State of Health Estimation for Lithium-Ion Batteries with Combined Methods

Von der Fakultät für Ingenieurwissenschaften
der Universität Bayreuth
zur Erlangung der Würde

Doktor-Ingenieur (Dr.-Ing.)

genehmigte Dissertation

von

Tobias Hofmann, M.Sc.

aus

Bogen

Erstgutachter: Prof. Dr.-Ing. Jan Philipp Schmidt
Zweitgutachter: Prof. Dr.-Ing. Weihan Li

Tag der mündlichen Prüfung: 23.02.2026

Lehrstuhl für Systemtechnik elektrischer Energiespeicher

Universität Bayreuth

2026

This work would not have been possible without the trust and guidance of my doctoral supervisor, Prof. Dr.-Ing. Jan Philipp Schmidt. Over countless hours, he was available for discussions and accompanied me through numerous revision cycles. His exceptionally prompt feedback on manuscripts—often within just a few days—as well as his continuous mentoring have been instrumental in the success of this work. I am equally grateful to Prof. Dr.-Ing. Weihan Li and Prof. Dr.-Ing. Vincent Lorentz for serving as my second and third examiners. Your valuable comments and constructive feedback have greatly enriched this thesis. At BMW Group, I especially want to thank Dr.-Ing. Jacob Hamar and Dr.-Ing. Simon Erhard for their support and guidance. They enabled me to directly implement my research findings in industrial practice and consistently placed their trust in me to pursue my own ideas. For this, I am deeply grateful. I would like to extend my sincere thanks to all colleagues who supported me in preparing my publications: Dr.-Ing. Jiahao Li, Marcel Rogge, Christoph Zörr, Bastian Mager, Cem Sayilgan, and Marco Duesdieker. I am also grateful to the students who contributed valuable work through their Bachelor's and Master's theses: Julian Raith, Bastian Mager, Severin Schumacher, Paul Lindner, and Kevin Herrnreiter. My thanks also go to my colleagues at BMW and at the chair for the many insightful discussions and professional exchanges. I would particularly like to highlight my fellow PhD colleagues Valentin Elender, Cem Sayilgan, and Kilian Stengel, who became close friends over the past three years. Whether exploring the city on our Nius or taking short trips to nearby European cities—you helped me manage the stress of doctoral studies and made the office a place I genuinely enjoyed spending time at. I also want to thank my BMW PhD colleagues with whom I enjoyed spending time outside of work: Nejira Hadzalic, Christoph Zörr, Sebastian Hölle, and Johannes Brehm. Thank you for keeping my spirits up throughout this journey and for your unwavering support. I am deeply grateful to my family and friends outside of BMW for their unconditional support—regardless of my career path. Your trust and encouragement kept me motivated even during challenging times. Special thanks go to my brother, Dr.-Ing. Simon Toni Hofmann, who embarked on his own PhD journey in parallel—albeit at a university and on a completely different topic. Despite our competitive nature, I know that deep down we support each other and are proud to be brothers.

Most importantly, I want to thank my fiancée Elena, who stands behind me and every decision I make. I could not wish for a more loving and supportive partner. Thank you for everything you have done for me—I love you.

Abstract

The ongoing transition towards sustainable transportation is driving the widespread adoption of battery electric vehicles (BEVs) in personal mobility. While many individuals in northern European regions and China are already convinced of the numerous advantages of BEVs over internal combustion vehicles – especially higher efficiency and less pollution – there remain several concerns in society, including range anxiety and insufficient charging infrastructure. Consumers worry about the accelerated aging of their high-voltage batteries, which could lead to a significant reduction in available range and residual value. This concern is particularly pronounced in the aftermarket for BEVs, where potential buyers are uncertain about the so-called state of health (SOH), suppressing the demand. Since measuring the SOH is not feasible during operation due to the need for controlled and lengthy testing, onboard estimation methods are required to accurately monitor the SOH throughout the lifetime of BEVs. These algorithms, however, are still lacking accuracy and are mostly limited to the SOH of capacity. This need is further emphasized by new regional regulations mandating manufacturers to transparently display the SOH to drivers.

This work presents several novel methods for estimating the SOH using available data, as detailed in four journal contributions. These studies collectively highlight the issue of insufficient data, leading to one final paper.

The first study introduces a novel adaptation of the well-known mechanistic modeling approach, applied to sparse real-world BEV fleet data. By modifying the objective function to minimize the charge difference instead of the voltage difference, this approach enables the estimation of not only the SOH of capacity but also the degradation modes (DMs) and the open-circuit voltage (OCV) of the lithium-ion cells within the high-voltage battery. Validation with measurement data from the BMW i3 customer fleet demonstrates robust results, achieving a SOH mean absolute error (MAE) of 2.5 % (in percentage points (pp)).

The subsequent three journal papers focus on integrating data-driven and physics-based models to accurately characterize batteries. Neural networks, as prominent representatives of data-driven models, face challenges related to data scarcity and dependence. Conversely, physics-based models are computationally intensive and require extensive input data. Combining these approaches is promising, as it mitigates individual weaknesses while leveraging their strengths. In the first study, the pseudo-two-dimensional model generates extensive battery aging data, which is combined with experimental data to estimate the SOH from random time-series segments of operation in a physics-informed neural network (PINN). This approach addresses data scarcity and maintains SOH of capacity MAE below 2.1 % (pp), although data dependence remains an issue. Consequently, two subsequent journal papers explore transfer learning. In both implementations, a physics-based model generates

constant-current (CC) charging profiles at various battery aging states. A novel neural network architecture is pre-trained with this extensive data and later fine-tuned with limited experimental data to monitor both the SOH of capacity and the OCV. The models are benchmarked against realistic CC charging events at various charging rates and the most commonly used state of charge (SOC) window from 30 % to 85 %, based on a field data analysis of nearly 2 million home-charging events. Both studies demonstrate excellent performance, with the first achieving a SOH MAE below 2.0 % (pp) and an OCV reconstruction MAE below 22 mV. In the second implementation, the transfer-learned neural network is coupled with an OCV model for updated estimates, showing even superior and more robust performance: The SOH MAE remains below 1.8 % (pp), the OCV MAE below 10 mV, and DMs can be estimated with an MAE under 3.1 % (pp), for all input SOC ranges.

Although the presented methods accurately estimate the state of batteries, they neglect dynamic effects during operation. This limitation arises from the lack of electrode aging information in public datasets. The final study addresses this gap by presenting a comprehensive battery aging study using a three-electrode setup with extensive characterization measurements.

The published articles contribute to the state of the art in several ways: The first study enables the mechanistic model to be applied to real-world BEV fleet data. The subsequent three studies solve the major issues of neural-network-based state estimation – data scarcity and data dependence – by introducing novel PINN and transfer learning architectures. The final study provides the first validated battery aging dataset for degradation mode estimation, linking equilibrium with dynamic cell effects, and with that allowing the extension of the SOH estimation to other SOH metrics.

These contributions not only enable the implementation of highly accurate SOH estimation models but also advance further development. This work especially bridges the gap between state estimation of individual lithium-ion cells and state estimation of high-voltage batteries. This ultimately allows for a comprehensive characterization of BEVs over their lifetime, encompassing dynamic effects, thereby addressing the fundamental concerns of hesitant buyers. This thesis contributes to the widespread adoption of BEVs by enhancing the reliability of battery SOH assessments and, thus, adds to the transition towards climate-neutral mobility.

Kurzfassung

Das Streben nach Klimaneutralität fördert die Verbreitung von Elektrofahrzeugen (engl. battery electric vehicles, BEVs) in der individuellen Mobilität. Während viele Menschen in nördlichen europäischen Regionen und China von den Vorteilen der BEVs überzeugt sind, bestehen in Teilen der Gesellschaft Bedenken hinsichtlich der Reichweite und Ladeinfrastruktur. Verbraucher sind besorgt über die beschleunigte Alterung der Hochvoltbatterie, wobei sie eine erhebliche Reduzierung der verfügbaren Reichweite und des Restwerts fürchten. Diese Sorge ist besonders im Gebrauchtwagenmarkt ausgeprägt, da der Gesundheitszustand (engl. state of health, SOH) schwer messbar ist. Daher sind präzise Schätzmethoden im Fahrzeug erforderlich, um den SOH über die Lebensdauer von BEVs zu ermitteln. Diese Algorithmen sind jedoch noch nicht präzise genug und beschränken sich meist auf den SOH der Kapazität. Diese Notwendigkeit wird durch neue regionale Vorschriften verstärkt, die Hersteller dazu verpflichten, den SOH für Fahrer transparent darzustellen.

In dieser Arbeit werden innovative Methoden zur Überwachung des SOH anhand vorhandener Daten vorgestellt, die in vier Zeitschriftenartikeln veröffentlicht wurden. Diese Studien beleuchten gemeinsam das Problem der unzureichenden Daten, das im letzten Artikel besonders deutlich wird.

Die erste Studie stellt eine neuartige Anpassung des mechanistischen Modellierungsansatzes vor, angewendet auf spärliche BEV-Flottendaten. Durch die Modifikation der Zielfunktion zur Minimierung der Ladungsdifferenz ermöglicht dieser Ansatz die Schätzung des SOH der Kapazität, der Degradationsmoden (engl. degradation modes, DMs) und der Ruhespannung (engl. open-circuit voltage, OCV) einzelner Zellen innerhalb einer Hochvoltbatterie. Die Validierung mit Messdaten aus der BMW i3 Kundenflotte zeigt robuste Ergebnisse mit einem mittleren absoluten Fehler (engl. mean absolute error (MAE)) des SOH von 2.5 % (in Prozentpunkten (pp)).

Die folgenden drei Artikel konzentrieren sich auf die Integration datengetriebener und physikalisch basierter Modelle zur genauen Batteriediagnose. Neuronale Netzwerke, als prominente Vertreter datengetriebener Modelle, stehen vor Herausforderungen in Bezug auf Datenknappheit und Datenabhängigkeit. Im Gegensatz dazu sind physikalisch basierte Modelle rechenintensiv und erfordern umfangreiche Eingabedaten. Die Kombination dieser Ansätze ist vielversprechend, da sie individuelle Schwächen mindert und ihre Stärken nutzt. In der ersten Studie generiert das pseudo-zweidimensionale Modell umfangreiche Batteriealterungsdaten, die mit experimentellen Daten in einem physikalisch-informiertem neuronalen Netzwerk (engl. physics-informed neural network (PINN)) kombiniert werden, um den SOH der Kapazität aus zufälligen Zeitreihensegmenten während des Betriebs zu schätzen. Dieser Ansatz adressiert die Datenknappheit und erreicht einen SOH-MAE unter 2.1 % (pp). Trotzdem bleibt die Datenabhängigkeit ein Problem. Folglich untersuchen

zwei nachfolgende Artikel das Transferlernen. In beiden Implementierungen generiert ein physikalisch basiertes Modell Konstantstrom (engl. constant-current (CC)) Ladeprofile bei verschiedenen Alterungszuständen. Eine neuartige neuronale Netzwerkarchitektur wird mit diesen umfangreichen Daten vortrainiert und später mit begrenzten experimentellen Daten fein-trainiert, um sowohl den SOH der Kapazität als auch die OCV zu schätzen. Die Modelle werden mit realistischen CC-Ladevorgängen bei unterschiedlichen Raten und einem Ladezustandsbereich von 30 % bis 85 % verglichen, basierend auf einer Felddatenanalyse von fast 2 Millionen privaten Ladevorgängen. Beide Studien zeigen hervorragende Ergebnisse, wobei die erste einen MAE des SOH unter 2.0 % (pp) und einen MAE der OCV-Rekonstruktion unter 22 mV erreicht. In der zweiten Implementierung wird das transfergelernte neuronale Netzwerk mit einem OCV-Modell für aktualisierte Schätzungen gekoppelt und erreicht noch bessere und robustere Ergebnisse: Der SOH-MAE bleibt unter 1.8 % (pp), der OCV-MAE unter 10 mV, und auch DMs können mit einem MAE unter 3.1 % (pp) geschätzt werden, unabhängig vom Ladezustandsfenster.

Obwohl die vorgestellten Methoden den Zustand von Batterien genau schätzen, vernachlässigen sie dynamische Effekte. Diese Einschränkung ergibt sich aus dem Mangel an Informationen zur Elektrodenalterung in öffentlichen Datensätzen. Die letzte Studie schließt diese Lücke, indem sie eine umfassende Batteriealterungsstudie mit einem Drei-Elektroden-Setup und umfangreichen Charakterisierungsmessungen präsentiert.

Die veröffentlichten Beiträge erweitern den Forschungsstand in vielerlei Hinsicht: Die erste Studie erlaubt erstmalig die Anwendung des mechanistischen Modellansatzes auf reale BEV-Flottendaten. Die drei darauffolgenden Studien lösen das Kernproblem neuronaler Netzwerke zur Zustandsschätzung – Datenknappheit und Datenabhängigkeit –, indem die neuartigen Architekturen PINN und Transferlernen eingeführt werden. Die finale Arbeit präsentiert einen validierten Batteriealterungsdatensatz zur DM-Schätzung, der nicht nur Gleichgewichtseffekte mit dynamischen Zelleffekten verbindet, sondern auch die Erweiterung der Zustandsschätzung auf beliebige SOH-Metriken erlaubt.

Diese Beiträge ermöglichen die Implementierung hochgenauer SOH-Schätzmodelle und fördern weitere Forschung. Diese Arbeit schließt insbesondere die Lücke zwischen der Zustandsschätzung einzelner Lithium-Ionen-Zellen und von Hochvoltbatterien. Dies ermöglicht letztlich eine umfassende Charakterisierung von BEVs über ihre Lebensdauer, die auch dynamische Effekte umfasst und damit die grundlegenden Bedenken zögerlicher Käufer anspricht. Diese Arbeit trägt zur breiten Akzeptanz von BEVs bei, indem sie die Zuverlässigkeit der SOH-Schätzung von Batterien verbessert, und liefert somit einen wichtigen Beitrag für den Übergang zu einer klimaneutralen Mobilität.

Contents

List of Abbreviations II

List of Symbols V

1 Introduction and Context 1
- 1.1 Lithium-Ion Batteries . . . 3
  - 1.1.1 Components and Working Principle . . . 4
  - 1.1.2 General Definitions . . . 5
  - 1.1.3 Aging and Degradation Mechanisms . . . 12
  - 1.1.4 Degradation Modes . . . 16
- 1.2 State of Health Estimation . . . 19
  - 1.2.1 Definitions and General Approaches . . . 20
  - 1.2.2 SOH Estimation based on OCV-Models . . . 28
  - 1.2.3 SOH Estimation based on Neural Networks . . . 38
- 1.3 Research Gap and Research Questions . . . 52
- 1.4 Outline of this Work . . . 52

2 Published Results 55
- 2.1 Conventional OCV-Models for SOH Estimation . . . 55
- 2.2 Solutions for Data Scarcity in Neural-Network-Based SOH Estimation . . . 73
  - 2.2.1 Physics-Informed Neural Networks for SOH Estimation . . . 73
  - 2.2.2 Transfer Learning for SOH and OCV Estimation . . . 100
  - 2.2.3 Physics-Constrained Transfer Learning for SOH and OCV Estimation 121
- 2.3 Generating a Comprehensive Battery Aging Database . . . 143

3 Discussion and Summary 168
- 3.1 Discussion of SOH Estimation based on OCV-Models . . . 168
- 3.2 Discussion of Data Scarcity and Neural Networks for SOH Estimation . . . 174
- 3.3 Discussion of the Extension of the SOH Metric to Cover Dynamic Effects . . . 177
- 3.4 Conclusion and Outlook . . . 179

References 183

List of Figures 204

List of Tables 207

List of Abbreviations

Abbreviation	Description
AI	artificial intelligence
BEV	battery electric vehicle
BMS	battery management system
CC	constant current
CNN	convolutional neural network
C-rate	charging rate
DC-IR	direct current internal resistance
DM	degradation mode
DOD	depth of discharge
DVA	differential voltage analysis
ECM	equivalent circuit model
EFC	equivalent full cycle
EIS	electrochemical impedance spectroscopy
EV	electric vehicle
FNN	feed-forward neural network
GITT	galvanostatic intermittent titration technique
HPPC	hybrid pulse power characterization
ICA	incremental capacity analysis
ICE	internal combustion engine
LAM	loss of active material
LAM_{NE}	loss of active material - negative electrode
LAM_{PE}	loss of active material - positive electrode
LCO	lithium cobalt oxide

Abbreviation	Description
LFP	lithium iron phosphate
LiB	lithium-ion battery
LLI	loss of lithium inventory
LMO	lithium manganese oxide
LSTM	long short-term memory neural network
MAE	mean absolute error
MAPE	mean absolute percentage error
MSE	mean squared error
NCA	nickel cobalt aluminum oxide
NMC	nickel manganese cobalt oxide
OCP	open-circuit potential
OCV	open-circuit voltage
P2D	pseudo-two-dimensional
PDE	partial differential equation
PHEV	plug-in hybrid electric vehicle
PINN	physics-informed neural network
pOCV	pseudo open-circuit voltage
pp	percentage points
REEV	range extender electric vehicle
ReLU	rectified linear unit
RMSE	root mean squared error
RNN	recurrent neural network
RoW	rest of the world
RPT	reference performance test
SEI	solid electrolyte interphase
SOC	state of charge
SOH	state of health
SPM	single particle model
tanh	hyperbolic tangent
TCN	temporal convolutional neural network
UBE	usable battery energy

List of Symbols

The symbols listed below, along with their description, are defined as they are used in the introduction and conclusion of this dissertation. It is important to note that the definitions and usage of these symbols may differ in the accompanying articles within the main body due to specific journal requirements or particular contexts presented within those works. Each integrated article contains its own definitions for the symbols utilized therein.

Symbol	Description	Unit
C	total cell capacity	Ah
C_{N}	nominal capacity	Ah
C_{NE}	capacity of the negative electrode	Ah
C_{PE}	capacity of the positive electrode	Ah
C_{lit}	available lithium inventory	Ah
C-rate	charging or discharging rate	h^{-1}
$\mathcal{D}$	dataset or domain	-
DOD	depth of discharge	%
ΔG	Gibbs free energy	$\mathrm{J\,mol}^{-1}$
$D_{\mathrm{l,eff}}$	effective diffusion coefficient liquid phase	$\mathrm{m}^2\,\mathrm{s}^{-1}$
$\mathcal{D}_{\mathrm{Source}}$	source domain	-
$\mathcal{D}_{\mathrm{Target}}$	target domain	-
E	energy	Wh
E_0	initial energy	Wh
$\mathcal{F}$	Faraday constant	96 485 As/mol
I	current	A
I_{applied}	applied current	A
I_{b}	boundary current	A
$\mathrm{LAM}_{\mathrm{NE}}$	loss of active material - negative electrode	%
$\mathrm{LAM}_{\mathrm{PE}}$	loss of active material - positive electrode	%
LLI	loss of lithium inventory	%
$\mathrm{OCP}_{\mathrm{NE}}$	open-circuit potential of the negative electrode vs. $\mathrm{Li/Li}^+$	V
$\mathrm{OCP}_{\mathrm{PE}}$	open-circuit potential of the positive electrode vs. $\mathrm{Li/Li}^+$	V
OCV	open-circuit voltage	V
$\mathrm{OCV}_{\mathrm{meas}}$	measured open-circuit voltage	V
$\mathrm{OCV}_{\mathrm{reco}}$	reconstructed open-circuit voltage	V
Q	electric charge	Ah

Symbol	Description	Unit
Q_{ava}	available electric charge	Ah
Q_{loss}	capacity loss	Ah
R	resistance	Ω
R_0	initial resistance	Ω
R_{DC}	direct current internal resistance	Ω
R_Ω	ohmic resistance	Ω
R	final receptive field per layer in a temporal convolutional neural network	-
$\mathcal{R}$	universal gas constant	$8.3144\,\text{J}\,\text{K}^{-1}\,\text{mol}^{-1}$
SOC	state of charge	%
SOC_0	reference state of charge	%
SOC_{NE}	state of charge of the negative electrode	%
SOC_{PE}	state of charge of the positive electrode	%
SOC_{mean}	average state of charge during cycling	%
$\text{SOC}_{\text{start}}$	start state of charge of the charging event	%
$\text{SOC}_{\text{storage}}$	storage state of charge	%
SOH	state of health	%
SOH_{C}	state of health - capacity	%
SOH_{R}	state of health - resistance	%
SOH_{UBE}	state of health - usable battery energy	%
$\mathcal{T}$	task	-
$\mathcal{T}_{\text{Source}}$	source task	-
$\mathcal{T}_{\text{Target}}$	target task	-
V	voltage	V
Z	fully connected neural network layer	-
a	neural network input neurons	-
α_{a}	transfer coefficient of anodic ractions	-
α_{c}	transfer coefficient of cathodic ractions	-
α_{NE}	scaling factor of the negative electrode	-
α_{PE}	scaling factor of the positive electrode	-
α_{cal}	fitting parameter calendar aging	-
α_{cyc}	fitting parameter cyclic aging	-
a_{s}	specific electrode area	m^{-1}
b	neural network biases	-
β_{NE}	shifting factor of the negative electrode	-
β_{PE}	shifting factor of the positive electrode	-
β_{cal}	fitting parameter calendar aging	-
β_{cyc}	fitting parameter cyclic aging	-
c_{s}	concentration solid phase	$\text{mol}\,\text{m}^{-3}$

Symbol	Description	Unit
$\Delta Q_{\text{measured}}$	measured charge difference between neighbouring relaxed voltage points	Ah
ΔQ_{reco}	reconstructed charge difference between neighbouring relaxed voltage points	Ah
ε_{l}	volume fraction liquid phase	-
η	overpotential	V
$\eta_{\text{transport}}$	transport overpotential	V
η_{Ω}	ohmic overpotential	V
$\eta_{\text{polarization}}$	polarization overpotential	V
f	filter of temporal convolutional neural network	-
i	current	A
i_0	exchange current density	$\mathrm{A\,m^{-2}}$
i_{l}	ionic current density liquid phase	$\mathrm{A\,m^{-2}}$
j_{n}	pore wall flux density	$\mathrm{mol\,m^{-2}\,s^{-1}}$
k	kernel size of temporal convolutional neural network	-
lb	lower boundary	-
μ	electrochemical potential	$\mathrm{V\,mol^{-1}}$
μ_{NE}	electrochemical potential of the negative electrode	$\mathrm{V\,mol^{-1}}$
μ_{PE}	electrochemical potential of the positive electrode	$\mathrm{V\,mol^{-1}}$
μ_{ref}	electrochemical potential of lithium in a reference electrode	$\mathrm{V\,mol^{-1}}$
n	number of electrons transferred per reaction	-
φ_{l}	electrical potential liquid phase	V
φ_{s}	electrical potential solid phase	V
r	radial coordinate in the particle domain	m
ρ_1	penalty parameter	-
ρ_2	penalty parameter	-
r_{p}	radius of the active material particle	m
t	time	s
t_+	transport number of lithium-ions	-
ϑ	alignment parameter set	-
ub	upper boundary	-
w	neural network weights	-
x	neural network input	-
y	neural network output	-

1 Introduction and Context

The widespread adoption and transfer from internal combustion engine (ICE) vehicles to battery electric vehicles (BEVs) in the private transport sector has long begun. Figure 1.1 gives a brief summary of the situation in late 2024 for representative countries.

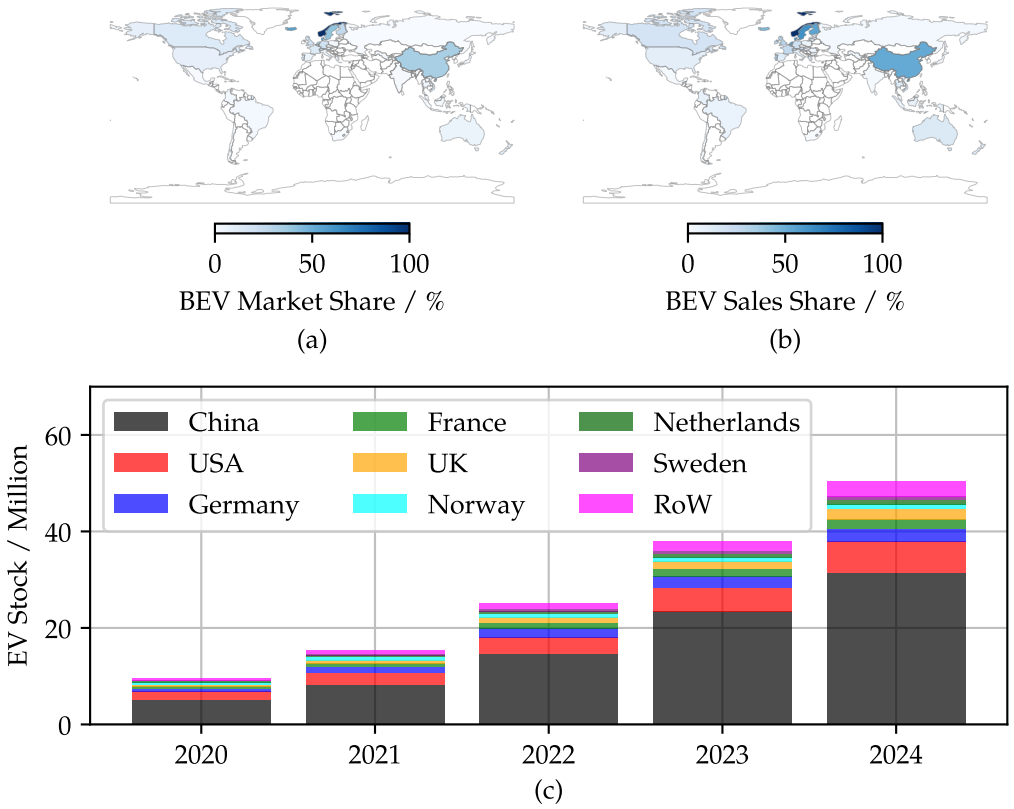

Figure 1.1: Current overview over the global electric vehicle (EV) market situation, with (a) the absolute battery electric vehicle (BEV) market share in 2024, (b) the BEV sales share in the same year, and (c) the development of the EV stock (including plug-in hybrid electric vehicles (PHEVs) and range extender electric vehicles (REEVs)) for selected countries. Data for the maps in Subfigure (a) and (b) is taken from IEA [1]. A list of the included countries in the world map can be found online [1]. Data for the EV stock development (c) is taken from ZSW [2].

While the total BEV market share is globally still inferior (Subfigure 1.1 (a)), the national yearly sales share of BEVs slowly overtakes those of ICE vehicles in selected countries (Subfigure 1.1 (b)). Especially the northern European countries and China experience high demand in pure BEVs [1]. In Germany, 19 % of all sold vehicles during 2024 were BEVs, increasing the

absolute national BEV share to 6.5 % [1]. Subfigure 1.1 (c) shows the detailed development of the national EV stock, i.e., also including plug-in hybrid electric vehicles (PHEVs) and range extender electric vehicles (REEVs), for selected countries in Europe, the USA, China, and the so-called rest of the world (RoW) from 2020 to 2024. China leads this trend and already operates more than 30 million EVs in their country [2], in which pure BEVs make up 11 % of the total vehicle share [1]. Interestingly, the adoption of BEVs depends on various factors, varying from region to region. While Europeans with high income tend towards a higher acceptance rate, higher salaries negatively correlate with the acceptance rate in the USA [3]. The Chinese market, in contrast, is heavily influenced by government regulations, which provide significant financial incentives [4; 5], at least in large cities [6]. As demonstrated in Figure 1.1, this strategy has proven to be effective [1; 2].

As illustrated in Subfigure 1.1 (c), millions of used BEVs continue to be operated or will eventually enter the aftermarket. The relatively simple and robust design of BEVs results in fewer parts, potentially allowing long-lasting vehicle generations. However, the most expensive component, the high-voltage battery composed of many lithium-ion battery (LiB) cells, also undergoes the most significant relative degradation. During operation, lithium-ions migrate between electrodes, leading to degradation effects known as cyclic aging. Factors such as frequent fast-charging cycles, high state of charge (SOC) operating ranges, and low operating temperatures exacerbate this effect. Additionally, intrinsic side reactions occur even when the vehicle is stationary, known as calendar aging, which are intensified by high storage SOC and elevated temperatures. In summary, from the moment of production, BEVs experience aging manifested as capacity decay and impedance rise, resulting in reduced available range and diminished power. Consequently, a metric to quantify these aging effects is crucial for both current owners and prospective buyers. This metric is referred to as the state of health (SOH).

Most countries have recognized the significance of monitoring this metric and have consequently implemented their own regulations. For instance, the Euro 7 norm in Europe, which is set to take effect in late 2027, addresses battery durability [7; 8]. The regulation requires that for passenger cars, including BEVs and PHEVs, the SOH must remain above 80 % after 5 years or 100 000 km of usage, whichever comes first. Additionally, the SOH must not be lower than 72 % after 8 years or 160 000 km, whichever occurs first. Importantly, the SOH must be accessible and retrievable by the vehicle user [7; 8].

Measuring the usable battery capacity demands a full discharge and charge with a predefined profile, which is not possible during normal vehicle operation. Thus, accurate onboard SOH estimation is of highest priority. These aspirations are aggravated by the reduced available data in real-world BEV fleets, which often comprises cumulated data or low sampled time-series data [9].

Therefore, there is a need for methods that leverage the sparse operational data from BEVs to monitor SOH decay. Promising research directions include data-driven methods and open-

circuit voltage (OCV)-based models, which incorporate changes in OCV to enable accurate SOC estimation over the vehicle's lifetime.

In this context, this work introduces innovative methods based on the OCV model and data-driven approaches that are applicable to real-world BEV data. The proposed methods are evaluated for their ability to thoroughly characterize battery aging, including changes in OCV and degradation modes (DMs). To achieve this, several integrated methods are presented, combining physics-based approaches with neural networks to harness their individual strengths while physically constraining the output. These integrated methods include physics-informed neural networks (PINNs) and physics-constrained transfer learning. Analyzing the limitations of individual studies and the current state of the art reveals a significant research gap in the availability of public aging data. Therefore, the final research topic addresses the creation of a comprehensive battery aging database. In summary, this dissertation advances the field by introducing innovative methods for SOH estimation, OCV reconstruction, and DM estimation. The development of new algorithms facilitates the application to sparse real-world BEV fleet data, enabling not only fleet monitoring but also the reliable determination of SOH in the aftermarket. The provision of a publicly accessible dataset, which includes internal electrode degradation information, further enhances the current state of the art. Ultimately, the research presented bridges the gap towards accessible SOH estimation methods, thereby increasing trust in the BEV sector, enhancing general acceptance rates, and promoting a shift towards climate-friendly mobility alternatives.

This thesis is organized into three main chapters, with Chapter 1 providing the essential fundamentals, Chapter 2 including the research papers and the core of this dissertation, and Chapter 3 concluding and discussing the results. The following background section is organized as follows: Section 1.1 provides essential knowledge about LiBs and their degradation behavior, Section 1.2 provides insights into existing SOH estimation techniques and state-of-the-art methods. Section 1.3 outlines the research gap and research questions behind this work, while Section 1.4 concludes with the structure of the thesis.

1.1 Lithium-Ion Batteries

In order to understand and discuss the proposed methods and results within this thesis, fundamental knowledge about LiBs is required. The following section guides as a brief introduction, with Section 1.1.1 detailing the components and working principle of LiBs, Section 1.1.2 providing common definitions in this field, including the fundamental theory behind the OCV and overpotentials, and Section 1.1.3 and 1.1.4 offering insights into battery aging, degradation mechanisms and DMs.

1.1.1 Components and Working Principle

LiBs are electrochemical energy storage devices that are based on lithium-ion exchange between two electrodes. Besides the electrodes, they consist of a separator and a liquid electrolyte. A single LiB is the fundamental unit, comprising a negative electrode (anode), a positive electrode (cathode), and the intervening separator. The typical structure is depicted in Figure 1.2.

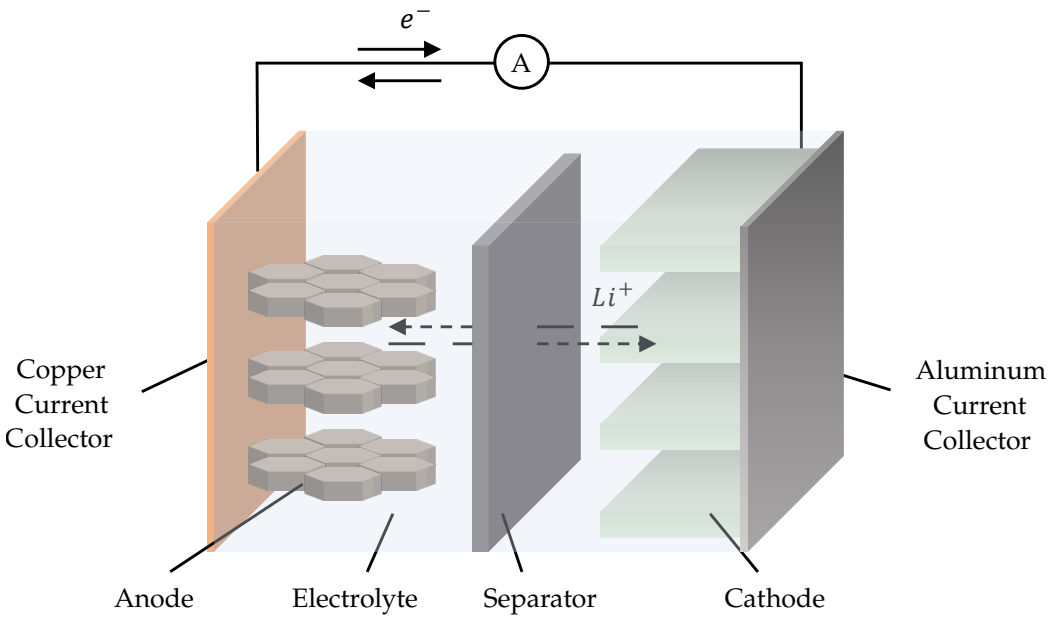

Figure 1.2: Schematic illustration of the components and basic operating principle of a lithium-ion battery (LiB).

As shown in Figure 1.2, the anode is typically coated on a copper current collector, while the cathode is deposited on an aluminum current collector. The porous separator, made of a polymeric material, electrically isolates the two electrodes while allowing the transport of lithium-ions between them. The most common anode material is graphite, which has a layered crystal structure that can accommodate lithium-ions through a reversible intercalation mechanism. Graphite exhibits a high specific capacity of around $372\,\mathrm{mAh\,g^{-1}}$ and excellent cycling stability, making it a widely adopted anode material in commercial LiBs [10; 11]. Advances in anode properties are achieved by adding silicon to the anode because it has ten times the theoretical specific capacity of $4200\,\mathrm{mAh\,g^{-1}}$. The large volume expansion of silicon during cycling ($\approx 300\,\%$), however, still presents challenges in widespread industrialization [10; 11].

The choice of cathode active material is a crucial factor in determining the performance characteristics of LiBs. Table 1.1 summarizes the properties of the most commonly used cathode materials, including their operating voltage, specific capacity, and expected cycle life. Conventional cathode materials include lithium cobalt oxide (LCO) and lithium manganese oxide (LMO), while recent battery generations usually focus on materials such as lithium iron

phosphate (LFP), nickel manganese cobalt oxide (NMC), and nickel cobalt alumnium oxide (NCA), which offer improved safety, energy density, and cycle life [10].

Table 1.1: Comparison of the key properties of common cathode materials for lithium-ion batteries (LiBs) [10; 12–14].

Cathode Material	Voltage vs. Li/Li^+	Spec. Capacity	Cycle Count
Lithium iron phosphate (LFP)	3.4 V	165 mAh g^{-1}	2000 - 5000
Nickel manganese cobalt oxide (NMC)	3.7 V	170 mAh g^{-1}	800 - 2000
Nickel cobalt alumnium oxide (NCA)	3.7 V	200 mAh g^{-1}	800 - 2000
Lithium cobalt oxide (LCO)	3.8 V	145 mAh g^{-1}	500 - 1000
Lithium manganese oxide (LMO)	4.1 V	120 mAh g^{-1}	500 - 2000

The electrodes and the separator are immersed in the electrolyte, which is typically composed of lithium salts dissolved in organic solvents, along with various additives. LiBs are manufactured in different geometries, including cylindrical, pouch, and prismatic configurations [14].

The working principle is based on de-/intercalation of lithium-cations from/between the electrodes while dis-/charging the cell. During charging the full cell – this means the full cell voltage increases and energy is transferred from an external load to the cell – lithium-ions move from the cathode to the anode to intercalate into the layered structure. For a graphite anode this reaction is [14–16]:

$$x\mathrm{Li}^+ + \mathrm{C}_6 + x\mathrm{e}^- \longrightarrow \mathrm{Li}_x\mathrm{C}_6 \tag{1.1}$$

While the lithium-ions lead to an oxidization on the anode side, a reduction takes place at the cathode side due to ions deintercalating from the host structure. This reduction during charging is as follows for a LCO half cell:

$$\mathrm{LiCoO}_2 \longrightarrow \mathrm{Li}_{1-x}\mathrm{CoO}_2 + x\mathrm{Li}^+ + x\mathrm{e}^- \tag{1.2}$$

Summarized the full cell charging process can be described by:

$$\mathrm{Li}_x\mathrm{C}_6 + \mathrm{LiCoO}_2 \longrightarrow \mathrm{C}_6 + \mathrm{LiCoO}_2 \tag{1.3}$$

These reactions reverse during discharging, where the external electron movement frees energy and can be used to operate an external load [14–16].

1.1.2 General Definitions

This thesis uses certain key terms frequently, and having a basic understanding of these terms is important for following the discussion throughout.

Capacity

The capacity of a LiB is defined as the maximum amount of electric charge, typically measured in ampere-hours (Ah), that can be extracted from the battery. While the scientific symbol for electric charge is Q, the capacity of LiBs is conventionally denoted by the symbol C [17].

This capacity value is dependent on numerous external factors, including the applied current, ambient temperature, and pressure. Battery manufacturers typically provide a nominal capacity C_N for their produced cells, which is measured under predefined conditions – for example in discharge direction at a temperature of 25 °C and a charging rate (C-rate) of 0.2C [18; 19].

C-Rate

The C-rate is a metric used to quantify the applied current I_{applied} in relation to its nominal capacity C_N. It is defined mathematically as follows:

$$\text{C-rate} = \frac{I_{\text{applied}}}{C_N} \tag{1.4}$$

The C-rate is expressed in units of h^{-1}, which indicates the reciprocal of the charging time. For instance, a C-rate of 2C signifies that the cell can be fully charged or discharged within a duration of thirty minutes. An increase in the C-rate corresponds to a faster charging process. Recent advancements in LiBs have achieved C-rates of up to 10C for certain electrode materials [20].

As the cell undergoes degradation, the available capacity C diminishes. However, the C-rate continues to reference the nominal capacity C_N, resulting in more aggressive charging and discharging behaviors for the same C-rate throughout the cell's lifespan.

Open-Circuit Voltage

The potential curves of the electrodes in equilibrium state can be expressed by the open-circuit potentials (OCPs): OCP_{NE} for the negative electrode and OCP_{PE} for the positive electrode [16; 21]. The OCV is the potential difference between both OCPs. Hence, it is the full cell voltage when no current flows and both electrodes are in equilibrium state:

$$\text{OCV} = \text{OCP}_{\text{PE}} - \text{OCP}_{\text{NE}} \tag{1.5}$$

This relationship is visualized in Figure 1.3 for the initial full cell SOC.

Electrochemically, the driving force between the Faradaic reactions in LiBs is the electrochemical potential difference of the lithium atoms which is highly dependent on the species, the concentration, and the temperature. Based on Newman and Balsara [16], in thermodynamic

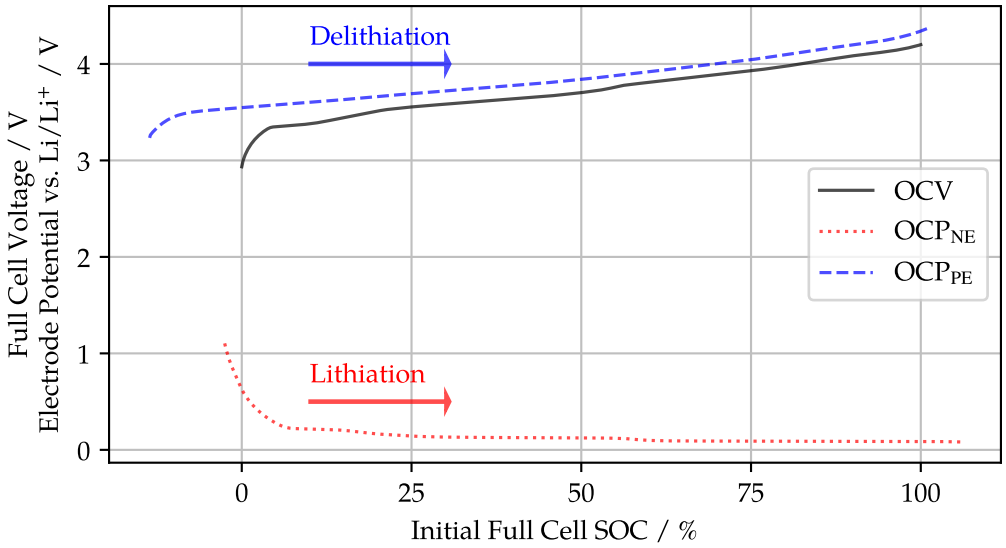

Figure 1.3: Schematic illustration of the open-circuit voltage (OCV) and its underlying open-circuit potentials (OCPs), including the de-/lithiation direction (adopted from [22]).

equilibrium, the OCV is dependent on the change in Gibbs free energy per reaction ΔG:

$$\mathrm{OCV} = \frac{-\Delta G}{n\mathcal{F}} \tag{1.6}$$

where n is the number of electrons transferred per reaction (in LiBs: $n = 1$), $\mathcal{F}$ is Faraday's constant and the change in Gibbs free energy depends on the electrochemical potential of both electrodes:

$$\Delta G = \mu_{\mathrm{PE}} - \mu_{\mathrm{NE}} \tag{1.7}$$

These electrochemical potentials of both electrodes is defined in relation to the electrochemical potential of lithium in a reference electrode μ_{ref}:

$$\mu - \mu_{\mathrm{ref}} = -n\mathcal{F} \cdot \mathrm{OCP} \tag{1.8}$$

Plugging in Equation 1.8 for both electrodes into Equation 1.7 yields:

$$\Delta G = (-n\mathcal{F} \cdot \mathrm{OCP_{PE}} + \mu_{\mathrm{ref}}) - (-n\mathcal{F} \cdot \mathrm{OCP_{NE}} + \mu_{\mathrm{ref}}) = -n\mathcal{F} \cdot (\mathrm{OCP_{PE}} - \mathrm{OCP_{NE}}) \tag{1.9}$$

Moving $-n\mathcal{F}$ to the left side, results in:

$$\frac{-\Delta G}{n\mathcal{F}} = \mathrm{OCP_{PE}} - \mathrm{OCP_{NE}} = \mathrm{OCV} \tag{1.10}$$

Comparing Equation 1.10 with Equation 1.6, yields the final equation which is identical to Equation 1.5 [16]. From this equation, Figure 1.3 can be interpreted: The resulting full-cell OCV curve is the result of the potential difference between the overlapping section of the cathode and the anode. The underlying OCPs of the OCV are material-specific, making the

OCV one of the most important characteristic of LiBs. The relation between the full cell SOC and the OCV (compare Figure 1.3) is, hence, an important property for accurate state estimation.

The measurement of the OCV necessitates specialized and time-intensive experiments, as achieving true equilibrium is theoretically impossible due to the presence of overpotentials which can never be fully stopped, i.e., self-discharge or aging processes. In most common material combinations, however, reaching practically equilibrium is possible if sufficient relaxation time is provided. The most prevalent method for determining the OCV is the galvanostatic intermittent titration technique (GITT) [23; 24]. In this procedure, a cell is gradually charged, usually with a C-rate below C/3, to predefined SOCs, where the cell is allowed to relax for a minimum duration of, e.g., 1 h, although a relaxation period of 3 h is more commonly employed. It is assumed that all overpotentials have decayed during this relaxation period, allowing for the collection of a relaxed voltage point that approximates the OCV. Interpolation between these voltage points provides the complete OCV profile.

An alternative and more efficient approach is the measurement of the pseudo open-circuit voltage (pOCV) [24–27]. The pOCV method approximates the true equilibrium state by applying a minimal current, specifically C/20 [26] or lower [27], with the aim of keeping the resulting overpotentials at negligible levels [24]. For common cell chemistries, both methods present valid options for measuring the OCV.

The measurement of OCPs requires similar experimental setups, albeit with additional complexities due to the initial configuration requirements. OCPs are typically measured in half-cell [23; 25; 28] configurations including a reference electrode – mostly pure lithium [25; 28], necessitating the opening of cells to extract electrode sheets or the use of specialized laboratory cells with fresh electrode sheets. This additional effort enables the measurement of the complete operating range of both electrodes individually.

Incorporating a reference electrode into a full-cell configuration provides a means to measure the OCPs during full-cell operation [29–31]. However, this arrangement restricts the measurement of OCPs to the operating range of the full cell, thereby omitting critical sections of the electrodes in the edge regions (see Figure 1.3). Due to the increased effort involved, OCP curves are predominantly available only for pristine cells [31]. For simplicity, however, it is assumed that the qualitative shape of the OCP curves remain constant over lifetime, while only the resulting OCV changes due to shifting and scaling of the OCP in relation to each other [32].

State of Charge

The SOC quantifies the currently available charge amount Q_{ava} in relation to the total cell capacity C [17; 33]. It is mathematically expressed as follows:

$$\text{SOC} = \frac{Q_{\text{ava}}}{C} \cdot 100\,\% \tag{1.11}$$

The SOC can be directly measured through Ah-counting and lookups of the OCV:

$$\text{SOC}(t) = \text{SOC}_0 + \frac{\int i(t)\mathrm{d}t}{C} \tag{1.12}$$

where the reference SOC_0 is derived from the OCV lookup and C is determined by the SOH.

As indicated by Equation 1.12, the SOC is significantly dependent on accurate knowledge of both the SOH and the OCV. This relationship serves as an initial indication of the interconnectedness of these state metrics.

State of Health

The SOH lacks a universally accepted definition and is subject to multiple interpretations [33]. The most prevalent definition is the SOH in terms of capacity, which will be primarily utilized throughout this thesis and is interchangeably referred to as SOH or SOH_{C} [17]:

$$\text{SOH}_{\text{C}} = \frac{C}{C_{\text{N}}} \cdot 100\,\% \tag{1.13}$$

Another widely recognized representation is the SOH in terms of resistance, denoted as SOH_{R}, which expresses the actual resistance R in relation to its initial resistance R_0 [33]:

$$\text{SOH}_{\text{R}} = \frac{R}{R_0} \cdot 100\,\% \tag{1.14}$$

Note that the SOH_{R} counterintuitively increases and other definitions exist [33]. It is crucial that the resistance values are consistently defined, taking into account factors such as temperature, SOC, and C-rate. A commonly referenced resistance value is the direct current internal resistance (DC-IR) at 50 % SOC, 25 °C at 1C, measured after 10 s:

$$R = \frac{U(t_0 + 10\,\text{s}) - U(t_0)}{I(t_0 + 10\,\text{s}) - I(t_0)} \tag{1.15}$$

where the current $I(t)$ is applied at time t_0 and is considered to be constant.

More recently, particularly in the context of BEVs, the SOH in terms of usable battery energy (UBE) (denoted as SOH_{UBE}) has emerged as a new, more practical, and user-oriented state

variable [34]. A possible definition is given by:

$$\mathrm{SOH}_{\mathrm{UBE}} = \frac{E}{E_0} \cdot 100\,\% \tag{1.16}$$

where E_0 represents the energy extracted from the battery during a predefined driving cycle in its initial state, and E is the measured energy at the current state. The energy can be interpreted as the *area under the curve* of the voltage discharge trajectory and can thus be calculated using the equation $E = \int V \mathrm{d}Q$ [34]. It therefore is a combination of the capacity and resistance and, with that, a more customer-oriented metric as it reflects the currently achievable range.

Overpotentials

In LiBs, true equilibrium can never be achieved due to the presence of overpotentials. Consequently, the measurable terminal voltage V is always the result of the superposition of the OCV and the overpotential η:

$$V = \mathrm{OCV} + \eta \tag{1.17}$$

Figure 1.4 illustrates the accumulation of overpotentials during a current pulse of 1C for 10 seconds at 50 % SOC, followed by the relaxation phase for a commercial NCA-graphite battery.

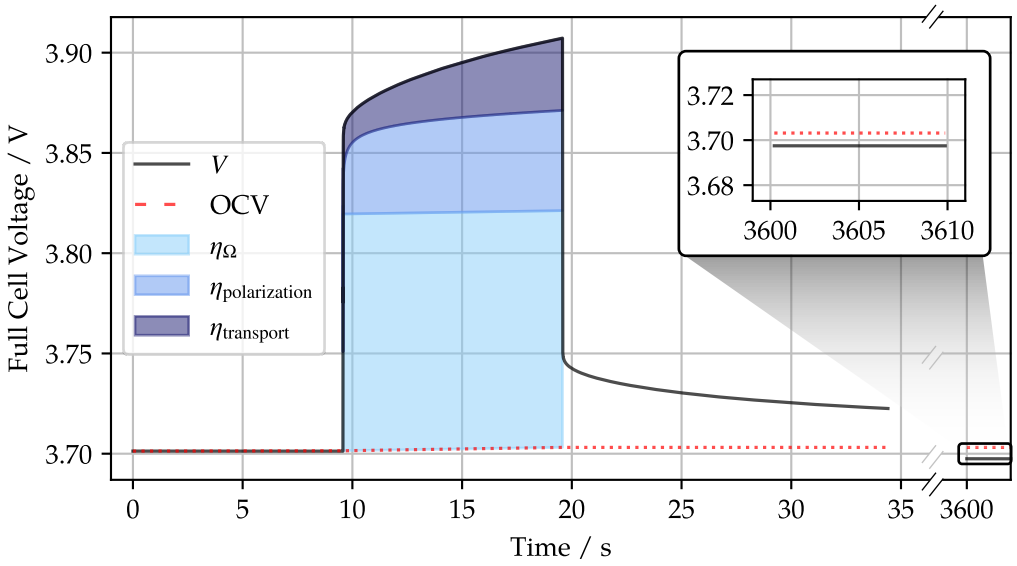

Figure 1.4: Pulse analysis for a nickel cobalt alumnium oxide (NCA)-graphite battery during a 1C pulse for 10 seconds at 50 % state of charge (SOC) including the schematic division of the overpotentials. An additional inlet shows the deviation of the measured voltage signal and the open-circuit voltage (OCV) 1 h after the applied pulse.

As depicted in Figure 1.4, the phenomena leading to overpotentials can be attributed to various processes within the LiB, which can be described by established mathematical equations [16; 35–39].

Simplified, these overpotentials consist of ohmic losses, polarization effects (also referred to as charge transfer polarization), and transportation effects [16; 38]. In a simplified manner, Equation 1.17 can be expressed as:

$$V = \mathrm{OCV} + (\eta_\Omega + \eta_{\mathrm{polarization}} + \eta_{\mathrm{transport}}) \tag{1.18}$$

Each component can be further divided into the respective shares of the individual electrodes.

From another perspective, the overpotentials can also be categorized based on their respective time scales: The ohmic overpotential develops within milliseconds, the polarization overpotential within seconds, and the transport polarization can persist for hours or even days [40; 41]. Additional reaction overpotentials arising from side reactions, including self-discharge and aging, are not considered in this work. Their influence, however, is visualized in the inlet of Figure 1.4, where already after 1 h of relaxation the measured voltage drops below the OCV due to side reactions.

The *ohmic overpotential* develops instantaneously and is described by Ohm's law:

$$\eta_\Omega = R_\Omega \cdot I \tag{1.19}$$

The ohmic overpotential is directly proportional to the applied current I and the ohmic resistance R_Ω, which arises from the electronic conductivity of the electrode active material, the ionic conductivity of the electrolyte, and the electronic conductivity of the current collectors [16; 36]. The ohmic resistance is highly dependent on temperature, SOC, and SOH: Generally, R_Ω increases at the boundary regions of the SOC and rises with decreasing SOH due to alterations in the electrode material [40; 41].

The Butler-Volmer equation describes the fundamental driving force for the reactions occurring in the electrodes and, with that, the kinetics of the de-/intercalation processes. The *polarization overpotential* $\eta_{\mathrm{polarization}}$ is related to the applied current I and expresses the rates of anodic and cathodic reactions:

$$I = i_0 \left[\exp\left(\frac{\alpha_\mathrm{a} \mathcal{F}}{\mathcal{R}T} \eta_{\mathrm{polarization}} \right) - \exp\left(\frac{-\alpha_\mathrm{c} \mathcal{F}}{\mathcal{R}T} \eta_{\mathrm{polarization}} \right) \right] \tag{1.20}$$

In Equation 1.20, the first term represents the anodic reaction (deintercalation), while the second term corresponds to the cathodic reaction (intercalation) [39]. The apparent transfer coefficients α_a and α_c govern the ratio of anodic to cathodic reactions [16]. Typically, these coefficients are set to 0.5 for LiBs [39]. The constants $\mathcal{F}$ and $\mathcal{R}$ denote the Faraday constant and the universal gas constant, respectively, while T represents the temperature, and i_0 is referred to as the exchange current density [16]. As indicated by Equation 1.20, the

polarization overpotential is primarily driven by the current, with an additional dependence on temperature.

The polarization overpotential exhibits a linear relationship with the current if $\eta_{\text{polarization}}$ is small. However, for larger values of $\eta_{\text{polarization}}$, the current changes exponentially with respect to $\eta_{\text{polarization}}$, and is predominantly influenced by either the first or the second term, meaning that either the intercalation or the deintercalation process governs the resulting current [16]. These simplifications, first illustrated using the Tafel plot, facilitate the determination of $\eta_{\text{polarization}}$ at high current densities [16]:

$$\eta_{\text{polarization}} = \frac{\mathcal{R}T}{\alpha_{\text{a}}\mathcal{F}} \ln\left(\frac{I}{i_0}\right) \qquad \text{for} \quad \alpha_{\text{a}}\mathcal{F}\eta_{\text{polarization}} >> \mathcal{R}T \tag{1.21}$$

$$\eta_{\text{polarization}} = \frac{\mathcal{R}T}{\alpha_{\text{c}}\mathcal{F}} \ln\left(\frac{I}{i_0}\right) \qquad \text{for} \quad \alpha_{\text{c}}\mathcal{F}\eta_{\text{polarization}} << -\mathcal{R}T \tag{1.22}$$

Transportation effects, also referred to as concentration polarization or diffusion, exhibit time constants that range from a few seconds to several days, primarily due to the limited diffusion of charge carriers. The transport overpotential, denoted as $\eta_{\text{transport}}$, acts as a corrective term for the thermodynamic properties of active materials within an electrode. This term becomes essential when concentration gradients develop at the interphase between the electrode surface and the electrolyte, resulting in a change in the electrode and electrolyte potentials. Such variations in the OCP must be incorporated into overpotential considerations. The diffusion overpotential is quantified through an extension of the Nernst equation, which accounts for the effects of concentration gradients, with the boundary current I_{b} calculated using Fick's laws [16; 42]:

$$\eta_{\text{transport}} = \frac{\mathcal{R}T}{\mathcal{F}} \ln\left(\frac{I_{\text{b}}}{I_{\text{b}} - I}\right) \tag{1.23}$$

This diffusion process is significantly influenced by the geometry, including the thickness of the active material, as well as the temperature [16; 36; 42].

In a simplified manner, all overpotentials can be combined into a single equation derived from Equation 1.17:

$$V = \text{OCV} + I \cdot R_{\text{DC}} \tag{1.24}$$

where R_{DC} is the DC-IR measured via Ohm's law, typically after a few seconds. Since R_{DC} encompasses all sources of overpotentials, its main dependencies are deducible, making it highly sensitive to temperature, SOC, and the aging state [40; 41].

1.1.3 Aging and Degradation Mechanisms

LiBs experience capacity fade and impedance rise during their lifetime, both of which can be described by the well-established SOH definitions in Equations 1.13 and 1.14. The extent of degradation, however, depends on the electrode material, the usage conditions, and various

external factors. The relation between cause, mechanism, mode and effect is illustrated in Figure 1.5. As all battery data used within the published work of this thesis relate to Nickel-containing cathodes and graphite-based anodes, all further descriptions are based on the NMC-graphite LiB, with NMC as the most common Nickel-containing cathode material.

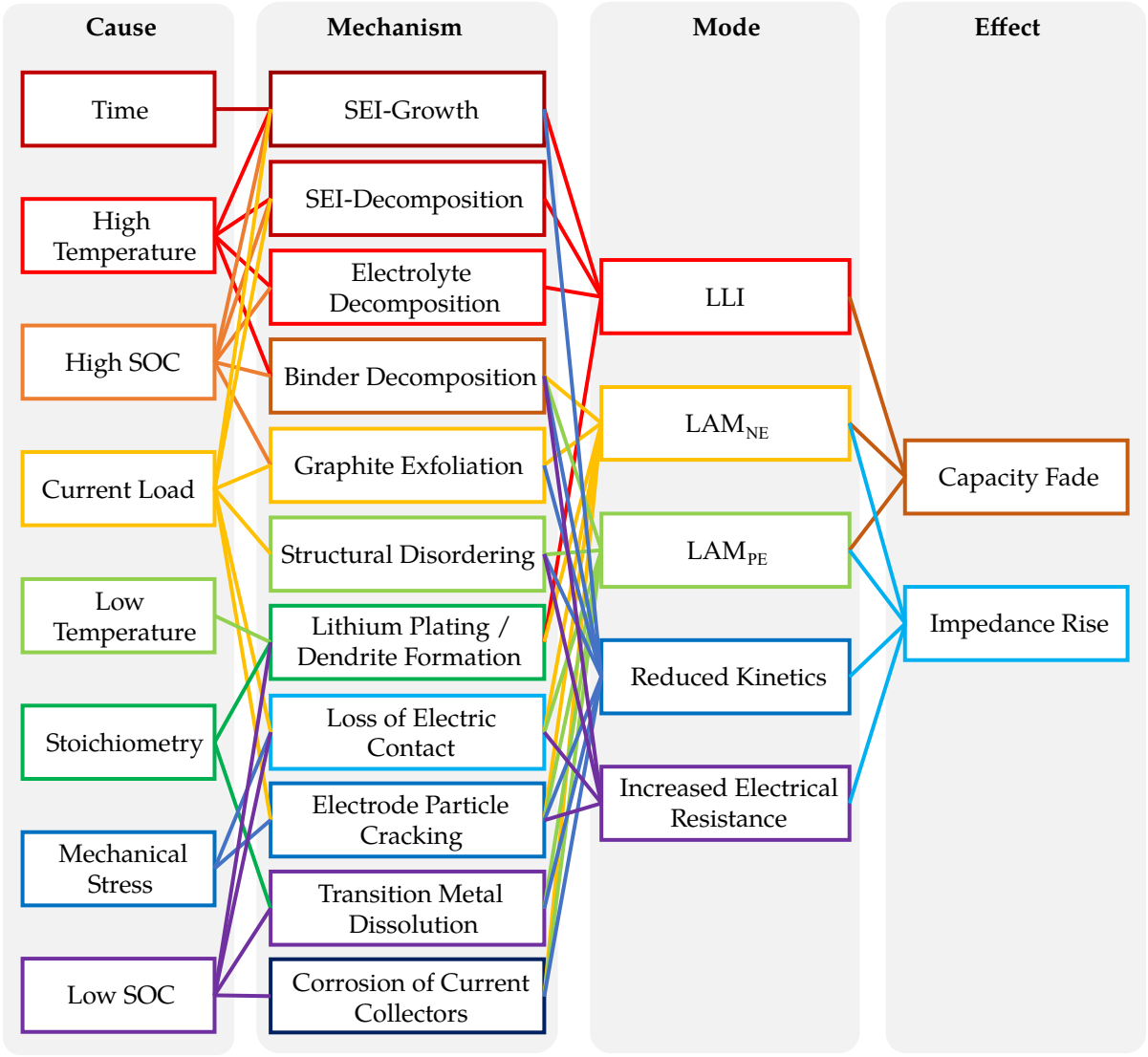

Figure 1.5: Relationship between the causes, degradation mechanisms, degradation modes (DMs), and effects of battery degradation, based on [43–45]. The color solely aims to guide the reader.

While the causes and effects (on the left and right in Figure 1.5) can be directly measured, there exist two additional levels of abstraction: Degradation modes (DMs) and the underlying physico-chemical degradation mechanisms. DMs cluster several degradation mechanisms and combine them in a mechanistic modeling approach [32]. DMs can be partially measured and estimated via optimization methods. While loss of lithium inventory (LLI) and loss of active material (LAM) are commonly considered as DMs, recent literature also identifies resistance rise and reduced kinetics as DMs [46].

The degradation mechanisms are the underlying physico-chemical reactions that occur within the LiB and lead to the DMs and, consequently, to capacity fade and impedance rise. Figure 1.6 illustrates the most important degradation mechanisms within conventional LiBs. Only the predominant degradation mechanisms – solid electrolyte interphase (SEI) formation, particle cracking on the anode side, lithium plating, particle cracking on the cathode side, transition metal dissolution, and structural disordering – are briefly introduced:

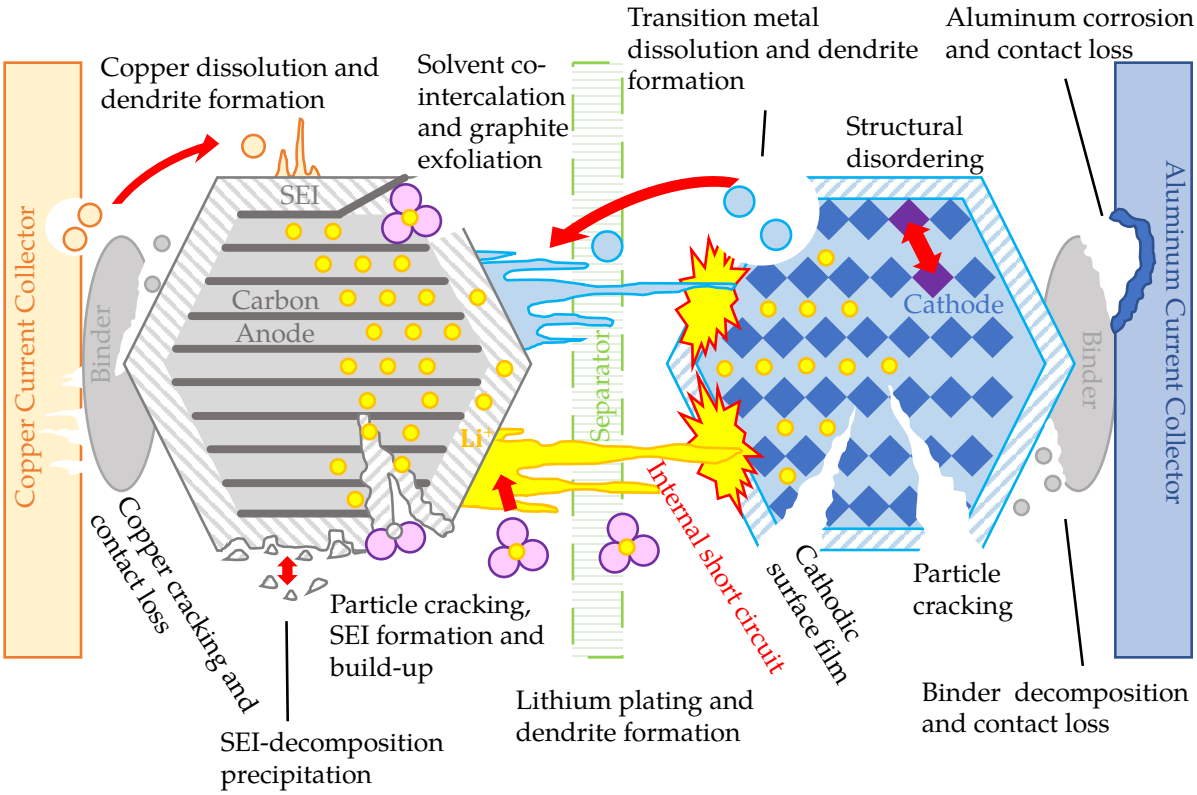

Figure 1.6: Schematic illustration of the degradation mechanisms occurring within a lithium-ion battery (LiB), based on Birkl et al. [43].

The reaction of the anode with the electrolyte at the electrode/electrolyte interphase is seen as the major source of degradation on the anode side [44]. As graphite-based anodes are operated outside the stability window of common electrolytes, reductive electrolyte decomposition and lithium-ion consumption lead to the build-up of the SEI. The SEI builds mainly during the formation process, but its growth does not suddenly stop over lifetime. The SEI itself, however, prevents the accelerated formation of more SEI as it is electronically isolating but ionically conductive [44]. As can be seen in Figure 1.5, SEI growth mainly leads to LLI as cyclable lithium is trapped inside the SEI and no longer available for cycling. Due to the additional layer on the interphase, it may also lead to reduced kinetics and, consequently, to impedance rise [43–45].

Cycling of the LiB leads to volumetric changes within the anode that may result in particle cracking. On the one hand, particle cracking on the anode side leads to a loss of ionic and electronic conductivity and, with that, to loss of active material - negative electrode (LAM_{NE})

and impedance rise [43; 45]. On the other hand, particle cracking may affect the SEI layer and result in the growth of new SEI areas. This again consumes cyclable lithium (LLI) and may lead to impedance rise [43–45].

One of the biggest concerns in BEV operation is the accelerated degradation during fast charging. This accelerated degradation is actually due to lithium plating and only occurs in unfavorable states, specifically, if the anode potential vs. Li/Li^+ drops below 0 V [43]. Lithium plating happens if the lithium-ions build metallic lithium instead of intercalating into the anode. If this plating mechanism forms dendrites, safety concerns may arise, as these dendrites eventually trigger an internal short-circuit if they grow through the separator [44]. Plating mainly leads to LLI and is favored either by thermodynamic causes, i.e., stoichiometry in Figure 1.5, or external factors, i.e., low temperature and high current loads [43–45].

Particle cracking may also occur on the cathode side and will lead to loss of active material - positive electrode (LAM_{PE}) and impedance rise [43]. Similar to the anode side, particle cracking on the cathode is aggravated by mechanical stress, including cycling with high current loads [43; 44]. In contrast to the anode, particle cracking of the cathode is not fully understood, and some researchers question whether particle cracking is just a symptom of structural disordering and, therefore, not a degradation mechanism itself [47; 48].

One of the most significant degradation mechanisms within the cathode is the so-called transition metal dissolution, which occurs for transition metals and lithium manganese oxides. The dissolution of the cathode material leads mainly to LAM_{PE}, but the dissolved metals may also pass through the separator and accelerate SEI growth there [44]. Reaction of the dissolved metals with the electrolyte is, similarly to the anode, referred to as cathode electrolyte interphase. This is an irreversible phenomenon that leads to impedance rise [43–45].

As discussed, Lee et al. [47] propose that particle cracking is rather a symptom of structural disordering instead of a mechanism itself. Structural disordering or phase change is aggravated for Nickel-rich materials in high-voltage segments and describes the formation of resistive, electrochemically inactive layers on the cathode particles' surface [44; 47; 49]. This phase change primarily leads to LAM_{PE} but also strongly increases the impedance. As pictured in Figure 1.5, structural disordering is mainly driven by high current loads [43–45]. More recently, Jung et al. [50] explore a new degradation mechanism – rocksalt formation – that is especially triggered by cycling in the upper voltage region and the reaction of released oxygen with the electrolyte at the cathode.

While a general understanding of the underlying degradation mechanisms is beneficial for interpreting the results of this thesis, more emphasis is laid on the DMs and their relation to the OCV change. The DMs are one of the state variables in this thesis that are estimated with appropriate methods.

1.1.4 Degradation Modes

Understanding the relationship between OCV and DMs is fundamental to this thesis. DMs categorize degradation mechanisms by the affected region, as illustrated in Figure 1.5. Although DMs cannot be directly measured in full cells, optimization methods enable highly accurate estimations [27; 32; 51]. Figure 1.7 outlines the three common DMs and their impact on the OCV.

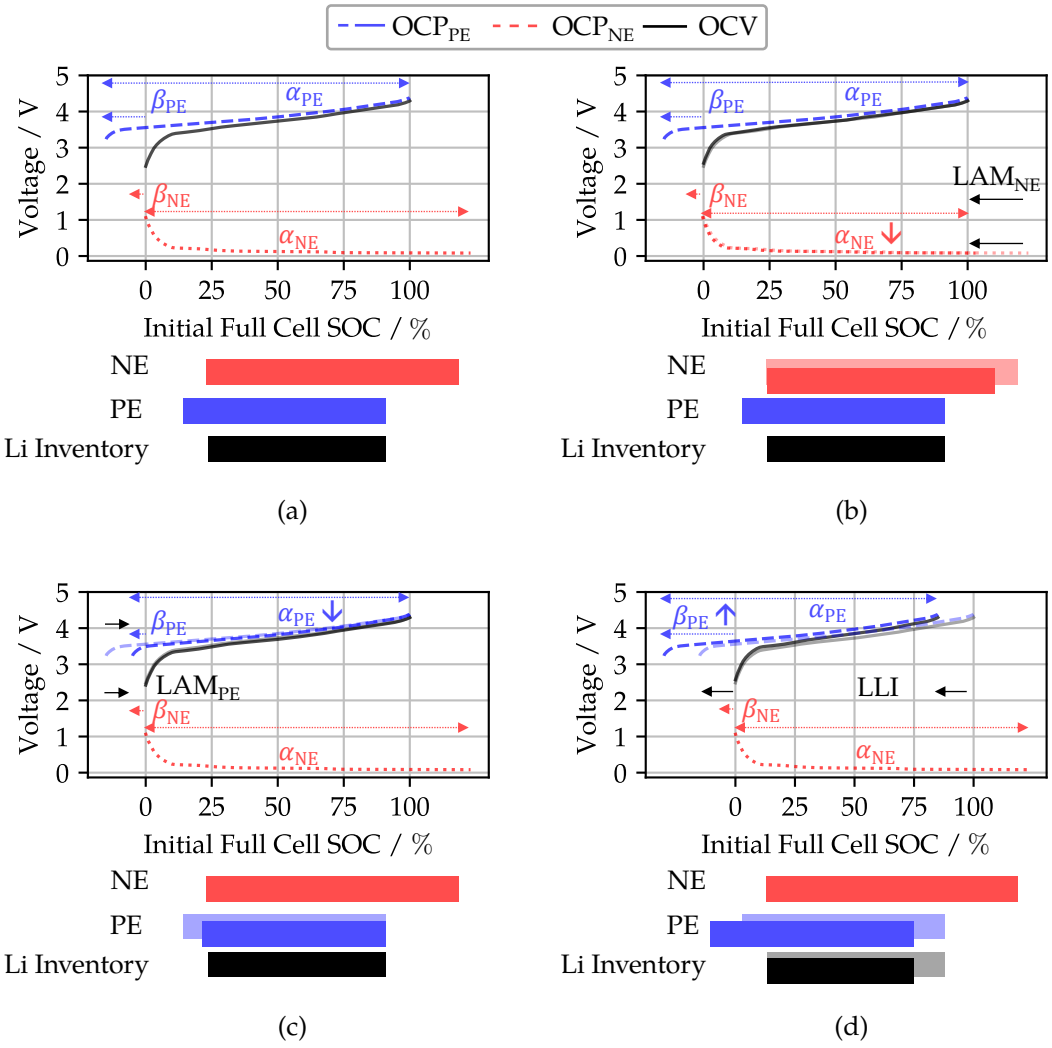

Figure 1.7: Relation of open-circuit voltage (OCV) changes, alignment parameter change, and underlying degradation modes (DMs) for a nickel cobalt alumnium oxide (NCA)-graphite battery. (a) Initial cell balancing and resulting OCV including the alignment parameter set α_{NE}, α_{PE}, β_{NE}, and β_{PE}; (b) Resulting OCV after loss of active material - negative electrode (LAM_{NE}); (c) Resulting OCV after loss of active material - positive electrode (LAM_{PE}); and (d) Resulting OCV after loss of lithium inventory (LLI) (Figure inspired by Birkl et al. [43]).

Figure 1.7 (a) illustrates the pristine state and the relationship between the OCPs, OCV and the initial full cell SOC. In other words, the initial full cell SOC is the SOC normalized to the capacity in initial or pristine state and is therefore suitable for a fair comparison.

In this example, the initial anode capacity is approximately 1.09 times the cathode capacity. This initial ratio, also known as the cell balancing or n/p ratio, is a key design parameter for LiBs and controls the available lithium inventory [14]. Typically, the n/p ratio is greater than one where the cathode is limiting in charge direction and the anode is limiting in discharge direction. This arrangement enables control of the full cell via the full cell voltage while avoiding electrode potentials that would accelerate degradation [43; 52].

LAM encompasses all degradation mechanisms that reduce the available electrode active material. LLI includes processes that decrease the cyclable lithium inventory. While these three DMs are widely recognized as primary DMs due to their description of the equilibrium behavior of LiB, additional DMs are necessary under real operational conditions: As shown in Figure 1.5, increased electrical resistance and reduced kinetics may be considered DMs as they describe the full cell voltage slope under current flow [32; 46]. Particularly when the OCV is approximated by the measured pOCV, inclusion of these new DMs may be required.

In Figure 1.7, the concept of alignment parameters is introduced. The alignment parameters α_{NE}, α_{PE}, β_{NE}, and β_{PE} describe the scaling and shifting of the electrodes' OCPs within the initial full cell SOC or normalized capacity coordinate system. First introduced by Dubarry et al. [32], these parameters function within the mechanistic model to calculate DMs.

As depicted in Figure 1.7, the alignment parameters consistently refer to the same coordinate system, with the full cell SOC as the abscissa throughout this thesis.

Subfigure 1.7 (a) illustrates the ideal, pristine case for a typical NCA-graphite LiB. Both OCPs have alignment parameters α and β: The scalar α-value represents the relative electrode capacity compared to the nominal capacity C_{N} of the full cell. The scalar β-values are defined negative if the arrows show to the left and indicate the relative shift to the charge onset, typically $|\beta_{\mathrm{NE}}| << |\beta_{\mathrm{PE}}|$. This relationship strongly depends on the measurement range of the initially captured OCPs [53–55].

The capacity of each electrode is shown with colored bars at the bottom of Subfigure 1.7 (a) and can be calculated by:

$$C_{\mathrm{NE}} = \alpha_{\mathrm{NE}} \cdot C_{\mathrm{N}} \tag{1.25}$$

$$C_{\mathrm{PE}} = \alpha_{\mathrm{PE}} \cdot C_{\mathrm{N}} \tag{1.26}$$

The resulting full cell capacity C is the overlapping section, i.e., the lithium inventory (depicted at the bottom of Subfigure 1.7 (a)) of both electrode curves within the usable voltage range, e.g., 2.8 V to 4.2 V for NMC-graphite batteries. Typically, the anode is limiting in discharge, while the cathode is limiting in charge direction. This implies that to some extent LAM does not affect the resulting full cell capacity [43].

Loss of Active Material - Negative Electrode

LAM_{NE} can arise from two primary causes, each potentially triggered by distinct events: Particle cracking or the loss of electronic contact between particles within the active material or between the active material and the current collector [43; 44]. These phenomena are exacerbated by high current loads and extensive cycling windows, particularly during overcharge conditions [44].

LAM_{NE} quantifies the available anode capacity relative to the pristine state, calculated as follows:

$$LAM_{NE} = \frac{\alpha_{NE,pristine} - \alpha_{NE}}{\alpha_{NE,pristine}} \tag{1.27}$$

Subfigure 1.7 (b) illustrates the impact of LAM_{NE} on the alignment parameters. A reduction in α_{NE} corresponds to a decrease in anode capacity, depicted by the shortened red bar at the bottom of Subfigure 1.7 (b). Despite this reduction, the anode retains an excess in the charge direction, leaving the lithium inventory unaffected.

Loss of Active Material - Positive Electrode

The specific causes of LAM_{PE} are highly dependent on the material used. However, the primary causes are similar to those of the anode: Particle cracking and loss of electronic contact [43; 44].

As shown in Subfigure 1.7 (c), the effect of LAM_{PE} mirrors that of LAM_{NE}. The resulting LAM_{PE} can be calculated as follows:

$$LAM_{PE} = \frac{\alpha_{PE,pristine} - \alpha_{PE}}{\alpha_{PE,pristine}} \tag{1.28}$$

Similar to LAM_{NE}, in this case (Subfigure 1.7 (c)) LAM_{PE} only reduces the excess, resulting in no decrease in lithium inventory or full cell capacity.

Loss of Lithium Inventory

Finally, LLI is the DM that mainly influences the full cell performance. Importantly, LLI can arise from two different causes: Either LLI is triggered by degradation mechanisms itself and a corresponding shift of both OCPs in relation to each other (compare Subfigure 1.7 (d)) or excessive LAM conditions LLI. If LAM on one electrode side consumes its respective excess, further LAM will also lead to LLI.

The degradation mechanisms behind conventional LLI, however, are SEI formation, build-up and decomposition, binder decomposition and lithium plating. While the first two are aggravated by high temperature and high SOC, lithium plating is triggered by low temperatures and high charging currents [44].

The conventional case of LLI is illustrated in Subfigure 1.7 (d), where the OCP_{PE} shifts relatively to the left while both electrode capacities stay the same. Hence, the α values are consistent while β_{PE} decreases. As depicted in the bottom Subfigure (d) this leads to a reduction in the overlapping section and, with that, to LLI. Finally, LLI gives the relative reduction of this lithium inventory:

$$\mathrm{LLI} = \frac{C_{\mathrm{lit,pristine}} - C_{\mathrm{lit}}}{C_{\mathrm{lit,pristine}}} \tag{1.29}$$

Due to the many different possible scenarios of LLI, the available lithium inventory C_{lit} demands a case-sensitive definition [51]:

$$C_{\mathrm{lit}} = \begin{cases} (\alpha_{\mathrm{PE}} - \beta_{\mathrm{NE}} + \beta_{\mathrm{PE}}) \cdot C_{\mathrm{N}} & \text{, for } (\alpha_{\mathrm{PE}} - \beta_{\mathrm{NE}} + \beta_{\mathrm{PE}}) \leq \alpha_{\mathrm{NE}} \wedge (\beta_{\mathrm{PE}} - \beta_{\mathrm{NE}}) \leq 0 \\ (\alpha_{\mathrm{NE}}) \cdot C_{\mathrm{N}} & \text{, for } (\alpha_{\mathrm{PE}} - \beta_{\mathrm{NE}} + \beta_{\mathrm{PE}}) > \alpha_{\mathrm{NE}} \wedge (\beta_{\mathrm{PE}} - \beta_{\mathrm{NE}}) \leq 0 \\ (\alpha_{\mathrm{NE}} + \beta_{\mathrm{NE}} - \beta_{\mathrm{PE}}) \cdot C_{\mathrm{N}} & \text{, for } (\alpha_{\mathrm{NE}} + \beta_{\mathrm{NE}} - \beta_{\mathrm{PE}}) \leq \alpha_{\mathrm{PE}} \wedge (\beta_{\mathrm{PE}} - \beta_{\mathrm{NE}}) > 0 \\ (\alpha_{\mathrm{PE}}) \cdot C_{\mathrm{N}} & \text{, for } (\alpha_{\mathrm{NE}} + \beta_{\mathrm{NE}} - \beta_{\mathrm{PE}}) > \alpha_{\mathrm{PE}} \wedge (\beta_{\mathrm{PE}} - \beta_{\mathrm{NE}}) > 0 \end{cases} \tag{1.30}$$

As can be seen in Figure 1.7, the usable voltage window within the available lithium inventory returns the full cell capacity. While LAM_{NE} or LAM_{PE} may occur without reducing the usable cell capacity, LLI always directly reflects the lost capacity. Hence, the LLI linearly correlates with the SOH_C. All of the aforementioned DMs are usually defined within the range from 0 % to 100 %, although slight negative values in the first few cycles are possible and realistic [56; 57].

1.2 State of Health Estimation

This thesis encompasses multiple studies on SOH estimation, employing two primary types of methods and their integration: OCV-models – as a type of mechanistic model – and neural networks – as a type of data-driven model. These methods are categorized and contextualized within the framework of commonly available SOH estimation techniques by presenting various categories and discussing the current state of the art. Prior to this, the standard definition of SOH used throughout this work is reiterated. Section 1.2.1 presents general approaches for SOH estimation, including physics-based, mechanistic, data-driven, and empirical models. The two employed architectures within this thesis, i.e., the mechanistic or OCV model and data-driven approaches, are intensively discussed in Section 1.2.2 and 1.2.3.

1.2.1 Definitions and General Approaches

As introduced in Section 1.1.2, the SOH_C is utilized throughout this thesis. Additionally, the OCV and the associated DMs extend the SOH_C, aiding in the identification of degradation mechanisms during operation, as shown in Figure 1.5. The SOH_C can be directly observed from the complete OCV curve, with C representing the available capacity within the usable voltage window. Thus, DMs are a valid extension of the SOH_C concept, bridging the gap between observable effects and underlying degradation mechanisms.

The following overview includes methods that are capable of estimating the SOH_C while some of them also include the OCV and, with that, the DMs. This clustering approach represents one method to categorize various SOH estimation models. Due to the close relationships among some models, separation can be challenging and heavily dependent on the perspective taken.

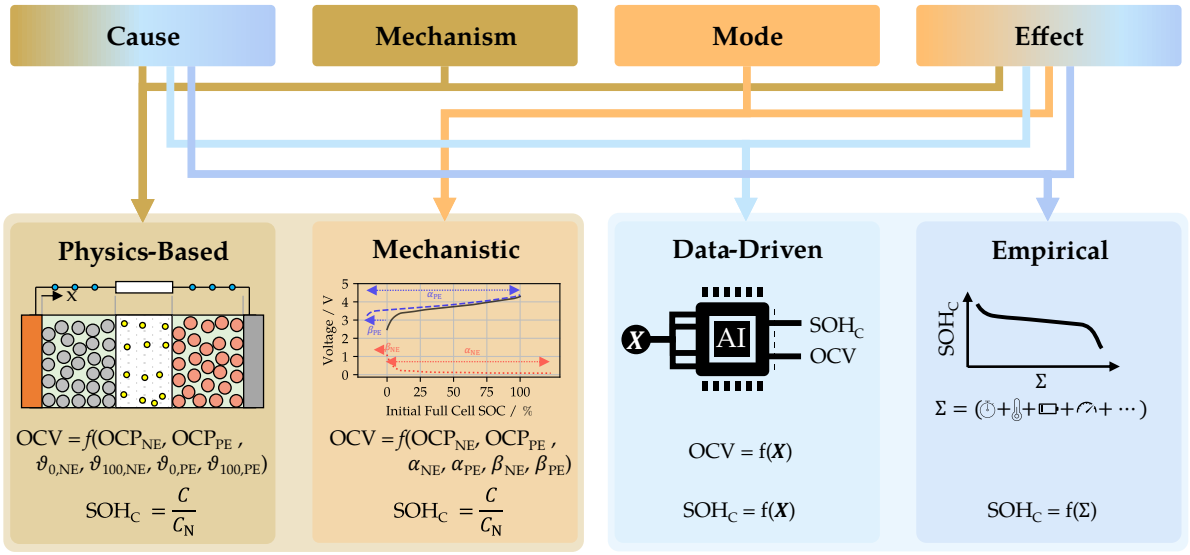

Figure 1.8: Overview of common state of health (SOH) estimation models and their relation to cause, mechanisms, modes, and effects of battery degradation. (Figure inspired by Schmitt [58] and Karger [59]).

Figure 1.8 illustrates the interconnection of model types with the abstraction and relation with the causes, mechanisms, modes and effects of battery degradation, as introduced in Figure 1.5. Empirical models utilize correlations between usage history — such as storage time and cycle count — and the decay of SOH_C, derived from historical data, to develop approximation functions [60]. Data-driven models, particularly neural networks, are akin to empirical models as they are also fitted to historical data to map usage history to effects. This close relation is indicated with a shared box around both models in Figure 1.8. However, neural networks can capture complex patterns in the data that simple empirical models cannot. Recent advancements in neural networks for battery state estimation even incorporate OCV and DMs [61–66]. Mechanistic models [32] exploit the relationship between OCPs and OCV to ascertain the current state by relating mode and effect. For state estimation, these models

must be reformulated as multivariate non-convex optimization problems. The solution variables, including alignment parameters, allowing for the estimation of OCV, DMs, and SOH_C. As indicated by the shared box around the mechanistic and physics-based model in Figure 1.8, mechanistic models, however, may be also assigned to the class of physics-based models, as their underlying theory follows thermodynamic laws. The most detailed models are physics-based models, notably the pseudo-two-dimensional (P2D) model [16], as depicted in Figure 1.8. These models directly link the causes of battery degradation to degradation mechanisms, providing deep insights into the current battery state. In the P2D model, state variables such as SOH_C, OCV, and DMs can be directly calculated from model parameters, including electrode stoichiometry [16; 67–69].

Empirical Models

Empirical models offer a direct approach for modeling battery degradation based on historical data. These models focus on SOH metrics, particularly SOH_C and SOH_R. Training data is usually sourced from laboratory aging studies, where cells are subjected to cyclic or calendar aging processes [60; 70–77]. During reference performance tests (RPTs), the relevant metric is evaluated, such as through a complete constant current (CC) discharge for SOH_C or a hybrid pulse power characterization (HPPC) test for SOH_R.

Empirical models encounter two major challenges: The requirement for extensive datasets to develop the model, and the lack of generalization, as these models are specific to particular batteries and experimental conditions. The complexity of generalized aging behavior, due to the nonlinear dependence of capacity decay and resistance rise on various stress factors, exceeds the scope of empirical models. Nevertheless, data-driven approaches can provide valuable support. Both model types are limited to replicating degradation behaviors present in the data; for instance, if temperature effects are not studied during aging tests, they cannot be represented in the empirical model.

Numerous studies have been conducted to empirically model capacity decay [60; 70–77] and impedance rise [71; 74; 75]. Typically, either calendar or cyclic aging studies are performed to isolate their effects on SOH_C decline, as demonstrated in:

$$SOH_C = \frac{C_N - Q_{loss,cal} - Q_{loss,cyc}}{C_N} \tag{1.31}$$

where capacity loss is divided into $Q_{loss,cal}$ and $Q_{loss,cyc}$. It is widely recognized that distinct stress factors drive calendar and cyclic aging: Calendar aging is affected by temperature and storage SOC, whereas cyclic aging is primarily influenced by temperature, depth of discharge (DOD), and applied current [72; 76; 77].

One foundational empirical aging model was presented by Schmalstieg et al. [60]: They modeled capacity decay using two equations:

$$Q_{\text{loss,cal}} = \beta_{\text{cal}} \cdot t^{\alpha_{\text{cal}}} \tag{1.32}$$

$$Q_{\text{loss,cyc}} = \beta_{\text{cyc}} \cdot Q^{\alpha_{\text{cyc}}} \tag{1.33}$$

where t represents total storage time and Q is the absolute charge throughput. The β parameters are adjustable fitting variables determined by experimental conditions, including the temperature T, the storage SOC ($\text{SOC}_{\text{storage}}$), the DOD, and the average SOC during cyclic aging SOC_{mean}:

$$\beta_{\text{cal}} = f(T, \text{SOC}_{\text{storage}}) \tag{1.34}$$

$$\beta_{\text{cyc}} = f(\text{DOD}, \text{SOC}_{\text{mean}}) \tag{1.35}$$

In their study [60], α parameters were fixed at 0.5 for calendar and 0.75 for cyclic aging, leading to the final SOH_{C} estimation equation:

$$\text{SOH}_{\text{C}} = \frac{C_N - \beta_{\text{cal}} t^{0.75} - \beta_{\text{cyc}} \sqrt{Q}}{C_N} \tag{1.36}$$

Equations 1.33 and 1.36 highlight a key limitation: Since the applied current was not varied during the aging study of Schmalstieg et al. [60], it was excluded from the cyclic capacity loss fitting function, despite being a significant factor in cyclic aging [72; 76; 77].

The mathematical modeling of capacity decay reveals inherent limitations in distinguishing calendar and cyclic influences on degradation. While laboratory-generated data can yield reasonable results, real-world application remains constrained. In practical scenarios, cyclic and calendar aging effects are interconnected, and path-dependency [78] significantly impacts field aging behavior. Path-dependency is often absent in empirical studies [60; 70–75; 77]. Consequently, there is a growing need for more comprehensive models, bridging the gap to physics-based, mechanistic, and data-driven approaches, as illustrated in Figure 1.8.

Physics-Based Models

While a variety of physics-based modeling approaches exist, this section focuses on the most fundamental: The P2D model [16] and its simplified version, the single particle model (SPM) [79–81]. As illustrated in Figure 1.8, physics-based models connect degradation causes to their underlying mechanisms. To extract the aging state from the model, the relevant parameters must be utilized. This necessitates that physics-based models are updated over the cell's lifetime by incorporating degradation mechanisms to accurately replicate cell behavior. In the following, the basics of the P2D and SPM models are presented, along with a review of the state-of-the-art degradation-adapted implementations found in the literature.

The P2D model, introduced by Doyle, Fuller, and Newman [16], describes a battery cell on a macroscopic scale with two porous electrodes, a separator, and a liquid electrolyte, visualized in Figure 1.9. The formulas are universally applicable for most common LiBs, allowing them to be used across different material combinations and cell designs without being limited to a specific chemistry. The model is built in one dimension x along the cell stack and includes a second pseudo-dimension r for lithium-ion diffusion within particles, hence the name.

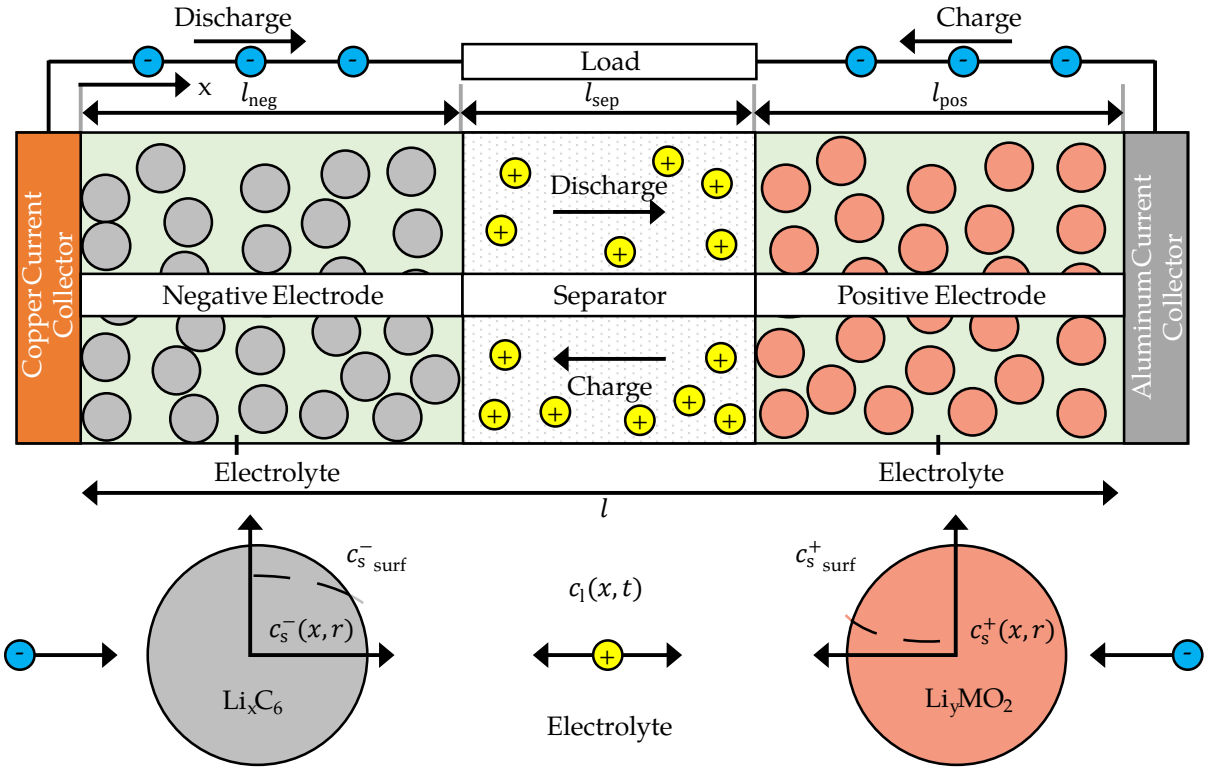

Figure 1.9: Schematic overview of a lithium-ion battery (LiB) and its modeling in the pseudo-two-dimensional (P2D) model with its respective dimensions through the cell layers x and the pseudo dimension r within the particle radius. Figure adapted from Jokar et al. [79].

The model solves for concentrations c_s, c_l and potentials φ_s, φ_l within the active material (s for solid phase) and electrolyte (l for liquid phase). Figure 1.9 schemes the concentration in the solid phase and its dependencies. Key equations of the P2D model, specifically the mass balance, include:

Separator domain:

$$\varepsilon_l \frac{\partial c_s}{\partial t} = \nabla \left(D_{l,\text{eff}} \nabla c_l - \frac{i_l t_+}{\mathcal{F}} \right) \tag{1.37}$$

Electrode domain:

$$\varepsilon_l \frac{\partial c_s}{\partial t} = \nabla \left(D_{l,\text{eff}} \nabla c_l - \frac{i_l t_+}{\mathcal{F}} \right) + a_s \left(1 - t_+\right) j_n \tag{1.38}$$

In these equations ε is the volume fraction, D_{eff} is the efficient diffusion coefficient, i is the current density, and j_n is the molar flux density, t is the transport number, a_s is the specific

surface and can be calculated from the particle radius r_p by $a_s = \frac{3\varepsilon_s}{r_p}$, and $\mathcal{F}$ is the Faraday constant.

For a detailed description of these equations including the remaining auxiliary conditions, the interested reader is referred to the original work by Doyle, Fuller and Newman [16].

The model is not analytically solvable and requires numerical methods like the finite element method [79]. It does not initially account for degradation, necessitating extensions or coupling with aging models for accurate SOH estimation. Uddin et al. [67] have built an optimization framework that identifies the most influential parameters for varying aging scenarios and, with that, updated the model. From these adapted parameters it is possible to yield the SOH_C [67]. The review by Miguel et al. [68] highlights the critical role of accurate parameter estimation in using physics-based models, especially the P2D model, for battery management systems (BMSs) and state estimation. It emphasizes that, while single-optimization approaches may offer good accuracy, multi-optimization analyses provide more comprehensive parameter estimations. These methods, especially when combined with physico-chemical tests, can enhance the robustness of the P2D model by ensuring precise parameter estimation and accurate state predictions [68]. While the parameter and optimization choice itself is already challenging, Laue et al. [69] further discuss the sensitivity to parametrization tests. Following their results, adequate P2D parameter updates are not feasible with the common C-rate tests as the reaction and conductivity coefficients cannot be differentiated. They propose the usage of constant and dynamic current tests, including the measurement of the half-cell potentials during these tests [69]. Due to these limitations, the P2D model, despite its high accuracy, is still not applicable in real-world scenarios, as continuous measurement of electrode potentials can only be conducted in controlled laboratory settings. Modifying the P2D model for SOH estimation requires the inclusion of degradation models that update dependent parameters. This integration, however, is aggravated by the highly sensitive parameters [67–69] and the high computational cost [79].

Reduced order models, such as the SPM, decrease computational complexity and parameter sensitivity by simplifying the P2D model. They assume uniform current density across electrode thickness and ignore lithium concentrations in the electrolyte, focusing on the mass balance for electrode particles and a nonlinear output voltage function [80; 81]. The SPM can be extended to include thermal behavior and aging mechanisms, achieving high state estimation accuracy [82; 83]. The main benefits of reduced order models are simplicity, low computational cost, and adaptability for various purposes, although they require fine-tuning for specific conditions [79]. Li et al. [82] have integrated SEI growth and crack propagation as the main degradation mechanisms into a SPM and coupled them with LLI to allow SOH_C estimation. Their model accurately estimates battery capacity fade and voltage profiles across various temperatures, emphasizing the dominant role of SEI layer formation. Building on their previous work, Li et al. [83] presented an extended capacity fade model using an SPM, which further addressed SEI layer formation and growth on the anode, and volumetric changes in the cathode. This enhanced model effectively estimates the SOH_C

with minimal error, though it requires empirical data for parameter determination and is cycle-based. Future advancements will focus on dynamic loading situations to enhance prediction accuracy [83]. While SPM offer a simplified approach compared to the more complex P2D models, they still face significant challenges: Due to the simplification of a single particle, they cannot accurately capture the depletion of electrolyte salt concentration across the dimension of thick electrodes, leading to poor reproduction of voltage drop under high current conditions [84]. One major disadvantage is the multitude of degradation mechanisms that need to be accurately modeled, which complicates the model development process. Additionally, the effort required for parameterization is substantial, posing critical challenges for onboard diagnostics in BMSs. In contrast, mechanistic models, which can also be considered physics-based models, offer a different approach. Rather than modeling individual degradation mechanisms, these models focus on DMs that directly influence the OCV. This approach potentially reduces complexity and computational demands, providing a more direct assessment of battery health.

Mechanistic Models

Dubarry et al. [32] was the pioneer in introducing the mechanistic modeling approach. This model adheres to the theory presented in Section 1.1.2, where the OCV is defined as the potential difference between the positive electrode potential $\mathrm{OCP_{PE}}$ and the negative electrode potential $\mathrm{OCP_{NE}}$. It is assumed that the OCPs remain constant throughout the lifetime of the system; however, they scale and shift relative to one another, resulting in corresponding changes in the OCV [32].

As discussed in Section 1.1.4, LAM leads to scaled electrode curves, while LLI results in shifts in the relationship between the electrodes. This leads to the fundamental concept of the mechanistic modeling approach for prognosis and diagnosis. Prognosis refers to the simulation of various aging states, allowing for the adjustment of DMs by simply shifting and scaling the OCPs. This can be efficiently achieved through programming tools, such as the *alawa toolbox* [32; 85], and allows the generation of battery aging data with low computational cost. In contrast, diagnosis involves estimating the DMs by minimizing the deviation between the measured and reconstructed OCV.

Schmidt et al. [25] were the first to validate the mechanistic modeling approach through laboratory measurements. In their study, they disassembled cells to establish specific rates of LLI and LAM. Their experiments involved six different cells and they found that for a C-rate below C/20 the deviation between the measured and reconstructed OCPs and OCV consistently remained a mean absolute error (MAE) below 21 mV or 0.5 %. With that, they achieved the proof of concept for the mechanistic model and gave rise to model modifications [46; 86–92].

The mechanistic modeling approach has been applied to various scenarios [27; 28; 54; 55; 88; 93–99], including full [25; 28; 43; 88; 93–99] and partial OCV measurements [27; 55]. There is an increasing number of publications [27; 54; 55; 91; 92] that leverage the mechanistic modeling approach for real-world charging events, particularly at higher C-rates and during partial charging segments. One work [100] contained in this thesis, the so-called ΔQ-method, modifies the cost function to optimize the charge difference between relaxed voltage point pairs which allows the application to real-world BEV fleet data. The mechanistic model has been modified for more accurate prognosis by integrating blended electrodes [27; 28; 88], kinetics [46; 89; 91], temperature effects [92], and inhomogeneities [87].

Recent advancements have begun to couple the mechanistic model with data-driven models [61–63]. For instance, alignment parameters can be estimated using neural networks [61]. However, it is important to note that data-driven methods do not necessarily require a physics-based core, as they can learn directly from raw data.

Data-Driven Models

In the context of artificial intelligence (AI) and data-driven models, neural networks are a fundamental component, particularly within the domain of machine learning. In the context of this work, Figure 1.10 visualizes the location of neural networks for battery SOH estimation within the AI landscape [9; 101]. The general areas are depicted in orange, while the concrete fields are colored in blue and highlighted with dashed circles.

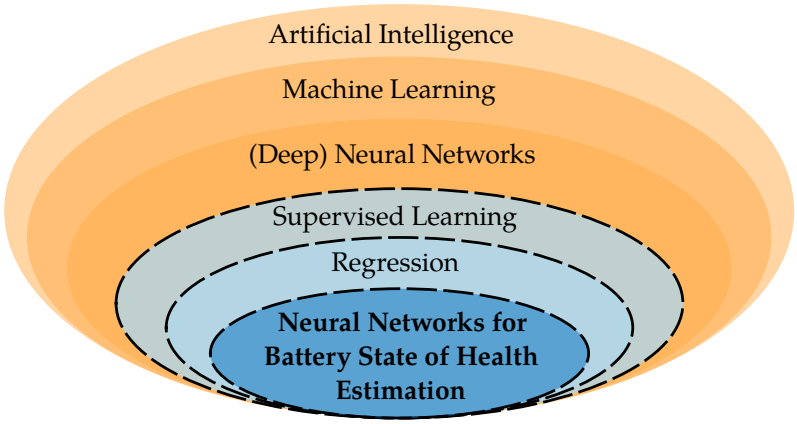

Figure 1.10: Schematic visualization of the location of battery state of health (SOH) estimation within the artificial intelligence (AI) landscape in orange. The dashed, blue circles offer a more detailed perspective, where the methods solve regression problems with supervised learning approaches [9; 101].

Neural networks can be employed in both supervised and unsupervised learning paradigms. In supervised learning, which is the focus of this dissertation, models are trained using labeled datasets to predict outcomes based on input features. This contrasts with unsupervised learning, where models identify patterns and structures in unlabeled data. Deep learning is

a subset of machine learning that involves neural networks with multiple layers, known as deep neural networks. These layers enable the model to learn hierarchical representations of data, making deep learning particularly effective for complex tasks such as image and speech recognition, and increasingly, battery SOH estimation.

Neural networks do not incorporate the underlying electrochemical mechanisms into their architecture. Instead, they learn the mapping function between input data streams, such as voltage, current, and temperature, and the SOH of a battery, as can be seen in Figure 1.8. The performance of these models is heavily dependent on the quality of the dataset and the preprocessing techniques employed, i.e., the so called feature set. The challenges in developing a data-driven SOH estimation model lie in data preprocessing and model fine-tuning to achieve effective generalization. As this thesis only deals with neural networks as one representation of data-driven models, as can be seen in Figure 1.10, focus is set on these methods.

Neural networks have become a key tool for estimating the SOH of batteries in recent years [102–121]. The simplest form, the perceptron, has been known for over six decades but gained practical application in the 21st century. An artificial neuron mimics biological neurons by processing multiple inputs with associated weights and applying an activation function. Training involves minimizing the deviation between expected and estimated outputs using gradient descent methods [122]. The feed-forward neural network (FNN) [102–104] builds on the perceptron by incorporating multiple layers and neurons. Variants such as the convolutional neural network (CNN) [105–108] excel with grid-like data, while recurrent neural networks (RNNs) [109; 110] are designed for time-dependent tasks. Long short-term memory neural networks (LSTMs), a specialized type of RNN, are particularly effective for sequential data, addressing the vanishing gradient problem (will be discussed in Section 1.2.3) through memory cells that retain information over time, thus enhancing accuracy [111–115]. Novel modifications, i.e., the temporal convolutional neural network (TCN) – a combination of LSTM and CNN, have gained attention [116–121]. For example, Bockrath et al. [120] have shown that TCNs work with raw sensor data and outperform several other neural network architectures, reaching a SOH_C root mean squared error (RMSE) of 1 %.

In recent years, neural networks have been adapted to DM estimation [61–66], including mostly CNN, LSTM, and novel modifications. Tian et al. [65], for example, have reached an OCV reconstruction RMSE below 15 mV by developing a CNN that estimates the stoichiometry. From these values, it is possible to directly output the DMs and the OCV.

Advancements have focused on solving the two major problems of neural networks in the field of battery state estimation: Data scarcity is tackled by leveraging the capabilities of transfer learning [51; 61; 123–146] and learning from previous battery aging datasets [61; 123–125; 127–130; 132–136; 139; 140; 142; 144–146] or from synthetic data [51; 126; 131; 137; 138]. The solution to data dependence, i.e., generalization, is aimed to be achieved

by integrating physics-based models into neural networks [51; 135; 147–165] by developing PINNs and, with that, physically constraining the estimation.

1.2.2 SOH Estimation based on OCV-Models

While many possibilities for successful SOH estimation exist, only two of the previously introduced approaches are utilized in this work, as both of them allow the extension to OCV reconstruction and DM estimation, although maintaining low parametrization effort and the possibility for online application: The mechanistic model and neural networks. As shown in Figure 1.8 and detailed in Section 1.2.1, the mechanistic model is of high interest, as it reveals the OCV.

The mechanistic modeling approach was initially published by Dubarry et al. [32], later validated by Schmidt et al. [25], and has since undergone multiple adaptations, modifications, and extensions [26; 27; 51; 53; 87; 91; 92; 94–96; 100; 166; 167]. The application of the mechanistic model for SOH_C estimation will also be referred to as the OCV model throughout this thesis.

The theoretical OCV is the superposition of both OCPs in the full cell design, i.e., the cell balancing, which can be expressed using the alignment parameter set ϑ, including the scaling and shifting factors which determine the electrode capacities and the electrode balancing:

$$\vartheta = [\alpha_{NE}, \alpha_{PE}, \beta_{NE}, \beta_{PE}] \tag{1.39}$$

These factors ultimately allow the reconstruction of the full OCV, the estimation of DMs, and the calculation of SOH_C. Mathematically, this implies solving an optimization problem, where the optimal alignment parameter set ϑ is sought to minimize a predefined cost function. In the following sections, the mathematical derivation for the optimization problem of the OCV model is presented, where the full cell SOC (herein simply denoted as SOC) is chosen as the common abscissa. This common abscissa, however, can also be the absolute capacity within given voltage limits.

Equation 1.5 can be transformed to:

$$OCV(SOC) = OCP_{PE}(SOC_{PE}) - OCP_{NE}(SOC_{NE}) \tag{1.40}$$

The OCPs of both electrodes must be transformed to the full cell SOC space:

$$SOC = \alpha_{NE} \cdot SOC_{NE} + \beta_{NE} \tag{1.41}$$

$$SOC = \alpha_{PE} \cdot SOC_{PE} + \beta_{PE} \tag{1.42}$$

This results in the following expression:

$$\mathrm{OCV}(\mathrm{SOC}) = \mathrm{OCP}_{\mathrm{PE}}\left(\frac{\mathrm{SOC} - \beta_{\mathrm{PE}}}{\alpha_{\mathrm{PE}}}\right) - \mathrm{OCP}_{\mathrm{NE}}\left(\frac{\mathrm{SOC} - \beta_{\mathrm{NE}}}{\alpha_{\mathrm{NE}}}\right) \tag{1.43}$$

Thus, the reconstructed full cell $\mathrm{OCV}_{\mathrm{reco}}$ can be described as a function of SOC and ϑ:

$$\mathrm{OCV}_{\mathrm{reco}} = f(\mathrm{SOC}, \vartheta) \tag{1.44}$$

To finally determine the optimal alignment parameter set, a measured $\mathrm{OCV}_{\mathrm{meas}}$, such as a pOCV or GITT measurement, is compared to the reconstructed curve, and the minimum deviation is sought. This process is visualized for a pristine NCA-graphite battery in Subfigure 1.11 (a). Manually, the OCPs of both electrodes must be shifted and squeezed until the error vanishes. In this example, the current alignment parameter set is $[1.05, 1.1, -0.07, -0.18]$. As can be seen, $\mathrm{OCV}_{\mathrm{meas}}$ and $\mathrm{OCV}_{\mathrm{reco}}$ still have large deviations, and $\mathrm{OCV}_{\mathrm{meas}}$ has more capacity. Increasing α_{PE} might reduce the cost. This example, however, already shows that manual tweaking is cumbersome and error-prone.

Automating this curve alignment is much more feasible and well-established [26; 27; 51; 53; 87; 91; 92; 94–96; 100; 166; 167]. To achieve this, a multivariate non-convex optimization problem must be solved, which generally has the following form:

$$\begin{aligned} \vartheta = \arg\min_{\vartheta} \quad & f(\vartheta) \\ \text{s.t.} \quad & \vartheta \geq \mathrm{lb} \\ & \vartheta \leq \mathrm{ub} \\ & f_{\mathrm{eq}}(\vartheta) = 0 \\ & f_{\mathrm{ineq}}(\vartheta) \geq 0 \end{aligned} \tag{1.45}$$

where $f(\vartheta)$ is the cost or objective function, and ϑ is the optimization argument. Additionally, lower and upper boundaries (lb and ub) of the optimization argument and additional equality and inequality constraints ($f_{\mathrm{eq}}(\vartheta)$ and $f_{\mathrm{ineq}}(\vartheta)$) may be included. In this case, as shown in Subfigure 1.11 (a), the cost function $f(\vartheta)$ can be expressed as:

$$f(\vartheta) = \| \mathrm{OCV}_{\mathrm{meas}}(\mathrm{SOC}) - \mathrm{OCV}_{\mathrm{reco}}(\mathrm{SOC}, \vartheta) \|_2^2 \tag{1.46}$$

where both OCV curves must be transformed to the same full cell SOC.

The cost function is the squared Euclidean norm of the measured and reconstructed OCV. While this optimization problem seems straightforward, it has several major influencing factors, including the cost function itself, the choice of the search space, the constraints, the solver, and finally, the input data, which will be discussed in the following.

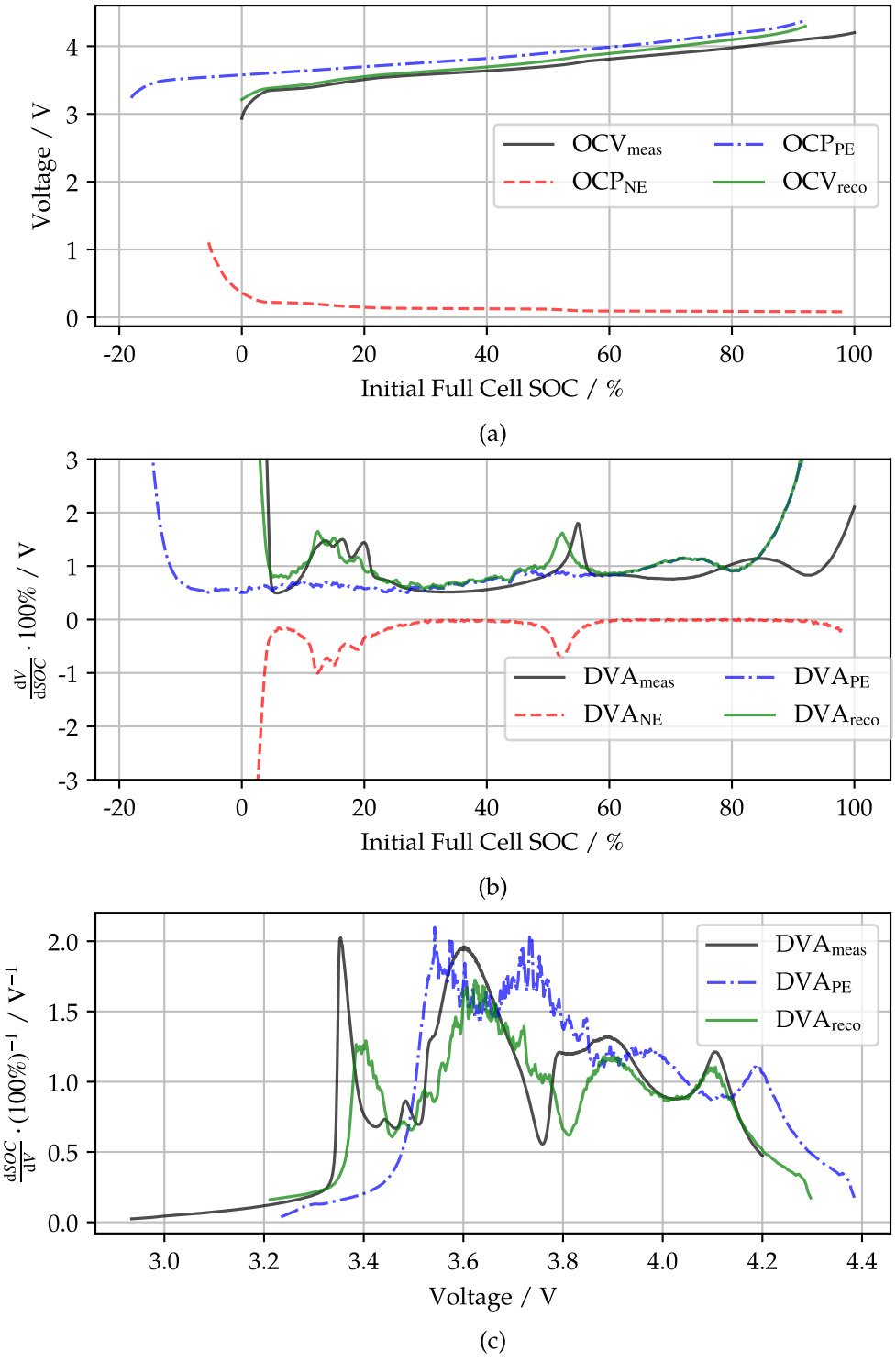

Figure 1.11: Different approaches for the cost function of the open-circuit voltage (OCV) model including the shifted and scaled open-circuit potentials (OCPs), the reconstructed OCV, and the measured signal for an initial alignment parameter set of $[1.05, 1.1, -0.07, -0.18]$ for α_{NE}, α_{PE}, β_{NE}, β_{PE}, respectively. Subfigure (a) shows the voltage, (b) the differential voltage, and (c) the incremental capacity.

Cost Function

The calculated error is mostly defined at equidistant SOC points and follows, for example, the squared Euclidean norm. The cost function, however, may also be expressed with non-equidistant points to weigh several regions higher than others. Besides the Euclidean norm, it is possible to use any other norm, e.g., the absolute value norm. Note that these norms may be expressed as error metrics, such as the MAE or the RMSE, however, they are convertible between each other. While the RMSE is very commonly used in the context of OCV reconstruction, the perfect configuration is problem-specific [58].

As can be seen in Subfigures 1.11 (b) and (c), the cost function may be changed or extended by the differential voltage analysis (DVA) or incremental capacity analysis (ICA). The general concept of the DVA and ICA is visualized in Figure 1.12, including information about the phase transitions of graphite which also leads to peaks and valleys in the full cell DVA and ICA.

The DVA is calculated with:

$$\mathrm{DVA} = \frac{\mathrm{dOCV}}{\mathrm{dSOC}} \tag{1.47}$$

in the SOC domain, and with:

$$\mathrm{DVA} = \frac{\mathrm{dOCV}}{\mathrm{d}Q} \tag{1.48}$$

in the capacity domain. For easier visualization, the curves are mostly multiplied by either 100 % or C_N, respectively. Subfigure 1.11 (b) shows that the full cell DVA can be determined from both electrode DVAs:

$$\frac{\mathrm{dOCV}}{\mathrm{dSOC}} = \frac{\mathrm{dOCP_{PE}}}{\mathrm{dSOC}} - \frac{\mathrm{dOCP_{NE}}}{\mathrm{dSOC}} \tag{1.49}$$

Hence, the full cell DVA includes features that can be attributed to individual electrodes and is a very important tool for diagnosis [22; 59; 91; 98; 169–174]. As can be seen in Subfigure 1.11 (b) and Figure 1.12, the DVA incorporates features which are not that prominent in the voltage curve. Equation 1.49 implies that steep gradients, i.e., phase transitions in the active material [59; 175], lead to peaks in the DVA. These phase transitions are illustrated in Subfigure 1.12 (c) and (d). The distinctive features observed in the anode are attributed to the lithiation process of graphite, during which various stages are sequentially traversed, each resulting in a distinct electrochemical potential. For a more comprehensive explanation, interested readers are encouraged to consult the works of Dahn [175] or Insinna et al. [168]. The characteristic anode plateau change around 50 % SOC is very visible in the DVA, while it is diminishing in the voltage curve. Besides that, the edge areas experience high peaks, as there the electrode OCPs are limiting. Other researchers even use the DVA curve to directly estimate the DMs by quantifying the change in length between several peaks [22; 91; 169–171; 173; 174]. For example, $Q_{\mathrm{NE},1}$ and $Q_{\mathrm{NE},2}$ quantify $\mathrm{LAM_{NE}}$, while $Q_{\mathrm{PE},1}$ quantifies $\mathrm{LAM_{PE}}$. The DMs are calculated by Equation 1.27 and 1.28, where the α variables are simply exchanged by

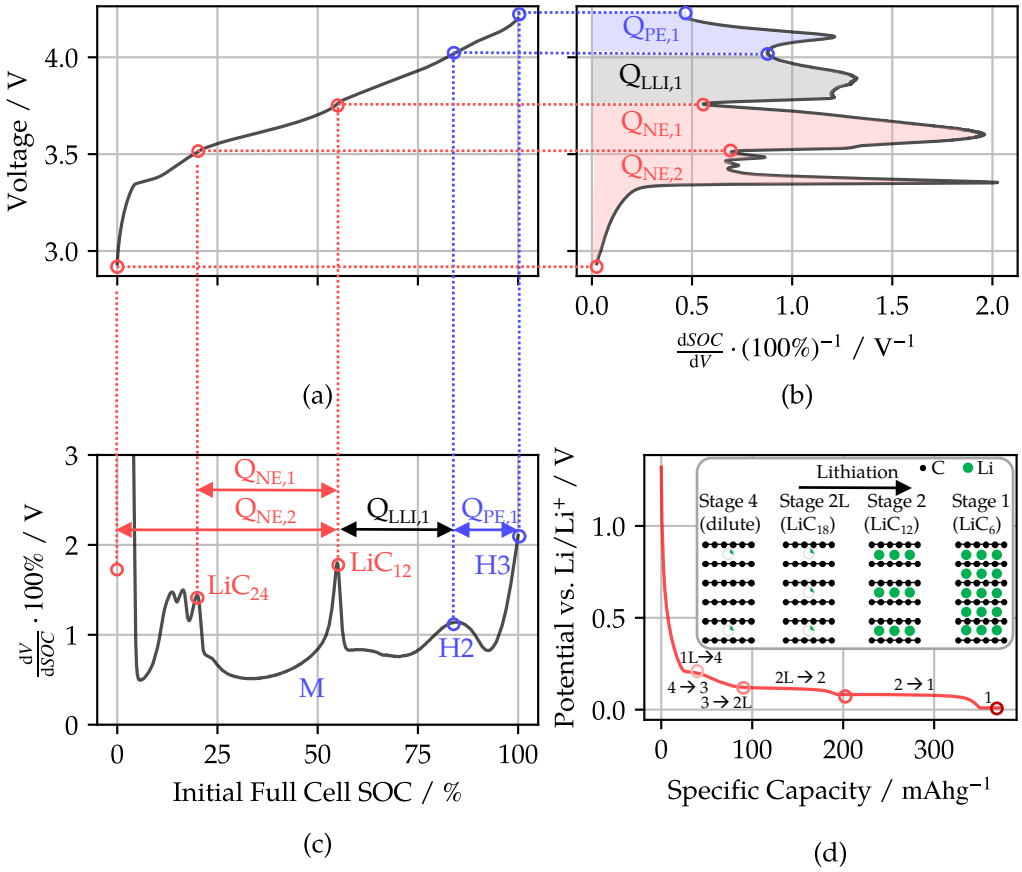

Figure 1.12: Illustration of the relation between the (a) open-circuit voltage (OCV), (b) the incremental capacity analysis (ICA), and (c) the differential voltage analysis (DVA) for a nickel cobalt alumnium oxide (NCA)-graphite battery. The location of the phase transitions in the DVA (c) is related to the phase equilibria in the ICA (b). The length between these peaks/valleys can be used for peak-tracking, i.e., degradation mode (DM) estimation. Figure is adapted from Karger et al. [59]. Subfigure (d) additionally illustrates the phase transitions of graphite during lithiation and the respective potential vs. Li/Li$^+$ (Figure adapted from Insinna et al. [168]).

the respective capacity $Q_{NE,1}$, $Q_{NE,2}$ or $Q_{PE,1}$. The capacity between peaks of the anode and cathode $Q_{LLI,1}$ correlates with LLI. Direct calculation of LLI, however, is not possible [59; 170]. For example, graphite experiences several phase transitions $LiC_{24} \rightarrow LiC_{12} \rightarrow LiC_6$, with the perfect configurations visible as peaks in the DVA in Subfigure 1.12 (c) [22; 59; 91; 169; 170; 175–178]. Especially, the LiC_{12} configuration is a prominent marker [59; 177]. Similarly, for a NCA cathode, several structural transitions occur, from hexagonal (H) to monoclinic (M), with the sequence H1 → M → H2 → H3 for delithiation [59; 179]. The two peaks associated with the H2 → H3 transitions are mostly visible; for example, in Subfigure 1.11 (b) or 1.12 (c), the last two peaks in the DVA [59; 179]. This so-called peak-tracking [91] follows the same theoretical considerations as the mechanistic model and the connected DM equations [22; 98; 169–171].

Similar to the DVA, the ICA is a well-established tool for direct cell diagnosis [91; 98; 173; 174; 180–182]. As can be seen in Subfigure 1.12 (b), however, the peaks are located in phase equilibria [59; 178], i.e., where large quantities of capacity are allocated in the electrode without significant potential changes. Mathematically, the ICA can be expressed as:

$$\left(\frac{\mathrm{dOCV}}{\mathrm{dSOC}}\right)^{-1} = \frac{1}{\frac{\mathrm{dOCP_{PE}}}{\mathrm{dSOC}} - \frac{\mathrm{dOCP_{NE}}}{\mathrm{dSOC}}} \tag{1.50}$$

The full cell ICA can be calculated from both electrode ICAs. In this case, however, the ICA of the negative electrode is subject to high noise as the $\mathrm{OCP_{NE}}$ is extremely flat. Hence, the $\mathrm{ICA_{NE}}$ is not included in Subfigure 1.11 (c). Further, the visual mapping of individual features from the electrodes to the full cell ICA is complicated as the ICAs are plotted against the voltage, yielding a corresponding shift of the peaks and valleys, as can be seen in Subfigure 1.11 (c). Nevertheless, the full cell ICA, displayed in Subfigure 1.12 (b), allows for very strong identification of cathode markers in the upper SOC region, including the H2 → H3 plateau for NCA cathode materials [59; 179]. Peak-tracking – although in this case it should rather be called valley-tracking – is, thus, also commonly used for DM estimation [91; 98; 173; 174; 180; 182], following the same equations as peak-tracking with the DVA.

If the cost function is modified to include the DVA and ICA, it will result in:

$$\begin{aligned} f(\vartheta) =& x_1 \cdot \| \mathrm{OCV_{meas}}(\mathrm{SOC}) - \mathrm{OCV_{reco}}(\mathrm{SOC}, \vartheta) \|_2^2 \\ &+ x_2 \cdot \| \mathrm{DVA_{meas}}(\mathrm{SOC}) - \mathrm{DVA_{reco}}(\mathrm{SOC}, \vartheta) \|_2^2 \\ &+ x_3 \cdot \| \mathrm{ICA_{meas}}(V) - \mathrm{ICA_{reco}}(V, \vartheta) \|_2^2 \end{aligned} \tag{1.51}$$

where x_1, x_2, and x_3 are the weighting factors for the individual components. Bin-Mat-Arishad et al. [93] have researched the optimum configuration and found evidence that a combination of all three is beneficial for a NMC-graphite battery. The exact choice of the cost function, however, remains highly cell-specific and must be optimized individually.

Recent modifications [87; 91] have included peak-tracking as additional terms in the cost function or directly in the constraints, which is especially helpful for correct anode alignment, as the $\mathrm{LiC_{12}}$ peak in the DVA [59; 177] just marginally influences the total cost.

Search Space and Constraints

The optimization problem is highly sensitive to the definition of the search space due to the non-convex nature of the objective function. The search space is determined by the upper and lower boundaries, as well as the equality and inequality constraints, as outlined in Equation 1.45. Additionally, some solvers require an initial starting point to perform the optimization effectively.

Following the barrier method for non-convex problems [183; 184], the problem can be simplified by incorporating the constraints directly into the objective function. In this approach, infeasible points are penalized, typically through a quadratic penalty term. Applying this method to Equation 1.45 results in the following reformulated objective function:

$$\begin{aligned} \vartheta = \arg\min_{\vartheta} \quad & f(\vartheta) + \rho_1 f_{\text{eq}}(\vartheta)^2 + \rho_2 \max(0, -f_{\text{ineq}}(\vartheta))^2 \\ \text{s.t.} \quad & \vartheta \geq \text{lb} \\ & \vartheta \leq \text{ub} \end{aligned} \tag{1.52}$$

where $\rho_1 > 0$ and $\rho_2 > 0$ are penalty parameters for the equality and inequality constraints, respectively.

In recent studies, only a limited number of authors [27; 87; 94] have explicitly incorporated equality and inequality constraints into their optimization frameworks. Schmitt et al. [27] included the inequality constraint that the reconstructed OCV must at least reach a voltage of 4.2 V. In other words, this implies that the electrodes keep their balancing with the cathode being the limiting factor in charge direction, as otherwise the full cell voltage of 4.2 V could not be reached. Fath et al. [87] employed the barrier method [183; 184] and integrated peak-tracking into the objective function of the OCV model, as shown in Equation 1.52. They also added the inequality constraint that all DMs must remain positive.

More commonly, researchers have relied on the use of boundaries and initial values, which appear to play a more significant role than explicit constraints [27; 51; 93; 100]. For instance, Schmitt et al. [27] developed an automated analysis tool for RPTs in an aging study. In their approach, initial values were provided for the pristine cell, corresponding to the first RPT. Subsequent iterations utilized the solution from the previous run as initial values, with boundaries set to 30 %. Another implementation [51] further reduced the boundaries to −20 % and +10 % for the same aging study. However, this procedure is not feasible for most real-world applications. A proposed OCV model for a BEV fleet leveraged the estimated SOH_C from the BMS to determine the initial values and boundaries [100].

Solver

The choice of solver plays a critical role in the optimization process, as it significantly impacts the convergence behavior and computational cost. Solvers can generally be categorized into global and local optimization methods [184]. Local algorithms exploit gradient descent to find the optimum, while global algorithms mostly work iteratively by comparing subsequent evaluation runs [184]. Each type has distinct characteristics, with some solvers capable of incorporating constraints and search space definitions, while others may not support such features. Global optimization methods address the problem on a global scale but are often more computationally demanding, as they typically require solving multiple local optimization problems [184].

The selection of an appropriate solver depends not only on the objective function and search space but also on the specific knowledge available about the problem. For instance, if the initial alignment parameters are known, it may be advantageous to choose a solver that allows the specification of initial values. This can improve convergence and reduce computational effort [93].

In literature, global solvers have been applied across a wide range of problems [53; 91; 92; 95; 166], with their performance varying depending on the complexity of the objective function and the dimensionality of the search space. Especially, particle swarm [53; 92; 95] and the genetic algorithm [53; 91; 92; 95] are popular choices.

Similarly, local solvers have been employed for problems [26; 27; 51; 87; 94; 96; 100; 167], where the search space is well-defined, and initial values are available, often achieving faster convergence but at the risk of finding suboptimal solutions in non-convex landscapes. Herein, mostly the pattern search algorithm [87], sequential quadratic programming [26; 94] or least-squares solvers [27; 51; 96; 100; 167] are used.

Despite the importance of selecting the optimal solver, objective function, and search space, these factors alone cannot guarantee success. The quality and sufficiency of the input database remain fundamental to achieving reliable and meaningful optimization results.

Input Data

Figure 1.13 illustrates charging curves at various C-rates from C/50 up to C/4, which pose increasing levels of difficulty to the OCV model. In the easiest case, a full measured pOCV or GITT is available, e.g., the pOCV curve at C/50 or C/25 in Subfigure 1.13 (a). The optimization problem gets increasingly challenging for partial pOCV and higher C-rates.

Partial voltage curves exclude several important regions. For example, a measured pOCV from 30 % to 80 % misses characteristic features of the OCV. Compared to Figure 1.12 and Figure 1.13, the most informative peaks in the DVA (c) and ICA (b) vanish and, with that, the possibility for peak-tracking. Similarly, the features vanish for higher current loads. As can be seen in Figure 1.13, the voltage curve at C/4 incorporates drastically less visible features, hence, tools as the DVA and ICA cannot robustly detect peaks. As the displayed data in Figure 1.13 is from a pristine cell, this trend is expected to worsen for degraded batteries as the impedance rises even more and, with that, fewer features are detectable.

If the full measured OCV curve is available, the objective function is typically defined by Equation 1.46 or extended as shown in Equation 1.51. Xu et al. [185] published a method to collect the full OCV from discrete curve fragments, allowing the original reconstruction.

In cases where only a partially measured OCV curve is available as input data, the objective function can be adapted in two ways:

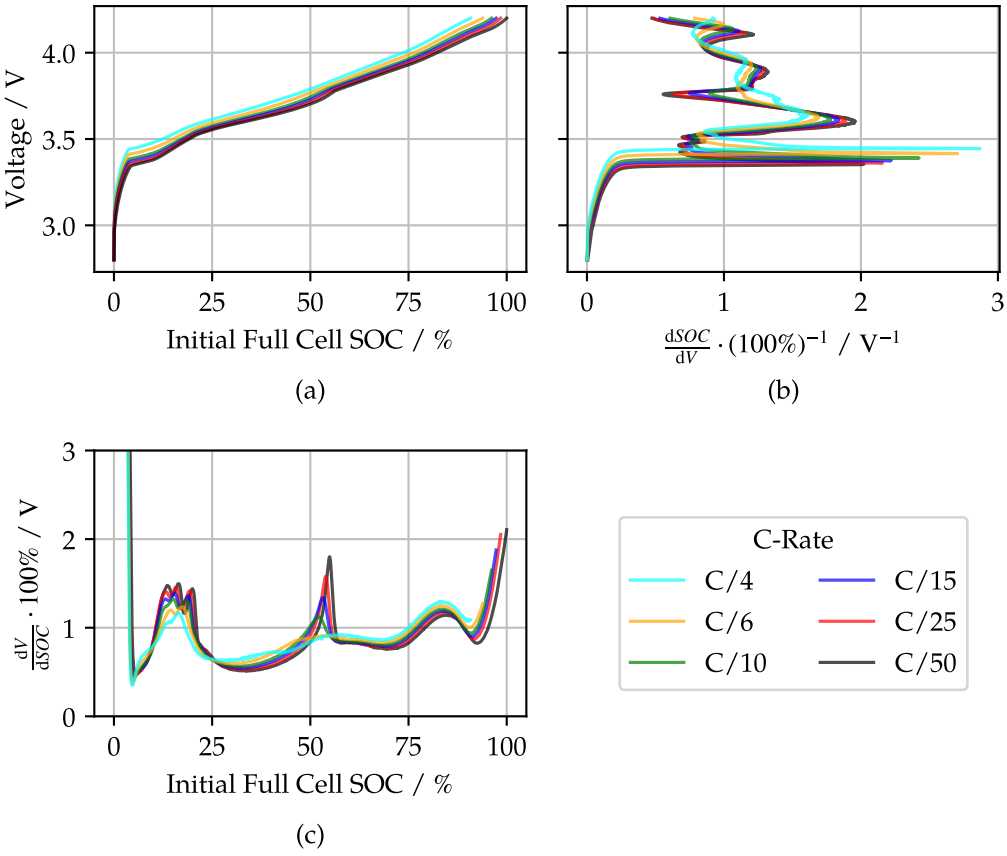

Figure 1.13: Illustration of potential input data for the open-circuit voltage (OCV) model derived from the mechanistic modeling approach. With higher C-rates of the voltage charging curve (a), the features in the incremental capacity analysis (ICA) (b), and differential voltage analysis (DVA) (c) vanish. The complexity of the optimization process increases with higher C-rate values and narrower available charging windows. The displayed charging curves correspond to a pristine nickel cobalt alumnium oxide (NCA)-graphite battery.

If the cathode OCP exhibits a detectable gradient, as is the case for materials such as NMC or NCA, Equation 1.46 can be modified to calculate the deviation only within the overlapping section of the measured data. This section is defined between $\mathrm{OCV}_{\mathrm{meas,min}}$ and $\mathrm{OCV}_{\mathrm{meas,max}}$, which represent the minimum and maximum values of the measured partial OCV curve. This condition can be added as inequality constraint:

$$\begin{aligned} \vartheta = \arg\min_{\vartheta} \quad & \| \mathrm{OCV}_{\mathrm{meas}}(\mathrm{SOC}) - \mathrm{OCV}_{\mathrm{reco}}(\mathrm{SOC}, \vartheta) \|_2^2 \\ \text{s.t.} \quad & \mathrm{OCV}_{\mathrm{reco}}(\mathrm{SOC}, \vartheta) \geq \mathrm{OCV}_{\mathrm{meas,min}} \\ & \mathrm{OCV}_{\mathrm{reco}}(\mathrm{SOC}, \vartheta) \leq \mathrm{OCV}_{\mathrm{meas,max}} \end{aligned} \tag{1.53}$$

For materials with a flat OCV characteristic, such as LFP, this approach is not feasible. Schmitt et al. [27] and Yang et al. [55] proposed alternative methods in such cases. Schmitt et al. [27]

adjusted the β-parameters to account for the estimated starting SOC, denoted as $SOC_{start,est}$:

$$\beta'_{NE} = \beta_{NE} - SOC_{start,est} \tag{1.54}$$

$$\beta'_{PE} = \beta_{PE} - SOC_{start,est} \tag{1.55}$$

This adjustment limits the comparable SOC window to the range of the measured data. A subsequent back-transformation restores the original alignment parameter set, enabling the reconstruction of the full OCV curve, the DMs, and the SOH_C. Similar, Yang et al. [55] transformed the input data to the fresh cell SOC for cost calculation. For relaxed voltage points [100] and low C-rates [27], the minimum available SOC span is reported as 40 % to 100 % [100] and 20 % to 70 % [27].

Various approaches exist for real-world charging data with higher C-rates [27; 54; 55; 91; 166]. Again, Schmitt et al. [27] and Yang et al. [55] have used similar approaches and reconstructed the measured partial OCV curve by subtracting a constant ohmic offset from the partial voltage charging curve. As can be seen in Figure 1.13, the features of the OCV vanish for higher C-rates. Lu et al. [54] and Friedrich et al. [166], however, stated that a SOC-dependent overpotential correction is superior. Recent findings state various upper limits for these methods and accurate SOH_C estimation: Schmitt et al. [27] propose C-rates up to C/4 and a SOC window from 10 % to 80 %, Yang et al. [55] and Chen et al. [91] even state a maximum C-rate up to C/3 and a SOC window from 20 % to 70 % [55] or 40 % to 100 % [91], respectively. Accurate OCV reconstruction and, with that, DM estimation, however, is yet only feasible for C-rates below C/15 [27].

Kunz et al. [186] have introduced a novel approach by modifying the OCV model to utilize heat flow measurements instead of voltage for assessing DMs in commercial cylindrical cells. Although industrialization is infeasible, the approach offers a valid alternative for laboratory studies. This method leverages isothermal calorimetry and surface temperature measurements combined with a zero-dimensional thermal model, enabling efficient entropy-based diagnostics that eliminate the need for thermodynamic equilibrium and predefined markers.

The literature indicates that accurate OCV reconstruction and DM estimation are only feasible under specific conditions, such as low C-rates (e.g., below C/15 [27]) and sufficiently large SOC windows, such as 20 % to 70 % [27; 55], 40 % to 100 % [91; 100], or 20 % to 70 % [55]. However, data-driven methods, particularly neural networks, offer the potential to overcome these limitations by uncovering hidden patterns in the input data. Such approaches could enable the use of higher C-rates, shorter charging segments, or even dynamic driving profiles, thereby expanding the applicability of OCV reconstruction and DM estimation to more realistic and challenging scenarios.

1.2.3 SOH Estimation based on Neural Networks

Neural networks have been a foundational concept in AI for over six decades [122], yet their application within the battery research community has significantly accelerated only in the past decade [66; 111–115; 117–121]. As empirical models often struggle to accurately capture the intricate dynamics of battery degradation, neural networks offer a powerful alternative by uncovering hidden patterns within complex datasets. Neural networks are computational models inspired by the human brain, designed to recognize patterns and relationships in data. They can be considered empirical models because they learn from data through experience. In Figure 1.8, they are, however, classified into a unique category as their working principle varies greatly from default empirical models.

While a multitude of different realizations for AI exist, this introduction only focuses on the required building blocks to follow the chosen approach of this work, as shown in Figure 1.10: The working principle, neural network architectures, and hyperparameter tuning. The fundamental problems of data scarcity and data dependence in neural network applications are discussed, introducing two possible solution strategies: PINNs and transfer learning.

Working Principle

The core of neural networks lies in their iterative training process, which is composed of three fundamental steps: (1) Initial parameterization, typically performed randomly; (2) computation of the loss, which involves comparing the model's predictions to the ground truth; and (3) updating the model parameters in the direction that reduces the loss. This process can be illustrated through the example of linear regression: In linear regression, the goal is to find a function $f(x)$ that predicts the outcome y based on some input x. This relationship can be expressed as:

$$f(x) = wx + b \tag{1.56}$$

where w represents the weights and b is the bias term.

Given a dataset $\mathcal{D}_{\text{train}} = \{(x_i, y_i)\}_{i=1}^{n}$, which is a subset of the dataset $\mathcal{D}$, the task is to determine the optimal parameter configuration (w^*, b^*). This is achieved by minimizing the loss function over a subset of the dataset $\mathcal{D}_{\text{train}}$, which typically comprises about 50 % to 80 % of the entire dataset $\mathcal{D}$ [122; 187; 188]. For instance, using the mean squared error as the loss function, the objective can be formulated as:

$$(w^*, b^*) = \arg\min_{(w,b)} f_{(w,b)}(x) = \arg\min_{(w,b)} \frac{1}{n} \sum_{i=1}^{n} \left((wx_i + b) - y_i\right)^2 \tag{1.57}$$

Most neural network strategies employ differentiable objective functions, allowing the use of gradient descent for optimization. The differentiability of the loss function enables the

calculation of partial derivatives with respect to the weights and biases, facilitating updates that reduce the loss:

$$\frac{\partial f_{(w,b)}(x)}{\partial w} = \frac{1}{n}\sum_{i=1}^{n}(-2x_i(y_i-(wx_i+b))) \tag{1.58}$$

$$\frac{\partial f_{(w,b)}(x)}{\partial b} = \frac{1}{n}\sum_{i=1}^{n}(-2(y_i-(wx_i+b))) \tag{1.59}$$

This iterative process continues through all samples i in the training dataset $\mathcal{D}_{\text{train}}$ to find the optimal parameters (w^*, b^*) that minimize the loss function. As neural networks are composed of numerous such functions, the linear regression example provides key insights into their working principle [9; 122; 187].

In the case of neural networks, this structure is extended to several layers l each with several input neurons $a_0^{(l-1)}, \ldots, a_j^{(l-1)}$ which are each processed with individual weights $w_n^{(l-1)}$, where n corresponds to the index of the current neuron, and biases $b^{(l-1)}$ processed by a scaling or activation function σ. Subfigure 1.14 (a) illustrates the relation for two layers and one output. Common scaling functions are the sigmoid function, the rectified linear unit (ReLU) or the hyperbolic tangent (tanh) function, visualized in Subfigure 1.14 (b).

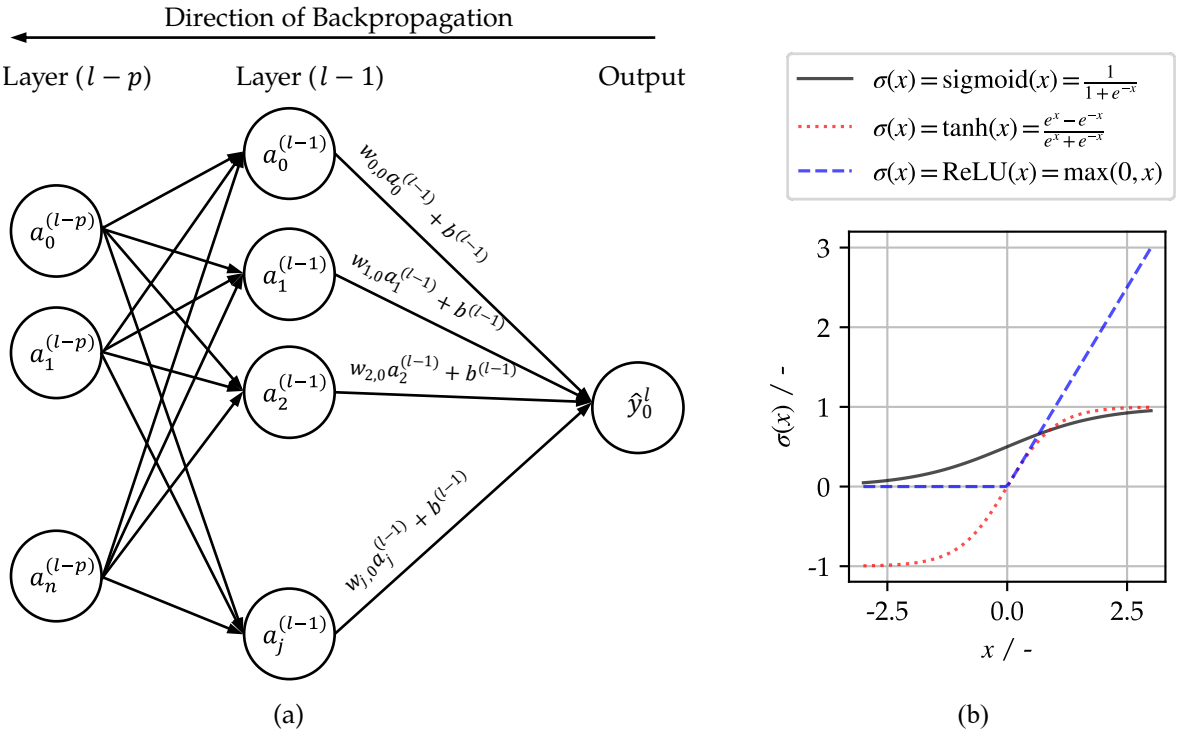

Figure 1.14: (a) Representation of a neural network with two layers and one output, including the individual weights w and biases b. Figure adapted from Burkov [189] and Hamar et al. [9]. (b) Overview of the three most common activation functions.

The function in Equation 1.56 is thus expressed as:

$$\hat{y}_0^l = \sigma(w_n^{(l-1)} a^{(l-1)} + b^{(l-1)}) \tag{1.60}$$

For a fully connected layer Z^l this can be expressed in matrix form:

$$Z^l = \begin{bmatrix} z_0^l \\ z_1^l \\ \dots \\ z_k^l \end{bmatrix} = \sigma\left(\begin{bmatrix} w_{0,0} & w_{0,1} & \dots & w_{0,j} \\ w_{1,0} & w_{1,1} & \dots & w_{1,j} \\ \dots\dots & \dots & \dots & \\ w_{k,0} & w_{k,1} & \dots & w_{k,j} \end{bmatrix} \begin{bmatrix} a_0^0 \\ a_1^0 \\ \dots \\ a_j^0 \end{bmatrix} + \begin{bmatrix} b_0^l \\ b_1^l \\ \dots \\ b_j^l \end{bmatrix} \right) \tag{1.61}$$

where j is the neuron index of the previous layer and k is the neuron index in the subsequent layer.

Similar to the linear regression task, the estimated output Z_i^l is compared to the true output y_i in a cost function δ, e.g., for the squared error:

$$\delta = \sum_{i=0}^{l} (Z_i^l - y_i)^2 \tag{1.62}$$

Backpropagation minimizes the cost function by iteratively adjusting parameters using gradient descent, moving towards a local minimum. This involves calculating the partial derivatives of the cost function with respect to each parameter (a, w, and b) for each layer, using the chain rule:

$$-\nabla\delta = -\nabla \sum_{i=0}^{l} \left(Z_i^l - y_i\right)^2 = \frac{\partial \delta}{\partial W^l} \cdot \frac{\partial \delta}{\partial a^{(l-p)}} \cdot \frac{\partial \delta}{\partial b^l} \tag{1.63}$$

$$\frac{\partial \delta}{\partial W^l} = \frac{\partial Z^l}{\partial W^l} \cdot \frac{\partial a^l}{\partial Z^l} \cdot \frac{\partial \delta}{\partial a^l} \tag{1.64}$$

$$\frac{\partial \delta}{\partial a^{(l-p)}} = \frac{\partial Z^l}{\partial a^{(l-p)}} \cdot \frac{\partial a^l}{\partial Z^l} \cdot \frac{\partial \delta}{\partial a^l} \tag{1.65}$$

$$\frac{\partial \delta}{\partial b^l} = \frac{\partial Z^l}{\partial b^l} \cdot \frac{\partial a^l}{\partial Z^l} \cdot \frac{\partial \delta}{\partial a^l} \tag{1.66}$$

In practical applications, the entire training process is seamlessly integrated into machine learning packages such as TensorFlow [190], scikit-learn [191], and PyTorch [192].

With this understanding, it becomes evident that linear algebra underpins successful neural network training. This also highlights the distinction between empirical and data-driven models: Neural networks provide significant flexibility due to their numerous parameters, which vary with the number of layers and neurons. Additionally, various topologies exist, further altering the model's structure [9; 122; 187].

Architectures

The principle of hierarchical feature engineering highlights that the strength of deep learning models lies in their use of nonlinear activation functions, which enable each layer to construct progressively complex features relevant to the predictive task [122; 188]. This inherent capability makes deep neural networks particularly powerful, which is why this work focuses exclusively on them. Despite the multitude of neural network variations, only a few have been successfully adapted for battery SOH estimation [61–66; 102–121]. This work focuses on three types of layers: feed-forward neural network (FNN) layers, long short-term memory neural network (LSTM) layers, and temporal convolutional neural network (TCN) layers.

As illustrated in Subfigure 1.14 (a), in a fully connected layer, each neuron in layer $(l-2)$ is connected to every neuron in the subsequent layer $(l-1)$, and so on. Due to this structure and the direction of information flow, these layers are often referred to as dense layers or, when multiple layers are involved, as in FNN [188]. Fully connected layers offer several advantages: They have the capability to approximate any function, provided there are sufficient neurons and layers, which makes them highly versatile. Fully connected layers are straightforward to implement and comprehend, as each neuron in one layer is connected to every neuron in the subsequent layer. They are also capable of learning complex feature representations, especially when used in conjunction with nonlinear activation functions [188]. However, they also have some drawbacks: Because of their many parameters, FNN are computationally demanding and prone to overfitting [188]. Fully connected layers cannot take advantage of spatial or temporal structures, thus, they frequently struggle to extract features from raw data. To extract features from the data, they are therefore frequently combined with sophisticated layer structures like LSTM or TCN [64–66; 105–108; 112; 113; 119]. Figure 1.15 shows the main building blocks of the LSTM layer (Subfigure 1.15 (a)) and the TCN layer (Subfigures 1.15 (b) and (c)).

LSTM layers, first introduced by Hochreiter and Schmidhuber [194], are an advanced form of RNN layers. Unlike fully connected layers, RNNs process a sequence of inputs, i.e., time-series data. Their variable number of layers corresponds to a specific timestep in the sequence, where each layer utilizes the same set of parameters. The recurrent structure is achieved by a repetitive structure, allowing the RNN to handle sequences of data [188]. RNNs, however, suffer under the so-called vanishing or exploding gradient problem that originates from the multiple propagation over many stages during backpropagation, and hinders RNNs from learning long-term dependencies [122]. Hochreiter and Schmidhuber [194] introduced LSTM layers as the solution for this problem. The main building blocks of an LSTM memory cell are shown in Subfigure 1.15 (a). The cell has an internal recurrent connection, where the input is calculated by a regular neuron. The input gate allows accumulation of the input data flow through a sigmoid activation function, which is also used in all other gates of the LSTM memory cell. The output gate can shut down the output when necessary. The core idea of LSTM is that the gradient can flow through self-loops connected to the state unit.

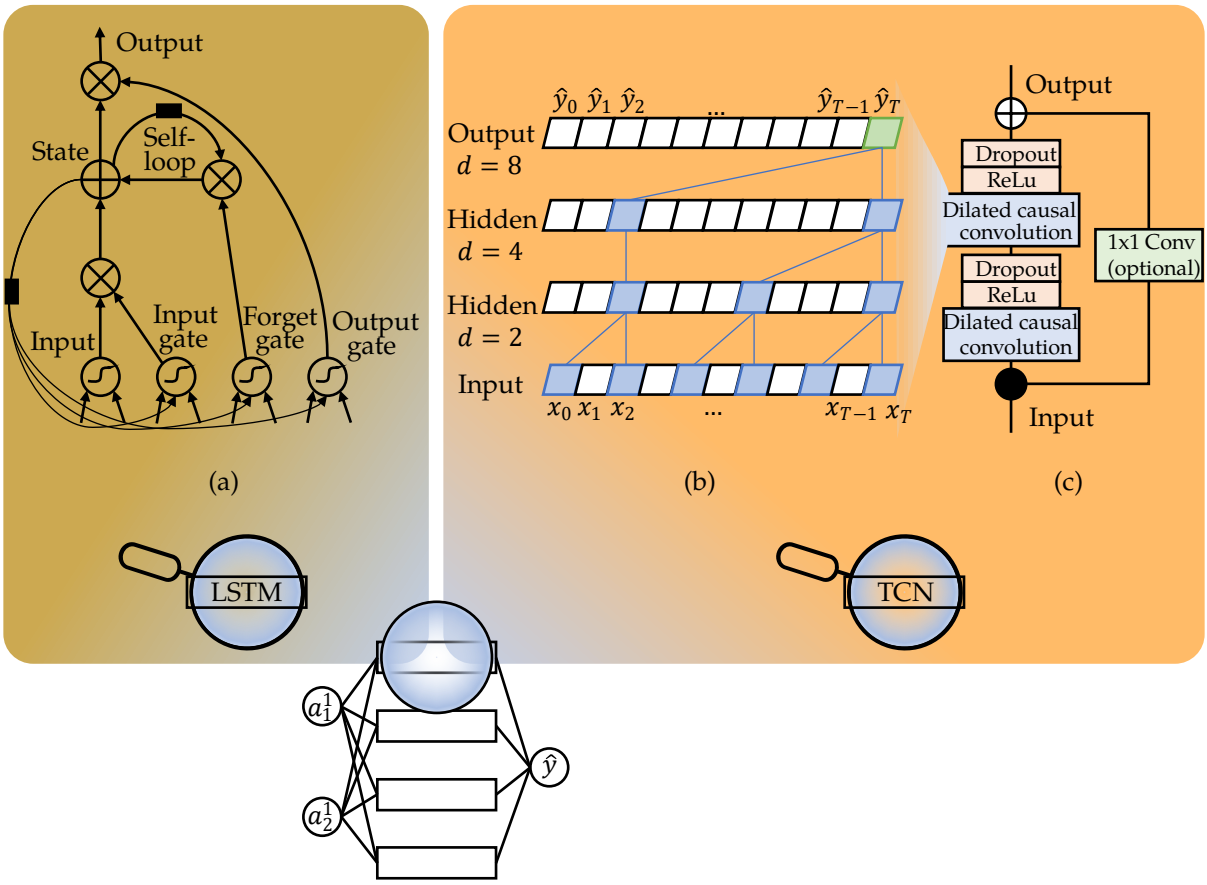

Figure 1.15: Illustration of a neural network with two different layer architectures: (a) long short-term memory neural network (LSTM) memory cell, adapted from Goodfellow et al. [122]. (b) Dilated causal convolution for a kernel size of 2 and dilation factors d within (c) a temporal convolutional neural network (TCN) residual block, which is interconnected with dropout and rectified linear unit (ReLU) layers. Figure adapted from Bai et al. [193] and Bockrath et al. [120]

Modifications of the self-loop weight allow dynamic control of the time scale integration via the forget gate [122; 188; 194]. This unique structure enables the cells to capture both long- and short-term dependencies within sequence data, making them extremely useful for time-series forecasting or regression tasks from time-series data, as in many battery state estimation applications [111–115].

CNNs follow a completely different working principle, as they exploit mathematical convolution instead of matrix multiplication [122]. Initially inspired by a biological experiment on a cat's visual cortex [188], they have been widely adapted for many different applications [122; 188]. CNNs are especially applicable to grid-like data, i.e., images or occasionally time-series data. One default convolutional layer has a three dimensional structure with height, width, and channels. For example, a colorful image with $32 \times 32 \times 3$ pixels has 32 height, 32 width, and 3 channels, each one for red, green, and blue [188]. A kernel or filter, which is generally smaller than the input, allows rapid reduction of the data and enhances efficiency. In general, by appropriately selecting the kernel size, stride, and padding, the feature map can be

efficiently reduced while retaining the essential information. In the case of an $5 \times 5 \times 3$ filter with a stride of 1 and no zero padding, the $32 \times 32 \times 3$ image is reduced to $28 \times 28 \times 5$ due to the filter convolving over the image. CNNs are further perfectly suited for feature extraction including edge detection from raw data as they exhibit equivariant representations and are capable of handling variable input size [122; 188]. CNNs are modifiable by many other settings and layers, including input data modifications such as padding, strides, pooling, and ReLU-layers, which is well documented in literature [122; 188].

Standalone CNNs, however, are not perfectly suited for time-series data as they must be coupled with LSTM layers to not only extract but also interpret features. Lea et al. [116], therefore, introduced the novel TCN architecture that was initially introduced for action segmentation and detection. In one of the first benchmarks [193], TCNs outperform RNNs in terms of efficiency and accuracy as they require less parameter and can process raw data [193].

The main building blocks are schemed in Subfigures 1.15 (b) and (c). As shown in Subfigure 1.15 (b) dilated TCNs can work for sequence modeling $\hat{y}_0, \ldots, \hat{y}_T = f(x_0, \ldots, x_T)$. The dilated convolution circumvents information leakage from the future as the output $\hat{y}_T$ only processes features from time step T and earlier. In contrast to CNNs, TCNs exploit dilated convolution which allows the processing of large receptive field by dilating a kernel of size k by a dilation factor d. This results in the convolution operation $F()$ on the element s:

$$F(s) = (x *_d f)(s) = \sum_{i=0}^{k-1} f(i) \cdot x_{s-d \cdot i} \tag{1.67}$$

for a 1D-sequence input $x \in \mathbb{R}^n$ and the filter $f : \{0, \ldots, k-1\} \rightarrow \mathbb{R}$. The final receptive field per layer can be calculated by:

$$\mathrm{R} = 2^l(k-1) \tag{1.68}$$

with l as the number of layers [120; 126; 193].

In Subfigure 1.15 (b), this dilated causal convolution is exemplarily shown for $k = 2$ and $d = (2, 4, 8)$, visualizing the high data compression. The dilated causal convolution is arranged in a residual block including ReLU and dropout layer (Subfigure 1.15 (c)). A dropout layer is a very common regularization technique that randomly sets the inputs to the layers to zero (randomly dropping out) during each update of the training phase. In Subfigure 1.15 (c) an optional 1×1 CNN processes the input in case of differing dimensions. The final output y is the applied transformation $\mathcal{F}$ of the input x added to the input x before flowing through the activation function σ [193]:

$$y = \sigma(x + \mathcal{F}(x)) \tag{1.69}$$

Due to these advantages for time-series modeling, LSTMs and TCNs are often employed for battery SOH estimation [66; 111–115; 117–121]. Many publications [111–115] explore the usage of LSTM networks for $\mathrm{SOH_C}$ estimation, demonstrating their effectiveness in capturing temporal dependencies for accurate battery health predictions. Peng et al. [114] proposed

a method combining multi-health feature extraction with an improved LSTM model, optimized using an improved quantum particle swarm optimization algorithm. Their approach improved SOH_C estimation accuracy and robustness, achieving a MAE (percentage points (pp)) within 1 % for the NASA dataset [195]. For the same dataset, Zhang et al. [115] developed an SOH_C estimation method using incremental capacity and LSTM networks. They introduced an improved feature extraction method based on voltage time-series data, which retains key information and reduces computational efforts. The LSTM model achieved superior accuracy with a mean absolute percentage error (MAPE) of less than 2 % across different battery samples. A recent publication by Guo et al. [66] revealed the ability of LSTM networks to reconstruct the OCV and estimate the underlying DMs. Their LSTM network was capable of estimating the partial OCV from partial charging curves, which is later fed into an optimization regime. There, the OCV is reconstructed by the mechanistic modeling approach and linear regression. The approach achieves a MAE of less than 20 mV in OCV reconstruction and a SOH_C MAE of less than 1.3 % (pp) for the Oxford dataset [196]. The method is verified across different charging segment lengths, demonstrating consistent results and improved estimation accuracy and stability in comparison to purely data-driven or purely mechanistic models [66].

Recently, TCNs are handled as the benchmark architecture for battery SOH estimation from time-series data [117–121]. Li [119] proposed a hybrid model combining TCN and LSTM for SOH_C estimation. The TCN-LSTM model was tested against CNN-LSTM, TCN, and LSTM models using the public NASA [195] and Oxford [196] datasets. The TCN layers were designed to extract the health features out of the voltage, current, and temperature time-series signals during discharge cycles. The TCN-LSTM network showed significant accuracy improvements in SOH_C estimation in comparison to the other architectures, with RMSE reductions of over 16 % in NASA [195] and 14 % in Oxford [196] datasets. Similarly, Liu et al. [121], compared their improved TCN with default TCN and LSTM networks. Different features were extracted using principal component analysis and derived from empirical mode decomposition of the capacity decay curve. The improved TCN model incorporates a channel attention module and a residual shrinkage network to enhance feature processing and adaptive threshold training. Tested on the NASA battery dataset [195], the improved TCN network achieved a MAE of 2 %, outperforming LSTM and default TCN networks.

This work presents new research [51; 126] accelerating the usage of combined TCN-LSTM networks for OCV reconstruction and DM estimation, marking the first exploration of TCNs in these areas.

Hyperparameter Tuning

While the dataset is the most crucial component for successful deep learning applications, the selection of hyperparameters also plays a significant role. Hyperparameters refer to any parameter within a neural network that is not a weight and, therefore, is not updated during

the training process. In other words, hyperparameters are chosen by the model developer. Generally, hyperparameters can be categorized into those that define the architecture, such as the number and type of layers, number of neurons, activation functions, and specific settings within the layer itself (e.g., filter size in a CNN), and those that guide the learning process, including the optimizer, data split, batch size, and epochs. Depending on the specific implementation, there can be many more [122; 188].

Hyperparameter tuning aims to assess various combinations to identify the hyperparameters that yield the lowest cost. Hence, it is an optimization problem itself, where the objective function is the training or validation loss [122]. The most common tuning strategies include grid search, random search, and Bayesian optimization. Grid search is a straightforward approach, where the search space, i.e., the space of tunable parameters, is covered with equidistant points. The set of parameters that returns the lowest cost is selected as the optimal parameter set. However, the search space is non-convex, and several local optima may exist between the selected grid points. Random search, an advancement of grid search, aims to minimize this risk by defining search points randomly within the search space. Both approaches can become infeasible for larger search spaces, as the number of evaluations grows exponentially with the number of hyperparameters [122]. For instance, if seven parameters are to be tuned during grid search and five different search points are defined for each parameter, a total of $5^7 = 78,125$ models must be evaluated. Even if one trial takes only 1 min, the entire grid search would take more than 54 days. Bayesian hyperparameter tuning significantly reduces the computational cost by introducing a surrogate model that follows the rules of exploration and exploitation [122]. This probabilistic surrogate model, based on Bayes' theorem, considers past evaluations to prune unpromising combinations. It effectively moves in the direction of gradient descent, even if the objective function is non-differentiable, and, hence, the gradient cannot be computed, and is likely to yield a local optimum within a few trials. Hyperparameter tuning requires initializing the set of parameters to be tuned and defining the range of the search space. After evaluating an initial set of points, the probabilistic analysis begins, leading to a local optimum [122; 188; 197].

Due to these beneficial properties of the Bayesian hyperparameter, it is regarded as the state of the art for neural network optimization in the context of battery SOH estimation [51; 119; 120; 126; 149; 197–201]. Li et al. [200] introduced a deep neural network combining CNN and LSTM layers for battery SOH_C and remaining useful life estimation. The study utilized Bayesian optimization, guided by a prior distribution obtained through the Kolmogorov–Smirnov test [202], to automatically configure hyperparameters, significantly reducing manual tuning efforts. This approach demonstrated superior accuracy, compared to existing neural network models, and highlighted Bayesian optimization as the state-of-the-art method for hyperparameter tuning in battery SOH estimation. Similarly, Mazzi et al. [201] introduced a hybrid deep neural network for battery SOH_C estimation. The study employed Bayesian optimization to efficiently tune hyperparameters, achieving a low MAE of 2.1 % (pp) in just 19 iterations. While Bayesian tuning is highly efficient, they emphasized

the importance of smart selection of tunable parameters to reduce the search space. Choosing default values for certain hyperparameters, such as using Adam [203] as the default optimizer or fixing the batch size, is a promising strategy to minimize effort and complexity [201].

Despite all the recent advances in developing and tuning neural network architectures, the crucial ingredient for successful data-driven modeling remains the source data.

Data Scarcity and Solution Approaches: Transfer Learning and Physics-Informed Neural Networks

The lack of sufficient training data is referred to as data scarcity. Data scarcity is seen as the biggest hurdle for the generalized application of neural networks in any discipline [122; 188]. Common strategies employ data augmentation or semi-supervised learning to overcome this hurdle [122]. They, however, still have to face the challenge of data dependence and domain shifts, limiting the generalization [204]. In the automotive sector, the issue of insufficient training data is exacerbated by the limited number of BEV SOH references available. Validated SOH labels are particularly inaccessible for new vehicle generations due to the insufficient time within the development cycle to accumulate degradation data. Additionally, training data cannot typically be directly obtained from the BMS because of limited memory and often inadequate sampling frequency [9; 123; 141]. Consequently, transferring knowledge from the cell level to real-world BEVs or between varying vehicle generations is a critical task in the automotive industry.

This thesis presents two novel approaches on how to circumvent this fundamental issue and helps to bridge the gap towards generalizable data-driven models. The core idea of both methods, transferring knowledge via the model itself or the data, is illustrated in Figure 1.16. The detailed description, on which this summary is based on, can be found in the included publications of this dissertation [126; 149].

As can be seen in Subfigure 1.16 (a), transfer learning exploits two different domains: The source domain $\mathcal{D}_{\text{Source}}$ and the target domain $\mathcal{D}_{\text{Target}}$. Conventional deep learning requires both domains to be independent and identically distributed. Transfer learning circumvents this necessity. The following introduction to transfer learning refers to the published work [126] and to Tan et al. [204] and Weber et al. [205]:

A domain $\mathcal{D} = \{\chi, P(X)\}$ is characterized by the feature space χ and the edge probability distribution $P(X)$ over the features, where $X = \{x_1, \ldots, x_n\} \in \chi$. A task $\mathcal{T} = \{y, f(x)\}$ comprises the label space y and the target prediction function $f(x)$, which can also be interpreted as the conditional probability function $P(y \mid x)$ [126; 204; 205].

Definition 1 (Transfer Learning)**.** Transfer Learning seeks to improve the performance of the predictive function $f_{\mathcal{T}}$ for the primary learning task $\mathcal{T}_{\text{Target}}$ by utilizing latent knowledge obtained from an auxiliary learning task $\mathcal{T}_{\text{Source}}$ and its corresponding dataset $\mathcal{D}_{\text{Source}}$, where $\mathcal{D}_{\text{Source}} \neq \mathcal{D}_{\text{Target}}$ or $\mathcal{T}_{\text{Source}} \neq \mathcal{T}_{\text{Target}}$ [126; 204; 205].

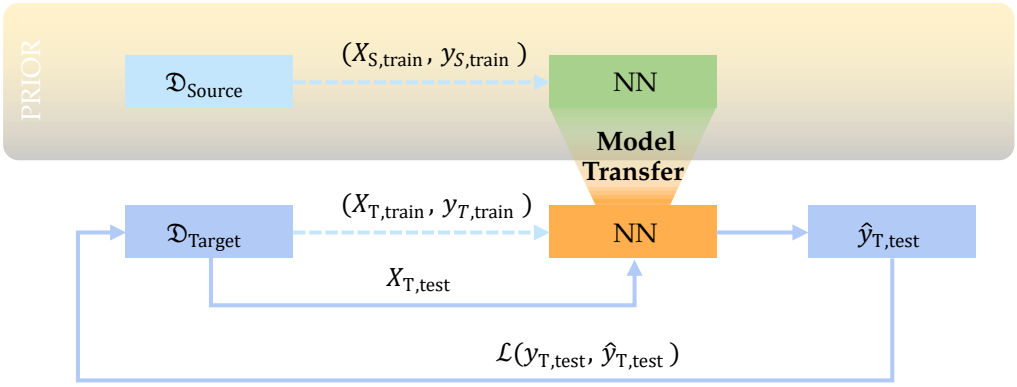

(a)

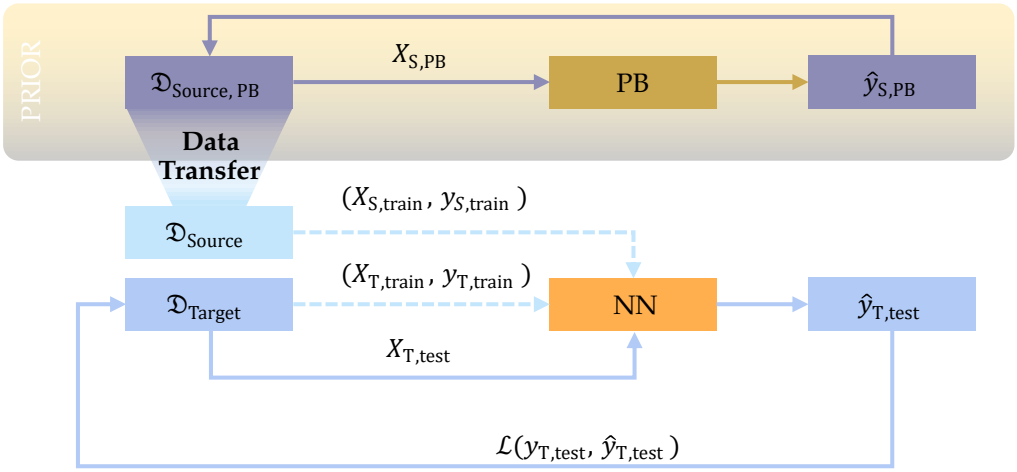

(b)

Figure 1.16: The problem of data scarcity and two possible solution approaches. (a) The model-based transfer learning approach solves the problem by pretraining a blank model on extensive data from other datasets $\mathcal{D}_{\text{Source}}$ prior and transferring the knowledge to another domain $\mathcal{D}_{\text{Target}}$. (b) The sequential PINN approach [147] accumulates more training data $\mathcal{D}_{\text{Source}}$ by running physics-based simulations with unlabeled data $\mathcal{D}_{\text{Source,PB}}$ prior.

Although no universal guideline exists for the ratio between $\mathcal{D}_{\text{Source}}$ and $\mathcal{D}_{\text{Target}}$, it is advisable for the dataset $\mathcal{D}_{\text{Source}}$ to be substantially larger than $\mathcal{D}_{\text{Target}}$. This approach enhances the likelihood of rapid generalization within the target domain [122]. With these properties, transfer learning reduces training time, improves generalization, and has a decreased dependency on large-scale data collection for the target task [206].

For time-series regression problems transfer learning employs domain adaptation, i.e., $\mathcal{D}_{\text{Source}} \neq \mathcal{D}_{\text{Target}}$ [205]. As surveyed by Tan et al. [204] deep transfer learning with time-series data can be broadly categorized into four main types:

- **Instance-based Transfer Learning**: The strategy focuses on identifying and re-weighting data samples from the source domain $\mathcal{D}_{\text{Source}}$ that are most relevant to the target domain $\mathcal{D}_{\text{Target}}$. The fundamental idea is that even if the source and target domains differ, a carefully selected subset of source instances can enhance the performance of the target model. The relevance of these instances is typically scaled to maximize their beneficial impact [204].
- **Adversarial-based Transfer Learning**: Inspired by generative adversarial networks, this approach establishes an adversarial relationship between two components. A feature extractor learns to produce feature representations that are indistinguishable between the source and target domains. Concurrently, a *domain discriminator* attempts to identify the origin of these features. The goal is to derive representations that are both highly effective for the main learning task and domain-invariant, ensuring successful knowledge transfer [204; 205].
- **Feature-based Transfer Learning**: This method aims to find a common feature space, where the data distributions of the source and target domains are more aligned. Data from both domains $\mathcal{D}_{\text{Source}}$ and $\mathcal{D}_{\text{Target}}$ are projected into this new, shared representation $\mathcal{D}_{\text{Shared}}$, which reduces domain discrepancy. This facilitates applying a model trained on the source data to the target data within this unified space [204].
- **Model-based Transfer Learning**: This widely adopted method, particularly prominent in deep learning, is visualized in Subfigure 1.16 (a). It involves leveraging a model, or parts of it, pre-trained on a large source dataset $\mathcal{D}_{\text{Source}}$. As the diagram illustrates, parameters or entire layers are transferred to initialize a new model for the target task $\mathcal{T}_{\text{Target}}$. This new model is then typically *fine-tuned* by continuing the training process on the target dataset $\mathcal{D}_{\text{Target}}$. The final performance can be evaluated by the loss calculation $\mathcal{L}(y_{\text{T,test}}, \hat{y}_{\text{T,test}})$. The core justification is that the initial layers of a pre-trained network learn general-purpose features that are widely applicable, providing an excellent starting point for the target task [204–206].

These transfer learning methods enable the development of robust and accurate models even with limited target data, where model-based transfer learning is the most prominent approach for battery SOH estimation [141; 143].

As the literature and Figure 1.16 reveal, a clear separation between transfer learning and PINN is not always possible. Many PINN approaches leverage methods which traditionally belong to transfer learning and vice versa. The following state of the art, however, presents recent publications, where a clear assignment, following Definition 1, is possible. While initially transfer learning methods were mostly applied for battery SOH estimation [61; 124; 125; 127–132; 134–136; 138–146], more recent implementations even tackle the problem of OCV reconstruction and DM estimation [51; 123; 126; 133; 137].

Chen et al. [124] compared different transfer learning strategies for varying degrees of domain shift in the context of battery SOH estimation. With uniform features derived from partial charging voltage segments, the degree of domain shift was defined by the battery type and the charging strategy. They propose that model-based transfer learning, namely direct transfer learning or fine-tuning, are optimal for minimal domain shifts. Adversarial-based transfer learning, i.e., domain-adversarial neural networks, are recommended for substantial domain shifts.

Huang et al. [127] compared two different fine-tuning strategies applied to an LSTM network. The first strategy involved fine-tuning the fully connected layers and the second strategy fine-tuning of all layers. Features were extracted from partial CC charging voltage curves. Regardless the strategy or the domain shift, all transfer learning models kept an SOH_C estimation RMSE under 1.44 %. This demonstrates the reduced requirements for training data in the target domain and increased accuracy in comparison to conventional deep learning methods.

Chen et al. [123] extended the fine-tuning approach to DM estimation and explored domain shifts between experimental and BEV batteries. With features derived from the ICA, their LSTM model yielded a MAE below 6 % (pp) for all DMs and batteries.

The extension to full OCV reconstruction was accomplished by Zhou et al. [133] with a deep neural network. Only 50 seconds of partial charging sufficed to train and fine-tune the transfer learning model. Even across battery types, their model achieved relative OCV curve reconstruction RMSEs below 0.5 % and 2.5 % for NCA and LFP batteries, respectively.

While harvesting suitable degradation datasets including OCVs and DM labels is challenging, synthetically generated source datasets offer an easy solution. Especially this direction is heavily researched in recent work [131; 137; 138]. Within this work, two novel approaches [51; 126] are presented that extend the state of the art. Both methods explore the application of transfer learning for precise OCV reconstruction and DM estimation between synthetic source and experimental target domains.

Subfigure 1.16 (b) presents an alternative solution approach, namely PINNs. PINNs couple neural networks with physics-based models to exploit the extrapolation capability of simulation with the interpolation capability of deep learning. There exist, however, many different architectures which greatly vary in their structure and application. This thesis follows the introduced definitions for PINNs by Aykol et al. [147]. There, they state that PINNs in the context of battery state estimation are either hybrid or sequential, where hybrid PINNs integrate one model into the other, and sequential PINNs have a sequential structure.

This brief introduction of the varying architectures follows the description by Aykol et al. [147] and is further discussed in one of the included publications [149] of this thesis. Aykol et al. [147] stated that there are three sequential and two hybrid approaches. This PINN landscape, however, is not complete and is continuously extended by recent research.

- **Sequential Residual Learning Approach**: This approach feeds the output of a physics-based degradation model into a neural network update model. The neural network learns the residual between the physics-based model's estimation ($\hat{y}_{\text{PB}}$) and the true label ($\hat{y}_{\text{true}}$), using this learned residual to update the estimation and minimize error. While the physics-based model captures basic aging effects, the neural network is promising for learning more complex degradation mechanisms. The application, however, is limited by the complexity of the numerical solution for the physics-based model and its implemented degradation mechanisms [147; 149].
- **Sequential Transfer Learning Approach**: This approach is shown in Subfigure 1.16 (b) and runs the complex physics-based model temporally decoupled (prior) with arbitrary input data $\mathcal{D}_{\text{Source,PB}}$. The estimated output data $\hat{y}_{\text{S,PB}}$ may include internal battery states such as concentrations and potentials and yields a generated dataset $\mathcal{D}_{\text{Source}}$. This dataset is combined with experimental data from the target domain $(X_{\text{T,train}}, y_{\text{T,train}}) \in \mathcal{D}_{\text{Target}}$ to train the neural network. During operation, time-series data from the target domain $X_{\text{T,test}} \in \mathcal{D}_{\text{Target}}$ can be used to estimate $\hat{y}_{\text{T,test}}$ with low computational cost and physical constraints. The loss $\mathcal{L}(y_{\text{T,test}}, \hat{y}_{\text{T,test}})$ is calculated to evaluate the final performance. The final PINN does not depend on the complexity of the physics-based model and is capable of learning the hidden physics of battery degradation [147; 149].
- **Sequential Parameter Learning PINNs**: This approach uses a prior neural network to learn battery parameters over its lifetime, updating the physics-based model with accurate parameters. The physics-based model uses this information to solve for, e.g., SOH_{C}, internal states, or DMs. Reduced physics-based models are necessary to reach onboard applicability [147; 149].
- **Hybrid Physics-Constrained Neural Networks**: This hybrid approach integrates physics-based elements into the neural network, such as in the loss function during training. There is optimism to physically constrain the output by following physico-chemical laws [147; 149]. An adaptation of this approach, leveraging a mechanistic model instead of a purely physics-based model, is presented in this thesis in one of the included publications [51].
- **Hybrid Neural-Network-Accelerated Physics-Based Models**: These models exploit the approximation ability of neural networks to solve underlying partial differential equations (PDEs) of physics-based models with less computational burden. The urgency to integrate degradation mechanisms into physics-based models, however, still limits the application of accurate neural-network-accelerated physics-based models for SOH estimation [147; 149]. This hybrid approach is closely related to the general definition of PINNs, as introduced by Raissi et al. [207; 208]. They exclusively define PINNs as neural networks for PDE approximation. This definition, however, was loosened up by Aykol et al. [147].

Since the introduction of PINNs for battery SOH estimation, many publications explored the usage for varying data [51; 131; 135; 147–165]. Within the PINN SOH estimation landscape, mostly the sequential transfer learning [131; 148; 149; 162–165] and the hybrid physics-constrained neural networks [135; 150–155; 158; 160; 161; 163] are present. Only few publications exploit the approximation ability of neural networks to solve for underlying PDEs of physics-based models [156; 157; 159]. Notably, recently many hybrid PINNs exploit traditional transfer learning strategies, such as the before discussed fine-tuning, to adapt models from one battery type to another [151; 153; 159].

The sequential transfer learning PINN approach, presented by Tian et al. [131], is particularly effective in reducing data requirements for SOH estimation. As synthetic data is fused with experimental data, it is also referred to as *data augmentation* [163]. A physics-based model is employed to generate synthetic charging curves at various aging states. A CNN is then trained using a fused dataset that combines synthetic and experimental data, leveraging the internal knowledge embedded in the variables of the synthetic dataset. This method not only reduces data requirements but also achieves higher performance compared to benchmark models. Furthermore, it is highly scalable and transferable to other battery types.

Ye et al. [150] developed a hybrid PINN for SOH estimation. They extracted features from ICA and differential temperature curves, using the peaks of ICA to form a monotonic relationship with SOH_C decay. This relationship was included as a physical constraint in the loss function. The model achieved a SOH_C RMSE below 1.5 % on the public Oxford [196] and NASA [195] datasets, outperforming conventional deep learning methods.

Similarly, Xiong et al. [161] incorporated a mechanistic modeling approach into the loss function of their hybrid PINN. This integration enables the generation of complete OCV curves and DMs while following physical constraints. Their CNN provides the alignment parameters, which are used internally to reconstruct and compare the OCV within the loss function. Using input data consisting of partial charging voltage segments of 300 mV at C/2, their model outperformed other deep learning models, achieving RMSEs for SOH_C, OCV, and DMs estimation of less than 2.5 %, 12.5 mV, and 1.8 %, respectively.

Méndez-Corbacho et al. [156] employed a hybrid PINN to solve the underlying PDEs of an SPM. This approach enabled the model to process unlabeled data and determine internal states, including stoichiometry, thereby calculating the OCV and DMs. They enhanced the loss function with physics-based terms to ensure adherence to physical laws and achieve generalization. The developed PINN was benchmarked against a SPM solved using the finite element method. The simulation of a complete 1C discharge curve required only 100 ms with the PINN, compared to 2.9 s for the conventional SPM, excluding mesh generation time. The RMSE between the simulation results was 19 mV, demonstrating the significant potential of PINNs for rapid and precise battery diagnosis and prognosis.

1.3 Research Gap and Research Questions

Reviewing the state of the art, several research gaps in the field of battery state estimation are detectable: First, the application of mechanistic models to vehicles necessitates time-series data, which is not feasible for most existing vehicle fleets, giving rise to the first research question:

1. How can the mechanistic model for OCV reconstruction be applied to real-world vehicle data?

Second, conventional deep learning methods demand extensive training data, which not only poses challenges of data scarcity but also leads to issues of data dependence and a lack of adherence to physical laws and interpretability. These interconnected challenges undermine the trustworthiness of the models. Consequently, the second research question which needs to be answered within this thesis is:

2. How can the issue of data scarcity in deep learning be resolved?

To address the broader implications of these challenges, which are also discussed within the scope of the second research question, the third research question is formulated:

3. How can deep learning models be integrated with physics-based models to ensure adherence to physical laws and improve interpretability?

Lastly, while there is a lack of publicly available datasets related to battery aging, particularly for OCV aging, this thesis also considers the potential for future research in this area. The availability of such datasets could enable comprehensive SOH estimation across various metrics, including SOH_C, SOH_R, and SOH_{UBE}, to fully characterize the current state of a LiB in terms of energy, power, and lifetime. The final research question, which serves as an outlook for future exploration, is:

4. What dataset is required to extend SOH estimation to other SOH metrics, such as SOH_R and SOH_{UBE}?

This thesis sets the stage for exploring the research questions outlined above. It aims to provide comprehensive insights and detailed answers to each question.

1.4 Outline of this Work

The comprehensive outline of this work is depicted in Figure 1.17. The core of this thesis is presented through five journal papers in Chapter 2, organized into sections corresponding to the respective research question.

In Section 2.1, a conventional OCV model, specifically the mechanistic model, is adapted for application to real-world vehicle fleet data. This work, titled *The ΔQ-method: State of health and degradation mode estimation for lithium-ion batteries using a mechanistic model with relaxed voltage*

points, involves collecting relaxed voltage points and the accumulated charge between these points from the BMS of the BMW i3 vehicle fleet. The modified OCV model facilitates OCV updates, SOH_C, and DM estimation.

Section 2.2 presents several deep learning approaches addressing not only the data scarcity issue, but also the integration with physics-based models. In Subsection 2.2.1, the work *Physics-Informed Neural Networks for State of Health Estimation in Lithium-Ion Batteries* is presented. The developed PINN enables the fusion of synthetic data, generated from a full P2D model including internal states, with experimental data. This sequential PINN approach not only reduces data requirements but also enhances accuracy by incorporating physical knowledge of LiB degradation into the learning process.

Subsection 2.2.2 addresses data scarcity through an alternative approach, transfer learning from synthetic data, as detailed in *Transfer learning from synthetic data for open-circuit voltage curve reconstruction and state of health estimation of lithium-ion batteries from partial charging segments*. A transfer learning neural network, trained on synthetic data generated by the mechanistic model, is developed to reconstruct the full OCV curve using partial voltage charging segments as input.

This work is further extended in the publication *Physics-constrained transfer learning: Open-circuit voltage curve reconstruction and degradation mode estimation of lithium-ion batteries*, included in Subsection 2.2.3. By sequentially integrating a mechanistic model with the aforementioned transfer learning neural network, physical constraints on the output are achieved, allowing for the estimation of DMs.

Section 2.3 introduces a novel battery aging database in the work *Database of Lithium-Ion Battery Aging: Degradation Modes, Electrode Resistance Rise, and Impedance*. This database serves as a foundational resource for generalized battery state estimation models concerning any SOH metric. It successfully bridges the gap between capacitive and resistive SOH metrics, enabling a comprehensive characterization of LiBs.

Chapter 3 provides an extensive discussion of the thesis, with a particular focus on OCV models, the challenge of data scarcity, and the extension of the SOH metric. Section 3.1 examines the contribution of the modified OCV model and its classification within the research context. Section 3.2 elaborates on the work related to deep learning methods for SOH estimation. Section 3.3 discusses the undergone studies in order to extend the state of the art of public battery datasets. Finally, Section 3.4 summarizes and concludes the entire thesis, offering an outlook on future research directions.

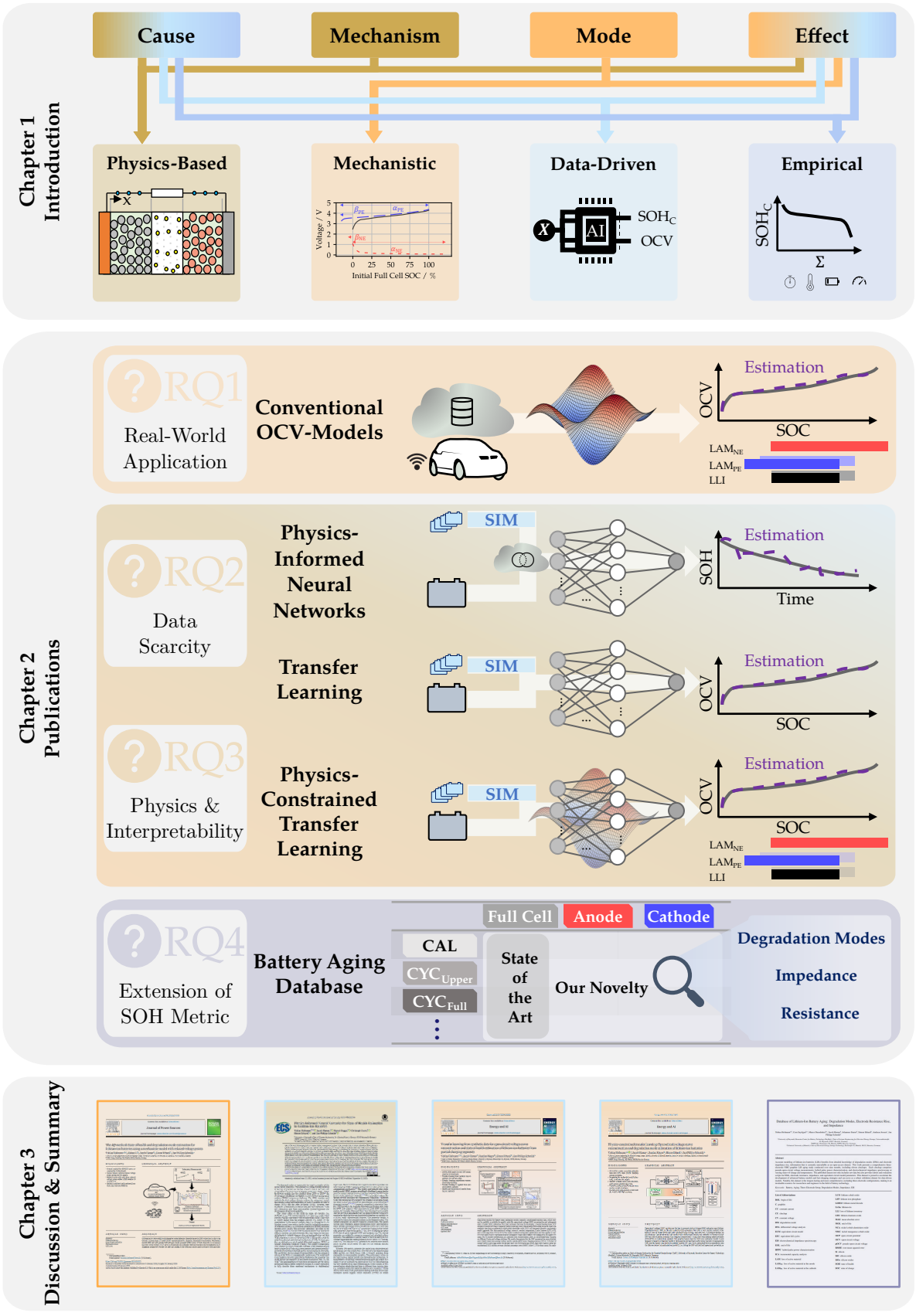

Figure 1.17: The outline of this thesis indicating the used methods within the publication by the color shade.

2 Published Results

This chapter presents the main findings of this cumulative thesis in the form of four published peer-reviewed journal papers and one draft version that will be submitted in 2026. Prior to each included publication, a concise summary is provided, along with its classification within the scope of this dissertation, the broader research context, publication notes, and the contributions of the authors.

2.1 Conventional OCV-Models for SOH Estimation

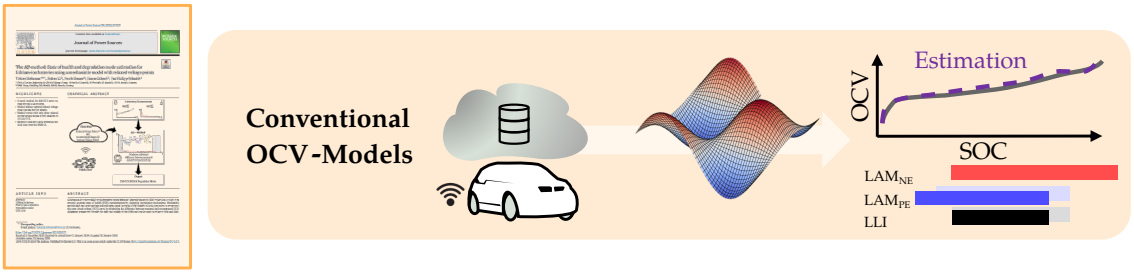

Figure 2.1: The trimmed outline of the thesis structure with focus on this chapter.

As discussed in the introduction, the SOH_C alone is insufficient to fully describe a battery's state. The aging of electrodes leads to changes in the OCV, making OCV updates crucial for BEVs. Accurate OCV curves are crucial for optimizing charging algorithms and enhancing SOC estimation. Incorrect OCV estimates result in imprecise SOC calculations, requiring a reduction in the displayed range to prevent running out of battery energy. Conversely, precise OCV updates enhance SOC estimation accuracy, thereby increasing the displayed range in BEVs. The application of mechanistic models, however, requires time-series data from (partial) charging events at low C-rates, which is not available for most existing BEV fleets [9]. Additionally, such measurements would require significant time and data storage, depending on the sampling frequency. This research, hence, addresses the question: How can the mechanistic model for OCV reconstruction be applied to real-world BEV fleet data?

To date, mechanistic models have been applied primarily to time-series data, initially using fully measured pOCV curves [25; 32; 185], extended to partially measured pOCV curves [27; 55], and finally adapted to partial charging events with C-rates up to C/3 [27; 54; 55; 91; 166]. The state of the art demonstrates that accurate reconstruction is possible for partial segments from 20 % to 70 % with C-rates up to C/15 [27; 55]. No existing method, however, can operate without knowledge of time-series data.

This work modifies the mechanistic modeling approach to reconstruct the full OCV curve using relaxed voltage point pairs and the associated charge throughput, data typically stored for existing BEV fleets for SOC calibration [209]. For example, the BMW i3, one of the oldest electric BMWs, has this type of data available. The approach combines multiple points from recent weeks to assemble the full OCV. Consequently, the objective function is adjusted to optimize the deviation between charge differences ΔQ of neighboring points, giving rise to the name of the algorithm: ΔQ-method.

The method is validated at both the cell and vehicle levels. In laboratory tests with an NMC-graphite cell dataset of 116 Ah capacity, the method achieved an MAE of 1.11 % (pp) for SOH_C estimation and 9.09 mV for OCV reconstruction. At the vehicle level, validation was performed using data from the BMW i3 fleet, comprising over 550 vehicles, each with a measured SOH_C label obtained during service visits. Although the true OCV is unknown, the OCV error is based on the optimization error. The ΔQ-method achieved an SOH_C MAE of 2.52 % (pp) and an OCV optimization error of 7.19 mV. The fleet's aging behavior was analyzed by calculating the DMs from the reconstructed OCV curves. A comprehensive sensitivity analysis of the fleet dataset revealed that the algorithm is robust against variations in input data and solver choice. As few as three relaxed voltage points, including one below 3.8 V and a minimum voltage window of 300 mV (equivalent to an SOC window from 40 % to 100 %), were sufficient to achieve an SOH_C MAE below 3 % (pp). For lower start SOCs the required SOC reduces even further to 30 % to 75 %.

For the first time, this work enables the application of the mechanistic model to real-world fleet data. By incorporating labeled vehicle data, the approach is validated. Compared to existing literature, the findings confirm the required SOC ranges and highlight the importance of lower segments for accurate reconstruction.

The paper introduces the method and develops the optimization problem. The ΔQ-method is initially presented using the cell dataset and subsequently validated with the fleet dataset. In addition to OCV and SOH_C, the DMs are calculated and discussed, despite the absence of true OCV measurements for the fleet data. A comprehensive sensitivity analysis of the method applied to the fleet dataset compares various input data filters and solvers (global vs. local, number of iterations, and stop tolerance).

Publication Notes

The article *The ΔQ-method: State of health and degradation mode estimation for lithium-ion batteries using a mechanistic model with relaxed voltage points* is presented in the following. The article was submitted to the Journal of Power Sources for peer review in December 2023 and was accepted in January 2024 [100]. The permanent web link to this publication is available under `https://doi.org/10.1016/j.jpowsour.2024.234107`.

Author Contributions

T. Hofmann and J. Li developed the method. T. Hofmann evaluated the data, developed the software, and wrote the manuscript. J. Hamar, S. Erhard and J.P. Schmidt supervised the research project, discussed the findings, and reviewed the manuscript.

Journal of Power Sources 596 (2024) 234107

Contents lists available at ScienceDirect

Journal of Power Sources

journal homepage: www.elsevier.com/locate/jpowsour

The ΔQ-method: State of health and degradation mode estimation for lithium-ion batteries using a mechanistic model with relaxed voltage points

Tobias Hofmann [a,b,*], Jiahao Li [b], Jacob Hamar [b], Simon Erhard [b], Jan Philipp Schmidt [a]

[a] Chair of Systems Engineering for Electrical Energy Storage, University of Bayreuth, Weiherstraße 26, Bayreuth, 95448, Bavaria, Germany
[b] BMW Group, Petuelring 130, Munich, 80809, Bavaria, Germany

HIGHLIGHTS

- A novel method for full OCV curve reconstruction is introduced.
- Method utilizes captured relaxed voltage points within the last month.
- Method works with only three relaxed voltage points within a SOC window of 30 % to 75 %.
- Method is validated with real-world vehicle data from the BMW i3.

GRAPHICAL ABSTRACT

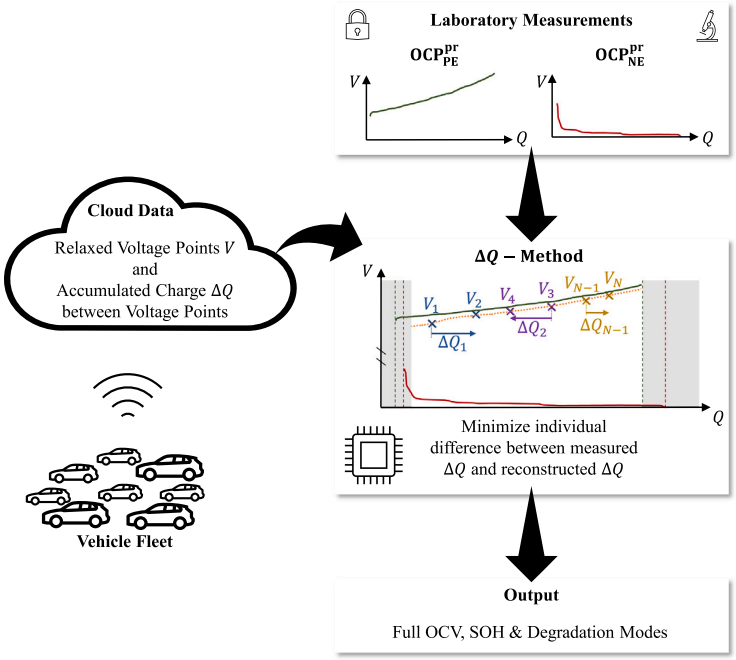

ARTICLE INFO

Keywords:
Lithium-ion battery
State of health estimation
Degradation modes
OCV curve

ABSTRACT

Lithium-ion batteries exhibit path-dependent aging behavior. Degradation mode (DM) estimation is a first step towards accurate state of health (SOH) representations by clustering degradation mechanisms. Mechanistic models shift and scale pristine half-cell open circuit potential (OCP) curves of both electrodes to reconstruct the open circuit voltage (OCV) curve by minimizing the difference between measured and reconstructed OCV. Alignment parameters describe the shift and scaling of the OCPs and can be used to estimate SOH and DMs.

* Corresponding author.
E-mail address: tobias.th.hofmann@bmw.de (T. Hofmann).

https://doi.org/10.1016/j.jpowsour.2024.234107
Received 6 December 2023; Received in revised form 11 January 2024; Accepted 18 January 2024
Available online 24 January 2024

T. Hofmann et al. Journal of Power Sources 596 (2024) 234107

Mechanistic model
Relaxed voltage points
Battery electric vehicle
Partial charging

This study introduces the ΔQ-method, which relies on relaxed voltage points and accumulated charge between these points. It is independent of current rates and applicable after almost every event. The optimization problem minimizes deviation between measured and reconstructed ΔQ. The method is developed with an automotive cell dataset and validated with real-world vehicle data from the BMW i3. The ΔQ-method achieves a mean absolute SOH estimation error of 2.52 % and a mean absolute OCV reconstruction error of 7.19 mV. Reliable estimations are ensured by predefined filters. The method remains effective with restricted state of charge (SOC) windows or limited data points. It is robust against variations in input data, solver choice, and optimization settings. Convergence is improved by constraining the solution space.

Nomenclature

List of Symbols

α	Scaling parameter
β	Shifting parameter
ΔQ	Charge difference between two relaxed voltage points
Δt	Time horizon of data acquisition in one data sample
ΔV	Voltage difference in one data sample
LAM	Loss of active material
LLI	Loss of lithium inventory
MAE	Mean absolute error
OCP	Open circuit potential
OCV	Open circuit voltage
SOC	State of charge
SOH	State of health
ϑ	Alignment parameter set
C	Capacity
N_{Points}	Number of points in one data sample
V	Voltage
V_{end}	Highest voltage in one data sample
V_{start}	Lowest voltage in one data sample

Subscripts

est	Estimated
FC	Full cell
interpolated	Interpolated
max	Maximum
meas	Measured
NE	Negative electrode
N	Nominal
OCV	Open circuit voltage
PE	Positive electrode
reco	Reconstructed
SOH	State of health
true	True value

Superscripts

aged	Aged
pr	Pristine

1. Introduction

With the rapid advent of battery electric vehicles (BEVs), modern battery management systems must be able to estimate internal states with high accuracy and robustness. Especially the SOH, which is commonly defined as the actual capacity in relation to the capacity at BOL, is crucial for optimal and safe operation, and prolonged battery life. Notice about the SOH, however, does not ensure knowledge about the aging path. Lithium-ion batteries age particularly path-dependent and have strong nonlinear dependencies on their operational strategy [1–3]. Two cells with the same SOH but a different history can behave completely different in future operation. A first step towards understanding path-dependent aging are the DMs [4,5]. These modes cluster the electrochemical degradation mechanisms into loss of active material at the negative electrode (NE) (LAM_{NE}), loss of active material at the positive electrode (PE) (LAM_{PE}) and loss of lithium inventory (LLI). These modes not only allow current characterization of the cell but also a more precise future prediction and strategies to mitigate degradation [6]. The DMs are connected to the change of the OCV over lifetime and hence existing DM estimation models output the OCV as well [4,5,7]. The updated OCV is beneficial for accurate SOC estimation [8] and optimal charging strategies over lifetime. Consequently, understanding the DMs provides valuable information for accurate SOH estimation and enables proactive maintenance and control strategies.

While DM estimation models rise in popularity, numerous other SOH estimation models exist which vary in complexity and accuracy: The most common electrochemical battery model is the Newman type pseudo-two dimensional model [9–11] which needs to be modified in order to add the SOH as a solution variable. It is usually reduced in order to decrease the computational complexity. Recent reduced order models [12–14] implement the SEI-growth into an aging-dependent voltage loss equation. Other approaches [15] implement the DMs directly by adapting the stoichiometries. Either way, the parameters of interest are updated by a comparison of the modeled and measured voltage response.

With the constant rise of machine learning, it is more and more used for battery state estimation [16]. Machine learning utilizes the hidden features in measurable signals like current, voltage and temperature to exploit the correlation between these features and the SOH. Within machine learning, deep-learning gains significant attention. Especially decision-tree models, convolutional and recurrent neural networks are eligible for processing time-series data and estimating the SOH [17]. Promising publications [16,18–20] reach root-mean squared errors below 2.5 % with neural networks that process time-series data from partial charging segments. The availability of more comprehensive input data, such as electrochemical impedance spectra, has enabled even greater accuracy in estimation. For instance, Luo et al. [21] achieve a mean absolute percentage error of 1.63 % using transformer-based neural networks that leverage the electrochemical impedance spectrum. Their study demonstrates the superiority of transformer-based neural networks over recurrent neural networks in effectively processing information from complete input data or long-term data sequences.

Similar to machine learning, empirical fits use the correlation between measurable features and the SOH [22,23]. In contrast to neural networks and other ML approaches, empirical fits are designed by the engineer. These methods allow to describe the SOH as a function of multiple input signals including the operational history.

All of the aforementioned methods require data from costly and long aging studies. This major drawback makes the application of these models to new generation of cells extremely challenging, especially for fast development sequences. The mechanistic model approach, introduced by Dubarry et al. [4], however, avoids this limitation by solely relying on pristine measurement data. Hence the mechanistic model is an

efficient, cheap and non-invasive diagnostic tool. The model describes the OCV over degradation as the difference of the half-cell potentials and assumes that the OCV only changes relative to the shifting and scaling of the OCPs. How the OCPs shift and scale further determines the DMs and the SOH which allows more knowledge about the aging path.

Since the first publication of the mechanistic model approach [4], numerous papers [5,7,24–35] were published which evaluate the method for different cells including electrode composites [7,28,29] and other cost functions depending on the differential voltage analysis (DVA) or incremental capacity analysis (ICA) [26,27,30,31,33]. Schmidt et al. [7] were the first to validate the mechanistic model approach with laboratory measurements. They disassembled cells to set specific rates of LLI and LAM_{PE}. For six different cells and a C-rate below C/20, the deviation between measured and reconstructed OCPs or OCV was always below 0.5 %.

There is a noticeable increase in scientific publications [36–41] exploring the application, extension and utilization of the method at higher C-rates and during partial charging segments, making the method applicable to real-world conditions. In their study, Schindler et al. [36] demonstrated the applicability of the model to higher C-rates and varying temperatures by incorporating the Arrhenius-dependent ohmic resistance increase and rate degradation factor as additional factors. The researchers assessed the performance of the model at different C-rates (C/35, C/5, C/3) and temperatures (10 °C, 25 °C, 45 °C) and observed that the residual error in OCV reconstruction remained below 2 %. This indicates that the model provides accurate predictions even under these challenging conditions. Progress has also been made by Yang et al. [37] in the application of the method to partial charging segments from a NMC–graphite cell, even when subjected to higher C-rates. Their investigation revealed that, for a C-rate of C/3, a SOC window spanning from 20 % to 70 % is essential to achieve accurate results for various aging paths. These findings were corroborated by Chen et al. [38]: By employing DVA and ICA on C/3 partial charging segments from a NMC/LCO–graphite cell within the range of 40 % to 100 % SOC, they also successfully determined the SOH and estimated the DMs with a root mean squared error below 3.5 %. In a recent study, Schmitt et al. [39] conducted a comprehensive sensitivity analysis of the method, considering higher C-rates and varying SOC windows for a NMC–Si/graphite cell. They addressed the issue of overpotentials at higher C-rates by introducing a correction method based on subtracting constant overpotential offsets. These offsets were computed by multiplying the applied current with the measured internal resistance. Interestingly, their results diverged from those of Yang et al. [37], as they revealed that achieving accurate DM estimation requires lower C-rates (≤ C/15). Furthermore, the study demonstrated that for sufficiently low C-rates (≤ C/30), even partial charging segments covering the SOC range of 20 % to 70 % are adequate. For precise SOH estimation, C-rates up to C/4, and partial charging segments spanning at least the SOC window of 10 % to 80 %, were shown to be feasible [39].

Mainly due to the availability of public battery aging data and the introduction of the *alawa* toolbox [42,43] for big data generation, various machine learning approaches [44–47] using the mechanistic model approach were published. Similar to existing methods [38], these models interpret the hidden features of raw [45,47] or postprocessed [44,46] charging curves.

The major drawback of existing methods, which rely on time-series data, is the dependency on wide SOC ranges and low C-rates. Hence, the application to real-world data is severely limited by the operational strategy of the customer.

In contrast to available methods, our novel ΔQ-method solely relies on a small number of relaxed voltage points and the accumulated charge between these points which are normally stored for BEVs. It is thus applicable to relaxed voltage points after almost every charging or driving event, independent of the applied current. This makes the ΔQ-method a promising algorithm for existing vehicle fleets.

The study at hand presents a novel algorithm for OCV reconstruction, SOH and DM estimation based on relaxed voltage points and the accumulated charge between these points. The ΔQ-method is evaluated with laboratory data from an automotive cell. The method is validated with real-world vehicle data from the BMW i3 fleet and its sensitivity to specific data filters is accessed. The influence of specific solvers and their settings is evaluated in terms of SOH error. We further highlight the advantages over conventional methods by evaluating the minimum requirements. The ΔQ-method is applicable to data from vehicles in operation with at least three measured relaxed voltage points, collected over a time-horizon up to six months. To the best of the authors knowledge, this is the first publication to design a mechanistic model approach using relaxed voltage points and accumulated charge for SOH and DM estimation.

2. Method

Knowledge about the DMs gives insight about the path-dependent aging behavior of lithium-ion batteries because the DMs correlate with the knee-point in battery aging trajectories [6]. Roeder and Ramasubramanian [48] suggested to define path dependence in three levels. While in level one, the aging path solely depends on the usage schedule, we refer in this work to level two: The current battery SOH depends on the order of usage conditions and not just their cumulative influence. As introduced by Dubarry et al. [49], extending the SOH definition with DMs helps to incorporate path-dependent battery degradation into the current state itself.

Conventional methods utilize the OCPs of the electrodes to reconstruct the full cell (FC) OCV by shifting and scaling the respective curves. Hence, it is assumed that the OCV is a function of the half cell potentials and these will only change in relation to each other which can be described by the alignment parameter set $\vartheta = [\alpha_{NE}, \alpha_{PE}, \beta_{NE}, \beta_{PE}]$. The α-parameters specify the squeezing and the β-parameters describe the shifting of the OCPs. If the OCPs or the OCV are captured at very low C-rates, they are pseudo-OCP/OCV because even at low C-rates the measured values will deviate from the truly relaxed voltage. For simplicity, in the following the terms pseudo-OCP/OCV and OCP/OCV will be used as synonyms.

2.1. Method description

Along a battery's lifetime its OCPs can be described with respect to the electrode SOC (SOC_{NE} and SOC_{PE}) or charge amount

$$OCP_{NE} = f_{NE}(SOC_{NE}) \tag{1}$$

$$OCP_{PE} = f_{PE}(SOC_{PE}). \tag{2}$$

Fig. 1 summarizes the steps to set up the algorithm: First, the OCV and OCPs must be captured in either charge or discharge direction. The direction of charge should be kept constant throughout the application of the algorithm to reduce the influence of hysteresis. All curves are normalized to their respective SOC. The C-rate is usually set below C/20 to decrease the influence of overpotentials. All inputs are transformed into the coordinate system of the full cell, i.e., the full cell SOC (SOC_{FC}), by scaling the specific electrode SOCs by the α-parameter and finally shifting them by the β-parameter.

$$SOC_{FC} = \alpha_{NE} \cdot SOC_{NE} + \beta_{NE} \tag{3}$$

$$SOC_{FC} = \alpha_{PE} \cdot SOC_{PE} + \beta_{PE} \tag{4}$$

Hence, Eqs. (1) and (2) transform to

$$OCP_{NE} = f_{NE}((SOC_{FC} - \beta_{NE})/\alpha_{NE}) = f_{NE}(SOC_{FC}, \vartheta) \tag{5}$$

$$OCP_{PE} = f_{PE}((SOC_{FC} - \beta_{PE})/\alpha_{PE}) = f_{PE}(SOC_{FC}, \vartheta). \tag{6}$$

The full mathematical derivation of the coordinate transformation can be found in the publication by Schmitt et al. [39].

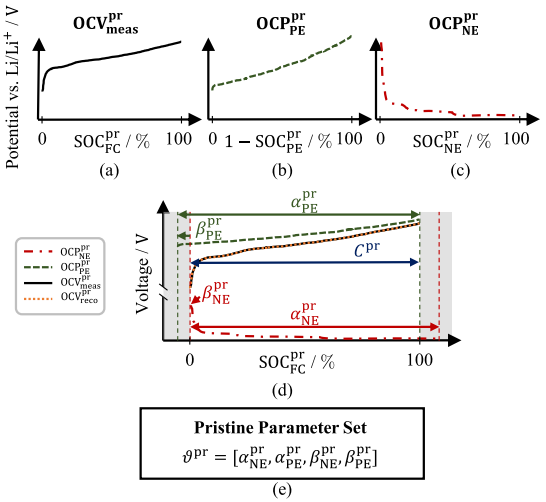

Fig. 1. Initialization process of conventional OCV reconstruction models. The OCV (a) together with the positive (b) and negative (c) electrode OCPs in the pristine state are captured at the same C-rate. In this example, all curves are measured in charge direction. (d) The pristine alignment parameters are fitted to minimize the error between the pristine OCV measurement and the reconstructed curve. (e) The resulting pristine alignment parameters are later mandatory to derive the SOH and DMs.

Finally, the OCV can be described with the help of the OCPs and the alignment parameters

$$\mathrm{OCV}(\mathrm{SOC_{FC}}) = f_{\mathrm{FC}}(\mathrm{OCP_{NE}},\ \mathrm{OCP_{PE}},\ \vartheta,\ \mathrm{SOC_{FC}}). \tag{7}$$

Second, the pristine (pr) alignment parameters are fitted to minimize the error between the measured (meas) and reconstructed (reco) OCV curve $\mathrm{OCV_{meas}}$ and $\mathrm{OCV_{reco}}$. The cell's BOL capacity is defined as the accumulated charge between the minimum and maximum cell voltage. Per definition, the SOH is always 100 % for this scenario. Last, the pristine alignment parameter set ϑ^{pr} must be stored in order to calculate the DMs in the application phase. In Fig. 2 the application phase is visualized for the conventional but also the ΔQ-method. The conventional algorithm, illustrated in Figs. 1 and 2, takes the raw OCV measurement $\mathrm{OCV_{meas}}$ (Fig. 1a) and the pristine OCPs: $\mathrm{OCP^{pr}_{PE,meas}}$, $\mathrm{OCP^{pr}_{NE,meas}}$ (Fig. 1b and c) as an input. By shifting and scaling the OCPs in relation to each other, the OCV reconstruction error is minimized (Fig. 1d) to finally yield the alignment parameters (Fig. 1e) and hence the SOH and DMs. Advances are made to use DVA and ICA for optimization [36–38]. The optimization happens in the coordinate system of the pristine full cell SOC ($\mathrm{SOC^{pr}_{FC}}$) or the absolute Ah-space. If a local optimum is found and no further feasible direction is detectable, the algorithm stops and returns the aged alignment parameter set

$$\vartheta^{\mathrm{aged}} = \arg\min_{\vartheta} \|\mathrm{OCV_{meas}}(\mathrm{SOC_{FC}}) - \mathrm{OCV_{reco}}(\vartheta,\ \mathrm{SOC_{FC}})\|_2. \tag{8}$$

The choice of optimization algorithm, i.e., gradient descent, particle swarm or genetic algorithm, can influence the final parameter solution.

In contrast to conventional methods, the ΔQ-method requires only three measured relaxed voltage points V_1, V_2, V_3 and the accumulated charge between these points ΔQ_1, ΔQ_2. By definition, the ΔQ is positive for charging events. For negative ΔQs and consequently discharge events, the ΔQ is inverted and the order of the voltage pair is reversed to meet the requirements. The algorithm minimizes the objective function $f(\vartheta)$, which is the vector of accumulated charge between adjacent points, and fixates the OCV points

$$\begin{aligned}\vartheta^{\mathrm{aged}} &= \arg\min_{\vartheta} \|f(\vartheta)\|_2 \\ &= \arg\min_{\vartheta} \|\Delta Q_{\mathrm{meas}}(V) - \Delta Q_{\mathrm{reco}}(\vartheta,\ V)\|_2,\end{aligned} \tag{9}$$

where ΔQ_{meas} is the vector of measured ΔQs and ΔQ_{reco} is the vector of the reconstructed ΔQs.

Instead of optimizing with respect to the y-axis, the ΔQ-method uses the x-axis. One of its advantages lies in the fact that no fixed reference voltage is required. Hence, every voltage pair is fitted individually. The alignment parameters not only yield the aged OCV-curve (Eq. (7)) but are further used to calculate the DMs. Because the aged OCV is reconstructed in the charge coordinate system, the SOH is easily derived by Eq. (10). The capacity of the pristine cell C^{pr} is simply the accumulated charge between the voltage limits for the pristine fit in Fig. 1d. The same applies for the estimated capacity of the aged cell $C^{\mathrm{aged}}_{\mathrm{est}}$.

$$\mathrm{SOH} = \frac{C^{\mathrm{aged}}_{\mathrm{est}}}{C^{\mathrm{pr}}} = \frac{Q^{\mathrm{aged}}(V^{\mathrm{aged}}_{\mathrm{max}})}{Q^{\mathrm{pr}}(V^{\mathrm{pr}}_{\mathrm{max}})} \tag{10}$$

In Eq. (10), Q^{aged} and Q^{pr} are the aged and the pristine charge vector, while $V^{\mathrm{aged}}_{\mathrm{max}}$ and $V^{\mathrm{pr}}_{\mathrm{max}}$ are the maximum voltage values of the aged and pristine voltage curves.

Loss of active material describes the available electrode capacity with respect to the pristine state. For both electrodes, the definition is similar:

$$\mathrm{LAM_{NE}} = \frac{\alpha^{\mathrm{pr}}_{\mathrm{NE}} - \alpha^{\mathrm{aged}}_{\mathrm{NE}}}{\alpha^{\mathrm{pr}}_{\mathrm{NE}}} \tag{11}$$

$$\mathrm{LAM_{PE}} = \frac{\alpha^{\mathrm{pr}}_{\mathrm{PE}} - \alpha^{\mathrm{aged}}_{\mathrm{PE}}}{\alpha^{\mathrm{pr}}_{\mathrm{PE}}} \tag{12}$$

Lithium inventory C_{lit} is the available lithium for cycling in both electrodes, i.e. the superposition of both OCPs. The loss of lithium inventory is defined with respect to the pristine amount of available lithium inventory $C^{\mathrm{pr}}_{\mathrm{lit}}$.

$$\mathrm{LLI} = \frac{C^{\mathrm{pr}}_{\mathrm{lit}} - C_{\mathrm{lit}}}{C^{\mathrm{pr}}_{\mathrm{lit}}} \tag{13}$$

When examining both OCPs across the entire delithiation and lithiation range, it is observed that the cathode builds a capacity overhang during discharge, while the anode exhibits a capacity overhang during charge [5], as depicted in Fig. 1. This remains generally true throughout the lifespan, leading to the definition of lithium inventory primarily as

$$C_{\mathrm{lit}} = (\alpha_{\mathrm{PE}} + \beta_{\mathrm{PE}} - \beta_{\mathrm{NE}}) \cdot C_{\mathrm{N}}. \tag{14}$$

There are instances, however, where the minimum or maximum lithiation degree for the initial measurement deviates from the standard definition due to varied measurement settings. This results in the possibility of mathematically determining an overhang in the discharge direction for the anode or an overhang in the charge direction for the cathode. In Fig. 4(a) for example, the cathode is limiting in charge and discharge direction. Besides the deviations in initial measurement settings, even if the pristine alignment parameters are set as in Fig. 1, a rapid $\mathrm{LAM_{NE}}$, without $\mathrm{LAM_{PE}}$ and LLI, may lead to the need for a new lithium inventory definition. Hence, it becomes necessary to introduce a case-sensitive definition for the lithium inventory, as shown in Eq. (15).

$$C_{\mathrm{lit}} = \begin{cases} (\alpha_{\mathrm{PE}} - \beta_{\mathrm{NE}} + \beta_{\mathrm{PE}}) \cdot C_{\mathrm{N}} \ , \text{for } (\alpha_{\mathrm{PE}} + \beta_{\mathrm{NE}} - \beta_{\mathrm{PE}}) < \alpha_{\mathrm{NE}} \\ \qquad \wedge \ (\beta_{\mathrm{PE}} - \beta_{\mathrm{NE}}) \le 0 \\ (\alpha_{\mathrm{NE}} - \beta_{\mathrm{NE}}) \cdot C_{\mathrm{N}} \ , \text{for } (\alpha_{\mathrm{PE}} + \beta_{\mathrm{NE}} - \beta_{\mathrm{PE}}) > \alpha_{\mathrm{NE}} \\ \qquad \wedge \ (\beta_{\mathrm{PE}} - \beta_{\mathrm{NE}}) \le 0 \\ (\alpha_{\mathrm{NE}} + \beta_{\mathrm{NE}} - \beta_{\mathrm{PE}}) \cdot C_{\mathrm{N}} \ , \text{for } (\alpha_{\mathrm{NE}} + \beta_{\mathrm{NE}} - \beta_{\mathrm{PE}}) < \alpha_{\mathrm{PE}} \\ \qquad \wedge \ (\beta_{\mathrm{PE}} - \beta_{\mathrm{NE}}) \ge 0 \\ (\alpha_{\mathrm{PE}} - \beta_{\mathrm{PE}}) \cdot C_{\mathrm{N}} \ , \text{for } (\alpha_{\mathrm{NE}} + \beta_{\mathrm{NE}} - \beta_{\mathrm{PE}}) > \alpha_{\mathrm{PE}} \\ \qquad \wedge \ (\beta_{\mathrm{PE}} - \beta_{\mathrm{NE}}) \ge 0 \end{cases} \tag{15}$$

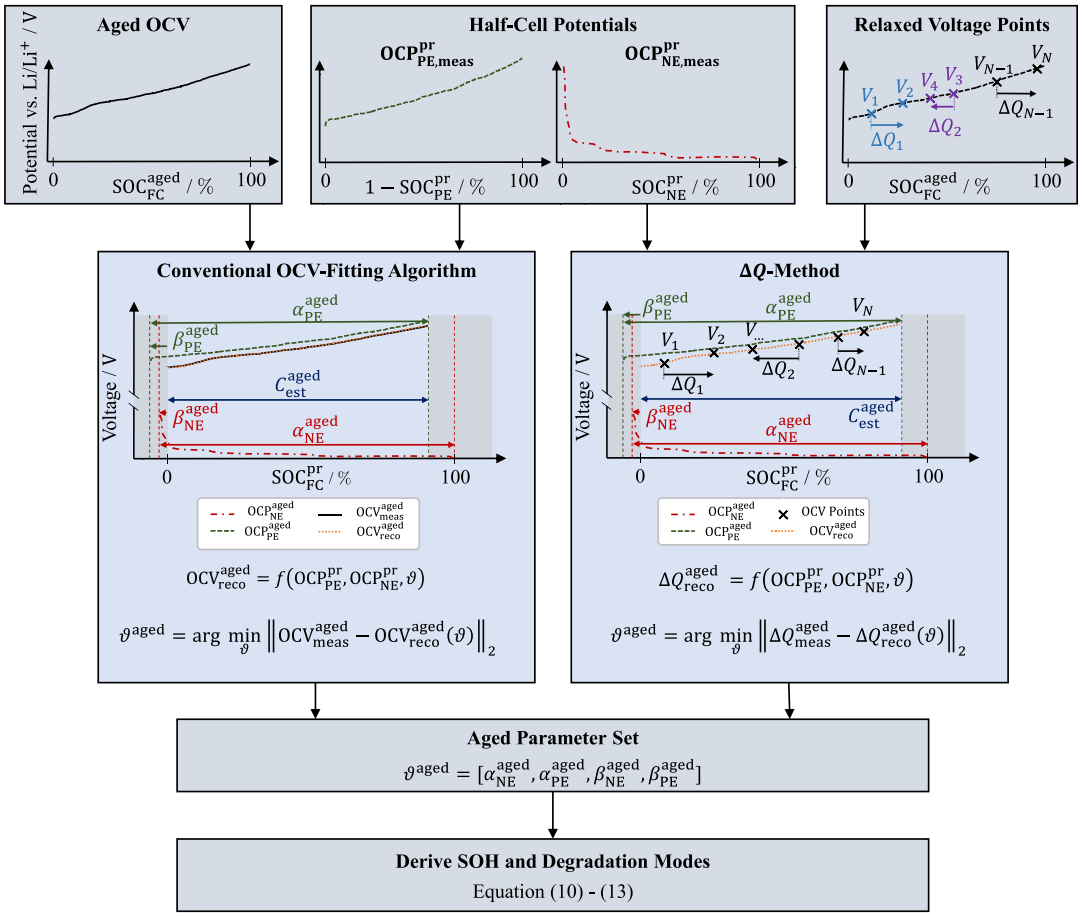

Fig. 2. Description of conventional OCV reconstruction methods and the novel ΔQ-method. For both algorithms the pristine OCPs are mandatory. While conventional methods use time-series measurements of the OCV, the ΔQ-method solely requires relaxed voltage points and the accumulated charge between those points. Conventional methods fit the pristine OCPs to the measured OCV by shifting and scaling the curve to minimize the OCV reconstruction error. The ΔQ-method, however, pursues the same target by minimizing in respect to the x-axis, i.e., the accumulated charge between two relaxed voltage points. The optimization argument yields the optimal alignment parameters which are used to estimate the SOH and DM.

2.2. Dataset

This paper introduces the basic idea of the ΔQ-method. First, the method is developed with measurements under laboratory conditions from a cyclic aging study of an automotive cell. The used automotive cell has a NMC811-cathode, a graphite-anode and a nominal capacity of 116 Ah [50]. Second, the developed algorithm is applied to real-world vehicle field data from the BMW i3, which was captured over eight years, not relying on accelerated aging tests. The BMW i3 uses a different cell with a NCA/NMC/LMO-blended-cathode, a graphite-anode and a nominal capacity of 60 Ah measured by a constant-current constant-voltage (CCCV) charge with C/3 at 25 °C.

The cell dataset comprises of twelve samples with 27 relaxed voltage points, the accumulated charge between these points and the respective SOH_{true} label. All points were measured at 25 °C in charge direction. Half of the samples were taken at BOL, while the remaining samples are distributed between 77 % to 93 % SOH after performing 500 to 1000 continuous cycles with C/3 charge and C/2 discharge at 10 °C and 35 °C. The pristine, true alignment parameter set is known from a previous publication [50] investigating the same cell.

In contrast to the standardized cell dataset, the vehicle dataset is captured at various conditions for 574 vehicles. The vehicle dataset is visualized in Fig. 3 with special focus on the variables of interest: SOH, number of relaxed voltage points, voltage level and accumulated charge between two adjacent voltage points. While the signals voltage and charge were captured on pack level, they are transformed to cell-level by multiplication by a fixed scaling factor. All vehicles in this dataset have undergone at least one and a maximum of eight testbench capacity measurements to create the SOH_{true} label. The testbench capacity measurement consists of a CCCV charge with C/3 at the service. The capacity is defined as the full accumulated charge throughput during this service. The dataset is categorized into three degradation states based on mileage: BOL for vehicles with mileage below 25 000 km, MOL for vehicles with mileage between 25 000 km and 100 000 km, and EOL for vehicles with mileage exceeding 100 000 km. The total mileage correlates with the aging state of the high voltage storage system. The SOH remains above 75 % even for vehicles with over 100 000 km and a vehicle age above eight years. While all BOL vehicles have a SOH above 90 % and all EOL vehicles have a SOH below 85 %, the MOL vehicles show ranges over the entire extreme, where one can see more clearly the influence of other factors on the vehicle SOH. The dataset was recorded within a time window of eight years. As a result, not every historical relaxed voltage point is included in the dataset. For this dataset, BOL vehicles are operated more frequently than MOL or EOL vehicles and inhibit more data points. Regarding voltage levels and SOC, the majority of data points in the entire dataset

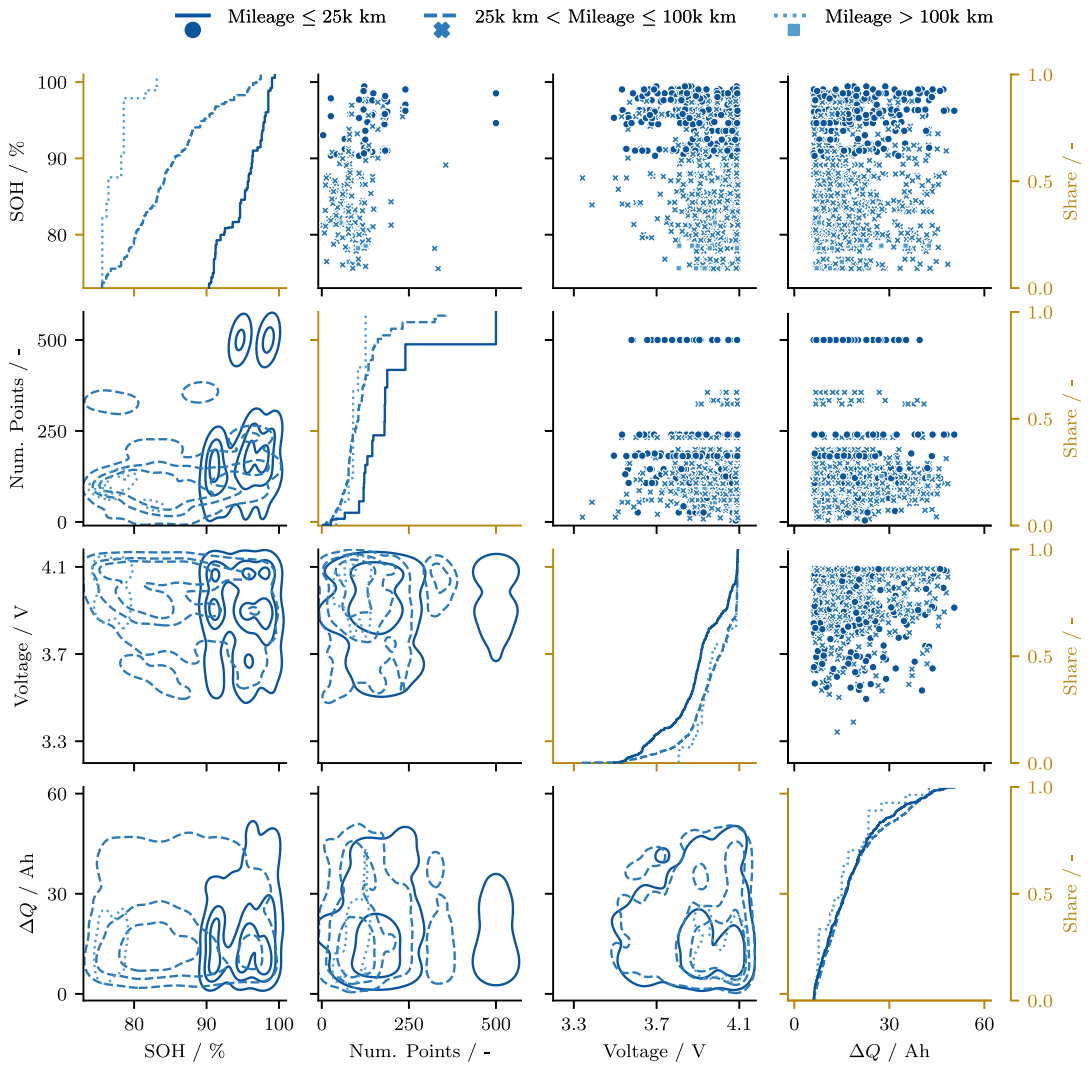

Fig. 3. Visualization of the validation dataset gathered from aged vehicles in the field. The upper diagonal figures show the scatter plot and the lower diagonal figures visualize the kernel densities. Both refer to the first y-axis on the left. The second y-axis on the right side refers to the cumulative distribution plots in the diagonal, in golden color. The hue indicates the milage of the investigated vehicles, which shows good agreement with the SOH.

are distributed at higher voltage levels. This observation is reasonable since there is high probability that a relaxed voltage point is recorded after a charging event. Due to the relatively small capacity of the first BMW i3, customers tended to show high frequent charging behavior. Additionally, the OCV increases with degradation, leading to even more data points at higher voltage levels. The accumulated charge between two adjacent points provides insights into user behavior. A higher value indicates longer charging events or that the vehicle is operated for a longer duration between stops. Comparing these key charging features, the cumulative distribution exhibits remarkable similarity for all three datasets, implying that user behavior remains consistent over the lifetime of the vehicles.

The dataset does not include the history between two points, i.e., current profile or the temperature, but makes sure that between two points charging events are not mixed with driving events. The combination of OCV points derived from both charging and discharging events, irrespective of their prior history, may be achieved under negligible hysteresis assumptions for the given cell. This objective can be realized by assigning a positive ΔQ value to a charging event, and multiplying the discharge event, which yields a negative ΔQ, by -1. To this end, the order of the measured voltage pair needs to be reversed.

3. Results

The proposed method is first implemented on cell data. The developed method is validated with actual field data from the BMW i3, which uses a different cell.

3.1. Application of the method to laboratory cell data

Fig. 4 provides a comprehensive visualization of the complete application of the ΔQ-method. In Fig. 4(a), the pristine OCPs, OCV, and measurement results are depicted. Additionally, the interpolation of the OCV voltage points is included to enhance the visualization of the actual OCV trajectory. The OCPs are appropriately adjusted based on their corresponding pristine alignment parameters, which are

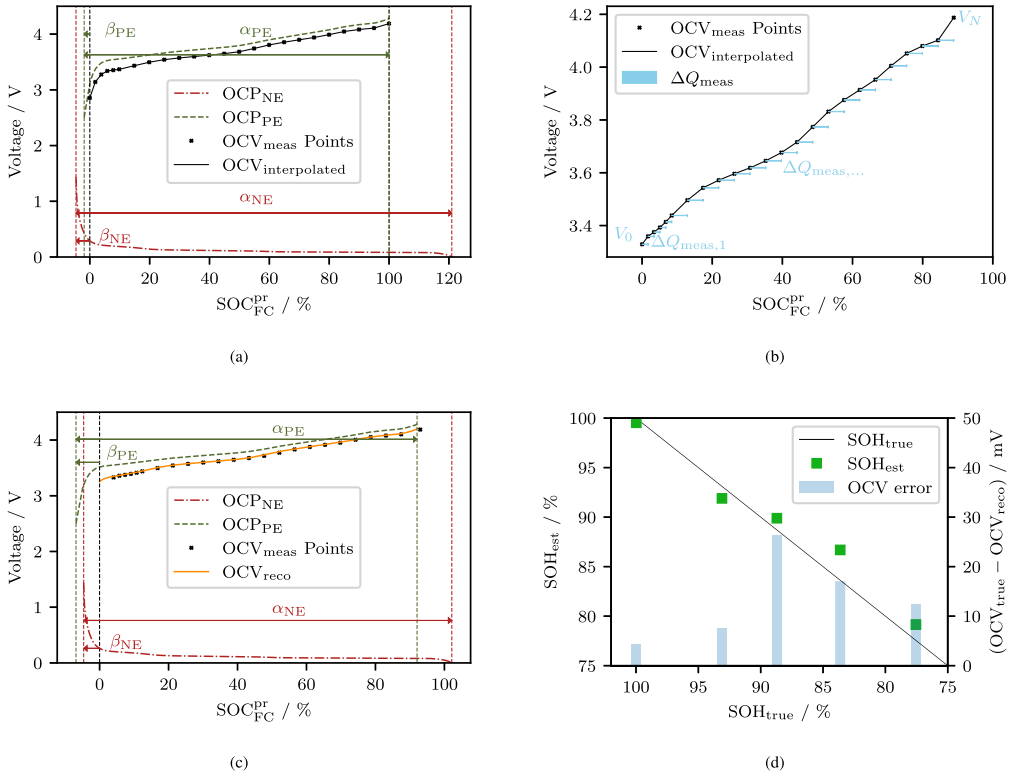

Fig. 4. Application of the algorithm to a single sample at an aged state from the standardized cell dataset. (a) Pristine Fit for investigated cell. (b) Input for ΔQ-algorithm: aged relaxed OCV points with accumulated charge between points. (c) Optimization result for aged cell. For this cell: $\mathrm{MAE}_{\mathrm{SOH}} = 1.05\,\%$ and OCV reconstruction error: $\mathrm{MAE}_{\mathrm{OCV}} = 12.4\,\mathrm{mV}$. (d) Result for all samples: $\mathrm{MAE}_{\mathrm{SOH}} = 1.11\,\%$ and OCV reconstruction error: $\mathrm{MAE}_{\mathrm{OCV}} = 9.09\,\mathrm{mV}$.

given in Table 1. In this paper all alignment parameters refer to a normalized SOC-axis between zero and one. It is worth noting that the observed anode-overhang in the discharge direction, as discussed earlier, is a result of the high cutoff voltage set to 1.5 V during the $\mathrm{OCP}_{\mathrm{NE}}$ measurement.

Fig. 4(b) illustrates the relaxed voltage measurements obtained from an aged cell. Again, an interpolation of the voltage points is visualized.

In order to apply the algorithm, the data needs to undergo preprocessing and to be organized into a matrix where the columns contain a vector with the voltage and charge difference value pairs, with each row representing a complete set for a sample at a consistent SOH. Specifically, the voltage points V_1 and V_2 are set in the first column, along with the corresponding charge difference $\Delta Q_1 = Q(V_2) - Q(V_1)$. Subsequently, the second column is filled with V_3, V_4, and $\Delta Q_2 = Q(V_4) - Q(V_3)$, as shown in Eq. (16).

$$\begin{bmatrix} V_1 & V_2 & \Delta Q_1 \\ V_3 & V_4 & \Delta Q_2 \\ \cdots & & \end{bmatrix} \tag{16}$$

Again, if for example ΔQ_1 is negative due to a driving event, Eq. (16) changes, as in Eq. (17).

$$\begin{bmatrix} V_2 & V_1 & -\Delta Q_1 \\ V_3 & V_4 & \Delta Q_2 \\ \cdots & & \end{bmatrix} \tag{17}$$

For the cell laboratory measurements V_3 equals V_2 and so forth. Along with the measured data, the pristine OCPs are normalized to equal length and stored to be used within the optimization process.

Table 1
Alignment parameter for the pristine state (SOH=100 %) and the estimation for an aged cell (SOH=93 %) (sample from Fig. 4(c)).

	α_{NE}	α_{PE}	β_{NE}	β_{PE}
Pristine	1.26	1.02	−0.05	−0.02
Aged Estimation	1.07	0.99	−0.05	−0.07

The optimization problem is formulated within MATLAB and the built-in nonlinear least-squares solver *lsqnonlin()* [51]. Instead of minimizing a scalar value, the nonlinear least-squares solver minimizes the vector of differences, as in Eq. (9). The default algorithm *trust-region-reflective* and all default settings from MATLAB are used for the solver [51]. The settings must be further redefined for more challenging datasets, i.e., the BMW i3 dataset in the consecutive subsection.

The optimization constraints and initial start points are set according to Table 2, which were found to be the best fit for pristine state and reflect most of the battery degradation. The algorithm does not rely on any additional constraints except the lower and upper boundaries.

Defining broader boundaries which make up to the full SOH-range lead to several local optima and the high risk of returning a result with an optimal solution with respect to the loss function but unreasonable alignment parameters. This means that for a specific set of voltage points several combinations of parameters exist which lead to equally low cost values of the objective function. Nevertheless, just a single combination yields the correct result. Limiting the solution space with adequate constraints helps to marginalize unwanted local optima.

The objective function $f(\vartheta)$, as it appears in Eq. (9), is defined as the vectorized difference between the measured $\Delta Q_{\mathrm{meas}}(V)$ and the

Table 2
Optimization constraints and initial values of the *lsqnonlin()* solver for the cell dataset.

Parameter	α_{NE}	α_{PE}	β_{NE}	β_{PE}
	BOL			
Initial Value	1.23	1.00	−0.05	−0.04
Lower Bound	1.21	0.99	−0.05	−0.04
Upper Bound	1.26	1.02	−0.05	−0.02
	MOL			
Initial Value	1.13	0.92	−0.05	−0.04
Lower Bound	1.07	0.87	−0.07	−0.07
Upper Bound	1.22	0.99	−0.05	−0.02
	EOL			
Initial Value	0.98	0.80	−0.05	−0.02
Lower Bound	0.94	0.76	−0.07	−0.07
Upper Bound	1.02	0.83	−0.05	−0.02

BOL: SOH ≥ 95 %, MOL: 80 % ≤ SOH < 95 %,EOL: SOH < 80 %.

reconstructed $\Delta Q_{reco}(\vartheta, V)$. Because all charge vectors are consecutive, i.e., in Eq. (16) V_3 equals V_2 and so forth, the optimization problem can be further simplified.

$$\begin{aligned} f(\vartheta) &= \Delta Q_{meas}(V) - \Delta Q_{reco}(\vartheta, V) \\ &= \begin{bmatrix} f_1(\vartheta) \\ f_2(\vartheta) \\ \dots \\ f_{N-1}(\vartheta) \end{bmatrix} = \begin{bmatrix} \Delta Q_{meas,1} - \Delta Q_{reco,1} \\ \Delta Q_{meas,2} - \Delta Q_{reco,2} \\ \dots \\ \Delta Q_{meas,N-1} - \Delta Q_{reco,N-1} \end{bmatrix} \\ &= \begin{bmatrix} (Q_{meas,2} - Q_{meas,1}) - (Q_{reco}(V_2, \vartheta) - Q_{reco}(V_1, \vartheta)) \\ (Q_{meas,3} - Q_{meas,3}) - (Q_{reco}(V_3, \vartheta) - Q_{reco}(V_2, \vartheta)) \\ \dots \\ (Q_{meas,N} - Q_{meas,N-1}) - (Q_{reco}(V_N, \vartheta) - Q_{reco}(V_{N-1}, \vartheta)) \end{bmatrix} \end{aligned} \tag{18}$$

The nonlinear least-squares problem is

$$\begin{aligned} \vartheta_{est} &= \arg\min_{\vartheta} \|f(\vartheta)\|_2^2 \\ &= \arg\min_{\vartheta}(f_1(\vartheta)^2 + f_2(\vartheta)^2 + \dots + f_{N-1}(\vartheta)^2) \quad \text{s.t.} \\ &\quad \vartheta \geq \text{lb} \\ &\quad \vartheta \leq \text{ub} \end{aligned} \tag{19}$$

where lb is the lower and ub is the upper boundary, according to Table 2.

Fig. 4(c) shows the optimization result for the sample in Fig. 4(b). The alignment parameters change according to Table 1.

With Eqs. (10), (11), (12) and (15) the SOH and DMs can be calculated. According to Table 2 the highest reachable DMs are 25.4 % for LAM_{NE}, 25.5 % for LAM_{PE} and 27.9 % for LLI. For the sample in Fig. 4(c) the estimated SOH is 92.1 %, which underestimates the actual SOH by absolute 1.05 %. $LAM_{NE,\ est}$ is 20.6 %, $LAM_{PE,\ est}$ is 16.7 % and LLI, est is 19.1 %. Mainly LAM_{PE} is responsible for LLI due to the anode overhang and the negligible relative shift of the OCPs. Further, LLI highly correlates with the SOH fade once the capacity overhangs of the anode is consumed, i.e., LAM_{NE} exceeds 16.7 %. If the cathode OCP does not shift, every LAM_{PE} directly leads to LLI and consequently to a decreasing SOH. The OCV reconstruction error is 12.4 mV. While SOH and OCV estimation is validated with the true value, it is not evaluated for the DMs. A detailed validation of the DM estimation exceeds the scope of this publication.

Fig. 4(d) presents the final result for all eleven samples of the cell dataset. All results are evaluate in terms of the mean absolute error (MAE). The MAE is defined as

$$\text{MAE} = \frac{1}{N}\sum_{i=1}^{N}\left|Y - \hat{Y}\right| \tag{20}$$

where Y is the true value, $\hat{Y}$ is the estimate and N is the total number of samples.

The MAE of SOH estimation is 1.11 % and the OCV MAE is 9.09 mV. The green squares show the estimated versus the true SOH. Due to the small amount of samples per SOH-value and the similar estimation result of those samples, the standard deviation is too small to be visible. The light blue bars indicate the OCV reconstruction error. While the estimation accuracy of SOH and OCV is very high for samples above 90 %, it decreases for higher degraded cells. The OCV error seems to directly correlate with the SOH error. Although this trend can be generally observed in Fig. 4(d), the samples with a true SOH of 88 % show the highest OCV error, while the SOH error is smaller than average.

For the laboratory dataset, one set of boundary conditions and a fixed initial start point, i.e., using the BOL upper boundary, EOL lower boundary, and MOL initial point, leads to accurate results. The reconstruction algorithm achieves a SOH MAE of 1.29 % (+0.18 % compared to clustered conditions, Fig. 4(d)) and an OCV reconstruction MAE of 9.70 mV(+0.61 mV compared to clustered conditions, Fig. 4(d)).

3.2. Validation of the method with vehicle field data

To evaluate the commercial viability, the proposed algorithm is validated with actual field data from the BMW i3. This dataset, on the one side, includes more samples and increases statistical significance. On the other side, the more challenging boundary conditions prove the real-world applicability of the ΔQ-method.

Fig. 5 gives a brief summary of the algorithm workflow, the dataset and the final result. As shown in Fig. 5(a), the method starts with an existing testbench capacity measurement as a reference. For this specific vehicle, a set of relaxed voltage points and the accumulated charge information are accessed. This dataset is preliminary checked and filtered to align with the requirements. The preset filters are a result of an availability-accuracy tradeoff, which is discussed in detail in Section 4. At least 10 data points, captured within the last 25 to 40 days before the testbench capacity measurement, must be available. The time horizon extends with higher vehicle age, i.e., older vehicles are closer to 40 on average. Additionally, the vehicle must be above 75 % SOH to align with the preset alignment parameter boundaries in Table 3. This criterion is simply checked by assessing the previous testbench capacity measurement. If no earlier measurement is available, the criterion is always fulfilled. For the investigated vehicle dataset, however, barely any samples below 75 % are available (see Fig. 3). Hence, this filter excludes a negligible amount of EOL vehicles. If all criteria are met, the boundary conditions of the algorithm are set according to Table 3. To prefilter the boundary conditions, the last maximum onboard (ob) SOH estimation $\max(SOH_{ob})$ is used as a criterion. This values is generally available and accurate enough to distinguish between BOL, MOL and EOL, but limited due to computing resources. The ΔQ-method processes this information and increases the quality and reliability of estimation. The ΔQ-method is validated against testbench capacity measurements instead of the onboard estimation.

The boundary conditions per degradation state are set such that they have an overlap with the other degradation states. This means, even if the latest maximum SOH onboard estimate implies that the boundary conditions are set according to BOL-conditions, the final estimate can still lay in the MOL-range. Hence, rough preliminary knowledge about the vehicle age is enough to run the algorithm. As shown with Eq. (19), the optimization uses the pristine OCPs to reconstruct the most accurate voltage curve. The optimization returns the adopted OCV, which is essential to estimate the SOH (Eq. (10)). In combination with the pristine parameter set, the estimated parameter set yields the DMs (Eqs. (11), (12), (15)).

In comparison to the cell dataset, the vehicle data demand tuned settings, as given in Table 3. The specific settings are a result of a detailed sensitivity analysis, which is further discussed in Section 4.

The maximum function evaluations (MaxFunEvals) are reduced to 100 from the default value of 400 to decrease the time-effort but

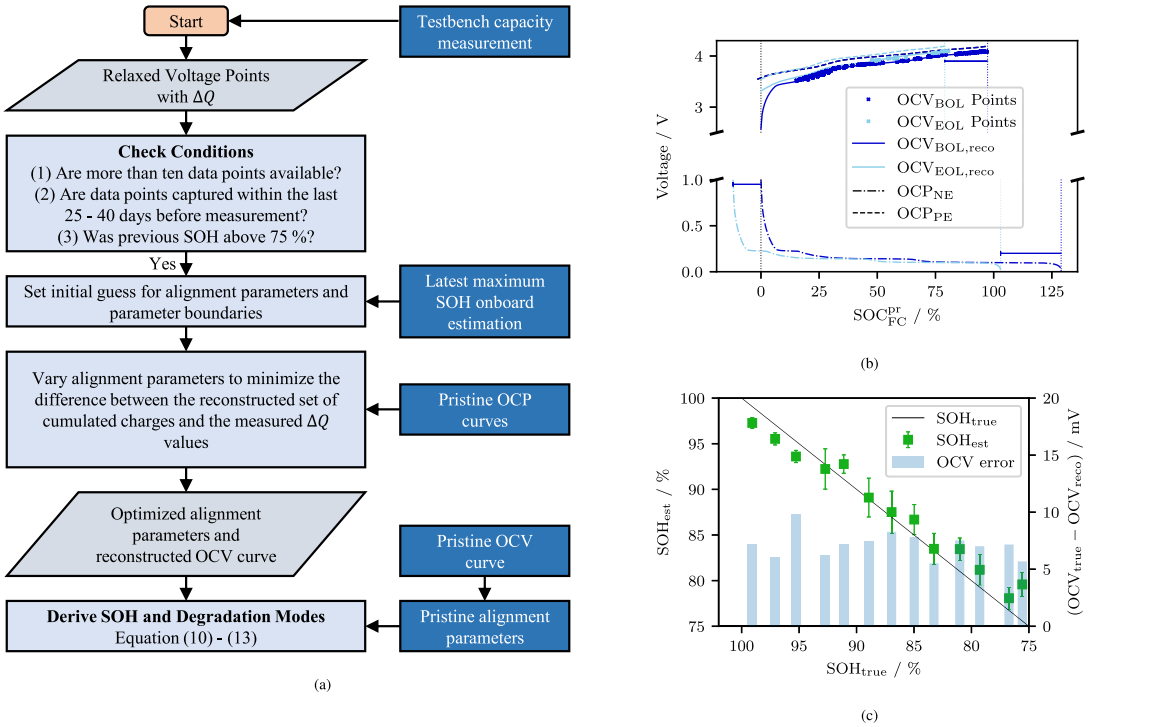

Fig. 5. Application of the algorithm to the vehicle dataset. (a) Workflow of the ΔQ-method. Input fields are colored in dark blue. (b) Input samples and optimization results for a BOL and EOL measurement. The arrows indicate the shift of the half cell potentials due to LAM and LLI. It must be noted that the cathode OCP was measured within a narrow voltage range leading to the appearance of a limiting cathode in discharge direction for the EOL sample. (c) Result for all samples: $MAE_{SOH} = 2.52\,\%$ and OCV reconstruction error: $MAE_{OCV} = 7.19\,mV$. The OCV reconstruction error is solely calculated in respect to the measured points which are used for the fitting process.

Table 3
Optimization settings, constraints and initial values of the *lsqnonlin()* solver for the BMW i3 vehicle dataset. The criteria for the BOL, MOL and EOL condition is realized by accessing the latest maximum SOH onboard estimation.

Setting	Value			
MaxFunEvals	100			
DiffMaxChange	1×10^{-5}			
DiffMinChange	1×10^{-5}			
FinDiffType	central			
Parameter	α_{NE}	α_{PE}	β_{NE}	β_{PE}
	BOL			
Initial Value	1.29	1.01	−0.10	0.00
Lower Bound	1.16	0.96	−0.16	−0.02
Upper Bound	1.29	1.01	0.00	0.00
	MOL			
Initial Value	1.23	0.91	−0.15	0.00
Lower Bound	1.16	0.77	−0.19	0.00
Upper Bound	1.25	0.96	−0.06	0.00
	EOL			
Initial Value	1.16	0.81	−0.16	0.00
Lower Bound	0.97	0.76	−0.20	0.00
Upper Bound	1.23	0.91	−0.08	0.00

BOL: $\max(SOH_{ob}) \geq 95\,\%$, MOL: $80\,\% \leq \max(SOH_{ob}) < 95\,\%$,
EOL: $\max(SOH_{ob}) < 80\,\%$.

still allow convergence. The minimum change in finite-difference for the variables (DiffMinChange) increases from zero to 1×10^{-5}. The maximum change (DiffMaxChange) is reduced from infinity to the same value as DiffMinChange, 1×10^{-5}. These settings allow fast computation while significant optimization steps are performed. It further hinders the algorithm from taking too large steps and potential skipping of optima. The finite difference type (FinDiffType) is switched from forward to centered, which doubles function evaluations but increases accuracy.

Table 4
Alignment parameter for the pristine state (SOH=100 %) and the estimation for an aged storage (SOH=80 %, sample from Fig. 5(b)).

	α_{NE}	α_{PE}	β_{NE}	β_{PE}
Pristine	1.29	1.02	0.00	−0.02
Aged Estimation	1.15	0.79	−0.12	0.00

While these tuned settings lead to a marginal SOH-estimation accuracy increase, they drastically reduce runtime: The MAE_{SOH} reduces from 2.57 % to 2.52 % and the computation time decrease by 41.5 %, on average.

As can be seen, the boundaries of the degradation states overlap, to make up for imprecise classification by the latest maximum SOH onboard estimation. The maximum reachable DMs are 24.8 % for LAM_{NE}, 25.5 % for LAM_{PE} and 26.9 % for LLI. The pristine alignment parameter set is given in Table 4. It further includes the parameter estimation result for the aged sample of Fig. 5(b).

Fig. 5(b) reveals the optimization result for a BOL and EOL sample. The BOL sample is estimated with an absolute SOH error of 1.82 % and underestimates the value to be at 97.2 %. Nevertheless, the OCV reconstruction error stays below 5.62 mV which indicates an accurate fit. The EOL sample reaches an absolute SOH error of 0.13 % and the OCV reconstruction error is 8.21 mV. The alignment parameters in Table 4 yield the DMs: The $LAM_{NE,\,est}$ is 11.2 %, the $LAM_{PE,\,est}$ is 22.4 % and the LLI_{est} adds up to 22.4 %. Due to the oversized anode, the LLI_{est} approximately equals $LAM_{PE,\,est}$ and leads to the estimated SOH of 80 %, which is further visible in Fig. 5(b). It must be noted that the anode overhang in discharge direction for the EOL sample may appear due to the limited voltage range for the cathode OCP measurement. On the contrary, this type of degradation is possible, following the

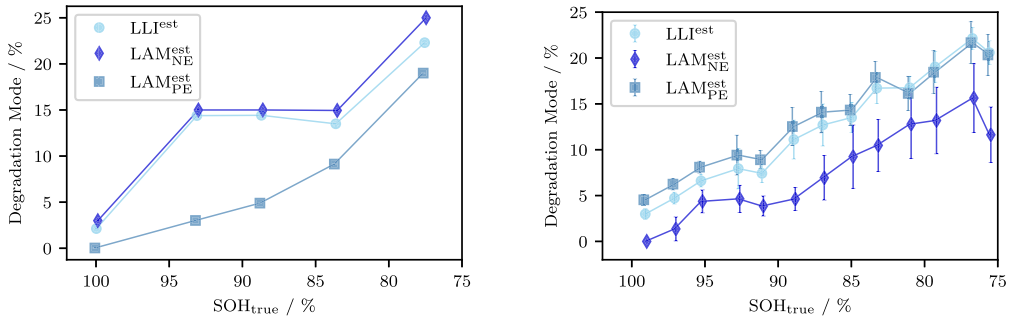

Fig. 6. Evolution of the DMs and their standard deviation, clustered per 2 % SOH range, for the (a) cell dataset and the (b) vehicle dataset. The markers for the LAM modes are slightly shifted to the left and right of the true SOH value in order to increase visibility.

explanations by Birkl et al. [5], who contribute this type of electrode shifting to delithiated LAM_{PE}.

The evaluation for the full dataset is presented in Fig. 5(c). The ΔQ-method achieves reasonable results with an MAE_{SOH} of 2.52 % against the testbench capacity measurements and an MAE_{OCV} of 7.19 mV. The standard deviation implies high estimation confidence for a broad spectrum of vehicles. For the larger and more diverse i3 dataset, the correlation of SOH and OCV accuracy is less prominent.

4. Discussion

One big advantage of the proposed method (or in general, the mechanistic model approach [43]) lies in the reconstructed OCV which is used to not only estimate the SOH but also the DMs. The OCV further is an important input for other vehicle functions, i.e., SOC estimation [8] or the fast charging strategy [52]. The studied datasets do not include a validated DM label due to the missing full OCV readouts for every SOH and the further challenging DM estimation, usually based on DVA and ICA [5]. It is possible, however, to evaluate the accuracy of the estimation by the OCV reconstruction error and the SOH estimation error. With these metrics, the ΔQ-method is further analyzed in terms of sensitivity to input data and solver settings.

4.1. Degradation mode estimation

Fig. 6 illustrates the trajectory of the estimated DMs for the cell dataset (Fig. 6(a)) and the vehicle dataset 6(b).

As expected, the DMs of the cell dataset in Fig. 6(a) generally increase with higher age. While the LAM_{PE} shows a reasonable continuous rise, LAM_{NE} and LLI increase rapidly after the first check-up at approximately 97 %. Moreover, LAM_{NE} stays constant for the consecutive two checkups. It is suspicious that the LLI decreases again. This, however, is not physically but mathematically possible if the β-parameters get closer to zero and their offset $\|\beta_{PE}\| - |\beta_{NE}\|$ decreases. Hence, mathematically more lithium inventory is available for cycling again. Measured by the SOH and OCV error, the first two checkups (100 % to 97 % SOH) are estimated with high accuracy, making the DM estimation feasible. The third and fourth check-up (87 % to 84 %), however, underestimate the SOH and contain a relatively high OCV error. This makes an underestimation of the LAM_{PE} very likely. In this degraded state, LLI shows high correlation to both types of LAM due to the consumed capacity overhang. Hence, the underestimated LAM_{PE} probably leads to an underestimation of LLI and consequently the lower SOH estimate. The last check-up overestimates the SOH and shows an acceptable OCV error. The most viable option is an underestimated β_{PE} which further increases LLI.

For more samples, as visualized in Fig. 6(b) for the i3 vehicle dataset, the consistent trend of the DMs is more visible. The LAM_{NE} contains the highest fluctuation, especially with the underestimation at 92 % SOH. At BOL the LLI is a result of LAM at both electrodes once the electrode capacity overhangs are consumed. Below 90 % SOH the LAM_{PE} exceeds the LAM_{NE} and LLI matches LAM_{PE} due to the oversized anode. This is reasonable due to the restricted search space of β_{PE} (Table 3) which results from the narrow voltage range of the cathode OCP measurement. This yields the fact that a decreasing α_{PE} directly influences the LLI. A strong anomaly for LAM_{PE} is visible at 82 % SOH with a decreasing slope. Analyzing Fig. 5(c) makes clear that the SOH is overestimated and hence it is reasonable that LAM_{PE} might be underestimated. Besides that, the highest SOC and OCV errors are located at 92 %, 82 % and especially 75 %. All these samples lead to anomalies in the course of the DMs. Hence, this strengthens the previous assumption of the correlation of SOH and OCV reconstruction with the DM estimation accuracy.

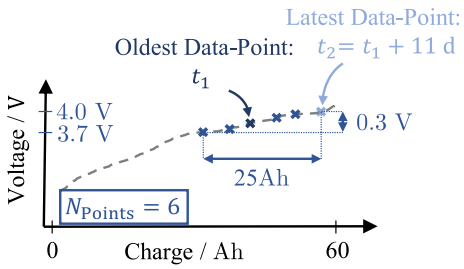

Fig. 7. Fictional sample as an example for the evaluation of applied data filters. This sample includes six data points, which were captured within a time-window of 11 days. The data points span a charge section of 25 Ah and a voltage window of 0.3 V. The minimum voltage is 3.7 V and the maximum voltage is 4.0 V.

4.2. Sensitivity of the method to input data

In comparison to the cell dataset, the i3 vehicle dataset has relatively sparse information included. The dataset was captured from the field without focus on the ΔQ-method and hence does not include the full operational strategy between the captured points. Nevertheless, it is insightful to explore the sensitivity of the method to the initially defined settings and further to understand why the filters are set as depicted in Fig. 5(a).

To better understand the applied filters and their impact, the process of dataset filtering is explored for an example sample, as depicted in Fig. 7. The filters always refer to the full input dataset per vehicle. Hence, the Δt, $\max(\Delta Q)$ and ΔV relate to several relaxed voltage points between multiple charging and driving events.

Table 5
Applied filters, their criteria and the final evaluation for the random sample in Fig. 7. For this specific example all example filters hold true and the sample could be further processed in the algorithm. The default filters do not hold true and the sample would be excluded.

Filter	Criterion	Check	Result
Example			
N_{Points}	$N \geq 5$	$6 \geq 5$	✓
Δt	$\Delta t \leq 20\,\text{d}$	$11\,\text{d} \leq 20\,\text{d}$	✓
$\max(\Delta Q)$	$\max(\Delta Q) \leq 30\,\text{Ah}$	$25\,\text{Ah} \leq 30\,\text{Ah}$	✓
ΔV	$\Delta V \leq 0.5\,\text{V}$	$0.3\,\text{V} \leq 0.5\,\text{V}$	✓
V_{start}	$V_{\text{start}} \geq 3.5\,\text{V}$	$3.7\,\text{V} \geq 3.5\,\text{V}$	✓
V_{end}	$V_{\text{end}} \leq 4.1\,\text{V}$	$4.0\,\text{V} \leq 4.1\,\text{V}$	✓
Default			
N_{Points}	$N \geq 10$	$6 \ngeq 10$	✗
Δt	$\Delta t \leq 25\,\text{d}$ *to* $40\,\text{d}$	$11\,\text{d} \leq 25\,\text{d}$	✓

Table 5 evaluates the example sample for the randomly set and the default filters. With this background knowledge, it should be straightforward to interpret the following discussion.

The possible filter variations and resulting SOH and OCV errors are visualized in Fig. 8. The default number of required points is set to 10. In contrast to the absolute variation in Fig. 8(b), the default value of the time threshold is set relative to the age (time since delivery) of the vehicle. Per default, for a BOL vehicle the last 25 days, while for an EOL vehicle up to 40 days, are used. Similar to the mileage feature, the age highly correlates with the SOH. These filters are mainly set due to the smaller number of available points for older vehicles (compare Fig. 3). Hence, increasing the time threshold for older vehicles, allows more samples with a higher number of points which cancels out the negative effect of itself. For the proposed algorithm, no filters are set regarding available voltage window, minimum and maximum voltage or maximum ΔQ. For every subfigure in Fig. 8, one variable is varied while all others are fixated to the default value. All used default settings are listed in the bottom section of Table 5. In Fig. 8 the rate of use is normalized to the number of investigated vehicles (574) and gives the number of available samples after the filtering. A small fraction ($< 10\,\%$) is initially unavailable due to the preset filters in Fig. 5(a) checking for feasible SOH values between $75\,\%$ to $100\,\%$.

In practice, the algorithm already works with at least three points. As can be seen in Fig. 8(a), more sample points lead to higher accuracy. On the contrary, by requiring more points less samples fulfill these conditions. The amount of usable samples in relation to the total number of samples is referred to as rate of use. A sample size of 10 points allows high accuracy and a high rate of use. On the contrary, more points continuously lead to slightly higher OCV reconstruction errors because more points increase the complexity of the fitting process. It must be noted that the statistical significance decreases with more required points due to the smaller rate of use.

For every sample, the date of the testbench capacity measurement is not only the reference for the SOH but also to select past relaxed voltage and ΔQ pairs. In Fig. 8(b) an upwards trend in the SOH error is detectable for a longer allowed data acquisition time. This behavior is reasonable due to the continuous nature of battery aging. The OCV error slightly decreases continuously. With a looser time-threshold more points over a broader SOC range and hence more samples are available for estimation. The voltage and ΔQ information provided by additional points seems to counteract the error from increasing time windows between points. This is especially the case for MOL and EOL vehicles which have a lower frequency of recordings within specific time periods (see Fig. 3).

Fig. 8(c) shows the influence of the accumulated charge amount between relaxed voltage points. Starting with a ΔQ of $8\,\text{Ah}$, enough points for some samples are available to pass the prefilter. The SOH error increases over $4\,\%$ with a $\max(\Delta Q)$ of approximately $12\,\text{Ah}$. The error continuously decreases for higher ΔQ constraints, making clear that with $50\,\text{Ah}$ all possible samples are available. The OCV error follows the slope of the SOH error. This again, gives rise to the assumption of an existing correlation between the OCV reconstruction accuracy and the SOH error. The interpretation, however, must be seen in the context of the error, which fluctuates between low values of $6.6\,\text{mV}$ to $8.0\,\text{mV}$.

The voltage window is analyzed in Fig. 8(d). The voltage boundaries are set according to Fig. 3. For BOL vehicles this voltage window of $0.9\,\text{V}$ equals the SOC width from $4\,\%$ to $100\,\%$. The correct SOC value is unknown for aged vehicles because the full and validated OCV is only known for pristine state. Hence an estimation aided by a look-up table is only possible for BOL vehicles. Due to the shifting of the OCV with degradation, huge errors are possible if the pristine OCV curves is used for a look-up table based SOC estimation. Consequently, the accuracy of the method is evaluated against varying available voltage windows instead of SOC windows. Fig. 8(d) shows the big advantage of the ΔQ-method. Accurate results are already feasible with small voltage windows, starting at $0.3\,\text{V}$, which equals approximately $60\,\%$ SOC for BOL vehicles if the start SOC is set to $40\,\%$, or $45\,\%$ if the start SOC is set to $30\,\%$, as can be seen in Fig. 5(b). The SOH error decreases with broader voltage windows and the rate of use increases. The OCV reconstruction error shows an upwards trend for broader voltage windows, giving more support to the following interpretation: It is most probable that broader voltage windows allow more uncertainty in the exact position of the relaxed voltage points which, as a result, yields a more inaccurate reconstruction.

In Figs. 8(e) and 8(f) the accuracy in dependence of the minimum and maximum voltage is depicted. With a higher minimum voltage a smaller voltage window and hence less points per sample are available. This leads to not only a lower rate of use but also a higher SOH estimation error. The dependence of the OCV reconstruction error on the minimum voltage strengthens the previously made interpretation: A smaller available voltage and charge window leads to less uncertainty and hence more precise reconstruction. In summary, a preset minimum voltage below $3.8\,\text{V}$ is sufficient for an adequate OCV reconstruction and SOH estimation. Due to mostly present relaxation voltages at higher SOCs in all samples, the maximum voltage must be set relatively high. As can be seen in Fig. 3 most of the data is distributed at high voltage values because of many charging events. The minimum maximum voltage allowing for an adequate rate of use is $4.10\,\text{V}$. The error behaves mostly as expected: With a higher allowed maximum voltage more samples and points are included in the reconstruction and the SOH and OCV error decreases. Both errors inhibit a minimum for an allowed maximum voltage of $4.09\,\text{V}$. This, however, lacks statistical significance due to an rate of use below $20\,\%$.

4.3. Sensitivity of the method to different solvers and settings

The solver choice and algorithm settings are evaluated. Table 6 shows the SOH error for five solvers in dependence to two varied setting: maximum evaluations or generations and function tolerance. For all solvers except *lsqnonlin()* the cost function is modified to return a scalar value.

As can be seen in Table 6, the solver choice has marginal impact on performance. The nonlinear least squares solver *lsqnonlin()* shows the best performance. The pattern search algorithm with five evaluations has the second highest accuracy but is computationally more complex [53]. The chosen maximum function tolerance of 100 assures to find the optimum without wasting computational effort and could be reduced even further. On the other side, the function tolerance does not seem to influence the accuracy at all, see Table 6. The termination tolerance on the objective function has no influence until it reaches relatively high values of almost 1×10^{-1}. Consequently, the optima in the objective functions are reached early within the optimization process, i.e., the higher function tolerance and possibly slower convergence do not hinder the algorithm to find the lowest cost function value. Starting

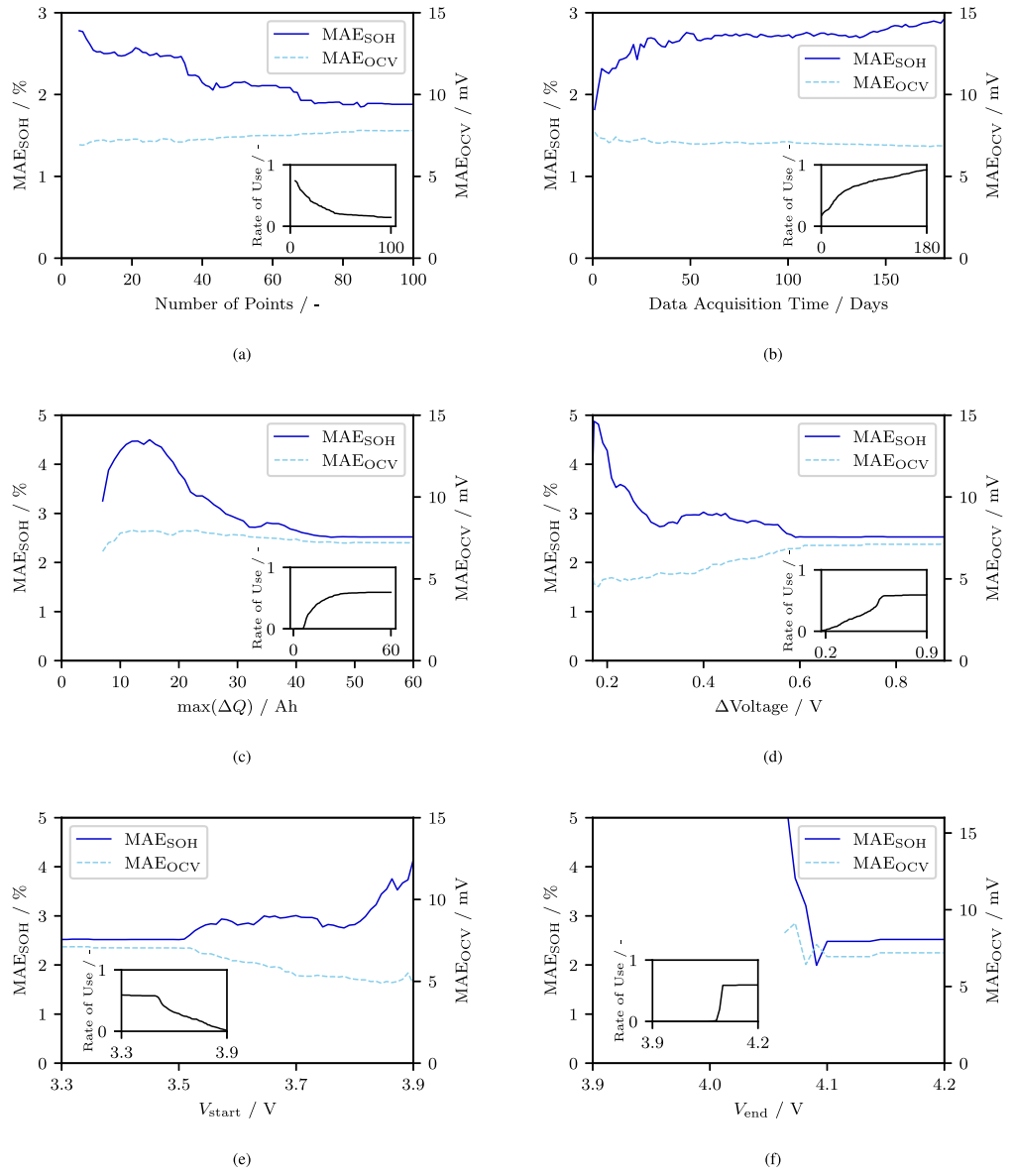

Fig. 8. Sensitivity of the ΔQ-method to specific input data filters and the resulting rate of use for the vehicle dataset. (a) Number of data points. (b) Data acquisition time horizon. (c) Maximum allowed amount of charge between two consecutive points. (d) Available voltage window in sample, where 0.9 V equals the SOC range from 4 % to 100 % for BOL batteries. (e) Minimum voltage threshold. (f) Maximum voltage threshold.

with function tolerances of 1×10^{-1} the optimization eventually stops too early and might miss the local optimum.

In summary, the designed cost function (Eq. (9)) is mathematically well-designed and robust against varying solvers and their settings. The chosen settings, as shown in Table 3, assure to find the local optimum with lowest SOH estimation and OCV reconstruction error.

4.4. Comprehensive analysis and discussion

The present study introduces a novel method for OCV reconstruction and subsequent SOH and DM estimation. The main research question at hand was whether the method is applicable to real-world data and how robust the algorithm is against varying input data and optimization settings. The application to real-world vehicle data from the BMW i3 could quantify the uncertainty of the method for the SOH estimation and demonstrate the robustness of the algorithm with respect to filter parameters and solver settings. As can be seen in Fig. 8(a), with already three relaxed voltage points and two ΔQ values, the method reaches an SOH error below 3 % and reconstructs the OCV with an average error below 10 mV. In contrast to conventional methods, the ΔQ-method does not require a fixed reference voltage for the fitting process but rather fits every voltage pair individually.

Established methods for OCV reconstruction [5,7,24–35] demand the full SOC range with relatively low C-rates to yield accurate results for DM estimation. Improved studies [37–39] established the possibility to reduce the SOC window and further increase the C-rate. Yang et al. [37] managed to use partial charging segments from 20 % to 70 % SOC with a C-rate of C/3. Similar, Chen et al. [38] reconstructed the OCV

Table 6
Sensitivity of the ΔQ-method's SOH estimation accuracy to the selected solver and specific algorithm settings, i.e., maximum function evaluations and function tolerance for termination. In the case of the genetic algorithm, the maximum function evaluations refer to the maximum number of generations and for the particle swarm it is the maximum number of iterations. The OCV fitting accuracy is almost independent (sensitivity below ±1 mV) of the investigated settings and hence not included in this Table.

	Maximum Evaluations/Generations			
Solver	5	50	100	200
lsqnonlin	3.76 %	2.46 %	2.52 %	2.54 %
fmincon	3.34 %	2.91 %	2.88 %	2.89 %
Genetic Algorithm	2.79 %	2.96 %	2.92 %	2.86 %
Particle Swarm	2.88 %	2.88 %	2.90 %	2.90 %
Pattern Search	2.69 %	2.94 %	3.01 %	3.01 %
	Function Tolerance			
Solver	10^{-10}	10^{-8}	10^{-4}	10^{-1}
lsqnonlin	2.53 %	2.53 %	2.52 %	2.40 %
fmincon	2.88 %	2.88 %	2.88 %	2.88 %
Genetic Algorithm	2.94 %	2.88 %	2.88 %	2.91 %
Particle Swarm	2.90 %	2.90 %	2.97 %	2.96 %
Pattern Search	3.01 %	3.01 %	3.01 %	3.01 %

with partial charging segment from 40 % to 100 % SOC and a C-rate of C/3. Schmitt et al. [39] raised the applicable C-rate up to C/4 by introducing a constant overpotential offset to reconstruct the partial OCV. The offset is calculated by repetitive pulse measurements to make up for the increasing internal resistance due to aging. Nevertheless, for a C-rate of C/4 a SOC window of at least 10 % to 80 % is mandatory to create accurate capacity estimations. Accurate DM estimation is feasible for C-rates below C/15 and a maximum SOC of at least 70 %. For lower C-rates of C/30 a smaller window of 20 % to 70 % is sufficient to yield an SOH error below 2 %. The ΔQ-method, however, works without any preprocessing because the relaxed voltage points, which equal the actual OCV, are utilized in the first place. These relaxed voltage points are gathered after almost every charging or driving event, independent of the applied current and history. Figs. 8(d), 8(e) and 8(f) prove that a voltage window of at least 300 mV and a starting voltage below 3.8 V suffice to reconstruct the OCV with an error below 7 mV and estimate the SOH with an error $\leq$ 3 %. For the pristine battery, these values correspond to a SOC window from 40 % to 100 %. For a lower starting voltage of 3.7 V the required SOC window spans from 30 % to 75 % which reduces the minimum required SOC range in comparison to known studies [37–39]. In contrast to existing methods [4,5,7,24–41], the ΔQ-method is independent of any reference charging process. It utilizes existing data from any vehicle fleet with very low sample rate and thus also low requirements with respect to bandwidth and/or storage capabilities that could be easily implemented in existing architectures. As there are no available data sources suitable for both the mechanistic model approach involving higher C-rates and partial charging segments, as well as the ΔQ-method, a comparison is performed using individual aging datasets.

The proposed method proves its suitability for given vehicle datasets, as in Fig. 5(c). With the default filters of at least 10 data points per sample, a maximum time-horizon of 25 to 40 days and the dependence on the last maximum SOH onboard estimation, a big fraction of over 59 % of the investigated vehicles with an existing testbench capacity measurement can be evaluated. The data is stored without any limitation on the operation between relaxed voltage points or temperature. It further shows in Figs. 8(b) and 8(c), that the algorithm is only slightly influenced by the time-horizon of data acquisition or the maximum allowed accumulated charge in-between voltage points, once $\max(\Delta Q) \geq 20$ Ah. These dependencies are further canceled out by the large benefit of more sample points distributed between a large voltage window which have the biggest influence on SOH and OCV error, as Figs. 8(a), 8(d), 8(e) and 8(f) show.

Existing methods [37] usually set the constraints and boundary conditions in respect to the last evaluation. Because this method is proposed for a vehicle fleet with at least one testbench capacity measurement during its lifetime, the boundary conditions must be set initially. The solution space, however, must be limited to reduce the risk of reaching the wrong local optimum. For this matter, the upper and lower boundaries of the α- and β-parameter are set according to the last maximum SOH onboard estimation which divides the storage into BOL, MOL and EOL, as in Table 3. Although this seems to bias the estimation towards the onboard estimation values, it must be kept in mind, that the onboard estimation is limited by the computation resources. The alignment parameter boundaries are defined loosely, to even allow out-of-bound estimations if the onboard value is completely off. Fig. 3 visualizes the strong correlation of mileage with the true SOH. It is thus possible to exchange the condition variable with either mileage or total time since production.

The total time since production is already used for setting the time-horizon filters as proposed in Fig. 5(a). Depending on this value, older vehicles use more of their history than new vehicles. While this filter hardly influences accuracy, it helps to increase the rate of use as Fig. 8(b) shows.

In comparison to the cell data results (Fig. 4(d)), the vehicle data OCV is reconstructed with similar precision over all samples (Fig. 5(c)). The OCV is only evaluated at its measured points. The reconstructed OCV is interpolated and evaluated at the respective measured charge points to calculate the OCV reconstruction error. The average number of available points for optimization, however, is 70 for the i3 dataset, assuring higher OCV reconstruction accuracy with statistical significance.

The proposed dataset is not applicable to verify the DM estimation because no full OCV measurement in aged state is available. It is only possible to evaluate the accuracy in dependence of their plausibility over SOH (Fig. 6(b)) and in terms of OCV error (Fig. 5(c)). With this mitigated criteria, the DM estimation shows reasonable trajectories.

In contrast to known methods for OCV reconstruction [4,5,7,24–41], the ΔQ-algorithm collects data from a broader time-horizon instead of relying on continuous measurements. The results in Fig. 8(b) give strong evidence that the influence of aging in data acquisition windows up to half a year is negligible. This further gives rise to the possibility to exploit this data collection scheme for time-series based algorithms, i.e., collection of several partial charging segments at a specific C-rate and subsequent reassembly.

5. Conclusion

In this work, the novel ΔQ-method was introduced and validated with real-world vehicle data gathered from more than 8 years of customer operation. The analysis showed that the method is robust to input data, solver choice and optimization settings. For the BMW i3, a minimum number of three relaxed voltage points, at least a voltage point below 3.8 V, and a minimum voltage window of 0.3 V – which combined equals a SOC window of 40 % to 100 % – were sufficient to yield SOH estimation errors below 3 %.

The algorithm is an adoption of the known mechanistic modeling approach [4] and eases the utilization for existing BEV fleets. The method does not require explicit charging segments with low C-rates but rather is applicable to relaxed voltage points and the accumulated charge between these points. No fixed reference voltage is required for the optimization process and rather every voltage pair is fitted individually during the minimization task. Analysis of the BMW i3 dataset shows that a large fraction of the studied vehicles ($\geq$ 59 %) are enabled for application.

The proposed method shows its suitability for existing BEV fleets. Most monitoring systems collect the relaxed voltage points and track the accumulated charge. Hence, it is straightforward to use these existing datasets for OCV reconstruction if the pristine OCPs and parameter sets are known. Updated OCVs further allow calibrated SOC estimation and improved charging strategies.

The algorithm requires the latest SOH onboard estimation to constrain the solution space which is usually available for modern BEV fleets. This dependence is solvable with exchanging the criteria with aging-correlating variables, i.e., time or mileage. The method can be further enhanced by leveraging the remaining available vehicle aging data to restrict the solution space using machine learning techniques. Alternatively, combining existing methods for OCV reconstruction with the ΔQ-method can reduce uncertainty. The method's validity for DM estimation remains unconfirmed and exceeds the scope of this publication. Therefore, further evaluation of this aspect is imperative in future research endeavors. It stays an open research question whether the proposed ΔQ-method is suitable to estimate the DMs, even with narrow SOC windows of 50 %. It is therefore desired to prove this assumption with an extended measurement series with full OCV measurements in the checkups, to derive the DVA and ICA which can be used to create comparable DM labels.

CRediT authorship contribution statement

Tobias Hofmann: Writing – original draft, Visualization, Validation, Software, Methodology, Investigation, Formal analysis, Conceptualization. **Jiahao Li:** Methodology, Conceptualization. **Jacob Hamar:** Writing – review & editing, Supervision. **Simon Erhard:** Writing – review & editing, Supervision. **Jan Philipp Schmidt:** Writing – review & editing, Supervision.

Declaration of competing interest

The authors declare the following financial interests/personal relationships which may be considered as potential competing interests: Tobias Hofmann reports financial support was provided by BMW Group. Jiahao Li has patent Verfahren zur Bestimmung der SOC-OCV Kennlinien und Kapazität einer Batterie mit Blendmaterialien pending to BMW Group. If there are other authors, they declare that they have no known competing financial interests or personal relationships that could have appeared to influence the work reported in this paper.

Data availability

The data that has been used is confidential.

Acknowledgments

This work was funded by the BMW Group and was performed in cooperation with the University of Bayreuth - Chair of Systems Engineering for Electrical Energy Storage.

References

[1] Z. Ma, J. Jiang, W. Shi, W. Zhang, C.C. Mi, Investigation of path dependence in commercial lithium-ion cells for pure electric bus applications: Aging mechanism identification, J. Power Sources 274 (2015) 29–40, http://dx.doi.org/10.1016/j.jpowsour.2014.10.006.

[2] L. Su, J. Zhang, J. Huang, H. Ge, Z. Li, F. Xie, B.Y. Liaw, Path dependence of lithium ion cells aging under storage conditions, J. Power Sources 315 (2016) 35–46, http://dx.doi.org/10.1016/j.jpowsour.2016.03.043.

[3] T. Raj, A.A. Wang, C.W. Monroe, D.A. Howey, Investigation of path-dependent degradation in lithium-ion batteries, Batteries Supercaps 3 (2020) 1377, http://dx.doi.org/10.1002/batt.202000160.

[4] M. Dubarry, C. Truchot, B.Y. Liaw, Synthesize battery degradation modes via a diagnostic and prognostic model, J. Power Sources 219 (2012) 204–216, http://dx.doi.org/10.1016/j.jpowsour.2012.07.016.

[5] C.R. Birkl, M.R. Roberts, E. McTurk, P.G. Bruce, D.A. Howey, Degradation diagnostics for lithium ion cells, J. Power Sources 341 (2017) 373–386, http://dx.doi.org/10.1016/j.jpowsour.2016.12.011.

[6] P.M. Attia, A. Bills, F.B. Planella, P. Dechent, G.d. Reis, M. Dubarry, P. Gasper, R. Gilchrist, S. Greenbank, D. Howey, O. Liu, E. Khoo, Y. Preger, A. Soni, S. Sripad, A.G. Stefanopoulou, V. Sulzer, Review—Knees in lithium-ion battery aging trajectories, J. Electrochem. Soc. 169 (2022) 060517, http://dx.doi.org/10.1149/1945-7111/ac6d13.

[7] J.P. Schmidt, H.Y. Tran, J. Richter, E. Ivers-Tiffée, M. Wohlfahrt-Mehrens, Analysis and prediction of the open circuit potential of lithium-ion cells, J. Power Sources 239 (2013) 696–704, http://dx.doi.org/10.1016/j.jpowsour.2012.11.101.

[8] G.L. Plett, Extended Kalman filtering for battery management systems of LiPB-based HEV battery packs: Part 1. Background, J. Power Sources 134 (2) (2004) 252–261, http://dx.doi.org/10.1016/j.jpowsour.2004.02.031.

[9] J. Newman, N.P. Balsara, Electrochemical Systems, 4th Edition, John Wiley % Sons, ISBN: 978-1-119-51459-6, 2021.

[10] M. Doyle, T.F. Fuller, J. Newman, Modeling of galvanostatic charge and discharge of the lithium/polymer/insertion cell, J. Electrochem. Soc. 140 (1993) 1526, http://dx.doi.org/10.1149/1.2221597.

[11] T.F. Fuller, M. Doyle, J. Newman, Simulation and optimization of the dual lithium ion insertion cell, J. Electrochem. Soc. 141 (1994) 1, http://dx.doi.org/10.1149/1.2054684.

[12] A. Allam, S. Onori, Online capacity estimation for lithium-ion battery cells via an electrochemical model-based adaptive interconnected observer, IEEE Trans. Control Syst. Technol. 29 (2021) 1636–1651, http://dx.doi.org/10.1109/TCST.2020.3017566.

[13] X. Zhao, Y. Bi, S.-Y. Choe, S.-Y. Kim, An integrated reduced order model considering degradation effects for LiFePO4/graphite cells, Electrochim. Acta 280 (2018) 41–54, http://dx.doi.org/10.1016/j.electacta.2018.05.091.

[14] P. Gambhire, K.S. Hariharan, A. Khandelwal, S.M. Kolake, T. Yeo, S. Doo, A physics based reduced order aging model for lithium-ion cells with phase change, J. Power Sources 270 (2014) 281–291, http://dx.doi.org/10.1016/j.jpowsour.2014.07.127.

[15] Y. Gao, K. Liu, C. Zhu, X. Zhang, D. Zhang, Co-estimation of state-of-charge and state-of- health for lithium-ion batteries using an enhanced electrochemical model, IEEE Trans. Ind. Electron. 69 (2022) 2684–2696, http://dx.doi.org/10.1109/TIE.2021.3066946.

[16] X. Sui, S. He, S.B. Vilsen, J. Meng, R. Teodorescu, D.-I. Stroe, A review of non-probabilistic machine learning-based state of health estimation techniques for lithium-ion battery, Appl. Energy 300 (2021) 117346, http://dx.doi.org/10.1016/j.apenergy.2021.117346.

[17] K. Luo, X. Chen, H. Zheng, Z. Shi, A review of deep learning approach to predicting the state of health and state of charge of lithium-ion batteries, J. Energy Chem. 74 (2022) 159–173, http://dx.doi.org/10.1016/j.jechem.2022.06.049.

[18] Q. Gong, P. Wang, Z. Cheng, A data-driven model framework based on deep learning for estimating the states of lithium-ion batteries, J. Electrochem. Soc. 169 (2022) 030532, http://dx.doi.org/10.1149/1945-7111/ac5bac.

[19] W. Li, N. Sengupta, P. Dechent, D. Howey, A. Annaswamy, D.U. Sauer, Online capacity estimation of lithium-ion batteries with deep long short-term memory networks, J. Power Sources 482 (2021) 228863, http://dx.doi.org/10.1016/j.jpowsour.2020.228863.

[20] Y. Choi, S. Ryu, K. Park, H. Kim, Machine learning-based lithium-ion battery capacity estimation exploiting multi-channel charging profiles, IEEE Access 7 (2019) 75143–75152, http://dx.doi.org/10.1109/ACCESS.2019.2920932.

[21] K. Luo, H. Zheng, Z. Shi, A simple feature extraction method for estimating the whole life cycle state of health of lithium-ion batteries using transformer-based neural network, J. Power Sources 576 (2023) 233139, http://dx.doi.org/10.1016/j.jpowsour.2023.233139.

[22] J. Yang, B. Xia, W. Huang, Y. Fu, C. Mi, Online state-of-health estimation for lithium-ion batteries using constant-voltage charging current analysis, Appl. Energy 212 (2018) 1589–1600, http://dx.doi.org/10.1016/j.apenergy.2018.01.010.

[23] J. Cannarella, C.B. Arnold, State of health and charge measurements in lithium-ion batteries using mechanical stress, J. Power Sources 269 (2014) 7–14, http://dx.doi.org/10.1016/j.jpowsour.2014.07.003.

[24] M. Dubarry, M. Berecibar, A. Devie, D. Anseán, N. Omar, I. Villarreal, State of health battery estimator enabling degradation diagnosis: Model and algorithm description, J. Power Sources 360 (2017) 59–69, http://dx.doi.org/10.1016/j.jpowsour.2017.05.121.

[25] Z. Ma, Z. Wang, R. Xiong, J. Jiang, A mechanism identification model based state-of-health diagnosis of lithium-ion batteries for energy storage applications, J. Clean. Prod. 193 (2018) 379–390, http://dx.doi.org/10.1016/j.jclepro.2018.05.074.

[26] C. Pastor-Fernández, T.F. Yu, W.D. Widanage, J. Marco, Critical review of non-invasive diagnosis techniques for quantification of degradation modes in lithium-ion batteries, Renew. Sustain. Energy Rev. 109 (2019) 138–159, http://dx.doi.org/10.1016/j.rser.2019.03.060.

[27] J.P. Fath, D. Dragicevic, L. Bittel, A. Nuhic, J. Sieg, S. Hahn, L. Alsheimer, B. Spier, T. Wetzel, Quantification of aging mechanisms and inhomogeneity in cycled lithium-ion cells by differential voltage analysis, J. Energy Storage 25 (2019) 100813, http://dx.doi.org/10.1016/j.est.2019.100813.

[28] K.M. Mbeya, N. Damay, G. Friedrich, C. Forgez, M. Juston, Off-line method to determine the electrode balancing of li-ion batteries, Math. Comput. Simulation 183 (2021) 34–47, http://dx.doi.org/10.1016/j.matcom.2020.02.013.

[29] D. Anseán, G. Baure, M. González, I. Cameán, A.B. García, M. Dubarry, Mechanistic investigation of silicon-graphite/LiNi0.8Mn0.1Co0.1O2 commercial cells for non-intrusive diagnosis and prognosis, J. Power Sources 459 (2020) 227882, http://dx.doi.org/10.1016/j.jpowsour.2020.227882.

[30] S. Lee, J.B. Siegel, A.G. Stefanopoulou, J.-W. Lee, T.-K. Lee, Electrode state of health estimation for lithium ion batteries considering half-cell potential change due to aging, J. Electrochem. Soc. 167 (2020) 090531, http://dx.doi.org/10.1149/1945-7111/ab8c83.

[31] B. Pan, D. Dong, J. Wang, J. Nie, S. Liu, Y. Cao, Y. Jiang, Aging mechanism diagnosis of lithium ion battery by open circuit voltage analysis, Electrochim. Acta 362 (2020) 137101, http://dx.doi.org/10.1016/j.electacta.2020.137101.

[32] M. Dubarry, D. Beck, Perspective on mechanistic modeling of li-ion batteries, Accounts Mater. Res. 3 (2022) 843–853, http://dx.doi.org/10.1021/accountsmr.2c00082.

[33] I. Bin-Mat-Arishad, B. Wimarshana, A. Fly, Influence of voltage profile and fitting technique on the accuracy of lithium-ion battery degradation identification through the voltage profile model, J. Energy Storage 70 (2023) 107884, http://dx.doi.org/10.1016/j.est.2023.107884.

[34] M. Dubarry, V. Agrawal, M. Hüske, M. Kuipers, Accurate LLI and LAMPE estimation using the mechanistic modeling approach with layered oxides, J. Electrochem. Soc. 170 (2023) 070503, http://dx.doi.org/10.1149/1945-7111/ace21c.

[35] J. Schmitt, M. Schindler, A. Oberbauer, A. Jossen, Determination of degradation modes of lithium-ion batteries considering aging-induced changes in the half-cell open-circuit potential curve of silicon–graphite, J. Power Sources 532 (2022) 231296, http://dx.doi.org/10.1016/j.jpowsour.2022.231296.

[36] S. Schindler, G. Baure, M.A. Danzer, M. Dubarry, Kinetics accommodation in li-ion mechanistic modeling, J. Power Sources 440 (2019) 227117, http://dx.doi.org/10.1016/j.jpowsour.2019.227117.

[37] S. Yang, C. Zhang, J. Jiang, W. Zhang, Y. Gao, L. Zhang, A voltage reconstruction model based on partial charging curve for state-of-health estimation of lithium-ion batteries, J. Energy Storage 35 (2021) 102271, http://dx.doi.org/10.1016/j.est.2021.102271.

[38] J. Chen, M.N. Marlow, Q. Jiang, B. Wu, Peak-tracking method to quantify degradation modes in lithium-ion batteries via differential voltage and incremental capacity, J. Energy Storage 45 (2022) 103669, http://dx.doi.org/10.1016/j.est.2021.103669.

[39] J. Schmitt, M. Rehm, A. Karger, A. Jossen, Capacity and degradation mode estimation for lithium-ion batteries based on partial charging curves at different current rates, J. Energy Storage 59 (2023) 106517, http://dx.doi.org/10.1016/j.est.2022.106517.

[40] D. Lu, M.S. Trimboli, G. Fan, R. Zhang, G.L. Plett, Implementation of a physics-based model for half-cell open-circuit potential and full-cell open-circuit voltage estimates: Part II. Processing full-cell data, J. Electrochem. Soc. 168 (2021) 070533, http://dx.doi.org/10.1149/1945-7111/ac11a5.

[41] Z. Cui, N. Cui, C. Li, J. Lu, C. Zhang, Online identification and reconstruction of open-circuit voltage for capacity and electrode aging estimation of lithium-ion batteries, IEEE Trans. Ind. Electron. 70 (2023) (2023) 4716–4726, http://dx.doi.org/10.1109/TIE.2022.3187596.

[42] M. Dubarry, D. Beck, Big data training data for artificial intelligence-based li-ion diagnosis and prognosis, J. Power Sources 479 (2020) 228806, http://dx.doi.org/10.1016/j.jpowsour.2020.228806.

[43] M. Dubarry, D. Beck, Analysis of synthetic voltage vs. Capacity datasets for big data li-ion diagnosis and prognosis, Energies 14 (2021) 2371, http://dx.doi.org/10.3390/en14092371.

[44] N. Costa, L. Sánchez, D. Anseán, M. Dubarry, Li-ion battery degradation modes diagnosis via convolutional neural networks, J. Energy Storage 55 (Part C) (2022) 105558, http://dx.doi.org/10.1016/j.est.2022.105558.

[45] J. Tian, R. Xiong, W. Shen, F. Sun, Electrode ageing estimation and open circuit voltage reconstruction for lithium ion batteries, Energy Storage Mater. 37 (2021) 283–295, http://dx.doi.org/10.1016/j.ensm.2021.02.018.

[46] X. Liu, S. Li, J. Tian, Z. Wei, P. Wang, Health estimation of lithium-ion batteries with voltage reconstruction and fusion model, Energy 282 (2023) 128216, http://dx.doi.org/10.1016/j.energy.2023.128216.

[47] W. Li, J. Chen, K. Quade, D. Luder, J. Gong, D.U. Sauer, Battery degradation diagnosis with field data, impedance-based modeling and artificial intelligence, Energy Storage Mater. 53 (2022) 391–403, http://dx.doi.org/10.1016/j.ensm.2022.08.021.

[48] F. Roeder, S. Ramasubramanian, A review and perspective on path dependency in batteries, Energy Technol. 10 (2022) 2200627, http://dx.doi.org/10.1002/ente.202200627.

[49] M. Dubarry, G. Baure, D. Anseán, Perspective on state-of-health determination in lithium-ion batteries, J. Electrochem. Energy Convers. Storage 17 (4) (2020) 044701, http://dx.doi.org/10.1115/1.4045008.

[50] T. Hofmann, J. Hamar, M. Rogge, C. Zoerr, S. Erhard, J.P. Schmidt, Physics-informed neural networks for state of health estimation in lithium-ion batteries, J. Electrochem. Soc. 170 (2023) 090524, http://dx.doi.org/10.1149/1945-7111/acf0ef.

[51] Matlab, Lsqnonlin Documentation, The MathWorks, Inc., 2023, https://de.mathworks.com/help/optim/ug/lsqnonlin.html. (accessed 19 July 2023).

[52] C. Zoerr, J.J. Sturm, S. Solchenbach, S.V. Erhard, A. Latz, Electrochemical polarization-based fast charging of lithium-ion batteries in embedded systems, J. Energy Storage 72 A (2023) 108234, http://dx.doi.org/10.1016/j.est.2023.108234.

[53] S. Jiang, B. Peng, O. Weinstein, The complexity of dynamic least-squares regression, 2023, http://dx.doi.org/10.48550/arXiv.2201.00228, arXiv preprint.

2.2 Solutions for Data Scarcity in Neural-Network-Based SOH Estimation

Besides the mechanistic OCV model, neural networks are emerging as a promising technology for accurate SOH, OCV, and DM estimation. Training of neural networks demands extensive amounts of data and suffers from data dependence. Especially for new generations of LiBs, training data is scarce and development of generalizable methods is, thus, challenging. This chapter presents several strategies on how to overcome the big issue of data scarcity and physical interpretability with novel methods, including PINN, transfer learning, and the fusion of physical constraints with transfer learning. Each section contributes to answering the overarching research questions:
How can the issue of data scarcity in deep learning be resolved?
How can deep learning models be integrated with physics-based models to ensure adherence to physical laws and improve interpretability?

2.2.1 Physics-Informed Neural Networks for SOH Estimation

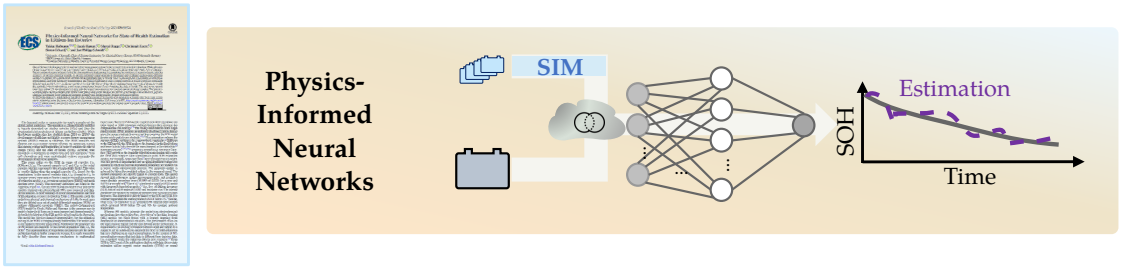

Figure 2.2: The trimmed outline of the thesis structure with focus on this chapter.

Neural networks are often regarded as black boxes that do not inherently adhere to physical laws, necessitating extensive amounts of training data to develop accurate and valid models. PINNs address the issue of data scarcity and physical interpretability by integrating physics-based models with neural networks. This work introduces a sequential PINN that utilizes simulation data from the P2D model, incorporating internal states for SOH estimation.

PINNs for SOH estimation were initially introduced by Aykol et al. [147], who distinguished between sequential and hybrid PINNs. Sequential models employ physics-based models and neural networks in a sequential manner. The state of the art involves combining synthetic with experimental data to reduce data requirements and expand the data space, leveraging the extrapolation capabilities of simulations and the interpolation power of neural networks [131; 148; 162–164]. Hybrid models integrate one model into the other, with the state of the art focusing on solving for internal states of the SPM by approximating the governing PDEs using a neural network [156].

Regarding sequential PINNs, the inclusion of internal states in the training dataset for SOH estimation has not been thoroughly researched. Additionally, adapting the P2D model for aging serves as the neural network training data generator.

In this article, the P2D model is adapted to generate a substantial amount of time-series data for various aging paths. This P2D data is fused with experimental cell and in-vehicle data. A comprehensive correlation, sensitivity, and feature analysis is conducted to enhance the dataset, with particular focus on the influence of internal states from the P2D aging dataset. Bayesian hyperparameter optimization is employed to refine the model architecture. Model performance is evaluated across various driving profiles and compared against other benchmark models.

The developed LSTM PINN surpasses benchmark models, achieving an average SOH_C MAE of 2.11 % (pp) across all datasets, using random 30 min driving time-series data as input with a 5 s sampling rate. The PINN performs optimally for CC (dis-)charging events, regardless of temperature. However, the PINN struggles to accurately monitor the in-vehicle dataset, as data analysis reveals significant structural differences from the extensive training data generated by the P2D model and extracted from laboratory cell data. Sensitivity and correlation analysis indicate that the inclusion of internal states, such as concentrations in the solid and liquid phases, enhances performance, even for experimental data lacking these features. This suggests that SOH estimation of experimental data benefits from the additional internal states included from the P2D data.

In comparison to existing literature, this work analyzes the use of highly accurate P2D aging data, the impact of data fusion, and the inclusion of internal states. This research presents an accurate aging parametrization for the P2D model and demonstrates that synthetic data, particularly when highly accurate, and inclusive of internal states, accelerates neural network performance. The publication proposes a default pipeline, i.e., guidelines, for neural network development in the context of battery state estimation.

The paper begins with a comprehensive literature survey, followed by an explanation of data sources, particularly data generation via the P2D model. It details model development, including feature engineering, correlation and sensitivity analysis, and hyperparameter tuning. Results are presented and compared against state-of-the-art neural network architectures, including LSTM, CNN, RNN, and FNN.

Publication Notes

The article *Physics-Informed Neural Networks for State of Health Estimation in Lithium-Ion Batteries* is presented in the following. The article was submitted to the Journal of The Electrochemical Society for peer review in June 2023 and was accepted in August 2023 [149]. The permanent web link to this publication is available under `https://doi.org/10.1149/1945-7111/acf0ef`.

Author Contributions

T. Hofmann developed the method, evaluated the data, developed the software, and wrote the manuscript. C. Zoerr assisted during the P2D model development and writing of the P2D appendix. M. Rogge, J. Hamar, S. Erhard and J.P. Schmidt supervised the research project, discussed the findings, and reviewed the manuscript.

Journal of The Electrochemical Society

The Electrochemical Society
Advancing solid state & electrochemical science & technology

Physics-Informed Neural Networks for State of Health Estimation in Lithium-Ion Batteries

To cite this article: Tobias Hofmann *et al* 2023 *J. Electrochem. Soc.* **170** 090524

Journal of The Electrochemical Society, 2023 **170** 090524

Physics-Informed Neural Networks for State of Health Estimation in Lithium-Ion Batteries

Tobias Hofmann,[1,2,z] Jacob Hamar,[2] Marcel Rogge,[3] Christoph Zoerr,[2] Simon Erhard,[2] and Jan Philipp Schmidt[1]

[1]*University of Bayreuth, Chair of Systems Engineering for Electrical Energy Storage, 95448 Bayreuth, Germany*
[2]*BMW Group AG, 80809 Munich, Germany*
[3]*Technical University of Munich, Chair of Electrical Energy Storage Technology, 80333 Munich, Germany*

One of the most challenging tasks of modern battery management systems is the accurate state of health estimation. While physico-chemical models are accurate, they have high computational cost. Neural networks lack physical interpretability but are efficient. Physics-informed neural networks tackle the aforementioned shortcomings by combining the efficiency of neural networks with the accuracy of physico-chemical models. A physics-informed neural network is developed and evaluated against three different datasets: A pseudo-two-dimensional Newman model generates data at various state of health points. This dataset is fused with experimental data from laboratory measurements and vehicle field data to train a neural network in which it exploits correlation from internal modeled states to the measurable state of health. The resulting physics-informed neural network performs best with the synthetic dataset and achieves a root mean squared error below 2% at estimating the state of health. The root mean squared error stays within 3% for laboratory test data, with the lowest error observed for constant current discharge samples. The physics-informed neural network outperforms several other purely data-driven methods and proves its advantage. The inclusion of physico-chemical information from simulation increases accuracy and further enables broader application ranges.
 [DOI: 10.1149/1945-7111/acf0ef]

Manuscript submitted June 23, 2023; revised manuscript received August 8, 2023. Published September 21, 2023.

The transport sector is responsible for nearly a quarter of the global carbon emissions.[1] The transition to climate friendly mobility is heavily dependent on electric vehicles (EVs) and thus the development and production of lithium-ion batterys (LiBs). While the battery market size has doubled from 2014 to 2019,[2] the development of efficient and highly accurate battery management systems (BMSs) remains a challenge. The BMS monitors and controls the high-voltage storage systems by measuring signals like current, voltage and temperature, in order to estimate the state of charge (SOC) and the state of health (SOH). Accurate state estimation is mandatory to enable long and safe operation.[3] New cell chemistries and more sophisticated systems aggravate the development of universal methods.

This paper refers to the SOH in terms of capacity, i.e., $SOH_C = C/C_{init}$. The current capacity is C and C_{init} is the initial capacity, which is a measured value at begin-of-life (BOL). This value is usually higher than the nominal capacity C_N, issued by the manufacturer. In the case of synthetic data, C_{init} is equal to C_N. In literature several error metrics can be found to evaluate the accuracy of estimation models, e.g., root mean squared error (RMSE) and mean absolute error (MAE). The necessary definitions are listed in the Appendix, Table XI. Various SOH estimation models exist and can be roughly clustered into physics-based (PB), semi-empirical and data-driven methods. A brief summary of recent implementations and their SOH estimation accuracy is listed in Table I. PB models catch the underlying physical and chemical mechanisms of LiBs. In most cases they are defined as a set of partial differential equations (PDEs) or ordinary differential equations (ODEs). The pseudo-2-dimensional (P2D) model by Doyle, Fuller and Newman is the common way to model a battery with focus on its mass transport and thermodynamics.[4] A detailed description of the P2D model can be found in the Appendix. The model has physico-chemical interpretability, but the numerical solving of the PDEs is computationally cumbersome. The model itself is not capable to describe aging effects. Furthermore the parameter sets of PB models are snapshots of the current degradation state, i.e., the SOH.[4] The implementation of degradation mechanisms into the model architecture leads to further complexity increase. It is nearly impossible to fully describe these numerous mechanisms in mathematical expressions. Reduced P2D models coupled with filter algorithms are often found in SOH estimation methods because they decrease the computational cost heavily.[5–9] The widely used reduced order single particle model (SPM) assumes an uniformly distributed current density along the porous electrode thickness and thus simplifies the P2D model to one single particle per electrode.[9–11] This assumption reduces the amount of PDEs and hence the computational complexity.[11] Different to the P2D model, the SPM neglects the dynamics in the liquid phase and hence fails to fully describe the mass transport in the electrolyte.[12] Recentpublications[5,7–9,13,14] frequently assume solid electrolyte interface (SEI) growth as the dominant degradation mechanism and couple the SPM with adaptive filter algorithms to yield SOH estimation models. For example, Allam and Onori[5] have developed such a model. The SEI growth is implemented into an aging-dependent voltage loss equation in which the relevant degradation parameters are updated via a sliding mode interconnected observer. The parameter update is achieved by fitting the simulated voltage to the measured signal. The updated parameters are directly linked to capacity fade. The model showed high robustness against measurement noise and reached a mean absolute percentage error (MAPE) of 0.92% for a new and 1.65% for an aged cell.[5] Gao et al.[7] introduced a simplified P2D model with integrated degradation modes,[15] i.e., loss of lithium inventory (LLI), loss of active material (LAM) and resistance rise. The internal parameters are updated by comparing measured and calculated voltage responses. The adaptation is directly linked to the SOC and SOH. For constant temperature the method reached a MAE below 1%.[7] Similar, Zhao et al.[9] or Gambhire et al.[8] presented PB reduced order models which achieved MAE below 2% and 1% for constant ambient temperature.

Whereas PB models integrate the underlying electrochemical mechanisms into the architecture, data-driven or machine learning (ML) models are black boxes with a learned mapping from measurable to immeasurable variables. The performance relies on the input training dataset and the user-defined model architecture. A requirement is an existing correlation between input and output. It is simple to set up a data-driven approach for SOC or SOH estimation but very challenging to reach generalization. In the context of ML generalization means that test data is different from training data, i.e., a method works for unknown data in new scenarios.[16] From 2018 to 2022 most of the publications dealing with data-driven state estimation utilize support vector machines (SVMs) or neural

[z]E-mail: tobias.th.hofmann@bmw.de

Journal of The Electrochemical Society, 2023 **170** 090524

Table I. Recent realizations of PB models and NNs with their SOH estimation accuracy. If not stated otherwise, the datasets were captured on cell level.

Method	Dataset	Limitation/Remark	Accuracy	References
SPM with sliding mode interconnected observer	Experimental dataset with two capacity measurements	—	1.65% RMSE	5
Simplified P2D model with integrated degradation modes	Experimental dataset with 21 capacity measurements	Constant temperature	1% MAE	7
PB reduced order model	Experimental cyclic aging data	Constant temperature (25, 40, 55 °C)	2% MAE	9
PB reduced order model	Experimental cyclic and calendaric aging data	Constant temperature (25, 45 °C)	1% MAE	8
LSTM NN	Oxford Battery Degradation dataset	CC charging voltage curves at constant temperature	0.5% RMSE	20
LSTM NN	Experimental cyclic aging cell data	CC charging voltage curves at 25 °C	2.08% RMSE	21
LSTM NN	NASA Battery Degradation dataset	CC charging voltage, current and temperature curves at temperature from 20 °C to 30 °C	2.5% RMSE	22
FNN	Experimental cyclic and calendaric aging data	Only applicable to narrow temperature window (25 °C to 35 °C)	0.9% RMSE	23
CNN–FNN	Real-world data from 40 EV buses	Long CC charging windows at low currents mandatory to reach high accuracy	2.79% RMSE	25

networks (NNs).[17] Especially long-short-term memory networks (LSTMs), first introduced by Hochreiter and Schmidhuber,[18] are in the focus because they are the most efficient and widely used sequential networks in the field.[17–19] For example, Gong et al.[20] published a combined SOC and SOH estimation model that uses unprocessed charging voltage curves as input. For the Oxford Battery Degradation dataset the LSTM model reached a RMSE below 0.5% and a maximum absolute error (MAX) below 1% at constant temperature. Similar, Li et al.[21] developed a LSTM model which uses unprocessed voltage charging curves as input and reached a MAPE below 2.08% at constant temperature of 25 °C. Choi et al.[22] have demonstrated up to absolute 3.57% RMSE reduction by utilizing a combined dataset from voltage, current and temperature. In a temperature range from 20 °C to 30 °C the LSTM model achieved a RMSE below 2.5% for the NASA Battery dataset. Rahimian et al.[23] showed a SOH estimation RMSE below 0.9% when training a feedforward neural network (FNN) with partial voltage, current and temperature data from automotive cells.

A more recent publication by She et al.[24] combined multiple equivalent circuit modelss (ECMs) on cell level with incremental capacity analysis (ICA) to build a full battery storage SOH estimation model. By utilizing the features gathered from ICA and a subsequent update of the battery parameters, the model estimated the SOH of an EV fleet with a RMSE of 2.04%. Similar, Wang et al.[25] combined health-indicating features gathered from coulomb-counting and ICA to inform a hybrid deep NN. The combined convolutional neural network (CNN) and FNN reached a SOH MAE of 2.79% for an EV bus fleet. More information about recent SOH estimation models can be drawn from recent review papers, e.g., by Yang et al.[26]

Aykol et al.[27] first recognized the potential of the physics-informed neural network (PINN) for SOH estimation in 2021. While PB models require high computational effort, ML models lack physical interpretability. The fusion of both models is promising to eliminate the respective disadvantage and rather strengthen the benefits.

As Fig. 1 shows, Aykol[27] extended the possible model architectures to sequential and hybrid PINNs. Strongly related to PINNs, and often falsely described as such, is physics-informed machine learning (PIML). These methods utilize other ML approaches like a SVM or Gaussian process regression (GPR). Sequential PINNs are generable with existing PB and ML models. The sequential residual learning approach S1 from Fig. 1 feeds the output of a PB degradation model into a ML update model. The ML model learns the residual between the PB model estimation SOH_{PB} and the true label SOH_{true}. The learned residual is used to update the estimation and minimize the error. While the PB model captures basic aging effects, the ML model is promising to learn more complex degradation mechanisms. The output SOH_{est} is partially constrained by physics but the application is still limited by the complexity of the PB model and its implemented degradation mechanisms.[27]

The **transfer learning approach S2** tackles this limitation by running the complex PB model temporally decoupled with arbitrary input data ***{X}***. The output data y_{PB} includes internal battery states such as concentrations and potentials. This data is combined with experimental data X_{meas} to train the ML model. During operation, time-series data $X(t)$ can be used to estimate the SOH_{est} with low computational cost and physical constraints. The final PINN does not depend on the complexity of the PB model and is prospective to learn the hidden physics of battery degradation.[27] Relatively few publications exist on sequential PINN or PIML for SOH estimation. Thelen et al.[28] researched the sequential PINN approaches S1 and S2 in two subsequent studies.[28,29] The first transfer learning PINN (S2) was trained to co-estimate the SOH and the primary degradation mode, LAM and LLI, by fusing experimental data with simulated data from a half-cell model. Both datasets were captured at two temperatures and current rates. The half-cell model output the open-circuit-potential (OCP) curves of both electrodes which can be used to reconstruct the open-circuit-voltage (OCV) of the full cell. Finally a differential voltage analysis (DVA) determines the degradation mode. These features were used to train a single hidden layer NN to estimate the SOH and degradation modes. The advantages of the data fusion was confirmed by a comparison to models trained solely with one input dataset. The combined training dataset lead to best performance with a RMSE of 0.74% for SOH and 2.85% for degradation mode estimation. In the consecutive study[29] the first approach was compared to the residual learning approach S1 with almost identical settings. The residual learning approach performed worse with an average RMSE of 2.35% for SOH and 5.09% for degradation mode estimation. Similarly, Kohtz et al.[30] developed a transfer learning PIML with three subsequent steps. SEI-growth was implemented as the major degradation mechanism in the initial PB model to describe capacity loss. It must be noted that SEI growth is yet not fully understood and building accurate models is an ongoing research question.[31] A succeeding GPR was trained to map partial charging voltage, current and temperature curves to SEI-layer thickness. The final multi-fidelity look-up table directly correlated the SEI-thickness with capacity, accepting an initial 1.5% error.

Journal of The Electrochemical Society, 2023 **170** 090524

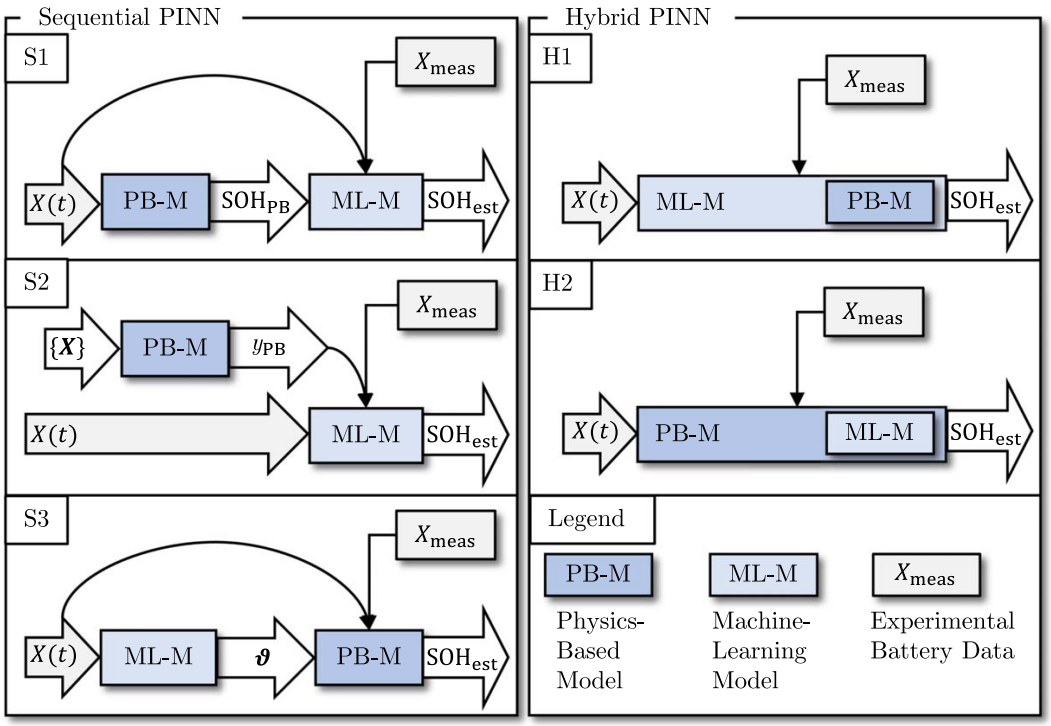

Figure 1. PINN architecture model landscape for SOH estimation (adapted from Aykol et al.[27]). In architecture S1, S3 and H2 it is assumed that the PB model has degradation mechanisms implemented and is thus able to estimate the SOH. $X(t)$ can be any time-series battery data used to perform the SOH estimation, X_{meas} can be any experimental battery data including time-series data, $\{X\}$ describes the necessary input data including battery parameters for the PB model, ϑ are the battery parameters and y_{PB} can be any output from a PB model.

Training data consisted of charging curves at 0.2, 0.33, 0.5, 1, 2C and 25, 35, 45 °C, while validation was carried out by samples at 1.5C, 30 °C and avarying duration of 150 s to 400 s. Assuming the exclusion of errors in the upper regions of the SOH, the RMSE of the estimated SEI thickness was found to be 8.97%.

The identification of physico-chemical battery parameters is a well discussed research topic.[27,32,33] First, more information about the influence of degradation on these parameters is necessary in order to implement validated **parameter learning PINNs (S3)**. This approach uses a prior ML model to learn the parameter set of a battery over its lifetime and eventually update the PB model with an accurate parameter set. The PB model uses this information to solve for the internal states and SOH_{est}. Reduced PB models are necessary to reach online applicability.[27] To the best of the authors knowledge, Li et al.[33] were the first to realize a parameter identification ML model. The model estimated degradation dependent PB parameters from voltage and current signals at a constant temperature of 25 °C with a MAPE of 12.5%.

The hybrid PINN approaches integrate one model into the other architecture. **Physics-constrained ML (H1)** implements PB elements in the ML model, e.g., in the loss function during training. There is optimism to physically constrain the output by following physico-chemical laws.[27] Nascimento et al. contributed with several publications[34–36] to the field of hybrid PINN for SOC estimation and remaining useful life (RUL) prediction. In their studies, they implemented physis-based knowledge into deep NN, for example by embedding it into recurrent neural network (RNN) cells, to simulate the time-dependent response of a battery to applied current.[36]

The **ML-accelerated PB models (H2)** are the original implementation of PINN, first introduced by Raissi et al.[37] Hence in other research areas these models are only referred to as PINNs. The approximation ability of NNs is exploited to solve the underlying PDEs of PB models with less computational burden. Due to the relation of the internal state lithium-ion concentration to the SOC, more H2 PINNs are already developed for SOC estimation.[38] In contrast, the urgency to integrate degradation mechanisms into PB models still limits the application of accurate ML-accelerated PB models for SOH estimation.[27] Pepe et al.[39] introduced a NN which solves the underlying differential equations of a PB system. For training with the NASA and Oxford Battery dataset, the PINN reached an SOH RMSE of 5.81% and 1.55%, respectively. The data was limited to a narrow current and temperature region. Thus, challenges remain to develop accurate, generalizable, ML-accelerated PB models. Recently, Xu et al.[40] set the benchmark for hybrid battery models by publishing a physics-informed deed autoencoder with an SOH RMSE of 0.64%. Similar, Wen et al.[41] proved the ability of NNs to approximate the underlying PDEs of a Verhulst model in order to estimate the SOH and predict the RUL.

While available PINNs show promising results for internal state estimation,[42–45] few publications exist on accurate, robust and generalizable SOH estimation. Especially, there are no studies utilizing these aforementioned immeasurable internal states, such as concentrations and potentials. To the best of the authors knowledge, this is the first publication to develop a transfer learning PINN which fuses experimental data from in-vehicle and laboratory sources with simulation data (including internal states), generated by a P2D model. The developed model fuses data with different dimensions from a broad operational region with a variety of load profiles and charging strategies, including temperatures from 0 °C to 50 °C and currents from −2.5C to 2.5C. The benefit of including synthetic data and especially immeasurable internal states is discussed in detail. The proposed method is further analyzed in regards of its sensitivity to current profiles and temperature and finally benchmarked to purely data-driven models.

Journal of The Electrochemical Society, 2023 **170** 090524

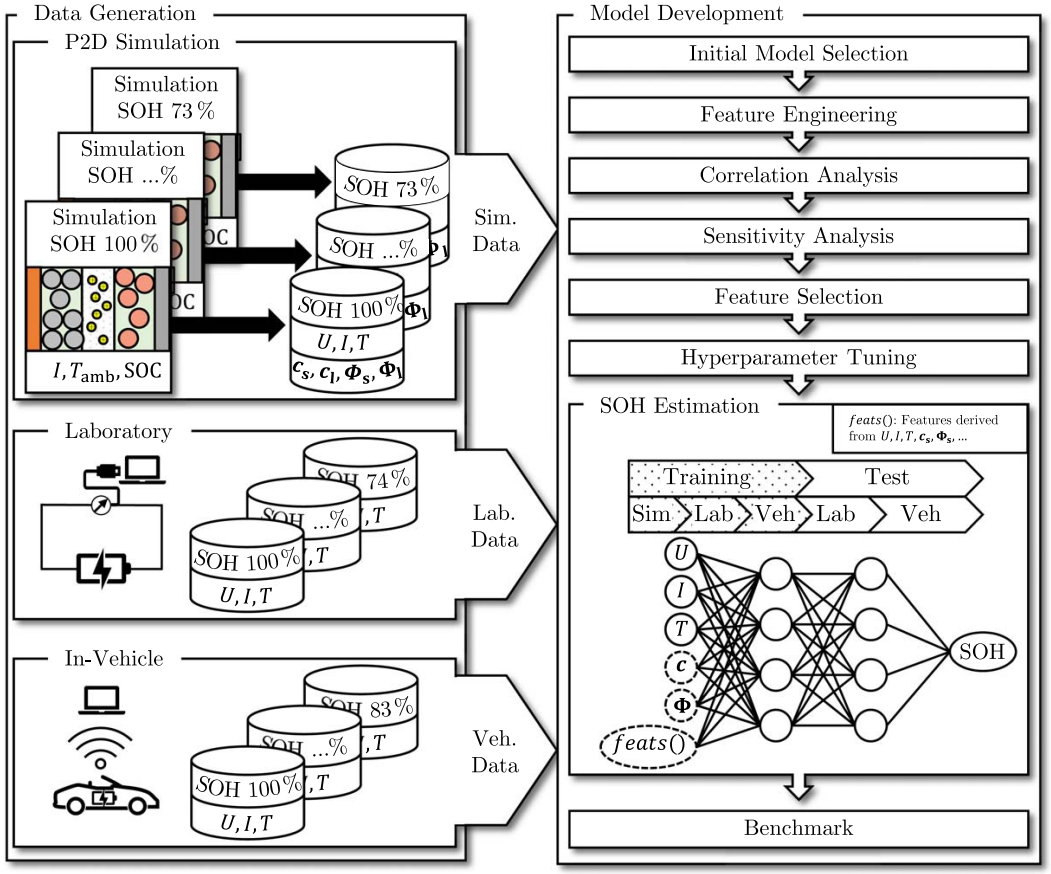

Figure 2. General approach with subsequent work tasks. Data is collected from simulation and measurement sources and a PINN for SOH estimation is developed.

Experimental

The outline of the proposed method is illustrated in Fig. 2. For this work a Newman-P2D model is used to generate data which is merged with experimental data. The combined dataset is randomly split into training and testing data.

The initial model is selected based on a literature research and optimized with additional features. The best features are chosen based on the results of a correlation and sensitivity analysis. The NN is finetuned in accordance to the results of a Bayes hyperparameter tuning approach.

Data generation.—The simulation of cell internal states over lifetime demands a parameter set, which represents the cell in its aged state. For the investigated cell 16 parameter sets at SOHs ranging from 73% to 100% are developed and validated against laboratory measurements. Table XV in the Appendix offers a more detailed description of the parameter set and the dependencies of single parameters on degradation. Further, a resimulation of the measurement profiles (Fig. 12 in the Appendix) yields an acceptable voltage MAE below 35 mV, even for degraded batteries. Nevertheless, it is crucial to remember that selecting correct parameters is still an open research question. Although the simulated voltage and temperature signals fit the true measurements, it cannot be proven that every physical and electrochemical parameter is correct.

The simulation dataset includes charging events, dynamic driving profiles and check-up tests. Figure 3 summarizes the simulated drive cycles together with the experimental current profiles.

The laboratory data was captured with a battery cycler in a climate chamber at 25 °C. Prior to testing, the cells were acclimatized and set to a default SOC of 50%. The laboratory measurements (Fig. 3i) refer to a predefined check-up-profile with four alternating C/3 charge and discharge sections which are applied within voltage limits. The constant current (CC) charging profiles are followed by a constant voltage (CV) section until the remaining cell current reaches a predefined threshold. The laboratory tests do not include dynamic load profiles. In total almost 150 d of time-series data from laboratory check-ups are used in the proposed method.

The in-vehicle data was collected from a development fleet with 18 EVs in Germany. A mobile data recorder directly accesses and stores the measured signals by the BMS. The recorder collects the signals during driving and charging and checks the SOH of the battery storage before and after the trip. The in-vehicle data (Fig. 3j) consists of dynamic driving profiles and charging sections. An in-vehicle profile is shown in Fig. 3j, as an example of a dynamic driving sample. In total nine days of in-vehicle time series data are available in the dataset. It must be noted that respective SOH labels of the in-vehicle dataset are generated at a test bench with similar measurements as in the laboratory dataset. Hence, the SOH represents the available capacity during a constant current (CC) C/3 discharge.

The simulation covers multi-step constant current (MSCC) fast charge events. Figure 3a illustrates a MSCC profile for a pristine cell at 25 °C. Two out of three sections from the dynamic stress test (DST) are included in the simulation (Figs. 3b and 3c). Similarly one section of the federal urban driving schedule (FUDS, Fig. 3d) and

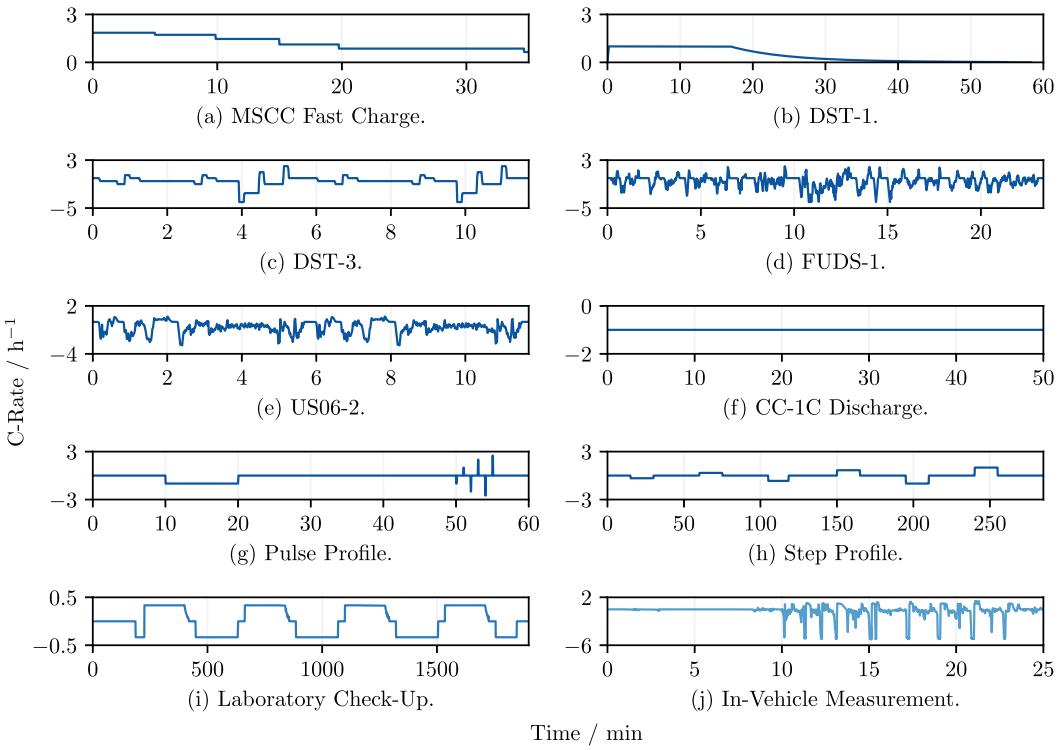

Figure 3. Current profiles of the simulated and measured dataset. For the dynamic profiles DST-3, FUDS-1, US06-2, pulse profile and the in-vehicle measurement just a snippet of the full profile is displayed.

Table II. Test matrix for the data generation process with the simulated starting SOC, ambient temperature and duration of the drive cycle.

Start SOC	10%	20%	30%	40%	50%	60%	70%	80%	90%	Duration
DST-1[a]	x	x	x	x	x					60 min
DST-3[a]		x	x	x	x	x	x	x	x	12 min
FUDS-1[a]								x	x	25 min
US06-2[a]		x	x	x	x					12 min
CC 1C[a]								x	x	50 min
Pulses[a]								x	x	180 min
Steps[a]				x	x	x				285 min
Fast Charge[b]	x	x	x	x	x					35 min

a Simulation at 0 °C, 15 °C, 25 °C, 35 °C, 45 °C. b Simulation at 0 °C, 15 °C, 25 °C, 35 °C.

one section of the high acceleration aggressive driving cycle (US06, Fig. 3e) are simulated. The DST, FUDS and US06 are based on public driving profiles which are available at the website of the University of Maryland.[46,47] The 1C CC discharging (Fig. 3f) generally accounts for low current discharging. The pulse profile (Fig. 3g) is a three times repeated test with a 1C discharge section and alternating pulses with 1C, 2C and 2.5C. The step profile (Fig. 3h) includes short CC charge and discharge sections with C/3, 2C/3 and 1C.

Further, Table II displays the simulation profiles, their duration and the varied start SOC and temperature. Some settings must be excluded due to exceeding of safety limits, i.e., minimum or maximum cell voltage or temperature. The simulations run with a time-step resolution of 5 s as a tradeoff between runtime and accuracy. In total almost 7000 simulations with a duration of 250 d are performed.

Figure 4 illustrates the data distribution of 1000 random samples from the full data. All datasets inhibit the full and evenly distributed voltage range, which directly correlates to the SOC. While the simulation data is evenly distributed along temperature, current and SOH, the laboratory data is mainly captured at 25 °C and current rates of −C/3 and C/3. The synthetic dataset is distributed at temperatures from 0 °C to 50 °C because the used P2D model was validated for this cell with these boundaries. Nevertheless, it is realistic to apply the method only to data captured at battery temperatures above 0 °C due to preconditioning of the battery pack before operation or charging. The intelligent, anticipating preconditioning–function results in a relatively low probability of operating the battery pack at sub–zero temperature. The in-vehicle measurements include a broader temperature region due to seasonal and daily variety in Germany. Unfortunately, the data is mainly distributed around 100% SOH, even including SOH values above 100%. While the synthetic dataset inhibits highly dynamic driving profiles and thus covers a current range from −2.5C up to 2.5C, the experimental dataset is mainly distributed at low current rates between −C/3 and C/3. For the laboratory cell dataset this is due to the check up profile in Fig. 3i, which refers to a standardized test protocol. Unfortunately, no dynamic driving profiles are available

Journal of The Electrochemical Society, 2023 **170** 090524

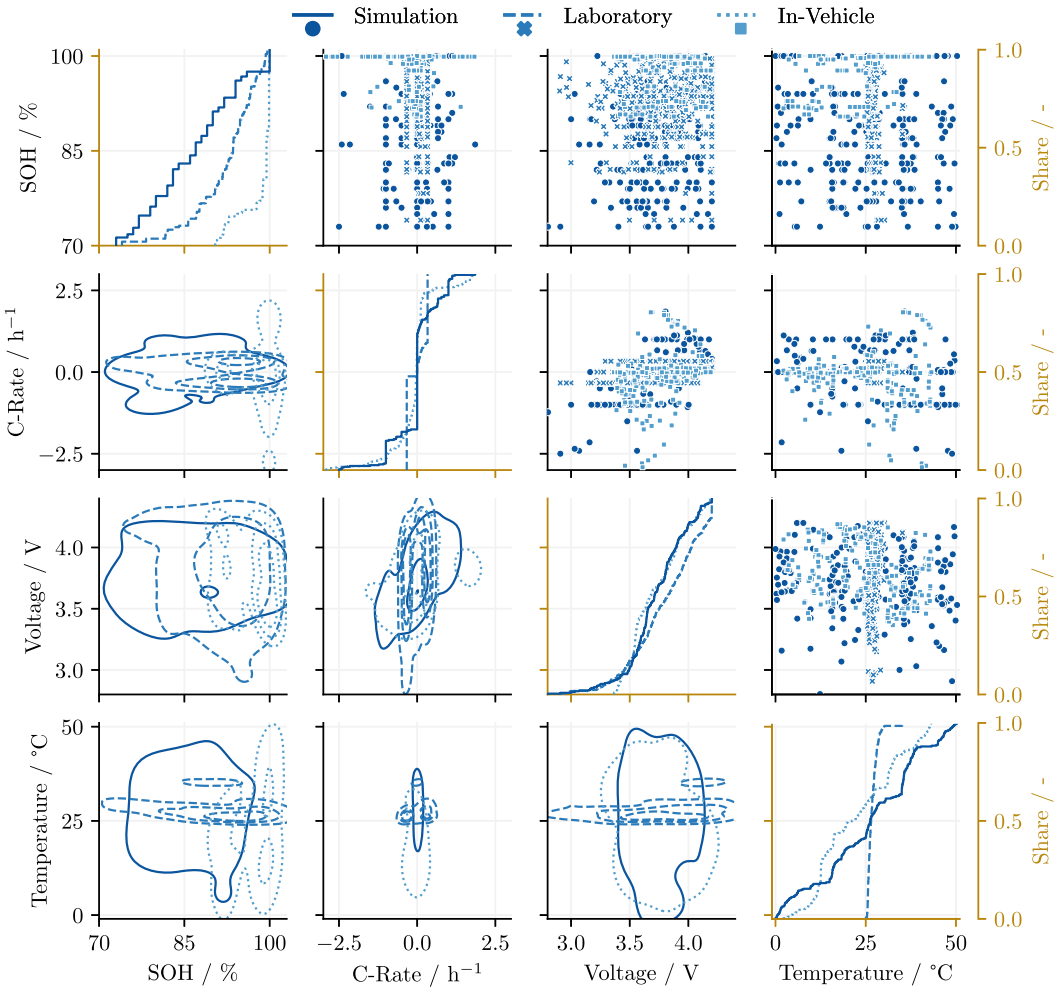

Figure 4. Visualization of the three datasets for 1000 random samples. The upper figures show the scatter plot and the lower figures visualize the kernel densities. Both refer to the first *y*-axis on the left. The second *y*-axis on the right side refers to the cumulative distribution plots in the diagonal, in golden color. While most of the simulation data is uniformly distributed, laboratory and in-vehicle measurements are mainly captured at fixed temperature and current operating points.

from laboratory cell measurements. On the other side, the in-vehicle dataset reflects real-world driving and charging behavior from our development fleet. Hence, lower current rates show realistic operational strategies. As can be seen in Fig. 4 more than 50% of the in-vehicle data are dynamic load profiles.

The simulation data has the lowest sampling rate, with one signal per five seconds, and consequently sets the reference. Higher sampling rates increase the computational effort for the P2D data generation heavily. Due to the low frequency, the fast effects during a change in charge direction are not discernible in the signal trajectory. Nevertheless, effects with longer time-constants give enough information about the degradation state to estimate the SOH. This issue is discussed in more depth in the Results and Discussion section. The combined dataset includes over 409 d of time-series including voltage, current, temperature and SOH. Simulation data further includes SOC and internal states, i.e., concentration and potential of the solid and liquid phase.

The full, combined dataset runs through a preprocessing scheme before it is used for model development. First, every signal is normalized to a range between zero and one. This has been shown to be optimal for NN training because it speeds up training and can improve performance.[48] The data is split into 70% of training and 30% of testing data which differ in the SOH label to avoid overfitting. The data split is applied to the simulation, laboratory and in-vehicle dataset. The chosen SOH values are selected randomly at the beginning for every subdataset. The data split, however, is kept during the whole model development process to ensure comparability throughout the development process. Hence, the data split ensures that subsamples from the same source and SOH belong to either the training or testing dataset.

Model optimization.—A transfer learning PINN runs the complex PB model simulations temporally decoupled[27] as in Fig. 1 S2. The output data, which includes internal battery states is fused with experimental data and processed in a NN. The final transfer learning PINN inhibits physico-chemical information from battery internal states and reduces the complexity in the application phase to that of the ML model. It is therefore crucial to design an efficient and accurate NN.

Recent publications[17,21] suggest the usage of LSTM networks, a specialized RNN, for processing time-series data and SOH estimation. A promising approach from Li et al.[21] is taken as the initial model and adopted to suit the database. The model complexity is reduced in order to start with a more basic approach. The LSTM

Journal of The Electrochemical Society, 2023 **170** 090524

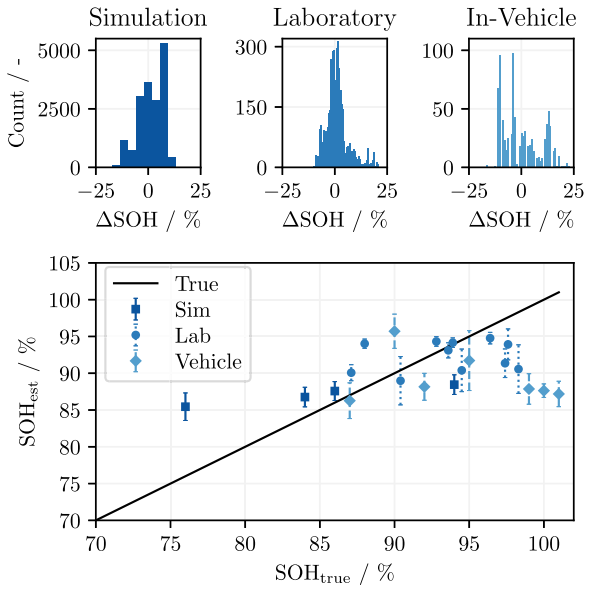

Figure 5. SOH estimation accuracy of the initial model for each test dataset. In the lower graph, the estimated SOH_{est} is plotted against the true SOH. The upper histograms visualize the error distribution with $\Delta SOH = SOH_{est} - SOH_{true}$ for every test dataset.

Table III. Accuracy of the initial SOH estimation model.

Evaluation Test Data	RMSE	MAE	MAX
Combined	5.94%	4.79%	23.2%
Simulation	5.92%	4.99%	20.9%
Laboratory	5.56%	3.85%	21.1%
In-Vehicle	8.89%	7.58%	23.2%

takes the three input signals current, voltage and temperature, sampled to 300 s with a time step of 5 s. The sampling routine is further optimized by using 50% sliding windows to increase the amount of data. For example, a full signal of 900 s length leads to five samples with 300 s duration instead of three.

Unfortunately, sampling also generates useless samples that, for example, have no current flow and no subsiding overpotentials, and thus no information. An outlier removal script excludes these samples. Nevertheless, samples with a short duration of applied current are included in the dataset on purpose. These samples are not associated as outliers but rather as data anomalies and hence are important elements of the training data.[49] Prior investigation proves the positive influence of the natural regularization effect of these data anomalies. Indeed, the removing of all these anomalies yields a local optimum where the model overfits on the simulation data and underfits on experimental data.

The model processes the input data with three dimensions, i.e., $\mathbb{R}^{samples \times 61 \times 3}$ through three LSTM layers with each 50, 50 and three memory cells, a reshape layer and a dense layer with one neuron to the final scalar output, the SOH. The architecture is visualized in Fig. 8a. The model is optimized with the state-of-the-art algorithm Adam (the reader is referred to the publication by Kingma and Ba[50]) and MAE as the loss function. The NN trains with no validation split and a batch size of 128 for 100 epochs.

Figure 5 visualizes the performance of the initial model for the three test datasets. In Fig. 5, the errorbars visualize the standard deviation of the estimations. Additionally, the distribution of the SOH estimation error is visualized in a histogram.

More information can be drawn from Table III, in which the model accuracy is measured in RMSE, MAE and MAX. While the MAE seems acceptable, the RMSE and MAX reveal the bad performance of the model. Most of the samples are estimated around the mean value and due to the low complexity of the model it struggles to fit the training data. This indicates underfitting in ML.[19]

Feature engineering.—The preprocessing of training data influences the performance of NNs. So-called features, which can range from arbitrary measured signals to statistical transformations, improve the accuracy and efficiency of the model if they correlate with the desired output.[19] Features with negligible correlation hinder the generalization of model training and slow down the computation. Therefore, the selection of the final feature set is guided by a correlation and sensitivity analysis. Statistical features are calculated via available input data. The available dataset includes voltage, current and temperature signals and even internal states for the simulation data subset. Cell voltage U is defined as the potential difference between both current collectors. The temperature signal T is the cell core temperature in the synthetic dataset and the cell surface temperature for experimental data. The resulting deviation is further analyzed in the Discussion section and visualized in the Appendix, Fig. 12. Table IV summarizes and clusters the available input data. As the internal states have temporal and spatial dependencies, the cell is discretized along its x-dimension. Indices used in Table IV provide information about the spatial characteristics of a time-series signal. It must be noted that the SOC is an internal state, too. For convenience the SOC is defined as the weighted average of the solid concentration $c_{s,NE}$ along the negative electrode with respect to the maximum solid concentration. The SOC is assumed as unknown for the experimental datasets. Further information regarding the spatial discretization and the calculation of respective signals can be found in the Appendix.

Table V shows a comprehensive list of possible features.[41–51,53] They are clustered in scalar and vectorized features. The scalar

Table IV. Input signals, clusters and the availability for each data subset. The solid concentration is distinguished between surface concentrations $c_{s,s}$ and average particle concentrations in the negative and positive electrode along the respective electrode $c_{s,NE}$, $c_{s,PE}$.

Cluster	Signals	Simulation	Laboratory	In-Vehicle
U	U	x	x	x
I	I	x	x	x
T	T	x	x	x
SOC	SOC	x		
Φ_s	$\Phi_{s,NE}$, $\Phi_{s,PE}$	x		
Φ_l	$\Phi_{l,NE/CC}$, $\Phi_{l,PE/CC}$, $\Phi_{l,SEP}$, $\Phi_{l,NE/SEP}$, $\Phi_{l,PE/SEP}$	x		
c_s	$c_{s,NE,avg}$, $c_{s,PE,avg}$, $c_{s,s,NE/SEP}$, $c_{s,s,PE/SEP}$	x		
c_l	$c_{l,NE/CC}$, $c_{l,PE/CC}$, $c_{l,SEP}$, $c_{l,NE/SEP}$, $c_{l,PE/SEP}$	x		

s: solid, l: liquid, s, s: solid surface, NE: negative electrode, PE: positive electrode, SEP: separator, CC: current collector.

Journal of The Electrochemical Society, 2023 **170** 090524

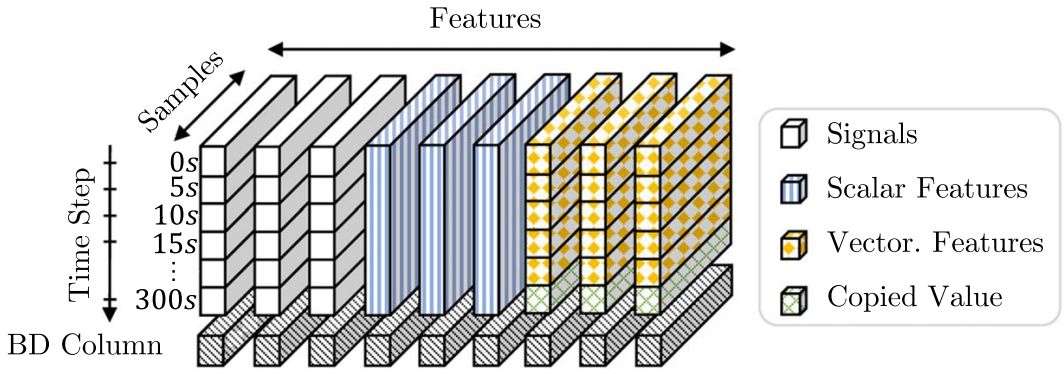

Figure 6. Structure of the three dimensional dataset. In this example one scalar and one vectorized feature are included and calculated for every input signal. After each feature the binary decision (BD) column informs the network about availability. The vectorized feature columns yield 60 data points for a 300 s sample with 61 data points. Thus, the last entry is copied into the empty cell.

Table V. Possible features derived from the raw time-series data $x(t) = X = \{x_1, x_2, ...x_N\}$, where p_j describes the probability of occurrence of one event x_j. $x(t)$ can be any time-series signal in the input dataset, e.g., voltage $u(t)$ or current $i(t)$.

Abbreviation	Feature	Formula
	Scalar Features	
min()	Minimum Value	$\min(\boldsymbol{X})$
max()	Maximum Value	$\max(\boldsymbol{X})$
mean()	Mean Value	$\frac{1}{N}\sum_{j=1}^{N} x_j$
mad()	Median Absolute Deviation	$\frac{1}{N}\sum_{j=1}^{N} \lvert x_j - \text{mean}(\boldsymbol{X})\rvert$
mode()	Mode	*Most Frequent Value in the Dataset* $\boldsymbol{X}$
$\Delta()$	Delta per Sample	$\max(\boldsymbol{X}) - \min(\boldsymbol{X})$
std()	Standard Deviation	$\sqrt{\frac{1}{N}\sum_{j=1}^{N}(x_j - \text{mean}(\boldsymbol{X}))^2}$
max $\Delta()$	Maximum Change per Timestep	$\max_{1\leqslant j\leqslant N-1} \lvert x_{j+1} - x_j\rvert$
rms()	Root Mean Square	$\sqrt{\frac{1}{N}\sum_{j=1}^{N} x_j^2}$
skew()	Skewness[54]	$\frac{\frac{1}{N}\sum_{j=1}^{N}(x_j - \text{mean}(\boldsymbol{X}))^3}{\left[\frac{1}{N}\sum_{j=1}^{N}(x_j - \text{mean}(\boldsymbol{X}))^2\right]^{3/2}}$
se()	Shannon Entropy[51]	$-\frac{1}{\log N}\sum_{j=1}^{N} p_j \log p_j$
wv()	Wavelet Variance[52]	*Last Coefficient of Wavelet Variance Transform*
dft()	Discrete Fourier Transform Coefficients[53]	$\sum_{j=1}^{N-1} \exp^{-2\pi i\frac{jk}{N}} \cdot x_j$ for $k = 1,...,N-1$
	Vectorized Features	
d/dt()	First Windowed Derivative	$\frac{x_{k+1}-x_k}{t_{k+1}-t_k}$ for $k = 1,...,N-1$
d^2/dt^2()	Second Windowed Derivative	$\frac{x_{k+1}-x_k}{(t_{k+1}-t_k)^2}$ for $k = 1,...,N-1$
$\text{rms}_{\text{vec}}()$	Windowed Root Mean Square	$\sqrt{\frac{1}{k+1}\sum_{j=1}^{k+1} x_j^2}$ for $k = 1,...,N-1$
	Additional (vectorized) Features	
$R()$	Windowed Resistance	$\frac{u_{k+1}-u_k}{i_{k+1}-i_k}$ for $k = 1,...,N-1$
CB()	Charge Balance	$\sum_{j=1}^{k} i_k(t_{k+1} - t_k)$ for $k = 1,...,N-1$

features include basic and advanced features. The scalar features yield one value per input sample. The vectorized features are generated by scanning the input signal between two adjacent points. Hence, a sample with N data points leads to $N-1$ data points for a vectorized feature. To align with the data size of the time-series signals, the last entry is replicated and placed in the final column. Figure 6 illustrates the process of combining the signals with its features in the three dimensional dataset.

Few statistical features demand a more detailed explanation. Skewness (skew()) is an asymmetry measure of the underlying data distribution.[54] Shannon entropy (se()) returns the amount of information contained in a signal, where information refers to the definition in information theory.[51] The wavelet variance (wv()) measures the variability in a signal.[52] The discrete Fourier transform coefficients (dft()) can be used to describe a periodic signal. This means a periodic signal is split into its constituent frequencies,[53] where the first six coefficients are used in this approach. The six coefficients are treated as scalar features in this approach. The windowed resistance feature ($R()$) calculates the theoretical resistance with respect to the investigated window. The charge balance

Journal of The Electrochemical Society, 2023 **170** 090524

(CB()) measures the added or removed charge amount and hence directly correlates to the SOC and can work as a substitute for the SOC column in the experimental dataset.

In this study, we utilize snipped time-series signals, such as voltage, current, temperature, and additional internal states, as the base for our input sample. By performing feature engineering, we augment our dataset with multiple vectorized time-series signals, which are added to the original dataframe. Additionally, scalar features are included in each input sample. The final input data can be represented as a three-dimensional dataframe that incorporates three distinct categories of information. It should be noted that, with the exception of the features $R()$ and CB(), all features are computed for every input signal. As a result, the total number of variables in each input sample is given by $N_{\text{signals}}\cdot(1 + N_{\text{features}}) + N_{\text{features,add}}$, where N_{signals} represents the number of signals used, and N_{features} represents the number of features employed. Notably, the count of N_{features} does not include $R()$ or CB(), which are classified as $N_{\text{features,add}}$.

Correlation and sensitivity analysis—feature selection.—Before selecting features, a correlation analysis helps to understand the relation between different input features and their relation to the output. After selecting the first set of useful features a sensitivity analysis returns the most promising feature set and leads to the final feature selection.

The correlation analysis uses the Pearson correlation coefficient r to calculate the correlation between two signals $\boldsymbol{X} = \{x_1, x_2,...,x_N\}$ and $\boldsymbol{Y} = \{y_1, y_2,...,y_N\}$, where N is the total number of samples.

$$r = \frac{\sum_{i=1}^{N} (x_i - \text{mean}(\boldsymbol{X}))(y_i - \text{mean}(\boldsymbol{Y}))}{\sqrt{\sum_{i=1}^{N} (x_i - \text{mean}(\boldsymbol{X}))^2 \sum_{i=1}^{N} (y_i - \text{mean}(\boldsymbol{Y}))^2}} \quad [1]$$

Equation 1 can be easily calculated between two scalar features, but it is not directly possible between two time-series datasets or between a time-series signal and a scalar feature, e.g., the voltage time signal to the SOH. The vectorized features in Table V serve as a substitute. The correlation coefficient is computed individually for each value with its corresponding data point in the other signal, followed by averaging.

The feature list in Table V applies to every input signal from Table IV. To decrease the computational effort, all features belonging to one data cluster (see Table IV) are kept together for analysis. Hence, correlation analysis is performed for every feature cluster to the SOH. The cross-correlation between features gives insights about redundant features.

Detailed results regarding the direct correlation of features to the SOH for 300 s samples can be found in the Appendix, Table XII. It must be noted that correlation will increase if the sample length increases. Features derived from $\boldsymbol{c}_s$ and $\boldsymbol{c}_l$ show non-negligible correlation to the SOH for basic scalar features mean(), max(), min(), mode() and rms(). Also more advanced features like wv() and dft() show higher correlation. The evaluation leads to the conclusion to exclude the features std(), $\Delta()$, mad(), skew(), max $\Delta()$ and $d^2/dt^2()$ from further analysis because they show no correlation to the output or have strong cross-correlation to already included features.

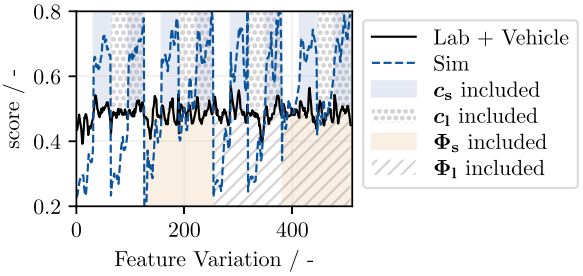

Figure 7. Resulting score (Eq. 4) from the sensitivity analysis. The final score is calculated only in respect to the laboratory and in-vehicle data. The feature variations include all possible 512 combinations of signals and their respective scalar and vectorized features. The included features are separated into the lower and upper y-range for better readability.

The remaining features and all possible input data clusters are evaluated in the following sensitivity analysis.

A sensitivity analysis describes the process of searching the possible feature space for the best combination of input features. The feature space includes the available signals but also the selected statistical features. While the signals current, voltage and temperature are included in any case, the additional input features from the simulation dataset are varied. Those signals are not available for experimental data, hence a so-called binary decision column is introduced. The column is located after the last time step and assigned with the value one in the case of available data, and with a zero in case of unavailable data. This allows the NN to either use or ignore the feature depending on availability. This method was already validated for battery temperature prediction with CNNs.[55] The combined data structure is visualized in Fig. 6.

The statistical features are clustered into four subsets as to reduce computational complexity. The charge balance feature CB() is included in any case, as it works as a substitute for the SOC. The clusters are listed in Table VI.

Combined with five possible input data signals (SOC, Φ_s, Φ_l, $\boldsymbol{c}_s$, $\boldsymbol{c}_l$) in total $1 + \sum_{i=0}^{9} \binom{9}{i} = 512$ combinations must be evaluated. The trained models are evaluated based on the decision metric in Eq. 4. The RMSE ϵ_{RMSE} and MAX ϵ_{MAX} for the experimental sub-test dataset are normalized and combined with a weighting factor to attribute the RMSE and MAX with equal importance. Simulation data is excluded from the decision metric. The final score results from both error metrics and yields the highest value for the best performing model.

$$\epsilon_{\text{RMSE}} = \frac{0.5\cdot\epsilon_{\text{RMSE}}^{\text{lab}} + 0.5\cdot\epsilon_{\text{RMSE}}^{\text{vehicle}}}{\max(\max(\boldsymbol{\epsilon}_{\text{RMSE}}^{\text{lab}}, \boldsymbol{\epsilon}_{\text{RMSE}}^{\text{vehicle}}))} \quad [2]$$

$$\epsilon_{\text{MAX}} = \frac{0.5\cdot\epsilon_{\text{MAX}}^{\text{lab}} + 0.5\cdot\epsilon_{\text{MAX}}^{\text{vehicle}}}{\max(\max(\boldsymbol{\epsilon}_{\text{MAX}}^{\text{lab}}, \boldsymbol{\epsilon}_{\text{MAX}}^{\text{vehicle}}))} \quad [3]$$

Table VI. Feature clusters, their abbreviation and content.

Abbreviation	Feature cluster	Content
F1	Statistical, scalar features	min(), mean(), max(), mode()
F2	Scalar, physical interpretable features	wv(), rms(), dft()
F3	Vectorized, related features	d/dt(), $R()$
F4	Vectorized, adapting features	$\text{rms}_{\text{vec}}()$

Journal of The Electrochemical Society, 2023 **170** 090524

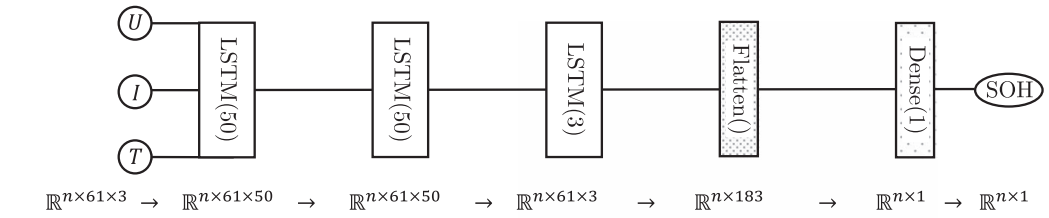

(a) Initial Model.

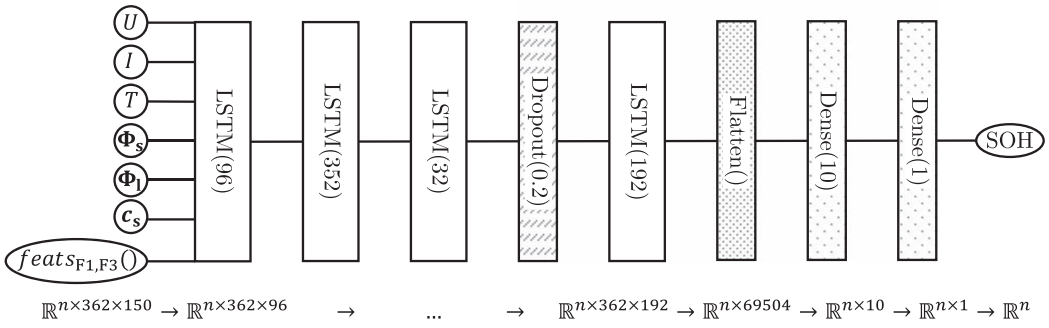

(b) Final Model.

Figure 8. Architecture of the initial (a) and final model (b) and corresponding dimensions of output data from each layer with n as the number of samples.

Table VII. Accuracy of the best performing model after sensitivity analysis for each test dataset and the relative error change in relation to the initial model.

Evaluation Test Data	RMSE	Δ_ϵ(RMSE)	MAE	Δ_ϵ(MAE)	MAX	Δ_ϵ(MAX)
Combined	3.96%	−33.3%	3.14%	−34.3%	12.3%	−47.0%
Simulation	3.48%	−41.2%	2.89%	−42.1%	7.98%	−61.8%
Laboratory	5.00%	−10.1%	3.66%	−4.94%	12.3%	−42.2%
In-Vehicle	5.45%	−38.7%	5.17%	−31.8%	10.0%	−56.9%

$$score = 1 - (0.5 \cdot \epsilon_{\mathrm{RMSE}} + 0.5 \cdot \epsilon_{\mathrm{MAX}}) \quad [4]$$

In Fig. 7 the results from the sensitivity analysis are displayed. The shaded areas refer to feature variations with signals from $\boldsymbol{c}_\mathrm{s}$, $\boldsymbol{c}_\mathrm{l}$, Φ_s or Φ_l included. Hence, in total $2^4 = 16$ different signal combinations are displayed. For better readability and to shift the focus toward the influence of signal combinations, the trajectories within a certain area are smoothed with a Savitzky-Golay filter with window size 11 and a polynomial order of three. Note that the final score solely emerges from the laboratory and in-vehicle results.

It is challenging to interpret the multidimensional visualization in Fig. 7. The usage of the features from the solid concentration $\boldsymbol{c}_\mathrm{s}$ leads to slight accuracy increase for the experimental data and excellent performance for synthetic data. For the simulation data, however, inclusion of features from both concentrations $\boldsymbol{c}_\mathrm{s}$ and $\boldsymbol{c}_\mathrm{l}$ leads to the best result. This result also supports the correlation analysis findings. The model with highest score includes features from cluster F2, and uses the signals U, I, T, SOC, Φ_s, Φ_l and $\boldsymbol{c}_\mathrm{s}$. Table VII gives the detailed report about estimation accuracy with the relative error $\Delta_\epsilon(x) = \frac{x_\mathrm{new} - x_\mathrm{old}}{x_\mathrm{old}}$. The accuracy increases for every dataset and metric. In particular the error related to simulation data decreases heavily, due to the inclusion of the internal states as an input variable and its correlation to the SOH.

Hyperparameter tuning.—Prior to hyperparameter tuning, a sample length analysis is conducted, resulting in 1800 s as the optimal trade-off between training runtime and accuracy. The sample length analysis for the initial model (Fig. 8a) and the priory selected feature set is given in the Appendix, Table XIII. An additional dense layer before the last layer further improves accuracy. These settings are used for hyperparameter tuning.

During model training, the weights of the individual neurons are adopted. These weights generally are referred to as parameters. In contrast, the hyperparameters cannot be learned during training and must be set initially. Hence, the hyperparameters are the settings of the model and must be tuned by the engineer in order to design a useful NN. The process of optimizing hyperparameters is called hyperparameter tuning. Most important, during this process one must not solely rely on the training accuracy. This always leads to deeper, more complex models and finally in overfitting the training data. Instead, test or validation accuracy must be included into the evaluation metric.[19]

Manual tweaking is cumbersome and prone to miss the global or even local optimum. Automated tuning scripts promise to ease the application and return global optima. Bayesian optimization is a powerful technique for tuning hyperparameters in a LSTM network.[19,56] It involves selecting a set of hyperparameters to optimize, defining a range of values for each hyperparameter, and then using Bayesian statistical methods to efficiently explore the hyperparameter space and identify the combination of hyperparameters that minimizes the validation loss. During the optimization process, the algorithm learns from previous evaluations and updates its estimate of the hyperparameters that are most likely to produce

Journal of The Electrochemical Society, 2023 **170** 090524

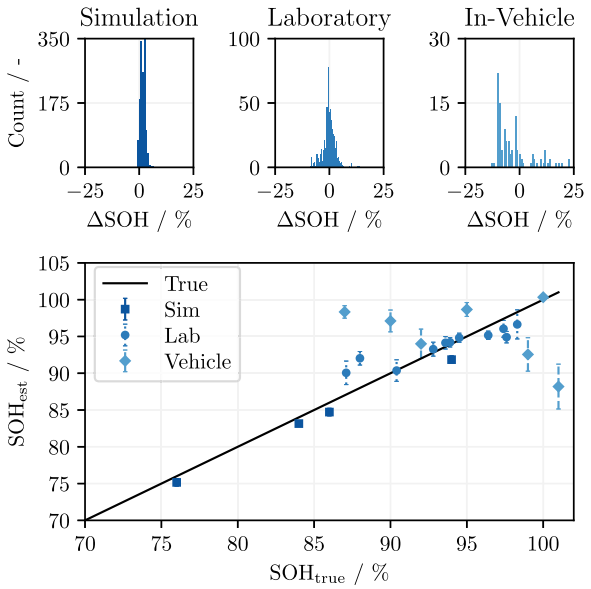

Figure 9. SOH estimation accuracy of the final model for each test dataset. In the lower graph, the estimated SOH_{est} is plotted against the true SOH. The upper histograms visualize the error distribution with $\Delta SOH = SOH_{est} - SOH_{true}$ for every test dataset.

the best results, while also pruning out non-promising directions of optimization. This approach can significantly reduce the time and effort required to find the optimal set of hyperparameters for a given LSTM network, and has been shown to improve performance compared to manual tuning or other automated methods.[56] The Keras-made solution KerasTuner[57] is used in this paper.

The search space and the maximum number of iterations used for Bayesian optimization are defined beforehand, as listed in Table VIII. The number of neurons and the dropout rate can be set individually for every layer. All resulting models from hyperparameter tuning are trained with the same dataset as the initial model, with the exception of small reversed subset for validation.

A fraction of the training dataset from laboratory and in-vehicle data is used as validation data to monitor the model's performance for unknown samples. The simulation data is excluded from validation because the main goal is to minimize the loss for experimental data. The Bayes optimization solves for the best choice of hyperparameters to minimize the validation loss, which means in this case the accuracy at estimating the SOH of experimental data. Every permutation is executed twice and the average validation loss is stored. More than 200 permutations are evaluated. The best hyperparameter set is found to be four LSTM layers, one dropout layer, a batch size of 256 and 1500 epochs. The architecture of the final model is visualized in Fig. 8b. The flattening layer maps a three dimensional input to a two dimensional output. Along with the architecture, the output dimensions of every layer are given.

Table VIII. Defined hyperparameter search space for Bayesian optimization.

Hyperparameter	Search space
LSTM Layers	1 to 5
Neurons in LSTM Layers	32 to 512
Dropout Layers	0 to 4
Dropout Rate	0.1 to 0.5
Batch Size	32 to 256
Epochs	50 to 2000

Results and Discussion

The performance evaluation of the final PINN is visualized in Fig. 9. The individual errors are listed in the first part of Table X. The model is evaluated against the tree different datasets: simulation, laboratory and in-vehicle data. The model performs best with simulation data and estimates the SOH with a RMSE of 1.98%. The SOH of the laboratory test data can be estimated with a RMSE of 2.95%. The standard deviation error bars in Fig. 9 show little deviation from the mean estimate for simulation and laboratory data, indicating increased estimation confidence. Nonetheless, the findings presented in Table X and Fig. 9 demonstrate that the in-vehicle data samples pose a significant challenge to the model. This subset of data is characterized by a higher RMSE of 8.56%. The model's failure to capture the overall degradation trend for the in-vehicle data is evident, resulting in decreased performance solely for this dataset when compared to the post-sensitivity-analysis model. Despite the higher in-vehicle error, the model achieves the lowest validation loss because the in-vehicle dataset represents a small subset of the validation data with less than 5% of the total validation data. Consequently, the worse estimation of in-vehicle samples is compensated by better performance for laboratory samples.

Model sensitivity.—The performance of the PINN model is strongly influenced by driving profiles and temperature ranges, as demonstrated in Table IX. While the sensitivity analysis was

Table IX. Accuracy of the PINN for different temperature regions and current profiles.

	Simulation		Laboratory		In-Vehicle	
	T_1	T_2	T_1	T_2	T_1	T_2
			MAE			
CC Charge	—	—	2.37%	—	7.65%	6.79%
CC Discharge	1.50%	1.36%	1.79%	—	12.2%	—
Dynamic Profile	1.69%	1.71%	2.09%	0.60%	7.21%	7.26%
Average	1.68%	1.69%	2.08%	0.60%	8.12%	7.23%
			RMSE			
CC Charge	—	—	3.46%	—	7.96%	6.79%
CC Discharge	1.72%	1.61%	2.43%	—	13.6%	—
Dynamic Profile	2.00%	2.01%	2.92%	0.60%	9.03%	8.02%
Average	1.98%	1.99%	2.95%	0.60%	9.57%	7.93%
			MAX			
CC Charge	—	—	14.1%	—	11.6%	6.98%
CC Discharge	2.73%	2.71%	7.54%	—	23.4%	—
Dynamic Profile	5.60%	6.73%	14.1%	0.60%	23.4%	13.0%

Journal of The Electrochemical Society, 2023 **170** 090524

Table X. Benchmark of the PINN with other state-of-the-art machine learning (ML) models for each test dataset. For every test dataset and every error metric the lowest error value is printed bold.

Evaluation Test Data	RMSE	MAE	MAX
		PINN	
Combined	**3.03%**	**2.11%**	23.4%
Simulation	**1.98%**	**1.69%**	**6.73%**
Laboratory	**2.95%**	**2.08%**	**14.1%**
In-Vehicle	8.56%	7.28%	23.4%
		$LSTM_{exp}$	
Combined	4.81%	3.29%	**20.9%**
Simulation	—	—	—
Laboratory	4.65%	3.01%	20.9%
In-Vehicle	5.76%	5.10%	13.1%
		LSTM	
Combined	3.36%	2.30%	29.5%
Simulation	2.97%	1.97%	13.86%
Laboratory	3.33%	2.45%	15.1%
In-Vehicle	6.65%	5.52%	29.5%
		FNN	
Combined	6.09%	4.97%	52.9%
Simulation	6.08%	5.24%	15.5%
Laboratory	6.11%	4.41%	52.9%
In-Vehicle	6.17%	4.99%	11.4%
		RNN	
Combined	7.00%	4.64%	30.4%
Simulation	8.25%	5.45%	30.4%
Laboratory	3.81%	3.00%	15.3%
In-Vehicle	**4.98%**	**4.60%**	**9.79%**

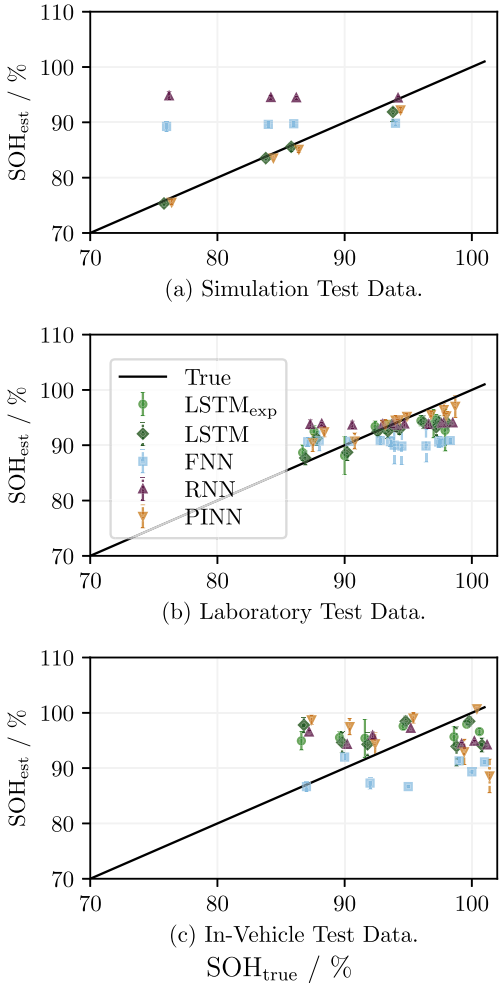

Figure 10. Benchmark of the PINN to other state-of-the-art machine learning (ML) models. The estimated SOH_{est} is plotted against the true SOH for every model and dataset.

employed during the model development process to identify the most promising features, we utilize it here to evaluate the PINN's dependency on current and temperature profiles. The selected driving profiles consist of CC charging, CC discharging, and dynamic profiles. Two temperature regions are defined. The first region T_1 includes all samples with a measured temperature between 20 °C to 30 °C. The region T_2 inhibits all samples outside of T_1, which means below 20 °C and above 30 °C.

Simulation data is estimated best with samples from CC discharge events in the temperature region T_2. It can be seen in Fig. 3 that the simulation data does not include CC charging events. Higher accuracy for CC events is expected, due to more data with similar profiles in the training data. Although more data with dynamic profiles is included in the training set, it is very challenging for data-driven models to transfer knowledge gained from one dynamic profile to another dynamic profile if current rates and gradients differ strongly. Additionally, the time-step of 5 s is too large to differentiate between the instantaneous processes inside the battery like ohmic and charge-transfer overpotentials. The model's performance exhibits a minor temperature dependency, potentially stemming from statistical uncertainty during the training phase. A more detailed analysis yields similar performance even for very low or high temperatures, which is explainable by the evenly distributed simulation dataset (Fig. 4). The worst performance, i.e., the MAX error, originates in both temperature regions from a sample with a negative current pulse of 1C (Steps-Profile from Fig. 3). This high error emerges from a relatively small portion of data with this profile in comparison to CC discharging events which leads to a biased estimation.

As can be seen in Fig. 4, most of the laboratory data is captured for CC charging and discharging events at the temperature region T_1. Dynamic profiles also include parts of CC charging and discharging events with at least 360 s of current flow and hence include the overpotential buildup or relaxation process. This additional information allows the PINN to reach high estimation accuracy for dynamic profiles with a RMSE below 3% for both temperature regions even with a large time-step of 5 s. The performance of the model with dynamic profiles within the temperature range T_2 lacks statistical significance due to the limited number of samples. In fact, just a single sample from the laboratory dataset lies within temperature range T_2. Excluding this data segment, the PINN performs best for CC discharging events, benefiting from additional data obtained during the training process from the simulation dataset. In contrast, less amount of data for CC charging events and possible outliers lead to poorer performance. These outliers are identified by unusual temperature profiles which originate from unknown history. For example the temperature decreases ($\Delta T < 0.5$ K) although the battery is operated due to prior heating. These data anomalies are not included in the CC discharging, nor the dynamic profiles.

Across all data subsets, the RMSE of the in-vehicle estimations exceeds 7%. The performance for all in-vehicle data subsets is insufficient, making the interpretation of the sensitivity analysis unnecessary. The PINN struggles to transfer knowledge from simulation and laboratory data to in-vehicle data, particularly due to significant mismatches in most current profiles. Notably, the

Journal of The Electrochemical Society, 2023 **170** 090524

highest errors emerge from CC discharging samples with a current rate below 0.1C.

Benchmark.—To further investigate the performance and the influence of physico-chemical information on the PINN, it is compared to purely data-driven approaches. The other approaches are chosen as they represent the most common NNs in the field.[17,19] The data-driven approaches are tuned with respect to the proposed hyperparameter–tuning procedure, presented in Table VIII. This allows a fair comparison because the hyperparameters are optimized to their individual best for the specific reduced dataset. They all keep the flattening and the two dense layers with ten and one neuron to produce the final scalar output. Table XIV in the Appendix presents the final architecture for every NN. Table X and Fig. 10 show the benchmark. All other models train with the full dataset but exclude internal states, with the exception of the $LSTM_{exp}$. The $LSTM_{exp}$ trains solely with experimental data to evaluate the impact of synthetic training data.

In Fig. 10 it is clearly visible, that the FNN and the RNN underfit the training data and hence fail to accurately estimate the SOH of any test dataset. It is evident that FNNs fail to capture the temporal context and are thus not qualified to process the dependencies of time-series signals.[18,58] The findings further support the initial statement, that LSTMs are superior to RNNs. The LSTM solves the vanishing gradient problem[18,59] and thus estimates the SOH with an average RMSE of 3.36%. Nevertheless, it has a worse performance than the PINN and estimates the laboratory samples with a RMSE of 3.33%. The error further increases to 4.65% if simulation data is completely excluded, as in the $LSTM_{exp}$.

Discussion.—The present study aims to investigate the effect of physical information and synthetic data on the performance of machine learning SOH estimation models. The main research question was whether incorporating such data can improve the accuracy and generalization ability of these models. Our results provide strong evidence that physical information and synthetic data indeed have a positive impact on model performance. Table X supports the statement by giving the accuracy of the PINN in comparison to the same model architecture trained without simulation data, nor internal states ($LSTM_{exp}$) and trained without internal states (LSTM). The PINN model trained with both types of data consistently outperforms other models for laboratory test data. The inclusion of synthetic data to the LSTM provides more training data and hence improves the accuracy for laboratory test data. Additional information from internal states further boosts performance.

Our results confirm previous findings by Thelen et al.,[28] who showed that a sequential PINN trained on a combined dataset achieved the best performance in estimating the SOH. Thelen et al.,[28] however, used less but more detailed data, including a DVA of half cells, and hence, reported a lower RMSE of 0.74% at estimating the SOH at 37 °C or 55 °C. Similarly, Son et al.[60] demonstrated that incorporating more detailed features, such as mechanical and electrochemical responses, in the form of health indicators optimized a PINN to estimate the SOH with a lower RMSE of 0.49%. In contrast, the current study utilizes easily derivable signals during operation and does not require complex measurements to initialize the method, thereby competing with the PIML model developed by Kohtz et al.[30] The latter model processes charging voltage segments and estimates the SEI thickness, which is directly mapped to the SOH, with an RMSE of 8.97% at an unseen test case at 30 °C. Notably, the developed PINN in the present study outperforms the PIML by Kohtz et al.[30] for any given laboratory test dataset. Furthermore, this study first introduces internal states from a P2D model as additional features in the synthetic dataset. The model is forced to link the measurable states to the internal variables that correlate to the SOH due to the binary decision column. This work thus extends previous research by demonstrating the efficacy of utilizing easily obtainable signals and internal states in estimating the SOH of batteries.

Nevertheless, the data and the method must be critically discussed. The following paragraphs are structured to align with the workflow of the model development process. Initially, a thorough analysis of the data sources is presented, encompassing aspects such as sampling methodologies, parameter validity, potential imperfections in the experimental data, and the integration of multiple data sources. Subsequently, the focus shifts toward a critical evaluation of the model, including an assessment of hyperparameter tuning and feature selection techniques.

First, the sampling itself reduces the signal duration and makes the model generalizable to snippets with constant length from any SOC window. On the other hand, by sampling the data, the previous history of operation is unknown and may lead to scenarios in which important information is missing. For example, the worst performance for laboratory data (Table IX) is due to a decreasing temperature signal, which is falsely interpreted by the model because the previous history is unknown. A more similar data structure eventually leads to higher performance, especially the usage of full CC charging events. The sampling further leads to a loss of information in the experimental datasets due to the low sampling rate of 0.2 Hz, which is set by the simulation data. Dynamic samples with relaxation processes profit from higher sampling rates because more information about the overpotentials with fast time-constants are included.[61] The additional information from higher sampling rates positively contributes to the final performance. In other works,[28,30,42,43,60,62] the sample rate is not explicitly stated.

Second, the validity of the P2D parameter set, particularly under degraded conditions, is limited to predefined measurements. For this particular cell, the degraded parameter set is fitted to a repeated C/3 CC charge–discharge test, as in Fig. 3i. In general, several parameter sets lead to accurate result due to the ambiguity of the combination. A perfect alignment between the observed battery response, voltage and temperature, does not necessarily guarantee the uniqueness of the assumed parameter set. The precise measurement of all internal states and parameters during operation is still a challenge. Nevertheless, the experimental data shows good agreement between the measurable signals and the simulation results (see Fig. 12).

Third, the accuracy is influenced by imperfections in the experimental dataset, i.e., noise or varying ambient temperature. Especially, the in-vehicle dataset presents these challenges for the PINN. More important, the in-vehicle dataset only comprises of 2.20% of the total data amount, whereas laboratory data makes up to 36.7% and simulation data 61.1%. Hence, it is reasonable for the model to be biased toward the other data sources and further to disregard the in-vehicle training loss during optimization. The model is likely to end in a local optimum with underfitted in-vehicle training data. The possibility to achieve comparable results with even sparser experimental data should be addressed in future studies.

This work tries to combine signals from cell level, which is simulation and laboratory data, with signals from storage level. The current flow into the storage is divided by the number of parallel cells to yield the average cell current. The voltage and temperature signal is only captured for the minimum, maximum and average value per signal. The average values are used in this approach. Hence, giving rise to various error sources. The samples from the in-vehicle dataset itself statistically vary from the other data sources, as can be seen in Fig. 4. Most of the data is distributed at high SOHs, even above 100%. The in-vehicle dataset includes more aggressive profiles with higher current rates than the other data sources. Hence, a large amount of the in-vehicle dataset is poorly represented in the training data. The interaction of these challenges leads to the reduced performance for in-vehicle data.

The model itself might be prone to overfitting because it trains with a large batch size of 256 for 1500 epochs and is relatively deep, i.e., many neurons and layers. Generally, more complex models are rather prone to overfit on training data.[19] To assess this problem, the data has been split independently priorly. This strategy ensures to use test data with different SOH labels than the training data. Bayes optimization uses the validation loss as the cost function and hence

Journal of The Electrochemical Society, 2023 **170** 090524

stops training before overfitting on training data occurs. Further, the dropout layer and the inclusion of data anomalies act as regularization techniques and thus prevent overfitting.[19]

Feature selection plays a vital role in determining the accuracy and interpretability of the final PINN. Although a comprehensive feature selection process including correlation and sensitivity analysis was performed, the initial selection of possible features may not be ideal, and there are several limitations to the process. In this study, the final feature selection indeed reduced the error, but it cannot be disproven that there exist another feature set that truly result in the global optimum of the feature space.

Finally, it is very challenging to prove the cause of superior performance of the PINN over the LSTM in Table X. It is most plausible and there is strong evidence that the NN exploits correlation between the measurable signals current, voltage, temperature, and the internal states which increase the correlation to the SOH. In other words, there are connections from the first layer with current, voltage and temperature as input to the hidden layers, which fuses this information with knowledge from internal states. Previous analyses support the statement about feature correlation from both signal types, corroborating this assertion.

To improve the efficacy of the proposed method, it is desired to employ an advanced synthetic dataset containing full CC charging events with higher sampling rates. Furthermore, to enhance the performance, more precise P2D parameters are required that exhibit improved conformity with experimental data, even at degraded state. In order to facilitate the utilization of PINNs in the context of in-vehicle or field data, it is imperative to minimize the discrepancies between combined datasets. To this end, processing the signals of individual cells holds promise as an alternative to relying on mean cell voltage and temperature.

The proposed method demonstrates its suitability for real-time SOH estimation in many applications. Especially the low requirement on signals allow the realization in EVs because only one current, voltage and temperature signal with a sampling rate of 0.2 Hz are mandatory. If we assume that one signal value equals one integer with two bytes, the whole data package comprises of 2.06 kB. A cloud connection and frequent data exchange further enable a BMS to monitor the SOH with remote updates, i.e., the 2.06 kB package is sent to the backend where the model is employed, the resulting scalar SOH is returned to the BMS. The final model demands 17.7 MB of storage in H5-format and estimation of one sample takes 55 ms with CPU-computing on a 11th generation Intel i7 core (3.00 GHz, 8 CPUs, 16 GB RAM).

PB simulations have the capability to enhance existing data-driven approaches through the provision of additional physico-chemical battery data or to establish new PINNs, even with sparse experimental data. The utilization of a synthetic dataset facilitates the acquisition of comprehensive information concerning cell-internal states, including the previously unknown degradation states. It enables a reduction in the number of required experiments and ultimately reduces associated time and cost requirements.

The utilization of conventional transfer learning for the PINN model presents a promising avenue for improving its usability and accuracy. In this context, transfer learning describes the training of base models with big data and the followed retraining with individual, sparse data. Transfer learning enables pre-training and publication of data-driven models with large-scale synthetic data, which can include internal states. The usability of conventional transfer learning for capacity estimation in lithium-ion batteries was exemplary proven by Shen et al.[63] and Zou et al.[64]

Conclusions

This research paper presents an analysis of the key challenges in the development process of ML projects, with a focus on the critical role of data and their preprocessing in optimizing model architecture. Physico-chemical simulations act as a powerful tool for generating large quantities of highly accurate data, including both measurable and non-measurable internal states in synthetic datasets, to yield improved results. Nevertheless, this study highlights the need for a detailed understanding of the limitations and development process of PINN. The developed sequential PINN architecture, which temporally decouples the complex P2D model, enables fast estimation using 30 min samples from current, voltage, and temperature signals. The PINN achieves estimation errors below 2% RMSE and 3% RMSE for simulation and laboratory data, respectively. The fusion of experimental data with synthetic data leads to increased accuracy and through inclusion of internal states in the simulation dataset, the performance is further improved. The comparison of the PINN with state-of-the-art NNs highlights the positive impact of incorporating physical information. Moreover, comparable current profiles, e.g., CC events, improve the estimation accuracy. The developed PINN demonstrates high accuracy for laboratory data, particularly for comparable samples to those in the simulation dataset. Unfortunately, it fails to generalize to in-vehicle data due to dataset size, differences in current profiles, and signal acquisition. Furthermore, the performance of the model is constrained by the sample rate of 5 s, which does not capture relaxation behavior in the high frequency domain. Ultimately, this study shows that a well chosen combination of experimental and synthetic data, equal data splits and structure, improves the performance of data-driven SOH estimation models. Hence, physical informing a NN is a low complex solution to boost performance of ML models, not limited to battery state estimation.

Acknowledgments

This work was funded by the BMW Group AG and was performed in cooperation with the University of Bayreuth and the Technical University of Munich.

Appendix A. Error Metrics

Table XI lists the most widely used error metrics. In the context of SOH estimation, Y is equal to the true SOH, while $\hat{Y}$ is the estimated SOH_{est}. The MAPE exhibits a more pronounced violation of errors around zero compared to the MAE or the RMSE.

Table XI. Common error metrics, their abbreviations and formula.[65]

Error Metric and Abbreviation	Formula
Mean Absolute Error (MAE)	$\frac{1}{N}\sum_{i=1}^{N}\lvert Y-\hat{Y}\rvert$
Root Mean Squared Error (RMSE)	$\sqrt{\frac{1}{N}\sum_{i=1}^{N}(Y-\hat{Y})^2}$
Mean Absolute Percentage Error (MAPE)	$\frac{1}{N}\sum_{i=1}^{N}\left\lvert\frac{Y-\hat{Y}}{Y}\right\rvert$
Maximum Absolute Error (MAX)	$\max_{1\leqslant i\leqslant N}\lvert Y-\hat{Y}\rvert$

Y: True value, $\hat{Y}$: Estimated value, N: Number of samples.

Journal of The Electrochemical Society, 2023 **170** 090524

Appendix B. Results from the Correlation Analysis

Table XII gives insights about the results from the correlation analysis performed to derive the best suitable features for SOH estimation. All scalar features are calculated on the 300 s samples from the combined dataset. The features derived from internal states solely utilize the synthetic data samples. The correlation between the vectorized feature CB() and the SOH is not calculated, because it is assumed to directly correlate with the SOC. Hence, CB() acts as a substitute for the SOC signal in the experimental dataset. The Pearson correlation coefficient between the windowed resistance $R()$ and the SOH is 2.16% for a window length of 10 s.

Table XII. Pearson correlation coefficient between the SOH and every feature of every signal from a 300 s sample. All values are given in percent in a range between −100% to 100%, where −100% indicates indirect proportionality and 100% direct proportionality.

Feature	U	I	T	SOC	Φ_s	Φ_l	$\boldsymbol{c}_s$	$\boldsymbol{c}_l$
min()	5.11	1.04	−1.20	4.15	9.08	4.17	28.8	8.94
max()	1.60	1.16	2.16	3.81	11.0	8.18	29.0	9.00
mean()	3.75	1.94	−1.48	3.47	10.9	6.59	29.0	7.46
mad()	−6.26	0.36	−6.90	−5.50	8.35	8.54	3.65	11.0
mode()	3.12	2.01	−1.31	2.99	10.5	6.07	28.3	6.57
Δ()	−4.84	0.54	−6.36	−6.24	7.19	6.53	4.02	10.8
std()	−5.67	−0.22	−5.94	−6.27	7.61	7.98	4.07	10.5
max Δ()	−1.24	−0.81	2.15	−3.81	1.96	1.07	3.13	1.21
rms()	3.72	2.24	−1.48	3.45	11.2	8.65	29.0	7.37
skew()	0.87	−0.32	−1.23	−0.20	0.82	1.15	1.90	1.12
se()	0.99	1.77	0.95	0.99	0.99	3.27	11.6	9.09
wv()	−0.78	1.93	−1.49	3.49	2.08	1.47	29.0	7.56
dft()	2.03	0.55	2.99	3.69	10.8	6.57	29.1	7.57
$d/dt()$	1.30	0.56	2.93	3.13	2.1	2.13	2.72	3.02
$d^2/dt^2()$	1.50	0.74	1.73	2.39	2.14	2.24	1.83	2.27
$rms_{vec}()$	3.89	2.63	1.49	3.68	11.4	8.65	29.2	7.54

Journal of The Electrochemical Society, 2023 **170** 090524

Appendix C. Results from the Sample Length Analysis

The initial model from Fig. 8a is trained with the final feature set and samples with varying duration from 300 s to 2400 s. Table XIII lists the RMSE of the individual models for every sub dataset and the training duration normalized to the training duration for the model with 300 s samples. A sample duration of 1800 s is selected due to its optimal accuracy in laboratory samples while ensuring reasonable runtime.

Table XIII. Results of the sample length analysis. For a sample length between 300 s to 2400 s the relative training duration and the accuracy for each test dataset is listed for the initial model.

Sample Length	$\Delta t_{\text{train}}/\Delta t_{\text{train,300 s}}$	Sim. RMSE	Lab. RMSE	Veh. RMSE
300 s	1.00	3.48%	5.00%	5.45%
600 s	1.23	2.14%	4.40%	7.50%
900 s	1.52	4.76%	4.34%	7.10%
1200 s	2.02	2.28%	4.41%	6.74%
1500 s	3.63	2.03%	4.73%	7.58%
1800 s	3.74	2.86%	4.11%	6.51%
2100 s	3.87	3.26%	4.45%	6.89%
2400 s	3.97	1.56%	4.60%	8.37%

Journal of The Electrochemical Society, 2023 **170** 090524

Appendix D. Results from the Bayes Optimization of the Benchmarked Models

The benchmarked NNs were tuned to their respective optimum by Bayes optimization. For all models, the search space is defined as in Table VIII. The resulting hyperparameters for every NN are listed in Table XIV.

Table XIV. Results of the Bayes hyperparameter tuning for all benchmarked NNs. The first dropout–layer is placed after the second neural layer.

Hyperparameters	LSTM	$LSTM_{exp}$	FNN	RNN
Layers	2	2	4	4
Neurons	352, 32	256, 128	480, 256, 64, 128	192, 384, 96, 480
Dropout Layers	1	1	3	3
Dropout Rate	0.2	0.4	0.3, 0.1, 0.4	0.3, 0.4, 0.2
Batch Size	265	64	256	96
Epochs	891	1437	1426	1303

Journal of The Electrochemical Society, 2023 **170** 090524

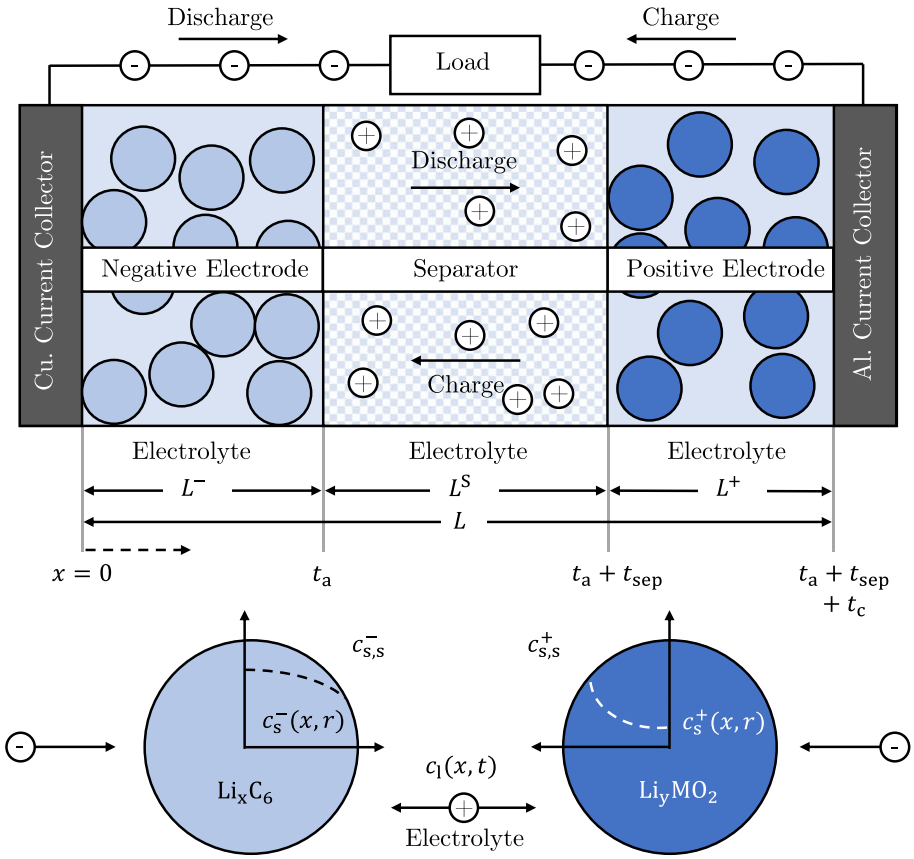

Figure 11. Domains and geometry of the Newman P2D model (adapted from Jokar et al.[68]).

Appendix E. Newman Pseudo Two-dimensional Model

The pseudo-2-dimensional (P2D) model, introduced by Doyle, Fuller and Newman,[4,66,67] describes the cell on a macroscopic scale with two porous electrodes, an insulating separator and liquid electrolyte, as depicted in Fig. 11. The model solves the mass and charge balance and the electrode kinetics along the *x*-dimension of the full cell. The insertion of lithium-ions into the particle, i.e., diffusion, is modelled with the second pseudo-dimension in *r*-direction. The two dimensions are coupled via the mass balance and the electrode kinetics.

Table XV presents a summary of the input parameters required for the Newman P2D model, including their dependencies on the proposed model and literature. The theoretical range of parameter variations over degradation is also included when available. The assumed parameter variations over degradation are in good agreement with the literature references.[33,69,70]

The accuracy of the aged parameter set is validated by laboratory measurements that include CC C/3 charge–discharge tests as in Fig. 3i. These tests are conducted at 25 °C and various SOHs during a cyclic and calendar lifetime study with varying boundary conditions. Figure 12 shows the resimulation of random samples from both laboratory and in-vehicle datasets. The absolute voltage error for laboratory data remains below 50 mV, except for very low SOC, due to the definition of stoichiometries in the P2D model referring to relaxed voltage data points. As a result, the deposited OCV curve in the model is not defined between 2.8 V to 4.2 V, but rather between 3.1 V to 4.2 V. A full discharge, as in the laboratory check-up, hence leads to slight deviation from measurement to simulation. The temporal signal course, however, aligns well. Similarly, the simulated cell core temperature and the measured cell surface temperature align well, although larger gradients build up during discharge, resulting in minor deviations. In contrast to the laboratory check-ups, the selected in-vehicle samples exhibit highly dynamic driving profiles in both pristine and aged states. For both samples, the voltage simulation agrees well with the measurement, and the absolute error remains below 100 mV at all times. Although the simulated temperature is close to reality for higher ambient temperatures (Fig. 12d), the error increases for lower temperatures (Fig. 12c). Nevertheless, the temporal courses align well, with a maximum error of less than 3 K.

The model solves for the concentrations $c_s(x, r, t)$, $c_l(x, t)$ and potentials $\Phi_s(x, t)$, $\Phi_l(x, t)$ within the active material (solid phase, index *s*) and electrolyte (liquid phase, index *l*). The surface concentration $c_s(x, r, t)|_{r=R_p}$ is considered as $c_{s,s}(x, t)$ in this paper. The simplification of a porous structure and the assumption of an infinite expansion in *y*- and *z*-direction lead to the interpretation of an available active material particle with radius R_p at every point along the *x*-direction in the electrodes. Hence, the concentrations and potentials can be calculated at every point along the *x*-dimension. The current densities in the liquid and solid phase i_l, i_s and further the ionic flux i_n are dependent variables.

The subsequent description of the model equation does not aim to be comprehensive but rather to give the main limitations and assumptions of the model. The interested reader is referred to Refs. 4, 44, 66, 67, 71, 72 for more details.

The mass balance in the liquid phase which is deduced from diffusion and migration yields

$$\varepsilon_l \frac{\partial c_l(x,\,t)}{\partial t} = \frac{\partial}{\partial x}\left(D_{l,\mathrm{eff}} \frac{\partial c_l(x,\,t)}{\partial x} + \frac{i_l(x,\,t)\left(1 - t_+^0\right)}{\mathrm{F}} \right) \qquad [5]$$

Table XV. P2D parameter set and their dependencies on SOH, SOC and geometry x for the investigated cell. If a value range cannot be stated, the parameter is described by a function. Begin-of-life (BOL) refers to the pristine state with 100% SOH, end-of-life (EOL) refers to 73% SOH. Table taken from Hamar et al.,[44] extended with the aid of Li et al.,[33] Andersson et al.[69] and Uddin et al.[70]

Parameter	Unit	Geometry						Dependencies
		Anode		*Separator*	*Cathode*			
		BOL	EOL		BOL	EOL		
Thickness L	m	7.3×10^{-5}		1.4×10^{-5}	5.5×10^{-5}			SOH[69]
Particle radius R_p	m	7×10^{-6}			7×10^{-6}			x[69], SOH[69]
Bruggeman exponent α_B		2.6		2.5	2.1			
Porosity ε_l		0.24	0.15	0.39	0.256			x[33,69], SOH^M[33,69]
Active material volume fraction ε_s		0.7164			0.65	0.48		SOH[33,69]
Electrode equilibrium potential E_{eq}	V vs Li/Li$^+$	$E^-_{eq}(c_{s,s})$			$E^+_{eq}(c_{s,s})$			T[69], SOC^M[69], SOH^M[69]
Entropic coefficient $\frac{\partial E_{eq}}{\partial T}$	V K^{-1}	$\frac{\partial E^-_{eq}}{\partial T}(c_{s,s})$			1×10^{-4}			T[69], SOC^M[69], SOH^M[69]
Stoichiometry at 0% SOC $\theta_{0\%}$		0.037	0.0076		0.93	0.81		SOH^M[70]
Stoichiometry at 100% SOC $\theta_{100\%}$		0.83	0.59		0.19	0.19		SOH^M[70]
Max. lithium-ion concentration $c_{s,max}$	molm^{-3}	31085.2			49240			SOH[69]
Electrical conductivity of the solid matrix σ	S m^{-1}	25			0.225			
Film resistance R_f	Ω m^2	0.13×10^{-3}	7.1×10^{-3}		0.1×10^{-3}	11×10^{-3}		SOH^M
Reference diffusion coefficient $D_{s,ref}$	m^2 s^{-1}	1.6×10^{-14}			1×10^{-13}			
Diffusion coefficient D_s	m^2 s^{-1}	$D^-_{s,ref}(T, c_{s,s})$			$D^+_{s,ref}(c_{s,s}, T)$			T[M,69], SOC^M[69], SOH^M[69]
Reference reaction rate k_{ref}	m s^{-1}	6.4016×10^{-9}			1.6839×10^{-9}			
Reaction rate activation energy $E_{a,k}$	J mol^{-1}	6.8×10^4			5×10^4			
Charge transfer coefficient $\alpha_{a/c}$		0.5			0.5			
				Electrolyte				
Initial concentration $c_{l,0}$	mol m^{-3}			1120				
Reference concentration $c_{l,ref}$	mol m^{-3}			1120				
Transport number t_+				0.38				T[69], c_l[69]
Ionic conductivity κ	S m^{-1}			$\kappa(T, c_l)$				T[M,69], c_l[M,69]
Diffusion coefficient D_l	m^2 s^{-1}			$D_l(T, c_l)$				T[M,69], c_l[M,69], SOH[69]
Activity coefficient $\frac{\partial \ln f_\pm}{\partial \ln c_l}$				$\frac{\partial \ln f_\pm}{\partial \ln c_l}(T, c_l)$				T[M,69], c_l[M,69]
				Full Cell				
Specific double layer capacitance C_{dl}	F m^{-2}			0.2				
Reference temperature T_{ref}	K			298.15				
Diffusion coefficient activation energy E_{a,D_s}	J mol^{-1}			3×10^4				
Reaction rate $k_{a/c}$	m s^{-1}			$k_{a/c}(T)$				T[M,69], SOC[69]
Contact resistance R_c	Ω m^2			1.2×10^{-3}				
Grid resistance outside the cell R_{ext}	Ω m^2			3×10^{-4}				
Specific heat capacity c_p	J kg^{-1} K^{-1}			880				

M Model.

Journal of The Electrochemical Society, 2023 **170** 090524

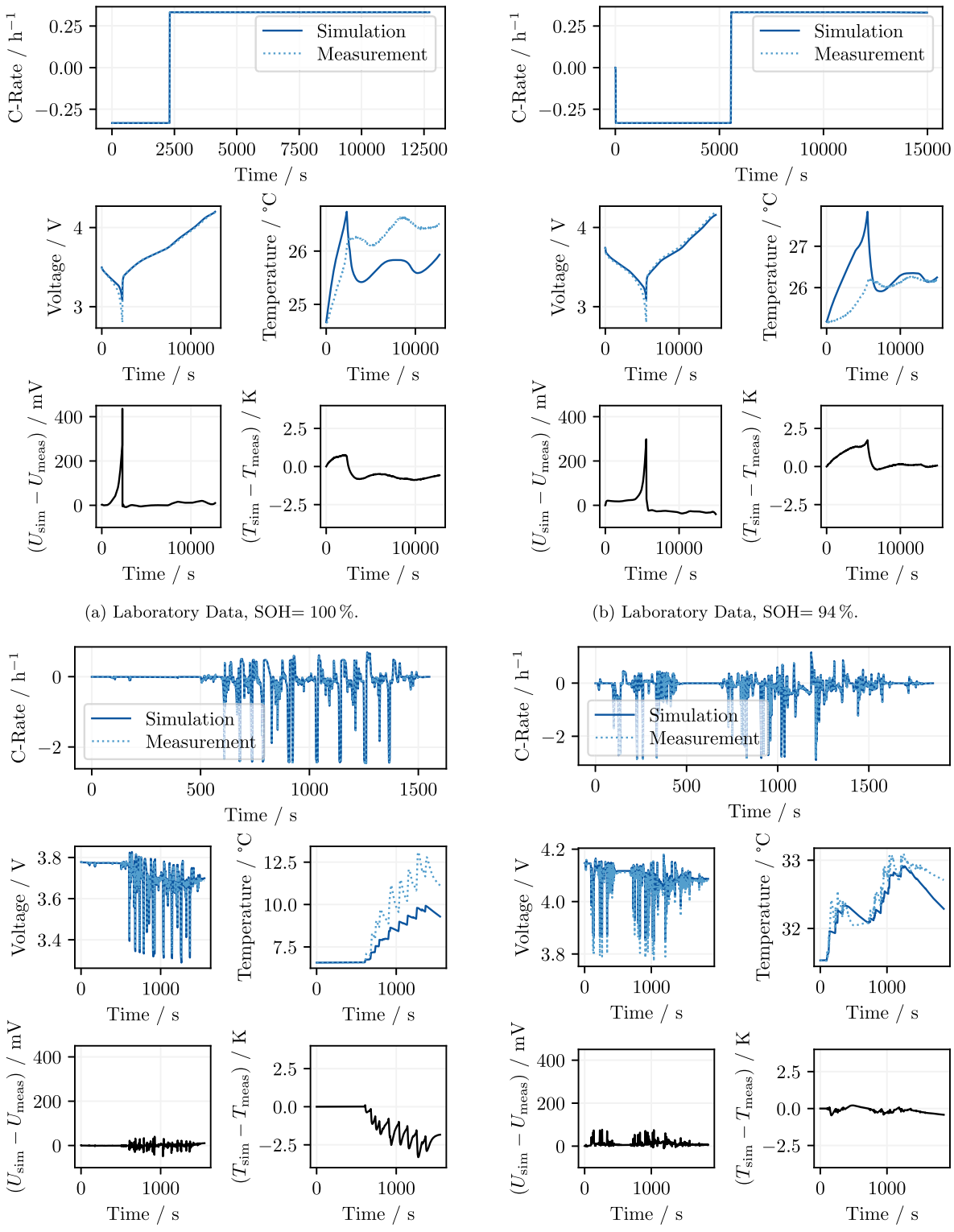

(a) Laboratory Data, SOH= 100 %.

(b) Laboratory Data, SOH= 94 %.

(c) In-Vehicle Data, SOH= 100 %.

(d) In-Vehicle Data, SOH= 92 %.

Figure 12. Random samples from the laboratory (12a and 12b) and in-vehicle dataset (12c and 12d) and their simulation results from the P2D model. The figures include the respective voltage and temperature estimation error. (a) Laboratory Data, SOH = 100%. (b) Laboratory Data, SOH = 94%. (c) In-Vehicle Data, SOH = 100%. (d) In-Vehicle Data, SOH = 92%.

Journal of The Electrochemical Society, 2023 **170** 090524

with the porosity ε_l, the effective diffusivity in the liquid phase $D_\mathrm{l,eff}$ and the transference number of cations in the solution t_+^0. Further, it must be assumed that the gradient of the liquid concentration is zero at the boundaries of the electrodes to the current collectors.

$$\left.\frac{\partial c_\mathrm{l}(x,\,t)}{\partial x}\right|_{x=0} = 0$$
$$\left.\frac{\partial c_\mathrm{l}(x,\,t)}{\partial x}\right|_{x=t_\mathrm{a}+t_\mathrm{sep}+t_\mathrm{c}} = 0 \qquad [6]$$

The potential in the liquid phase Φ_l is linked to the lithium-ion concentration in the liquid phase c_l via

$$i_\mathrm{l}(x,\,t) = -\kappa_\mathrm{eff}\frac{\partial\Phi_\mathrm{l}(x,\,t)}{\partial x} + \frac{2\kappa_\mathrm{eff}\mathrm{R}T}{\mathrm{F}}\left(1 + \frac{\partial \ln f_\pm}{\partial \ln c_\mathrm{l}(x,\,t)}\right) \times\left(1 - t_+^0\right)\frac{\partial \ln c_\mathrm{l}(x,\,t)}{\partial x} \qquad [7]$$

where κ_eff is the effective conductivity and $f_\pm$ is the activity coefficient. Again, the gradient of the liquid potential is zero toward the electrode—current collector boundary and the value itself is zero for the boundary at the positive electrode.

$$\left.\frac{\partial\Phi_\mathrm{l}(x,\,t)}{\partial x}\right|_{x=0} = 0$$
$$\left.\frac{\partial\Phi_\mathrm{l}(x,\,t)}{\partial x}\right|_{x=t_\mathrm{a}+t_\mathrm{sep}+t_\mathrm{c}} = 0$$
$$\Phi_\mathrm{l}(x,\,t)|_{x=t_\mathrm{a}+t_\mathrm{sep}+t_\mathrm{c}} = 0 \qquad [8]$$

In both electrodes the charge balance applies

$$\frac{\partial i_\mathrm{l}(x,\,t)}{\partial x} + \frac{\partial i_\mathrm{s}(x,\,t)}{\partial x} = 0 \qquad [9]$$

which couples the current density in the solid and liquid phase. In the separator the current in the liquid phase $i_\mathrm{l}(x,\,t)$ is equal to the applied current i_app. The x- and r-dimension are coupled via the correlation of the pore wall flux j_n and the divergence of the current density

$$\frac{\partial i_\mathrm{s}(x,\,t)}{\partial x} = -\frac{3\varepsilon_\mathrm{s}}{R_\mathrm{p}}\mathrm{F}j_n(x,\,t) = -a_\mathrm{s}\mathrm{F}j_n(x,\,t) \qquad [10]$$

where the specific surface a_s expresses the geometrical coupling. The specific surface is defined as the ratio of surface to volume in the spherical active particles with the volume fraction of the active material ε_s and the radius of the particles R_p.

The ionic pore-wall flux j_n of lithium-ions is related to the surface overpotential η by the Butler-Volmer relation

$$j_n(x,\,t) = \frac{i_0(x,\,t)}{\mathrm{F}}\left(\exp\left(\frac{\alpha_\mathrm{a}\mathrm{F}}{\mathrm{R}T}\eta(x,\,t)\right) - \exp\left(-\frac{\alpha_\mathrm{c}\mathrm{F}}{\mathrm{R}T}\eta(x,\,t)\right)\right)$$
$$i_0(x,\,t) = \mathrm{F}k_\mathrm{c}^{\alpha_\mathrm{a}}k_\mathrm{a}^{\alpha_\mathrm{c}}(c_\mathrm{s,max} - c_\mathrm{s,s}(x,\,t))^{\alpha_\mathrm{a}}\,(c_\mathrm{s,s}(x,\,t))^{\alpha_\mathrm{c}}\left(\frac{c_\mathrm{l}(x,\,t)}{c_\mathrm{l,ref}}\right)^{\alpha_\mathrm{a}} \qquad [11]$$

where i_0 is the exchange current density and $c_\mathrm{l,ref}$ is the reference lithium-ion concentration in the liquid phase. The reaction rate constants are k_a, k_c; and α_a, α_c are the charge transfer coefficients for the anodic and cathodic path, respectively. The surface overpotential η is the driving force of the electrochemical reaction and can be expressed with the electrode and electrolyte potentials, the equilibrium potential and the potential drop across a film resistance R_f

$$\eta(x,\,t) = \Phi_\mathrm{s}(x,\,t) - \Phi_\mathrm{l}(x,\,t) - E_\mathrm{eq}(c_\mathrm{s,s}(x,\,t)) - j_n(x,\,t)\mathrm{F}R_\mathrm{f}. \qquad [12]$$

The equilibrium potential depends on the surface concentration and thus on the SOC.

The potential in the solid phase of the electrodes is finally derived by Ohm's law as

$$\frac{\partial\Phi_\mathrm{s}(x,\,t)}{\partial x} = -\frac{i_\mathrm{s}(x,\,t)}{\sigma_\mathrm{s,eff}} \qquad [13]$$

with $\sigma_\mathrm{s,eff}$ as the effective electrical conductivity. The gradient of the solid potential is zero at the boundary between electrodes and separator.

$$\left.\frac{\partial\Phi_\mathrm{s}(x,\,t)}{\partial x}\right|_{x=t_\mathrm{a}} = 0$$
$$\left.\frac{\partial\Phi_\mathrm{s}(x,\,t)}{\partial x}\right|_{x=t_\mathrm{a}+t_\mathrm{sep}} = 0 \qquad [14]$$

Further, the gradient can be explicitly stated for the boundary of the positive electrode to the current collector

$$\left.\frac{\partial\Phi_\mathrm{s}(x,\,t)}{\partial x}\right|_{x=t_\mathrm{a}+t_\mathrm{sep}+t_\mathrm{c}} = -\frac{i_\mathrm{s} + i_\mathrm{l}}{\sigma_\mathrm{s,eff}}. \qquad [15]$$

The particle mass balance is described with spherical coordinates as

$$\frac{\partial c_\mathrm{s}(x,\,r,\,t)}{\partial t} = \frac{1}{r^2}\frac{\partial}{\partial r}\left(D_\mathrm{s}r^2\frac{\partial c_\mathrm{s}(x,\,r,\,t)}{\partial r}\right). \qquad [16]$$

The solid diffusion coefficient is given as D_s. The concentration gradient of lithium-ions is assumed to be zero at the center of particles, i.e.,

$$\left.\frac{\partial c_\mathrm{s}(x,\,r,\,t)}{\partial r}\right|_{r=0} = 0. \qquad [17]$$

In contrast, on the particle surface it is expressed by the pore-wall flux perpendicular to its surface

$$\left.\frac{\partial c_\mathrm{s}(x,\,r,\,t)}{\partial r}\right|_{r=R_\mathrm{p}} = -\frac{j_n(x,\,t)}{D_\mathrm{s}} \qquad [18]$$

The presented P2D model is coupled with a zero-dimensional thermal model to account for the temperature-dependent character of electrochemical reactions. The thermal model includes heat generation within the cell and convective heat transfer with the environment. The local temperature distribution is neglected and hence all equations are calculated without dependency on x or r. The simplified energy balance is given by

$$\rho V c_\mathrm{p}\frac{\partial T}{\partial t} = \dot{Q}_\mathrm{irr} - \dot{Q}_\mathrm{rev} - \dot{Q}_\mathrm{con} \qquad [19]$$

where ρ, V and c_p are the cell's density, volume and specific heat capacity. The irreversible heat generation

$$\dot{Q}_\mathrm{irr} = (V_\mathrm{OCV} - V_\mathrm{cell})\cdot I \qquad [20]$$

depends on the potential difference between cell voltage V_cell and the open-circuit-voltage (OCV) V_OCV, and the applied current I. The reversible heat generation is directly related to the entropy and depends on the absolute temperature T, the applied current I and the temperature dependency of the OCV

$$\dot{Q}_\mathrm{rev} = TI\frac{\partial V_\mathrm{OCV}}{\partial T}. \qquad [21]$$

The convective heat transfer between the cell's surface and the environment calculates as

$$\dot{Q}_{\text{con}} = hA(T - T_{\text{amb}}) \quad [22]$$

where h is the heat transfer coefficient, A is the intersectional area and T_{amb} is the ambient temperature. The simplified energy balance is coupled with the electrochemical model by introducing temperature dependent parameters, as indicated in Table XV. While the temperature dependency of the solid phase diffusion D_{s} and the reaction rate constants k_{a}, k_{c} are expressed by the general Arrhenius equation, the diffusion coefficient of the liquid phase $D_{\text{l,eff}}$, the ionic conductivity κ and the activity coefficient $f_{\pm}$ depend on an empirical fitting. For a more detailed explanation and the equations, the interested reader is referred to Ref. 44.

ORCID

Tobias Hofmann https://orcid.org/0009-0000-2511-9006
Jacob Hamar https://orcid.org/0000-0002-0845-3667
Marcel Rogge https://orcid.org/0000-0002-5805-4840
Christoph Zoerr https://orcid.org/0000-0002-6361-2296
Simon Erhard https://orcid.org/0000-0002-5029-7477
Jan Philipp Schmidt https://orcid.org/0000-0001-7220-377X

References

1. Y.-F. Sun, Y.-J. Zhang, and B. Su, "How does global transport sector improve the emissions reduction performance? A demand-side analysis." *Applied Energy*, **311**, 118648 (2022).
2. Y. Zhao, O. Pohl, A. I. Bhatt, G. E. Collis, P. J. Mahon, T. Rüther, and A. F. Hollenkamp, "A review on battery market trends, second-life reuse, and recycling." *Sustainable Chemistry*, **2**, 167 (2021).
3. A. Fotouhi, K. Propp, D. J. Auger, and S. Longo, "State of charge and state of health estimation over the battery lifespan." *Behaviour of Lithium-Ion Batteries in Electric Vehicles*, ed. G. Pistoia and B. Liaw (Springer Link Bücher; Springer, Cham) p. 267 (2018).
4. J. Newman and K. E. Thomas-Alyea, *Electrochemical Systems* (Wiley, Somerset) 3rd ed. (2012).
5. A. Allam and S. Onori, "Online capacity estimation for lithium-ion battery cells via an electrochemical model-based adaptive interconnected observer." *IEEE Transactions on Control Systems Technology*, **29**, 1636 (2021).
6. J. M. Reniers, G. Mulder, and D. A. Howey, "Review and performance comparison of mechanical-chemical degradation models for lithium-ion batteries." *J. Electrochem. Soc.*, **166**, A3189 (2019).
7. Y. Gao, K. Liu, C. Zhu, X. Zhang, and D. Zhang, "Co-estimation of state-of-charge and state-of- health for lithium-ion batteries using an enhanced electrochemical model." *IEEE Trans. Ind. Electron.*, **69**, 2684 (2022).
8. P. Gambhire, K. S. Hariharan, A. Khandelwal, S. M. Kolake, T. Yeo, and S. Doo, "A physics based reduced order aging model for lithium-ion cells with phase change." *Journal of Power Sources*, **270**, 281 (2014).
9. X. Zhao, Y. Bi, S.-Y. Choe, and S.-Y. Kim, "An integrated reduced order model considering degradation effects for LiFePO4/graphite cells." *Electrochimica Acta*, **280**, 41 (2018).
10. S. Dey, B. Ayalew, and P. Pisu, "Combined estimation of state-of-charge and state-of-health of Li-ion battery cells using SMO on electrochemical model." *13th International Workshop on Variable Structure Systems (VSS), IEEE* (2014), 10.1109/VSS.2014.6881140.
11. M. Guo, G. Sikha, and R. E. White, "Single-particle model for a lithium-ion cell: thermal behavior." *J. Electrochem. Soc.*, **158**, A122 (2011).
12. W. Li, Y. Fan, F. Ringbeck, D. J¨ost, X. Han, M. Ouyang, and D. U. Sauer, "Electrochemical model-based state estimation for lithium-ion batteries with adaptive unscented Kalman filter." *Journal of Power Sources*, **476**, 228534 (2020).
13. M. B. Pinson and M. Z. Bazant, "Theory of SEI formation in rechargeable batteries: capacity fade, accelerated aging and lifetime prediction." *J. Electrochem. Soc.*, **160**, A243 (2013).
14. E. Prada, D. Di Domenico, Y. Creff, J. Bernard, V. Sauvant-Moynot, and F. Huet, "Simplified electrochemical and thermal model of LiFePO4-graphite Li-ion batteries for fast charge applications." *J. Electrochem. Soc.*, **159**, A1508 (2012).
15. M. Dubarry, C. Truchot, and B. Y. Liaw, "Synthesize battery degradation modes via a diagnostic and prognostic model." *Journal of Power Sources*, **219**, 204 (2012).
16. W. Shen and R. Xiong, *Advanced Battery Management Technologies for Electric Vehicles* (Wiley, Incorporated, Newark, United Kingdom) (2019).
17. X. Sui, S. He, S. B. Vilsen, J. Meng, R. Teodorescu, and D.-I. Stroe, "A review of non-probabilistic machine learning-based state of health estimation techniques for Lithium-ion battery." *Applied Energy*, **300**, 117346 (2021).
18. S. Hochreiter and J. Schmidhuber, "Long short-term memory." *Neural Computation*, **9**, 1735 (1997).
19. I. Goodfellow, A. Courville, and Y. Bengio, *Deep Learning; Adaptive Computation and Machine Learning* (The MIT Press, Cambridge, Massachusetts) (2016).
20. Q. Gong, P. Wang, and Z. Cheng, "A data-driven model framework based on deep learning for estimating the states of lithium-ion batteries." *J. Electrochem. Soc.*, **169**, 030532 (2022).
21. W. Li, N. Sengupta, P. Dechent, D. Howey, A. Annaswamy, and D. U. Sauer, "Online capacity estimation of lithium-ion batteries with deep long short-term memory networks." *Journal of Power Sources*, **482**, 228863 (2021).
22. Y. Choi, S. Ryu, K. Park, and H. Kim, "Machine learning-based lithium-ion battery capacity estimation exploiting multi-channel charging profiles." *IEEE Access*, **7**, 75143 (2019).
23. S. Khaleghi Rahimian and Y. Tang, "A practical data-driven battery state-of-health estimation for electric vehicles." *IEEE Trans. Ind. Electron.*, **70**, 1973 (2023).
24. C. She, L. Zhang, Z. Wang, F. Sun, P. Liu, and C. Song, "Battery state-of-health estimation based on incremental capacity analysis method: synthesizing from cell-level test to real-world application." *IEEE J. Emerg. Sel. Top. Power Electron.*, **11**, 214 (2023).
25. Q. Wang, Z. Wang, L. Zhang, P. Liu, and L. Zhou, "A battery capacity estimation framework combining hybrid deep neural network and regional capacity calculation based on real-world operating data." *IEEE Trans. Ind. Electron.*, **70**, 8499 (2023).
26. K. Yang et al., "Battery state of health estimate strategies: from data analysis to end-cloud collaborative framework." *Batteries*, **9**, 351 (2023).
27. M. Aykol, C. B. Gopal, A. Anapolsky, P. K. Herring, B. van Vlijmen, M. D. Berliner, M. Z. Bazant, R. D. Braatz, W. C. Chueh, and B. D. Storey, "Perspective—combining physics and machine learning to predict battery lifetime." *J. Electrochem. Soc.*, **168**, 030525 (2021).
28. A. Thelen, Y. H. Lui, S. Shen, S. Laflamme, S. Hu, and C. Hu, "Physics-informed machine learning for degradation diagnostics of lithium-ion batterie." *Proceedings of the ASME 2021 International Design Engineering Technical Conferences and Computers and Information in Engineering Conference (IDETC-CIE2021), The American Society of Mechanical Engineers and Curran Associates Inc: New York, NY, USA and Red Hook, NY* (2021), 10.1115/DETC2021-71407.
29. A. Thelen, Y. H. Lui, S. Shen, S. Laflamme, S. Hu, H. Ye, and C. Hu, "Integrating physics-based modeling and machine learning for degradation diagnostics of lithium-ion batteries." *Energy Storage Materials*, **50**, 668 (2022).
30. S. Kohtz, Y. Xu, Z. Zheng, and P. Wang, "Physics-informed machine learning model for battery state of health prognostics using partial charging segments." *Mechanical Systems and Signal Processing*, **172**, 109002 (2022).
31. A. Wang, S. Kadam, H. Li, S. Shi, and Y. Qi, "Review on modeling of the anode solid electrolyte interphase (SEI) for lithium-ion batteries." *npj Computational Materials*, **4**, 15 (2018).
32. J. J. Sturm, S. Ludwig, J. Zwirner, C. Ramirez-Garcia, B. Heinrich, M. F. Horsche, and A. Jossen, "Suitability of physicochemical models for embedded systems regarding a nickel-rich, silicon-graphite lithium-ion battery." *Journal of Power Sources*, **436**, 226834 (2019).
33. W. Li, I. Demir, D. Cao, D. J¨ost, F. Ringbeck, M. Junker, and D. U. Sauer, "Data-driven systematic parameter identification of an electrochemical model for lithium-ion batteries with artificial intelligence." *Energy Storage Materials*, **44**, 557 (2022).
34. R. G. Nascimento, M. Corbetta, C. S. Kulkarni, and F. A. Viana, "Hybrid physics-informed neural networks for lithium-ion battery modeling and prognosis." *Journal of Power Sources*, **513**, 230526 (2021).
35. R. G. Nascimento, "Lithium-ion battery prognosis with variational hybrid physics-informed neural networks." *Ph.D. Thesis*, University of Central Florida (2022).
36. R. G. Nascimento, F. Viana, M. Corbetta, and C. S. Kulkarni, "Quantifying uncertainty in Li-ion battery aging due to unknown usage with hybrid physics-informed neural networks." *AIAA SCITECH 2023 Forum*, 0536 (2023).
37. M. Raissi, P. Perdikaris, and G. E. Karniadakis, *arXiv* (2017), Physics informed deep learning (Part I): data-driven solutions of nonlinear partial differential equations ArXiv, abs/1711.10561.
38. W. Li, D. W. Limoge, J. Zhang, D. U. Sauer, and A. M. Annaswamy, "Estimation of potentials in lithium-ion batteries using machine learning models." *IEEE Transactions on Control Systems Technology*, **30**, 680 (2022).
39. S. Pepe, J. Liu, E. Quattrocchi, and F. Ciucci, "Neural ordinary differential equations and recurrent neural networks for predicting the state of health of batteries." *Journal of Energy Storage*, **50**, 104209 (2022).
40. Z. Xu, Y. Guo, and J. H. Saleh, "A physics-informed dynamic deep autoencoder for accurate state-of-health prediction of lithium-ion battery." *Neural Computing and Applications*, **34**, 15997 (2022).
41. P. Wen, Z.-S. Ye, Y. Li, S. Chen, and S. Zhao, *arXiv* (2023), Fusing models for prognostics and health management of lithium-ion batteries based on physics-informed neural networks. arXiv:2301.00776.
42. W. Li, J. Zhang, F. Ringbeck, D. Jöst, L. Zhang, Z. Wei, and D. U. Sauer, "Physics-informed neural networks for electrode-level state estimation in lithium-ion batteries." *Journal of Power Sources*, **506**, 230034 (2021).
43. M. B. Mckay, B. Wetton, and R. B. Gopaluni, "Learning physics based models of Lithium-ion Batteries." *IFAC-PapersOnLine*, **54**, 97 (2021).
44. J. C. Hamar, S. V. Erhard, C. Zoerr, and A. Jossen, "Anode potential estimation in lithium-ion batteries using data-driven models for online applications." *J. Electrochem. Soc.*, **168**, 030535 (2021).
45. J. Kuchly, A. Goussian, M. Merveillaut, I. Baghdadi, S. Franger, D. Nelson-Gruel, C. Nouillant, and Y. Chamaillard, "Li-ion battery SOC estimation method using a neural network trained with data generated by a P2D model." *IFACPapersOnLine*, **54**, 336 (2021).
46. M. Pecht, (2022), Battery Data: Dynamic Test Profile, Maryland https://calce.umd.edu/battery-data (Last accessed: August 16, 2022).
47. F. Zheng, Y. Xing, J. Jiang, B. Sun, J. Kim, and M. Pecht, "Influence of different open circuit voltage tests on state of charge online estimation for lithium-ion batteries." *Applied Energy*, **183**, 513 (2016).

48. J. Sola and J. Sevilla, "Importance of input data normalization for the application of neural networks to complex industrial problems." *IEEE Trans. Nucl. Sci.*, **44**, 1464 (1997).
49. Z. S. Abdallah, L. Du, and G. I. Webb, "Data preparation." *Encyclopedia of Machine Learning and Data Mining*, ed. C Sammut and G. I. Webb (Springer, US: Boston, MA) p. 318 (2017).
50. D. P. Kingma and J. Ba, *arXiv* (2014), Adam: a method for stochastic optimization. arXiv:1412.6980.
51. C. E. Shannon, "A mathematical theory of communication." *The Bell System Technical Journal*, **27**, 623 (1948).
52. MathWorks Signal Classification Using Wavelet-Based Features and Support Vector Machines: Online Documentation The MathWorks, Inc. (2022), https://de.mathworks.com/help/wavelet/ug/ecg-classification-using-wavelet-features.html (Last accessed: August 24,2022).
53. D. Sundararajan, "The Discrete Fourier Transform: Theory." *The Discrete Fourier Transform: Theory, Algorithms and Applications* (World Scientific) p. 31 (2001).
54. D. P. Doane and L. E. Seward, "Measuring skewness: a forgotten statistic?" *Journal of Statistics Education*, **19**, 1 (2011).
55. A. M. Billert, M. Frey, and F. Gauterin, "A method of developing quantile convolutional neural networks for electric vehicle battery temperature prediction trained on cross-domain data." *IEEE Open Journal of Intelligent Transportation Systems*, **3**, 411 (2022).
56. A. H. Victoria and G. Maragatham, "Automatic tuning of hyperparameters using Bayesian optimization." *Evolving Systems*, **12**, 217 (2021).
57. T. O'Malley, E. Bursztein, J. Long, F. Chollet, H. Jin, and L. Invernizzi et al., (2019), KerasTuner https://github.com/keras-team/keras-tuner.
58. Y. Bengio, P. Simard, and P. Frasconi, "Learning long-term dependencies with gradient descent is difficult." *IEEE Transactions on Neural Networks*, **5**, 157 (1994).
59. T. Oji, Y. Zhou, S. Ci, F. Kang, X. Chen, and X. Liu, "Data-driven methods for battery SOH estimation: survey and a critical analysis." *IEEE Access*, **9**, 126903 (2021).
60. S. Son, S. Jeong, E. Kwak, J.-H. Kim, and K.-Y. Oh, "Integrated framework for SOH estimation of lithium-ion batteries using multiphysics features." *Energy*, **238**, 121712 (2022).
61. L. Cai, J. Meng, D.-I. Stroe, J. Peng, G. Luo, and R. Teodorescu, "Multiobjective optimization of data-driven model for lithium-ion battery soh estimation with short-term feature." *IEEE Transactions on Power Electronics*, **35**, 11855 (2020).
62. H. Tu, S. Moura, and H. Fang, "Integrating electrochemical modeling with machine learning for lithium-ion batteries." *2021 American Control Conference (ACC)* 4401 (2021).
63. S. Shen, M. Sadoughi, M. Li, Z. Wang, and C. Hu, "Deep convolutional neural networks with ensemble learning and transfer learning for capacity estimation of lithium-ion batteries." *Applied Energy*, **260**, 114296 (2020).
64. G. Zou, Z. Yan, C. Zhang, and L. Song, "Transfer learning with CNN-LSTM model for capacity prediction of lithium-ion batteries under small sample." *J. Phys.: Conf. Ser.*, **2258**, 012042 (2022).
65. R. J. Hyndman and A. B. Koehler, "Another look at measures of forecast accuracy." *International Journal of Forecasting*, **22**, 679 (2006).
66. M. Doyle, T. F. Fuller, and J. Newman, "Modeling of galvanostatic charge and discharge of the lithium/polymer/insertion cell." *J. Electrochem. Soc.*, **140**, 1526 (1993).
67. T. F. Fuller, M. Doyle, and J. Newman, "Simulation and optimization of the dual lithium ion insertion cell." *J. Electrochem. Soc.*, **141**, 1 (1994).
68. A. Jokar, B. Rajabloo, M. Désilets, and M. Lacroix, "Review of simplified Pseudo-two-dimensional models of lithium-ion batteries." *Journal of Power Sources*, **327**, 44 (2016).
69. M. Andersson, M. Streb, J. Y. Ko, V. L. Klass, M. Klett, H. Ekstr¨om, M. Johansson, and G. Lindbergh, "Parametrization of physics-based battery models from input-output data: a review of methodology and current research." *Journal of Power Sources*, **521**, 230859 (2022).
70. K. Uddin, S. Perera, W. D. Widanage, L. Somerville, and J. Marco, "Characterising lithium-ion battery degradation through the identification and tracking of electro-chemical battery model parameters." *Batteries*, **2**, 13 (2016).
71. J. J. Sturm, "State-estimation of lithium-ion batteries using physicochemical models and experimental characterization techniques,." *Ph.D. Thesis*, Technische Universität München, 296 (2021).
72. C. Zoerr, J. Sturm, S. Solchenbach, S. Erhard, and A. Latz, "Electrochemical polarization-based fast charging of lithium-ion batteries in embedded systems." *Journal of Energy Storage*, **72**, 108234 (2023).

2.2.2 Transfer Learning for SOH and OCV Estimation

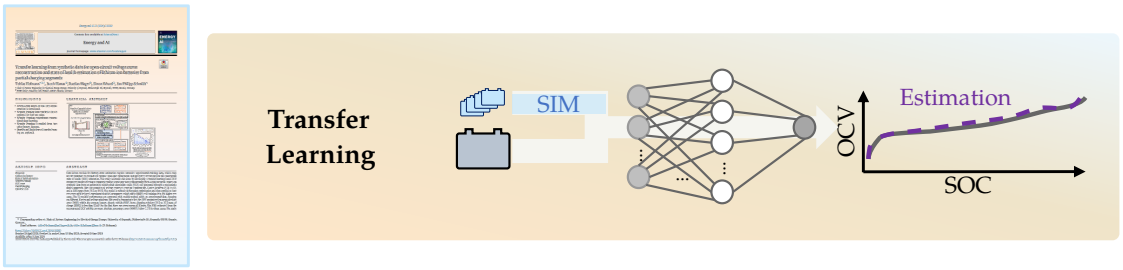

Figure 2.3: The trimmed outline of the thesis structure with focus on this chapter.

The exploration of PINNs has demonstrated that the issue of data scarcity can be addressed, but the problem of data dependency persists. Specifically, for successful PINN implementation, the training data must originate from the same domain as the test data. However, this is not always feasible. To address this challenge, an alternative neural network approach is explored: Transfer learning. A significant change to the previously discussed PINN article, is the data handling: While in the PINN framework synthetic and experimental data were fused and processed within the neural network at once, the transfer learning approach handles the datasets sequentially. The neural network pretrains with the full synthetic dataset and is fine-tuned with parts of the experimental data.

This research investigates whether it is possible to accurately reconstruct the OCV of experimental data using neural networks primarily trained on synthetic data. This article reveals the limitations and the underlying knowledge that is truly transferred within these black box models.

Typically, optimization problems must be solved to derive the full OCV from partial charging segments, as discussed in Section 2.1. Accurate estimation of the full OCV is feasible only for partial charging windows from 20 % to 70 % and a maximum C-rate of up to C/15 [27]. Transfer learning, as an alternative to optimization, was initially applied for SOH estimation and knowledge transfer between varying experimental datasets [61; 124; 125; 127–132; 134–136; 138–146]. Recent advancements explore the estimation of the full OCV and the estimation of DMs [123; 133; 137]. While the substitution of training data with synthetic data is extensively researched [131; 137; 138], the state of the art lacks contributions regarding the use and limitations of synthetic data for OCV reconstruction.

In this work, a mechanistic modeling approach to generate extensive training data for an NCA-graphite battery is employed. The dataset comprises partial charging events at varying C-rates and the corresponding OCV labels at different aging states. A novel TCN-LSTM model is pretrained on the synthetic data and subsequently fine-tuned on varying amounts of experimental data from a public NMC-silicon/graphite dataset. The model is compared to the same optimized architecture for different use cases. From an extensive field data analysis, including 1.9 million BEV low C-rate charging events ($P \leq 22$ kW), the default partial

charging window is defined. To elucidate the real transferred knowledge, two additional source datasets are generated: A LFP dataset and a completely artificial dataset.

The transfer-learned TCN-LSTM outperforms the conventional deep learning model for every use case within the default charging window from 30 % to 85 % SOC. For the first three use cases, the model achieves an OCV reconstruction MAE below 22.0 mV and a SOH_C MAE under 2.0 % (pp). Notably, in the third use case, only 13.2 % of the experimental data are used for fine-tuning. Results demonstrate that transfer learning to a new domain is feasible if the fine-tuning data encompasses the boundaries of the target dataset, i.e., the lowest and highest SOH and C-rate. The findings further confirm that lower charging segments are advantageous for accurate OCV reconstruction. For the first three use cases, the MAE of the OCV reconstruction and the MAE of the SOH_C estimation drop below 14.0 mV and 1.0 % (pp), respectively, if the charging segments start below 3.4 V.

In comparison to the state of the art, the approach expands the usable input data for reconstruction to charging segments with C-rates up to 1C and a voltage span of at least 400 mV. Transfer learning from the synthetic LFP and the completely artificial dataset reveals that the positional shift of gradient changes alone suffices as the core information learned by the neural network.

The article begins with the theoretical background of the mechanistic model, neural networks, and transfer learning. Next, the data is presented and the default charging window, extracted from the field data analysis, is defined. The method section follows a clear structure, including data preprocessing and model optimization, aided by Bayesian tuning. The results and discussion section is structured around the use case definition and compares the transfer-learned neural network to the benchmark deep learning model for each use case. Finally, the potential knowledge transfer between varying cell chemistries and purely artificial data is discussed, guiding the discussion on the essence of knowledge transfer in these data-driven OCV models.

Publication Notes

The article *Transfer learning from synthetic data for open-circuit voltage curve reconstruction and state of health estimation of lithium-ion batteries from partial charging segments* is presented in the following. The article was submitted to the Journal Energy and AI for peer review in April 2024 and was accepted in June 2024 [126]. The permanent web link to this publication is available under `https://doi.org/10.1016/j.egyai.2024.100382`.

Author Contributions

T. Hofmann developed the method, evaluated the data, developed the software, and wrote the manuscript. B. Mager assisted during the synthetic data generation. J. Hamar, S. Erhard

and J.P. Schmidt supervised the research project, discussed the findings, and reviewed the manuscript.

Energy and AI 17 (2024) 100382

Contents lists available at ScienceDirect

Energy and AI

journal homepage: www.elsevier.com/locate/egyai

Transfer learning from synthetic data for open-circuit voltage curve reconstruction and state of health estimation of lithium-ion batteries from partial charging segments

Tobias Hofmann [a,b,*], Jacob Hamar [b], Bastian Mager [b], Simon Erhard [b], Jan Philipp Schmidt [a]

[a] Chair of Systems Engineering for Electrical Energy Storage, University of Bayreuth, Weiherstraße 26, Bayreuth, 95448, Bavaria, Germany
[b] BMW Group, Petuelring 130, Munich, 80809, Bavaria, Germany

HIGHLIGHTS

- A TCN-LSTM model for full OCV reconstruction is introduced.
- Transfer learning from synthetic data is explored for four use cases.
- Transfer learning outperforms conventional deep learning.
- Transfer learning is applied from two other battery datasets.
- Benefits and limitations of transfer learning are explored.

GRAPHICAL ABSTRACT

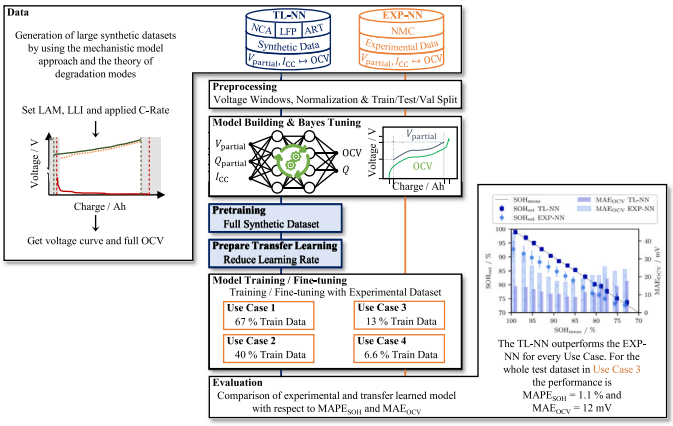

ARTICLE INFO

Keywords:
Lithium-ion battery
State of health estimation
Transfer learning
OCV curve
Partial charging
Synthetic data

ABSTRACT

Data-driven models for battery state estimation require extensive experimental training data, which may not be available or suitable for specific tasks like open-circuit voltage (OCV) reconstruction and subsequent state of health (SOH) estimation. This study addresses this issue by developing a transfer-learning-based OCV reconstruction model using a temporal convolutional long short-term memory (TCN-LSTM) network trained on synthetic data from an automotive nickel cobalt aluminium oxide (NCA) cell generated through a mechanistic model approach. The data consists of voltage curves at constant temperature, C-rates between C/30 to 1C, and a SOH-range from 70 % to 100 %. The model is refined via Bayesian optimization and then applied to four use cases with reduced experimental nickel manganese cobalt oxide (NMC) cell training data for higher use cases. The TL models' performances are compared with models trained solely on experimental data, focusing on different C-rates and voltage windows. The results demonstrate that the OCV reconstruction mean absolute error (MAE) within the average battery electric vehicle (BEV) home charging window (30 % to 85 % state of charge (SOC)) is less than 22 mV for the first three use cases across all C-rates. The SOH estimated from the reconstructed OCV exhibits an mean absolute percentage error (MAPE) below 2.2 % for these cases. The study

* Corresponding author at: Chair of Systems Engineering for Electrical Energy Storage, University of Bayreuth, Weiherstraße 26, Bayreuth, 95448, Bavaria, Germany.
E-mail addresses: tobias1.hofmann@uni-bayreuth.de, tobias.th.hofmann@bmw.de (T. Hofmann).

https://doi.org/10.1016/j.egyai.2024.100382
Received 8 April 2024; Received in revised form 14 May 2024; Accepted 2 June 2024
Available online 6 June 2024

further investigates the impact of the source domain on TL by incorporating two additional synthetic datasets, a lithium iron phosphate (LFP) cell and an entirely artificial, non-existing, cell, showing that solely the shifting and scaling of gradient changes in the charging curve suffice to transfer knowledge, even between different cell chemistries. A key limitation with respect to extrapolation capability is identified and evidenced in our fourth use case, where the absence of such comprehensive data hindered the TL process.

1. Introduction

With newer generations of battery electric vehicles (BEVs), more computing resources – either directly in the car or accessible via the backend – accelerate the development of state estimation algorithms. The state of health (SOH) plays an important role because it determines the available energy and power over lifetime. It is mostly defined as the available capacity in relation to its capacity at begin of life (BOL) [1]. Additionally the open-circuit voltage (OCV) is an important characteristic of the lithium-ion battery which is crucial for accurate state of charge (SOC) estimation, algorithms concerning safety, healthy fast-charging and a prolonged lifetime [2,3]. Available methods [4,5] use the pristine open-circuit potential (OCP) curves to reconstruct the aged OCV curve. These reconstruction methods, however, simplify the degradation of the OCV based on the mechanistic model approach [6] and require constant current measurements with very low C-rates [4] or relaxed voltage points [5].

Data-driven methods can bridge this gap by relying on empirical datasets and thus are promising to eliminate the need for specific input measurements. They are capable of discovering data patterns leading to qualitative features for SOH estimation and OCV reconstruction. Especially the combination of deep learning (DL) and explicit input measurements was successful for accurate SOH estimation: Zhang et al. [7] compared their combined incremental capacity analysis (ICA) and broad learning system algorithm with other available data-driven methods. They proved that highly correlating health features from the IC-curve allowed their method to outperform other algorithms and reached SOH mean absolute percentage errors (MAPEs) below 0.42% for three different batteries. In a subsequent study [8] they identified the difficulties incorporated by varying charging manners and working conditions for real-world BEVs. Hence, they introduced a method which solely relies on the raw measurement data from the constant voltage phase, i.e., the gradually decreasing current. Via their proposed double correlation analysis several health features are extracted from that raw sensor data to finally estimate the SOH with a gated recurrent unit. Again, they reached excellent results with SOH MAPEs below 0.48%. Recently, Zhang et al. [9] focused on the available input data from partial charging segments during the constant current phase. With health indicators derived from their newly defined incremental energy per SOC curve, they have trained a bidirectional long short-term memory neural network (LSTM) to estimate the SOH. With random partial charging events at different C-rates (0.5C: 11% to 36%, 0.3C: 23% to 75%, 0.2C: 35% to 82%, 0.1C: 15% to 53%) they have reached SOH mean absolute errors (MAEs) below 0.43%. Dubarry et al. [10] explored the usage of synthetic data for model training and subsequent degradation mode (DM) estimation within photovoltaic systems. They used a mechanistic model to generate voltage curves with varying aging paths and trained several data-driven models on these data. They have validated the method with synthetic data from over 10 000 different degradation paths and reached DM root mean squared errors (RMSEs) of 2.75%.

In recent years, partial charging data has also emerged as a suitable input for OCV reconstruction via DL. Tian et al. [11] introduced a convolutional neural network (CNN) that processes the charge amount from parts of the daily charging voltage curves at 1 C to estimate the stoichiometries and hence the OCV curve of aged lithium-ion batteries. With usage of these raw segments they reached an OCV reconstruction RMSE below 15 mV and an SOH estimation error below 1.0%. In the work by Ruan et al. [12] they have used a CNN as a quick analysis tool to estimate DMs from OCV curves. They developed the method fully with synthetic data but have shown the real-world applicability by using partial OCV segments from an experimental battery. With a voltage segment from 3.4 V to 4.18 V they have estimated the DMs with a RMSE of 1.75%. These DMs were further used to reconstruct the full OCV with a RMSE of 21.05 mV. Guo et al. [13] used a similar approach where they required partial charging segments at 1C to estimate partial OCV curves with a LSTM. The partial OCV was fed into an optimizer which reconstructed the full OCV with a MAE below 20 mV and estimated the SOH with a MAPE below 1.3%. In contrast to the CNN developed by Tian et al. [11], the proposed LSTM by Guo et al. [13] struggled to directly interpret raw data and, hence, first calculated health-indicators from the charging curves.

Both, CNNs and LSTMs, have specific benefits for battery state estimation from time-series data: CNNs, which were initially proposed for computer vision [14], do not require additional feature engineering and can process raw data segments. LSTMs, however, are beneficial for time-series data processing due to their ability to handle sequential data including internal feedback loops. Specifically in the last years, temporal convolutional neural networks (TCNs) [15], which combine the benefits from CNNs and LSTMs, have gained attraction in the field of battery state estimation [16–20]. These new types of neural networks (NNs) outperform former architectures, eliminate the need for cumbersome preprocessing and are optimized for time-series data [16]. Without preprocessing, Bockrath et al. [16] have fed raw sensor data from partial discharging segements into a TCN network and reached an overall SOH RMSE for unseen test data of 1.0%. Their model outperformed several other NN architectures. In their study the middle and upper SOC-range was more suitable for SOH estimation. Li et al. [17] compared the performance of different NN architectures for SOH estimation using the same dataset as Bockrath et al. [16]. They proved that TCN-LSTM networks increase the accuracy by more than 16% compared to TCN, LSTM and CNN-LSTM networks, i.e., the MAE decreased from 3.11% (TCN), 3.38% (LSTM), 2.78% (CNN-LSTM) to 2.5% (TCN-LSTM).

DL, however, is accompanied by challenges such as data dependence and limited training data availability [21]. DL models typically require vast amounts of data to effectively capture complex data patterns. The training data must encompass a significant portion of the data space to enable the model to interpolate between different locations. To address this issue, transfer learning (TL) has been introduced, eliminating the requirement for training and test data to be independent and identically distributed [21]. In the developed TL model by Sahoo et al. [22], they mapped features from the voltage curve to the SOH which lead to SOH estimation errors below 2% for unseen data. A two-layered feed-forward neural network (FNN) was pretrained with an experimental dataset. Finally, TL was applied by freezing the first layer and fine-tuning the second layer with other public datasets. Zou et al. [23] followed the same model-based TL approach with a different dataset and architecture: They used experimental battery aging data from the public NASA degradation dataset. Source and target domain, however, were selected from this dataset which was divided into groups based on varying usage conditions. Their work, hence, evaluated TL within the same cell chemistry to new degradation paths. Their NN processed features from the constant current charging voltage curve to the CNN input layer. A LSTM layer interpreted the output of the CNN layer and passed its output through a FNN layer which produced the SOH value. The freezing mechanism was limited to the LSTM layer and the

amount of training data from the target domain was varied during fine-tuning. They showed that with limited training data from the target domain, TL models outperform stand-alone NNs. In contrast, Shen et al. [24] took a different approach by omitting the freezing mechanism and instead focused on retuning multiple models to construct an ensemble model. Their base model consisted of five CNN and three FNN layers, which were utilized to process the raw voltage, current, and charge time-series data from partial constant current charging curves for estimating the SOH. Rather than fine-tuning a single model, the authors replicated the architecture to create several new models, each of which was subsequently fine-tuned using different subsets of the training data domain. Tian et al. [25] finally explored the transferable knowledge between synthetic and experimental data by creating a CNN for SOH estimation. They have pretrained the model with synthetic data from a voltage capacity model, simulating the experimental cell. Fine-tuning was carried out with 300 mV partial charging segments. They repeated the experiment for three public available datasets and reached SOH RMSEs of 1.00%, 3.13% and 0.52% for the Oxford, CALCE and Tongji dataset [25], respectively. Zhou et al. [26] were the first to apply TL for full OCV reconstruction from daily partial charging data. With a generative DL model, they successfully applied TL from different cell chemistries with SOH RMSEs of 0.47% and 2.73% for nickel cobalt aluminium oxide (NCA) and lithium iron phosphate (LFP) cells, respectively.

A critical limitation identified in these models is their reliance on extensive experimental training datasets. While a multitude of public datasets are available, they may not always align with specific research objectives or provide the ideal conditions for model training. Zhou et al. [26] highlighted the potential for TL in OCV reconstruction, a topic that has received limited attention in the existing literature.

The present study introduces a novel approach for OCV reconstruction and SOH estimation utilizing a TL framework with a TCN-LSTM architecture. This approach is distinctive in its exclusive use of synthetic data from a different cell derived from partial voltage charging curves to train the model. Synthetic data for an automotive NCA cell are generated using a mechanistic model approach, with the dataset partitioned according to different voltage windows. The use of synthetic data allows fast data generation and detailed analytics. A base model is trained on this dataset and optimized using Bayesian optimization techniques. Subsequently, TL is applied to four distinct use cases (UCs), each characterized by varying quantities of experimental, measured nickel manganese cobalt oxide (NMC) cell data, to evaluate the efficacy and constraints of TL. The performance of TL models is benchmarked against models trained solely on experimental data for each UC, thereby assessing the influence of TL on model outcomes. The evaluation focuses on the effects of varying C-rates and voltage windows. Notably, we determine from a field data analysis that the average BEV home charging pattern is compatible with the proposed algorithm. Additionally, the study explores the influence of the source domain on TL by incorporating two alternative synthetic datasets for base model training, one based on a LFP cell and the other entirely artificial. This allows to interpret the hidden features in voltage trajectories necessary to reconstruct the OCV. We give evidence that the shift of plateaus in the voltage curve is the main information captured by DL and especially TL models.

To our knowledge, this is the first study to employ synthetic data as the source domain for TL between varying cells in the context of OCV reconstruction, as well as the first to investigate TL from wholly artificial cells. This approach provides novel insights into the learning dynamics of DL models.

2. Theory

The proposed NN estimates the full OCV curve from constant current partial charging segments. The estimated SOH is finally calculated from that OCV curve. The NN, hence, only processes the raw voltage curve, the capacity throughput during this partial charging event and the applied C-rate. The utilization of machine learning (ML) techniques for battery modeling and state estimation, however, is currently constrained by the substantial data prerequisites. The application of TL on synthetic data presents an alternative approach to circumvent the necessity for expensive aging experiments. This section, hence, is mandatory to follow the subsequent method section and introduces the synthetic data generation model and elucidates the fundamentals of TL. In the remainder of this paper, we refer to the following definition for the SOH: The SOH is defined as the measured charge capacity at a low C-rate, e.g., C/25, relative to its nominal capacity at BOL. The amount of charge is measured between lower and upper voltage limits.

$$\mathrm{SOH} = \frac{C_{\mathrm{meas,C/25}}}{C_{\mathrm{N}}} \tag{1}$$

We further simplify the OCV definition to include pseudo-OCV measurements at C-rates as low as C/25.

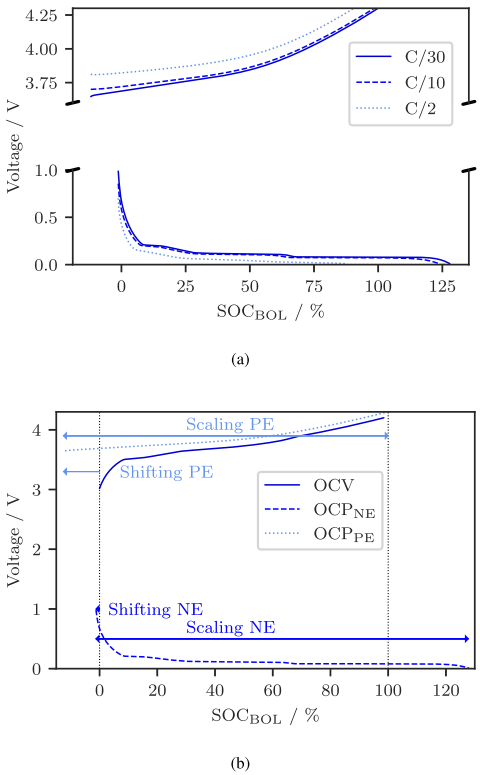

Fig. 1. Fundamentals of the mechanistic model approach from Dubarry et al. [6]. The C-rate refers to the full-cell capacity measurable during a constant current charge. (a) To generate constant current charging curves at different C-rates the model relies on half-cell potential measurements at different C-rates. (b) The user has to define the degradation parameters, which results in a scaling and shifting of the half-cell potential curves and finally output the voltage curve as the difference between the positive and the negative half-cell potential curve.

2.1. Mechanistic model for battery data generation

The mechanistic model approach, originally proposed by Dubarry et al. [6], posits that the OCV of a lithium-ion battery throughout its lifespan can be determined by the disparity between the half-cell OCP curves of the positive and negative electrode [27,28]. The shape of the OCV is primarily influenced by a relative shift and scaling of the OCPs. If the degradation-induced impedance rise is disregarded,

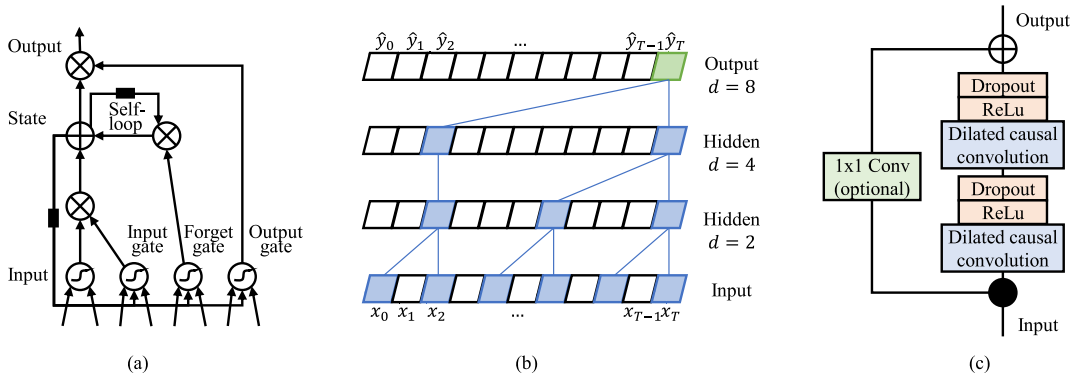

Fig. 2. The main building blocks of LSTM ((a) adopted from Goodfellow et al. [29]) and TCN ((b), (c) adopted from Bai et al. [34] and Bockrath et al. [16]) networks. (a) Memory cell of a LSTM network. (b) Example for one dilated causal convolution within a residual block for a kernel size of 2 and dilation factors $d = 8, 4, 2$. (c) TCN residual block with the optional 1×1 convolutional in case of different dimensions between input and output. ReLU is the most common activation function which only passes positive input, i.e., $f_{\text{ReLu}}(x) = \max(0, x)$.

this concept can be extended to voltage responses to applied current, allowing for the reconstruction of voltage curves at higher C-rates using the measured half-cell potential curves at corresponding C-rates [6]. To generate data, the mechanistic model employs pristine half-cell potential curves at various C-rates, as illustrated in Fig. 1(a). In the mechanistic model, the degradation rate is determined solely by the user-defined shifting and scaling parameters, as illustrated in Fig. 1(b). This fundamental theory allows the simulation and generation of mass synthetic data with predefined DMs and SOH based on real measurements. For a more comprehensive understanding of these alignment parameters, readers are encouraged to refer to the works of Dubarry et al. [6] or Hofmann et al. [5]. In our example (Fig. 1), the model generates the OCV curve from the OCP measurements, along with the SOH. This implies that the process of constructing the OCV curve from Fig. 1(b) can also be applied to C-rates of C/10 and C/2. Consequently, the model can be utilized to produce constant current voltage curves at any given C-rate, provided that pristine half-cell potential measurements are available and overpotentials are linear.

2.2. Neural networks for battery state of health estimation

With the advances in ML, more network architectures arise to estimate the SOH from battery cycling data. The simplest architecture in DL is the FNN, which consists of multiple neurons and direct connections between layers. It can be described as a function approximator $\mathbf{y} = f(\mathbf{x}; \boldsymbol{\vartheta})$, where $\mathbf{y}$ represents the approximated value (e.g., SOH), $\mathbf{x}$ represents arbitrary features extracted from battery aging data (e.g., voltage level or C-rate), and $\boldsymbol{\vartheta}$ represents the hyperparameters [29,30]. The FNN does not have any feedback loops and information flows only in a forward direction.

In contrast, if the network includes feedback loops between neurons or layers, it is known as a recurrent neural network (RNN). RNN are particularly suitable for handling sequential data, such as time-series data [29].

LSTMs, as in Fig. 2(a), form a specific type of RNN. First introduced by Hochreiter and Schmidhuber [31], they have gained immense popularity in the field of battery diagnosis [32,33]. These memory cells (Fig. 2(a)) are compact, self-regulating networks that possess input, output, and forget gates. By means of an internal feedback loop, the LSTM mechanism adjusts the weights based on the temporal history. Consequently, the network determines both the type and quantity of memory to be stored or discarded [29].

Similar to RNNs, CNNs have recently gained increased attention in the field due to their ability to process grid-like data, i.e, multiple time-series data streams, without preprocessing [29,35,36]. Filters convolve over the n-dimensional input and pass the results to the next layer. These filters allow the inclusion of the present time-step, as well as historical data [35,36]. Some adaptions [17,23,37] leverage the feature extraction power of CNNs sequential to the feature processing ability of LSTMs to build accurate SOH estimation models.

TCNs were proposed to couple the benefits from CNNs and LSTMs: Lea et al. [15] introduced the novel TCN initially for action segmentation and detection. This special type of CNN uses causal convolution to produce output with the same length as the input, similar to RNNs [16]. TCNs outperform RNNs in terms of training efficiency, model size, model accuracy and do not require data preprocessing [16]. Bai et al. [34] evaluate the architecture for a variety of use cases against common RNN architectures and propose TCNs as a natural starting point for sequence modeling, i.e., $\hat{y}_0, \ldots, \hat{y}_T = f(x_0, \ldots, x_T)$. Fig. 2(b) and (c) illustrate the main building blocks of a TCN. Causal convolution leads to an output with same length as the input and avoids leakage from future information x_{N+1} to the past $\hat{y}_N$ [16]. The output at time $\hat{y}_T$ is only convolved with input data at time T and earlier $x_0, \ldots, x_T$. In contrast to CNNs, which use centered kernels, TCNs employ kernels where the rightmost value of the kernel is the considered time [16,34]. When it comes to DL or large receptive fields, causal convolution leads to many additional weights and stabilization problems. Dilated convolution (Fig. 2(b)) solves this problem by dilating the kernel of size k by the dilation factor d. The dilated convolution operation $F()$ on the element s is

$$F(s) = (x *_d f)(s) = \sum_{i=0}^{k-1} f(i) \cdot x_{s-d \cdot i} \tag{2}$$

for a 1D-sequence input $x \in \mathbb{R}^n$ and the filter $f : \{0, \ldots, k-1\} \to \mathbb{R}$. The final receptive field per layer is then calculated by

$$\mathrm{R} = 2^l (k-1) \tag{3}$$

where l is the number of layers. Hence, this allows the TCN to process exponentially large receptive field which is especially helpful for efficient processing of long time-series data [16,34]. Finally, a residual block (Fig. 2(c)) allows to learn modifications to the identity mapping instead of the entire transformation [16]. One residual block consists of stacked dilated causal convolutions, ReLU and dropout blocks. An optional 1×1 convolution processes the input in case of differing dimensions between input and output. The output o of a residual block is the applied transformation $\mathcal{F}$ added to the input x of the block [34]:

$$o = Activation(x + \mathcal{F}(x)) \tag{4}$$

2.3. Fundamentals of transfer learning

In the domain of TL it is essential to establish a mathematical understanding of its principles. While DL models encounter challenges related to data dependence and insufficient training data [21], TL aims for a solution. This approach eliminates the necessity for training and test data to adhere to the assumption of being independent and identically distributed.

To understand the mathematical definition of TL we require some basic annotations and refer to the publication by Tan et al. [21] and Weber et al. [38]: A domain $\mathcal{D} = \{\chi, P(X)\}$ is defined by the feature space χ and the edge probability distribution $P(X)$, where $X = \{x_1, \ldots, x_n\} \in \chi$. A task $\mathcal{T} = \{y, f(x)\}$ consists of the label space y and the target prediction function $f(x)$, which can be also understood as the conditional probability function $P(y \mid x)$.

Definition 2.1 (*Transfer Learning*)**.** TL aims to enhance the performance of the predictive function $f_{\mathcal{T}}()$ for the main learning task $\mathcal{T}_t$ by leveraging latent knowledge discovered from the supplementary learning task $\mathcal{T}_s$ and its associated dataset $\mathcal{D}_s$, where $\mathcal{D}_s \neq \mathcal{D}_t$ and/or $\mathcal{T}_s \neq \mathcal{T}_t$. Typically, the size of $\mathcal{D}_s$ is significantly larger than $\mathcal{D}_t$, i.e., $N_s \gg N_t$.

In most cases – and also in this paper – TL refers to *domain adaption* (DA), i.e., $\mathcal{D}_s \neq \mathcal{D}_t$ [38]. In the literature [21,38], TL for time-series data consists of three categories:

Instance-based TL assumes that instances from the source and target domain are similar. Hence, selected or reweighted samples from the source domain are included in the TL process.

Feature-based TL transfers both domains into the same feature representation, i.e., uses the same features for both datasets.

Model-based TL is the most common form of TL and reuses a pretrained model in the source domain for target model building. In this context, several possibilities exist: Parameter-based TL refers to only reusing the learned parameters. Ensemble TL describes the stacking of a pretrained model with a blank model for the target domain. Model controlled TL changes the objective function for retraining. Finally, adversarial-based TL utilize generative adversarial networks [21,38].

In the context of battery state estimation and OCV reconstruction mostly model-based TL exists [22–24,26]. Hence, we elaborate model-based TL for SOH estimation: A straightforward way to deploy TL for SOH estimation is partial freezing and fine-tuning, a strategy used within parameter-based TL, as in the work by Sahoo et al. [22]. Hence, an initial model is trained on the source domain, while just a subset of the pretrained model is retrained on the target domain. The remaining frozen parts of the retrained model do not change their parameters, i.e., the weights of the neurons, during retraining. The retraining process, also known as fine-tuning, typically involves reducing the learning rate and/or limiting the number of epochs to allow only slight modifications of the model parameters. Both mechanism, freezing and fine-tuning, hinder the TL model from catastrophic forgetting [38].

In summary, most researchers choose model-based TL approaches with partial freezing and/or fine-tuning to deploy their TL battery SOH estimation models.

2.4. Performance metrics

In our work we always refer to the MAPE for SOH estimation and to the MAE for OCV reconstruction accuracy. The MAPE and MAE are defined as follows:

$$\mathrm{MAPE} = \frac{1}{N}\sum_{i=1}^{N}\left|\frac{y_i - \hat{y}_i}{y_i}\right| \tag{5}$$

$$\mathrm{MAE} = \frac{1}{N}\sum_{i=1}^{N}\left|y_i - \hat{y}_i\right| \tag{6}$$

In Eqs. (5) and (6), y_i represents the ground truth, i.e., the measured OCV or SOH, whereas $\hat{y}$ corresponds to the estimation; N is the total number of samples. When considering the OCV reconstruction error $\mathrm{MAE}_{\mathrm{OCV}}$, it is crucial that both y_i and $\hat{y}_i$ must be vectors of the same length. Consequently, if the model outputs an OCV that is longer or shorter than the ground truth, the error is only calculated at the overlapping section. Eqs. (5) and (6) can be modified for our study as follows:

$$\mathrm{MAPE}_{\mathrm{SOH}} = \frac{1}{N}\sum_{i=1}^{N}\left|\frac{\mathrm{SOH}_{\mathrm{meas},i} - \mathrm{SOH}_{\mathrm{est},i}}{\mathrm{SOH}_{\mathrm{meas},i}}\right| \tag{7}$$

$$\mathrm{MAE}_{\mathrm{OCV}} = \frac{1}{N}\sum_{i=1}^{N}\left|\mathrm{OCV}_{\mathrm{meas},i} - \mathrm{OCV}_{\mathrm{est},i}\right| \tag{8}$$

3. Materials and method

The efficacy of ML techniques is heavily reliant on the underlying data and its distribution. A significant limitation of data-driven approaches for SOH estimation is the requirement for numerous aging experiments across multiple aging paths. Performing such experiments is both expensive and time-consuming. TL from synthetic data presents a promising avenue for developing ML methods with limited data. Given the crucial role of data sources, this paper presents them first, followed by a detailed exposition of the investigated TL approach.

3.1. Data

This work utilizes synthetic data created by a mechanistic model tool. The simulation toolbox relies solely on the measured pristine half-cell potential curves at various C-rates. Instead of modeling the physico-chemical degradation mechanisms in numerical equations it uses the simplified theory of DMs [6]. In this work, we consider loss of active material at the anode ($\mathrm{LAM}_{\mathrm{NE}}$), loss of active material at the cathode ($\mathrm{LAM}_{\mathrm{PE}}$) and loss of lithium inventory (LLI). Similar to the work of Dubarry et al. [6] the used approach shifts and scales the pristine half-cell potential curves to set specific DMs. One simulation always includes the charging profile for the set C-rate and also the OCV, because the half-cell potential curves are captured for various C-rates. For a detailed description of DMs and their utilization for voltage curve generation we refer to a previous publication [5].

The simulation data is based on pristine half-cell potential measurements of a prismatic automotive NCA-graphite cell with 70.2 Ah at an ambient temperature of 25 °C. The layer thicknesses are $t_{\mathrm{NE}} = 107\,\mu\mathrm{m}$ and $t_{\mathrm{PE}} = 62.5\,\mu\mathrm{m}$, respectively. The initial loading ratio (LR) and $\mathrm{SOC}_{\mathrm{PE}}$ offset (OFS) are 0.95 and 10.6%. For the concept of LR and OFS we refer to the work of Dubarry et al. [6]. The simulation is carried out by varying all three DMs: $\mathrm{LAM}_{\mathrm{NE}}$ and $\mathrm{LAM}_{\mathrm{PE}}$ are varied between 0% to 15% in steps of 3.75%. LLI is varied in steps of 5% between 0% to 20%. By setting this generic degradation parameters, in total $5 \cdot 5 \cdot 5 = 125$ voltage curves exist per C-rate. Per voltage curve, the corresponding OCV curve is available, too. All voltage and OCV curves are cut to the range from 3 V to 4.25 V.

The experimental dataset, comprising 10 commercial INR18650-MJ1 NMC-silicone/graphite cells (LR: 0.90, OFS: 11%, silicon mass ratio in anode between 1wt.% to 5wt.%), is taken from Schmitt et al. [4] and preprocessed to only include the constant current sections. The investigated cells were partioned into five different aging studies and hence different aging paths, as listed in Table 1. Between degradation phases, all cells underwent an OCV measurement and a charging rate test. The OCV measurement refers to a constant current charging measurement with C/30 and the charging rate test data, used within this work, refers to the constant current measurements at 0.26C ≈ C/3.85, C/2 and 1C. The C/3.85 charge is equivalent to a constant-power 11 kW charge for a 42 kWh storage with a 96s36p configuration, to evaluate the applicability of the proposed algorithm by Schmitt et al. [4] for real use cases. Again, the SOH refers to the OCV measurement. Due to the

Table 1
Aging conditions of the experimental dataset, taken from Schmitt et al. [4]. All degradation phases ran at an ambient temperature of 25 °C.

Cell number	Aging conditions
A1, A2	2.5 V–4.2 V cycling
B1, B2	2.5 V–4.0 V cycling
C1, C2	3.6 V–4.2 V cycling
D1, D2	WLTP cycling
E1, E2	Calendar aging at 3.7 V

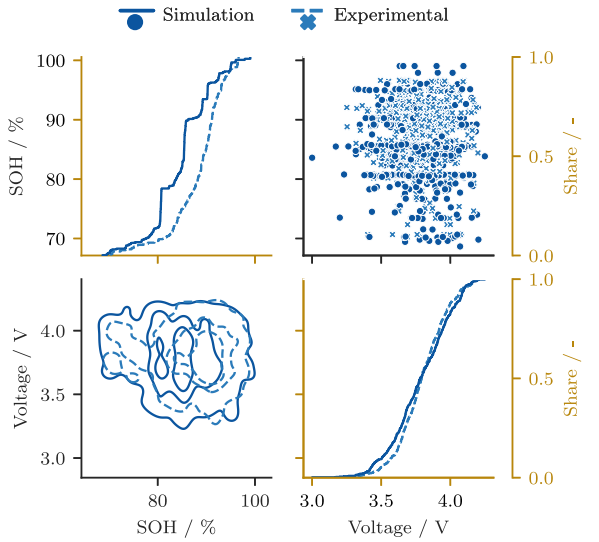

Fig. 3. Visualization of the synthetic NCA and the experimental NMC dataset. The upper right figure shows the scatter plot and the lower left figure visualizes the kernel densities. Both refer to the first y-axis on the left. The second y-axis on the right side refers to the cumulative distribution plots in the diagonal, in golden color. All voltage curves at any given C-rate are illustrated. (For interpretation of the references to color in this figure legend, the reader is referred to the web version of this article.)

increasing minimal voltage at begin of charge, all samples are cut to the voltage-range between 3.24 V to 4.2 V.

The synthetic dataset is visualized together with the experimental dataset in Fig. 3. For both datasets, the SOH for a given voltage curve refers to the accumulated charge between the lower and upper voltage limit during an OCV measurement. In both datasets, all samples with a SOH below 70% are excluded due to our definition of the end of life (EOL) at 70% SOH. While the SOH range seems evenly distributed for the experimental dataset, the predefined degradation states are visible in the synthetic SOH trajectory. Due to the similar cathode material of both datasets, the voltage distribution looks similar. This is, as well, visible in the kernel densities and the scatter plot.

Fig. 4 provides a more comprehensive analysis of the data. As shown in Fig. 4(a), the synthetic dataset encompasses charging trajectories ranging from C/15, C/10, C/6, C/3, C/2 and 1C, while the OCV is established through a constant current-charging process with C/25. Conversely, the experimental dataset in Fig. 4(b) includes constant current-charging events at C/3.85, C/2, and 1C. In contrast to the synthetic dataset, the OCV measurement is obtained from a C/30 charge. The voltage curve exhibits an increase for higher currents primarily due to the ohmic overpotentials, which display a direct correlation with the applied current. Consequently, the upper voltage limits are reached earlier, resulting in a shorter constant current-phase. In this study, we exclude the CV-phase from all calculations and base our SOH and SOC calculations solely on the constant current-phase. The SOH always refers to the full charge amount between the voltage limits in the OCV measurement. Fig. 4(c) and (d) illustrate pristine and aged OCV curves and the correlation between SOH and the OCV trajectory. The observations can be categorized into two fundamental aspects of battery aging: capacity fade and impedance rise. Capacity fade is directly evident in Fig. 4(c) and (d) by the earlier reached cutoff voltage. In the synthetic dataset, the capacity is modeled by the DMs. Impedance rise is only evident in the experimental datasets, visualized in Fig. 4(d). Impedance rise also contributes to reaching the cutoff voltage earlier. Impedance rise over lifetime is not included in the synthetic dataset because it aggravates the clear interpretation of plateau shifting and scaled OCPs. Hence, in this paper we focus on the effect of capacity drop and TL, while the influence of impedance rise will be discussed in future work.

Both datasets were captured at 25 °C to focus on the clear effect of transferred knowledge from different cell chemistries, C-rates and voltage windows. The real-world applicability of the method, however, is still given due to negligible temperature dependencies of the voltage and OCV curve between temperatures from 20 °C to 40 °C [39].

To further evaluate the data requirements for model fine-tuning and especially the urge to cover most of the dataset, several UCs are defined. The described UCs divide the experimental dataset for fine-tuning into differing data segments, which vary in their difficulty based on content and amount of training data. This separation aims to explore the boundaries of NNs and especially TL for battery state estimation. Fig. 5 visualizes the training, validation and test dataset per UC. The UCs for TL can be differentiated based on two factors: Firstly, they vary in terms of the included charging curves at different C-rates. Secondly, they differ in terms of the included degradation path. The data split comprises four distinct UCs, namely UC1 (Fig. 5(a)), UC2 (Fig. 5(b)), UC3 (Fig. 5(c)), and UC4 (Fig. 5(d)). These UCs cover different boundaries of the training dataset. UC1 to UC3 encompass the entire SOH range, including the lowest and highest C-rate. In contrast, UC4 only includes the entire SOH range for one specific C-rate. Approximately 67% of the entire experimental dataset is covered by UC1, while UC2 covers 40%, UC3 covers 13%, and UC4 covers only 6.6%. In UC1, all cells and charging curves are used for training, except for the curves at C/2. UC2 further complicates the TL process by excluding aging path B, as well as one cell each from aging path C and D from the training dataset. Similarly, UC3 reduces the training dataset even further by excluding the cells from aging path D and E completely. The most challenging UC4 solely includes the charging curves at C/3.85 from cell A2 and C2 for training.

3.2. Default charging window

To evaluate the appropriate charging window for analysis, we collect customer field data comprising 1.9 million BEV AC-charging events conducted at residential locations. The dataset includes the corresponding SOC windows of those charging events. Based on the findings depicted in Fig. 6, the most frequently utilized charging window is identified, which serves as the focus of our study. The distribution of start-SOC values is remarkably uniform, with the mean occurring at approximately 49%.

To establish a default start-SOC, we opt for the minimum start-SOC that encompasses at least 25% of all charging events. Consequently, a start-SOC of 30% is selected. Analysis of the end-SOC values reveals two prominent peaks at 80% and 100% SOC, resulting in a mean value of 85%. Consequently, this value is adopted as the default end-SOC.

In conclusion, we establish a default SOC charging window spanning from 30% to 85%. This window serves as a benchmark for our study and further demonstrates the practicality and applicability of our methodology to real-world charging events at resident locations.

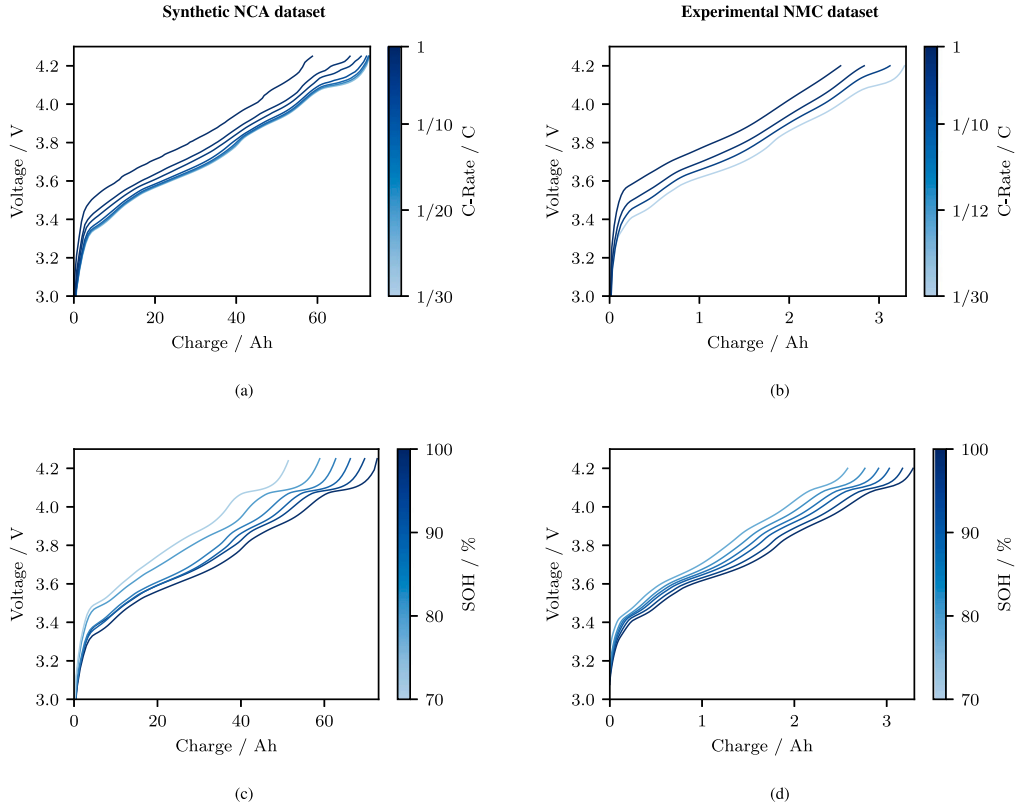

Fig. 4. Influence of C-rate and SOH on the voltage trajectory for the synthetic NCA and the experimental NMC dataset. (a) Influence of C-rate: Synthetic dataset. (b) Influence of C-rate: Experimental dataset. (c) Influence of SOH on OCV: Synthetic dataset. (d) Influence of SOH on OCV: Experimental dataset.

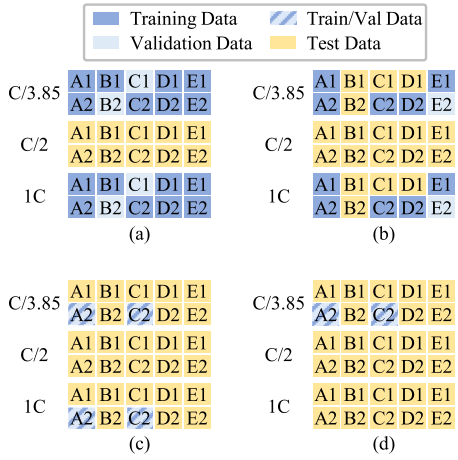

Fig. 5. Definition of different UCs for model comparison: (a) UC1, (b) UC2, (c) UC3 and (d) UC4. The UCs are distinctive in their used curves from different cells and C-rates of the experimental dataset for training data, visualized by different colors. In UC3 and UC4 a random 33% subset of the training data is used for validation. (For interpretation of the references to color in this figure legend, the reader is referred to the web version of this article.)

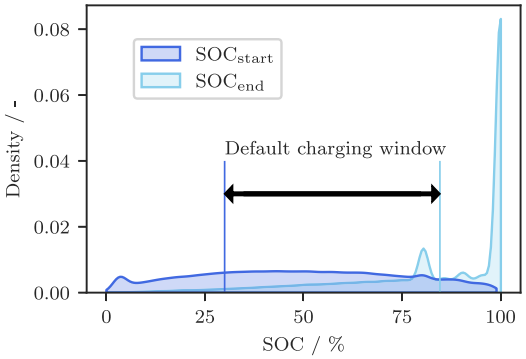

Fig. 6. Start- and end-SOC for 1.9 million BEV AC-charging events. The default partial charging window is selected from the SOC start point with at least 25% share. (In comparison: The average start-SOC is 49%.) The end-SOC is the average for all charging events. The default partial charging window is from 30% to 85%.

3.3. Method

The method is summarized in Fig. 7(a), which describes the steps necessary to build the transfer learned neural network (TL-NN) and the reference EXP-NN. The EXP-NN is only trained and evaluated with the experimental dataset to evaluate the influence of TL. In the main method, the TL-NN is pretrained with the NCA synthetic dataset, hence only referred to as TL-NN. For discussing the limitations and benefits of TL, and the exploration of the underlying transferred knowledge, additional TL-NNs are set up with a LFP and an artificial (ART) cell. These developed models are referred to as TL (LFP) and TL (ART) model, respectively. Both datasets undergo preprocessing, are normalized and split to training, test and validation sub-datasets as indicated

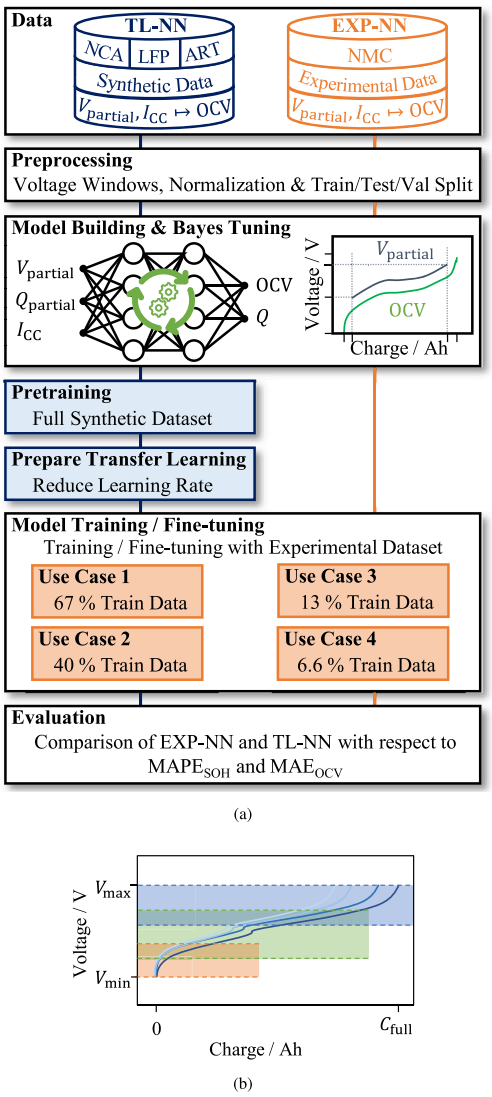

Fig. 7. Description of the TL approach. (a) Overview of the applied method and the differentiation between the TL and the reference EXP-NN path. The main TL path is carried out with the NCA cell. (b) Example for three different partial voltage segments extracted from four different constant current voltage curves.

in Fig. 5. Both models are optimized with Bayes tuning to yield the best architecture. The TL-NN is subsequently pretrained with the full synthetic dataset. The pretrained TL-NN and the not-trained EXP-NN are finally fine-tuned/trained with partial amounts of data from the UCs, defined in Fig. 5. Both models are evaluated with the MAE_{SOH} and MAE_{OCV}. We choose a similar approach as Bockrath et al. [16] and snipped the full voltage charge curve into multiple partial segments based on voltage boundaries in 200 mV steps, as in Fig. 7(b). In Fig. 7(b) C_{full} refers to the charged capacity during a full charge at the given C-rates. The example can be applied to every voltage curve and any C-rate. For the upper voltage segments above 4 V, the step-size is lowered to 100 mV, in order to allow more variation in the final end SOC. Instead of just three partial segments we utilize more steps and extract 19 different voltage windows from one simulated full voltage curve. From the experimental dataset, we extract 15 different voltage windows per full voltage curve. This generates more training data and allows a more

Table 2
Selected voltage windows from the simulation and experimental dataset during preprocessing.

	V_{min}	V_{max}		V_{min}	V_{max}
	3.25 V	3.8 V		3.0 V	3.8 V
	3.4 V	4.0 V		3.2 V	4.0 V
Exp. Data	3.6 V	4.1 V	Sim. Data	3.4 V	4.1 V
	3.8 V	4.2 V		3.6 V	4.25 V
				3.8 V	

detailed analysis of the sensitivity to different voltage segments. Table 2 summarizes the chosen minimum and maximum voltage values V_{min}, V_{max} from all selected windows. All possible combinations, e.g., V_{min} = 3.25 V and V_{max} = 4.2 V, are selected. A partial charge window is only extracted if $V_{min} < V_{max}$. Hence, with this approach, in real-world scenarios arbitrary charging data can be snipped into the respective voltage segments if and only if the start voltage is below 3.6 V and the end voltage is above 3.8 V or the start voltage is below 3.8 V and the end voltage is above 4.0 V.

All compared networks are trained with the same feature set comprising of the raw partial voltage curve, the partial charge curve (which is defined to start at 0), and the applied C-rate. The dimension of each feature is $\mathbb{R}^{1\times100}$ which requires a downsampling for all data sources. The scalar C-rate is also mapped to a $\mathbb{R}^{1\times100}$ vector to match the dimensions. The whole dataset undergoes normalization to lie in a range between zero and one for further processing. This has been shown to increase NN performance and efficiency [40]. Note that both datasets, the source and target dataset, are normalized individually. During every tuning or training process, the dataset is split into training, validation and test data as shown in Fig. 5. To ensure a representative validation dataset for UC3 and UC4, these datasets are selected as a random 33% subset of the training dataset.

TCNs have been shown to be advantageous for time-series modeling because they work as a type of automated feature extractor from raw data [34]. Many authors [16–20] have, besides that, already proven the ability to employ TCNs for SOH estimation. In our work, we combine TCN layers as a type of feature extractor with subsequent LSTM layers as a type of feature interpreter. Other works [17,23,37] show the mutual support of CNN with LSTM, and even TCN with LSTM. We select fine-tuning as our approach due to the similarity of both datasets. The TCN layer(s) extract similar features for both the source and target domains, while the LSTM layer(s) interpret these features in a similar manner. Hence, only small modifications of the network should be necessary during TL. To accomplish this, we reduce the learning rate and retrain the network for a smaller number of epochs, allowing only minor changes in the network configuration. The proposed method can, of course, be applied to different NN architectures as well. It is important, however, to note that the comparison of these architectures is beyond the scope of this publication.

Before applying TL, the NNs for both the experimental and synthetic datasets are optimized to their respective best performance using Bayesian hyperparameter tuning. Bayesian optimization is a highly effective hyperparameter tuning method as it enables exploration of a large search space with minimal trials [41]. This method employs a surrogate model to minimize the validation loss for different hyperparameter sets. The algorithm prunes unpromising directions and selects the most promising hyperparameter combination for its subsequent trial, thereby requiring only a few trials to achieve optimal performance. Table 3 lists the search space of the hyperparameter tuning. The batch-size is fixed to 128 and the number of epochs is set to a maximum of 500 with early stopping once the validation loss does not decrease for 50 consecutive epochs. Default values are used for all hyperparameters not listed in Table 3. We use the Adam optimizer with the default learning rate of 1×10^{-3}. The last layer is always a LSTM layer with 2 units to guarantee correct output dimensions. To optimize the performance of

Table 3
Search space for Bayesian hyperparameter tuning, where N refers to the layer number. Hence, for every additional TCN or LSTM layer, the respective hyperparameters can be tuned individually.

Hyperparameter	Definition
TCN layers	$\lambda_{TCN} \in \Lambda_{TCN}$ with $\Lambda_{TCN} := \{\lambda_{TCN} \in \mathbb{N}; 1 \leq \lambda_{TCN} \leq 3\}$
Kernel size	$\lambda_{K,N} \in \Lambda_K$ with $\Lambda_K := \{\lambda_K \in \mathbb{N}; 1 \leq \lambda_K \leq 8\}$
Filter size	$\lambda_{F,N} \in \Lambda_F$ with $\Lambda_F := \{\lambda_F \in \mathbb{N}; 8 \leq \lambda_F \leq 128\}$
LSTM layers	$\lambda_{LSTM} \in \Lambda_{LSTM}$ with $\Lambda_{LSTM} := \{\lambda_{LSTM} \in \mathbb{N}; 0 \leq \lambda_{LSTM} \leq 2\}$
Units	$\lambda_{U,N} \in \Lambda_U$ with $\Lambda_U := \{\lambda_U \in \mathbb{N}; 8 \leq \lambda_U \leq 128\}$
Dropout	$\lambda_{D,N} \in \Lambda_D$ with $\Lambda_D := \{\lambda_D \in \mathbb{D}; 0 \leq \lambda_D \leq 0.5\}$

our model, we explored a large search space. This includes tuning the number of TCN layers λ_{TCN} (range 1 to 3) with the number of filters $\lambda_{F,N}$ (range 8 to 128) and kernel size $\lambda_{K,N}$ (range 1 to 8), as well as the number of LSTM layers λ_{LSTM} (range 0 to 2) with the number of units $\lambda_{U,N}$ (range 8 to 128) and dropout $\lambda_{D,N}$ (range 0 to 0.5) between layers. By considering a wide range of hyperparameters, we aim to find the optimal configuration for our specific task. The optimization runs for 100 trials with the KerasTuner [42] and the goal to minimize the validation loss. To tune the architecture of the reference EXP-NN, we select cells with C-rate values of 1C and C/3.85 for training. Cells B2 and C1 with C-rate C/2 are chosen for validation, while the remaining cells serve as the test dataset to assess the model's generalization ability. This train/test/validation split, optimized for UC1, includes training data from other UCs, enabling the architecture to learn patterns in this data. Fig. 8(a) illustrates the optimized architecture. It consists of an input-TCN layer combined with three LSTM layers and dropout applied between them.

Similar to the EXP-NN, we split the synthetic dataset based on C-rates to create training, testing, and validation datasets.

All curves with C/6 are used for validation, while all curves with C/3 are used for testing, and the remaining data is used for training. The resulting model architecture is depicted in Fig. 8(b). Unlike the EXP-NN, this architecture only includes one TCN layer and no additional LSTM layers besides the output layer. The synthetic dataset is cleaner and does not include any measurement noise, allowing the model to learn data patterns quickly without the need for a complex architecture.

For all four UCs, both the EXP-NN and TL-NNs utilize the same data split, as outlined in Fig. 5: In UC1, cells B2 and C1 from the training dataset are selected as the validation data. In UC2, cell E2 from the training dataset is chosen. For UC3 and UC4, a random subset comprising 33% of the training data is used as the validation dataset to avoid further reduction of the training data space.

The EXP-NN trains in every UC for a maximum of 500 epochs with early stopping once the validation loss does not decrease for 50 consecutive epochs. The training runs for 250 epochs for UC1, 442 epochs for UC2, 500 epochs for UC3 and 471 epochs for UC4.

To achieve optimal learning, the base synthetic model is initially trained with the complete synthetic dataset before TL. A random subset comprising 33% of the data is used for validation during this training phase. The base model successfully achieves $MAPE_{SOH}$ and MAE_{OCV} values below 1% and 10 mV, respectively, for all samples across different C-rates. In contrast to the pretraining phase, the objective of TL is to make marginal modifications to the parameters of the base model. This is accomplished by setting the learning rate to 1×10^{-6} and training for only 200 epochs.

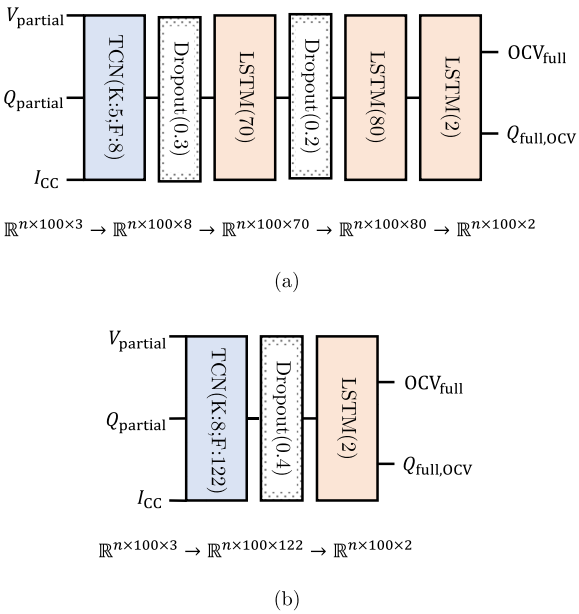

Fig. 8. Final architecture of the tuned (a) EXP-NN and (b) synthetic model / TL-NN and the corresponding dimensions of output data from each layer with n as the number of samples. In the TCN-layers the first number refers to the kernel size and the second number to the filter size.

4. Results and discussion

The present study aims to evaluate the benefits and limitations of TL, with the UCs defined in Fig. 5 guiding the subsequent discussion. While the EXP-NN is expected to perform comparably to the TL-NN when sufficient training data is available, the TL-NN is expected to outperform the EXP-NN in all other cases. In our approach, the cell chemistries used within the target and source domain are similar. Due to the underlying theory of the mechanistic model approach, the sole information of plateau shifting along degradation should be enough to reconstruct the OCV. Hence, the possibilities of TL from other cell chemistries is discussed in the latter subsection. We even designed a purely artificial synthetic dataset (ART) from self-designed half-cell potential curves to prove this assumption.

4.1. Benchmark

The evaluation of the UCs is based on the models derived from the Bayes optimization (Fig. 8). These UCs vary in terms of the amount and content of training data. Table 4 provides a summary of the results, with a focus on the MAE_{OCV} and MAE_{SOH} for reconstruction from partial segments between 3.6 V to 4.1 V. The voltage window is selected because it represents the available charging window from 30% to 85% at BOL, extracted from Fig. 6. Hence, Table 4 gives realistic results for possible applications.

While the more complex EXP-NN still achieves reasonable results for UC1 and UC2, it worsens drastically for the remaining UCs. In a similar manner, the advantage of the simpler TL-NN gets more visible once the training data for fine-tuning gets more and more limited. This, however, also implies the limitations of TL for sparse fine-tuning datasets which do not cover the boundaries of the target domain. For all UCs, the models are evaluated within different partial charging segments.

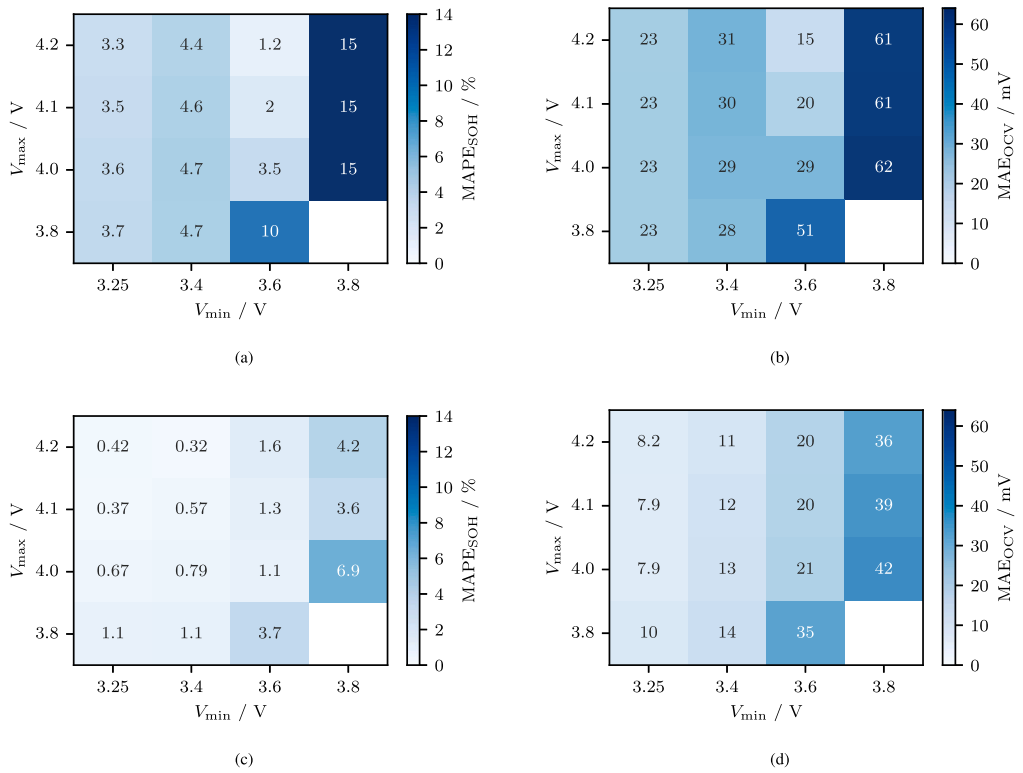

Fig. 9. Results for UC1: (a), (b) EXP-NN, (c), (d) TL-NN. (a) Average SOH error for the test datast with the reference EXP-NN. (b) Average OCV error for the test datast with the reference EXP-NN. (c) Average SOH error for the test datast with the TL-NN. (d) Average OCV error for the test datast with the TL-NN.

Table 4
Performance comparison of the EXP-NN and the TL-NN for different UCs in the voltage window between 3.6 V to 4.1 V. The UCs differ in the amount of training data for the training/fine-tuning process.

		$MAPE_{SOH}$			MAE_{OCV}		
		C/3.85	C/2	1C	C/3.85	C/2	1C
UC1	EXP-NN	–	2.0%	–	–	21 mV	–
	TL-NN	–	1.3%	–	–	20 mV	-
UC2	EXP-NN	2.8%	4.9%	2.5%	18 mV	18 mV	15 mV
	TL-NN	0.6%	2.0%	1.1%	8.0 mV	22 mV	10 mV
UC3	EXP-NN	7.2%	2.9%	3.3%	27 mV	22 mV	18 mV
	TL-NN	0.5%	2.2%	0.8%	7.0 mV	20 mV	8.0 mV
UC4	EXP-NN	1.2%	6.7%	20.4%	15 mV	140 mV	280 mV
	TL-NN	0.9%	6.8%	17.0%	7.0 mV	31 mV	25 mV

4.1.1. Use Case 1: Retraining from all cells at two C-rates

Fig. 9 illustrates the performance of both models across different partial charging segments. It is evident that both models exhibit higher accuracy for wider voltage-ranges. Interestingly, the EXP-NN shows a decrease in performance specifically for the partial charging segments starting at 3.4 V, while the TL-NN does not display this trend. This observation suggests that TL may have been successful in improving the performance of the TL-NN for these segments. The TL-NN consistently outperforms the EXP-NN across all voltage segments, except for the range between 3.6 V to 4.2 V. Notably, it becomes evident that the lower charging segment, starting at 3.25 V or SOC = 0%, is sufficient for reconstructing the OCV with a MAE below 10 mV, even with a lower upper voltage limit. This voltage window, spanning from 3.25 V to 3.8 V, corresponds to a SOC window between 0% and 30% to 50% over the battery's lifetime.

4.1.2. Use Case 2: Retraining from six cells at two C-rates

The results for UC2 are presented in Appendix A.1, Fig. A.14. We train and fine-tune the models using only 40.4% of the experimental dataset, with training data consisting of samples with C-rates of C/3.85 and 1C. The TL-NN outperforms the EXP-NN in terms of SOH and OCV accuracy. Table 4 shows that the TL-NN performs slightly worse by 4 mV for the test dataset at C/2 and in the voltage-range between 3.6 V to 4.1 V. The TL-NN, however, still achieves reasonable results. Notably, the TL-NN's performance for C/2 remains consistent compared to UC1, even with limited training data. On the other hand, the EXP-NN exhibits worsened SOH accuracy with a MAPE of 4.9%. Both models demonstrate a trend of better performance for wider voltage windows. Similar to UC1, we obtain the best results with a low starting voltage of 3.25 V, even with limited voltage windows. However, the accuracy decreases for the upper voltage segment, with an MAE_{OCV} above 30 mV. This is mainly due to two main factors: First, the low voltage segments include the steepest gradient at the begin of charge which allows accurate estimation of the anode degradation. Second, the lower voltage segments include more and significant gradient changes, as can be seen in Fig. 4. This effects provide useful information for the developed NNs and hence increase the reconstruction accuracy.

4.1.3. Use Case 3: Retraining from two cells at two C-rates

UC3 further reduces the experimental training data to only 13.2% at two C-rates. Appendix A.2 presents the performance matrix for different voltage windows in Fig. A.15. The TL-NN exhibits nearly the same accuracy as in the previous UCs. Even for the test data at C/2 and between 3.6 V to 4.1 V, as shown in Table 4, the TL-NN performs comparably. The TL-NN outperforms even its own previous realization for UC1, owing to the larger amount of test data from the same C-rate, as revealed in Table 4: The TL-NN performs significantly better

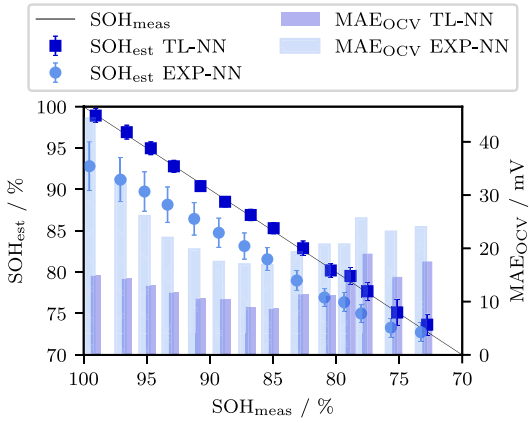

Fig. 10. Evaluation of the EXP-NN and the TL-NN for UC3 and the whole test dataset. One data point corresponds to the average estimation within a 2% region and bins them for better comparability. The markers for the SOH estimations indicate the mean value, while the bars correspond to the standard deviation. Similar, the mean OCV reconstruction error is evaluated with the bar plot. To increase comparability between the EXP-NN and TL-NN, the results from the TL-NN are shifted to the left by 0.25%, and the results from the EXP-NN are shifted to the right by 0.25%.

for C/3.85 and 1C. Also the EXP-NN seems to perform better for UC3, but only for lower voltage segments with $V_{min} \leq 3.4\,V$.

The advantages of TL become even more pronounced when comparing the accuracy along the degradation, as depicted in Fig. 10. The TL-NN shows excellent performance in terms of SOH accuracy with almost no recognizable error and barely any visible standard deviation. For the whole test dataset, i.e., all C-rates and voltage windows, the $MAPE_{SOH}$ is 1.1% and the MAE_{OCV} is 12 mV. Also, the OCV reconstruction accuracy stays below 18 mV for every SOH. Below 75% SOH, the standard deviation gets visible with values below 1.6% which is further recognizable by the higher OCV reconstruction error. A correlation between the OCV reconstruction error and the SOH estimation accuracy is thus probable.

Contrary, the EXP-NN underestimates the battery SOH along its lifetime by approximately 5.2% and further inhibits a large standard deviation of up to 2.9%. The MAE_{OCV} is 24 mV. The EXP-NN performs worse for the upper SOH region with higher SOH standard deviations and a larger OCV reconstruction error. Again, this supports the previously made assumption about an existing correlation between the OCV reconstruction error and the SOH estimation accuracy. In total, the OCV reconstruction accuracy deviates between 17 mV to 47 mV.

Fig. 11 presents the OCV reconstruction from partial voltage segments at C/2 and 1C for different SOHs for the TL-NN at UC3. The Figure is divided into three columns with different SOHs and four rows with varying input voltage windows: The low SOC-range ((a)–(c)) spans from 3.25 V to 3.8 V, the mid SOC-range ((d)–(f)) from 3.6 V to 4.1 V, the high SOC-range ((g)–(i)) from 3.8 V to 4.2 V and the full SOC-range ((j)–(l)) from 3.25 V to 4.2 V. Additionally, in every subplot, the MAE_{OCV} for both C-rates is given in its respective color and position. The TL-NN performs very well for the lower SOC-range for all three degradation states, as can be seen in Fig. 11(a)–(c). The error stays mostly below 12 mV. Solely, the OCV reconstruction with 1C at the lowest SOH (Fig. 11(c)), shows a worse result with a MAE_{OCV} of 22 mV. With higher SOC-ranges, the accuracy worsens. While the TL-NN reaches acceptable reconstruction results for mid of life (MOL) (Fig. 11(e) and (h)) and EOL (Fig. 11(f) and (i)), the BOL reconstruction (Fig. 11(d) and (g)) from the partial C/2 shows high deviations with a MAE_{OCV} of 37 mV. A more detailed analysis reveals that the trajectory of the reconstructed OCV shows a good fit but is shifted to the left. On average, the upper voltage segments in Fig. 11(g)–(i) lead to the worst results with OCV reconstruction errors between 9 mV and 37 mV. Again, for the BOL fit from the partial C/2 voltage curve the trajectory itself looks promising but is shifted to the left. More interesting, the input data from the partial segment at 1C lead to better results than the inputs from the C/2 data. This stands in contrast with recent literature findings about the applicability and limitations of mechanistic OCV reconstruction approaches [4,43–47]. The performance of the TL-NN heavily relies on the training data from the target domain. As long as gradient changes in the charging voltage curve are recognizable, the NN does not seem to be influenced by the C-rate. Similar results where already gathered from evaluations of the base simulation model, where also no C-rate dependency could be found. The full SOC-range (Fig. 11(j)–(l)) leads to similar results as the low SOC-range (Fig. 11(a)–(c)). This is already expected due to the heatmaps investigated from Fig. A.15. All OCVs are reconstructed with sufficient accuracy.

4.1.4. Use Case 4: Retraining from two cells at one C-rate - The limitations of transfer learning

Within UC4 the limitations of TL get visible, as Fig. A.16 in Appendix A.3 shows. As expected, the EXP-NN completely fails to estimate the OCV with a MAE_{OCV} up to 280 mV for test data at 1C from the voltage window between 3.6 V to 4.1 V due to insufficient training data. In comparison, the TL-NN performs well with an average OCV reconstruction error of 25 mV. Fig. A.16(b) indicates that the estimated OCV curves are shifted to the left or right and hence lead to less accurate results. The OCV reconstruction error can only be evaluated at charge positions where both curves – the measured and reconstructed OCV – are available. This explains the lower MAE_{OCV}. The previously seen patterns in the accuracy depending on the voltage windows are not visible for the EXP-NN. As can be seen in Fig. A.16 the model achieves the best approximation with errors below 130 mV for the upper voltage segments. Of course, this must be interpreted in the context of the already very high errors and thus should not lead to any conclusions. In contrast, the TL-NN still shows comparable OCV reconstruction dependency as the previous UCs: The OCV is reconstructed with a MAE_{OCV} below 20 mV for the full and lower voltage segments, while it worsens up to 26 mV for the upper voltage segments.

This indicates that TL is indeed able to transfer knowledge from the source domain to the target domain if, and only if, the fine-tuning process includes the boundaries of the target domain. In our study, these boundaries are samples with C/3.85 and 1C at BOL and EOL. Hence, TL works perfectly for UC3 but suddenly fails for UC4 once the samples with 1C are excluded from the training data, as can be seen in Fig. 5.

While this gives clear requirements for TL, it stays an open research questions which features actually lead to accurate OCV reconstruction. Thus, we further elaborate on the hypothesis of gradient changes in the voltage trajectories as the main feature.

4.2. Transfer learning from different cell chemistries

To validate our hypothesis that gradient changes is the sole requirement for transferring knowledge from the source to the target domain independent of its chemistry, we conduct additional experiments using two synthetic datasets. The synthetic datasets consist of constant current voltage curves, and Fig. 12 displays samples of the OCPs used to generate them. The samples include an LFP cathode with a graphite anode (Fig. 12(a)) and an artificial anode with an artificial cathode (Fig. 12(b)). It is important to note that the ART cell used in this study is completely self-designed and not the result of measurements. While the main trajectory is comparable to a conventional NMC- or NCA-graphite cell, the only information contained is a changing gradient at three and five positions in the anode and cathode OCP, respectively. Hence, this is the only transferable knowledge from the source domain and ultimately proves if this is the main feature for TL in the field of battery SOH estimation and OCV reconstruction.

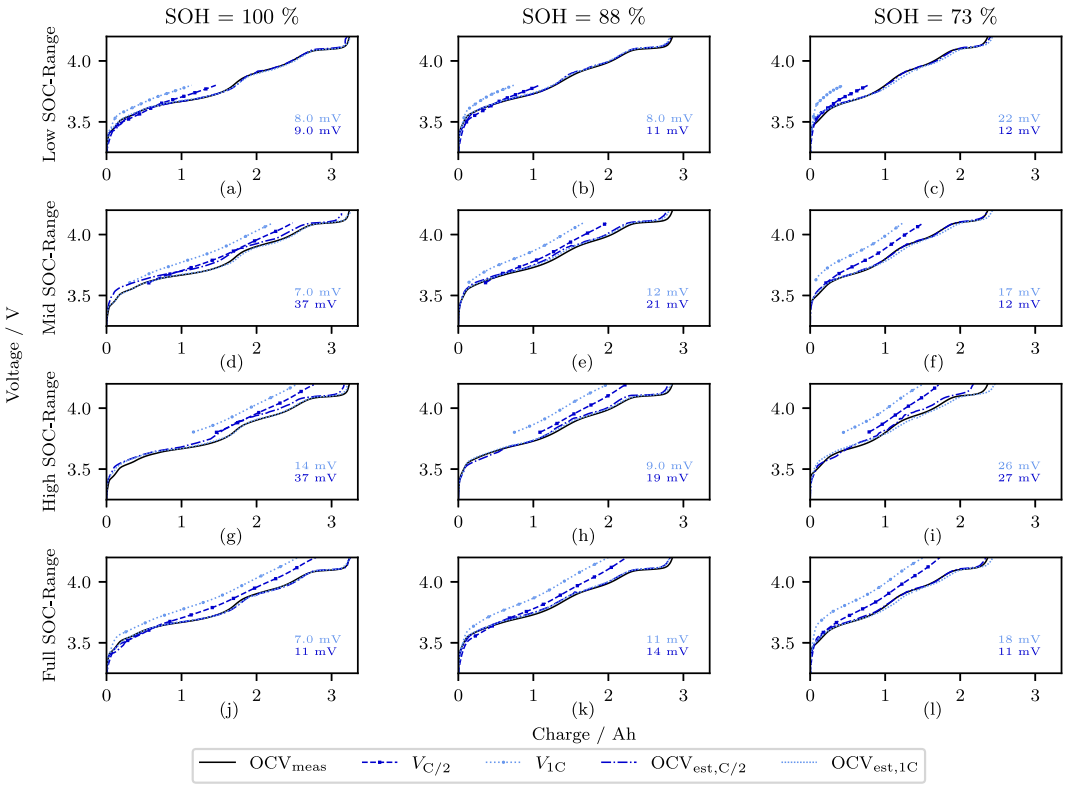

Fig. 11. Evaluation of the TL-NN performance for UC3 and test data drawn from partial charging events at C/2 and 1C. For both cases, three degradation states and four different voltage/SOC windows are evaluated. The low SOC-range ((a)–(c)) corresponds to a voltage window from 3.25 V to 3.8 V, the middle window ((d)–(f)) from 3.6 V to 4.1 V and the high SOC-range ((g)–(i)) from 3.8 V to 4.2 V. Subfigures (j)–(l) show the results for the full input voltage. For all evaluated scenarios the mean absolute OCV reconstruction error is included in the subplot, in its respective color. The upper text belongs to the 1C event, while the lower text corresponds to the C/2 charge. (For interpretation of the references to color in this figure legend, the reader is referred to the web version of this article.)

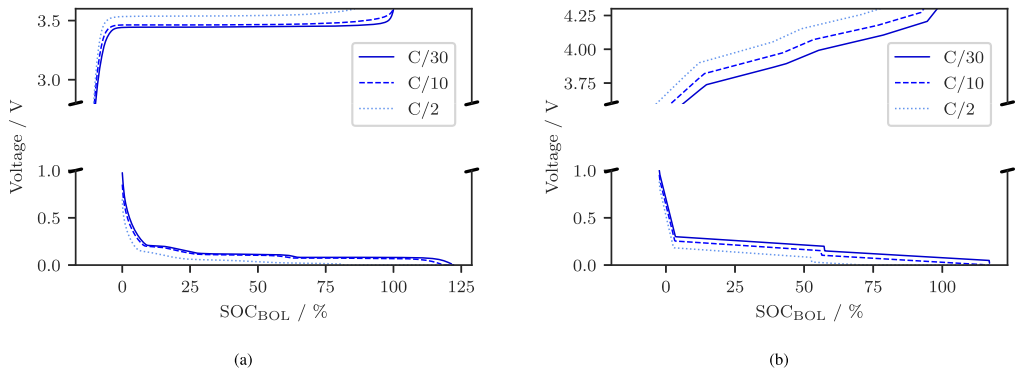

Fig. 12. Additional synthetic dataset generated from half-cell potential curves at various C-rates. Two additional datasets are created, one for a (a) LFP chemistry and another for an (b) artificial (ART) chemistry.

In this study, we follow a consistent workflow, as depicted in Fig. 7, to investigate the effectiveness of plateau shifting in transferring knowledge between domains. The synthetic datasets used in our experiments are generated under identical conditions, including the same C-rates and aging paths. In contrast to our previous synthetic dataset, we utilized the alawa-toolbox from Dubarry et al. [6] to generate these constant current voltage curves. To ensure consistency and comparability across the datasets, we apply the same preprocessing steps, including voltage windowing, normalization, and data splitting. While the ART dataset uses the same defined voltage windows as for the initial synthetic dataset in Table 2, the LFP cell undergoes a windowing with lower voltage levels: The minimum voltage V_{min} is set to 2.8 V, 3.0 V, 3.2 V and 3.4 V. The maximum voltage V_{max} varies between 3.4 V, 3.5 V and 3.6 V. To optimize the performance of the new base models, we employ Bayes tuning with the defined search space, as outlined in Table 3. This allows us to improve the models and achieve their respective optima. The final model architectures, along with their hyperparameters, are provided in the Appendix B to facilitate reproducibility and transparency. The base models are now trained and

Table 5
Performance comparison of the EXP-NN and the TL-NN (pretrained with a different cell chemistry) for different UCs in the voltage window between 3.6 V to 4.1 V. The UCs differ in the amount of training data for the fine-tuning process.

		$MAPE_{SOH}$			MAE_{OCV}		
		C/3.85	C/2	1C	C/3.85	C/2	1C
UC1	EXP-NN	–	2.0%	–	–	21 mV	–
	TL (LFP)	–	9.1%	–	–	50 mV	–
	TL (ART)	–	3.3%	-	–	21 mV	-
UC2	EXP-NN	2.8%	4.9%	2.5%	18 mV	18 mV	15 mV
	TL (LFP)	17.8%	8.6%	4.2%	78 mV	55 mV	26 mV
	TL (ART)	1.2%	5.4%	1.6%	11 mV	25 mV	11 mV
UC3	EXP-NN	7.2%	2.9%	3.3%	27 mV	22 mV	18 mV
	TL (LFP)	19.9%	15.3%	6.9%	74 mV	64 mV	40 mV
	TL (ART)	0.8%	4.7%	1.2%	12 mV	28 mV	11 mV
UC4	EXP-NN	1.2%	6.7%	20.4%	15 mV	140 mV	280 mV
	TL (LFP)	15.5%	8.3%	9.0%	66 mV	43 mV	43 mV
	TL (ART)	0.5%	5.6%	6.9%	11 mV	32 mV	47 mV

transfer-learned for the four defined UCs in Fig. 5. Specifically, we utilize fine-tuning with a reduced learning rate of 1×10^{-4} for 200 epochs. Noticeably, we must increase the learning rate in comparison to our initial TL-NN from 1×10^{-6} to 1×10^{-4} (Adam default value is 1×10^{-3}) due to the decreased similarity of the source and target datasets. In the fine-tuning process, more adoptions of the network weights are mandatory to achieve sufficient learning of the target dataset which is not possible with a learning rate lower than 1×10^{-4}. The base models are compared to the EXP-NNs for each UC, and the final comparison results are summarized in Table 5. These results provide insights into the performance and effectiveness of plateau shifting in transferring knowledge across different UCs. The pretrained model from the LFP dataset fails to transfer its past knowledge to the target domain. For a voltage input window from 3.6 V to 4.1 V and UC1 to UC3 the TL LFP model performs worse than the benchmark EXP-NN. The LFP OCV curve is very flat and barely shows any detectable gradient changes in its trajectory. At higher C-rates the voltage charging curve seems even faded and does not provide any information to the model. The sole advantage is a moderate estimation for UC4. Nevertheless, the fine-tuning process does not allow a sufficient adaption to the target domain and hence the performance stays equally low for every UC. Fig. 13(a) illustrates the performance for the model on UC3 for the complete test dataset: The insufficient fine-tuning process is visible by the almost constant estimations over lifetime. The learning-rate or number of epochs, however, cannot be increased any higher because this will lead to catastrophic forgetting and completely erase the impact of the learned knowledge from the source dataset.

Contrary the ART model outperforms the reference EXP-NN, as can be seen in Fig. 13(b). The model achieves accurate estimations over lifetime with a small standard deviation. The OCV curve is mostly reconstructed with a MAE below 20 mV. The deviation, however, is remarkably higher than the initial TL pretrained from a similar cell chemistry (see Fig. 10). Table 5 provides further insights and reveals the advantage of the ART TL-NN for all use cases and the voltage window from 3.6 V to 4.1 V: While the model performs comparably to the EXP-NN for test data with C/2 and UC1 to UC3, it is very accurate for test data with C/3.85 and 1C. This adds on to our theory of including fixed boundaries of the target dataset to accelerate the transfer of knowledge. Although the test data for these C-rates includes different cells, inclusion of another cell at this specific C-rates for training drastically improves performance. This may be due to the better interpretation of C-rate dependent gradient changes and the location of those in the voltage curve.

In conclusion, the ART TL-NN exhibits slightly lower performance compared to the original TL-NN. This finding, however, emphasizes that the specific chemical composition of the source dataset is not a critical factor. Instead, it is the presence of gradients and its changes

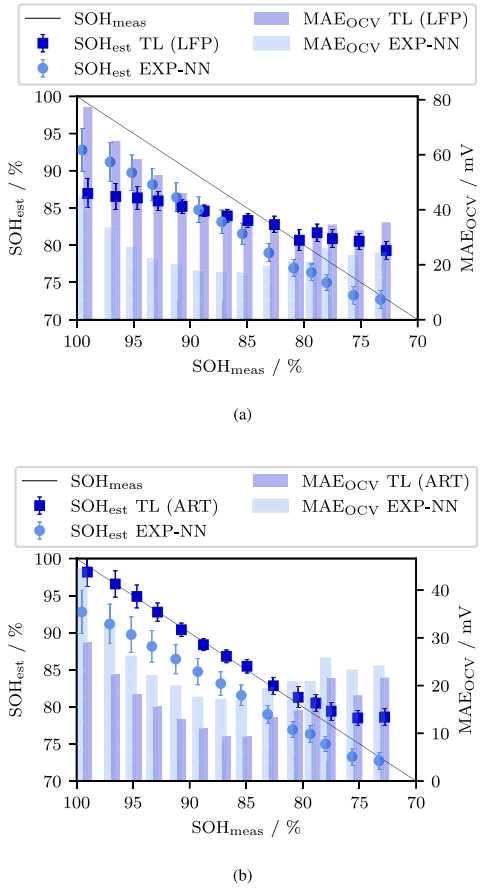

Fig. 13. Evaluation of the EXP-NN and the TL-NNs pretrained with (a) LFP and (b) ART cell for UC3 and the whole test dataset. One data point corresponds to the average estimation within a 2% region and bins them for better comparability. The markers for the SOH estimations indicate the mean value, while the bars correspond to the standard deviation. Similar, the mean OCV reconstruction error is evaluated with the bar plot. To increase comparability between the EXP-NN and TL-NNs, the results from the TL ART model are shifted to the left by 0.25%, and the results from the EXP-NN are shifted to the right by 0.25%.

in the voltage curves that play a crucial role. Especially the cathode OCP heavily influences the performance because in the LFP dataset, the graphite anode shows some detectable gradient changes which are not sufficient to reconstruct the OCV accordingly. Consequently, the TCN-LSTM approach can effectively identify degradation modes and their underlying patterns in the voltage curves, enabling the mapping of these patterns to the altered OCV curve.

4.3. Comprehensive discussion

The study at hand presents a TCN-LSTM network to reconstruct the full OCV curve from partial charging voltage segments at different C-rates. Our findings further confirm the research question that TL from synthetic data is possible and superior to traditional DL. For UC3 the TL-NN outperforms the more complex EXP-NN which are both trained / fine-tuned with 13.2% of the total experimental dataset. For every C-rate and a limited voltage window from 3.6 V to 4.1 V the TL-NN already reaches OCV-reconstruction MAEs below 20 mV which is in the range of literature values [4,11,13]. The SOH is calculated from the reconstructed OCV curves with MAPEs below 2.2%. We further highlight the influence of C-rate and voltage-range on the accuracy.

While lower voltage levels definitely lead to higher accuracies, the influence of the C-rate is obscured by the impact of the training data. Lower voltage segments may be beneficial because this allows an easier detection of the anode aging due to changing gradient of the voltage curve. Subsequent the identification of cathode aging is more straightforward due to the higher gradient in the OCP. By introducing two additional source synthetic datasets, we are able to answer the second research question about the actual learned knowledge from partial voltage curves: Our findings strongly suggest that the TCN-LSTM model comprehends the degradation patterns in the voltage curve, which are influenced by the shifting of plateaus caused by degradation modes.

In contrast to our findings, Bockrath et al. [16] concluded the middle and upper voltage-range to be more suitable for SOH estimation from partial discharge voltage segments. They claim that the middle and upper voltage ranges preserve more of the full capacity degradation measurements and that their learned knowledge differs from our hypothesis: Their TCN exploits the correlation between the measured capacity from partial measurements to the measured SOH. They show that their measured capacity throughput in the middle and upper voltage ranges correlates well with the SOH. This is not the main feature in our dataset, as we aim to reconstruct the full OCV curve and calculate the SOH from this curve. Hence, the sole information of the SOH is insufficient for accurate OCV reconstruction. Comparing our TL-NN from UC3 with the TCN developed by Bockrath et al. [16] for full voltage curves, we see that they have reached an SOH RMSE of 1.0%, while we were able to decrease the SOH MAPE to 0.64%. Zhou et al. [26] have for the first time introduced a TL approach for full OCV reconstruction from partial charging data. While they have successfully applied TL to different cell chemistries and reconstructed the OCV with errors below 2.73%, they failed to clarify the usability of synthetic data for the source domain. They have used a generative DL model and reached TL by fine-tuning the decoder basis. Contrary, we fine-tune our complete TCN-LSTM network by reducing the learning rate to 1×10^{-6} and epochs to a maximum of 200. Further, we have found no contributions towards a detailed analysis of the corresponding knowledge transferred between deep-learning models.

We prove that synthetic data indeed works as a source domain for TL, even for varying cells. Further, TL outperforms traditional DL as long as the fine-tuning data includes the boundaries of the target domain. TL increases its superiority against traditional DL with smaller training datasets. Generally, DL models for full OCV reconstruction reach higher accuracy for the lower voltage segments. The C-rate of the input data does not influence the performance as much as the training/testing split does. Hence, in most research studies, the clear influence of the C-rate is hard to identify. Pretraining from synthetic data sources and varying cell chemistries works as long as enough plateaus and gradient shifts are detectable in the voltage curves. Although pretraining the model with the source LFP dataset fails to detect any information, the use of an artificially designed dataset consisting of ART OCPs allows for the incorporation of knowledge regarding degradation modes and OCV degradation into the NN. Consequently, by including more detectable plateaus and a wider range of gradients in the voltage trajectory, the model is able to extract more information and exhibits a higher likelihood of successfully transferring its knowledge to a new target domain.

Table 4 shows that for UC2 and UC3 the performance is biased towards test data with C/3.85 and 1C. These data segments are included in the fine-tuning data and hence the possibility of overfitting arises on these parts of the data. This stands in contrast to the reduced learning rate and the smaller number of fine-tuning epochs. As Fig. 11 shows, the reconstructed OCV matches the true OCV well, even for test data with C/2 charging segments. Even though the MAE_{OCV} for UC2 and UC3 are similar for the TL and the EXP-NN (see Table 4), the MAE_{SOH} reveal a different result: The SOH estimation accuracy is higher for the TL-NN and hence proves a better fit of the whole reconstruction because the MAE_{OCV} is only calculated at Q-locations where both, the estimated and the true OCV, exist. Hence, a $MAE_{OCV} = 0\,mV$ in combination with $MAE_{SOH} \geq 10\,\%$ is possible and thus the reconstructed curve may be incomplete.

Future research should tackle the exploration of more and other experimental datasets, including more C-rates, varying temperatures and more challenging cell chemistries, i.e., LFP or Si-containing anodes. The usage of synthetic data for TL arises the opportunity for DM estimation due to the contained labels in the synthetic dataset. While generating these labels in the experimental dataset is challenging, differential voltage analysis (DVA) and ICA with OCV measurements still can give rough insights about the degradation patterns. Similar, the output of the developed TL-NN can be fed into a mechanistic model approach [6] to reconstruct the full OCV curve based on shifting and scaling of the pristine OCPs. This further enables to estimate the DMs and includes more physico-chemical relevance into the estimation.

5. Conclusion

The study proposes a data-driven method to reconstruct the full OCV curve from partial charging voltage segments at different C-rates. We prove the effectiveness of TL from synthetic data and evaluate the limitations of this shortcoming by comparing our TL models for four different UCs to purely experimental ML models. In every UC the experimental training/fine-tuning data gets reduced from 67% for UC1 to 40% for UC2, to 13% for UC3 until only 6.6% of the data are included for the fourth and last UC4. While the training/fine-tuning data for UC1 to UC3 incorporate the boundaries of the dataset, i.e., highest and lowest SOH and C-rate, data is limited to the lowest C-rate for UC4. The TL-NN with a simpler architecture outperforms the EXP-NN for every UC and reaches a MAE_{OCV} below 22 mV for the first three UCs and a partial voltage input curve from 3.6 V to 4.1 V. We conclude that a minimum voltage window spanning 400 mV is necessary to enable accurate OCV reconstruction. Further, the lower voltage segments are better suited for full OCV curve reconstruction due to the better recognition of features from the anode half-cell potential curve in the voltage segment. These segments allow accurate SOH estimation with errors below 14 mV MAE_{OCV} and 1.1% $MAPE_{SOH}$, respectively, for the first three UCs and $V_{min} \leq 3.4$ V. Reducing the training data amount to a minimum, requires the inclusion of the boundaries, i.e., the highest and lowest C-rate and SOH, in the fine-tuning datasets. We further find the influence of the C-rate to be negligible in our experiment but it may be a result of the train/test split. Pretraining from different source datasets and incorporating other cell chemistries allows for some interpretation of the actual learning patterns in the black-box TCN-LSTM. Using a completely artificial dataset with many plateaus and gradient switches allows the model to comprehend the theory of DMs and apply this prelearned knowledge to the new target domain. Pretraining from the LFP dataset, however, fails due to no detectable gradient changes in the voltage trajectory.

The positive results of the TL-NN suggest the general usage of TL from synthetic data for battery state estimation. Especially for SOC and SOH estimation over lifetime, the generation of comprehensive data at various aging paths might accelerate the industrialization for BEV fleets and the low-cost development of data-driven state estimation algorithms by reducing measurement time and cost. The generation of synthetic data for various batteries is publicly available (see alawa-toolbox [6]) and allows the pretraining of ML models for multiple UCs. Even the deployment of ML models for new cell chemistries is feasible due to the low requirements of fine-tuning data from the target domain. Hence, this research project takes a promising step towards generalizable ML models for almost every battery type.

The limitations of TL, however, must be kept in mind by fulfilling the minimum requirements of the pretraining and fine-tuning datasets. The application of ML models for OCV curve reconstruction from

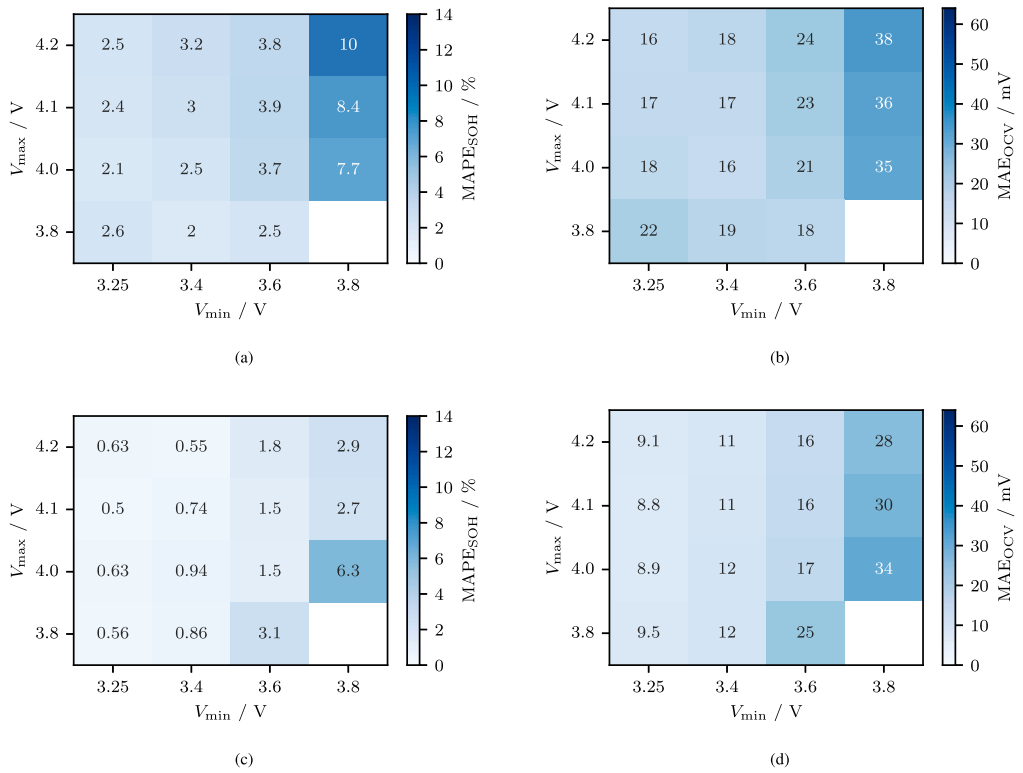

Fig. A.14. Results for UC2: (a), (b) EXP-NN, (c), (d) TL-NN. (a) Average SOH error for the test datast with the reference EXP-NN. (b) Average OCV error for the test datast with the reference EXP-NN. (c) Average SOH error for the test datast with the TL-NN. (d) Average OCV error for the test datast with the TL-NN.

charging voltage segments is generally limited to batteries with sufficient voltage trajectories, i.e., huge challenges arise for LFP cells. The application of TL to other cell chemistries in the target domain remains an open research question and must be explored in future studies. Hence, the inclusion of larger and more diverse experimental datasets in the target domain will answer many of the open questions. Moreover, the application of the method to real-world BEV data must be answered in the near future. Our proof-of-concept for TL-based SOH estimation opens new research perspectives for SOC, SOH and DM estimation. With the usage of synthetic data, many other state estimation models can be developed faster and more efficiently.

CRediT authorship contribution statement

Tobias Hofmann: Writing – original draft, Visualization, Validation, Software, Methodology, Investigation, Data curation, Conceptualization. **Jacob Hamar:** Writing – review & editing, Supervision. **Bastian Mager:** Investigation. **Simon Erhard:** Writing – review & editing, Supervision. **Jan Philipp Schmidt:** Writing – review & editing, Supervision.

Declaration of competing interest

The authors declare that they have no known competing financial interests or personal relationships that could have appeared to influence the work reported in this paper.

Data availability

Data will be made available on request.

Acknowledgments

Funded by the Open Access Publishing Fund of the University of Bayreuth. This work was performed in cooperation with the University of Bayreuth - Chair of Systems Engineering for Electrical Energy Storage and BMW Group. The authors would like to thank the team of Batemo GmbH for providing the Batemo Cell Models as high-precision physical battery cell models to generate the simulation data. The authors would also like to thank Matthieu Dubarry and the University of Hawai'i at Mānoa for sharing the alawa battery emulation toolbox.

Appendix A. Detailed benchmark results

This section provides a more detailed analysis of each TL and EXP-NN for UC2 to UC4. The Figures provide insights about the OCV curve reconstruction and the SOH estimation accuracy with different partial voltage windows as input data.

A.1. Use Case 2

See Fig. A.14.

A.2. Use Case 3

See Fig. A.15.

A.3. Use Case 4

See Fig. A.16.

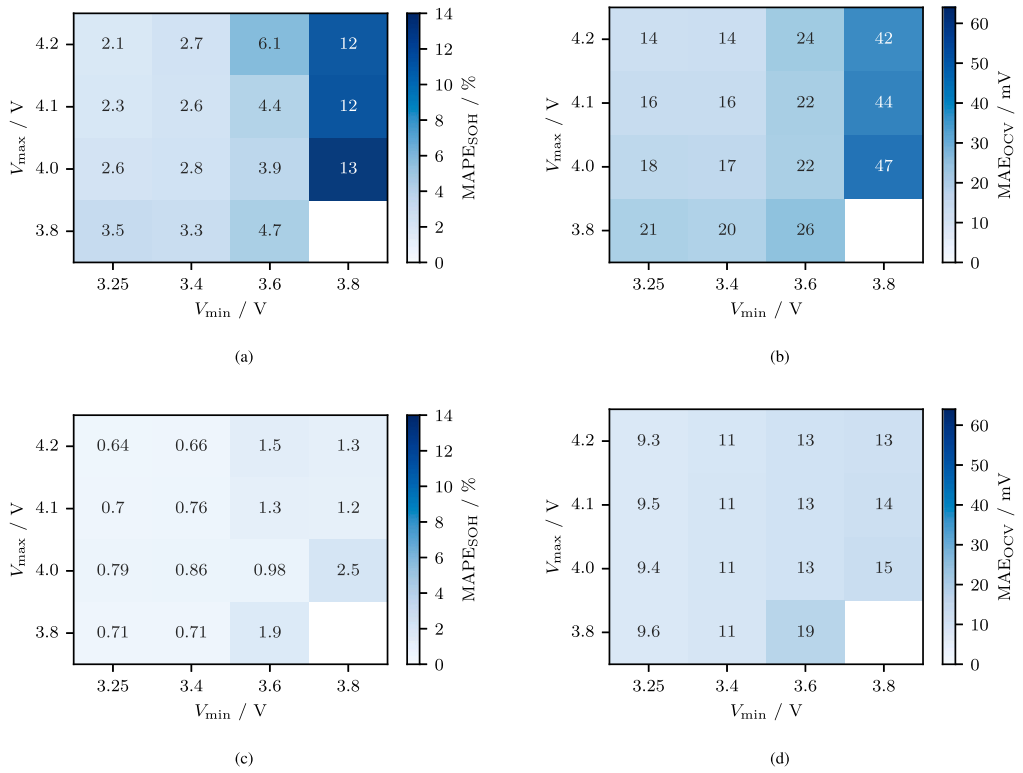

Fig. A.15. Results for UC3: (a), (b) EXP-NN, (c), (d) TL-NN. (a) Average SOH error for the test datast with the reference EXP-NN. (b) Average OCV error for the test datast with the reference EXP-NN. (c) Average SOH error for the test datast with the TL-NN. (d) Average OCV error for the test datast with the TL-NN.

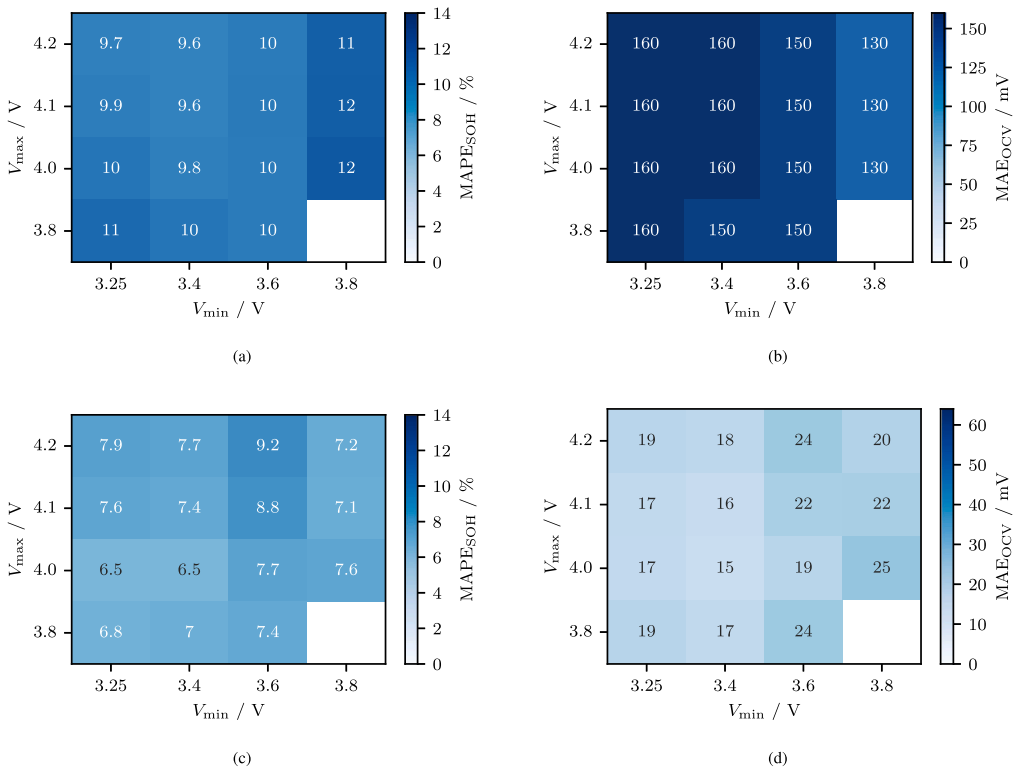

Fig. A.16. Results for UC4: (a), (b) EXP-NN, (c), (d) TL-NN. (a) Average SOH error for the test datast with the reference EXP-NN. (b) Average OCV error for the test datast with the reference EXP-NN. (c) Average SOH error for the test datast with the TL-NN. (d) Average OCV error for the test datast with the TL-NN.

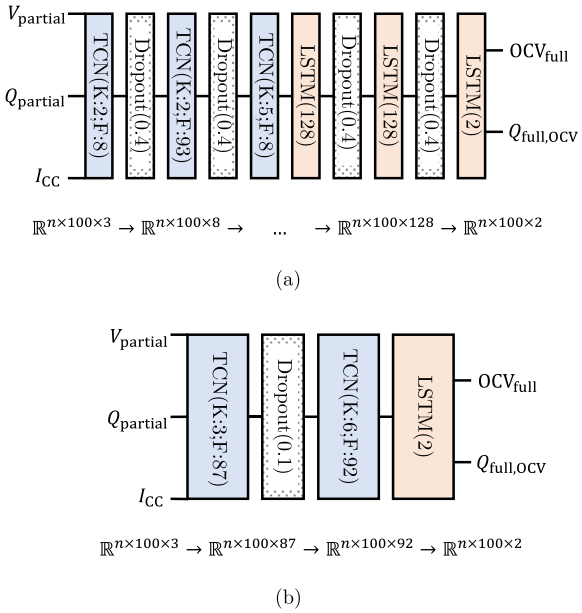

Fig. B.17. Final architecture of the tuned synthetic models optimized with data from the (a) LFP dataset and the (b) ART dataset and the corresponding dimensions of output data from each layer with n as the number of samples. In the TCN-layers the first number refers to the kernel size and the second number to the filter size.

Appendix B. Model architecture of the LFP and ART model

Fig. B.17 provides insights about the final model architectures trained from the additional source datasets LFP and ART. The final architectures are a result of an extensive Bayesian hyperparameter optimization with 100 trials.

References

[1] Sauer DU, Bopp G, Jossen A, Garche J, Rothert M, Wollny M. State of Charge — What do we really speak about. In: The 21st international telecommunications energy conference. 1999, p. 6–9.
[2] Plett GL. Extended Kalman filtering for battery management systems of LiPB-based HEV battery packs: Part 2. Modeling and identification. J Power Sources 2004;134(2):262–76. http://dx.doi.org/10.1016/j.jpowsour.2004.02.032.
[3] Plett GL. Extended Kalman filtering for battery management systems of LiPB-based HEV battery packs: Part 3. State and parameter estimation. J Power Sources 2004;134(2):277–92. http://dx.doi.org/10.1016/j.jpowsour.2004.02.033.
[4] Schmitt J, Rehm M, Karger A, Jossen A. Capacity and degradation mode estimation for lithium-ion batteries based on partial charging curves at different current rates. J Energy Storage 2023;59:106517. http://dx.doi.org/10.1016/j.est.2022.106517.
[5] Hofmann T, Li J, Hamar J, Erhard S, Schmidt JP. The ΔQ-method: State of health and degradation mode estimation for lithium-ion batteries using a mechanistic model with relaxed voltage points. J Power Sources 2024;596:234107. http://dx.doi.org/10.1016/j.jpowsour.2024.234107.
[6] Dubarry M, Truchot C, Liaw BY. Synthesize battery degradation modes via a diagnostic and prognostic model. J Power Sources 2012;219:204–16. http://dx.doi.org/10.1016/j.jpowsour.2012.07.016.
[7] Zhang C, Zhao S, Yang Z, Chen Y. A reliable data-driven state-of-health estimation model for lithium-ion batteries in electric vehicles. Front Energy Res 2022;10. http://dx.doi.org/10.3389/fenrg.2022.1013800.
[8] Zhang C, Luo L, Yang Z, Zhao S, He Y, Wang X, Wang H. Battery SOH estimation method based on gradual decreasing current, double correlation analysis and GRU. Green Energy Intell Transp 2023;2(5):100108. http://dx.doi.org/10.1016/j.geits.2023.100108.

[9] Zhang C, Luo L, Yang Z, Du B, Zhou Z, Wu J, Chen L. Flexible method for estimating the state of health of lithium-ion batteries using partial charging segments. Energy 2024;295:131009. http://dx.doi.org/10.1016/j.energy.2024.131009.
[10] Dubarry M, Costa N, Matthews D. Data-driven direct diagnosis of Li-ion batteries connected to photovoltaics. Nature Commun 2023;14:3138. http://dx.doi.org/10.1038/s41467-023-38895-7.
[11] Tian J, Xiong R, Shen W, Sun F. Electrode ageing estimation and open circuit voltage reconstruction for lithium ion batteries. Energy Storage Mater 2021;37:283–95. http://dx.doi.org/10.1016/j.ensm.2021.02.018.
[12] Ruan H, Chen J, Ai W, Wu B. Generalised diagnostic framework for rapid battery degradation quantification with deep learning. Energy AI 2022;9:100158. http://dx.doi.org/10.1016/j.egyai.2022.100158.
[13] Guo R, Xu Y, Hu C, Shen W. A curve relocation approach for robust battery open circuit voltage reconstruction and capacity estimation based on partial charging data. IEEE Trans Power Electron 2024;39(3):3760–73. http://dx.doi.org/10.1109/TPEL.2023.3347236.
[14] O'Shea K, Nash R. An introduction to convolutional neural networks. 2015, http://dx.doi.org/10.48550/arXiv.1511.08458, arXiv:1511.08458.
[15] Lea C, Flynn MD, Vidal R, Reiter A, Hager GD. Temporal convolutional networks for action segmentation and detection. In: Proceedings of the IEEE conference on computer vision and pattern recognition. CVPR, 2017, p. 156–65. http://dx.doi.org/10.48550/arXiv.1611.05267.
[16] Bockrath S, Lorentz V, Pruckner M. State of health estimation of lithium-ion batteries with a temporal convolutional neural network using partial load profiles. Appl Energy 2023;329:120307. http://dx.doi.org/10.1016/j.apenergy.2022.120307.
[17] Li C, Han X, Zhang Q, Li M, Rao Z, Liao W, Liu X, Liu X, Li G. State-of-health and remaining-useful-life estimations of lithium-ion battery based on temporal convolutional network-long short-term memory. J Energy Storage 2023;74(Part B):109498. http://dx.doi.org/10.1016/j.est.2023.109498.
[18] Liu S, Chen Z, Yuan L, Xu Z, Jin L, Zhang C. State of health estimation of lithium-ion batteries based on multi-feature extraction and temporal convolutional network. J Energy Storage 2024;75:109658. http://dx.doi.org/10.1016/j.est.2023.109658.
[19] Zhou D, Li Z, Zhu J, Zhang H, Hou L. State of health monitoring and remaining useful life prediction of lithium-ion batteries based on temporal convolutional network. IEEE Access 2020;8:53307–20. http://dx.doi.org/10.1109/ACCESS.2020.2981261.
[20] Zhou D, Wang B. Battery health prognosis using improved temporal convolutional network modeling. J Energy Storage 2022;51:104480. http://dx.doi.org/10.1016/j.est.2022.104480.
[21] Tan C, Sun F, Kong T, Zhang W, Yang C, Liu C. A survey on deep transfer learning. In: Artificial neural networks and machine learning – ICANN. 2018, p. 11141. http://dx.doi.org/10.1007/978-3-030-01424-7_27.
[22] Sahoo S, Hariharan KS, Agarwal S, Swernath SB, Bharti R, Han S, Lee S. Transfer learning based generalized framework for state of health estimation of Li-ion cells. Sci Rep 2022;12:13173. http://dx.doi.org/10.1038/s41598-022-16692-4.
[23] Zou G, Yan Z, Zhang C, Song L. Transfer learning with CNN-LSTM model for capacity prediction of lithium-ion batteries under small sample. J Phys Conf Ser 2022;2258:012042. http://dx.doi.org/10.1088/1742-6596/2258/1/012042.
[24] Shen S, Sadoughi M, Li M, Wang Z, Hu C. Deep convolutional neural networks with ensemble learning and transfer learning for capacity estimation of lithium-ion batteries. Appl Energy 2020;260:114296. http://dx.doi.org/10.1016/j.apenergy.2019.114296.
[25] Tian J, Ma L, Zhang T, Han T, Mai W, Chung CY. Exploiting domain knowledge to reduce data requirements for battery health monitoring. Energy Storage Mater 2024;67:103270. http://dx.doi.org/10.1016/j.ensm.2024.103270.
[26] Zhou Z, Liu Y, Zhang C, Shen W, Xiong R. Deep neural network-enabled battery open-circuit voltage estimation based on partial charging data. J Energy Chem 2024;90:120–32. http://dx.doi.org/10.1016/j.jechem.2023.11.009.
[27] Keil P, Schuster SF, Wilhelm J, Travi J, Hauser A, Karl RC, Jossen A. Calendar aging of lithium-ion batteries. J Electrochem Soc 2016;163(9):A1872. http://dx.doi.org/10.1149/2.0411609jes.
[28] Hamar JC, Stuckenberger M, Sturm J, Schmitt J, Rogge M, Erhard SV, Jossen A. Investigating the path dependent aging behavior of nickel cobalt aluminum oxide cathode batteries during high C-rate cycling conditions. J Electrochem Soc 2024;171(2):020555. http://dx.doi.org/10.1149/1945-7111/ad2952.
[29] Goodfellow I, Bengio Y, Courville A. Deep learning. MIT Press; 2016, http://www.deeplearningbook.org.
[30] Hamar JC, Erhard SV, Canesso A, Kohlschmidt J, Olivain N, Jossen A. State-of-health estimation using a neural network trained on vehicle data. J Power Sources 2021;512:230493. http://dx.doi.org/10.1016/j.jpowsour.2021.230493.
[31] Hochreiter S, Schmidhuber J. Long short-term memory. Neural Comput 1997;9(8):1735–80. http://dx.doi.org/10.1162/neco.1997.9.8.1735.
[32] Li W, Sengupta N, Dechent P, Howey D, Annaswamy A, Sauer DU. Online capacity estimation of lithium-ion batteries with deep long short-term memory networks. J Power Sources 2021;482:228863. http://dx.doi.org/10.1016/j.jpowsour.2020.228863.
[33] Gong Q, Wang P, Cheng Z. A data-driven model framework based on deep learning for estimating the states of lithium-ion batteries. J Electrochem Soc 2022;169:030532. http://dx.doi.org/10.1149/1945-7111/ac5bac.
[34] Bai S, Kolter JZ, Koltun V. An empirical evaluation of generic convolutional and recurrent networks for sequence modeling. 2018, http://dx.doi.org/10.48550/arXiv.1803.01271, arXiv preprint.
[35] Chemali E, Kollmeyer PJ, Preindl M, Fahmy Y, Emadi A. A convolutional neural network approach for estimation of li-ion battery state of health from charge profiles. Energies 2022;15(3):1185. http://dx.doi.org/10.3390/en15031185.
[36] Qian C, Xu B, Chang L, Sun B, Feng Q, Yang D, Ren Y, Wang Z. Convolutional neural network based capacity estimation using random segments of the charging curves for lithium-ion batteries. Energy 2021;227:120333. http://dx.doi.org/10.1016/j.energy.2021.120333.
[37] Xu H, Wu L, Xiong S, Li W, Garg A, Gao L. An improved CNN-LSTM model-based state-of-health estimation approach for lithium-ion batteries. Energy 2023;276:127585. http://dx.doi.org/10.1016/j.energy.2023.127585.
[38] Weber M, Auch M, Doblander C, Mandl P, Jacobsen H-A. Transfer learning with time series data: A systematic mapping study. IEEE Access 2021;9:165409–32.
[39] Lu Z, Yu XL, Wei LC, Cao F, Zhang LY, Meng XZ, Jin LW. A comprehensive experimental study on temperature-dependent performance of lithium-ion battery. Appl Therm Eng 2019;158:113800. http://dx.doi.org/10.1016/j.applthermaleng.2019.113800.
[40] Sola J, Sevilla J. Importance of input data normalization for the application of neural networks to complex industrial problems. IEEE Trans Nucl Sci 1997;44(3):1464–8. http://dx.doi.org/10.1109/23.589532.
[41] Victoria AH, Maragatham G. Automatic tuning of hyperparameters using Bayesian optimization. Evol Syst 2021;12:217–23. http://dx.doi.org/10.1007/s12530-020-09345-2.
[42] O'Malley T, Bursztein E, Long J, Chollet F, Jin H, Invernizzi L, et al. Keras tuner. GitHub; 2019, https://github.com/keras-team/keras-tuner.
[43] Schindler S, Baure G, Danzer MA, Dubarry M. Kinetics accommodation in Li-ion mechanistic modeling. J Power Sources 2019;440:227117. http://dx.doi.org/10.1016/j.jpowsour.2019.227117.
[44] Yang S, Zhang C, Jiang J, Zhang W, Gao Y, Zhang L. A voltage reconstruction model based on partial charging curve for state-of-health estimation of lithium-ion batteries. J Energy Storage 2021;35:102271. http://dx.doi.org/10.1016/j.est.2021.102271.
[45] Chen J, Marlow MN, Jiang Q, Wu B. Peak-tracking method to quantify degradation modes in lithium-ion batteries via differential voltage and incremental capacity. J Energy Storage 2022;45:103669. http://dx.doi.org/10.1016/j.est.2021.103669.
[46] Lu D, Trimboli MS, Fan G, Zhang R, Plett GL. Implementation of a physics-based model for half-cell open-circuit potential and full-cell open-circuit voltage estimates: Part II. Processing full-cell data. J Electrochem Soc 2021;168:070533. http://dx.doi.org/10.1149/1945-7111/ac11a5.
[47] Cui Z, Cui N, Li C, Lu J, Zhang C. Online identification and reconstruction of open-circuit voltage for capacity and electrode aging estimation of lithium-ion batteries. IEEE Trans Ind Electron 2023;70:4716–26. http://dx.doi.org/10.1109/TIE.2022.3187596.

2.2.3 Physics-Constrained Transfer Learning for SOH and OCV Estimation

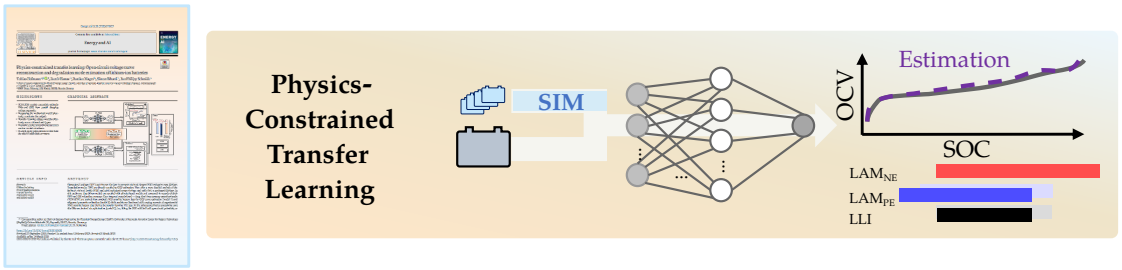

Figure 2.4: The trimmed outline of the thesis structure with focus on this chapter.

The previous article in Section 2.2.2 successfully explored the capabilities of transfer learning, yet it left room for improvement: DMs were not estimated and remained unknown, and the OCV output was noisy and did not adhere to physical laws. This study aims to address these issues by combining the mechanistic modeling approach with a transfer-learned neural network to physically constrain the output and enable DM estimation.

This research explores whether it is possible to physically constrain the output of a neural network by integrating data-driven models with mechanistic models.

While numerous articles investigate the application of transfer learning [123; 133; 137] or the mechanistic modeling approach for OCV and DM estimation [27; 54; 55; 91; 166], there is a notable lack of studies addressing the coupling of these methods. One study has explored generating alignment parameters via CNN as input for mechanistic models [61]. Other research has coupled various data-driven models and fused them into an optimization problem to individually weight the model components [210].

This study follows a methodology similar to the previous publication (Section 2.2.2). Extensive synthetic data is generated using a mechanistic model. Two transfer learning approaches are compared: One directly generates the full OCV curve based on partial charging segments, while the other yields alignment parameters. In the first approach, the OCV curve is fed into an optimization framework where the objective function minimizes the difference between measured and reconstructed OCV curves. The second approach uses simple equations to reconstruct the full OCV and calculate the DMs from the alignment parameters. Both approaches are compared against each other and further validated against a benchmark deep learning model for various use cases.

Both models demonstrate that a single aging path of the target domain suffices as fine-tuning data if it includes the maximum appearing DMs, meaning the fine-tuning dataset must encompass the boundaries of the target domain. Both models significantly outperform the benchmark, achieving a MAE for OCV reconstruction, DM, and SOH_C estimation of 10.0 mV, 3.10 % (pp), and 1.82 % (pp), respectively.

Two novel methods for OCV reconstruction and DM estimation are presented, each with distinct benefits and limitations. Previous findings that lower voltage segments are ad-

vantageous are reaffirmed. Most importantly, the findings reveal how much of a typical experimental design for training a neural network for SOH estimation and OCV reconstruction can be omitted if transfer learning is employed: Nearly 95 % of the experiments can be eliminated, significantly reducing costs.

The paper begins with the theoretical background of the mechanistic model, optimization, and transfer learning. The datasets and their generation process are presented, followed by the methodology section, which includes data preprocessing and model tuning. Results and discussion are structured according to the use case definition. In addition to the OCV and SOH error, the DM evolution over aging is compared to true values. Limitations of both approaches are discussed.

Publication Notes

The article *Physics-constrained transfer learning: Open-circuit voltage curve reconstruction and degradation mode estimation of lithium-ion batteries* is presented in the following. The article was submitted to the Journal Energy and AI for peer review in September 2024 and was accepted in March 2025 [51]. The permanent web link to this publication is available under `https://doi.org/10.1016/j.egyai.2025.100493`.

Author Contributions

T. Hofmann developed the method, evaluated the data, developed the software, and wrote the manuscript. B. Mager assisted during the synthetic data generation and software development of TL-NN-B. J. Hamar, S. Erhard and J.P. Schmidt supervised the research project, discussed the findings, and reviewed the manuscript.

Energy and AI 20 (2025) 100493

Contents lists available at ScienceDirect

Energy and AI

journal homepage: www.elsevier.com/locate/egyai

Physics-constrained transfer learning: Open-circuit voltage curve reconstruction and degradation mode estimation of lithium-ion batteries

Tobias Hofmann [a,b,*], Jacob Hamar [b], Bastian Mager [b], Simon Erhard [b], Jan Philipp Schmidt [a]

[a] Chair of Systems Engineering for Electrical Energy Storage (SysEE), University of Bayreuth, Bavarian Center for Battery Technology (BayBatt), Universitätsstraße 30, Bayreuth, 95447, Bavaria, Germany
[b] BMW Group, Petuelring 130, Munich, 80809, Bavaria, Germany

HIGHLIGHTS

- TCN-LSTM models accurately estimate DMs and OCV from partial charging voltage segments.
- Integrating the mechanistic model physically constrains the output.
- Transfer learning adapts models effectively across different cell types.
- Extensive testing across diverse use cases verifies model robustness.
- A single aging path suffices to fine-tune the models with high accuracy.

GRAPHICAL ABSTRACT

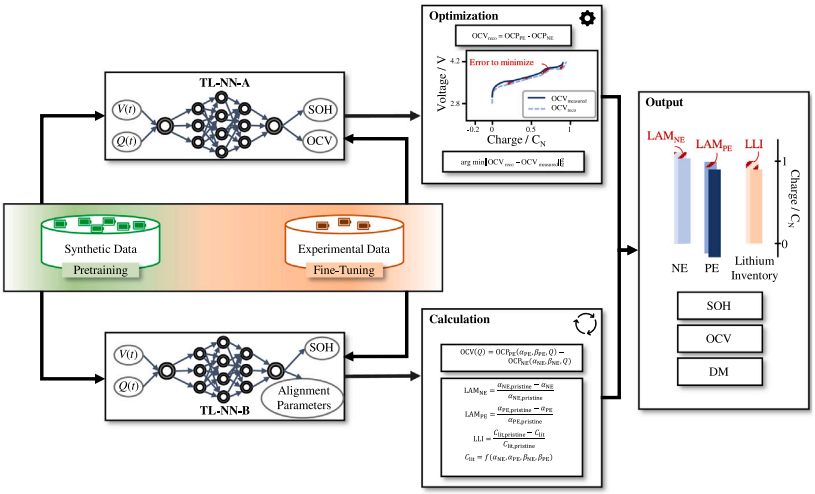

ARTICLE INFO

Keywords:
Lithium-ion battery
State of health estimation
Transfer learning
Degradation modes
Mechanistic model

ABSTRACT

Open-circuit voltage (OCV) updates are the key to accurate state of charge (SOC) estimates over lifetime. Degradation modes (DM) are directly coupled to OCV estimation. They offer a more detailed analysis of the battery's state of health (SOH) and yield optimized usage strategy, and with that, a prolonged lifetime. In this study two data-driven models are coupled with physics-based models and compared in regards of their OCV and DM estimation accuracy: Two temporal convolutional — long short-term memory neural networks (TCN-LSTM) are trained from synthetic NCA-graphite battery data for OCV curve estimation (model 1) and alignment parameter estimation (model 2). Both models are fine-tuned with varying amounts of experimental NMC-graphite battery data during the transfer learning (TL) step. In the subsequent physics-constraining part the DMs are derived via optimization (model 1), i.e., fitting the OCV with half cell open-circuit potentials, or

* Corresponding author at: Chair of Systems Engineering for Electrical Energy Storage (SysEE), University of Bayreuth, Bavarian Center for Battery Technology (BayBatt), Universitätsstraße 30, Bayreuth, 95447, Bavaria, Germany.
E-mail address: tobias1.hofmann@uni-bayreuth.de (T. Hofmann).

https://doi.org/10.1016/j.egyai.2025.100493
Received 27 September 2024; Received in revised form 6 February 2025; Accepted 3 March 2025
Available online 14 March 2025

directly via mathematical equations (model 2). Both models prove that fine-tuning data from one aging path suffices, if it includes the maximum appearing DMs of the target domain. For these use cases both models maintain OCV mean absolute errors (MAEs), DM MAEs and SOH mean absolute percentage errors (MAPEs) under 10 mV, 3.10 % and 1.98 %, respectively. The model 2 has less computational complexity and reaches slightly better results but requires labeled target data including alignment parameters for its application. This study shows that synthetic data is eligible for TL, even for varying cell chemistries, and that the mechanistic model helps to physically constrain the output.

1. Introduction

In recent years the new registrations of battery electric vehicles (BEVs) have rapidly increased [1]. With that, more used BEVs are available on the aftermarket, where customers are especially interested in the SOH. The SOH is the currently available energy relative to its value at begin of life (BOL). The definition is usually simplified to the currently available capacity relative to its pristine value [2]. The battery is the most costly component of BEVs and, hence, it heavily defines the residual value. The SOH, however, is not only important when selling a BEV but rather mandatory over the whole vehicle lifetime to allow accurate SOC or remaining range estimations, efficient operation and healthy charging. OCV updates for BEVs, unfortunately, have not yet been well documented or reached a sufficient state of the art. Knowledge about the OCV, however, is crucial and the backbone of accurate state estimation. Due to its aging-path-dependent variation, maintaining high OCV reconstruction accuracy is challenging [3,4]. It, additionally, allows the calculation of DMs [5], which help to realize adaptive, aging-path-individual, usage strategies. Such counteractions may help to, e.g., reduce the time at high storage SOCs which prevents the battery from further triggering a specific DM and might lead to a knee point [6].

Throughout this research paper, we refer to the simplified SOH definition as the currently available capacity $Q(t)$ in relation to the available capacity in its initial state $Q(t_0)$, as given in

$$\mathrm{SOH}(t) = \frac{Q(t)}{Q(t_0)}. \tag{1}$$

The automotive industry has long sought effective data-driven approaches to estimate battery SOH. Recent advancements [7–13] in data-driven SOH estimation have shown promising results. Bockrath et al. [8], for example, used a TCN to estimate SOH from raw partial constant-current discharge segments, achieving an SOH root mean squared error (RMSE) of 1.0 % for the NASA dataset. Costa et al. [9] extended the field to include DM estimation using a convolutional neural network (CNN) with synthetic data, achieving an RMSE of 2 % for all DMs of interest. Yet, a key challenge remains: Determining the OCV, and consequently DMs, over the lifetime of non-synthetic battery data still requires costly and time-consuming aging experiments to parametrize these aging models, making it difficult to keep pace with the rapid development cycles of new battery generations. Novel approaches for OCV reconstruction from real-world charging events are sought more than ever. TL allows the usage of pretrained models and adopting them to small target datasets. There has been a significant increase in publications [14–26] exploiting TL for SOH, DM, or OCV estimation: Yao and Han [14] explored the influence of different aging paths in a CNN-TL model, achieving an SOH RMSE of 2.2 %. Zhou et al. [15] extended TL-based OCV reconstruction to other cell chemistries, achieving SOH RMSEs 0.47 % and 2.73 % for nickel cobalt aluminium oxide (NCA) and lithium iron phosphate (LFP) cells, respectively. Hofmann et al. [17] demonstrated that TL from synthetic data is possible across different cell chemistries with a mean absolute error (MAE) of 12 mV for OCV reconstruction and a mean absolute percentage error (MAPE) of 1.1 % for SOH. On the other hand, optimization models based on mechanistic approach [5] only require pristine measurements but are heavily limited by the input data's precision requirements [5,27–32].

The combination of data-driven and physics-based models is a promising research avenue to reduce data requirements and integrate physical constraints [33–41]. Liang et al. [34], for example, have merged two machine learning (ML) models and weighted their output based on a nonlinear optimization result. They have used time-series data from battery charging as an input for two models that both output the SOH. During the training phase an optimization process yielded the weights of each SOH estimate. The final estimated SOH reached a RMSE below 1 % but required full charging cycles to deploy. Tian et al. [25] have used partial charging voltage curves at 1C as an input for a CNN model that estimated the alignment parameters which directly yield the DMs, as well as the OCV curve. Their supervised learning approach required labels which were generated via optimization, i.e., minimizing the difference between reconstructed and measured OCV in repetitive checkups of aging tests. The RMSE of the reconstructed OCV from the CNN model remained below 15 mV.

Reviewing the state of the art, we identify a research gap in the field of physics-constrained ML for OCV curve reconstruction and DM estimation. While substantial progress has been made in the field of TL for SOH [34] and OCV estimation [17,25], there remains a gap in the integration of TL with physics-based optimization models for real-world applications. Existing studies treat TL and optimization separately, missing the opportunity to leverage the strengths of both approaches in a combined framework. Especially the usage of synthetic data for DM estimation has not been reported before. We present a novel approach that directly couples TL with optimization, leveraging the strengths of both methods. Our model uses a TCN-LSTM architecture to estimate the OCV curve from partial charging segments, followed by an optimization step to refine the OCV and calculate DMs. By pretraining our TL model with high-quality synthetic data and fine-tuning with minimal experimental data, we significantly reduce the data requirements and associated costs of aging experiments. The inclusion of an optimization step based on the mechanistic model ensures that the estimated OCV and DMs are physically consistent and accurate, addressing a key limitation of purely data-driven approaches. This approach is compared to an alternative path that uses the same architecture to directly estimate the alignment parameters, and from that reconstruct the OCV. Our approach is validated across different UCs, demonstrating its versatility and potential for real-world applications, including scenarios with limited and noisy data. In summary, our work bridges the gap between data-driven TL models and physics-based optimization, providing a robust and efficient solution for SOH and OCV estimation that is both data-efficient and physically consistent.

To our knowledge this is the first study to directly couple synthetic data, ML and optimization for OCV curve reconstruction and DM estimation. By comparing various model architectures and UCs we are able to evaluate the individual strengths of model parts and data requirements. The incorporation of synthetic data as the source domain for TL yields low data requirements, allows rapid reduction in aging experiment costs and development time for model parametrization. The inclusion of the optimization, based on the mechanistic model

approach, however, integrates physical constraints and improves battery state estimation. Furthermore, the training of neural networks necessitates a large number of data points, which are often unavailable in the early stages due to cost and time constraints associated with aging experiments. By supplementing limited experimental data with synthetic data that mirrors physical behavior, these limitations can be overcome. This paper specifically investigates the utility and boundaries of synthetic data in this context by addressing key questions such as the optimal ratio of synthetic to real data, the required similarity between synthetic and real data, and the feasibility of extrapolation.

2. Theory

The combination of simulation, ML and optimization allows the generation of mass data, learning from that data and finally fusing the output with physico-chemical information from pristine half-cell potential curves. Hence, we introduce the basics of the used simulation toolbox (mechanistic model), the ML framework (TL) and the optimization (OCV reconstruction). For a more detailed description of the mechanistic model, TL, and optimization, we refer to previous publications [17,27]. While our prior work [17] established the theoretical foundation for the neural networks (NNs) and TL techniques used, this section introduces the novel aspects of our approach. Specifically, we emphasize the integration of the OCV model with the calculation of DMs through mathematical optimization. This unique combination ensures both accuracy and physical consistency in OCV and DM estimations. Nevertheless, the essential theoretical basics are briefly reintroduced for completeness.

2.1. Mechanistic model for battery data generation

Dubarry et al. [5] have introduced the mechanistic model approach as a simplification for battery degradation which breaks down the complex mechanisms to relative shifts and scalings between the open-circuit half-cell potential curves of the negative electrode (NE) $\mathrm{OCP_{NE}}$ and positive electrode (PE) $\mathrm{OCP_{PE}}$. These relative shifting and scaling can be determined by the alignment parameter set ϑ which is the set of scaling α_{NE}, α_{PE} and shifting parameters β_{NE}, β_{PE}. The resulting OCV is the difference between the positive and the negative open-circuit half-cell potential curve within its voltage boundaries

$$\begin{aligned}\mathrm{OCV}(Q) &= f(\mathrm{OCP_{NE}}, \mathrm{OCP_{PE}}, \vartheta, Q)\\ &= \mathrm{OCP_{PE}}(\alpha_{\mathrm{PE}}, \beta_{\mathrm{PE}}, Q) - \mathrm{OCP_{NE}}(\alpha_{\mathrm{NE}}, \beta_{\mathrm{NE}}, Q)\end{aligned} \tag{2}$$

where Q is the charge throughput. Eq. (2) can be applied to higher C-rates by exchanging the open-circuit half-cell potential curves with half-cell potential curves gathered at the desired C-rates. This implies that Eq. (2) transforms to

$$\begin{aligned}\mathrm{V}_{x\mathrm{C}}(Q) &= f(\mathrm{P_{NE,xC}}, \mathrm{P_{PE,xC}}, \vartheta, Q)\\ &= \mathrm{P_{PE,xC}}(\alpha_{\mathrm{PE}}, \beta_{\mathrm{PE}}, Q) - \mathrm{P_{NE,xC}}(\alpha_{\mathrm{NE}}, \beta_{\mathrm{NE}}, Q)\end{aligned} \tag{3}$$

with the half-cell potential curves $\mathrm{P_{NE,xC}}$, $\mathrm{P_{PE,xC}}$ at a given C-rate xC. Simulation toolboxes, e.g., the alawa-toolbox [5], exploit this theory to generate synthetic voltage charging curves at arbitrary degradation states (via ϑ) and C-rates (via xC).

The alignment parameter set ϑ directly transfers to the physico-chemical DMs with the following formula: The loss of active material (LAM) is the lost electrode capacity in relation to its pristine state.

$$\mathrm{LAM_{NE}} = \frac{\alpha_{\mathrm{NE,pristine}} - \alpha_{\mathrm{NE}}}{\alpha_{\mathrm{NE,pristine}}} \tag{4}$$

$$\mathrm{LAM_{PE}} = \frac{\alpha_{\mathrm{PE,pristine}} - \alpha_{\mathrm{PE}}}{\alpha_{\mathrm{PE,pristine}}} \tag{5}$$

The loss of lithium-inventory (LLI), however, is the lost cyclable lithium inventory, i.e., the superposition of both half-cell potential curves.

$$\mathrm{LLI} = \frac{C_{\mathrm{lit,pristine}} - C_{\mathrm{lit}}}{C_{\mathrm{lit,pristine}}} \tag{6}$$

The available lithium inventory C_{lit} demands a case-sensitive definition [27].

$$C_{\mathrm{lit}} = \begin{cases} (\alpha_{\mathrm{PE}} - \beta_{\mathrm{NE}} + \beta_{\mathrm{PE}}) \cdot C_{\mathrm{N}} & \text{, for } (\alpha_{\mathrm{PE}} - \beta_{\mathrm{NE}} + \beta_{\mathrm{PE}}) < \alpha_{\mathrm{NE}} \\ & \quad \wedge \ (\beta_{\mathrm{PE}} - \beta_{\mathrm{NE}}) \le 0 \\ (\alpha_{\mathrm{NE}}) \cdot C_{\mathrm{N}} & \text{, for } (\alpha_{\mathrm{PE}} - \beta_{\mathrm{NE}} + \beta_{\mathrm{PE}}) > \alpha_{\mathrm{NE}} \\ & \quad \wedge \ (\beta_{\mathrm{PE}} - \beta_{\mathrm{NE}}) \le 0 \\ (\alpha_{\mathrm{NE}} + \beta_{\mathrm{NE}} - \beta_{\mathrm{PE}}) \cdot C_{\mathrm{N}} & \text{, for } (\alpha_{\mathrm{NE}} + \beta_{\mathrm{NE}} - \beta_{\mathrm{PE}}) < \alpha_{\mathrm{PE}} \\ & \quad \wedge \ (\beta_{\mathrm{PE}} - \beta_{\mathrm{NE}}) \ge 0 \\ (\alpha_{\mathrm{PE}}) \cdot C_{\mathrm{N}} & \text{, for } (\alpha_{\mathrm{NE}} + \beta_{\mathrm{NE}} - \beta_{\mathrm{PE}}) > \alpha_{\mathrm{PE}} \\ & \quad \wedge \ (\beta_{\mathrm{PE}} - \beta_{\mathrm{NE}}) \ge 0 \end{cases} \tag{7}$$

2.2. Open-circuit voltage reconstruction via optimization

The mechanistic model approach can be used to reconstruct the OCV and determine the underlying DMs from either full or partial (pseudo) OCV measurements [28–30]. The process of this optimization workflow is displayed in Fig. 1. Fig. 1(a) shows the necessary input, namely the measured and normalized pristine electrode open-circuit potential (OCP) curves $\mathrm{OCP_{NE}}$ and $\mathrm{OCP_{PE}}$ and the measured and normalized $\mathrm{OCV_{measured}}$. Many different solvers can be used for optimization, with least-squares being the most prominent [42]. Boundaries, as stated in Eq. (8), should be set for improved performance [27]. Fig. 1(b) presents the optimization itself. The solver aims to find the optimum parameter set $\vartheta = [\alpha_{\mathrm{NE}}, \alpha_{\mathrm{PE}}, \beta_{\mathrm{NE}}, \beta_{\mathrm{PE}}]$ that minimizes the discrepancy between the measured $\mathrm{OCV_{measured}}$ and the reconstructed $\mathrm{OCV_{reco}}$. For every possible alignment parameter set, the reconstructed OCV is simply calculated by Eq. (2).

The final optimization problem states as follows

$$\begin{aligned}\vartheta_{\mathrm{est}} &= \arg\min_{\vartheta} \ ||\mathrm{OCV_{measured}}(Q) - \mathrm{OCV_{reco}}(Q)\ ||_2^2\\ &= \arg\min_{\vartheta} \ ||\mathrm{OCV_{measured}}(Q) - f(\mathrm{OCP_{NE}}, \mathrm{OCP_{PE}}, \vartheta, Q)\ ||_2^2\\ &\text{s.t.} \quad \vartheta \ge \mathrm{lb}\\ &\qquad \vartheta \le \mathrm{ub}\\ &\qquad f_{\mathrm{eq}}(\vartheta, \mathrm{OCV_{measured}}, \mathrm{OCV_{reco}}, ..) = 0\\ &\qquad f_{\mathrm{ineq}}(\vartheta, \mathrm{OCV_{measured}}, \mathrm{OCV_{reco}}, ..) \ge 0\end{aligned} \tag{8}$$

with lb and ub being the lower and upper boundaries, and $f_{\mathrm{eq}}(\vartheta, \mathrm{OCV_{measured}}, \mathrm{OCV_{reco}}, ..)$ and $f_{\mathrm{ineq}}(\vartheta, \mathrm{OCV_{measured}}, \mathrm{OCV_{reco}}, ..)$ as the equality and inequality constraints. The constraints can be any arbitrary functions that can be calculated from the available input. Fig. 1(c) finally visualizes the output of the method, based on the reconstructed OCV, including the SOH which is the available charge throughput within the voltage limits in comparison to its pristine values, and the DMs. With the help of Fig. 1(c) the DMs can be interpreted visually: The LAM is the decreased length of the electrode capacities and the LLI is the reduction in the overlapping section of both electrodes. Mathematically, Eqs. (4) to (7) are used to determine the DMs.

2.3. Transfer learning for battery state of health estimation

Supervised learning with NNs for battery state estimation, including SOH and DMs, and OCV reconstruction was extensively studied in available literature [7–13,15]. Supervised learning methods, however, rely on huge labeled training data, which are rare for the battery use case. For conventional methods, the training data must be representative for the target data, which further reduces suitable data. TL with NNs relaxes the strict requirements for training data.

In the context of TL, a domain $\mathcal{D}$ is formally defined as $\mathcal{D} = \{\chi, P(X)\}$, where χ represents the feature space and $P(X)$ denotes the edge probability distribution, with $X = \{x_1, \ldots, x_n\} \in \chi$ [17,43,44]. Similarly, a task $\mathcal{T}$ is defined as $\mathcal{T} = \{y, f(x)\}$, comprising the label space y and the target prediction function $f(x)$, which can also be

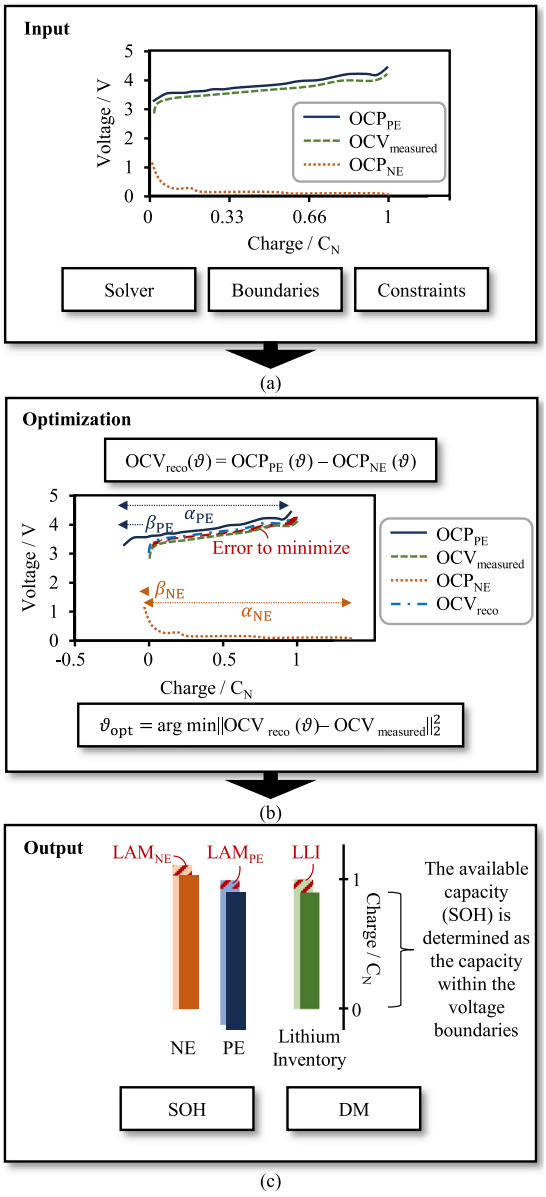

Fig. 1. Pipeline of OCV reconstruction via optimization. (a) Input, (b) Optimization, (c) Output.

interpreted as the conditional probability function $P(y \mid x)$ [17,43,44]. The number of samples within the source domain s and target domain t are given by N_s and N_t.

Definition 2.1 (*Transfer Learning*)**.** The goal of TL is to improve the performance of the predictive function $f_{\mathcal{T}}()$ for the primary learning task $\mathcal{T}_t$. This is achieved by leveraging the latent knowledge discovered from a supplementary learning task $\mathcal{T}_s$ and its associated data $\mathcal{D}_s$, where $\mathcal{D}_s \neq \mathcal{D}_t$ and/or $\mathcal{T}_s \neq \mathcal{T}_t$, typically with $N_s \gg N_t$ [17,43,44].

Several types of TL exist, whereas for our problem at hand, parameter-based TL in the context of model-based TL is the most promising [17, 33,44]. Parameter-based TL refers to methods with domain adaption, i.e., $\mathcal{D}_s \neq \mathcal{D}_t$. In parameter-based TL a model gets pretrained in the source domain and reuses its learned parameters in the target domain. This is realized by, e.g., partial freezing and/or fine-tuning [44]. Some layers of the NN keep their weights, while some layers, mostly the output layer(s) [44], adopt their weights during fine-tuning with a reduced learning rate and/or reduced epochs. It is important to only allow small modifications of the network to avoid catastrophic forgetting, which describes an overfitted model to the target domain which has lost its memory of the source domain [44].

2.4. Performance metrics

The accuracy of the developed methods in terms of SOH, DM or OCV is measured with the MAE and MAPE

$$\mathrm{MAPE} = \frac{1}{N}\sum_{i=1}^{N}\left|\frac{y_i - \hat{y}_i}{y_i}\right| \cdot 100\,\% \tag{9}$$

$$\mathrm{MAE} = \frac{1}{N}\sum_{i=1}^{N}|y_i - \hat{y}_i| \tag{10}$$

where y_i is the true label and $\hat{y}_i$ is the estimated label of sample i. The total number of samples is N. Both, the MAE and the MAPE, are given in percent. The MAPE is generally useful to compare the SOH estimation accuracy across varying degradation states, because the SOH in the used data never approaches zero, which would drastically bias the MAPE [45]. The MAE, on the other hand, works for near-zero estimates and does not show this bias. Hence, the MAE is used for DM estimation accuracy. For better interpretability, the MAE is selected for the OCV reconstruction accuracy. Note that the OCV error is only calculated at the overlapping sections of the estimated and real capacity range. Hence, the $\mathrm{MAE}_{\mathrm{OCV}}$ must always be interpreted together with the $\mathrm{MAPE}_{\mathrm{SOH}}$.

3. Materials and method

Our research compares two methods which both combine model-based TL with the mechanistic model approach, as can be seen in Fig. 2. The TL-NN-A builds upon our previous work [17] but extends the approach to correct the OCV via optimization which enables the estimations of DMs. The TL-NN-B, on the other hand, utilizes the same data but the prior TL model is trained to directly output the scalar values SOH and the alignment parameters. From these values it is directly possible to calculate the OCV curve without the subsequent optimization step from the first approach.

3.1. Data

In our study, we use simulation data from an automotive prismatic NCA-graphite cell with 70.2 Ah capacity. This specific choice allows us to maintain consistency with our previous work [17] and directly compare the results. Furthermore, our previous findings indicate that the selection of simulation data type has minimal impact on the outcomes, provided that essential characteristics such as gradient changes within the voltage slope and sufficient sample diversity are present. This reinforces the robustness of our TL approach across different cell chemistries and configurations. Simulation data for the source domain is generated by a physico-chemical mechanistic model toolbox. The simulation toolbox takes the DMs and a constant-current C-rate as input, and outputs the voltage curve, charge throughput during charging, OCV curve, charge throughput for the OCV curve, SOH, and DMs. For more details about the cell characteristics and the simulation we refer to our previous publication [17]. One of the key findings in our previous work [17] was that the source domain in TL should encompass a larger search space than the target domain. To fulfill this requirement for any possible output variable, we add additional simulation data to the source domain, including more aging paths and C-rates. We add the

Table 1
The experimental data, taken from Schmitt et al. [28], which includes ten identical cells without any pre-treatment. For each cell the aging condition as well as the final SOH, DM fade, charge throughput and experiment duration is given.

Cell	Aging condition	ΔSOH	ΔLAM_{NE}	ΔLAM_{PE}	ΔLLI	Charge throughput	Duration
A1	Cycling (2.5 V–4.2 V)	30 %	30 %	15 %	35 %	6610 Ah	433 d
A2	Cycling (2.5 V–4.2 V)	30 %	30 %	15 %	35 %	5900 Ah	348 d
B1	Cycling (2.5 V–4.0 V)	15 %	15 %	8 %	15 %	8720 Ah	486 d
B2	Cycling (2.5 V–4.0 V)	15 %	15 %	8 %	15 %	8630 Ah	486 d
C1	Cycling (3.6 V–4.2 V)	15 %	15 %	8 %	15 %	6700 Ah	489 d
C2	Cycling (3.6 V–4.2 V)	15 %	15 %	8 %	15 %	7400 Ah	486 d
D1	Cycling (WLTP)	25 %	25 %	15 %	30 %	5210 Ah	489 d
D2	Cycling (WLTP)	25 %	25 %	15 %	30 %	5740 Ah	483 d
E1	Storage (3.7 V)	10 %	8 %	2.5 %	10 %	1530 Ah	454 d
E2	Storage (3.7 V)	10 %	8 %	2.5 %	10 %	1690 Ah	486 d

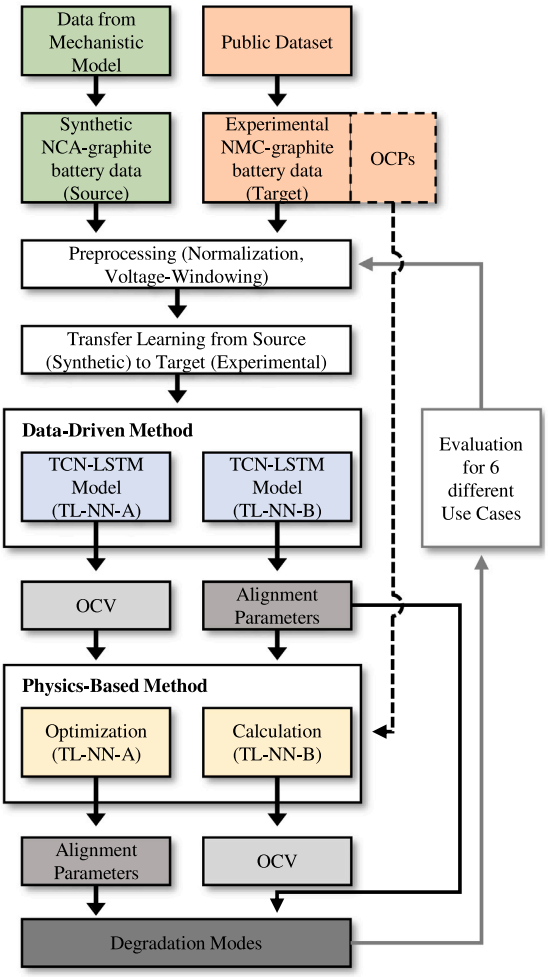

Fig. 2. Overview of the presented approach, from data generation and extraction to the coupling of data-driven and physics-based models.

C-rate of 3/2C to the simulation data, resulting in a total of seven C-rates: C/15, C/10, C/6, C/3, C/2, 1C and 3/2C. Besides that, we extend the aging path space by running simulations with each eight discrete steps in varying DMs. LAM is varied between 0 % and 40 %, while LLI is varied between 0 % and 60 %. In total 260 out of the possible 512 simulations are successful, due to constraints regarding the minimum voltage, and stored for later preprocessing. With these settings, the SOH ranges from 32.7 % to 100 % and in total $7 \cdot 260 = 1820$ samples are available.

The experimental data is taken from Schmitt et al. [28] and includes ten commercial INR18650 MJ1 nickel manganese cobalt oxide (NMC)-silicone/graphite cells with 3.35 Ah. As listed in Table 1, the cells were aged in five different scenarios. The aging test was performed for a total duration of maximum 489 d or until the cell surface temperature exceeded 60 °C at any time during the experiment. The operating ambient temperature during the experiment was set to 25 °C by a climate chamber. In the following we refer to the pseudo-OCV measurements as checkups, which took place during the reference performance test. The dataset not only includes the aging series of the ten cells, but also the pristine electrode potentials OCP_{NE} and OCP_{PE}. A pristine cell was opened within an argon-filled glove box and coin cells with lithium-metal counter-electrodes were built. The used OCPs within this study are constant-current measurements at C/90 and an ambient temperature of 25 °C [46,47]. Table 1 not only includes the aging condition but also the resulting SOH and DM fade in the final checkup. The SOH was calculated by a pseudo-OCV measurement with C/30. It is defined as the capacity throughput within the voltage limits from 3.25 V to 4.2 V during these checkups, in which 3.25 V is the highest minimum value during all pseudo-OCV measurements of all cells. As explained by Schmitt et al. [28] the minimum voltage value of the charging pseudo-OCV curve increases over time, i.e., with rising impedance. To allow comparable results, the pseudo-OCV, as well as the SOH, is defined within these limited voltage boundaries. Because the DMs were not available in the published data [28], we generate these labels via optimization and the pristine OCP curves of the electrodes. In every checkup, the OCV curve is known and can be used to map the OCPs to the OCV and generate the DM labels via Eq. (4) to (7). The cost function combines the OCV with the DVA and ICA fit, because this has been shown to increase accuracy [48]. We refer to the measured and reconstructed DVA and ICA with $DVA_{measured}$, DVA_{reco} and $ICA_{measured}$, ICA_{reco}, respectively. We use the scipy.optimize.minimize function with sequential least squares programming (SLSQP) and the default settings [49]. We exclude any additional constraints and solely pass upper and lower boundaries for the alignment parameter set ϑ. Hence, the optimization problem for one cell at iteration/checkup $i > 1$ is formulated as follows

$$\begin{aligned} \vartheta_{i,\text{est}} = \arg\min_{\vartheta} \Bigg(& x_1 \left\| \frac{\text{OCV}_{i,\text{measured}} - \text{OCV}_{i,\text{reco}}}{\max(\text{OCV}_{i,\text{measured}})} \right\|_2^2 \\ & + x_2 \left\| \frac{\text{DVA}_{i,\text{measured}} - \text{DVA}_{i,\text{reco}}}{\max(\text{DVA}_{i,\text{measured}})} \right\|_2^2 \\ & + x_3 \left\| \frac{\text{ICA}_{i,\text{measured}} - \text{ICA}_{i,\text{reco}}}{\max(\text{ICA}_{i,\text{measured}})} \right\|_2^2 \Bigg) \\ \text{s.t.} \quad & \vartheta_{i,\text{est}} \geq 0.8 \cdot \vartheta_{i-1,\text{est}} \\ & \vartheta_{i,\text{est}} \leq 1.1 \cdot \vartheta_{i-1,\text{est}} \end{aligned} \tag{11}$$

with x_1 (OCV), x_2 (DVA) and x_3 (ICA) being 10, 1 and 1, respectively. These values were motivated by literature findings [48] and manually optimized to reach the lowest possible error. The components of the cost function are normalized to values below one for better interpretability of the weighting factors. The optimization runs for every cell individually and sets the boundaries depending on the last

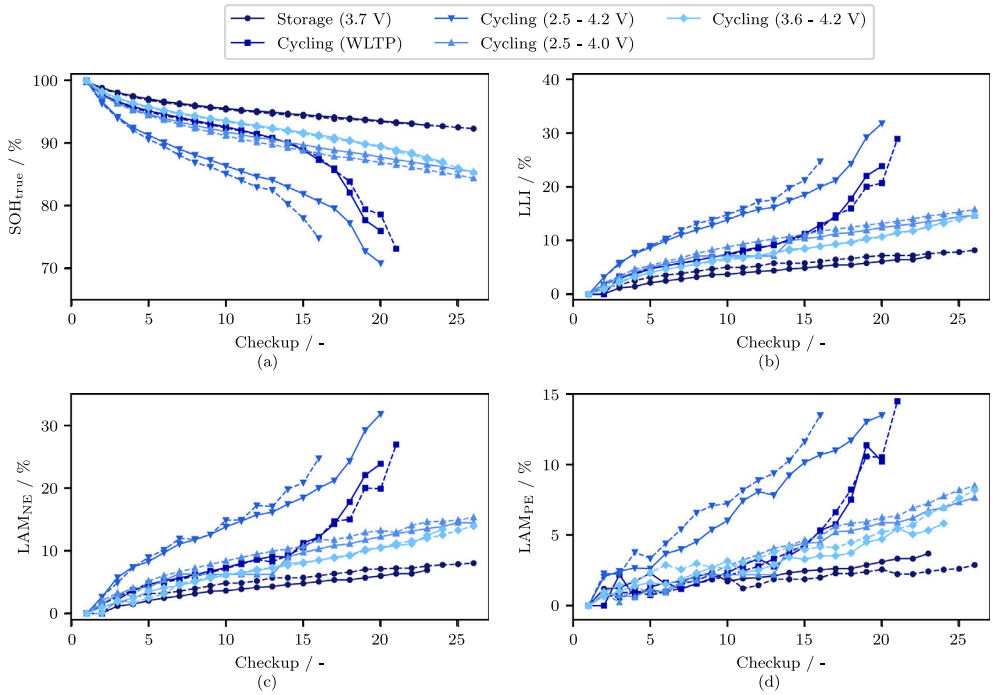

Fig. 3. The measured SOH (a) and estimated DMs ((b) LLI, (c) LAM_{NE}, (d) LAM_{PE}) from the OCV reconstruction of the experimental data.

iteration. The initial value is set to the optimization result from the previous iteration. For the initial run, the values for ϑ_0 are set to $[1.02, 1.14, -0.04, -0.14]$. The MAE_{OCV} stays below 3 mV for all samples along lifetime. The results of all checkups from all cells in regard to SOH and DMs is visualized in Fig. 3. One checkup took place approximately every 19 d. Each aging path includes two cells which mainly show very similar DMs over lifetime. All curves show good agreement with the visualized DMs in the publication by Schmitt et al. [28]. Note that they did not plot the DMs from checkups with a SOH below 80 %. As can be seen in Fig. 3(a), the partial cycling in the upper and lower region result in almost the same DMs at the final checkup. During the cycling, however, the cells cycled in the lower voltage region have shown higher degradation. Degrading the cell with full cycles lead to the highest degradation with a final SOH of approximately 70 %. The underlying DMs are higher than for any other aging condition. The WLTP cycling reaches similar DMs in the final checkup but showed a latter knee-point [6] after 15 checkups. In early checkups the cells behaved similar to those from the lower cycling phase. To analyze the influence of the checkups, a calendaric aging phase was conducted with cells stored at 3.7 V, 25 °C and the whole duration of the experiment (486 days) [28]. As expected, this aging phase has shown the least degradation and the SOH stays above 90 % for all checkups.

3.2. Method

The method overview is given by Fig. 2. Two models are developed with the same final output: The OCV, SOH and DMs. TL-NN-A directly estimates the OCV curve and feeds its output to an optimizer which fits the OCPs into the OCV curve to update its estimation and calculate the DMs. TL-NN-B does not require an optimization step because it estimates the alignment parameters. With these alignment parameters and the help of Eq. (2) and Eqs. (4) to (7) it is possible to calculate the OCV curve and also the DMs. Hence, the TL-NN-B approach offers an opportunity with less computational but stricter data requirements due to the explicit mandatory knowledge over all DMs.

Table 2
Selected voltage windows from the simulation and experimental data during preprocessing.

	V_{min}	V_{max}		V_{min}	V_{max}
Exp. Data	3.25 V	3.8 V	Sim. Data	2.8 V	3.8 V
	3.4 V	4.0 V		3.0 V	4.0 V
	3.6 V	4.1 V		3.2 V	4.1 V
	3.8 V	4.2 V		3.4 V	4.25 V
				3.6 V	
				3.8 V	

Table 3
Data size and input/output relation of both models. The estimated alignment parameters from TL-NN-B are reduced to $\vartheta_{reduced}$, consisting of three values α_{NE}, α_{PE} and $\beta_{NE} - \beta_{PE}$ because these values include the same information but final complexity is reduced.

Signal	Dimension	TL-NN-A	TL-NN-B
$Q_{partial}(t)$	$\mathbb{R}^{<1\times100>}$	Input	Input
$V_{partial}(t)$	$\mathbb{R}^{<1\times100>}$	Input	Input
$I(t)$	$\mathbb{R}^{<1\times100>}$	Input	Input
$Q_{OCV}(t)$	$\mathbb{R}^{<1\times100>}$	$Output_{TL}$	$Output_{PB}$
		$Output_{PB}$	
$OCV(t)$	$\mathbb{R}^{<1\times100>}$	$Output_{TL}$	$Output_{PB}$
		$Output_{PB}$	
SOH	$\mathbb{R}^{<1\times1>}$	$Output_{TL}$	$Output_{TL}$
		$Output_{PB}$	$Output_{PB}$
DMs	$\mathbb{R}^{<1\times3>}$	$Output_{PB}$	$Output_{PB}$
$\vartheta_{reduced}$	$\mathbb{R}^{<1\times3>}$		$Output_{TL}$
ϑ	$\mathbb{R}^{<1\times4>}$	$Output_{PB}$	

Both models process the same source and target domain. The data undergoes preprocessing which includes voltage windowing to later access the sensitivity of the models. The voltage windows are selected as in Table 2. Due to a larger voltage span in the simulation data, we extend the possible minimum voltages for this data. With these sampling, one simulation sample results in 23 windowed samples and one experimental sample in 15 windowed samples, respectively. In total, we

thus create 1820·23 = 41860 simulation data samples and 726·15 = 10890 experimental data samples. Both datasets are individually normalized to lie in a range between zero and one. The data structure can be accessed in Table 3. In Table 3 $\text{Output}_{\text{TL}}$ refers to the output of a TL model and $\text{Output}_{\text{PB}}$ is the estimated physics-based value, either from the optimization model (TL-NN-A) or the calculated output via Eqs. (2) and (4) to (7) (TL-NN-B). The information loss between describing the alignment parameters as three instead of four variables is zero because the absolute value for β_{NE} can be accessed as the distance between the first value of the OCP_{NE} curve and the minimum voltage of the full cell OCV curve. As shown in Table 3, both models utilize the same input from the partial charging segment: $Q_{\text{partial}}(t)$, $V_{\text{partial}}(t)$, and $I(t)$. The NN models are designed to process raw time-series signals without the need for feature processing or dimensionality reduction. The data-driven section of TL-NN-A directly generates the full OCV curve $Q_{\text{OCV}}(t)$ and $\text{OCV}(t)$, from which the SOH can be determined as the maximum charge throughput between the voltage limits. In the subsequent optimization step, TL-NN-A again outputs the full OCV curve $Q_{\text{OCV}}(t)$ and $\text{OCV}(t)$ along with the SOH. Additionally, this step allows for the calculation of DMs using the alignment parameters ϑ. Conversely, the data-driven section of TL-NN-B directly provides the SOH value and the reduced alignment parameters $\vartheta_{\text{reduced}}$. Through simple analytical equations, the complete TL-NN-B model can then compute the full OCV curve $Q_{\text{OCV}}(t)$ and $\text{OCV}(t)$, as well as the DMs.

The study at hand determines the minimum requirements for fine-tuning data necessary for adequate generalization. Hence, six different UCs, as defined in Fig. 4, are introduced. In Fig. 4, the experimental data is categorized for each cell along with its respective aging path (compare with Table 1) and the applied C-rates during the checkups. In Sub Fig. 4(g), the simulation data only shows the applied C-rates and the division for pretraining. During pretraining, the objective is to learn as much as possible from the source domain. Consequently, except for the data at C/6 and C/3, the simulation data is directly used for training.

The UCs are separated into three categories (UC1, UC2 and UC3) which differ in the included aging path for the fine-tuning. In every category itself, the B UCs (Fig. 4(b), (d), (f)) aggravate the TL process by reducing the fine-tuning data even further in regards to the included C-rate. UC1A and UC1B (Fig. 4(a), (b)) include cells from aging path A (Cycling (2.5 V–4.2 V)), D (Cycling (WLTP)) and E (Storage (3.7 V)). Comparing with Table 1, it gets clear that these fine-tuning data, aging path A and D, show the highest degradation in terms of SOH and DMs and, hence, will be the easiest to apply TL. Fine-tuning data in UC2A and UC2B (Fig. 4(c), (d)) reduces to aging path A, which again shows the highest degradation and should allow successful TL. On the other side, UC3A and UC3B (Fig. 4(e), (f)) only include fine-tuning data from aging path B (Cycling (2.5 V–4.0 V)), which only shows a 15 % SOH drop. Hence, UC3A and UC3B are the most challenging tasks because their fine-tuning data from aging path B roughly shows half the degradation of aging path A.

As outlined in Fig. 2, the prior model is a NN that either estimates the OCV curve (TL-NN-A) or directly estimates the alignment parameters (TL-NN-B). It is impossible to try every possible combination of available NN architectures to find the optimum. It is more efficient to tune the hyperparameters of a predefined architecture that has been shown to be advantageous for the given application in available literature [7,8,17,50–53]. TCNs have been found to be effective for time-series modeling as they can automatically extract relevant features from raw data [54]. Several studies have demonstrated the effectiveness of TCNs for SOH estimation [7,8,17,50–53]. In this work, we propose a hybrid approach that combines TCN layers as a feature extractor with subsequent LSTM layers as a feature interpreter. This approach is supported by previous research showing the mutual benefits of combining CNN with LSTM, and even TCN with LSTM [17,18,50,55]. The optimum hyperparameters are found via

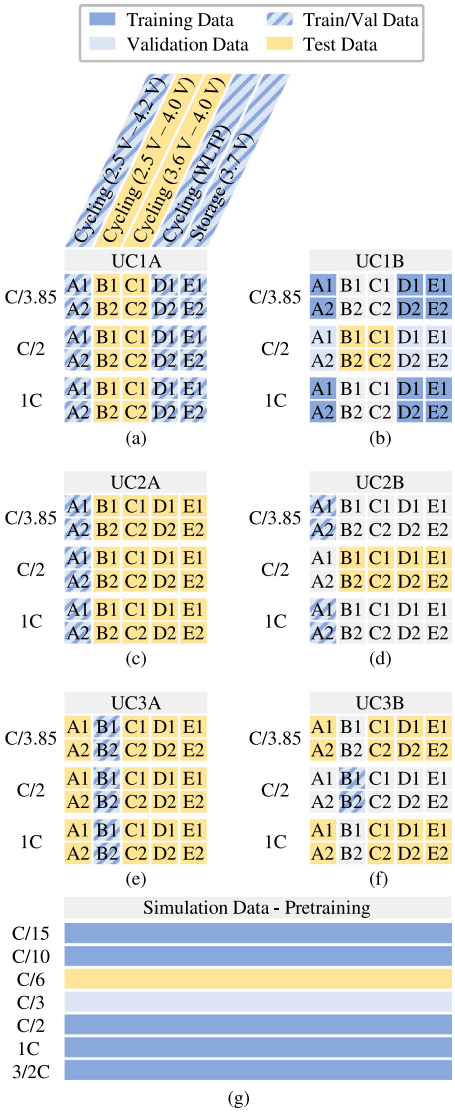

Fig. 4. Definition of use cases including data split for model training, validation and testing. (a) UC1A including the description of the relation between cell and the respective aging path, (b) UC1B, (c) UC2A, (d) UC2B, (e) UC3A, (f) UC3B, (g) simulation dataset used for pretraining. The used training data within each UC is displayed in dark blue, whereas the validation data is light blue. Both, training and validation data, are used for fine-tuning. The test data is yellow and if the data is excluded it is pictured white.

Bayesian optimization. Bayesian optimization is the state-of-the-art hyperparameter tuning method because it allows the exploration of large search spaces and the exploitation of promising valleys while being very efficient [17,56]. Bayesian optimization minimizes the required trials to find the optimum hyperparameter set because a surrogate model prunes unpromising directions and hence shrinks the search space continuously [17,56]. In this study, the KerasTuner [57] is used to optimize the NNs. Two different NNs, TL-NN-A and TL-NN-B, each adopted for six different UCs, are developed. The architecture tuning is limited to the source domain. The search space, however, stays consistent for every tuning operation and is listed in Table 4. In Table 4, for any hyperparameter λ for any layer N the possible set of values

Table 4
Search space for Bayesian hyperparameter tuning, where N refers to the layer number and λ is a hyperparameter that belongs to the set of possible hyperparameters Λ. Hence, for every additional TCN or LSTM layer, the respective hyperparameters can be tuned individually.

Hyperparameter	Definition
TCN layers	$\lambda_{\text{TCN}} \in \Lambda_{\text{TCN}}$ with $\Lambda_{\text{TCN}} := \{\lambda_{\text{TCN}} \in \mathbb{N}; 1 \leq \lambda_{\text{TCN}} \leq 3\}$
Kernel Size	$\lambda_{\text{K},N} \in \Lambda_{\text{K}}$ with $\Lambda_{\text{K}} := \{\lambda_{\text{K}} \in \mathbb{N}; 1 \leq \lambda_{\text{K}} \leq 8\}$
Filter Size	$\lambda_{\text{F},N} \in \Lambda_{\text{F}}$ with $\Lambda_{\text{F}} := \{\lambda_{\text{F}} \in \mathbb{N}; 8 \leq \lambda_{\text{F}} \leq 128\}$
LSTM layers	$\lambda_{\text{LSTM}} \in \Lambda_{\text{LSTM}}$ with $\Lambda_{\text{LSTM}} := \{\lambda_{\text{LSTM}} \in \mathbb{N}; 0 \leq \lambda_{\text{LSTM}} \leq 2\}$
Units	$\lambda_{\text{U},N} \in \Lambda_{\text{U}}$ with $\Lambda_{\text{U}} := \{\lambda_{\text{U}} \in \mathbb{N}; 8 \leq \lambda_{\text{U}} \leq 128\}$
Dropout	$\lambda_{\text{D},N} \in \Lambda_{\text{D}}$ with $\Lambda_{\text{D}} := \{\lambda_{\text{D}} \in \mathbb{D}; 0 \leq \lambda_{\text{D}} \leq 0.5\}$

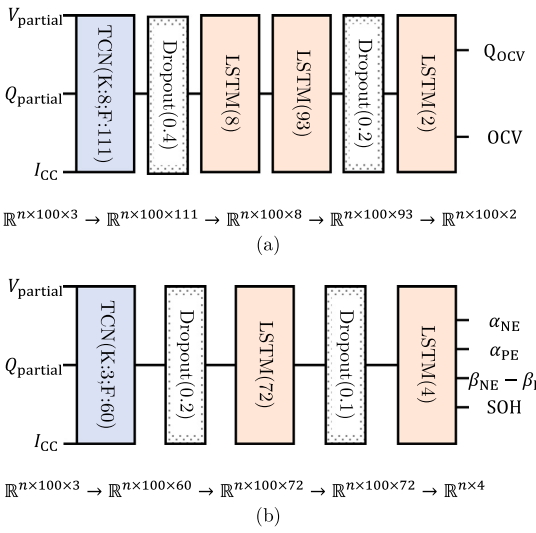

Fig. 5. Architecture of the optimized model for DM and SOH estimation, where (a) is the TL-NN-A and (b) is the TL-NN-B. In the TCN layers, K represents the kernel size and F the filter size.

is given by Λ. For any hyperparameter not listed in Table 4, we use the default parameter. Additionally, the models must end with a LSTM-layer which matches the output dimensions, i.e., two units for TL-NN-A and four units for TL-NN-B. All training run with the Adam optimizer [58]. The tuning process runs for 100 iterations with 60 initial points, a batch size of 128 and a maximum number of 500 epochs on a NVIDIA L4-2Q with 8 GB dedicated memory. One trial runs as long as the validation loss does not decrease for 50 consecutive epochs. Both TL-NNs use the data at C/3 from the simulation data as the validation data, the C/6 curves as the test data and the remaining simulation data serves as the training data. After successful tuning, the base TL-NNs are trained with the full simulation data in order to reach the optimum knowledge transfer. During this base-training process, 33 % of the simulation data are excluded from the training data and rather used as the validation data. The final architectures for the base transfer learned neural network (TL-NN)s are displayed in Fig. 5. Both the TL-NN-A (Fig. 5(a)) and TL-NN-B (Fig. 5(b)) show similar complexity. The TL-NN-A includes one more LSTM layer and the TL-NN-B reduces the dimension in the last LSTM layer to match the final output.

In this work, we employ a TL approach to leverage the knowledge gained from the source domain for the target domain. Specifically, we utilize a fine-tuning strategy with a reduced learning rate, which is a type of parameter-based TL. The parameter-based TL approach belongs to the broader category of model-based TL, which in turn is a sub-category of domain adaptation TL [44]. Given that our source and target domains are different while the task remains the same, parameter-based TL is optimal for our problem. Within parameter-based TL, the two primary options are partial freezing and fine-tuning. We choose fine-tuning because it allows for adjustments throughout the network, which can lead to improved performance. This approach has also been successfully employed in other studies, such as those by Yao and Han [14] and Zhou et al. [15], where fine-tuning yielded positive results. The rationale behind this hierarchical TL strategy is that the source and target domains are highly similar. Both datasets are obtained from battery cells with a similar chemistry (NCA-graphite vs. NMC-silicone/graphite), and the input and output data, as well as the underlying patterns, are analogous across the two domains. Prior literature has shown the effectiveness of TL techniques in such scenarios [15,17–20]. By employing the fine-tuning approach with a reduced learning rate, we can capitalize on the similarities between the source and target domains, while minimizing the need for extensive retraining or architectural changes. This TL strategy allows the model to effectively leverage the knowledge gained from the source domain to improve the performance on the target task, which is crucial for the practical deployment of the proposed approach. The fine-tuning process runs for a maximum of 1000 epochs with a learning rate of 1×10^{-5} and the early stopping criterion being 20 consecutive epochs without a decrease in the validation loss. A detailed overview, including the final performed epochs during fine-tuning, can be found in the Appendix A, Table A.7.

As can be seen in Fig. 2 the output of the TL models are later fed into an optimization model (TL-NN-A) or directly into equations (TL-NN-B) to calculate the DMs. The OCV curve from TL-NN-A is optimized via OCP fitting and the optimization problem defined in Eq. (11). The same procedure, as for generating the ground-truth labels of the experimental data, is followed for OCV fitting: In the first iteration for one cell, the pristine, ideal alignment parameters $\vartheta_{\text{ini}} = [1.02, 1.14, -0.04, -0.14]$ are set as the initial value with the upper and lower boundary being $0.8 \cdot \vartheta_{\text{ini}} \leq \vartheta_1 \leq 1.1 \cdot \vartheta_{\text{ini}}$. Every succeeding iteration/checkup assumes the prior solution as the initial value and allows the same variation as in the initial run. Because TL-NN-B directly estimates the alignment parameter set ϑ, Eqs. (4) to (7) are enough to calculate the OCV curve and the DMs.

4. Results and discussion

This work investigates the advantages of combining synthetic data with ML and the mechanistic model approach. Especially, the undergone study answers the question about which coupling is the most beneficial for accurate SOH, DM and OCV curve estimation from partial charging voltage segments. Guidelines for the mandatory experiments required to fine-tune pre-trained NNs are derived by defining varying UCs with reduced experimental fine-tuning data for the prior TL models, as shown in Fig. 4.

4.1. Benchmark

Table 5 offers an overview of the models' performance for the respective complete test data, regarding to Fig. 4. From Table 5 it can be seen at first glance that both TL models perform with comparable accuracy. The computationally less complex TL-NN-B, however, performs slightly better, especially in terms of DM accuracy.

4.1.1. Use case 1

Both models achieve high accuracy for UC1A: The MAE_{OCV} stays below 8 mV and the MAPE_{SOH} below 1.2 %. While LLI is also estimated with high accuracy, the LAM_{NE} shows MAEs up to 2.48 % for the

Table 5
Performance comparison of TL-NN-A and TL-NN-B for different UCs and their complete test data. The UCs differ in the amount of training data for the training/fine-tuning process.

		$MAPE_{SOH}$	MAE_{OCV}	$MAE_{LAM\text{-}NE}$	$MAE_{LAM\text{-}PE}$	MAE_{LLI}
UC1A	TL-NN-A	1.16 %	7.55 mV	2.48 %	2.13 %	0.82 %
	TL-NN-B	0.96 %	5.83 mV	0.97 %	0.73 %	0.81 %
UC1B	TL-NN-A	3.67 %	15.8 mV	2.57 %	3.81 %	2.80 %
	TL-NN-B	2.62 %	14.0 mV	2.41 %	1.17 %	2.36 %
UC2A	TL-NN-A	1.17 %	8.21 mV	2.83 %	2.03 %	0.97 %
	TL-NN-B	1.21 %	7.23 mV	1.40 %	0.61 %	1.11 %
UC2B	TL-NN-A	4.06 %	19.2 mV	3.22 %	3.71 %	3.43 %
	TL-NN-B	3.13 %	18.8 mV	2.99 %	1.55 %	3.29 %
UC3A	TL-NN-A	1.86 %	10.2 mV	2.97 %	2.27 %	1.21 %
	TL-NN-B	1.54 %	12.4 mV	1.28 %	1.26 %	1.27 %
UC3B	TL-NN-A	5.00 %	31.9 mV	5.49 %	3.78 %	5.24 %
	TL-NN-B	4.97 %	32.7 mV	5.06 %	4.18 %	4.16 %

TL-NN-A model. Due to less fine-tuning data in UC1B, the performance worsens for both models and the MAE_{OCV} rises above 15 mV. Obviously, due to a lower LAM_{PE} estimation accuracy, also the $MAPE_{SOH}$ is worse for TL-NN-A. Fig. 6 and Fig. B.14 (in Appendix B.1) offer a more detailed analysis in regards to varying input voltage windows. Interestingly, both models barely show any voltage-window-dependency. There is a slight tendency towards lower voltage segments, as discussed in our previous work [17]: Cells with graphite anodes show the highest gradient of their OCP during the begin of charge of the full cell, as can be seen in Fig. 1(a). This gradient is detectable in the full cell voltage response during constant-current charging and, hence, allows to estimate the anode degradation. On the other side, upper voltage segments only include one detectable change of gradient due to the anode. In some cases this is not only difficult to distinguish from the cathodic gradient changes but further does not include as much information as the gradient changes in the lower voltage segment. Even with very limited input data, i.e., a partial charging curve from 3.8 V to 4.0 V, the MAE_{OCV} stays below 10 mV and the DMs are estimated with adequate accuracy. This behavior drastically changes for UC1B: With limited fine-tuning data, the voltage-window-dependency increases. While segments from the lower range still achieve comparable results to UC1A, both models have resulting MAE_{OCV} above 30 mV for a lower cutoff voltage of 3.8 V, i.e., $V_{min} \geq 3.8$ V. Fig. B.14 in Appendix B.1 shows that TL-NN-A has more stable estimations and shows higher interpretability. This can also be attributed to the fact that TL-NN-A is not designed to directly produce the alignment parameters and, consequently, the DMs. TL-NN-B, however, seems to already include overfitted sections, i.e., voltage windows with a lower cutoff voltage of 3.6 V. The observation that nearly every estimated variable from these limited voltage windows surpasses the accuracy of those estimated with the full input voltage window suggests an increased likelihood of overfitting. The full voltage window encompasses more information than the partial segments and should, therefore, be capable of achieving higher estimation accuracy compared to any individual partial voltage window. Moreover, TL-NN-B reaches low LAM_{PE} errors, independent of the input data, leading to the same assumption. Figs. 7 and 8 display the reduction of the input data to only one sample at a specific SOH and with input data from the C/2 charging events for UC1A. Fig. 7, specifically, visualizes the measured and estimated OCV, ICA and DVA for samples at a SOH of 91 %. The OCV trajectory (Fig. 7(a), (d), (g), (j)) shows that all models underestimate the SOH. However, a more detailed analysis can be derived from the ICA (Fig. 7 (b), (e), (h), (k)) and DVA (Fig. 7(c), (f), (i), (l)). The prior TCN-LSTM model introduces high noise in the reconstructed signal, evident in several peaks. Despite this, the mean peaks and valleys caused by electrode degradation are accurately captured. The optimized models TL-NN-A and TL-NN-B align well with the positions of all peaks and valleys, though the peaks appear exaggerated and sharper compared to real measurements. This discrepancy is due to the impedance rise and increasing inhomogeneity in the real cell, causing the extrema in the ICA and DVA to diminish slightly [59]. The reconstructed signals fail to account for this behavior accurately because they are calculated from pristine OCP measurements. This behavior becomes clearer when comparing with Figs. B.12 and B.13 in Appendix B.1. At the pristine state, the amplitude of all peaks in the ICA matches for both TL-NN-A and TL-NN-B. For the aged cell with a SOH of 81 % (Fig. B.13), the measured peaks decrease in amplitude, and the mismatch between measured and reconstructed signals increases.

Since directly comparing the model output (OCV) with the measured voltage curve using Figs. 7, B.12, and B.13 is challenging, we evaluate the error trajectory for all analyzed input data, summarized in Fig. 8. It shows the error course of the estimated OCV from the prior TCN-LSTM network within TL-NN-A and the final OCV reconstructions error from TL-NN-A and TL-NN-B. This evaluation is presented for three distinct aging states SOH = 100 %, SOH = 91 % and SOH = 84 % and four varying SOC ranges: low range from approximately 0 % to 50 %, the mid range from approximately 20 % to 90 %, the high range from approximately 50 % to 100 % and the full range. Note that the input segments are snipped based on voltage boundaries, as described in Fig. 8, hence, the SOC ranges are rough estimates. As before, the evaluation shows both models perform with high accuracy and that the error mostly stays within the 20 mV boundaries. Even the first estimate from the stand-alone TCN-LSTM model in path A achieves satisfactory results. These estimations, however, still include noisy artifacts, as visible when comparing all three lines. Reconstructing the OCV via optimization not only allows the estimation of the DMs but also the correction of the OCV curve. Although the MAE_{OCV} barely reduces with optimization, the final results are more realistic and represent the physico-chemical effects of battery aging. In general, the reconstruction accuracy slightly decreases for higher degradation, as can be seen in Fig. 8. This is reasonable due to the increasing internal resistance leading to higher overpotentials and, hence, less visible features of the OCPs in the full cell voltage trajectory. Interestingly, the general course of the error course seems similar for one C/2 measurement at the same SOH with varying input voltage segments. The offset to zero, however, decreases for the full input segment. The models seem to interpret similar features of the input data, independent of the voltage segment. For all samples and models especially the error below 1 Ah has a dynamic trajectory due to the high gradient in the lower SOC region in combination with many gradient changes. Non-accurate estimations of the shifting between both OCPs, thus, generate this special trend. For each sample, an increasing OCV error is observed towards the end of the charge cycle. This phenomenon can be attributed to the model's imperfect estimation of the SOH, leading to a premature termination of either the reconstructed or the measured OCV. During this phase, the OCV rises rapidly, as illustrated in Fig. 1(a), thereby causing a substantial increase in the error. An unusual behavior is the negative error in the beginning of the reconstruction for the plain TCN-LSTM

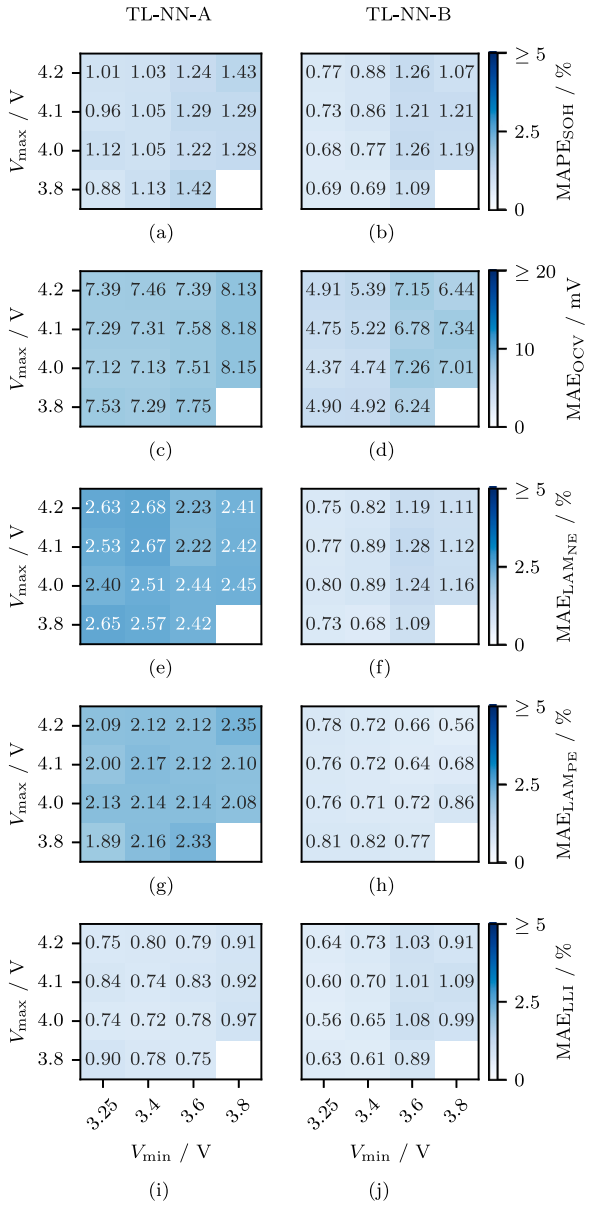

Fig. 6. SOH estimation, DM estimation and OCV reconstruction accuracy for model TL-NN-A and TL-NN-B for UC1A and varying partial voltage input charging curves. The Subfigures show in detail the $MAPE_{SOH}$ for (a) TL-NN-A and (b) TL-NN-B, the MAE_{OCV} for (c) TL-NN-A and (d) TL-NN-B, the $MAE_{LAM\text{-}NE}$ for (e) TL-NN-A and (f) TL-NN-B, the $MAE_{LAM\text{-}PE}$ for (g) TL-NN-A and (h) TL-NN-B, and the MAE_{LLI} for (i) TL-NN-A and (j) TL-NN-B.

model and the samples from 100 % SOH. The NN overestimates the OCV curve by up to 20 mV, independent of the input voltage segment. This behavior can be explained by an overestimation of LAM_{NE}. The OCV error reaches even −50 mV for end of charge which simply is due to an earlier cutoff and a lower estimated SOH.

4.1.2. Use case 2

We conduct the same analysis for UC2A and UC2B in Figs. 9 and B.15, Appendix B.2, with a similar result: Both approaches work excellent for UC2A, but struggle to achieve comparable performance for UC2B, which is also supported by Table 5. While the MAE_{OCV} still remains below 10 mV, the $MAPE_{SOH}$ below 2 % and all DMs mostly below 3 % for UC2A, this behavior changes for UC2B: The TL-NN-A reaches similar results only for the lower and full SOC ranges with a lower cutoff voltage below 3.4 V. The TL-NN-B even requires a start SOC of 0 % to maintain similar accuracy. The overall performance is highly influenced by the input data and a lower cutoff voltage generally leads to higher accuracy. As in UC1B, there seems to be an overfitted section with input data and a lower cutoff voltage of 3.6 V for TL-NN-B.

4.1.3. Use case 3

As listed in Table 5 both models perform comparably well for UC3A with an OCV reconstruction error below 13 mV and a $MAPE_{SOH}$ below 2 %. Interestingly, TL-NN-B shows higher estimation accuracy in terms of SOH and DMs while the OCV reconstruction error is higher. The UC3B, however, seems to mark the boundary of successful TL because for both models the OCV reconstruction error exceeds 30 mV and all states are estimated with unusable accuracy. Figs. 10 and B.16, Appendix B.3, compare both models and UCs according to varying input voltage windows. The voltage-window-dependency is strongly visible for both models in UC3A, Fig. 10. Both models achieve adequate reconstruction and estimation accuracy for voltage windows with $V_{min} \leq 3.6$ V. TL-NN-A struggles to maintain high accuracy for LAM_{NE} estimation, whereas TL-NN-B maintains a MAE below 2 % for all input windows. This behavior drastically changes for UC3B: Both models fail to apply their transferred knowledge and the OCV reconstruction error stays above 25 mV for all input data. Fig. B.16 in Appendix B.3 reveals that both models fail to estimate the anode aging which of course leads to worsened OCV reconstruction and, hence, less accurate loss of lithium inventory (LLI) and SOH estimation. For TL-NN-A, however, the voltage-window-dependency is still very visible, especially for the SOH and LAM_{PE} estimation. Fig. 11 presents the estimation accuracy per aging path from the test data for UC3A and TL-NN-A. UC3A offers the most challenging and still successful TL step with very limited fine-tuning data from cells which do not show the complete degradation, as can be seen in Fig. 3 and Table 1. According to the findings from our previous study [17] and the included information from Table 1 we expect TL-NN-A to not reach high accuracy for samples with SOH ≤ 85 %, $LAM_{NE} \geq 15$ %, $LAM_{PE} \geq 8$ % or LLI ≥ 15 %. In Fig. 11, however, this theory cannot be confirmed completely. For the degradation paths with lower degradation, i.e., path C (Cycling (3.6 V − 4.2 V)) and path E (Storage (3.7 V)), the model performs well besides a small overestimation of LAM_{PE}. The standard deviation remains narrow and especially LLI and SOH are estimated with high accuracy. Even for the two degradation paths with higher degradation, i.e., path A (Cycling (2.5 V − 4.2 V)) and path D (Cycling (WLTP)), the accuracy stays high for the LLI and SOH estimation. Again, LAM_{PE} is overestimated for all checkups but the standard deviation stays narrow until the last checkups. During the state of higher degradation, the TL-NN-A loses accuracy, estimations get worse and standard deviation increases. This trend, however, does not start once $LAM_{PE} \geq 8$ %, but rather once $LAM_{PE} \geq 15$ %. The LAM_{NE} estimations also start to show wide standard deviations ranging from 0 % to 25 % once the measured LAM_{NE} exceeds approximately 15 %. This is again in well agreement with the prior assumption [17].

In Table 5 the MAE for LAM_{NE} and LAM_{PE} stays below 3 % for TL-NN-A. Comparing with Fig. 11 this seems inconsistent because estimation for aging path A (Cycling (2.5 V–4.2 V)) and D (Cycling (WLTP)) gets highly inaccurate with absolute deviations up to 20 %. This high variance can be either be interpreted as low confidence estimation or as some samples with high deviations in relation to the full dataset performance. The final scalar metric is calculated from the entire test dataset. The influence of outliers in the dataset is diminished due to the large data size. Therefore, it is highly recommended to not solely rely on a single metric, but rather analyze individual samples and smaller

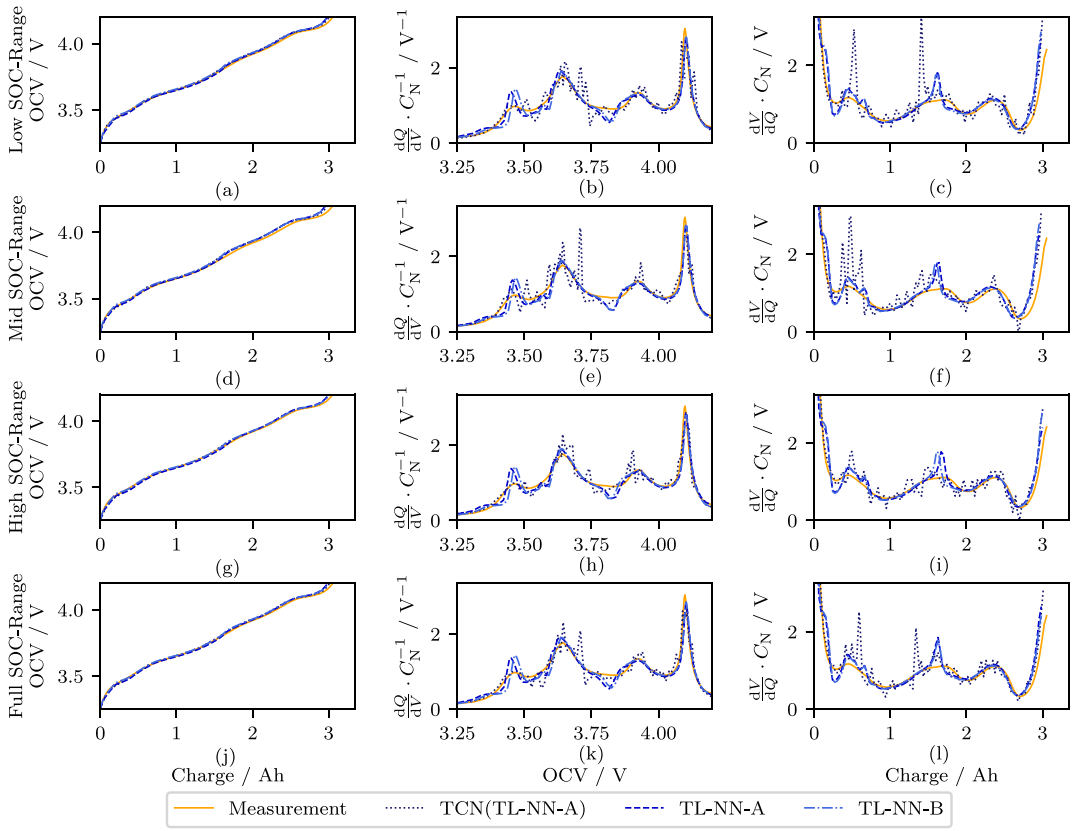

Fig. 7. Evaluation of the OCV, ICA and DVA reconstruction from the prior TCN-LSTM model from TL-NN-A, the final TL-NN-A and TL-NN-B, which includes the performance for UC1A and test data drawn from partial charging events at C/2 and a SOH of 91 %. Four different voltage / SOC windows are evaluated: The low SOC-range ((a)–(c)) corresponds to a voltage window from 3.25 V to 3.8 V, the middle window ((d)–(f)) from 3.6 V to 4.1 V and the high SOC-range ((g)–(i)) from 3.8 V to 4.2 V. Subfigures (j)–(l) show the results for the full input voltage.

subsets of the test dataset to identify high variance in the model's estimation performance.

4.2. Comprehensive discussion

The results of our study reveal the benefits of coupling simulation data with ML and the mechanistic model approach. Both models prove their applicability for OCV reconstruction and DM estimation, even for limited fine-tuning data. During the A UCs, fine-tuning data is limited even further but it includes samples from every C-rate. This allows the TL-NN-A and TL-NN-B to maintain high accuracy independent of the input voltage window. All B UCs aggravate the TL by eliminating some C-rates from the fine-tuning data. This leads to stronger requirements for the input voltage window, i.e., lower cutoff voltage, for UC1B and UC2B. For UC3B, however, an accurate reconstruction is not possible anymore because the fine-tung data only includes samples from C/2. Both models, TL-NN-A and TL-NN-B, perform comparably well. As can be seen in Table 5, TL-NN-B reaches lower DM estimation errors. Besides that, TL-NN-B convinces by reduced computational requirements: The initial output from the TL-NN-B only includes four scalars (Fig. 5(b)) and the OCV curve can be calculated with a simple equation, see Eq. (2). The coupling of TL with optimization, however, yields more interpretable results with more stable estimation and a stronger voltage-window-dependency, e.g., compare with Fig. B.14 in Appendix B.1 and B.15 in Appendix B.2. The TL-NN-A does not show any obvious overfitted section and yields reasonable LAM_{NE} errors for the upper voltage segments.

As can be seen in Fig. 5(a) the TL-NN-A model deviates from the tuned architecture in our previous work [17], i.e., the model is more complex and includes two additional LSTM-layers. The input TCN layer, however, has almost the same hyperparameters which is a result of the similar training data. The higher complexity can be explained by the extended data including more C-rates and voltage windows. The number of epochs increases for higher UCs which may be due to a challenging training dataset in the lower UCs: The models get eventually stuck in a local optimum early in the fitting process. For sparse data the optimization landscape may be more well-defined and the fitting process is likely to run into overfitting. On the other hand, the diverse experimental data in the early UCs works as a type of regularization and prevents the models from overfitting [60]. In our previous work [17], we have shown with our UCs that fine-tuning with data from multiple cells but only at one C-rate leads to worsened performance with OCV reconstruction errors around 20 mV for varying voltage windows. This extended study at hand reveals that also the implicit DMs play a crucial role. By selecting fine-tuning data from the cells which show the highest degradation, i.e., from path A (Cycling (2.5 V – 4.2 V), compare Table 1), and including all C-rates we optimize the performance of both models and consequently reach OCV reconstruction errors below 10 mV independent of the input data. Although the model developed in our prior study [17] was fine-tuned with two cells from varying aging

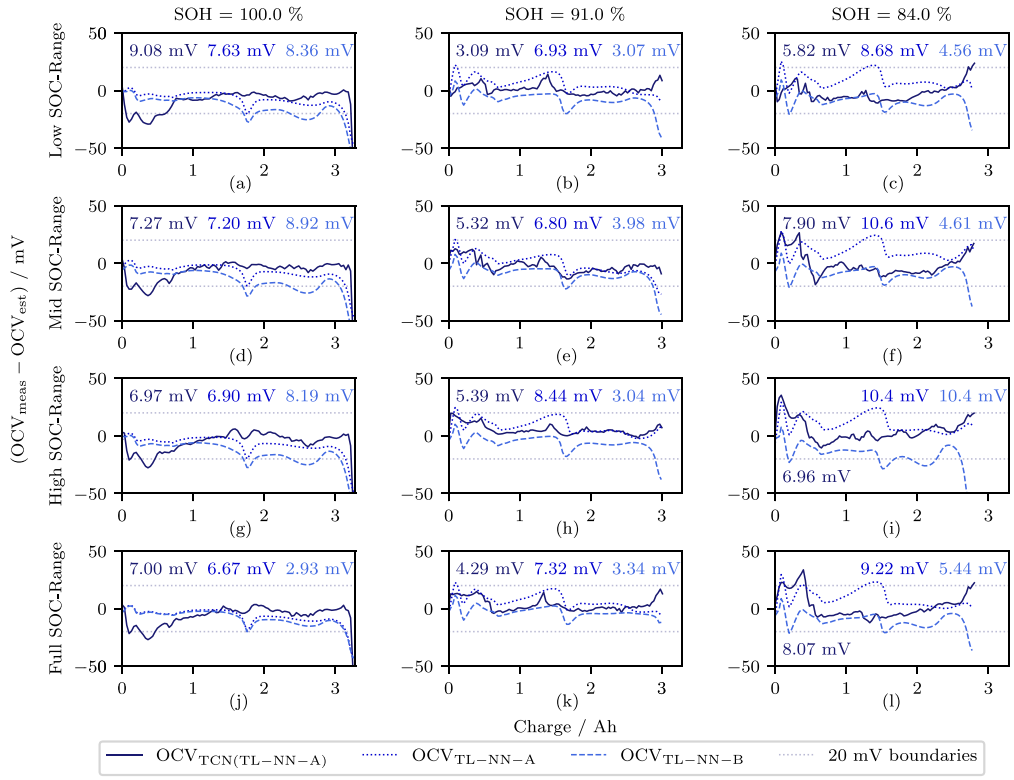

Fig. 8. Evaluation of the OCV reconstruction error from the prior TCN-LSTM model from TL-NN-A, the final TL-NN-A and TL-NN-B, which includes the performance for UC1A and test data drawn from partial charging events at C/2. The error course is plotted over the charge throughput of the OCV measurement during the respective checkup. Three degradation states and four different voltage / SOC windows are evaluated: The low SOC-range ((a)–(c)) corresponds to a voltage window from 3.25 V to 3.8 V, the middle window ((d)–(f)) from 3.6 V to 4.1 V and the high SOC-range ((g)–(i)) from 3.8 V to 4.2 V. Subfigures (j)–(l) show the results for the full input voltage. The 20 mV error boundaries are plotted for better visibility in dashed gray lines. For all evaluated scenarios the MAE_{OCV} error is included in the subplot, in its respective color. The left text belongs to the prior TCN-LSTM from TL-NN-A, the middle text to the final TL-NN-A, while the right text corresponds to the TL-NN-B.

paths and, hence, the learned degradation pattern is more diverse, the error is above 10 mV for any input data segment with a lower cutoff voltage $V_{min} \geq 3.4$ V. Comparing both studies, we can conclude that this behavior must be due to the included samples at C/2 in the fine-tuning of TL-NN-A and TL-NN-B. In contrast to our previous study [17], by introducing an alternative UC definition, according to Fig. 4, we have revealed that extrapolation of estimation is possible to some extent. For UC3A the TL-NN-A is able to estimate the correct DMs and SOH for two degradation paths which show higher DMs than the fine-tuning data. The standard deviations for the LAM estimations, however, increase once the input samples move too far away from the re-learned fine-tuning data. On the other hand, this extrapolation is not possible in combination with varying C-rates as in UC3B: The model cannot conclude the correct OCV just from fine-tuning with data at the medium C-rate and medium degradation.

Comparing our work to a purely optimization-based approach as in the work by Schmitt et al. [28], we can reach more accurate DM estimations even for partial charging events at higher C-rates. Schmitt et al. [28] concluded that at least a C-rate below C/15 or partial charging segments spanning at least the SOC range from 20 % to 70 % at an even lower C-rate of C/30 are necessary to yield accurate DM estimations. Especially for the upper voltage segments our approach outperforms the model by Schmitt et al. [28] in terms of DM estimation accuracy: For a partial voltage segment, measured at C/30 from 50 % to 85 % SOC, Schmitt et al. [28] have reached a $RMSE_{LAM\text{-}NE}$ of 14.4 %, a $RMSE_{LAM\text{-}PE}$ of 2.5 % and a $RMSE_{LLI}$ of 8.3 %. This SOC range approximates to the voltage window from 3.8 V to 4.1 V independent of the applied C-rate. For all of the UCs UC1A, UC2A and UC3A both models – TL-NN-A and TL-NN-B – maintain DM estimation MAEs below 3 % ($RMSE_{LAM\text{-}NE} \leq 5.08$ %, $RMSE_{LAM\text{-}PE} \leq 3.67$ %, $RMSE_{LLI} \leq 1.95$ %) even for a test data comprising of voltage curves solely captured at an applied current between C/3.85 and 1C (compare Figs. 6, 9 and 10). A similar improvement holds true for the OCV reconstruction and SOH estimation error: While Schmitt et al. [28] reached a $RMSE_{OCV}$ of 32 mV and $RMSE_{SOH}$ of 8.0 % our TL-NN-A maintains a MAE_{OCV} below 12.2 mV ($RMSE_{OCV} \leq 14.4$ mV) and a $MAPE_{SOH}$ below 2.47 % ($RMSE_{SOH} \leq 2.46$ %) for the A UCs. Similar, the TL-NN-B yields a MAE_{OCV} below 18.1 mV ($RMSE_{OCV} \leq 24.2$ mV) and a $MAPE_{SOH}$ below 1.63 % ($RMSE_{SOH} \leq 1.77$ %). While this example is only on selected voltage window, the general trend holds true for all input voltage segments and even applies for the lower voltage segments from UC1B and UC2B (compare Figs. 6, B.14 in Appendix B.1, 9, B.15 in Appendix B.2, 10, B.16 in Appendix B.3).

The comparison with the developed TCN network by Bockrath et al. [8], which directly estimates the SOH from partial discharge voltage segments at approximately C/2, allows to evaluate the benefit of the TL step from synthetic data: Their developed NN reaches a $RMSE_{SOH}$ of 1.0 % for 3.2 V to 4.2 V, 13.1 % for 3.2 V to 3.5 V, 2.9 % for 3.5 V to 3.7 V and 1.4 % for 3.7 V to 4.2 V [8]. These values lie in a comparable range to our $MAPE_{SOH}$ for varying UCs and both models TL-NN-A and TL-NN-B (compare Fig. 6, B.14 in Appendix B.1, 9, B.15 in Appendix B.2, 10, B.16 in Appendix B.3). Contrary to our thesis, they concluded

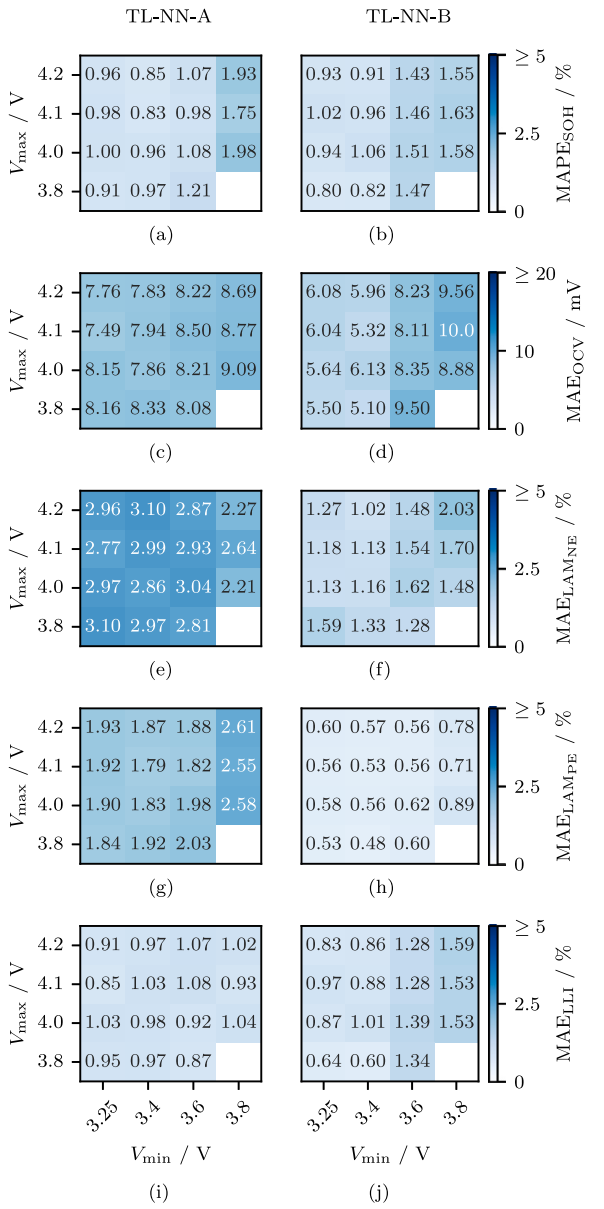

Fig. 9. SOH estimation, DM estimation and OCV reconstruction accuracy for model TL-NN-A and TL-NN-B for UC2A and varying partial voltage input charging curves. The Subfigures show in detail the $MAPE_{SOH}$ for (a) TL-NN-A and (b) TL-NN-B, the MAE_{OCV} for (c) TL-NN-A and (d) TL-NN-B, the $MAE_{LAM\text{-}NE}$ for (e) TL-NN-A and (f) TL-NN-B, the $MAE_{LAM\text{-}PE}$ for (g) TL-NN-A and (h) TL-NN-B, and the MAE_{LLI} for (i) TL-NN-A and (j) TL-NN-B.

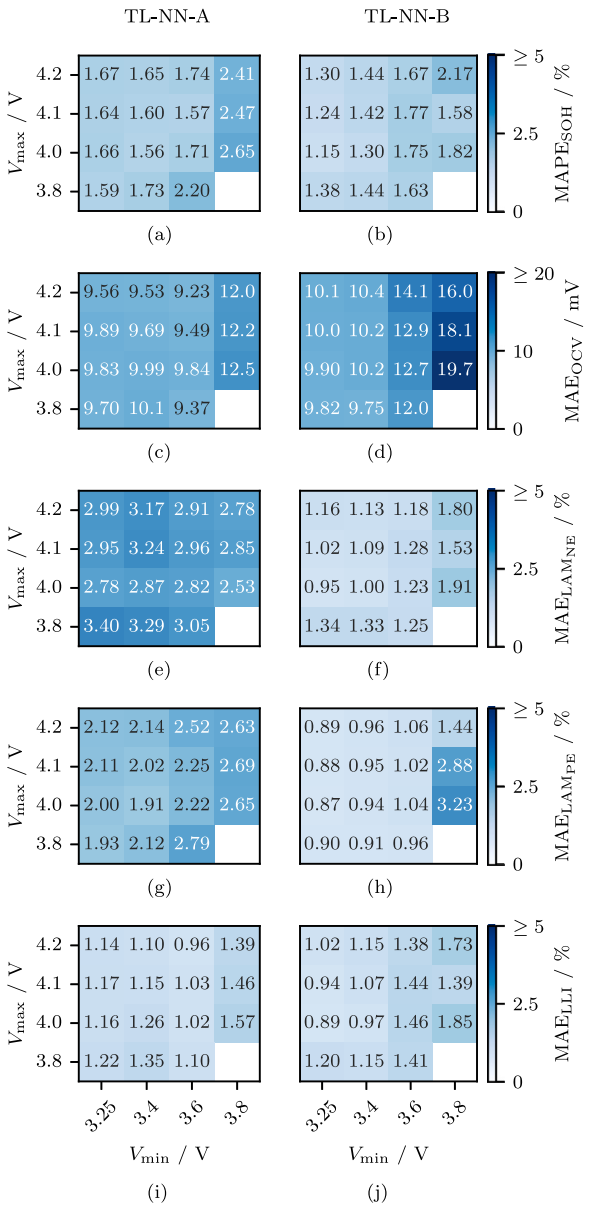

Fig. 10. SOH estimation, DM estimation and OCV reconstruction accuracy for model TL-NN-A and TL-NN-B for UC3A and varying partial voltage input charging curves. The Subfigures show in detail the $MAPE_{SOH}$ for (a) TL-NN-A and (b) TL-NN-B, the MAE_{OCV} for (c) TL-NN-A and (d) TL-NN-B, the $MAE_{LAM\text{-}NE}$ for (e) TL-NN-A and (f) TL-NN-B, the $MAE_{LAM\text{-}PE}$ for (g) TL-NN-A and (h) TL-NN-B, and the MAE_{LLI} for (i) TL-NN-A and (j) TL-NN-B.

that the upper voltage segments are better suitable for SOH estimation due to higher correlation between the accumulated charge in this segments and the full capacity throughput. When it comes to OCV reconstruction and DM estimation, however, our findings show that the lower voltage segments are better suited, which also aligns with the results from Schmitt et al. [28]. In essence, this phenomenon can be attributed to the geometrical characteristics, specifically the gradient variations within the voltage curve. Capturing and learning a greater number of these features across the potential degradation range of a battery cell enhances the accuracy of OCV reconstruction and SOH estimation. Ultimately, minimal electrochemical knowledge but rather mathematical understanding is required to develop data-driven models that effectively learn the trends of battery degradation.

The only comparable study to evaluate the coupling of ML and the mechanistic model approach was derived by Tian et al. [25]: They have trained a NN to estimate the stoichiometries from partial charging voltage segments at 1C and directly derived the OCV curve from that. For 200 mV voltage segments at varying SOC positions their reconstructed OCV curve maintained RMSEs below 15 mV and the derived MAE_{SOH} was under 3.7 %. Their estimated DMs accuracies were not

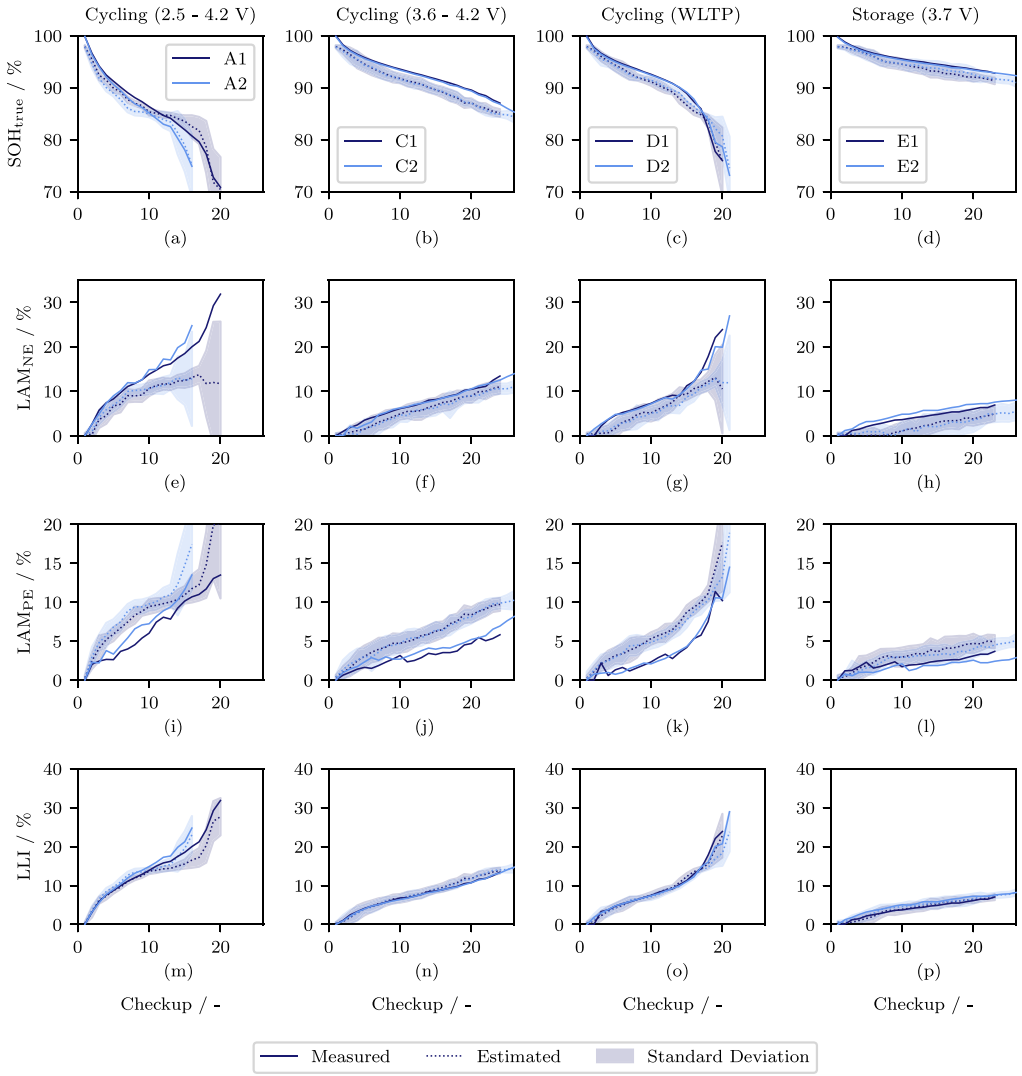

Fig. 11. Measured and estimated SOH and DMs for UC3A and TL-NN-A. The true values are displayed in solid lines, while the estimations from both cells per aging path are pointed with the shaded areas showing the standard deviation. The standard deviation shows the result of all estimations at one aging state with all different possible voltage windows.

fully specified but – visually analyzed – stayed in good agreement with their reference. Their LAM_{NE} estimation, however, starts to increase its deviation for later cycles. Our developed TL-NN-B follows a very similar approach but includes TL to aggravate more training data, which seems to benefit the OCV reconstruction. For 200 mV input segments the TL-NN-B reconstructs the OCV curve for UC1A and UC2A with a MAE below 9.5 mV ($RMSE_{OCV} \leq 16.1$ mV) and also the $MAPE_{SOH}$ stays under 1.58 % ($MAE_{SOH} \leq 1.46$ %, compare Figs. 6, 9).

As in any data-driven method, our results show that training data – source and target domain – heavily influence the performance. Previous findings [17] already prove the eligibility of synthetic data as the source domain and prove that the source domain must cover all possible variations in terms of C-rate, SOC window or DMs of the target domain. Additionally, our previous study [17] highlights that the choice and amount of synthetic data for pretraining do not matter as long as it includes a sufficient amount of supporting points within the boundaries of the describing parameters, ensuring accurate representation within the target domain. Due to our UC definition in Fig. 4 we can conclude that also the fine-tuning data from the target domain highly matters: To allow accurate OCV reconstruction it must at least include the boundaries of the test data, as can be seen in Table 5. This implies that the fine-tuning data should always be selected from the cells showing the highest degradation. Further, the lowest and highest C-rates of all samples, i.e., C/3.85 and 1C as in our UC3A, must be included as well. It remains an open research question to determine the extent to which this simplification of fine-tuning data can be pursued in real-world scenarios including battery cell validation in industry application. On one hand, it is crucial to understand the validity of this assumption across varying dataset sizes. On the other hand, research must be conducted to explore how much the fine-tuning data can be minimized to ascertain whether highly accelerated aging tests are sufficient for this purpose. With these findings it will be possible to conclude possible time and cost savings enabled by TL from synthetic data.

The comparison of both model architectures – TL-NN-A coupling TL and optimization, and TL-NN-B coupling TL and the mechanistic model – is challenging to conclude with a clear advantage on one

Table 6
A typical experiment design for aging model parametrization according to industry experience and literature [61]. The used experimental data [28] in our approach is highlighted (lightgray) including the resulting capacity fade and DMs, as well as the reduced fine-tuning data for UC2A (darkgray).

Aging condition	Current profile	Temperature	SOC / Voltage-range	ΔSOH	ΔLAM_{NE}	ΔLAM_{PE}	ΔLLI
Cyclic	0.5C	25 °C	2.5 V to 4.2 V				
			2.5 V to 4.0 V				
			3.6 V to 4.2 V				
		35 °C	2.5 V to 4.2 V				
			2.5 V to 4.0 V				
			3.6 V to 4.2 V				
	1C	25 °C	2.5 V to 4.2 V	30 %	30 %	15 %	35 %
			2.5 V to 4.0 V	15 %	15 %	8 %	15 %
			3.6 V to 4.2 V	15 %	15 %	8 %	15 %
		35 °C	2.5 V to 4.2 V				
			2.5 V to 4.0 V				
			3.6 V to 4.2 V				
	WLTP	25 °C		25 %	25 %	15 %	30 %
		35 °C					
	3N3F	10 °C					
		25 °C					
		35 °C					
Calendaric		25 °C	10 %				
			50 %	10 %	8 %	2.5 %	10 %
			100 %				
		50 °C	10 %				
			50 %				
			100 %				

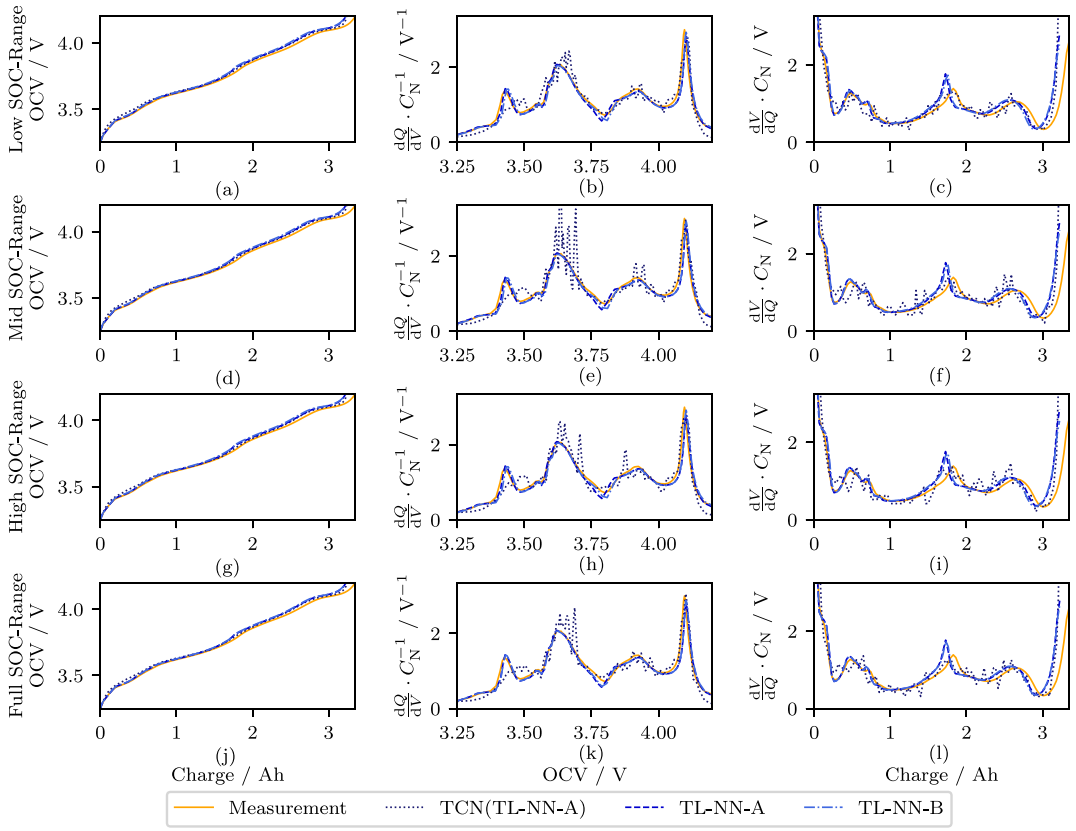

Fig. B.12. Evaluation of the OCV, ICA and DVA reconstruction from the prior TCN-LSTM model from TL-NN-A, the final TL-NN-A and TL-NN-B, which includes the performance for UC1A and test data drawn from partial charging events at C/2 and a SOH of 100 %. Four different voltage / SOC windows are evaluated: The low SOC-range ((a)–(c)) corresponds to a voltage window from 3.25 V to 3.8 V, the middle window ((d)–(f)) from 3.6 V to 4.1 V and the high SOC-range ((g)–(i)) from 3.8 V to 4.2 V. Subfigures (j)–(l) show the results for the full input voltage.

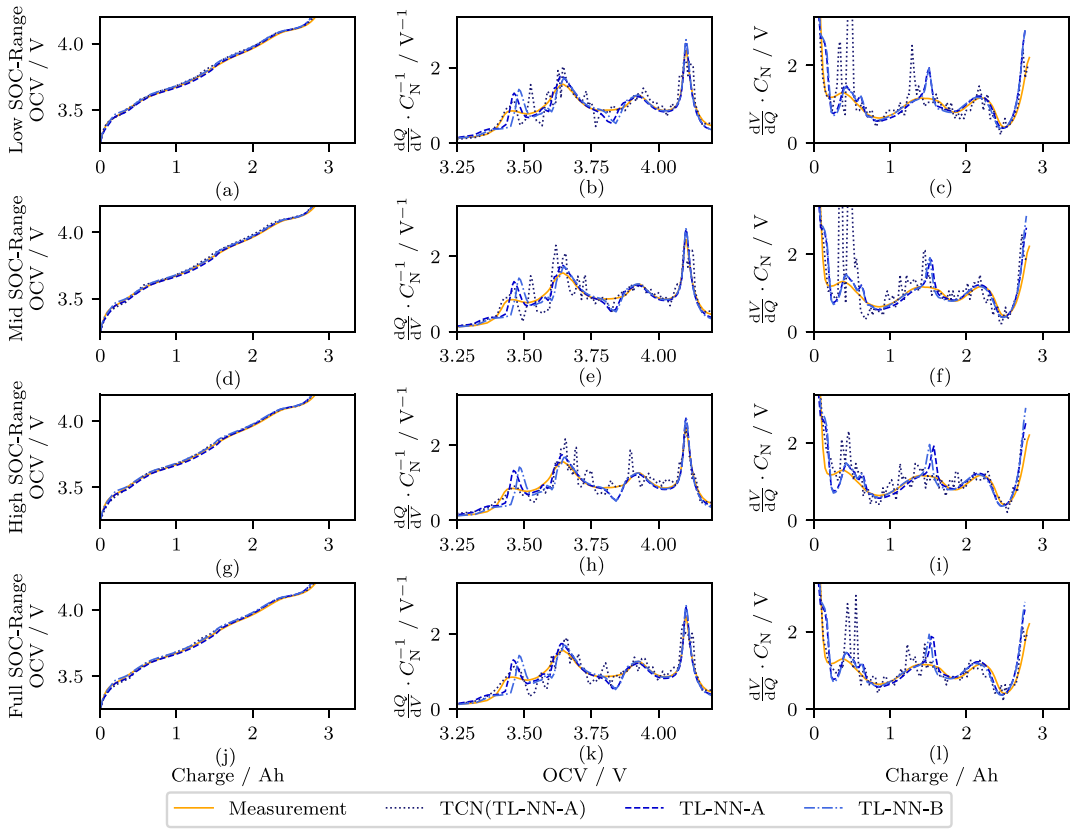

Fig. B.13. Evaluation of the OCV, ICA and DVA reconstruction from the prior TCN-LSTM model from TL-NN-A, the final TL-NN-A and TL-NN-B, which includes the performance for UC1A and test data drawn from partial charging events at C/2 and a SOH of 84 %. Four different voltage / SOC windows are evaluated: The low SOC-range ((a)–(c)) corresponds to a voltage window from 3.25 V to 3.8 V, the middle window ((d)–(f)) from 3.6 V to 4.1 V and the high SOC-range ((g)–(i)) from 3.8 V to 4.2 V. Subfigures (j)–(l) show the results for the full input voltage.

side. The TL-NN-B, however, has less computational complexity and slightly outperforms the TL-NN-A in almost any UC. It has the downside of requiring the exact alignment parameters for both, the source and target domain, for model training. This requirement can often not be fulfilled, whereas the TL-NN-A suffices with the captured OCV and the pristine alignment parameters, without any additional label. Hence, TL-NN-A allows the OCV reconstruction and DM estimation applied to almost any battery aging test.

The results from UC2A show that a huge reduction of the planned experiments is possible if a pretrained TL model is used. Our findings strongly suggest that the exact aging path does not matter as long as the explicit fine-tuning data provoke the highest degradation in terms of SOH and DMs. If we assume that Table 6 is the standard for data-driven aging model parametrization, we reduce the number of required experiments from 23 to 1. If we assume that one aging experiment runs for 500 days, a checkup is performed every 30 days and a climate chamber makes up 36 % of the aging costs (cycling + storage), the TL approach can reduce the costs by 95 %.

Especially TL-NN-A, due to its low requirements on fine-tuning data, offers a high probability of being successfully applied to onboard or backend BEV algorithms. Offering aging-path-individual OCV updates takes a huge step towards optimized battery usage strategy, increases the accuracy of state estimation and eventually prolongs the lifetime. The gathered knowledge from this study enables the refinement of typical experiment designs for their validity in advance. Many planned measurements can be pre-analyzed to determine their location in the source or target domain. Ultimately, this allows for the exclusion of unnecessary measurements that are implicitly covered by other measurements.

These promises, however, must be interpreted considering the inherent limitations of the chosen theory. DMs are primarily a mathematical construct used to describe OCV changes over the battery's lifetime. Nonetheless, they are valuable for roughly categorizing the degradation mechanisms occurring within the battery. For instance, electrolyte decomposition can be mainly attributed to LLI, while lithium plating affects both LLI and LAM_{NE} [62]. In this study, we limited the DMs to LLI, LAM_{NE}, and LAM_{PE}, although impedance rise is also a critical factor for battery performance over its lifetime. Impedance significantly impacts the available power of the system, especially in BEV applications, and thus affects fast-charging performance. Future studies should expand the DM terminology to include impedance rise to account for practical performance considerations.

Apart from that, TL opens the possibility to develop many SOH or SOC estimation algorithms by using synthetic data as the source domain. The proposed method can be extended to hysteresis-affected battery cells, such as LFP cells or those with a high silicon content in the anode, by substituting the pseudo-OCV with galvanostatic intermittent titration technique (GITT) measurements. This substitution results in even more pronounced cost and time savings.

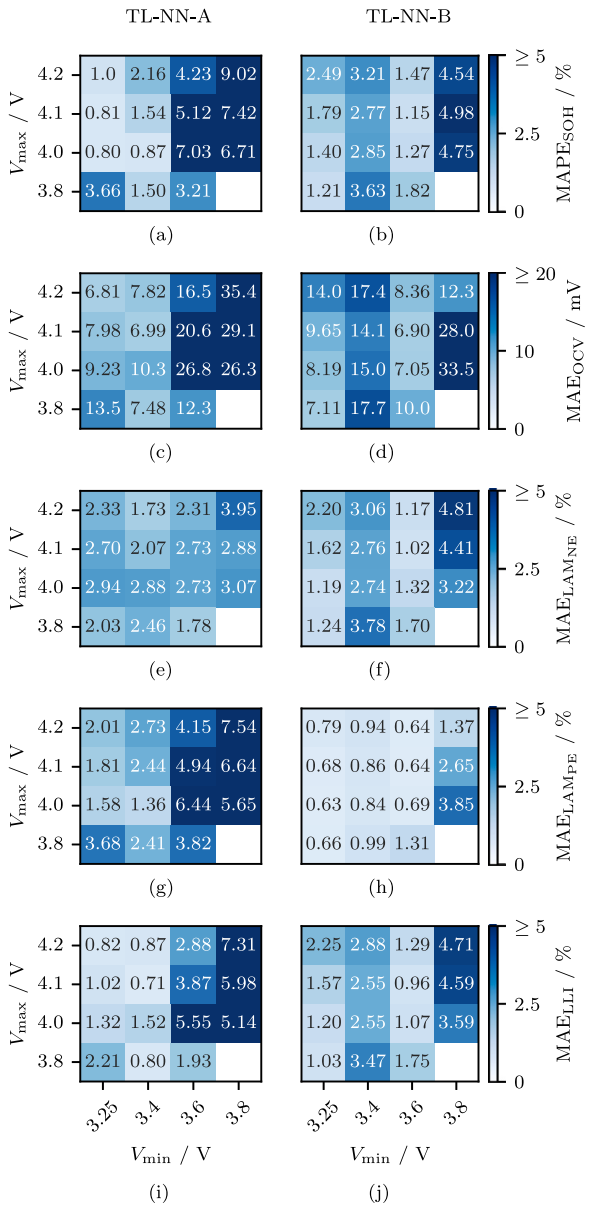

Fig. B.14. SOH estimation, DM estimation and OCV reconstruction accuracy for model TL-NN-A and TL-NN-B for UC1B and varying partial voltage input charging curves. The Subfigures show in detail the MAPE$_{SOH}$ for (a) TL-NN-A and (b) TL-NN-B, the MAE$_{OCV}$ for (c) TL-NN-A and (d) TL-NN-B, the MAE$_{LAM\text{-}NE}$ for (e) TL-NN-A and (f) TL-NN-B, the MAE$_{LAM\text{-}PE}$ for (g) TL-NN-A and (h) TL-NN-B, and the MAE$_{LLI}$ for (i) TL-NN-A and (j) TL-NN-B.

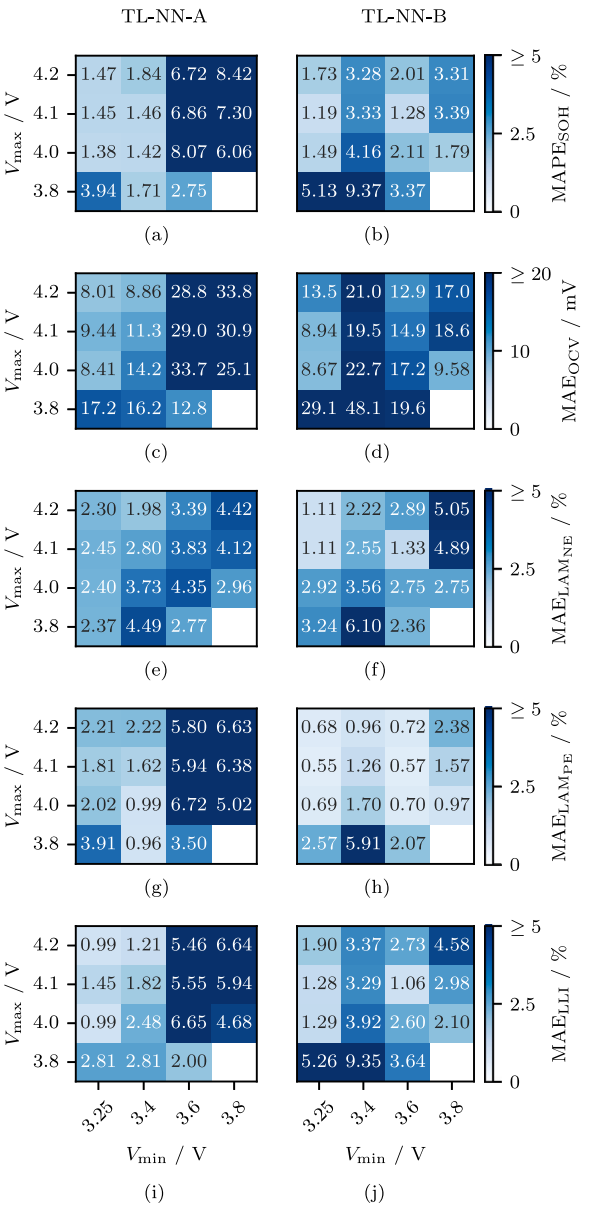

Fig. B.15. SOH estimation, DM estimation and OCV reconstruction accuracy for model TL-NN-A and TL-NN-B for UC2B and varying partial voltage input charging curves. The Subfigures show in detail the MAPE$_{SOH}$ for (a) TL-NN-A and (b) TL-NN-B, the MAE$_{OCV}$ for (c) TL-NN-A and (d) TL-NN-B, the MAE$_{LAM\text{-}NE}$ for (e) TL-NN-A and (f) TL-NN-B, the MAE$_{LAM\text{-}PE}$ for (g) TL-NN-A and (h) TL-NN-B, and the MAE$_{LLI}$ for (i) TL-NN-A and (j) TL-NN-B.

5. Conclusion

This study compares two approaches – TL and optimization – to couple synthetic data for battery state estimation. A base model is trained with a large synthetic dataset, including constant-current charging profiles at various C-rates and degradation states for a large-format automotive NCA-graphite cell. Two TCN-LSTM models are developed: TL-NN-A for estimating OCV and TL-NN-B for estimating alignment parameters from partial voltage segments. These models are fine-tuned with experimental data from a commercial NMC-silicone/graphite cell.

Both models achieve high accuracy, maintaining MAE$_{OCV}$ below 10 mV and MAPE$_{SOH}$ under 2 %, for most use cases even for voltage segments of 200 mV. For the challenging use case with less degradation data, the MAE$_{OCV}$ ranges from 9.23 mV to 19.7 mV, and MAPE$_{SOH}$ ranges from 1.15 % to 2.65 %. Our findings suggest that fine-tuning with one cell from one aging experiment is sufficient if the cell shows the highest

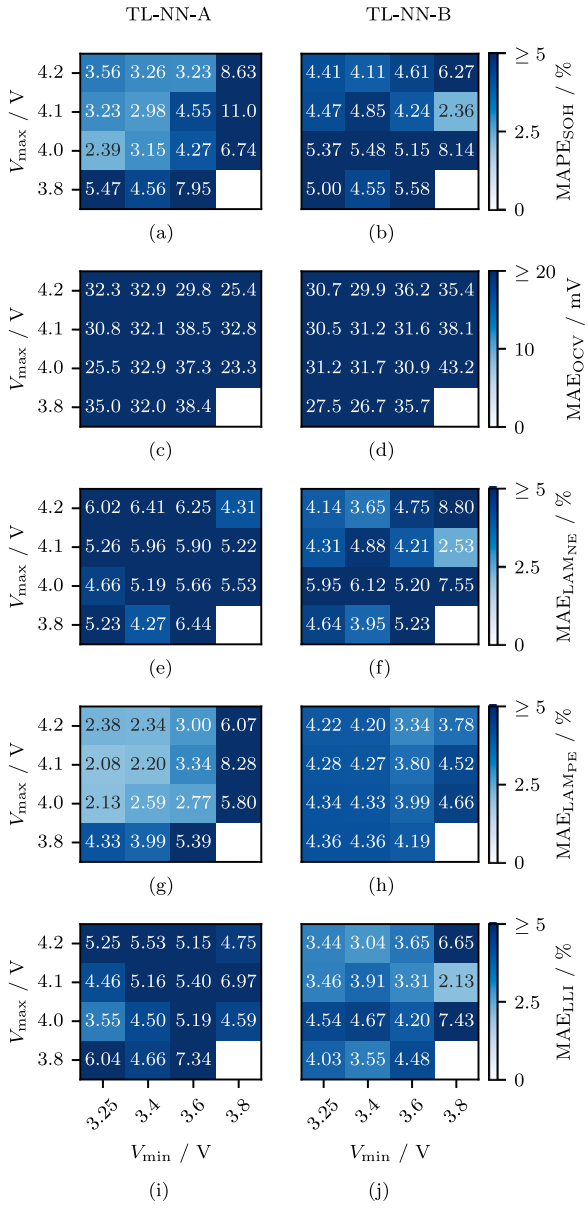

Fig. B.16. SOH estimation, DM estimation and OCV reconstruction accuracy for model TL-NN-A and TL-NN-B for UC3B and varying partial voltage input charging curves. The Subfigures show in detail the $MAPE_{SOH}$ for (a) TL-NN-A and (b) TL-NN-B, the MAE_{OCV} for (c) TL-NN-A and (d) TL-NN-B, the $MAE_{LAM\text{-}NE}$ for (e) TL-NN-A and (f) TL-NN-B, the $MAE_{LAM\text{-}PE}$ for (g) TL-NN-A and (h) TL-NN-B, and the MAE_{LLI} for (i) TL-NN-A and (j) TL-NN-B.

degradation in terms of capacity fade and all DMs. Specific triggering of isolated DMs is not necessary; instead, data generation should focus on evenly developed DMs. Lower cutoff voltages generally lead to better results due to more detectable gradient changes. While TL-NN-B has lower computational requirements and achieves slightly better results, TL-NN-A offers lower data requirements.

Utilizing TL from synthetic data has proven effective for developing battery state estimation models with minimal fine-tuning data. The key to this efficiency is the use of a single aging path with the highest degradation, allowing the model to capture essential features of battery degradation without extensive data. Coupling ML with optimization enables the generation of DMs and the creation of aging-path-specific OCV updates, crucial for optimized battery management systems.

Challenges remain in deploying the coupled model for vehicle applications. It is unclear whether ML can handle noisy and superimposed battery pack signals from multiple cells. Additionally, generalizing the ML model from accelerated lab aging data to real-world aging behavior needs validation. The validity of the assumed ground truth labels of the experimental data can be questioned, but generating the DMs via OCV fits is currently the only available method for non-invasive, reproducible long-term aging tests [63,64]. Future research should explore alternative approaches to combine ML and optimization. For instance, leveraging fleet data to train a Bayesian neural network could constrain the solution space during OCV reconstruction, increasing the likelihood of returning the global optimum.

Table A.7
Final number of epochs before the early stopping criterion was fulfilled during the fine-tuning process of the TL models TL-NN-A and TL-NN-B.

Use case	TL-NN-A	TL-NN-B
UC1A	359	524
UC1B	450	490
UC2A	610	1000
UC2B	829	1000
UC3A	521	873
UC3B	614	988

CRediT authorship contribution statement

Tobias Hofmann: Writing – original draft, Visualization, Validation, Software, Methodology, Investigation, Conceptualization. **Jacob Hamar:** Writing – review & editing, Supervision. **Bastian Mager:** Writing – review & editing, Validation, Methodology. **Simon Erhard:** Writing – review & editing, Supervision. **Jan Philipp Schmidt:** Writing – review & editing, Supervision.

Declaration of competing interest

The authors declare that they have no known competing financial interests or personal relationships that could have appeared to influence the work reported in this paper.

Acknowledgments

Funded by the Open Access Publishing Fund of the University of Bayreuth. This work was performed in cooperation with the University of Bayreuth - Chair of Systems Engineering for Electrical Energy Storage and BMW Group. The authors would like to thank the team of Batemo GmbH for providing the Batemo Cell Models as high-precision physical battery cell models to generate the simulation data.

Appendix A. Neural network optimization and fine-tuning

See Table A.7.

Appendix B. Detailed benchmark results

B.1. Use case 1

See Figs. B.12–B.14.

B.2. Use case 2

See Fig. B.15.

B.3. Use case 3

See Fig. B.16.

Data availability

Data will be made available on request.

References

[1] Şimşir M, Ghayth A. Global trends in electric vehicle battery efficiency and impact on sustainable grid. Sol Energy Sustain Dev J 2024;13(2):1–17. http://dx.doi.org/10.51646/jsesd.v13i2.202.

[2] Sauer DU, Bopp G, Jossen A, Garche J, Rothert M, Wollny M. State of charge — What do we really speak about. In: The 21st international telecommunications energy conference. 1999, p. 6–9.

[3] Plett GL. Extended Kalman filtering for battery management systems of LiPB-based HEV battery packs: Part 2. Modeling and identification. J Power Sources 2004;134(2):262–76. http://dx.doi.org/10.1016/j.jpowsour.2004.02.032.

[4] Plett GL. Extended Kalman filtering for battery management systems of LiPB-based HEV battery packs: Part 3. State and parameter estimation. J Power Sources 2004;134(2):277–92. http://dx.doi.org/10.1016/j.jpowsour.2004.02.033.

[5] Dubarry M, Truchot C, Liaw BY. Synthesize battery degradation modes via a diagnostic and prognostic model. J Power Sources 2012;219:204–16. http://dx.doi.org/10.1016/j.jpowsour.2012.07.016.

[6] Attia PM, Bills A, Planella FB, Dechent P, d. Reis G, Dubarry M, et al. Review—Knees in lithium-ion battery aging trajectories. J Electrochem Soc 2022;169(6):060517. http://dx.doi.org/10.1149/1945-7111/ac6d13.

[7] Bockrath S, Waldhör S, Ludwig H, Lorentz V. State of health estimation using a temporal convolutional network for an efficient use of retired electric vehicle batteries within second-life applications. In: Artificial intelligence for digitising industry–applications. 2022, p. 21–34, River Publishers.

[8] Bockrath S, Lorentz V, Pruckner M. State of health estimation of lithium-ion batteries with a temporal convolutional neural network using partial load profiles. Appl Energ 2023;329:120307. http://dx.doi.org/10.1016/j.apenergy.2022.120307.

[9] Costa N, Sánchez L, Anseán D, Dubarry M. Li-ion battery degradation modes diagnosis via convolutional neural networks. J Energy Storage 2022;55(C):105558. http://dx.doi.org/10.1016/j.est.2022.105558.

[10] Hofmann T, Hamar J, Rogge M, Zoerr C, Erhard S, Schmidt JP. Physics-informed neural networks for state of health estimation in lithium-ion batteries. J Electrochem Soc 2023;170:090524. http://dx.doi.org/10.1149/1945-7111/acf0ef.

[11] Lee S, Kim Y. Li-ion battery electrode health diagnostics using machine learning. In: American control conference. 2020, p. 1137–42. http://dx.doi.org/10.23919/ACC45564.2020.9147633.

[12] Dubarry M, Costa N, Matthews D. Data-driven direct diagnosis of li-ion batteries connected to photovoltaics. Nat Commun 2023;14:3138. http://dx.doi.org/10.1038/s41467-023-38895-7.

[13] Zhang L, Zhang J, Gao T, Lyu L, Wang L, Shi W, et al. Improved LSTM based state of health estimation using random segments of the charging curves for lithium-ion batteries. J Energy Storage 2023;74(B):109370. http://dx.doi.org/10.1016/j.est.2023.109370.

[14] Yao J, Han T. Data-driven lithium-ion batteries capacity estimation based on deep transfer learning using partial segment of charging/discharging data. Energy 2023;271:127033. http://dx.doi.org/10.1016/j.energy.2023.127033.

[15] Zhou Z, Liu Y, Zhang C, Shen W, Xiong R. Deep neural network-enabled battery open-circuit voltage estimation based on partial charging data. J Energy Chem 2024;90:120–32. http://dx.doi.org/10.1016/j.jechem.2023.11.009.

[16] Chen J, Han X, Sun T, Zheng Y. Analysis and prediction of battery aging modes based on transfer learning. Appl Energy 2024;356:122330. http://dx.doi.org/10.1016/j.apenergy.2023.122330.

[17] Hofmann T, Hamar J, Mager B, Erhard S, Schmidt JP. Transfer learning from synthetic data for open-circuit voltage curve reconstruction and state of health estimation of lithium-ion batteries from partial charging segments. Energy AI 2024;17:100382. http://dx.doi.org/10.1016/j.egyai.2024.100382.

[18] Zou G, Yan Z, Zhang C, Song L. Transfer learning with CNN-LSTM model for capacity prediction of lithium-ion batteries under small sample. J Physics: Conf Ser 2022;2258:012042. http://dx.doi.org/10.1088/1742-6596/2258/1/012042.

[19] Sahoo S, Hariharan KS, Agarwal S, Swernath SB, Bharti R, Han S, et al. Transfer learning based generalized framework for state of health estimation of li-ion cells. Sci Rep 2022;12:13173. http://dx.doi.org/10.1038/s41598-022-16692-4.

[20] Shen S, Sadoughi M, Li M, Wang Z, Hu C. Deep convolutional neural networks with ensemble learning and transfer learning for capacity estimation of lithium-ion batteries. Appl Energy 2020;260:114296. http://dx.doi.org/10.1016/j.apenergy.2019.114296.

[21] Chen X, Sun T, Lai X, Zheng Y, Han Xuebing. Transfer learning strategies for lithium-ion battery capacity estimation under domain shift differences. J Energy Storage 2024;90(A):111860. http://dx.doi.org/10.1016/j.est.2024.111860.

[22] Fu S, Tao S, Fan H, He K, Liu X, Tao Y, et al. Data-driven capacity estimation for lithium-ion batteries with feature matching based transfer learning method. Appl Energy 2024;353(A):121991. http://dx.doi.org/10.1016/j.apenergy.2023.121991.

[23] Huang K, Yao K, Guo Y, Lv Z. State of health estimation of lithium-ion batteries based on fine-tuning or rebuilding transfer learning strategies combined with new features mining. Energy 2023;282:128739. http://dx.doi.org/10.1016/j.energy.2023.128739.

[24] Sun Y, Tian H, Hu F, Du J. Method for evaluating degradation of battery capacity based on partial charging segments for multi-type batteries. Batteries 2024;10:187. http://dx.doi.org/10.3390/batteries10060187.

[25] Tian J, Xiong R, Shen W, Lu J, Yang X-G. Deep neural network battery charging curve prediction using 30 points collected in 10 min. Joule 2021;6(5):1521–34. http://dx.doi.org/10.1016/j.joule.2021.05.012.

[26] Tian J, Ma L, Zhang T, Han T, Mai W, Chung CY. Exploiting domain knowledge to reduce data requirements for battery health monitoring. Energy Storage Mater 2024;67:103270. http://dx.doi.org/10.1016/j.ensm.2024.103270.

[27] Hofmann T, Li J, Hamar J, Erhard S, Schmidt JP. The ΔQ-method: State of health and degradation mode estimation for lithium-ion batteries using a mechanistic model with relaxed voltage points. J Power Sources 2024;596:234107. http://dx.doi.org/10.1016/j.jpowsour.2024.234107.

[28] Schmitt J, Rehm M, Karger A, Jossen A. Capacity and degradation mode estimation for lithium-ion batteries based on partial charging curves at different current rates. J Energy Storage 2023;59:106517. http://dx.doi.org/10.1016/j.est.2022.106517.

[29] Zhu C, Sun L, Chen C, Tian J, Shen W, Xiong R. Lithium-ion battery degradation diagnosis and state-of-health estimation with half cell electrode potential. Electrochim Acta 2023;459:142588. http://dx.doi.org/10.1016/j.electacta.2023.142588.

[30] Yang S, Zhang C, Jiang J, Zhang W, Gao Y, Zhang L. A voltage reconstruction model based on partial charging curve for state-of-health estimation of lithium-ion batteries. J Energy Storage 2021;35:102271. http://dx.doi.org/10.1016/j.est.2021.102271.

[31] Xu X, Xu Z, Wang T, Xu J, Pei L. Open-circuit voltage curve reconstruction for degrading lithium-ion batteries utilizing discrete curve fragments from an online dataset. J Energy Storage 2022;56(B):106003. http://dx.doi.org/10.1016/j.est.2022.106003.

[32] Cui Z, Cui N, Li C, Lu J, Zhang C. Online identification and reconstruction of open-circuit voltage for capacity and electrode aging estimation of lithium-ion batteries. IEEE Trans Ind Electron 2023;70(5):4716–26. http://dx.doi.org/10.1109/TIE.2022.3187596.

[33] Aykol M, Gopal CB, Anapolsky A, Herring PK, van Vlijmen B, Berliner MD, et al. Perspective—Combining physics and machine learning to predict battery lifetime. J Electrochem Soc 2021;168(3):030525. http://dx.doi.org/10.1149/1945-7111/abec55.

[34] Liang Y, Wang S, Fan Y, Hao X, Liu D, Fernandez C. State of health prediction of lithium-ion batteries using combined machine learning model based on nonlinear constraint optimization. J Electrochem Soc 2024;171(1):010508. http://dx.doi.org/10.1149/1945-7111/ad18e1.

[35] Tian J, Xiong R, Shen W, Sun F. Electrode ageing estimation and open circuit voltage reconstruction for lithium ion batteries. Energy Storage Mater 2021;37:283–95. http://dx.doi.org/10.1016/j.ensm.2021.02.018.

[36] Bian X, Wei Z, Li W, Pou J, Sauer DU, Liu L. State-of-health estimation of lithium-ion batteries by fusing an open circuit voltage model and incremental capacity analysis. IEEE Trans Power Electron 2022;37(2):2226–36. http://dx.doi.org/10.1109/TPEL.2021.3104723.

[37] Li W, Chen J, Quade K, Luder D, Gong J, Sauer DU. Battery degradation diagnosis with field data, impedance-based modeling and artificial intelligence. Energy Storage Mater 2022;53:391–403. http://dx.doi.org/10.1016/j.ensm.2022.08.021.

[38] Ruan H, Chen J, Ai W, Wu B. Generalised diagnostic framework for rapid battery degradation quantification with deep learning. Energy AI 2022;9:100158. http://dx.doi.org/10.1016/j.egyai.2022.100158.

[39] Sun S, Zhang H, Ge J, Che L. State-of-health estimation for lithium-ion battery using model-based feature optimization and deep extreme learning machine. J Energy Storage 2023;72(E):108732. http://dx.doi.org/10.1016/j.est.2023.108732.

[40] Narayanan SSS, Thangavel S. Terminal voltage prediction of li-ion batteries using combined neural network and teaching learning based optimization algorithm. Appl Soft Comput 2023;133:109954. http://dx.doi.org/10.1016/j.asoc.2022.109954.

[41] Guo R, Xu Y, Hu C, Shen W. A curve relocation approach for robust battery open circuit voltage reconstruction and capacity estimation based on partial charging data. IEEE Trans Power Electron 2024;39(3):3760–73. http://dx.doi.org/10.1109/TPEL.2023.3347236.
[42] Nocedal J, Wright SJ. Numerical optimization. 2nd ed.. Springer; 2006, http://dx.doi.org/10.1007/978-0-387-40065-5.
[43] Tan C, Sun F, Kong T, Zhang W, Yang C, Liu C. A survey on deep transfer learning. In: Artificial neural networks and machine learning – ICANN. 2018, p. 11141. http://dx.doi.org/10.1007/978-3-030-01424-7_27.
[44] Weber M, Auch M, Doblander C, Mandl P, Jacobsen H-A. Transfer learning with time series data: A systematic mapping study. IEEE Access 2021;9:165. http://dx.doi.org/10.1109/ACCESS.2021.3134628.
[45] Hyndman RJ, Koehler AB. Another look at measures of forecast accuracy. Int J Forecast 2006;22–4:679–88. http://dx.doi.org/10.1016/j.ijforecast.2006.03.001.
[46] Schmitt J, Schindler M, Jossen A. Change in the half-cell open-circuit potential curves of silicon–graphite and nickel-rich lithium nickel manganese cobalt oxide during cycle aging. J Power Sources 2021;506:230240. http://dx.doi.org/10.1016/j.jpowsour.2021.230240.
[47] Schmitt J, Schindler M, Oberbauer A, Jossen A. Determination of degradation modes of lithium-ion batteries considering aging-induced changes in the half-cell open-circuit potential curve of silicon–graphite. J Power Sources 2022;532:231296. http://dx.doi.org/10.1016/j.jpowsour.2022.231296.
[48] Bin-Mat-Arishad I, Wimarshana B, Fly A. Influence of voltage profile and fitting technique on the accuracy of lithium-ion battery degradation identification through the voltage profile model. J Energy Storage 2023;70:107884. http://dx.doi.org/10.1016/j.est.2023.107884.
[49] Virtanen P, Gommers R, Oliphant TE, Haberland M, Reddy T, Cournapeau D, et al. SciPy 1.0 contributors, SciPy 1.0: Fundamental algorithms for scientific computing in Python. Nature Methods 2020;17(3):261–72, https://rdcu.be/b08Wh.
[50] Li C, Han X, Zhang Q, Li M, Rao Z, Liao W, et al. State-of-health and remaining-useful-life estimations of lithium-ion battery based on temporal convolutional network-long short-term memory. J Energy Storage 2023;74(Part B):109498. http://dx.doi.org/10.1016/j.est.2023.109498.
[51] Liu S, Chen Z, Yuan L, Xu Z, Jin L, Zhang C. State of health estimation of lithium-ion batteries based on multi-feature extraction and temporal convolutional network. J Energy Storage 2024;75:109658. http://dx.doi.org/10.1016/j.est.2023.109658.
[52] Zhou D, Li Z, Zhu J, Zhang H, Hou L. State of health monitoring and remaining useful life prediction of lithium-ion batteries based on temporal convolutional network. IEEE Access 2020;8:53307–20. http://dx.doi.org/10.1109/ACCESS.2020.2981261.
[53] Zhou D, Wang B. Battery health prognosis using improved temporal convolutional network modeling. J Energy Storage 2022;51:104480. http://dx.doi.org/10.1016/j.est.2022.104480.
[54] Bai S, Kolter JZ, Koltun V. An empirical evaluation of generic convolutional and recurrent networks for sequence modeling. 2018, http://dx.doi.org/10.48550/arXiv.1803.01271, arXiv preprint.
[55] Xu H, Wu L, Xiong S, Li W, Garg A, Gao L. An improved CNN-LSTM model-based state-of-health estimation approach for lithium-ion batteries. Energy 2023;276:127585. http://dx.doi.org/10.1016/j.energy.2023.127585.
[56] Victoria AH, Maragatham G. Automatic tuning of hyperparameters using Bayesian optimization. Evol Syst 2021;12:217–23. http://dx.doi.org/10.1007/s12530-020-09345-2.
[57] O'Malley T, Bursztein E, Long J, Chollet F, Jin H, Invernizzi L, et al. Keras tuner, GitHub. 2019, https://github.com/keras-team/keras-tuner.
[58] Kingma DP, Ba J. Adam: A method for stochastic optimization. 2014, http://dx.doi.org/10.48550/arXiv.1412.6980, arXiv, arXiv:1412.6980.
[59] Rogge M, Jossen A. Path-dependent ageing of lithium-ion batteries and implications on the ageing assessment of accelerated ageing tests. Batter Supercaps 2024;7:e202300313. http://dx.doi.org/10.1002/batt.202300313.
[60] Abdallah ZS, Du L, Webb GI. Data preparation. In: Encyclopedia of machine learning and data mining. 2016, p. 318–27. http://dx.doi.org/10.1007/978-1-4899-7502-7_62-1.
[61] Schmalstieg J, Käbitz S, Ecker M, Sauer DU. A holistic aging model for li(NiMnCo) O2 based 18650 lithium-ion batteries. J Power Sources 2014;257:325–34. http://dx.doi.org/10.1016/j.jpowsour.2014.02.012.
[62] Birkl CR, Roberts MR, McTurk E, Bruce PG, Howey DA. Degradation diagnostics for lithium ion cells. J Power Sources 2017;341:373–86. http://dx.doi.org/10.1016/j.jpowsour.2016.12.011.
[63] Sieg J, Schmid AU, Rau L, Gesterkamp A, Storch M, Spier B, et al. Fast-charging capability of lithium-ion cells: Influence of electrode aging and electrolyte consumption. Appl Energy 2022;305:117747. http://dx.doi.org/10.1016/j.apenergy.2021.117747.
[64] Epding B, Broda A, Rumberg B, Jahnke H, Kwade A. Development of durable 3-electrode lithium-ion pouch cells with LTO reference mesh: Aging and performance studies. J Electrochem Soc 2019;166(8):A1550. http://dx.doi.org/10.1149/2.0851908jes.

2.3 Generating a Comprehensive Battery Aging Database

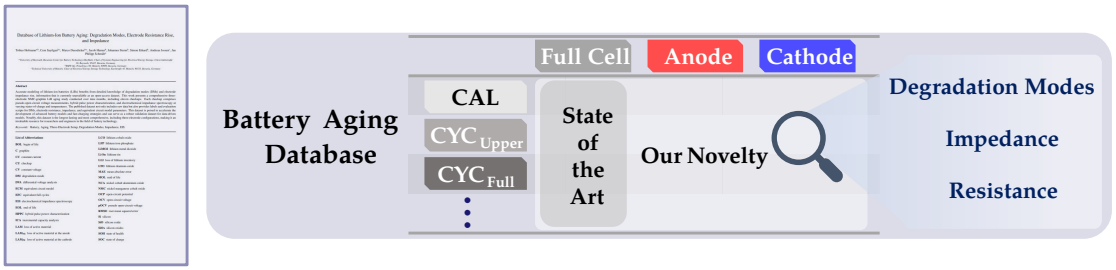

Figure 2.5: The trimmed outline of the thesis structure with focus on this chapter.

Until now, this thesis has focused on SOH_C, OCV, and DMs. However, to truly characterize a LiB, it is essential to also consider its dynamic behavior and the SOH in that context, specifically SOH_R and SOH_{UBE}. A significant challenge is the lack of data describing degradation at the electrode level, which makes it difficult to monitor this behavior and the relationship between DMs and resistance increase. Understanding this would enable several advancements: Developing more accurate OCV reconstruction methods by precisely attributing overpotentials to the respective electrode, and enabling more precise fast-charging by reducing the lithium plating buffer. Knowing the anode resistance allows for setting the C-rate as high as possible while maintaining a positive anode potential. This exploration not only addresses current challenges but also sets the stage for future research directions, highlighting the potential for further advancements in battery technology.

Thus, the research question is: What dataset is required to extend the SOH estimation to other SOH metrics, such as SOH_R and SOH_{UBE}?

A comprehensive survey of 23 public battery aging datasets [27; 29; 31; 77; 195; 196; 211–231] was conducted, focusing on the availability of OCV / pOCV, HPPC, and electrochemical impedance spectroscopy (EIS) measurements, as well as the inclusion of temperature and SOC variation, and – most importantly – the use of three-electrode configurations. This survey reveals that no dataset with a three-electrode configuration [29; 31; 211–213] fulfills all criteria. On a full-cell scale, many freely available datasets exist [27; 77; 195; 196; 214–231], however, they do not include measured half-cell data, making it impossible to yield validated DMs and electrode resistance values. Hence, there is a significant research gap in generating a comprehensive three-electrode database that includes DMs, resistance, and impedance labels at the electrode level.

Eighteen laboratory three-electrode cells (PAT-cells) were constructed using state-of-the-art cathode material (NMC955) and graphite as anode material, each with a capacity of approximately 10 mAh. Six distinct aging paths were defined, such as calendar aging, cyclic aging, and fast-charging, with three cells per aging path, each designed to trigger specific DMs. In total, three large and eight small RPTs thoroughly characterized the LiBs, including pOCV, EIS and HPPC at varying SOC and temperature reference points; large RPTs included dis-

charge direction and more SOC reference points. The generation of DMs and evaluation of resistance and impedance at the electrode level for every test point resulted in a substantial database. The dataset was enriched by fitted equivalent circuit model (ECM) parameters for each, the full cell, the cathode, and the anode, based on the EIS and HPPC measurement. Validation confirmed high measurement quality.

All cells were aged for more than nine months, maintaining an SOH above 67 %. The cells underwent between 20 to above 600 equivalent full cycles (EFCs). The study introduces state-of-the-art fitting protocols for pOCV, EIS, and HPPC.

One of the most comprehensive electrode aging datasets has been generated and is publicly available for researchers to utilize. All cycling and fitting protocols to accurately reproduce the experiment are published. This dataset enables the validated development of state-of-the-art SOH estimation algorithms, independent of the SOH metric.

The paper begins with background and summary, presenting a comprehensive literature survey and capturing available battery degradation datasets and their limitations, revealing a significant gap. The method section details the experimental design, cell assembly and formation, the aging test itself, and the RPT procedure, including the fitting procedure for the pOCV, HPPC, and EIS. The data records section presents the structure of the database, including raw data, cycling, and fitting protocols. Technical validation confirms the high quality of the database through examination of the battery cycling system, half-cell potential measurements, and fitting results. Lastly, usage notes for the reader are provided.

Publication Notes

The article *Database of Lithium-Ion Battery Aging: Degradation Modes, Electrode Resistance Rise, and Impedance* is presented in the following. The article will be submitted to the Journal Nature Scientific Data for peer review in 2026. The permanent web link to this draft version will be available under `https://epub.uni-bayreuth.de/`.

Author Contributions

T. Hofmann and C. Sayilgan developed the method and the test bench. T. Hofmann and C. Sayilgan built the laboratory cells, assisted by M. Duesdieker. T. Hofmann and C. Sayilgan conducted the experiments, supervised the test-bench, and evaluated the data. T. Hofmann developed the database and wrote the manuscript. J. Hamar, J. Sturm, S. Erhard, A. Jossen and J.P. Schmidt supervised the research project, discussed the findings, and reviewed the manuscript.

Database of Lithium-Ion Battery Aging: Degradation Modes, Electrode Resistance Rise, and Impedance

Tobias Hofmann[a,b], Cem Sayilgan[b,c], Marco Duesdieker[b,c], Jacob Hamar[b], Johannes Sturm[b], Simon Erhard[b], Andreas Jossen[c], Jan Philipp Schmidt[a]

[a] *University of Bayreuth, Bavarian Center for Battery Technology (BayBatt), Chair of Systems Engineering for Electrical Energy Storage, Universitätsstraße 30, Bayreuth, 95447, Bavaria, Germany*
[b] *BMW AG, Petuelring 130, Munich, 80809, Bavaria, Germany*
[c] *Technical University of Munich, Chair of Electrical Energy Storage Technology, Karlstraße 45, Munich, 80333, Bavaria, Germany*

Abstract

Accurate modeling of lithium-ion batteries (LiBs) benefits from detailed knowledge of degradation modes (DMs) and electrode impedance rise, information that is currently unavailable as an open-access dataset. This work presents a comprehensive three-electrode NMC-graphite LiB aging study conducted over nine months, including eleven checkups. Each checkup comprises pseudo-open-circuit voltage measurements, hybrid pulse power characterization, and electrochemical impedance spectroscopy at varying states-of-charge and temperatures. The published dataset not only includes raw data but also provides labels and evaluation scripts for DMs, electrode resistance, impedance, and equivalent circuit model parameters. This dataset is poised to accelerate the development of advanced battery models and fast-charging strategies and can serve as a robust validation dataset for data-driven models. Notably, this dataset is the longest-lasting and most comprehensive, including three-electrode configurations, making it an invaluable resource for researchers and engineers in the field of battery technology.

Keywords: Battery, Aging, Three-Electrode Setup, Degradation Modes, Impedance, EIS

List of Abbreviations

BOL begin of life

C graphite

CC constant current

CU checkup

CV constant voltage

DM degradation mode

DVA differential voltage analysis

ECM equivalent circuit model

EFC equivalent full cycles

EIS electrochemical impedance spectroscopy

EOL end of life

HPPC hybrid pulse power characterization

ICA incremental capacity analysis

LAM loss of active material

LAM_{NE} loss of active material at the anode

LAM_{PE} loss of active material at the cathode

LCO lithium cobalt oxide

LFP lithium iron phosphate

LiMO2 lithium metal dioxide

Li-Sn lithium-tin

LLI loss of lithium inventory

LTO lithium-titanium-oxide

MAE mean absolute error

MOL mid of life

NCA nickel cobalt aluminium oxide

NMC nickel manganese cobalt oxide

OCP open-circuit potential

OCV open-circuit voltage

pOCV pseudo open-circuit voltage

RMSE root mean squared error

Si silicon

SiO silicon oxide

SiOx silicon oxides

SOH state of health

SOC state of charge

1. Background and Summary

Lithium-ion batteries are extensively utilized in the automotive sector because of their superior energy storage capacity and extended lifespan. For users, two essential considerations are the durability of the battery and the speed of the charging process. These two requirements are inseparably interconnected: While advancements in technology have improved charging speeds for new vehicles, the duration of charging significantly increases with battery aging. This is primarily because internal battery management systems reduce the charging current to protect the battery from accelerated degradation caused by lithium plating. Lithium plating occurs when the potential of the negative electrode falls below 0 V vs. Li/Li^+, a phenomenon that is exacerbated by high current and low temperatures [1, 2, 3]. To effectively monitor the risk of lithium plating, it is essential for battery models to accurately estimate the impedance of the negative electrode. The decline in charging speed over the battery's lifetime can be attributed to the fact that pristine batteries are relatively easy to characterize, and there is a wealth of data available for them. In this optimal state, battery models can be finely parametrized to accurately estimate the potential of the negative electrode, allowing for the determination of the optimal current that maximizes charging speed while ensuring that the negative electrode potential remains above 0 V vs. Li/Li^+. However, the situation becomes significantly more complex for degraded batteries. Direct measurement of the negative electrode potential during operation over time is not feasible, necessitating the implementation of safety buffers to maintain positive electrode potentials.

Benefits may arise from open-access datasets that include information about the electrode resistance over lifetime. Table 1 summarizes available research studies and open-access datasets that incorporate impedance and capacity information over aging.

Especially the usage of three-electrode setups, enabling the measurement of electrode potentials, lacks quantitative data in current literature. Abrahm et al. [4] used NCA-C cells with a lithium-tin (Li-Sn) reference to study the impedance rise via HPPC and EIS during a calendar aging study. However, only a single aging path and no OCV measurement was conducted. Xu et al. [5] investigated the evolution of degradation modes (DMs) and impedance rise on electrode level by inserting either a lithium-metal or a lithium-titanium-oxide (LTO) coated copper wire into NMC-C cells. A subsequent post-mortem analysis validated their results from a differential voltage analysis (DVA) and enables further research with three-electrode configurations. As stated in their publication [5] they will make the data freely available on request. Many aging studies [6, 7, 8] were conducted with three-electrode configurations which reveal promising insights, however, without explicitly sharing the data with the community: Belt et al. [6] investigated the capacity fade and impedance rise of commercial NMC-C cells modified with a lithium-metal reference electrode to track the electrode shares. Their study revealed that especially the positive electrode experiences impedance rise and is therefore mostly responsible for the full-cell resistance. Epding et al. [7] analyzed the influence of varying three-electrode configurations over aging and yielded that a LTO coated aluminum mesh has minor influence on the impedance but accelerates the capacity fade. Friedrich et al. [8] yields that upper cycling is most beneficial for the lifetime of NCA-Si cells with a lithium-metal reference by reaching almost 600 equivalent full cycles (EFC).

Much more comprehensive aging datasets exist on full-cell level without three-electrode configurations [9, 10, 11, 12, 13, 14, 15, 16, 17, 18, 19, 20, 22, 23, 24, 25, 26, 27, 28, 29, 30, 31, 32]. E.g., Luh et al. [9] have aged 228 commercial NMC-(C+SiO) lithium-ion cells with varying calendar and cyclic aging conditions for more than one year. During their checkup (CU), they measured the HPPC and EIS at varying SOC and temperature reference points. However, the OCV change was not covered during their experiment. Geslin et al. [14] and Cui et al. [15] both included OCV and HPPC measurements during their CU to analyze the influence of varying cyclic aging paths [14] or the influence of formation protocols [15]. Many different authors [23, 28, 29, 30, 31] have analyzed the OCV change and incorporated HPPC and EIS measurements at varying SOC reference points during their CU for various long-term aging studies. While DMs can be accessed via OCV-reconstruction tools, i.e. DVA-fitting, the electrode specific impedance rise cannot be gathered.

A significant research gap exists in the availability of battery aging data at the electrode level, encompassing both electrode impedance rise and DMs. This lack of accessible data hinders the development of effective strategies for managing battery performance as it ages. Our proposed dataset addresses this gap by including 18 NMC-graphite experimental three-electrode lab cells, aged through six distinct aging paths. Each aging path is designed to trigger specific DMs, resulting in a comprehensive open-access dataset that can be utilized for various research questions.

The cells under investigation were aged over a period of nine months, with cyclic aged cells surpassing 600 EFC. The three-electrode setup enabled continuous measurement of the anode potential, which is available for characterization. The CU procedure incorporated pseudo open-circuit voltage (pOCV) measurements to generate DMs labels, as well as HPPC and EIS tests at various SOC and temperature reference points. These tests facilitated the numerical calculation of resistance values at both the full cell and electrode levels. Additionally, individual equivalent circuit models (ECMs) were fitted to the data in both the time and frequency domains to enrich the dataset.

Our dataset serves multiple purposes: It aids in the development of various innovative state estimation methods and functions as a validation tool by providing true labels for each cell. Furthermore, the novel provision of DMs alongside impedance rise at the electrode level enables the development of anode potential estimators, which ultimately enhance novel fast-charging algorithms.

2. Methods

The following sections provide a comprehensive overview of the experimental design and the post-processing steps em-

Table 1: State-of-the-art available battery aging datasets including their information of open-circuit voltage (OCV) change, hybrid pulse power characterization (HPPC) and electrochemical impedance spectroscopy (EIS) testing, temperature and state of charge (SOC) variation and the usage of three-electrode setups.

Study	OCV	HPPC	EIS	Temp.	SOC	Three Electrode	Type of lithium-ion cells and study
Abraham et al. [4]	No	Yes	Yes	No	Yes	Yes	NCA-C; Calendar aging at 55 °C
Xu et al. [5]	Yes	No	Yes	No	Yes	Yes	7 NMC-C; Analysis of DVA as a tool to evaluate DMs
Belt et al. [6]	Yes	Yes	No	No	Yes	Yes	85 NMC-C; 15 calendar and cyclic aging paths
Epding et al. [7]	No	No	Yes	No	No	Yes	18 NMC-C; Analysis of varying three-electrode configurations
Friedrich et al. [8]	No (only C/10)	Yes	No	No	Yes	Yes	8 NCA-Si; Analysis of varying voltage windows
Luh and Blank [9]	No	Yes	Yes	Yes	Yes	No	228 NMC-(C+SiO); Calendar and cyclic aging
Stroebl et al. [10]	Yes	Yes	No	Yes	Yes	No	279 NMC-C; 71 combined calendar and cyclic aging paths
Li et al. [11]	No (only C/10)	Yes	No	No	Yes	No	40 NMC-(C+SiO); 5 cyclic aging paths
van Vlijmen et al. [12]	No (only C/5)	Yes	No	No	Yes	No	363 NCA-(C+SiOx); 218 cyclic aging paths
Lam et al. [13]	No (only C/5)	No	No	No	No	No	232 LFP-C / NCA-C / NMC-C / LCO-C; 13 year calendar aging
Geslin et al. [14]	Yes	Yes	No	No	Yes	No	92 NCA-(C+SiO); 10 cyclic aging paths
Cui et al. [15]	Yes	Yes	No	No	Yes	No	186 NMC-C; Varying formation protocols
Schmitt et al. [16]	Yes	Yes	No	No	No	No	10 NMC-(C+SiO); 5 calendar and cyclic aging paths
Bole et al. [17, 18]	Yes	Yes	Yes	Yes	Yes	No	34 NCA-C; Various cyclic aging paths
Birkl [19, 20, 21]	Yes	No	No	No	No	No	8 LiMO2-C; One cyclic aging path
Catenaro and Onori [22]	Yes	No	No	Yes	No	No	6 NCA-C, 6 NMC-C, 6 LFP-C; Comparison of cell chemistries under different discharge tests
Pozzato et al. [23]	Yes	Yes	Yes	No	Yes	No	10 NMC-(C+Si); 23 months of cycling with real-world EV driving profiles
Li et al. [24, 25, 26]	No (only C/10)	Yes	No	No	Yes	No	28 NCA-(C+Si); One cyclic aging path
Wildfeuer et al. [27]	No (only C/10)	Yes	No	No	Yes	No	196 NCA-(C+SiO); Varying cyclic and calendar aging conditions
Bessmann et al. [28]	Yes	Yes	Yes	No	Yes	No	12 NMC-C cells; Analysis of AC harmonics
Mohtat et al. [29]	Yes	Yes	Yes	No	Yes	No	31 NMC-C; Varying cyclic aging paths
Raj et al. [30]	Yes	Yes	Yes	No	Yes	No	12 NCA-C; Analysis of path-dependent aging
Goldammer et al. [31]	Yes	Yes	Yes	No	Yes	No	60 NMC-C; Analysis of AC ripples

Cathode: nickel cobalt aluminium oxide (NCA), nickel manganese cobalt oxide (NMC), lithium iron phosphate (LFP), lithium cobalt oxide (LCO), lithium metal dioxide (LiMO2)

Anode: graphite (C), silicon (Si), silicon oxide (SiO), silicon oxides (SiOx)

ployed to generate the data labels presented in this study. We place significant emphasis on the raw data during the evaluation process, which includes measurements such as pOCV, HPPC, and EIS. These measurements are conducted at both the full cell and electrode levels to ensure a thorough analysis. Additionally, state-of-the-art processing techniques are utilized and provided

to derive labels that encompass various DMs, impedance rise, and fitted ECMs, thereby enhancing the robustness and utility of our dataset.

2.1. Experiment Design

The aging test series conducted in this study is illustrated in Figure 1, providing a general overview of the experimental process. The entire experiment spanned over nine months and comprised three main stages: cell assembly and formation (Figure 1a), the aging test itself (Figure 1b), and post-processing (Figure 1c).
In total, 11 CUs were performed, with each aging sequence running for exactly 18 d. Hence, a total of 10 aging sequences with a combined duration of 180 d were conducted. Three out of all CUs were extended to also include the discharge direction. These extended CUs took place initially after formation (begin of life (BOL)), after the first five CUs (mid of life (MOL)), and at the very end (end of life (EOL)). One standard CU took approximately 5 d, while an extended CU lasted for almost 11 d. Consequently, during the experiment, the cells were characterized for approximately 73 d. While the overall influence of the CU protocol must not be neglected, the actual influence is marginal, as the CUs only account for 29 % of the total duration and stress the cells with very low C-rates.
Each step of the process is described in detail in the following subsections. All code, test profiles, measurements, and the gathered data will be made available open-access in https://epub.uni-bayreuth.de/.

2.2. Cell Assembly and Formation

The PAT-Cell M from El-Cell [33] was used to enable three-electrode measurements. Prior research [34] reveals this three-electrode configuration as a subtle tool for small-scale aging experiments that reflect similar aging processes as commercial and even large scale cells. In total, 18 cells were manufactured, divided into six aging groups with three cells each.
The PAT-Cells were assembled with copper upper plungers (ECC1-01-0026-A), aluminum lower plungers (ECC1-01-0027-A_200), and aluminum sealing rings (ECC1-00-0232-G/X). The insulation sleeve (ECC1-00-0210-O/X) used lithium as the reference and a 260 µm glass fibre separator from El-Cell [33].
We used dual-coated sheets with NMC955 for the positive electrode and graphite for the negative electrode. The NMC had a specific capacity of 0.220 mAh/mg and the graphite had a specific capacity of 0.355 mAh/mg. In the first step, one side of each electrode sheet was cleansed with distilled water for the anode and NMP for the cathode, respectively, all under dry room conditions. All additional hardware of the PAT cells was cleansed with distilled water. 18 mm coins were punched out from the electrode sheets and measured three times for thickness and weight. Due to the configuration of the PAT cell, no anode overhang exists in the setup, i.e., $A_{PE}/A_{NE} = 1$. This, however, has negligible impact on the aging trajectroy [34]. In total, 28 cathode and 26 anode coins were manufactured. The corresponding raw data can be found in the data repository. All materials, including PAT-cell hardware and electrode sheets, were dried for at least 12 h under dry room conditions at 60 °C.
Before the final assembly of the cells, the electrodes were visually examined, and their weights and thicknesses were evaluated to ensure the most uniform distribution in the final electrode set. PAT-Cell manufacturing took place under dry room conditions. We used 100 µL of LP572 electrolyte per cell.
Within 2 h after final assembly, the formation protocols started with two initial constant current (CC)-constant voltage (CV) charge/discharge cycles at C/25 and the CV criterion at C/100. Finally, another C/10 CC-CV charge/discharge cycle was performed before the initial CU started.
Table 2 groups the cells into varying aging paths and maps their measurement system and channel. Depending on the available devices, EIS was possible on both full-cell and negative electrode levels, only on the full-cell level, or on neither. The last column shows the group for the test plans, as they were run sequentially to increase data quality.

2.3. Aging Test

The objective of the test series was to generate a comprehensive battery aging dataset, including electrode aging information for several aging paths. To achieve a diverse range of aging paths, we developed multiple degradation profiles that specifically target different DMs. This approach ensures that the parameter space of our dataset is extensive, facilitating the identification of patterns within the data.
To obtain statistically significant results, each aging path included three cells. For all test profiles, a rest phase of 30 min was maintained between consecutive charging and discharging phases. The current criterion during CV charging or discharging was fixed at C/100. It was only changed after the MOL CU because the prior aging phase showed CV-phases lasting over 3 hour and decreasing the effective cycle count. Hence, the CV-criterion was reduced to C/20 after the MOL CU. CC-CV charging was consistently performed in tests where a SOC of 0 or 100 % was set. The individual capacity per cell was calculated from the charge balance during the prior pOCV measurement in the CU. Individual SOCs were set based on this value. The C-rate always referred to the initial nominal capacity of the cells, i.e., 10.5 mAh. The ambient temperature was maintained at 25 °C, except for the calendar aging sequences, which were performed at 55 °C.
Two aging paths were designed to trigger loss of lithium inventory (LLI), a mode accelerated by high temperature and high storage SOCs [35, 36]. These conditions lead to accelerated solid electrolyte interphase (SEI) and electrolyte decomposition, two mechanisms primarily responsible for LLI [37, 38, 39]. For both aging paths, the cells were kept at an ambient temperature of 55 °C.

- **Standard Calendar Aging (CAL):** During the standard calendar aging phase, the cells were CC-CV-charged with C/2 up to 100 % SOC and then kept there.
- **Accelerated Calendar Aging (CAL_{acc}):** The accelerated calendar aging phase included additional slow cycling be-

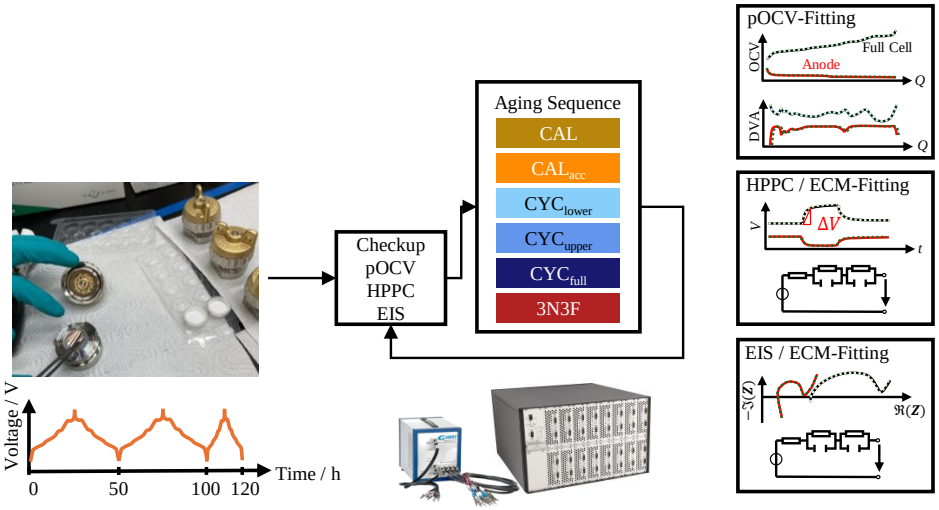

(a) Cell Assembly and Formation (b) Aging Test (c) Evaluation

Figure 1: Experiment Overview / Graphical Abstract

Table 2: Cell serial number (SN), their connected battery testing systems (CTS) and the assigned channels for the full cell (FC) and the negative electrode (NE). The possibility for EIS measurements is provided. The cells were grouped in clusters of four each, to increase sampling rates.

SN	Aging Path	CTS	Channel	EIS-FC	EIS-NE	Group
6297	CAL	1460	CH00/01	yes	yes	A
6298	CYC_{lower}	1460	CH02/03	yes	no	A
6299	CAL_{acc}	1460	CH04/05	yes	yes	A
6300	CYC_{full}	1460	CH06/07	yes	yes	A
6301	3N3F	1460	CH08/09	yes	yes	B
6302	CYC_{upper}	1460	CH10/11	yes	yes	B
6303	CAL	1460	CH12/13	yes	yes	B
6304	CYC_{lower}	1460	CH14/15	yes	yes	B
6305	CAL_{acc}	1460	CH16/17	yes	yes	C
6306	CYC_{full}	1460	CH18/19	yes	yes	C
6307	3N3F	1460	CH20/21	yes	yes	C
6308	CYC_{upper}	1460	CH22/23	yes	yes	C
6309	CAL	1460	CH24/25	yes	yes	D
6310	CYC_{lower}	1460	CH26/27	yes	yes	D
6311	CAL_{acc}	1460	CH28/29	yes	yes	D
6312	CYC_{full}	1460	CH30/31	yes	yes	D
6313	3N3F	1463	CH00/01	no	no	E
6314	CYC_{upper}	1463	CH02/03	no	no	E

tween 30 % to 70 % SOC with C/5. Although conventionally this aging path must be assigned to *cyclic aging*, we refer to *calendar aging* as it accelerates the predominant DMs from the purely calendar aging path. More precisely, the additional cycling procedure was selected to accelerate SEI decomposition [37, 38, 39, 40].

Three varying cyclic aging conditions were designed with different SOC spans to trigger various degradation mechanisms. All cycling sequences were performed with a C-rate of C/2.

- **Lower Cycling Aging (CYC_{lower}):** This phase consists of cycling between 0 % to 40 % SOC to trigger loss of active material at the anode (LAM_{NE}). Many low cycles are expected to particularly cause particle cracking and loss of electric contact in the anode, correlating with many crossings of voltage plateaus of the anode [38, 39, 41, 42].
- **Upper Cycling Aging (CYC_{upper}):** This phase stresses the positive electrode by cycling between 40 % to 100 % SOC, leading to accelerated loss of active material at the cathode (LAM_{PE}). This stress is mainly due to increased

structural disordering, loss of electric contact, and particle cracking, all enhanced by many cycles in the upper SOC region [38, 39, 43]. Especially in Ni-rich cathodes, oxygen evolution further accelerates degradation [44, 45].

- **Full Cycling Sequence (CYC_{full}):** This sequence is designed to equally trigger loss of active material (LAM) in both the anode and the cathode by inducing the subsequent degradation mechanisms [38, 39, 41, 42, 43, 46, 47].

Finally, a fast-charging sequence was designed.

- **3N3F:** After three normal full charges (0 % to 100 % SOC with C/2), three fast-charging procedures follow. The fast-charging is conducted between 10 % to 80 % SOC, with the initial C-rate set to 3C. The C-rate decreases once the full cell voltage exceeds 4.2 V or the anode potential drops below 25 mV. The fast-charging procedure sets the C-rate as high as possible while still fulfilling both constraints. While the three normal charging events equally trigger LAM_{NE} and LAM_{PE}, the fast-charging events accelerate LLI due to SEI decomposition [38, 39, 48, 49].

Besides the 3N3F aging phase, which depends on the electrode potential measurement, all other reference electrode connections were temporarily disconnected during the aging phase to reduce the risk of leakage currents and following degradation of the lithium reference ring.

2.4. Checkup

Both CU protocols, the standard and extended CU, were designed to gather relevant degradation-dependent parameters. They included pOCV measurements, HPPC, and EIS measurements, all conducted at both full-cell and half-cell levels, as shown in Table 2. During validation of the measurement equipment, it was observed that the sampling rate decreased drastically from below 10 ms to above 200 ms if more than four channels were active in parallel. Consequently, all HPPC test protocols were designed in groups, as shown in the last column of Table 2. While one group was active, i.e., a test protocol was running, all other groups remained idle. Since only one active EIS measurement was possible at a time and more than four cells waiting for the response of the EIS device led to errors during validation, the sequential approach was also adopted for EIS.

The pOCV protocol commenced with an initial CC-CV discharge at a rate of C/3, concluding at C/100 when the voltage reached 2.8 V. Following a 30 min relaxation period, the pOCV measurement proceeded with a CC-CV charge at C/25. The charge throughput for each cell was recorded separately and subsequently utilized for SOC calibration during HPPC, EIS, and aging protocols. In scenarios involving an extended CU, the pOCV protocol continued with another 30 min relaxation at 100 % SOC, followed by a CC discharge at C/25. To address artifacts in the anode potential which aggravated the pOCV fitting, the C-Rate was reduced to C/50 starting with the MOL CU. This adjustment effectively resolved the issue and contributed to maintaining high data quality throughout the aging series.

The HPPC and EIS test protocols were conducted at three different ambient temperatures: 10 °C, 25 °C, and 40 °C. Initially, all cells were completely discharged as in the pOCV protocol. After 30 min of relaxation, all cells were CC charged to the first SOC reference point at 10 % with C/3 and again relaxed for 30 min. While the first group (Group A) started with the EIS protocol, the other groups (Groups B-D) remained idle with no active test protocol.

The galvanostatic EIS ran from 100 kHz to 100 mHz with 20 reference points per decade. The current amplitude was fixed at C/20.

After Group A finished the EIS measurements, all cells in that group moved to idle and Group B started its EIS measurement, and so forth. After all EIS measurements were completed, Group A started the HPPC protocol, which consisted of a 20 s CC-CV pulse at 1C and 5 min of relaxation, while the other groups remained idle. After Group A completed the HPPC test, Group B followed, and so forth. Once all groups finished the HPPC test in the charge direction, Group A repeated the HPPC protocol in the discharge direction. After Group A completed the discharge pulse test, Group B followed, and so forth. Due to the sequential HPPC approach, no additional relaxation step was necessary between tests. After successful completion of all EIS and HPPC tests at the first SOC stage, all channels were synchronized again and charged in parallel to the next SOC stage where the whole process was repeated.

The SOC stages for the standard CU were 10 %, 20 %, 50 %, 80 %, and 90 %. The extended CU also included the discharge direction and incorporated two additional SOC stages (15 % and 85 %) during the HPPC and EIS tests.

2.5. pOCV Evaluation

The measured pOCV during the CU was used to generate labels for the DMs. This was achieved by using a sequential fitting regime, exploiting the mechanistic model approach [50]. Figure 2 visualizes the procedure and the fitting result, i.e., DVA and incremental capacity analysis (ICA) result, for an exemplary cell (cell 6300) at an arbitrary CU (CU2). Initially, both electrode open-circuit potential (OCP) curves, i.e., OCP_{NE} and OCP_{PE}, were measured in the pristine state in both charge and discharge directions. Figure 2 (d) and (g) show the charge direction. The pristine OCP curves were gathered from an additional PAT cell, following the same assembly protocol as described in Section 2.2, measured at C/50 CC at 25 °C. The OCP curves were normalized to the SOC scale from 0 to 1. During each CU, the pOCV was measured in the charge direction, and during the extended CUs, the discharge direction was covered as well. The measured voltage signals during a standard CU, in this case for cell 6300 at CU2, are depicted in Figure 2 (a), (d) and (g). The mechanistic model assumes that the qualitative shape of the OCPs does not change during degradation. They solely scale and shift their curves relative to each other, changing the shape of the resulting OCV of the full cell. This scaling and shifting can be described with the help of alignment parameters $\vartheta = [\alpha_{NE}, \alpha_{PE}, \beta_{NE}, \beta_{PE}]$, which describe the

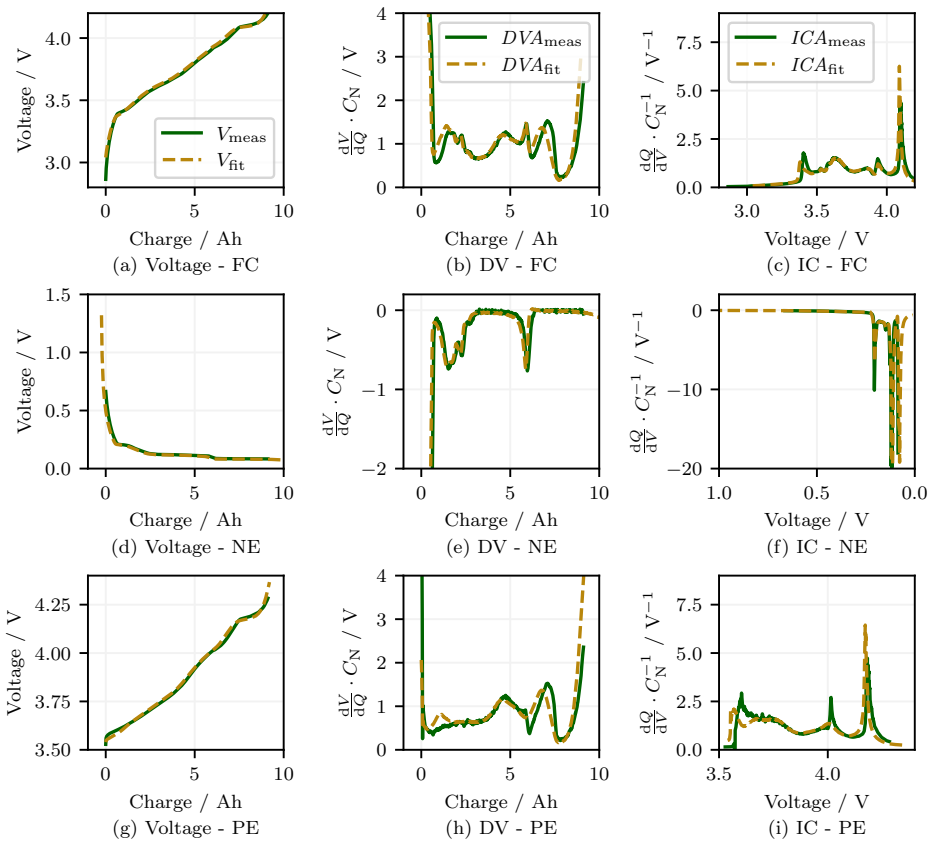

Figure 2: Fitting procedure and result for exemplary cell 6300 during CU2. All DVA and ICA curves are smoothed with the Savitzky-Golay filter using a window size of 15 and polynomial order of 2. Due to the high noise within the ICA of the anode (see (f)), the signal is additionally filtered by excluding all values below -20.

scaling (α values) and relative shifting (β values) of the OCPs. The scaled and shifted OCPs can be seen in Figure 2 (d) and (g). The resulting DMs can be finally calculated via simple equations [51, 52], where the loss of active material states how much capacity is lost within each electrode.

$$\mathrm{LAM_{NE}} = \frac{\alpha_{\mathrm{NE,pristine}} - \alpha_{\mathrm{NE}}}{\alpha_{\mathrm{NE,pristine}}} \tag{1}$$

$$\mathrm{LAM_{PE}} = \frac{\alpha_{\mathrm{PE,pristine}} - \alpha_{\mathrm{PE}}}{\alpha_{\mathrm{PE,pristine}}} \tag{2}$$

The LLI is the lost cyclable lithium inventory:

$$\mathrm{LLI} = \frac{C_{\mathrm{lit,pristine}} - C_{\mathrm{lit}}}{C_{\mathrm{lit,pristine}}} \tag{3}$$

The available lithium inventory C_{lit}, however, demands a case-sensitive definition [51, 52].

$$C_{\mathrm{lit}} = \begin{cases} (\alpha_{\mathrm{PE}} - \beta_{\mathrm{NE}} + \beta_{\mathrm{PE}}) \cdot C_{\mathrm{N}} & \text{, for } (\alpha_{\mathrm{PE}} - \beta_{\mathrm{NE}} + \beta_{\mathrm{PE}}) \leq \alpha_{\mathrm{NE}} \\ & \quad \wedge \ (\beta_{\mathrm{PE}} - \beta_{\mathrm{NE}}) \leq 0 \\ (\alpha_{\mathrm{NE}}) \cdot C_{\mathrm{N}} & \text{, for } (\alpha_{\mathrm{PE}} - \beta_{\mathrm{NE}} + \beta_{\mathrm{PE}}) > \alpha_{\mathrm{NE}} \\ & \quad \wedge \ (\beta_{\mathrm{PE}} - \beta_{\mathrm{NE}}) \leq 0 \\ (\alpha_{\mathrm{NE}} + \beta_{\mathrm{NE}} - \beta_{\mathrm{PE}}) \cdot C_{\mathrm{N}} & \text{, for } (\alpha_{\mathrm{NE}} + \beta_{\mathrm{NE}} - \beta_{\mathrm{PE}}) \leq \alpha_{\mathrm{PE}} \\ & \quad \wedge \ (\beta_{\mathrm{PE}} - \beta_{\mathrm{NE}}) \geq 0 \\ (\alpha_{\mathrm{PE}}) \cdot C_{\mathrm{N}} & \text{, for } (\alpha_{\mathrm{NE}} + \beta_{\mathrm{NE}} - \beta_{\mathrm{PE}}) > \alpha_{\mathrm{PE}} \\ & \quad \wedge \ (\beta_{\mathrm{PE}} - \beta_{\mathrm{NE}}) \geq 0 \end{cases} \tag{4}$$

These DMs are derived via optimization, where the optimum $\hat{\vartheta}$ is the solution of a minimization task. Usually the optimization problem is formulated as follows:

$$
\begin{aligned}
\hat{\vartheta} &= \arg\min_{\vartheta} \; ||\mathrm{OCV}(Q) - \mathrm{OCV}_{\mathrm{reco}}(Q)\,||_2^2 \\
&= \arg\min_{\vartheta} \; ||\mathrm{OCV}(Q) - f(\mathrm{OCP}_{\mathrm{NE}}, \mathrm{OCP}_{\mathrm{PE}}, \vartheta, Q)\,||_2^2 \\
&\text{s.t.} \qquad \vartheta \geq \mathrm{lb} \\
&\qquad\quad \vartheta \leq \mathrm{ub} \\
&\qquad\quad f_{\mathrm{eq}}(\vartheta, \mathrm{OCV}, \mathrm{OCV}_{\mathrm{reco}}, ..) = 0 \\
&\qquad\quad f_{\mathrm{ineq}}(\vartheta, \mathrm{OCV}, \mathrm{OCV}_{\mathrm{reco}}, ..) \geq 0
\end{aligned}
\tag{5}
$$

In Equation 5, the measured OCV is given as a function of the charge throughput $\mathrm{OCV}(Q)$. The reconstructed OCV $\mathrm{OCV}_{\mathrm{reco}}(Q)$ is a function of both OCPs and the respective alignment parameter set, as well as the charge throughput: $\mathrm{OCV}_{\mathrm{reco}}(Q) = f(\mathrm{OCP}_{\mathrm{NE}}, \mathrm{OCP}_{\mathrm{PE}}, \vartheta, Q)$. For a detailed description of this function, we refer to other publications with a deeper focus on the optimization itself [16, 51].

As seen in Equation 5, optional constraints can be defined to guide the solution finding. The boundaries, lb and ub, are usually set by the user and require some cell-specific knowledge. The equality and inequality constraints can be any arbitrary function that stabilizes the optimization. Furthermore, the cost function can be modified to also include the DVA and/or ICA [52, 53, 54]. Even peak tracking can be included in the cost function or the constraints [36, 55].

Mostly least-squares solvers are used for the minimization [51, 52, 54]. Other approaches modify global optimization methods, e.g., particle swarm [56] or the genetic algorithm [55], for the problem. The unique PAT-cell setup enables the in-situ measurement of the OCPs, and, with that, allows a novel OCV-reconstruction method: While conventional OCV-reconstruction tools, based on full-cell voltage data, aim to minimize the discrepancy between the measured and the reconstructed OCV, which is a result of the potential difference between $\mathrm{OCP}_{\mathrm{PE}}$ and $\mathrm{OCP}_{\mathrm{NE}}$, we can directly use the OCPs. With that, we can modify the optimization task to a sequential two-step minimization problem: The first step is to fit the $\mathrm{OCP}_{\mathrm{NE}}$, including the OCP-fit, the DVA-fit, and peak tracking into the cost function.

$$
\begin{aligned}
&[\hat{\alpha}_{\mathrm{NE},i}, \hat{\beta}_{\mathrm{NE},i}] = \\
&\arg\min_{\alpha_{\mathrm{NE},i}, \beta_{\mathrm{NE},i}} \Big(x_1 \Big\| \mathrm{OCP}_{\mathrm{NE},i}(Q) - \mathrm{OCP}_{\mathrm{NE},i,\mathrm{reco}}(\alpha_{\mathrm{NE}}, \beta_{\mathrm{NE}}, Q) \Big\|_2^2 \\
&\qquad + x_2 \Big\| \mathrm{DVA}_{\mathrm{NE},i}(Q) - \mathrm{DVA}_{\mathrm{NE},i,\mathrm{reco}}(\alpha_{\mathrm{NE}}, \beta_{\mathrm{NE}}, Q) \Big\|_2^2 \\
&\qquad + x_3 \Big\| Q_{\mathrm{peak},i}(\mathrm{DVA}_{\mathrm{NE},i})/C_N - \\
&\qquad\qquad Q_{\mathrm{peak,reco},i}(\mathrm{DVA}_{\mathrm{NE},i,\mathrm{reco}})/C_N \Big\|_2^2 \Big) \\
&\text{s.t.} \qquad \alpha_{\mathrm{NE},i} \geq 0.8 \cdot \alpha_{\mathrm{NE},i-1} \\
&\qquad\quad \beta_{\mathrm{NE},i} \geq 0.8 \cdot \beta_{\mathrm{NE},i-1} \\
&\qquad\quad \alpha_{\mathrm{NE},i} \leq 1.1 \cdot \alpha_{\mathrm{NE},i-1} \\
&\qquad\quad \beta_{\mathrm{NE},i} \leq 1.1 \cdot \beta_{\mathrm{NE},i-1}
\end{aligned}
\tag{6}
$$

where the DVA is calculated by $\mathrm{DVA}_{\mathrm{NE}}(Q) = \frac{\partial \mathrm{OCP}_{\mathrm{NE}}(Q)}{\partial Q}$ and the peak-tracking term is solved by

$$
\begin{aligned}
Q_{\mathrm{peak}} &= Q(\max |\mathrm{DVA}_{\mathrm{NE}}(Q)|) \\
&\text{s.t.} \quad 0.3 \cdot C_N \leq Q \leq 0.7 \cdot C_N.
\end{aligned}
\tag{7}
$$

Respectively for the cathode, where peak-tracking is disabled:

$$
\begin{aligned}
&[\hat{\alpha}_{\mathrm{PE},i}, \hat{\beta}_{\mathrm{PE},i}] = \\
&\arg\min_{\alpha_{\mathrm{PE},i}, \beta_{\mathrm{PE},i}} \Big(x_1 \Big\| \mathrm{OCP}_{\mathrm{PE},i}(Q) - \mathrm{OCP}_{\mathrm{PE},i,\mathrm{reco}}(\alpha_{\mathrm{PE}}, \beta_{\mathrm{PE}}, Q) \Big\|_2^2 \\
&\qquad + x_2 \Big\| \mathrm{DVA}_{\mathrm{PE},i}(Q) - \mathrm{DVA}_{\mathrm{PE},i,\mathrm{reco}}(\alpha_{\mathrm{PE}}, \beta_{\mathrm{PE}}, Q) \Big\|_2^2 \Big) \\
&\text{s.t.} \qquad \alpha_{\mathrm{PE},i} \geq 0.8 \cdot \alpha_{\mathrm{PE},i-1} \\
&\qquad\quad \beta_{\mathrm{PE},i} \geq 0.8 \cdot \beta_{\mathrm{PE},i-1} \\
&\qquad\quad \alpha_{\mathrm{PE},i} \leq 1.1 \cdot \alpha_{\mathrm{PE},i-1} \\
&\qquad\quad \beta_{\mathrm{PE},i} \leq 1.1 \cdot \beta_{\mathrm{PE},i-1}
\end{aligned}
\tag{8}
$$

The weighting factors x_1, x_2, and x_3 are set to 1, 4, and 4, based on literature findings [53] and individual optimization. In both equations, there are no additional constraints except the lower and upper boundaries which depend on the previous iteration, i.e., the previous CU result. For the first iteration, i.e., $i = 0$, the boundaries are set to 1.0 to 1.2 for the α-values and -0.05 to 0.2 for the β-values.

For both optimization problems, we use the particle swarm optimizer from *pyswarm* [57], with a swarm size of 350, the maximum number of iterations of 250, and a termination criterion of a minimum change in function value above $1e-7$.

The resulting voltage, DVA and ICA fits are visualized for the full cell (Figure 2 (b) and (c)), the anode ((e) and (f)) and the cathode ((h) and (i)). Visually, a high fitting accuracy can be determined. The optimization yields the alignment parameter set $\vartheta = [1.151, 0.940, 0.0134, -0.00740]$ which results in a mean absolute OCV-fitting accuracy of 6.02 mV. Finally, Equations 1 to 4 can be used to derive the DMs from the gathered optimum alignment parameters: $\mathrm{LAM}_{\mathrm{NE}} = -0.0890\,\%$, $\mathrm{LAM}_{\mathrm{PE}} = 9.74\,\%$ and $\mathrm{LLI} = 9.40\,\%$.

2.6. HPPC Evaluation

As discussed in Section 2.4, the HPPC includes charge and discharge pulses at varying SOC reference points and three ambient temperatures. The gathered time-series data are evaluated numerically and by a fitting regime. Figure 3 shows the extracted pulse and relaxation phase exemplary for cell 6300 at CU1_BOL, 50 % SOC and 25 °C together with the fitted ECM from the pulse section. The 1C-pulse is applied for 20 s and data is collected with the maximum possible sampling rate of almost 10 ms. Due to the sequential CU protocol, only parts of the relaxation process were stored, i.e., 180 s. These time sections, however, are sufficient to fit ECMs.

A simple two RC ECM was selected as our model. The fitting approach follows *Method 1* proposed by Peng et al. [58]. All four sections (charge pulse and its relaxation phase, discharge pulse and its relaxation phase) are fitted individually by minimizing the voltage difference with respect to predefined boundary values of the ECM parameters R_0, R_1, R_2, C_1, and C_2. This

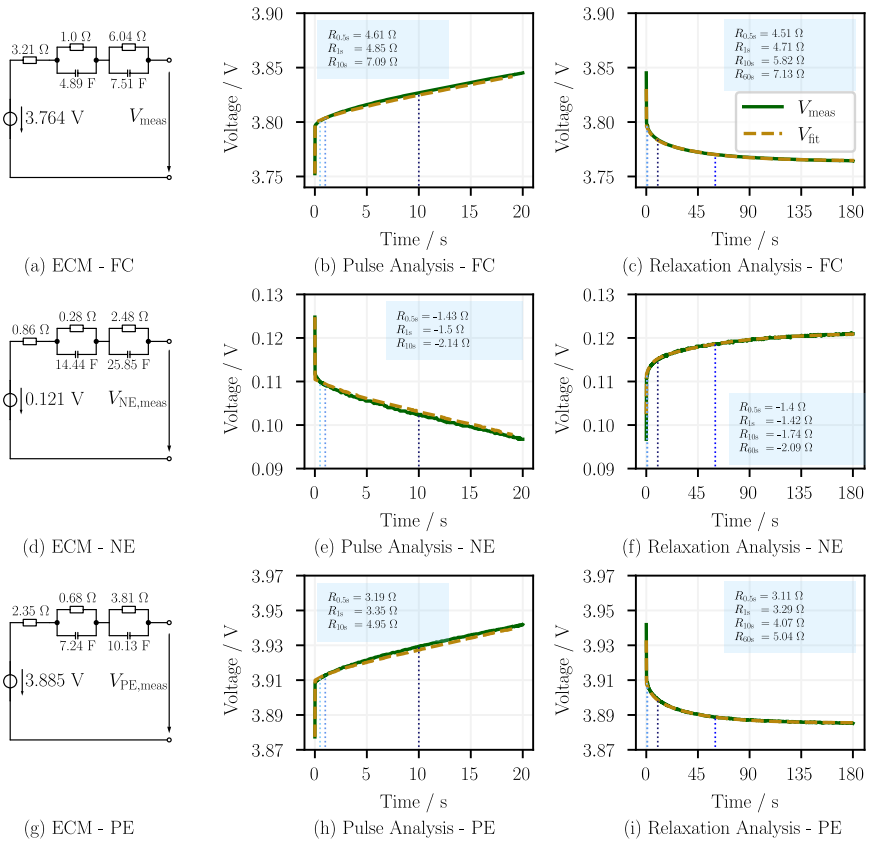

Figure 3: HPPC fitting procedure and result for exemplary cell 6300 during CU1_BOL at 50 % SOC, 25 °C and a 1C charge pulse for 20 s. An individual ECM is fitted for the full cell (a), the anode (d) and the cathode (g) based on the pulse analysis visualized in Subfigure (b), (e) and (h), respectively. The procedure is repeated for the relaxation process (Subfigure (c), (f) and (i)). For both, pulse and relaxation analysis, the calculated resistance values at constant time-steps from 0.5 s to 50 s are printed into the respective Subfigure.

fitting procedure is analogously applied to the electrode data, i.e., the negative and positive electrodes.
The voltage response, e.g., of the full cell in Figure 3 (b), can be described by the following equations

$$V_{\text{fit}} = \text{OCV}_{\text{fit/meas}} \pm V_1 \pm V_2 \pm IR_0 \tag{9}$$

$$\frac{\mathrm{d}V_1}{\mathrm{d}t} = \frac{-1}{R_1C_1}V_1 + \frac{1}{C_1}I \tag{10}$$

$$\frac{\mathrm{d}V_2}{\mathrm{d}t} = \frac{-1}{R_2C_2}V_2 + \frac{1}{C_2}I, \tag{11}$$

where $\text{OCV}_{\text{fit/meas}}$ is the measured or fitted voltage value prior to the pulse/relaxation period and I is the applied current. The sign of the individual summands depends on the pulse direction, i.e., positive for a charge pulse as the voltage increases, and negative for a discharge pulse as the voltage decreases.

Fitting during Relaxation
During the relaxation phase, as the current is zero, Equation 9 simplifies to:

$$V_{\text{fit,relax}} = \text{OCV}_{\text{fit}} \pm V_1 \pm V_2 \tag{12}$$

$$V_{\text{fit,relax}}(t) = \text{OCV}_{\text{fit}} \pm V_1(0)\exp\left(-\frac{t}{R_1C_1}\right) \pm V_2(0)\exp\left(-\frac{t}{R_2C_2}\right) \tag{13}$$

Here, OCV_{meas} is transformed to OCV_{fit} as the relaxation period of 180 s does not suffice to reach full relaxation. Hence, no value can be measured from the raw data, and fitting this value leads to higher accuracy. This can be further transformed into:

$$V_{\text{fit,relax}}(t) = A + B\exp(-\alpha t) + C\exp(-\beta t), \tag{14}$$

with the optimization parameters $\psi = [A, B, C, \alpha, \beta]$. The final optimization problem is formulated with additional boundary constraints as follows:

$$\begin{aligned}\hat{\psi} &= \arg\min_{\psi} \left\| V_{\text{meas}}(t) - V_{\text{fit,relax}}(t) \right\|_2^2 \\ &= \arg\min_{\psi} \left\| V_{\text{meas}}(t) - (A + B\exp(-\alpha t) + C\exp(-\beta t)) \right\|_2^2 \\ \text{s.t.} \quad & \psi \geq \text{lb} \\ & \psi \leq \text{ub}\end{aligned} \tag{15}$$

Cost function 15 is solved via a nonlinear least-squares solver, and the lower and upper boundaries are extracted from the optimal solution of the last CU during the same reference point, i.e., cell, temperature, SOC, and direction, by allowing the optimizer to search within 10 % to 200 % of this value. During CU1_MOL, the boundary for α and β were set to 0.01 to 2 and 0.001 to 0.2, respectively.
From Equation 15, the ECM-related parameters can be extracted via backtransformation:

$$\text{OCV}_{\text{fit}} = A \tag{16}$$

$$\tau_1 = \frac{1}{\alpha} = \frac{1}{R_1 C_1} \tag{17}$$

$$\tau_2 = \frac{1}{\beta} = \frac{1}{R_2 C_2} \tag{18}$$

$$R_1 = \frac{B}{(1 - \exp(-t_{\text{p}}\alpha))I} \tag{19}$$

$$R_2 = \frac{C}{(1 - \exp(-t_{\text{p}}\beta))I} \tag{20}$$

$$C_1 = \frac{1}{\alpha R_1} \tag{21}$$

$$C_2 = \frac{1}{\beta R_2} \tag{22}$$

Here, t_{p} is the duration of the applied pulse before the relaxation phase [58].

Fitting during Pulse
During the current section, Equation 9 requires all terms and can be written as:

$$\begin{aligned}V_{\text{fit,pulse}}(t) = \text{OCV}_{\text{meas}}(t) &\pm IR_0 \pm V_1(0)\exp\left(-\frac{t}{R_1 C_1}\right) \\ &\pm V_2(0)\exp\left(-\frac{t}{R_2 C_2}\right) \\ &\pm I\left[R_1\left(1 - \exp\left(-\frac{1}{R_1 C_1}\right)\right)\right. \\ &\left. + R_2\left(1 - \exp\left(-\frac{1}{R_2 C_2}\right)\right)\right]\end{aligned} \tag{23}$$

$$\begin{aligned}V_{\text{fit,pulse}}(t) = \text{OCV}_{\text{meas}} &\pm IR_0 \\ &\pm (A\exp(-\alpha t) + B\exp(-\beta t)) \\ &\pm I\left[C(1 - \exp(-\alpha t)) + D(1 - \exp(-\beta t))\right]\end{aligned} \tag{24}$$

Let's assume the current pulse starts at time t_0 and the highest possible sampling rate is Δt_{min}, i.e., 10 ms. During the current pulse, the ohmic resistance R_0 is directly calculated by the instantaneous voltage response:

$$R_0 = \left| \frac{V_{\text{meas}}(t_0 + \Delta t_{\text{min}}) - V_{\text{meas}}(t_0)}{I(t_0 + \Delta t_{\text{min}}) - I(t_0)} \right| \tag{25}$$

Note that in contrast to Equation 13, the OCV term is not an optimization parameter, but a measured quantity $\text{OCV}_{\text{meas}}(t)$ from the prior pOCV section. $\text{OCV}_{\text{meas}}(t)$ is defined as a lookup table that returns the measured OCV based on the charge quantity, where the first value $\text{OCV}_{\text{meas}}(0)$ is equal to the measured voltage before the applied current.
Thus, the optimization parameters in this case are $\psi = [A, B, C, D, \alpha, \beta]$, and the optimization problem is:

$$\begin{aligned}\hat{\psi} &= \arg\min_{\psi} \left\| V_{\text{meas}}(t) - V_{\text{fit,pulse}}(t) \right\|_2^2 \\ &= \arg\min_{\psi} \| V_{\text{meas}}(t) \\ &- \Big[\text{OCV}_{\text{meas}} \pm IR_0 \pm (A\exp(-\alpha t) + B\exp(-\beta t)) \\ &\pm I\Big(C(1 - \exp(-\alpha t)) + D(1 - \exp(-\beta t))\Big)\Big]\Big\|_2^2 \\ \text{s.t.} \quad & \psi \geq \text{lb} \\ & \psi \leq \text{ub}\end{aligned} \tag{26}$$

The search space is defined by an allowed deviation of up to 10 % to 200 % for R_1, C_1 and 1 % to 200 % for R_2, C_2, depending on the optimum parameters from the relaxation fitting. Again, the ECM parameters are calculated via backtransformation [58]:

$$\tau_1 = \frac{1}{\alpha} = \frac{1}{R_1 C_1} \tag{27}$$

$$\tau_2 = \frac{1}{\beta} = \frac{1}{R_2 C_2} \tag{28}$$

$$R_1 = C \tag{29}$$

$$R_2 = D \tag{30}$$

$$C_1 = \frac{1}{\alpha R_1} \tag{31}$$

$$C_2 = \frac{1}{\beta R_2} \tag{32}$$

One example is visualized in Figure 3 where the measured and fitted voltage response during a charge pulse and the following relaxation phase is compared for full cell ((b) and (c)), anode ((e) and (f)) and cathode ((h) and (i)). Subfigures 3 (a), (d) and (g) visualize the fitted ECM during the pulse section. Instead of interpreting the OCV as a function, the first measured value is shown for simplicity.
As the ECM parameters are not the only calculated parameters during the analysis, the subfigures further include a selection of the calculated DC resistances that are calculated by Ohm's law, see Equation 25, by adapting the Δt to 0.5 s, 1 s, 10 s and 20 s during the pulse and 0.5 s, 1 s, 10 s, 20 s, 30 s, 60 s, 120 s and 180 s during the relaxation. These evaluations are already included in the final published dataset, but, of course, further assessments are possible by extending the evaluation scripts.

2.7. EIS Evaluation

EIS measurements are conducted at the same SOC reference points as the pulse analysis during the HPPC. The EIS is conducted at full cell and anode level, respectively, with 20 reference points per decade within the frequency region from 100 kHz to 100 mHz. As can be seen in Figure 4 (h), and later validated in Figure 6, the Nyquist plot is additionally calculated for the cathode by

$$\mathbf{Z}_{\mathrm{PE}} = \mathbf{Z} - \mathbf{Z}_{\mathrm{NE}}. \tag{33}$$

During the EIS measurement, both the time-series data, as well as the frequency domain data are stored and will be made freely available at https://epub.uni-bayreuth.de/.

The *impedance.py* [59] package is used for data loading, preprocessing, error analysis and ECM-fitting. The full guide for the package can be found in the respective publication [59]. The used functions within this study are clearly explained within the code, and will be made available at https://epub.uni-bayreuth.de/.

As reported by Costard et al. [60] EIS in three-electrode configurations with a point-like lithium reference may raise measurement artifacts due to electrochemical asymmetry [60, 61]. A linear Kramers-Kronig (lin KK) analysis [62], however, allows to determine the invalid frequency range within a Nyquist plot as it requires causality and linearity of the complex signal. The validity of the impedance is checked by comparing the raw signal with the reproduced signal from a simple ECM that includes an ohmic resistance R_Ω and an arbitrary amount M of RC-elements.

$$\hat{\mathbf{Z}} = R_\Omega + \sum_{k=1}^{M} \frac{R_k}{1 + j\omega\tau_k} \tag{34}$$

Note that R_Ω and R_k are the only fitting variables, as the time constants τ_k are distributed logarithmically

$$\tau_1 = \frac{1}{\omega_{\max}}, \tag{35}$$

$$\tau_M = \frac{1}{\omega_{\min}}, \tag{36}$$

$$\tau_k = 10^{\log(\tau_{\min}) + \frac{k-1}{M-1}\log\left(\frac{\tau_{\max}}{\tau_{\min}}\right)}. \tag{37}$$

As proposed by Schönleber et al. [62] we integrate a regularization term to prevent under- or overfitting. The ratio of positive to negative resistor mass influences the optimal number of RC-elements via the following equation:

$$\mu = 1 - \frac{\sum_{R_k \geq 0} |R_k|}{\sum_{R_k < 0} |R_k|} \tag{38}$$

The algorithm iterates up to the maximum count of 100 and until the value μ falls below the threshold of 0.2.

The discrepancy between the modeled $\hat{\mathbf{Z}}$ and measured $\mathbf{Z}$ is visualized over the frequency axis in Figure 4 (c), (f) and (i) for the full and half cells, respectively. The complex deviation is divided into the real and imaginary part. As can be seen in Figure 4 (c) and (i), the deviation starts to increase rapidly around 1 kHz, while it still stays within a 5 % error band – at least for the full cell and the cathode. The anode signal, however, seems more noisy over the complete frequency spectrum with the highest deviation starting again at 1 kHz. Especially the imaginary part shows high deviations.

Concluding from these investigations, the full cell spectrum is fitted over the whole frequency range, while both half-cells are only fitted for the frequency spectrum below 1 kHz. As can be visually anticipated from the raw signal displayed in Figure 4 (e), the half-cell signal between 100 Hz and 1 kHz is slightly noisy which aggravates the fitting process. Hence, the measured half-cell signal between 100 Hz and 1 kHz is additionally smoothed by applying an one-dimensional Gaussian filter with a sigma value of 4 (compare scipy package [63]) as it reduces artifacts and increases fitting quality.

The wide frequency range has a high resolution and therefore allows to fit ECMs with a higher degree of freedom. Although the proposed ECM is an empirical model, the individual elements are chosen based on physical motivation. An additional modified inductance is necessary to model the high-frequency behavior [64, 65] with $Z_L = L \cdot (j\omega)^\alpha$. In the first RC-circuit, the capacitance is replaced with a constant-phase-element [64, 66, 67] $\left(Z_{CPE} = \frac{1}{Q\cdot(j\omega)^\alpha}\right)$ to better model the non-ideal semicircle, as can be seen in Figure 4 (b), (e) and (h). Additionally, a Warburg-impedance $\left(Z_w = \frac{Z_0}{\sqrt{j\omega\tau}}\coth\sqrt{j\omega\tau}\right)$ is added to the resistance of the second RC-element, which is necessary to model the diffusion line of the low frequency domain [64, 67]. This ECM is used for the full, as well as the half-cell data, and is displayed in Figure 4 (a), (d) and (g).

The fitting itself is performed with the *circuit_fit* function of the *scipy.optimization* package and 10000 maximum function evaluations. The optimizer runs without boundaries but with initial values for the first CU1_BOL, set as in Table 3.

For every following iteration, the last optimum is selected

Table 3: Initial values for the initial CU (CU1_BOL) for the ECM-fitting from the EIS data.

Parameter	Symbol	Full Cell	Anode	Cathode
Ohmic Resistance	R_Ω	1.65 Ω	0.429 Ω	1.58 Ω
Inductance	L	2.86×10^{-9} H	1.07×10^{-37} H	2.19×10^{-37} H
Phase Shift	α_{L}	1.00	0.48	1.00
Resistance	R_2	2.79 Ω	0.982 Ω	1.49 Ω
CPE Constant	Q_{CPE}	4.05 mF	6.84 mF	4.62 mF
CPE Exponent	α_{CPE}	0.608	0.672	0.717
Resistance	R_3	173 mΩ	6.66 mΩ	17.1 mΩ
Warburg Impedance	Z_0	18.6 mF	36.4 mF	18.8 mF
Warburg Time Constant	τ	17.6 s	35.6 s	20.7 s
Capacitance	C	0.618 F	2.27 F	1.62 F

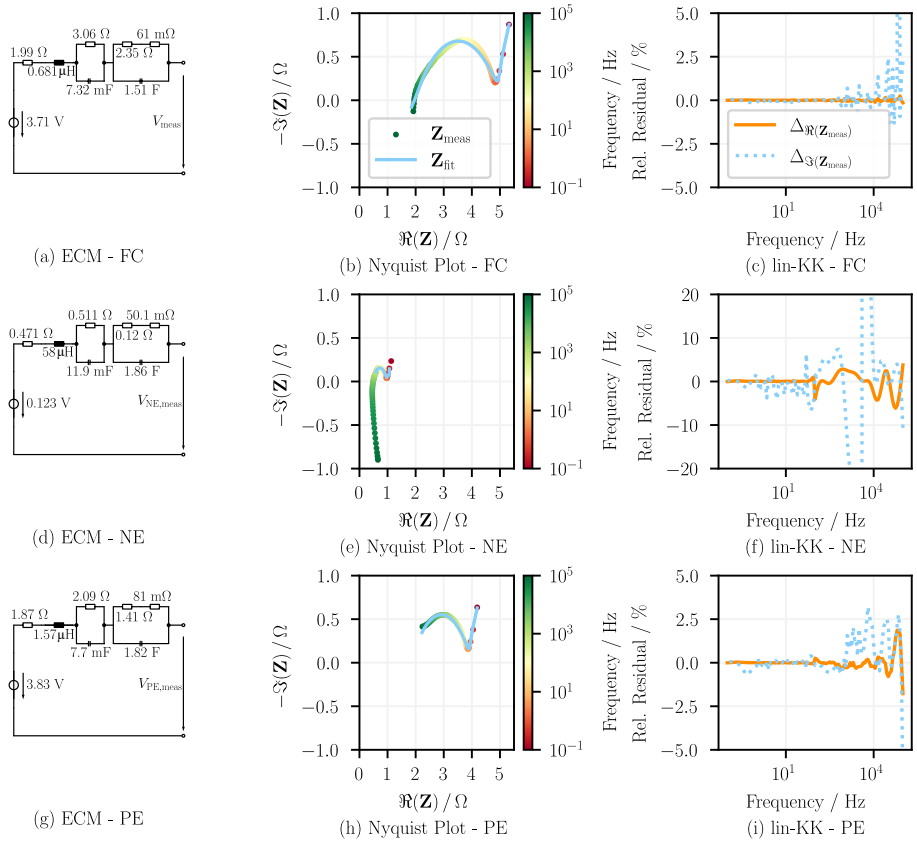

Figure 4: EIS fitting procedure and result for exemplary cell 6300 during CU2 at 50 % SOC and 25 °C. An individual ECM is fitted for the full cell (a), the anode (d) and the cathode (g) based on the impedance spectrum visualized in Subfigure (b), (e) and (h), respectively. A lin-Kramers-Kronig analysis (Subfigure (c), (f) and (i)) yields the validated frequency spectrum. The anode spectrum is only fitted for impedance measurement points below 1 kHz.

as the initial value for the optimization. The optimized ECM-parameters for cell 6300 during CU2 at 50 % SOC, 25 °C and in charge direction are visualized in Figure 4 (a), (d) and (g). The fitted impedance spectra, however, are compared to the measured data in Figure 4 (b), (e) and (h). For the full and the half cell a very high fitting accuracy is reached, demonstrated by the low residuals.

Additional features extracted from all three impedance spectra include the ohmic resistance, i.e. the impedance value at the intersection with the imaginary axis, and the characteristic impedance value at 1 kHz. In cases, where there is no intersection with the imaginary axis present due to rapid impedance rise, the ohmic resistance is replaced with the real part of the impedance value with the lowest imaginary value.

3. Data Records

The complete dataset, including raw data files, processed data files, code to generate the data, as well as the battery cycling protocols, will be made freely available at https://epub.uni-bayreuth.de/. The dataset is organized into several file types and formats, each serving a specific purpose in the analysis of the battery aging dataset. Below is a detailed overview of the file types, their organization, and guidance on accessing and processing the data. The folder structure for all measured raw data files is described with the aid of Figure 5. In Figure 5 the files for one exemplary CU, as well as the aging files, are listed.

The folder structure remains consistent for all cells and CUs, i.e., although a cell is aged cyclic, the calendar aging subfolder exists, which, however, will be empty. A detailed description is given below:

01_Formation All measured data during the formation process is stored as .txt files for both master and slave channels.

02_CU_ext The subfolder structure of 02_CU_ext is visible in Figure 5, where each folder exists for the BOL, MOL, and EOL CU. For the temperature $T = 25\,°C$, all subfolders exist, while for 10 °C and 45 °C, the pOCV measurement is missing. The direction is covered in CHA and DCH directions for all tests. In the pOCV subfolder, only two files exist, one for the master and one for the slave channel. In the HPPC subfolder, four files exist per SOC step: two

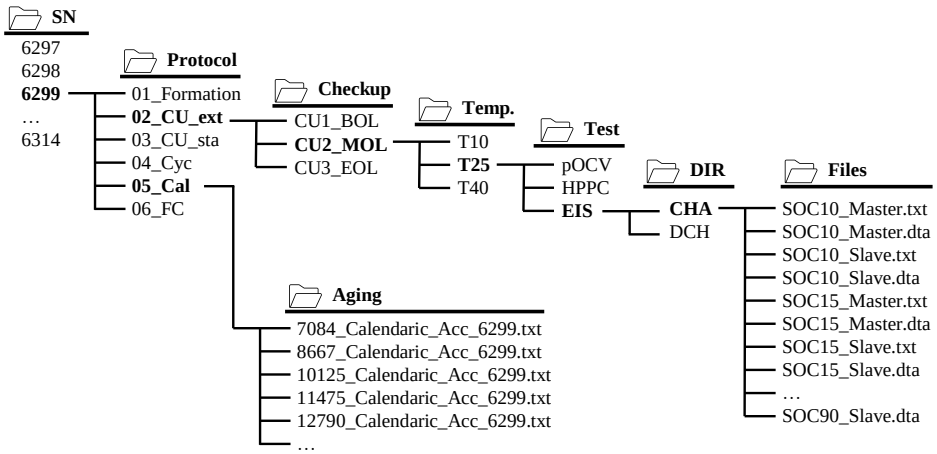

Figure 5: Folder structure of the raw data files. Each selected folder is printed bold, while all subfolders are presented again, and so on. In this example, all EIS files for cell 6299 during the MOL CU (CU2_MOL) at 25 °C and in charge direction are listed. Additionally, the files, captured during the aging phase, are listed below.

each for the charge and discharge pulse, one for the master and one for the slave channel, respectively.

03_CU_sta The standard CU folder shares its structure with the 02_CU_ext folder but incorporates only the CHA direction folder. Moreover, the SOC steps at 15 % and 85 % are not present.

04_Cyc One file per aging phase.

05_Cal One file per aging phase.

06_FC One file per aging phase.

3.1. File Types and Formats

Cell information Two Excel spreadsheets: *Cell_Assembly_Data.xlsx* contains measurements during the assembly in the laboratory; *Results_Formation_Final.xlsx* includes the calculated capacity from the assembly data and the measured capacity from the formation.

Formation protocols and data One .pln file for the formation protocols of all channels and one .txt file with the measurement for every cell.

Battery cycling protocols Organized in respective subfolders for each test step, i.e., CU_standard, CU_extended, and Aging. All files are stored in .pln format with a clear naming convention to map channel and cell, e.g., *HPPC_Standard_DCH_CH00.pln* or *pOCV_Extended_Master_CH08.pln*.

Validation files The measurement verification files of all BaSyTec and MUX channels are stored as .mat files, e.g., *BaSyTec_1981_Verification_Protocol 20-12-2024_13-24.mat*. The validation files regarding correct EIS measurement are stored as .txt and .dta files.

Raw data files CU Raw data files are stored under their respective cell folder, either as .txt files for time-series data, e.g., *8853_HPPC_DCH_SOC10_6300.txt*, or .dta files for Gamry EIS measurements, e.g., *Gamry_TE_0000005368_0022_0001_0001_0000.dta*. In total, 706 .txt files and 138 .dta files exist per cell, totaling 15,192 files for the entire aging experiment, excluding missing EIS files for cell 6298 on electrode level and cells 6313 and 6314. The files have a total size of approximately 1.9 GB per cell.

Raw data files aging phase The time-series data of the aging process is stored in respective subfolders (same folder as the raw data files CU) under each cell number in .txt format, e.g., *7081_Calendaric_6297.txt*, where *7081* is the counting measurement number, *Calendaric* is the aging path, and *6297* is the cell number. Each file exists per aging sequence, totaling 180 files, approximately 3 GB.

Preprocessing code The preprocessing code is stored in three subdirectories for pOCV, HPPC, and EIS fitting. Each subdirectory includes one Jupyter notebook and one Python file containing all functions in the subdirectory *A_Modell*.

Preprocessed data Preprocessed dataframes are stored as .csv files for each fitting result, i.e., *df_pOCV.csv*, *df_HPPC.csv*, and *df_EIS.csv*.

3.2. Battery Cycling Protocols

All battery cycling protocols are available in the BaSyTec-preferred .pln format. The files are organized in respective *CU*

standard, *CU extended*, and *Aging Phase* folders. Additional protocols include formation, temperature control, and discharge profiles.

Aging Phase The aging phase protocols include one file for each protocol, with an exception for the 3N3F protocols, and are organized in respective folders. To achieve anode-potential-controlled fast-charging, the measured anode potential must be added to the cycling protocol and included as a controlling variable. Hence, one individual 3N3F protocol is necessary for each cell, i.e., *Aging_3N3F_CH08.pln*.

CU standard The files for the standard CU are organized in subfolders for each test step:

- **pOCV** The pOCV protocols are divided into master and slave protocols, respectively. While one individual file exists for every master channel, only one general file exists for all slave channels.
- **EIS** Similarly, the EIS protocols are divided into master and slave: The protocols exist individually per channel group, as shown in Table 2. The master channel protocols are divided into test steps for each SOC adaptation, i.e., ±10 %, ±20 %, ±30 %.
- **HPPC** The HPPC protocols are divided into the pulse direction, i.e., charge or discharge, where one master channel file exists per channel.

CU extended The CU protocols for the extended CU have the same folder structure as the standard CU, solely the discharge direction is covered, with one parallel DCH folder in every test step.

3.3. Preprocessing Code

The preprocessing code is divided into three directories, each one for the pOCV, EIS, and HPPC processing. Each directory has the same general structure: A subdirectory *A_Modell* includes all necessary Python files for the actual fitting, while a Jupyter notebook in the main directory iterates through all raw data files and finally stores the results in a dataframe. All functions are well documented in the repository itself.

3.4. Preprocessed Data

For each fitting protocol, one final dataframe, stored as a .csv file, exists, which shares a common structure as displayed in Table 4. The data columns in Table 4 are filled individually for every dataframe. The unique identifiers in the first columns, however, allow merging of all dataframes and directly comparing their values. They also offer a great starting point for new model development, model validation, or visualization of trends within the aging series.

4. Technical Validation

The technical validation of our battery cycling system and measurement protocols ensures the reliability and accuracy of the data collected throughout the study. This section provides a detailed examination of the hardware calibration, data acquisition methods, and the robustness of the fitting results, highlighting the precision of our experimental setup and the integrity of the findings.

4.1. Battery Cycling System

Battery cycling and testing were performed using two BaSyTec CTS Lab measurement devices, i.e., CTS1460 and CTS1463. Each device is equipped with 32 channels, initially facilitating three-electrode measurements per channel. However, it is important to note that the sampling rate decreases when utilizing the three-electrode configuration. Consequently, each cell requires two channels: the master channel (e.g., CTS1460 channel 00) manages the full cell, while the slave channel (e.g., CTS1460 channel 01) is dedicated to controlling the anode. EIS measurements were enabled through the use of an auxiliary Gamry Reference 3000 potentiostat, in conjunction with a BaSyTec multiplexer. This setup allowed the connection of one CTS Lab to the Gamry device (in this case: CTS1460), thereby facilitating sequential EIS measurements across all connected cells. However, this configuration was limited to a single CTS Lab, encompassing only 32 channels, which corresponds to 16 cells. It is noteworthy that channel 03 on the multiplexer experienced irreparable issues, resulting in the absence of EIS data at the electrode level for cell 6298. For a comprehensive list of specifications, please refer to the BaSyTec and Gamry websites [68, 69].
To verify the accuracy of the chosen hardware, a calibration protocol was followed for both CTS labs. For the CTS1460 connected to the multiplexer and the Gamry device, the multiplexer was connected during the verification. The verification protocol included the comparison of two different voltage (approximately 2.5 V and 4 V) and one current regime (approximately −1 mA to 1 mA) with a calibrated Keysight 34470A multimeter. Three sample batteries, with low, medium and high SOC, serve as the reference for both measurement devices. The verification is repeated ten times to ensure statistical robustness. The results, including the mean μ and standard deviation σ of the difference to the Keysight 34470A, for each channel of both CTS Labs are listed in Table 5. As listed on the datasheet of the CTS Lab [68], the voltage and current uncertainty is stated to be 1 mV and 0.2 µA. Our measurements confirm that the stated uncertainty is not exceeded by any channel.

4.2. Half-Cell Potential Data

From the manufacturing data, i.e., the weights of the electrode coins, the theoretical capacity was calculated, as shown in Table 6. The theoretical capacity is calculated by multiplying the electrode mass, i.e., the coin mass minus the current collector mass, with the specific capacity of the material. These values always correspond the cathode capacities, as they limit the full cell capacity. These theoretical values were validated with

Table 4: Structure of the preprocessed dataframes (*df_pOCV.csv*, *df_HPPC.csv*, *df_EIS.csv*) stored as .csv files with each column filled with all unique values. The data column is respectively filled with the resulting values from each fitting protocol.

Cell	CU	Aging_Path	Temperature	SOC	Direction	Electrode	Cycle_Count	Data…
6297	CU1_BOL	CAL	T10	10	CHA	FC	0	…
6298	CU2_MOL	CAL_{acc}	T25	15	DCH	neg	…	…
6299	CU3_EOL	CYC_{full}	T40	20		pos	…	…
6300	CU1	CYC_{lower}		50			…	…
…	…	…		…			…	…
6314	CU8	3F3N		90			…	…

the measured capacity during the first C/10 CC-CV charge protocol during formation. The Pearson correlation coefficient between the theoretical and measured capacity values is at 0.8440, indicating a high quality during assembly.
One shortcoming of the provided dataset is that only the anode potential and EIS was measured during CUs. The cathode potential, however, was simply calculated from that via Equation 39 and 40.

$$\mathrm{OCP_{PE}} = \mathrm{OCV} + \mathrm{OCP_{NE}} \tag{39}$$

$$\mathbf{Z}_{\mathrm{PE}} = \mathbf{Z} - \mathbf{Z}_{\mathrm{NE}} \tag{40}$$

Due to the structure of the used PAT-cells, no additional validation for the cathode potential calculation is necessary. The cathode EIS calculation, however, remains to be validated against true measurements. Figure 6 provides this analysis in one common Nyquist plot where the measured anode, cathode and full cells EIS is compared to the calculated cathode EIS from Equation 40. As can be seen, especially by the additional vertical error plot next to the frequency colorbar in Figure 6, the alignment between measured and calculated cathode EIS is very high with the deviation mostly below 0.1 Ω. There is no systematic error in the middle frequency range, evident by the fluctuation error of the real part. The error significantly increases for very low and very high frequencies. Similar to the linear Kramers-Kroning evaluation by Figure 4, we suggest to solely use electrode EIS data up to a frequency of approximately 1 kHz.

4.3. Data Quality - Measurement and Fitting Results

To ensure statistical significant results, three cells were aged per aging path. All evaluations include the standard deviation of the fitting process indicating the statistical significance.

4.3.1. pOCV Evaluation

Figure 7 shows the gathered DMs for all cells over all CUs. In each subfigure, the respective DM is plotted per aging path over the measured state of health (SOH) including the standard deviation in both dimensions, SOH and DM. As can be seen in Figure 7 (a), the LLI rises linearly with the SOH decay, mathematically following Equation 4. Due to the dimensions of the OCPs in relation to each other, this behavior is reasonable.
The anode shows barely any aging, as shown in Figure 7 (b), with the maximum $\mathrm{LAM_{NE}}$ not exceeding 1.5 %. Visibly $\mathrm{LAM_{NE}}$ reduces in some CUs, especially for the calendar aging paths. This can be explained by additives in the electrolyte which leads to a softer SEI after the first few cycles and, with that, reduces the resistance. Due to the measurement of the pOCV at non-negligible C-Rates, there is a non-negligible overpotential, measurable as an offset in the electrode potentials. Reduction of this offset, as with decreased resistance, leads to less $\mathrm{LAM_{NE}}$.
The $\mathrm{LAM_{PE}}$ trajectory in Figure 7 (c) shows expected behavior: The 3N3F and $\mathrm{CYC_{full}}$ aging paths stress the cathode the most and thus lead to the – in comparison – excessive $\mathrm{LAM_{PE}}$. Notably, the partial cycling aging paths shows nearly the same trend. Both calendar aging paths experience the least cathode aging, especially the pure CAL path, shows only approximately 10 % of $\mathrm{LAM_{PE}}$, even after 25 % capacity decay. This implies that most aging there is due to a shift of both OCPs to each other, what is mostly referred to as LLI.
Overall, the standard deviation per CU and aging path is notably low, revealing the high data quality. While the standard deviation of $\mathrm{LAM_{NE}}$, displayed in Figure 7 (b), seems high, it must be interpreted in relation to the general low absolute anode aging values. The maximum standard deviation there is still below 1.2 %, ensuring the quality of the data and the fitting protocol.
During the aging study, we explored unexpected behavior in the captured $\mathrm{OCP_{PE}}$ which seemed to be additional overpotentials at high SOC states. Following the assumptions from Jung et al. [44] and Zhang [45], we believe to capture rocksalt formation in the cathode due to the very high nickel content. While the general fitting accuracy was still very high (mean absolute error (MAE) below 7 mV), the additional impedance in the upper SOC region lead to overestimated SOH values because the upper voltage limits was reached earlier during measurement.

4.3.2. HPPC Evaluation

While many resistance values were evaluated during the HPPC test, the $R_{\mathrm{DC,1s}}$ is well comparable to literature and allows valuable comparison between electrodes, SOC and over degradation. Figure 8 summarizes the $R_{\mathrm{DC,1s}}$ at 25 °C for anode, cathode and full cell for the lowest, mid and highest SOC, i.e., 10 %, 50 % and 90 %, for all aging paths along degradation. The three cells per path are combined in one datapoint, with the standard deviation shown by the vertical errorbars. The previously described odd behavior of the cathode is also visible in

Table 5: Results of the hardware verification of both BaSyTec CTS Lab for two voltage and one current regime. All measurements were repeated ten times to ensure statistical robustness.

Channel	Low Voltage Range		High Voltage Range		Current	
	μ / mV	σ / mV	μ / mV	σ / mV	μ / mA	σ / mA
CTS1460 CH00	2.63×10^{-1}	1.21×10^{-3}	-2.95×10^{-1}	6.23×10^{-4}	-7.16×10^{-8}	1.63×10^{-9}
CTS1460 CH01	-1.59×10^{-1}	9.86×10^{-4}	-2.38×10^{-1}	3.38×10^{-4}	-2.21×10^{-9}	1.81×10^{-9}
CTS1460 CH02	-5.26×10^{-1}	9.86×10^{-2}	-5.68×10^{-1}	3.32×10^{-4}	-2.78×10^{-9}	4.70×10^{-8}
CTS1460 CH03	6.03×10^{-2}	1.14×10^{-3}	-3.17×10^{-1}	6.01×10^{-2}	1.15×10^{-9}	1.99×10^{-9}
CTS1460 CH04	-5.69×10^{-2}	6.08×10^{-2}	-2.76×10^{-1}	-2.76×10^{-1}	-2.57×10^{-9}	1.90×10^{-9}
CTS1460 CH05	2.01×10^{-2}	8.04×10^{-2}	-1.44×10^{-1}	-1.44×10^{-1}	-1.77×10^{-9}	1.97×10^{-9}
CTS1460 CH06	-8.52×10^{-2}	5.99×10^{-2}	-1.77×10^{-2}	-1.77×10^{-2}	6.15×10^{-8}	1.69×10^{-9}
CTS1460 CH07	-3.14×10^{-3}	9.21×10^{-2}	1.96×10^{-1}	1.96×10^{-1}	2.62×10^{-9}	2.09×10^{-9}
CTS1460 CH08	-2.71×10^{-1}	5.93×10^{-4}	-2.65×10^{-1}	4.92×10^{-4}	9.41×10^{-8}	2.17×10^{-9}
CTS1460 CH09	9.77×10^{-2}	4.97×10^{-4}	3.06×10^{-3}	4.65×10^{-4}	-5.75×10^{-9}	1.45×10^{-9}
CTS1460 CH10	-2.88×10^{-1}	1.01×10^{-1}	-3.36×10^{-1}	4.93×10^{-4}	3.48×10^{-9}	1.65×10^{-9}
CTS1460 CH11	4.03×10^{-2}	5.51×10^{-4}	-1.15×10^{-1}	6.03×10^{-2}	2.42×10^{-9}	1.53×10^{-9}
CTS1460 CH12	-3.16×10^{-1}	6.02×10^{-2}	-3.43×10^{-1}	8.05×10^{-2}	2.38×10^{-9}	1.76×10^{-9}
CTS1460 CH13	2.42×10^{-1}	6.06×10^{-2}	1.44×10^{-1}	8.01×10^{-2}	2.09×10^{-9}	1.97×10^{-9}
CTS1460 CH14	-2.78×10^{-1}	8.78×10^{-4}	-4.23×10^{-1}	5.54×10^{-4}	-1.91×10^{-9}	2.02×10^{-9}
CTS1460 CH15	-1.72×10^{-1}	6.29×10^{-4}	-9.59×10^{-2}	4.91×10^{-4}	-2.05×10^{-9}	1.58×10^{-9}
CTS1460 CH16	-1.55×10^{-1}	6.18×10^{-4}	-2.86×10^{-2}	4.57×10^{-4}	-2.99×10^{-9}	2.32×10^{-9}
CTS1460 CH17	-1.88×10^{-1}	3.42×10^{-4}	-2.87×10^{-1}	9.85×10^{-2}	-6.81×10^{-9}	1.80×10^{-9}
CTS1460 CH18	-1.86×10^{-1}	5.94×10^{-4}	-4.90×10^{-2}	4.82×10^{-4}	-7.11×10^{-8}	4.38×10^{-8}
CTS1460 CH19	-7.99×10^{-2}	6.03×10^{-2}	-3.00×10^{-1}	3.83×10^{-4}	-3.00×10^{-7}	2.00×10^{-9}
CTS1460 CH20	3.08×10^{-3}	5.43×10^{-4}	-2.41×10^{-1}	8.05×10^{-2}	2.96×10^{-9}	1.64×10^{-9}
CTS1460 CH21	-1.14×10^{-1}	5.10×10^{-4}	-3.45×10^{-1}	9.20×10^{-2}	-4.43×10^{-9}	4.51×10^{-8}
CTS1460 CH22	-4.17×10^{-1}	9.23×10^{-2}	-4.02×10^{-1}	6.07×10^{-2}	1.20×10^{-9}	1.63×10^{-9}
CTS1460 CH23	-1.09×10^{-1}	8.96×10^{-4}	-4.03×10^{-1}	3.61×10^{-4}	-2.87×10^{-9}	1.81×10^{-9}
CTS1460 CH24	-2.18×10^{-1}	5.57×10^{-4}	-3.05×10^{-1}	2.66×10^{-4}	-4.72×10^{-8}	2.04×10^{-9}
CTS1460 CH25	5.47×10^{-2}	4.76×10^{-4}	1.04×10^{-1}	3.85×10^{-4}	1.68×10^{-9}	2.87×10^{-8}
CTS1460 CH26	-4.37×10^{-1}	5.71×10^{-4}	-6.11×10^{-1}	9.24×10^{-2}	-2.95×10^{-9}	2.22×10^{-9}
CTS1460 CH27	1.24×10^{-2}	5.01×10^{-4}	-2.65×10^{-1}	8.04×10^{-2}	-6.56×10^{-9}	1.57×10^{-9}
CTS1460 CH28	6.19×10^{-1}	7.16×10^{-4}	5.19×10^{-1}	4.58×10^{-4}	-1.66×10^{-9}	2.19×10^{-9}
CTS1460 CH29	5.53×10^{-1}	2.88×10^{-4}	6.41×10^{-1}	4.61×10^{-4}	-3.65×10^{-9}	1.47×10^{-9}
CTS1460 CH30	-2.90×10^{-2}	2.09×10^{-3}	-9.49×10^{-2}	8.41×10^{-4}	2.46×10^{-9}	1.89×10^{-9}
CTS1460 CH31	-1.10×10^{-1}	3.86×10^{-4}	-9.75×10^{-2}	6.04×10^{-2}	-4.56×10^{-8}	1.91×10^{-9}
CTS1463 CH00	5.96×10^{-2}	1.09×10^{-3}	-8.70×10^{-2}	5.10×10^{-4}	1.53×10^{-9}	1.17×10^{-9}
CTS1463 CH01	2.96×10^{-2}	7.94×10^{-4}	1.46×10^{-1}	1.01×10^{-1}	-9.81×10^{-8}	1.63×10^{-9}
CTS1463 CH02	-2.51×10^{-1}	7.13×10^{-4}	-3.89×10^{-1}	3.68×10^{-4}	-2.22×10^{-9}	1.21×10^{-9}
CTS1463 CH03	-1.28×10^{-1}	7.95×10^{-4}	-2.53×10^{-1}	9.21×10^{-2}	-2.64×10^{-9}	8.69×10^{-8}
CTS1463 CH04	1.79×10^{-3}	6.27×10^{-4}	-9.92×10^{-2}	6.89×10^{-4}	-7.25×10^{-8}	1.61×10^{-9}
CTS1463 CH05	1.18×10^{-1}	9.21×10^{-2}	-6.29×10^{-2}	7.22×10^{-4}	-3.85×10^{-9}	1.91×10^{-8}
CTS1463 CH06	-1.52×10^{-1}	8.93×10^{-4}	-1.96×10^{-1}	6.02×10^{-2}	-4.45×10^{-9}	1.54×10^{-9}
CTS1463 CH07	1.23×10^{-1}	8.41×10^{-4}	-1.42×10^{-1}	6.64×10^{-4}	3.07×10^{-9}	4.30×10^{-8}
CTS1463 CH08	3.52×10^{-2}	9.65×10^{-4}	2.64×10^{-1}	9.19×10^{-2}	-8.65×10^{-8}	1.25×10^{-9}
CTS1463 CH09	-9.39×10^{-2}	9.20×10^{-2}	-3.15×10^{-1}	9.21×10^{-2}	-2.85×10^{-9}	2.08×10^{-9}

Figure 8 (c): For the two most aggressive aging paths, 3N3F and CYC_{full}, $R_{DC,1s}$ exceeds values of 30 Ω, notably more than five times the initial value. The $R_{DC,1s}$, however, shows similar behavior also for the lower SOCs at 50 % (Figure 8 (b)) and 10 % (Figure 8 (a)). There the resistance increases similarly, but less pronounced, to values around 20 Ω. In all three SOC points, the partially cycled aging paths show the least resistance increase. As shown in Figure 8 (g) - (i), the full cell resistance is dominated by the cathode, which shows almost identical trajectories. The anode resistance course proves that the included additives in the electrolyte indeed lead to reduced anode resistances in the first few cycles, explaining the unexpected declining behavior in the LAM_{NE}. The SOC-dependency is almost negligible for the anode. Summarized the low standard

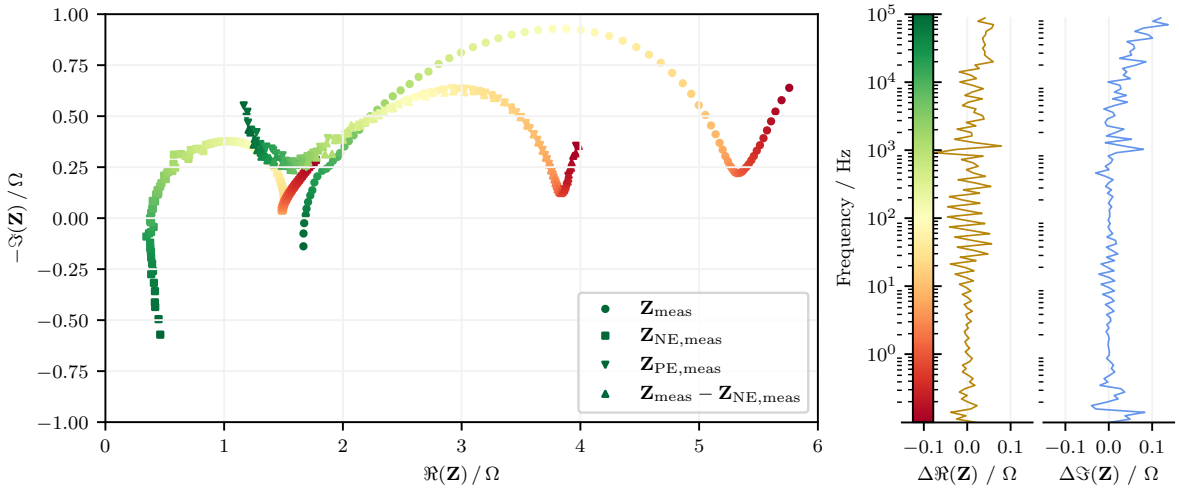

Figure 6: Technical validation of the cathode EIS measurement. The Nyquist plot compares the calculated with the measured cathode Nyquist plot. Additionally the impedance deviation is plotted, for the real and imaginary part, next to the frequency bar.

Table 6: Theoretical cell capacity value calculated from the electrode coin weight in comparison to the measured capacity during formation cycles.

SN	Theoretical Capacity	Measured Capacity
6297	10.08 mAh	9.900 mAh
6298	10.06 mAh	9.874 mAh
6299	10.06 mAh	9.880 mAh
6300	10.07 mAh	9.923 mAh
6301	10.10 mAh	9.939 mAh
6302	10.08 mAh	9.935 mAh
6303	10.15 mAh	10.01 mAh
6304	10.08 mAh	9.917 mAh
6305	10.10 mAh	9.912 mAh
6306	10.08 mAh	9.938 mAh
6307	10.08 mAh	9.929 mAh
6308	10.07 mAh	9.920 mAh
6309	10.14 mAh	9.974 mAh
6310	10.04 mAh	9.909 mAh
6311	10.07 mAh	9.952 mAh
6312	10.05 mAh	9.986 mAh
6313	10.10 mAh	9.957 mAh
6314	10.02 mAh	9.843 mAh

deviation between the three cells per aging path in each CU prove the high data quality of the cells itself, the aging series, but also the measurement.

4.3.3. EIS Evaluation

Instead of evaluating fitted values from the EIS fitting protocol, a direct comparison of the gathered Nyquist plots allows a fair comparison of all cells and especially the deviation between cells from the same aging path. Figure 9 summarizes all measured Nyquist plots from all cells on full cell level for 25 °C and 50 % SOC over the SOH. As can be seen, no measurements are available for cell 6313 (Figure 9 (r)) and 6314 (Figure 9 (l)) due to only 32 available MUX channels. Hence, only for the first 16 cells EIS measurements were taken for the full cell and the anode. Each row represents the Nyquist plot for all three cells of one aging path. Note that not all subfigures have the same *x* and *y* scaling. Again, the calendar aging paths (CAL and CAL_{acc}, Figure 9 (a) - (c) and Figure 9 (d) - (f)), the partial cycling paths ($\text{CYC}_{\text{lower}}$ and $\text{CYC}_{\text{upper}}$, Figure 9 (g) - (i) and Figure 9 (j) - (l)) and the most aggressive aging paths (CYC_{full} and 3N3F, Figure 9 (m) - (o) and Figure 9 (p) - (r)) show similar behavior, respectively. This again provides evidence for high data quality. Most interestingly, the Nyquist plots for the 3N3F and CYC_{full} aging path show tremendous impedance rise for the high frequency range. In comparison to the 3N3F case, the fully cycled cells even experience amplified rise of the imaginary impedance part.

5. Usage Notes

This section provides a brief description of each fitting protocol. The foundations and reasoning behind the selected protocols are documented in Section 2.

pOCV Fitting In the subdirectory *A_Modell* of the pOCV fitting, only one Python file is stored that includes all necessary functions, i.e., *fit_OCV()*, *cost_fun_anode()*, *cost_fun_cathode()*, *create_OCV_DVA_ICA()*, *get_DM()*, and *plot_OCV_DVA_ICA()*. In the main directory the controlling jupyter notebook *main_pOCV.ipynb* is stored. The *fit_OCV()* function is the main function called from within the notebook. In the notebook itself, the raw data file paths are iteratively loaded and checked if already evaluated. If not, the file path is handed to the *fit_OCV()*

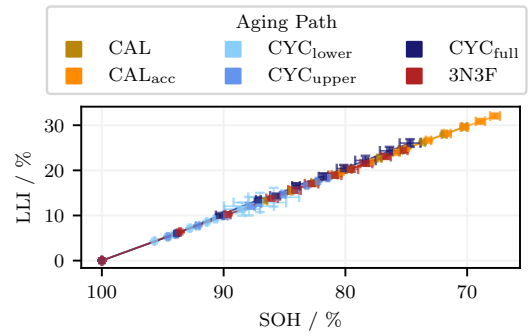

(a) Loss of Lithium Inventory

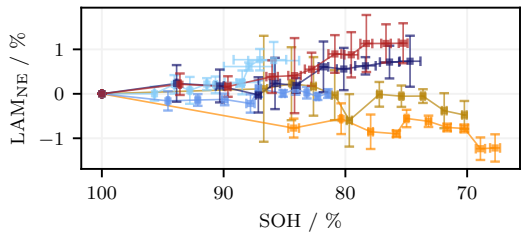

(b) Loss of Active Material - NE

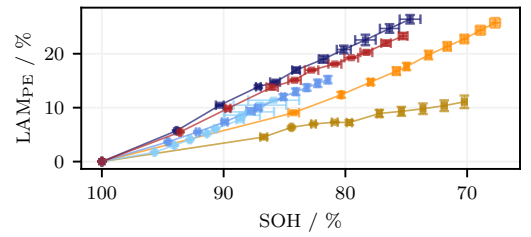

(c) Loss of Active Material - PE

Figure 7: Gathered DMs versus the estimated SOH for all aging paths. Each aging path includes three identical cells, where the standard deviation of the SOH and DM estimation is visualized by the error bar.

function and loaded there. In *fit_OCV()*, first some basic definitions are set, i.e., the boundaries and the sample length. The differential voltage and incremental capacity curves of the raw voltage signals are calculated, and the main DVA peak of the anode is detected. The prior CU results are loaded to select the initial and boundary values, as stated in Equation 5. First, the anode cost function *cost_fun_anode()* is called, followed by the cathode cost function *cost_fun_cathode()*. Both results, from the anode and cathode fitting, are handed to the *create_OCV_DVA_ICA()* and *get_DM()* functions, which return, as the names suggest, the full OCV, DVA, ICA curves, as well as the DMs. Optionally, the visualization function *plot_OCV_DVA_ICA()* is called to view the result. The main function *fit_OCV()* returns all important values, i.e., the resulting alignment parameters, the alignment parameters in pristine state, the measured capacity, the estimated as well as the calculated SOH, the OCV error, and all DMs. These values are processed in the notebook and stored in the respective location in the dataframe.

HPPC Fitting The main notebook *main_hppc.ipynb* controls the fitting procedure and iterates through the respective CUs and cells while calling the actual functions located within the subdirectory *A_Modell*. For every CU of every cell, the respective pOCV value is loaded by assessing the function *process_and_evaluate_pocv_data()*. Next, for every temperature and charge direction, the respective directory is located and the raw data is loaded, aided by the supporting function *process_and_evaluate_hppc_data()*. For every SOC and pulse direction, the actual fitting starts: First, the dataframe is checked for any prior results and the corresponding raw data, including the HPPC and pOCV files, is located. The first straightforward step is done via the *ohmic_resistance_calculation()* function, i.e., calculation of the ohmic resistance via Ohm's law. Next, the initial values for the fitting of the ECM parameters are loaded. If it is not the first CU, the prior results are loaded and the search space is set to 1 % to 200 % of the prior result. Finally, the ECM parameters are fitted with the core function *ecm_parameter_fitting()*. This process is subsequently iterated for the electrodes and the full cell, first for the relaxation phase and, finally, for the pulse phase. Lastly, the DC-IR calculation follows, aided by the function *dcir_calculation()*.

EIS Fitting The preprocessing code of the EIS fitting is divided into the evaluation function *eval_EIS()*, located in the Python file *eval_EIS.py* within the subdirectory *A_Modell*, and the main notebook *main_EIS.ipynb*. Analogous to the pOCV and HPPC fitting, the main EIS notebook simply creates or loads the dataframe and iterates through all raw data files. During these iterations, however, there are additional quality gates to maintain high accuracy: The fitting function *eval_EIS()* accepts initial values for its ECM parameters. During the first CU CU1_BOL, three different combinations are evaluated to yield the best fitting result. For every following CU, the prior result is selected as the initial values, if available. In the fitting function *eval_EIS.py*, we use the *impedance.py* package [59] to extract the frequency and impedance arrays from the Gamry .dta files and to finally fit the ECM. While the full spectrum of the full cell is fitted, the electrode data is truncated based on a prior Gaussian kernel to smooth the data and a Kramers-Kronig test to determine the valid frequency range. Besides the fitting, the *eval_EIS.py* function also calculates characteristic points from the Nyquist plot, i.e., the ohmic resistance as the intersection of the Nyquist curve with the imaginary axis and the impedance at 1 kHz. Finally, *eval_EIS.py* returns these values, as well as all fitted ECM parameters and the fitting root mean squared error (RMSE). If after 10000 iterations no valid result can be determined, the function returns NaN. This, however, is only the case for less than

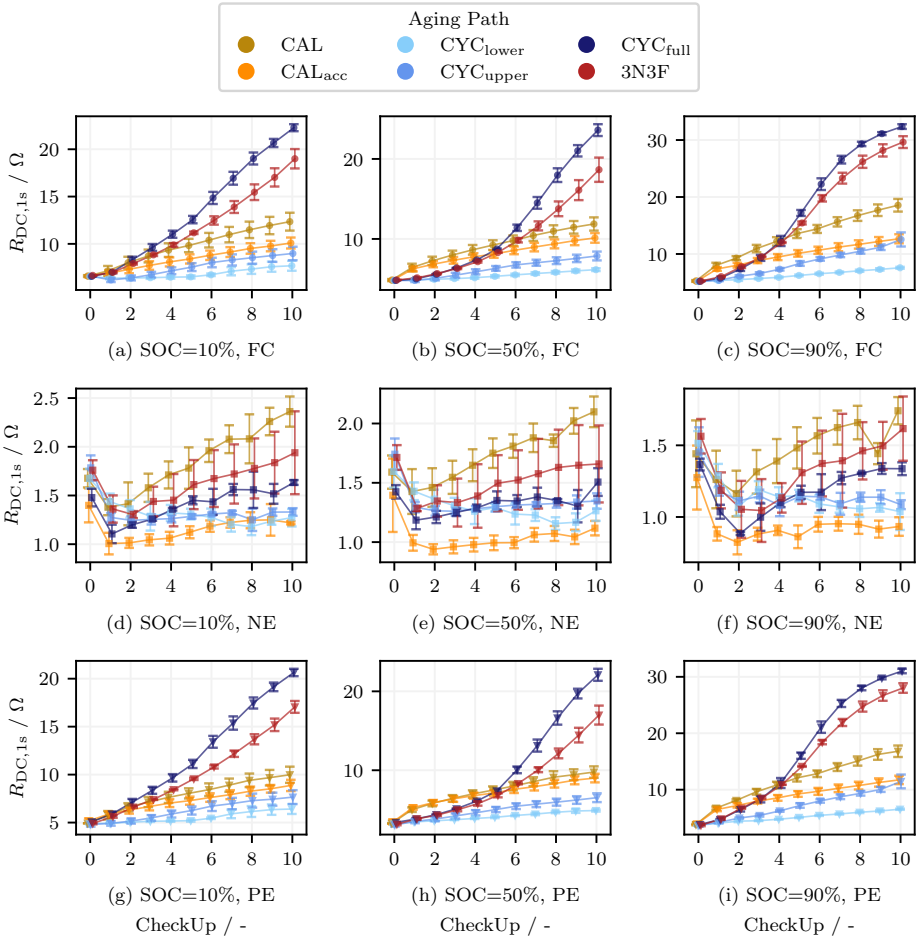

Figure 8: Calculated DC resistance value after 1 s for the full cell, the negative and the positive electrode at three distinct SOC reference points: 10 %, 50 % and 90 %. All measurements were taken at 25 °C and repeated with three identical cells per aging paths. The standard deviation is visualized by the error bar.

5 % of the data points, and mostly for electrode data in boundary regions.

6. Code Availability

All resources used to generate this dataset, as well as all raw data will be made freely available under: https://epub.uni-bayreuth.de/. The required python libraries are listed in the repository.

Acknowledgments

This work was performed in cooperation with the University of Bayreuth - Chair of Systems Engineering for Electrical Energy Storage, the Technical University of Munich - Chair of Electrical Energy Storage and the BMW AG. The authors would like to thank Jonathan Martin from BaSyTec and Dr. Matthias Hahn from El-Cell for their helpful feedback during the gathering of the dataset!

References

[1] Bugga, R.V., Smart, M.C., "Lithium Plating Behavior in Lithium-Ion Cells", ECS Transactions, vol. 25, pp. 241, 2010. DOI: 10.1149/1.3393860.

[2] Danzer, M.A., Petzl, M., "Voltage and Impedance Analysis for the Indirect Detection and Characterization of Lithium Plating in Commercial Lfp//Graphite Li-Ion Cells", ECS Meeting Abstracts, vol. MA2014-04, pp. 769, 2014. DOI: 10.1149/MA2014-04/4/769.

[3] Liu, Q., Du, C., Shen, B., Zuo, P., Cheng, X., Ma, Y., Yin, G., Gao, Y., "Understanding undesirable anode lithium plating issues in lithium-ion batteries", RSC Adv, vol. 6, pp. 88683–88700, 2016. DOI: 10.1039/C6RA19482F.

[4] Abraham, D.P., Poppen, S.D., Jansen, A.N., Liu, J., Dees, D.W., "Application of a lithium–tin reference electrode to determine electrode contributions to

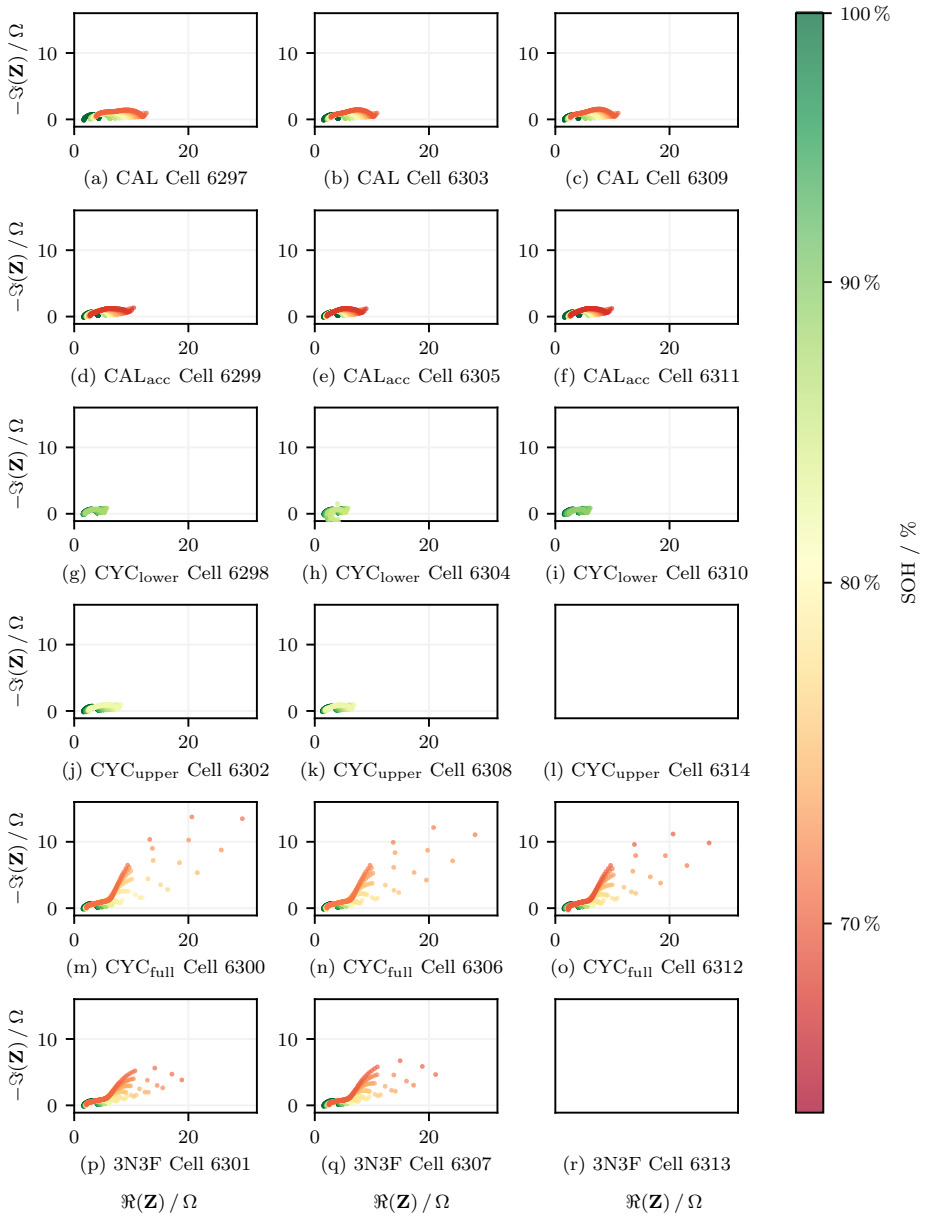

Figure 9: Nyquiyt plot for all full cells at 25 °C and 50 % SOC. The axes are fixed for each aging path to accommodate the significant impedance variations observed across different paths. The measured SOH is indicated by the colorbar. As can be seen, with the lower SOH the impedance spectra move toward the upper right and the semicircles expand.

impedance rise in high-power lithium-ion cells", Electrochimica Acta, vol. 49, pp. 4763–4775, 2004. DOI: 10.1016/j.electacta.2004.05.040.

[5] Xu, W., Zhu, J., Zhang, J., Tian, M., Cai, J., Wu, H., Wei, G., Chen, T., Wei, X., Dai, H., "Investigation of lithium-ion battery degradation by corrected differential voltage analysis based on reference electrode", Applied Energy, vol. 389, pp. 125735, 2025. DOI: 10.1016/j.apenergy.2025.125735.

[6] Belt, J.R., Bernardi, D.M., Utgikar, V., "Development and Use of a Lithium-Metal Reference Electrode in Aging Studies of Lithium-Ion Batteries", Journal of The Electrochemical Society, vol. 161, pp. A1116, 2014. DOI: 10.1149/2.062406jes.

[7] Epding, B., Broda, A., Rumberg, B., Jahnke, H., Kwade, A., "Development of Durable 3-Electrode Lithium-Ion Pouch Cells with LTO Reference Mesh: Aging and Performance Studies", Journal of The Electrochemical Society, vol. 166, pp. A1550, 2019. DOI: 10.1149/2.0851908jes.

[8] Friedrich, S., Bock, M., Jossen, A., "Cycling Aging in Different State of Charge Windows in Lithium-Ion Batteries with Silicon-Dominant Anodes", Journal of The Electrochemical Society, vol. 171, pp. 100503, 2024. DOI: 10.1149/1945-7111/ad71f8.

[9] Luh, M., Blank, T., "Comprehensive battery aging dataset: capacity and impedance fade measurements of a lithium-ion NMC/C-SiO cell", Scientific Data, vol. 11, pp. 1004, 2024. DOI: 10.1038/s41597-024-03831-x.

[10] Stroebl, F., Petersohn, R., Schricker, B., Schaeufl, F., Bohlen, O., Palm, H., "A multi-stage lithium-ion battery aging dataset using various experimental design methodologies", Scientific Data, vol. 11, pp. 1020, 2024. DOI: 10.1038/s41597-024-03859-z.

[11] Li, R., Kirkaldy, N.D., Oehler, F.F., Marinescu, M., Offer, G.J., O'Kane, S. E.J., "The importance of degradation mode analysis in parameterising lifetime prediction models of lithium-ion battery degradation", Nature Communications, vol. 16, pp. 2776, 2025. DOI: 10.1038/s41467-025-57968-3.

[12] van Vlijmen, B., Lam, V., Asinger, P.A., Cui, X., Ganapathi, D., Sun, S., Herring, P.K., Gopal, C.B., Geise, N., Deng, H.D. and others, "Interpretable data-driven modeling reveals complexity of battery aging", ChemRxiv, 2023. DOI: 10.26434/chemrxiv-2023-zdl2n.

[13] Lam, V.N., Cui, X. Stroebl, F., Uppaluri, M., Onori, S., Chueh, W.C., "A decade of insights: Delving into calendar aging trends and implications", Joule, vol. 9 (1), 2025. DOI: 10.1016/j.joule.2024.11.013.

[14] Geslin, A., Le Xu, Ganapathi, D., Moy, K., Chueh, W.C., Onori, S., "Dynamic cycling enhances battery lifetime", Nature Energy, vol. 10, pp. 172–180, 2025. DOI: 10.1038/s41560-024-01675-8.

[15] Cui, X., Kang, S.D., Wang, S., Rose, J.A., Lian, H., Geslin, A., Torrisi, S.B., Bazant, M.Z., Sun, S., Chueh, W.C., "Data-driven analysis of battery formation reveals the role of electrode utilization in extending cycle life", Joule, vol. 8, pp. 3072–3087, 2024. DOI: 10.1016/j.joule.2024.07.024.

[16] Schmitt, J., Rehm, M., Karger, A., Jossen, A., "Capacity and degradation mode estimation for lithium-ion batteries based on partial charging curves at different current rates", Journal of Energy Storage, vol. 59, pp. 106517, 2023. DOI: 10.1016/j.est.2022.106517.

[17] Bole, B., Kulkarni, C.S., Daigle, M., "Randomized Battery Usage Dataset", 2025. URL: https://data.nasa.gov (Last accessed: 25.09.2025).

[18] Bole, B., Kulkarni, C.S., Daigle, M., "Adaptation of an Electrochemistry-based Li-Ion Battery Model to Account for Deterioration Observed Under Randomized Use", Annual Conference of the PHM Society, vol. 6, pp. 1, 2014. DOI: 10.36001/phmconf.2014.v6i1.2490.

[19] Birkl, C., "Oxford Battery Degradation Dataset 1", 2017. URL: https://ora.ox.ac.uk (Last accessed: 25.09.2025).

[20] Birkl, C., "Diagnosis and prognosis of degradation in lithium-ion batteries", PhD Thesis, University of Oxford, 2017, URL: https://ora.ox.ac.uk (Last accessed: 25.09.2025).

[21] McTurk, E., Birkl, C.R., Roberts, M.R., Howey, D.A., Bruce, P.G., "Minimally Invasive Insertion of Reference Electrodes into Commercial Lithium-Ion Pouch Cells", ECS Electrochemistry Letters, vol. 4 (12), pp. A145, 2015. DOI: 10.1149/2.0081512eel.

[22] Catenaro, E., Onori, S., "Experimental data of lithium-ion batteries under galvanostatic discharge tests at different rates and temperatures of operation", Data in Brief, vol. 35, pp. 106894, 2021. DOI: 10.1016/j.dib.2021.106894.

[23] Pozzato, G., Allam, A., Onori, S., "Lithium-ion battery aging dataset based on electric vehicle real-driving profiles," Data in Brief, vol. 41, pp. 107995, 2022. DOI: 10.1016/j.dib.2022.107995.

[24] Li, W., Sengupta, N., Dechent, P., Howey, D.A., Annaswamy, A., Sauer, D.U., "One-shot battery degradation trajectory prediction with deep learning", Journal of Power Sources, vol. 506, pp. 230024, 2021. DOI: 10.1016/j.jpowsour.2021.230024.

[25] Li, W., Zhang, H., van Vlijmen, B., Dechent, P., Sauer, D.U., "Forecasting battery capacity and power degradation with multi-task learning", Energy Storage Materials, vol. 53, pp. 453–466, 2022. DOI: 10.1016/j.ensm.2022.09.013.

[26] Sauer, D.U., "Time-series cyclic aging data on 48 commercial NMC/graphite Sanyo/Panasonic UR18650E cylindrical cells", 2021. DOI: 10.18154/RWTH-2021-04545.

[27] Wildfeuer, L., Karger, A., Aygül, D., Wassiliadis, N., Jossen, A., Lienkamp, M., "Experimental degradation study of a commercial lithium-ion battery", Journal of Power Sources, vol. 560, pp. 232498, 2023. DOI: 10.1016/j.jpowsour.2022.232498.

[28] Bessman, A., Soares, R., Wallmark, O., Svens, P., Lindbergh, G., "Aging effects of AC harmonics on lithium-ion cells", Journal of Energy Storage, vol. 21, pp. 741–749, 2019. DOI: 10.1016/j.est.2018.12.016.

[29] Mohtat, P., Lee, S., Siegel, J.B., Stefanopoulou, A.G., "Reversible and Irreversible Expansion of Lithium-Ion Batteries Under a Wide Range of Stress Factors", Journal of The Electrochemical Society, vol. 168, pp. 100520, 2021. DOI: 10.1149/1945-7111/ac2d3e.

[30] Raj, T., Wang, A.A., Monroe, C.W., Howey, D.A., "Investigation of Path-Dependent Degradation in Lithium-Ion Batteries", Batteries & Supercaps, vol. 3, pp. 1377–1385, 2020. DOI: 10.1002/batt.202000160.

[31] Goldammer, E., Gentejohann, M., Schlüter, M., Weber, D., Wondrak, W., Dieckerhoff, S., Gühmann, C., Kowal, J., "The Impact of an Overlaid Ripple Current on Battery Aging: The Development of the SiCWell Dataset", Batteries, vol. 8, 2022. DOI: 10.3390/batteries8020011.

[32] Mayemba, Q., Mingant, R., Li, A., Ducret, G., Venet, P., "Aging datasets of commercial lithium-ion batteries: A review", Journal of Energy Storage, vol. 83, pp. 110560, 2024. DOI: 10.1016/j.est.2024.110560.

[33] EL-CELL GmbH, "PAT-Cell: The ideal 3-electrode test cell for high-throughput battery testing.", 2025. URL: https://www.el-cell.com (Last accessed: 25.09.2025).

[34] Schmid, A.U., Ridder, A., Hahn, M., Schofer, K., Birke, K.P., "Aging of Extracted and Reassembled Li-ion Electrode Material in Coin Cells—Capabilities and Limitations", Batteries, vol. 6 (2), 2020. DOI: 10.3390/batteries6020033.

[35] Keil, P., Schuster, S.F., Wilhelm, J., Travi, J., Hauser, A., Karl, R.C., Jossen, A., "Calendar Aging of Lithium-Ion Batteries", Journal of The Electrochemical Society, vol. 163, pp. A1872, 2016. DOI: 10.1149/2.0411609jes.

[36] Keil, P., Jossen, A., "Calendar Aging of NCA Lithium-Ion Batteries Investigated by Differential Voltage Analysis and Coulomb Tracking", Journal of The Electrochemical Society, vol. 164, pp. A6066, 2016. DOI: 10.1149/2.0091701jes.

[37] Vetter, J., Novák, P., Wagner, M.R., Veit, C., Möller, K.-C., Besenhard, J.O., Winter, M., Wohlfahrt-Mehrens, M., Vogler, C., Hammouche, A., "Ageing mechanisms in lithium-ion batteries", Journal of Power Sources, vol. 147, pp. 269–281, 2005. DOI: 10.1016/j.jpowsour.2005.01.006.

[38] Sarwar, W., "Hybridised energy storage systems for automotive powertrain applications", PhD Thesis, Imperial College London, 2016. DOI: 10.25560/44975.

[39] Birkl, C., Roberts, M.R., McTurk, E., Bruce, P.G., Howey, D.A., "Degradation diagnostics for lithium ion cells", Journal of Power Sources, vol. 341, pp. 373–386, 2017. DOI: 10.1016/j.jpowsour.2016.12.011.

[40] Safari, M., Delacourt, C., "Aging of a Commercial Graphite/LiFePO4 Cell", Journal of The Electrochemical Society, vol. 158, pp. A1123, 2011. DOI: 10.1149/1.3614529.

[41] Li, D., Danilov, D.L., Gao, L., Yang, Y., Notten, P.H.L., "Degradation Mechanisms of the Graphite Electrode in C6/LiFePO4 Batteries Unraveled by a Non-Destructive Approach", Journal of The Electrochemical Society, vol. 163, pp. A3016, 2016. DOI: 10.1149/2.0821614jes.

[42] Ecker, M., Nieto, N., Käbitz, S., Schmalstieg, J., Blanke, H., Warnecke, A., Sauer, D.U., "Calendar and cycle life study of Li(NiMnCo)O2-based 18650 lithium-ion batteries", Journal of Power Sources, vol. 248, pp. 839–851, 2014. DOI: 10.1016/j.jpowsour.2013.09.143.

[43] Wikner, E., Björklund, E., Fridner, J., Brandell, D., Thiringer, T., "How the utilised SOC window in commercial Li-ion pouch cells influence battery ageing", Journal of Power Sources Advances, vol. 8, pp. 100054, 2021. DOI: 10.1016/j.powera.2021.100054.

[44] Jung, R., Metzger, M., Maglia, F., Stinner, C., Gasteiger, H.A., "Oxygen Release and Its Effect on the Cycling Stability of LiNixMnyCozO2 (NMC) Cathode Materials for Li-Ion Batteries", Journal of The Electrochemical Society, vol. 164, pp. A1361, 2017. DOI: 10.1149/2.0021707jes.

[45] Zhang, S.S., "Understanding of performance degradation of LiNi0.80Co0.10Mn0.10O2 cathode material operating at high potentials", Journal of Energy Chemistry, vol. 41, pp. 135–141, 2020. DOI: 10.1016/j.jechem.2019.05.013.

[46] Venkatakrishnan, S., Ramasamy, R.P., "Effect of Fast-Charging and Cycling Window on Lithium-Ion Battery Performance and Aging", Journal of The Electrochemical Society, vol. 172, pp. 050529, 2025. DOI: 10.1149/1945-7111/add388.

[47] Jalkanen, K., Karppinen, J., Skogström, L., Laurila, T., Nisula, M., Vuorilehto, K., "Cycle aging of commercial NMC/graphite pouch cells at different temperatures", Applied Energy, vol. 154, pp. 160–172, 2015. DOI: 10.1016/j.apenergy.2015.04.110.

[48] Zhang, S.S., "The Puzzles in Fast Charging of Li-Ion Batteries", ENERGY & ENVIRONMENTAL MATERIALS, vol. 5, pp. 1005–1007, 2022. DOI: 10.1002/eem2.12330.

[49] Laforgue, A., Yuan, X.-Z., Platt, A., Brueckner, S., Perrin-Sarazin, F., Toupin, M., Huot, J.-Y., Mokrini, A., "Effects of Fast Charging at Low Temperature on a High Energy Li-Ion Battery", Journal of The Electrochemical Society, vol. 167, pp. 140521, 2020. DOI: 10.1149/1945-7111/abc4bc.

[50] Dubarry, M., Truchot, C., Liaw, B.Y., "Synthesize battery degradation modes via a diagnostic and prognostic model", Journal of Power Sources, vol. 219, pp. 204–216, 2012. DOI: 10.1016/j.jpowsour.2012.07.016.

[51] Hofmann, T., Li, J., Hamar, J., Erhard, S., Schmidt, J.P., "The ΔQ-method: State of health and degradation mode estimation for lithium-ion batteries using a mechanistic model with relaxed voltage points", Journal of Power Sources, vol. 596, pp. 234107, 2024. DOI: 10.1016/j.jpowsour.2024.234107.

[52] Hofmann, T., Hamar, J., Mager, B., Erhard, S., Schmidt, J.P., "Physics-constrained transfer learning: Open-circuit voltage curve reconstruction and degradation mode estimation of lithium-ion batteries", Energy and AI, vol. 20, pp. 100493, 2025. DOI: 10.1016/j.egyai.2025.100493.

[53] Bin-Mat-Arishad, I., Wimarshana, B., Fly, A., "Influence of voltage profile and fitting technique on the accuracy of lithium-ion battery degradation identification through the Voltage Profile Model", Journal of Energy Storage, vol. 70, pp. 107884, 2023. DOI: 10.1016/j.est.2023.107884.

[54] Pastor-Fernández, C., Yu, T. F., Widanage, W. D., Marco, J., "Critical review of non-invasive diagnosis techniques for quantification of degradation modes in lithium-ion batteries", Renewable and Sustainable Energy Reviews, vol. 109, pp. 138–159, 2019. DOI: 10.1016/j.rser.2019.03.060.

[55] Chen, J., Marlow, M.N., Jiang, Q., Wu, B., "Peak-tracking method to quantify degradation modes in lithium-ion batteries via differential voltage and incremental capacity", Journal of Energy Storage, vol. 45, pp. 103669, 2022. DOI: 10.1016/j.est.2021.103669.

[56] Ma, Z., Wang, Z., Xiong, R., Jiang, J.,, "A mechanism identification model based state-of-health diagnosis of lithium-ion batteries for energy storage applications", Journal of Cleaner Production, vol. 193, pp. 379–390, 2018. DOI: 10.1016/j.jclepro.2018.05.074.

[57] Miranda, L.J.V., "PySwarms, a research-toolkit for Particle Swarm Optimization in Python", Journal of Open Source Software, vol. 3(21), 2018. DOI: 10.21105/joss.00433.

[58] Peng, J., Meng, J., Wu, J., Deng, Z., Lin, M., Mao, S., Stroe, D.-I., "A comprehensive overview and comparison of parameter benchmark methods for lithium-ion battery application", Journal of Energy Storage, vol. 71, pp. 108197, 2023. DOI: 10.1016/j.est.2023.108197.

[59] Murbach, M.D., Gerwe, B., Dawson-Elli, N., Tsui, L.-k., "impedance.py: A Python package for electrochemical impedance analysis", Journal of Open Source Software, vol. 5, pp. 2349, 2020. DOI: 10.21105/joss.02349.

[60] Costard, J., Ender, M., Weiss, M., Ivers-Tiffée, E., "Three-Electrode Setups for Lithium-Ion Batteries", Journal of The Electrochemical Society, vol. 164, pp. A80, 2016. DOI: 10.1149/2.0241702jes.

[61] Middlemiss, L.A., Rennie, A.J.R., Sayers, R., West, A.R., "Characterisation of batteries by electrochemical impedance spectroscopy", Energy Reports, vol. 6, pp. 232–241, 2020. DOI: 10.1016/j.egyr.2020.03.029.

[62] Schönleber, M., Klotz, D., Ivers-Tiffée, E., "A Method for Improving the Robustness of linear Kramers-Kronig Validity Tests", Electrochimica Acta, vol. 131, pp. 20–27, 2014. DOI: 10.1016/j.electacta.2014.01.034.

[63] Virtanen, P. Gommers, R., Oliphant, T.E., Haberland, M., Reddy, T., Cournapeau, D., Burovski, E., Peterson, P., Weckesser, W., Bright, J., van der Walt, S.J., Brett, M., Wilson, J., Millman, K.J., Mayorov, N., Nelson, A.R.J., Jones, E., Kern, R., Larson, E., Carey, C.J., Polat, VanderPlas, J., Laxalde, D., Perktold, J., Cimrman, R., Henriksen, I., Quintero, E.A., Harris, C.R., Archibald, A.M., Ribeiro, A.H., Pedregosa, F., van Mulbregt, P. and SciPy 1.0 Contributors, "SciPy 1.0: Fundamental Algorithms for Scientific Computing in Python", Nature Methods, vol. 17, pp. 261–272, 2020. DOI: 10.1038/s41592-019-0686-2.

[64] Li, H., Lyu, Z., Han, M., "Robust and fast estimation of equivalent circuit model from noisy electrochemical impedance spectra", Electrochimica Acta, vol. 422, pp. 140474, 2022. DOI: 10.1016/j.electacta.2022.140474.

[65] BioLogic Instruments, "Battery – Application Note 42", 2024. URL: https://www.biologic.net (Last accessed: 25.09.2025).

[66] Jorcin, J.-B., Orazem, M.E., Pébère, N., Tribollet, B., "CPE analysis by local electrochemical impedance spectroscopy", Electrochimica Acta, vol. 51, pp. 1473–1479, 2006. DOI: 10.1016/j.electacta.2005.02.128.

[67] Metrohm Autolab, "EIS Data fitting – How to obtain good starting values of equivalent circuit elements: AN-EIS-007", 2019. URL: https://www.metrohm.com (Last accessed: 25.09.2025).

[68] BaSyTec, "BaSyTec CTS Battery Test Systems", 2024. URL: https://basytec.de (Last accessed: 25.09.2025).

[69] Gamry Instruments, "Reference 3000 Potentiostat/Galvanostat/ZRA Product Brochure", 2025. URL: https://www.gamry.com (Last accessed: 25.09.2025).

3 Discussion and Summary

This discussion particularly focuses on the advancements made in SOH estimation and OCV reconstruction algorithms for LiBs and BEVs. By integrating the findings from each article, this chapter elucidates the ways in which this thesis enhances the accuracy and reliability of SOH estimation, thereby contributing significantly to the field of battery technology and BEV performance. This thesis not only allows one to improve state estimation for LiBs but also bridges the gap towards onboard estimation for BEV fleets. This ultimately leads to higher transparency over used BEVs and, with that, to a higher acceptance rate – especially in the aftermarket. While new BEV generations are still too expensive to penetrate the entire market, increased trust in the aftermarket will allow the widespread adoption of BEVs throughout society, leading to fewer ICE cars on the road and, thus, to a more climate-friendly future.

A thematic connection between each research article is created and guides the process from SOH_C estimation, through OCV reconstruction and DM estimation, to finally creating a truly valid dataset, including all aging information necessary. The synthesis provided herein demonstrates how the collective insights from these articles contribute to answering the overarching research questions defined earlier in the thesis.

This chapter presents an individual discussion of the research questions in Sections 3.1, 3.2, and 3.3, while still maintaining the overall connection between all articles. Section 3.4 concludes with a brief summary and an outlook for future research.

3.1 Discussion of SOH Estimation based on OCV-Models

As outlined in the introduction, the OCV model, based on the mechanistic modeling approach, traditionally requires time-series data during charging to operate. However, such data is not available for most existing BEV fleets. In Section 2.1, a novel OCV model is introduced that utilizes an alternative data source: Relaxed voltage points and the accumulated charge between these points, which is already captured in most BMSs for SOC adaptation.

The initial research question regarding how the mechanistic model must be modified to operate with real-world BEV fleet data is addressed by altering the objective of the optimization problem:

$$f(\vartheta) = \| \Delta Q_{\mathrm{meas}}(V) - \Delta Q_{\mathrm{reco}}(V, \vartheta) \|_2^2 \tag{3.1}$$

where $\Delta Q_{\text{meas}}(V)$ is the measured vector of N charge differences between each two neighboring relaxed voltage points:

$$\Delta Q_{\text{meas}}(V) = \begin{bmatrix} \Delta Q_1 \\ \Delta Q_2 \\ \dots \\ \Delta Q_N \end{bmatrix} = \begin{bmatrix} Q(V_2) - Q(V_1) \\ Q(V_4) - Q(V_3) \\ \dots \\ Q(V_{2N}) - Q(V_{2N-1}) \end{bmatrix} \tag{3.2}$$

This adaptation of the objective function offers several benefits: Reduced computational cost due to processing less data. In other adaptations of the mechanistic model with time-series data, vectors of significant length are processed. In contrast, the novel ΔQ-method operates with as few as three data points and typically does not process more than 20 relaxed voltage points. Consequently, the calculation of the cost in the objective function is less complex, facilitating easier operation on onboard BMS. This modification allows the mechanistic model to be applied to existing BEV fleet data for the first time. While this is a substantial benefit for onboard applications and accurate OCV updates, it also serves as a diagnostic tool to monitor fleet behavior. Understanding degradation patterns in the field can influence the design of future battery cells and the working principles of onboard algorithms, such as SOC estimation or fast-charging strategies.

For the voltage points in Equation 3.2, it is, e.g., possible for V_2 to equal V_3, indicating that two values of the vector are connected. This can occur if a customer charges the BEV to a specific SOC, pauses until the criteria for a relaxed voltage point measurement are met (e.g., 3 h of relaxation), and then continues charging to another SOC point where the criteria are again fulfilled. This adaptation also enables usage in laboratory environments. For example, using relaxed voltage points during GITT or HPPC tests can reconstruct the full OCV. The use of the connected relaxed voltage points from the HPPC is particularly promising, as it can significantly reduce testing time. This connects to the last section (Section 2.3) in the main chapter: The novel battery degradation database at the electrode level allows validation of such novel methods because it includes validated DMs and HPPC measurements.

Figure 3.1 compares the estimated DMs from the ΔQ-method with the generated DMs from the measurement series in Section 2.3. In Figure 3.1, all measured DMs from all cells over all aging paths are combined to validate the ΔQ-method with the largest possible dataset.

The data used includes relaxed voltage points from the HPPC section, i.e., SOC points at 10 %, 20 %, 50 %, 80 %, and 90 % SOC. The relaxation period was at least 1 h, and the cumulative charge between these points was tracked by the cycling system. Hence, the matrix for the objective function in Equation 3.2 consists of four segments, totaling five relaxed voltage points, where V_1 is the measured voltage at SOC = 10 %, V_2 at SOC = 20 %, and so on. These estimated DMs are compared to the valid DMs generated by the fitting protocol introduced in Section 2.3. The measured electrode potentials are used to track changes in DMs, providing the most accurate estimation of DMs, which are considered the reference.

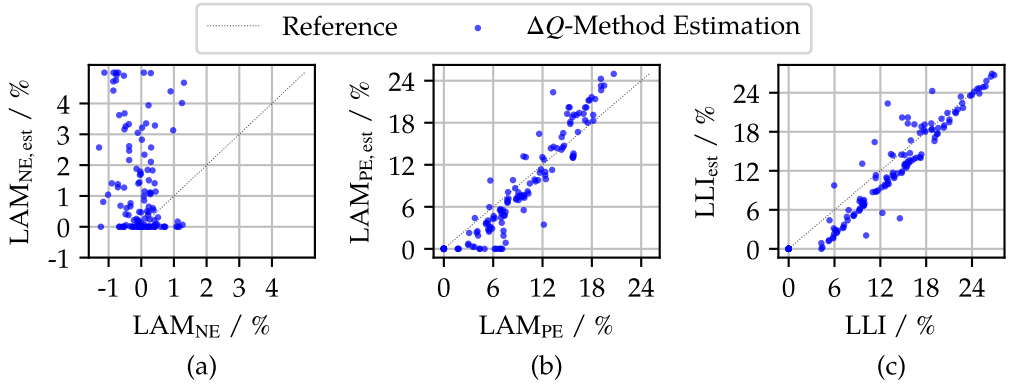

Figure 3.1: The ΔQ-method applied on relaxed voltage points, gathered from the hybrid pulse power characterization (HPPC) of the dataset introduced in Section 2.3. The true labels are generated from the measured electrode potentials, which are fitted based on the algorithm described in Section 2.3, and are compared to the estimated loss of active material - negative electrode (LAM_{NE}) (a), loss of active material - positive electrode (LAM_{PE}) (b) and loss of lithium inventory (LLI) (c).

Figure 3.1 demonstrates that the ΔQ-method yields accurate results for LAM_{PE} and LLI estimation – now also validated for another cell chemistry than in the initial publication [100]. However, the estimation of the nearly constant LAM_{NE} is challenging due to the absence of anode features in the data matrix. The lower SOC segment is particularly important for the ΔQ-method because it provides a steeper gradient in the OCP_{NE}, which influences the full-cell voltage. This allows for better estimation of the alignment parameters for the anode, α_{NE} and β_{NE}. Figure 3.2 visualizes the OCV (a) and DVA (b) of the pristine LiB, including the measured electrode potentials, investigated in Figure 3.1 in comparison to the included relaxed voltage points at 10 %, 20 %, 50 %, 80 %, and 90 % SOC.
This comparison makes it clear that the anode just marginally influences the cost function, i.e., only the lowest segment ΔQ_1 is influenced by the gradient change of the OCP_{NE}. Hence, the objective function is biased towards accurate reconstruction of the OCP_{PE}, while the influence of LAM_{NE} on the full cell OCV is negligible. Inclusion of an additional relaxed voltage point at 0 % state of charge (SOC) would drastically change the objective and increase the fitting accuracy for the OCP_{NE} due to the high gradient in this region, as can be seen in Subfigure 3.2 (b).

This work extends the state of the art by presenting a novel method for OCV reconstruction applicable to virtually any dataset, independent of the system level, whether laboratory cell, cell, pack, or BEV. This research confirms earlier findings regarding the optimal SOC range, noting that lower SOC segments are beneficial for accurate OCV reconstruction. Table 3.1 compares the findings from the study to the state of the art utilizing the mechanistic modeling approach on partial charging events for OCV reconstruction. While many novel state estimation models are benchmarked against the NASA [195] or Oxford [196] datasets, this is not the case for the proposed models within this thesis as these common datasets are not

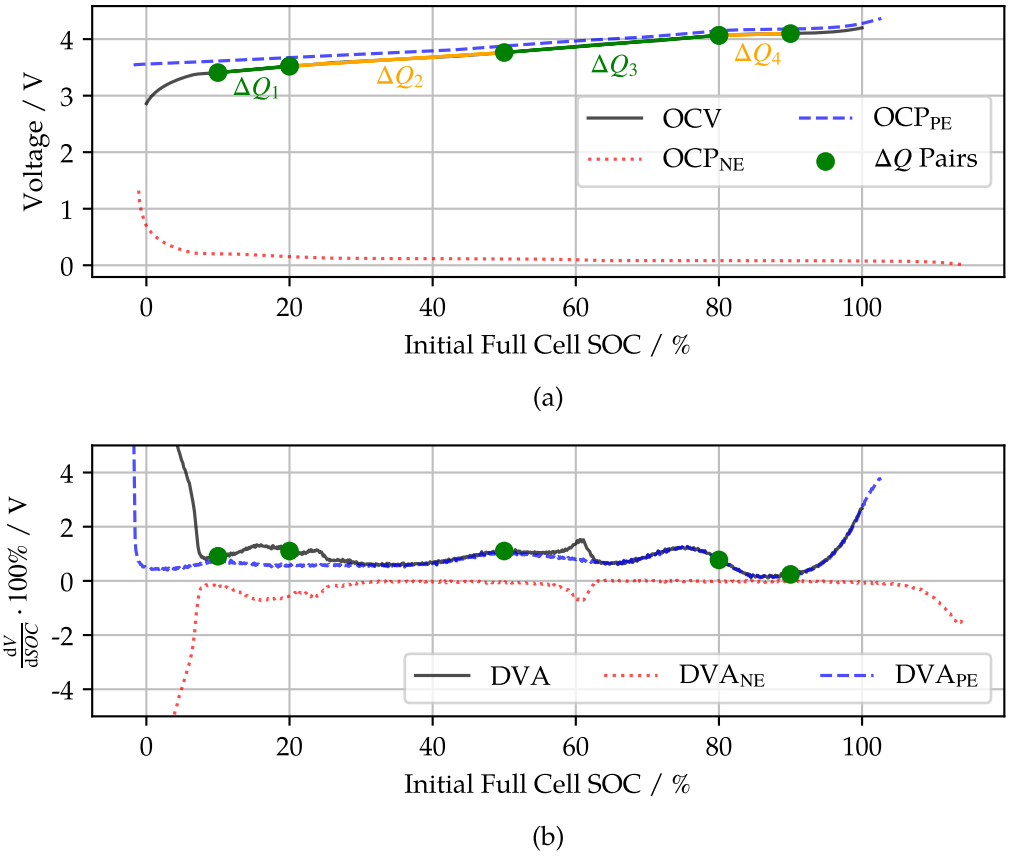

Figure 3.2: Relaxed voltage points and ΔQ-pairs, gathered from the hybrid pulse power characterization (HPPC) of the dataset introduced in Section 2.3, in comparison to the measured open-circuit voltage (OCV), open-circuit potentials (OCPs) (a), and differential voltage analysis (DVA) (b) from a pristine lithium-ion battery (LiB).

representative. Table 3.1 reveals that most authors [27; 46; 55; 91] state a maximum C-rate between C/3 and C/4 to achieve accurate results. This, however, must be interpreted in the context of their studies: For example, Chen et al. [91] state that they have achieved DM RMSEs below 3.5 % while only using partial charging events from 40 % to 100 % at C/3. They have gathered synthetic data for these results, which highly simplifies the problem at hand because synthetic data still includes detectable features, even if they are marginal, at higher C-rates.

Yang et al. [55] propose that a partial charging voltage segment from 20 % to 70 % SOC at C/3 suffices to reach acceptable results. Their findings were limited on SOH_C estimation, while the estimation of DMs was carried out with 20 % to 80 % SOC segments at C/20. For their dataset at C/3 they further state, that even accurate SOH_C estimation is not possible if the starting SOC is above 30 %. Schindler [46] and Friedrich et al. [166] both modified the mechanistic model to cover charging events at higher C-rates. They did not analyze the influence of partial voltage curves. Schmitt et al. [27], finally, initialized a detailed sensitivity analysis and concluded that accurate OCV reconstruction – and, with that, DM estimation

Table 3.1: Comparison of literature findings on the application of the mechanistic modeling approach to (partial) charging voltage curves with the novel ΔQ-method.

Study	Minimum SOC range	Maximum C-rate	Comment
Hofmann et al. [100]	40 % to 100 % or 30 % to 75 %	relaxed voltage pairs	Usage of relaxed voltage points
Schindler et al. [46]	0 % to 100 %	C/3	Focus on current and temperature
Friedrich et al. [166]	0 % to 100 %	C/10	Focus on methods
Yang et al. [55]	20 % to 70 %	C/3	Evaluation of SOH_C
Chen et al. [91]	40 % to 100 %	C/3	Synthetic data
Schmitt et al. [27]	10 % to 80 %	C/4	For SOH_C estimation
Schmitt et al. [27]	20 % to 70 %	C/15	For OCV reconstruction

– from partial voltage curves is only possible with C-rates as high as C/15. Otherwise, the features in the full cell voltage curve vanish and especially for the OCP_{NE} no significant marker is detectable. They claim that the C-rate can be higher if the full SOC window is available.

As can be seen in Table 3.1, the ΔQ-method requires less wide SOC windows if the starting SOC reduces. This again, confirms the earlier findings presented in Figure 3.1 and 3.2: The lower segments are extremely beneficial for detecting features in the OCP_{NE} and, with that, guide an accurate OCV reconstruction. It must be further noted that all compared studies [27; 46; 55; 91; 166] have used laboratory data on cell level instead of real-world vehicle fleet data. Hence, the results partly confirm the prior investigations and, for the first time, prove the applicability of the OCV model for BEV data. This was achieved by using the mean cell voltage in the battery pack of the BMW i3. For the application of the ΔQ-method, this implies that relaxed voltage points in the low SOC region are mandatory to achieve high OCV reconstruction accuracy, forcing the customers to discharge, i.e., drive, their vehicle to a very low SOC and keep the vehicle at this state for at least some hours before plugging it in to start charging. While this seems unrealistic, it becomes very likely if (smart) bidirectional charging is activated, e.g., the vehicle could wait with the full charge to fulfill the relaxation criteria or even discharge the BEV to reach lower SOC regions.

Despite these advances in comparison to the state of the art, some challenges remain. The only valid labels were the SOH_C measurements. It was not possible to validate the OCV update as this true measurement was unavailable. Only the comparison between the ΔQ error and the resulting OCV error from reconstruction and measurement was possible. DM labels were generated but not validated. This issue was addressed with additional data from the final journal publication in Section 2.3, as shown in Figure 3.1.

Input data variations, i.e., charge direction, number of relaxed voltage pairs, temperature, relaxation period or SOC range, can be critical as many influencing factors are ignored. Point

pairs during charging and discharging are combined by solely changing the sign, which may not accurately reflect the true conditions. Additionally, two relaxed voltage points during a discharge event likely include charging segments from recuperation, affecting accuracy, as hysteresis is completely neglected. Temperature effects are not considered, nor is the applied current before the relaxation phase. The relaxation period itself is also not taken into account. Furthermore, the average cell voltage might not be ideal, as the most degraded cell limits the overall SOH of the BEV. Ideally, capturing cell-individual voltage data would provide a more accurate assessment of the whole high-voltage battery.

Criticism of the method includes search space constraints based on the SOH onboard estimate, which already bias the estimation towards the correct SOH label. It is unclear if the preset search space covers the entire degradation paths of the vehicle fleet and this cannot be validated. Moreover, the pristine OCP of the positive electrode from the BMW i3 was only measured in a very narrow voltage range, which might negatively influence the estimation accuracy for degraded batteries. Some degradation states, specifically certain alignment parameter combinations, might not be covered with the measured OCPs due to their limited range.

Previously, many automotive manufacturers might have considered capturing time-series data of charging events for their algorithms to perform OCV updates. The novel method offers a solution that eliminates this time- and data-storage-intensive requirement. The ΔQ-method is already applicable to existing BEV fleets and was already validated against measured SOH_C labels. The OCV reconstruction results repeatedly highlight the need for a comprehensive battery aging database that can serve as a validation tool, such as the presented database in the last section (Section 2.3) of the main chapter.

The findings can guide future OCV reconstruction methods in several ways: Both methods (mechanistic model and ΔQ-method) follow the same working principle and show that lower SOC segments are beneficial as they reveal the most information about the anode. These results can also be transferred to LFP, as LFP has a very flat voltage characteristic. To make the mechanistic model work for LFP, whether using the time-series or the ΔQ-approach, very high and low SOCs are required, as only there are changes in the LFP OCP reflected in the full-cell voltage. In addition, due to the significant hysteresis of LFP cathodes, the input data must be collected exclusively during either the charging or discharging process.

Applications include fleet monitoring, laboratory measurement evaluation, and test plan reduction. As demonstrated in Figure 3.1, LAM_{PE} and LLI are accurately estimated from relaxed voltage points in HPPC measurements, removing the need for lengthy pOCV or GITT measurements to track OCV changes. The lightweight algorithm allows for the application to onboard BMS, facilitating rollout to most BEV fleets. As observed in this study and discussed by literature findings [27; 46; 55; 91; 166], the use of voltage data in the lower SOC region is essential. While this presents a challenge, it also offers an opportunity to enhance state estimation through smart charging strategies. For instance, controlled charging with

predefined steps in the lower SOC regions appears feasible in the near future. This approach not only increases the number of data points in the low SOC segments but also enriches the overall dataset, thereby improving accuracy.

The sensitivity of the method must be critically discussed, especially in terms of input data. Further application of the method to recent BEVs, particularly those including LFP LiBs, is of high interest as the flat voltage characteristic poses significant challenges to the method. To accurately validate the OCV and DM estimation accuracy, full pOCV measurements of degraded BEVs are necessary.

3.2 Discussion of Data Scarcity and Neural Networks for SOH Estimation

While the mechanistic model provides an opportunity to estimate SOH_C, OCV, and DMs from a single measurement, it is computationally complex during operation and constrained by the physics-based rules embedded in the model itself. Adhering strictly to these rules may be erroneous, and learning from past data could be a more effective approach [9; 102]. Deep learning models, although cumbersome during offline training, are efficient once trained and can easily operate onboard. They are not completely restricted to predefined physical laws, which can be both an advantage and a disadvantage. Besides that, deep learning models face two substantial challenges: Data scarcity and data dependence.

The publications introduced in Section 2.2 aim to address how these major issues can be resolved. Three different approaches are discussed: PINN (Subsection 2.2.1 [149]), transfer learning (Subsection 2.2.2 [126]), and their combination (Subsection 2.2.3 [51]). The PINN approach offers several solutions to these challenges [147] and presents a sequential model architecture where synthetic data generated by a P2D model, including internal states, was fused with the target experimental data. Results indicate that PINNs effectively address data scarcity by leveraging information from physics-based synthetic data. Accuracy can be further enhanced by including internal states, which guide the internal information flow of the deep learning network by connecting neurons that map measured signals to the desired SOH.

The proposed transfer learning approach extends SOH_C estimation to OCV reconstruction. Similarly, synthetic data is generated using the mechanistic model, with the distinction that the synthetic data is based on a different cell. The study reveals that transfer learning is highly promising for overcoming challenges in deep learning, as the requirements for adequate source and target domain training datasets are minimal: The source domain training dataset must encompass all possible aging paths and labels, which is easily achieved with simulation data. The target domain fine-tuning dataset must include the boundaries of the desired domain. For instance, if a model is to function across a current range from C/50 to 1C and a temperature range from 10 °C to 40 °C, the fine-tuning dataset must contain

at least eight samples: C/50 and 10 °C, C/50 and 40 °C, 1C and 10 °C, 1C and 40 °C, all in pristine and degraded states. This demonstrates that transfer learning effectively exploits the extrapolation capability of simulation and the interpolation capability of neural networks.

The most effective approach was the combination of transfer learning and PINN: By integrating the developed transfer learning model with a mechanistic modeling approach, the reconstructed OCV was updated to adhere to the rules of the mechanistic model, and it further enabled the estimation of DMs. It was irrelevant whether the prior transfer learning model returned the full OCV or just the alignment parameters. Both methods outperform the state of the art: In comparison to the most similar study by Tian et al. [61], the proposed method reduced the SOH_C MAE for 200 mV input segments from approximately 3.7 % (pp) to 1.5 % (pp). The study's results also emphasize the importance of fine-tuning data, as the known DMs clarified that the maximum appearing DMs must be included in the dataset. This highlights another major benefit of transfer learning: Setting up a deep learning model guided by transfer learning reduces data requirements by approximately 95 % [51].

The PINN results extend the state of the art and demonstrate that synthetic data can not only substitute for training data, but also the inclusion of internal states is beneficial – a finding not previously observed [131; 148; 162–164]. While prior realizations of PINN [131; 148; 162–164] focused on the simplicity of the sequential approach and mainly on the benefit created by fusing data sources, this approach reveals more underlying advantages. The results lead to the assumption that the incorporation of unmeasurable states in the training data forces the neural network to link neurons within the hidden layers to exploit the correlation between measurable states, internal battery states, and the state of interest, the SOH_C. As discussed in the work by Thelen et al. [162] and Navidi et al. [163], the PINN approach can be easily extended to DM estimation [164] and, with that, OCV reconstruction.

The transfer learning approaches move in this direction by defining the OCV as the target variable. The published transfer learning study [126] extends the state of the art by proving that the choice of the source domain is not critically important. It demonstrated that even completely synthetic data, with self-designed OCP curves, can serve as the source domain if it adheres to the physics-based rules of battery degradation, such as LAM leading to shrunken electrode potential curves and LLI causing a relative shift. In comparison to other transfer learning studies [61; 123–125; 127–146], this study further advances the state of the art by combining the strengths of PINNs and transfer learning in a single model that achieves highly accurate results for OCV reconstruction, even with partial charging data. Especially the analysis of more than 1.9 million BEV low C-rate charging events ($P \leq 22$ kW) provides valuable insights, as it detects customer charging patterns and yields the SOC window from 30 % to 85 % as the default. While previously transfer learning was already applied for DM estimation and OCV reconstruction [123; 133; 137], the usage of synthetic data from the mechanistic modeling approach for this target lacked sufficient research [137]. Lu et al. [137], however, only compared the performance regarding SOH_C estimation for full charging events because explicit DM knowledge of their experimental dataset was missing.

Comparing the results to Table 3.1, this work extends the state of the art to realistic charging events, i.e., narrower SOC ranges and higher C-rates. Both proposed methods, achieve reasonable results for the newly defined default SOC window from 30 % to 85 %. The first approach [126] kept an OCV reconstruction MAE and an SOH_C estimation MAE below 20 mV and 2.0 % (pp), respectively, independent of the C-rate (C/3.85 to 1C), also for very challenging use cases with only 13 % of available fine-tuning data. The second approach [51] extended these findings by narrowing the fine-tuning data to only one out of all available aging paths. On average, the developed methods kept the MAE of the reconstructed OCV below 13 mV, the SOH_C MAE below 1.8 % (pp), and all relevant DM MAEs below 3 % (pp). Especially the detailed analysis of the deviation between reconstructed and measured OCV, DVA and ICA, reveals the huge advantage of fusing physics-based models with deep learning approaches. Both findings clearly outperform the state of the art, while maintaining very low data requirements.

Despite these advantages, several drawbacks in the study design and results can be identified. For PINNs, the sampling rate was too low, causing dynamic effects to vanish. The lack of variation in laboratory data, with only constant-current (dis)charging events, was another limitation. The failure to estimate in-vehicle data might be related to the minimal amount of data (2.2 %) compared to the complete dataset.

In the transfer learning model, the claim is expanded by asserting that including the boundaries of the target domain is sufficient. As a result, the accuracy for samples close to these boundaries is higher than for those further away. Despite that, accuracy for other samples remains higher than the benchmark and is sufficient. The combined PINN and transfer learning approach initially suggested that using purely physics-based or mechanistic models forces the estimation to follow predefined rules. By fusing transfer learning with the mechanistic model, the approach reinforces this constraint. This is because general assumptions of degradation hold true, especially regarding the mechanistic model.

All proposed methods do not fully leverage the benefits of deep learning because, instead of learning from full history, as seen in literature examples [9; 102], they rely on explicit measurements. For transfer learning and the physics-constrained transfer learning, OCV reconstruction is limited to partial charging segments, but performance for random driving segments is also of interest. In general, PINNs exhibit high data dependence, making it crucial that synthetic data closely resembles experimental data. This is not the case for both transfer learning projects, where there is relatively low data dependence, as the source and target domains can be derived from completely different cell chemistries without issue. Most importantly, all investigated models focus solely on characterization of the equilibrium, i.e., SOH_C, OCV, and DMs – dynamic effects remain unexplored.

All methods could be directly applied to an onboard BMS to estimate the current SOH_C, OCV, or DMs from partial charging segments. This can also be done in cloud-based systems for fleet diagnosis, where especially the last method – physics-constrained transfer learning

– and the ability to estimate DMs provide crucial insights into battery degradation. Transfer learning, in particular, can be applied to other cell chemistries, and adaptation from cell to system level is highly sought after. Low data dependence has already been observed, suggesting that transfer learning should work with relatively few labels, even for real-world fleet data. Yet, time-series data of BEV charging events are scarce, especially for older BEVs.

Further research is needed, particularly in applying these methods to BEV fleets. Most importantly, extending the methods to dynamic effects and more in-depth characterization, including inhomogeneity, is crucial. For transfer learning, this would involve a large source domain where impedance and homogeneity at the electrode level are modified. For fine-tuning, a database is necessary that includes electrode potential and resistance information along aging, provided within this dissertation and presented in the comprehensive battery degradation database in Section 2.3.

3.3 Discussion of the Extension of the SOH Metric to Cover Dynamic Effects

In the first four studies [51; 100; 126; 149], various methods were proposed for estimating SOH_C, reconstructing OCV, and estimating DMs. These methods utilized different data sources and were validated with diverse datasets. Yet, a common limitation emerged: A comprehensive SOH metric, specifically SOH_{UBE}, could not be generated from these methods. The primary reason is the inability to dynamically model impedance effects at the electrode level without the necessary data. Consequently, prior research within this thesis concluded that a novel database at the electrode level is essential to serve as a baseline for future investigations. Figure 3.3 illustrates this effort by comparing the data sections covered in each publication. It becomes clear that prior investigations exclusively dealt with the equilibrium effects of battery degradation, i.e., capacity loss, DM rise, and resulting OCV changes. While two of the studies also researched the applicability of BEV fleet data, there is a lack of utilized electrode aging data and, with that, the information about specific effects within the battery.

The novel database significantly expands the available data sources by incorporating information about electrode resistance rise in relation to DMs across various aging paths.

This database establishes a new state of the art, surpassing available literature and public datasets [27; 29; 31; 77; 195; 196; 211–231]. Previous literature primarily focused on limited datasets that did not encompass comprehensive electrode-level data. With this dataset, it is possible to truly characterize the SOH of batteries, including electrode information. For the first time, this dataset allows for the true validation of models for SOH estimation, independent of the specific definition used.

The dataset preserves high data quality, consisting of 18 cells and 11 RPTs, with no information loss. Notably, no cell or channel experienced failure throughout the aging series. The

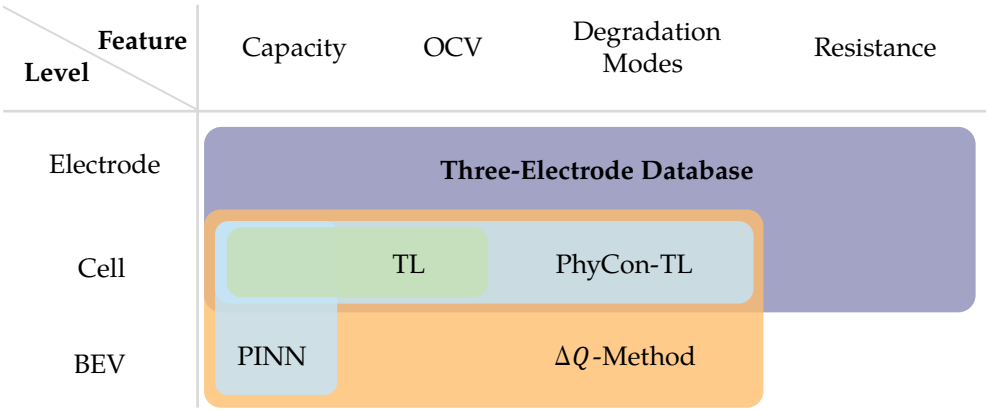

Figure 3.3: Comparison of the proposed publications and their investigated system level and included features.

investigated cells have undergone up to 600 EFCs while maintaining an SOH_C above 67 %. Additionally, fitting quality was ensured by accurately tracking errors, maintaining high data integrity.

A challenge remains in validating all generated labels, particularly since LAM_{NE} exhibits unusual behavior and is often negative. However, all methods employed directly utilize measured electrode potentials and adhere to state-of-the-art techniques. Furthermore, all results reflect the mathematical optimum by employing a global optimization routine. All raw data and software are published, allowing for straightforward recalculation of DMs and ECM values if the state of the art evolves. For the first time in the literature, aside from the NASA [195] or Oxford [196] dataset, a comparison between research groups can be drawn, allowing for the examination of exceptionally high physical relevance and precision.

The correlation between DMs and resistance rise can be exploited to develop models that estimate the resistance contribution of electrodes based on the full cell resistance rise and estimated DMs from the discussed methods. This can be applied, for example, in fast-charging scenarios. Another possibility is to extend the SOH metric to SOH_{UBE} by dynamically monitoring electrode resistance rise and integrating these terms into the objective function. The most important application is the validation of any estimation model in the field using a truly validated dataset.

Further research is necessary to recreate the database for other cell chemistries, particularly for LFP and silicon-containing anodes. Extending this to commercial cells requires developing a large measurement series, where cells are extracted and disassembled during each RPT to monitor electrode changes. This, however, demands extensive and costly degradation studies with multiple batteries.

3.4 Conclusion and Outlook

This section summarizes the key findings of this dissertation. The studies demonstrated that both data-driven and mechanistic OCV models accurately monitor the SOH_C of battery cells and are capable of analyzing real-world BEV fleet data. For a comprehensive characterization, understanding the underlying DMs and the OCV is equally important as precise knowledge of the SOH_C. The OCV plays a critical role in determining the accuracy of SOC estimations and significantly influences most charging algorithms. Therefore, the methods were examined for their applicability in estimating the DMs and the OCV. Additionally, the challenge of data scarcity in neural networks was addressed, exploring how transfer learning and PINNs could effectively bridge this gap. Ultimately, the types of data necessary to construct a comprehensive database for thorough battery characterization were identified, accounting for both equilibrium and dynamic effects, such as SOH_R and SOH_{UBE}.

To this end, the following research questions were formulated and answered in the three sections and five journal contributions:

1. How can the mechanistic model for OCV reconstruction be applied to real-world vehicle data? (Section 2.1)
2. How can the issue of data scarcity in deep learning be resolved? (Section 2.2)
3. How can deep learning models be integrated with physics-based models to ensure adherence to physical laws and improve interpretability? (Section 2.2)
4. What dataset is required to extend SOH estimation to other SOH metrics, such as SOH_R and SOH_{UBE}? (Section 2.3)

The first research question was addressed by modifying the objective function of the OCV model. By adapting this function to utilize the gathered relaxed voltage points in conjunction with the accumulated charge between these points, the mechanistic model was successfully applied to real-world BEV fleet data. The objective function minimized the charge difference between adjacent relaxed voltage points, which was validated using a laboratory cell dataset and subsequently applied to fleet data from the BMW i3. Validation at the fleet data level involved comparing the estimated SOH_C to a measured value obtained during a service visit. A comparison across all 550 vehicles resulted in a SOH_C MAE of 2.52 % (pp). Although the accuracy of the OCV reconstruction and the estimation of DMs cannot be definitively proven, it is possible to analyze the general trend of the DMs, which aligned with expectations based on literature observations.

OCV models based on the mechanistic modeling approach require input data which fulfill many requirements regarding SOC range, C-rate, and temperature, whereas neural networks offer more flexible options but demand extensive amounts of training data and might produce unphysical results. Consequently, for new battery and BEV generations, the most significant challenges are data scarcity, data dependence, and the adherence to physical laws. The

second research question aims to address the major issue of data scarcity, which is inherently linked to data dependence. The third research question expands the requirements by demanding deep learning models that are integrated with physics-based models to ensure adherence to physical principles and enhance interpretability. This goal is approached from two directions: PINNs and transfer learning. One study analyzed PINN architectures, while two studies investigated the utilization of transfer learning.

The proposed PINN architecture exclusively estimated SOH_C and investigated three different data sources: A synthetic cell dataset, an experimental cell dataset, and a vehicle fleet dataset. The issue of data scarcity was resolved by generating extensive synthetic training data from a P2D model. This synthetic dataset included internal states, such as concentrations and potentials, and was combined with experimental data sources before training a neural network. Results demonstrated that synthetic data can serve as a substitute and enhance accuracy. Furthermore, the inclusion of internal states, which showed a high correlation with capacity decay, improved performance as it guides the model to follow physical principles. Using random time-series segments, the PINN achieved SOH_C MAEs below 2.11 % (pp). However, the transfer to real-world fleet data was unsuccessful due to significant differences between the data sources. Consequently, while the proposed PINN could address data scarcity, it failed to tackle the problem of data dependence.

Another approach was designed to address both data scarcity and data dependence: Transfer learning. In the first study on transfer learning, the targets were SOH_C and OCV. A neural network was pre-trained with synthetic data generated from the mechanistic model. This network utilized partial charging segments and directly returned the full OCV. The default partial charging segment was extracted from an extensive field data analysis, comprising nearly 2 million BEV home-charging events, yielding a default SOC window from 30 % to 85 %. From the resulting full OCV, the SOH_C could be determined as the available capacity within the voltage boundaries. The network was later fine-tuned with decreasing amounts of experimental cell data. Its performance was compared to a conventional neural network trained exclusively with the same amount of experimental data. The transfer-learned neural network outperformed conventional deep learning in every use case and further advanced the state of the art by adapting the model to higher C-rates and smaller charging windows. For limited fine-tuning data down to 13 % of the full dataset, the SOH_C MAE remained below 2.0 % (pp), and the OCV reconstruction MAE was below 22 mV for the default charging window from 30 % to 85 %, independent of the C-rate, which varied from C/3.85 to 1C.

Within this study, the limitations were noisy, partly nonphysical, reconstructed OCVs and the absence of DM estimation. A novel combination of the proposed transfer-learned neural network with the OCV model addressed both issues by sequentially coupling them. Two methods were proposed: The first utilized the prior transfer-learned neural network to output the full OCV and fed this OCV into an optimization routine where electrode OCPs were fitted to reconstruct the full-cell OCV. The second approach modified the neural network architecture to directly estimate alignment parameters, enabling reconstruction of the OCV

via the mechanistic model and calculation of the DMs. Both approaches outperformed previous realizations and advanced the state of the art. The study revealed the underlying requirements for transfer learning: The source domain must be at least as large as the target domain, and the fine-tuning dataset must encompass the boundaries of the target domain. For the minimum fine-tuning dataset that met these requirements, both models achieved a MAE for OCV reconstruction, DM estimation, and SOH_C estimation below 10 mV, 3.1 % (pp), and 1.82 % (pp) for the default SOC window of 30 % to 85 %.

While previous studies revealed several methods for SOH_C, OCV, and DM estimation, they neglected dynamic effects, including impedance rise, which is gaining significant attention in BEV applications as the SOH_{UBE} is the metric to be monitored. Therefore, the final research question focused on creating a comprehensive database to address this shortcoming in future research. To this end, an extensive laboratory study was conducted, incorporating three-electrode lab cells aged over nine months, with some exceeding 600 EFCs. During RPTs, the pOCV, EIS, and HPPC were measured. This dataset enables the next generation of state estimation, as the measured electrode potentials allow adequate localization of effects and accurate partitioning of impedance rise – freely available for every researcher as the dataset is public. Consequently, not only SOH_C, SOH_R, and SOH_{UBE} estimation is possible, but also state-of-the-art fast charging algorithms can be implemented.

The outlook for future research highlights several key areas. Extending the SOH metric to include SOH_{UBE} is advised. For the OCV model, smarter boundary and initial value settings based on historical data could improve accuracy. In PINNs, adding more aging paths to synthetic datasets, combining different cell chemistries, and testing alternative architectures could enhance results. Transfer learning should address the model's inability to distinguish between impedance rise and LAM by including impedance rise in target variables. Investigating transfer between cell and high-voltage battery levels is promising. Research should also expand to other cell chemistries, such as LFP cathodes, cathodes with high nickel content, and silicon-containing anodes, to increase applicability. Silicon-containing anodes require blend electrode models due to the rapid degradation of silicon [28]. A similar approach could be adapted for cathodes with high nickel content, as this chemistry often results in unexpected behavior due to accelerated impedance rise [50]. This rise in impedance poses significant challenges for OCV measurements, as the magnitude of the increase can hinder the approximation of OCV using pOCV measurements at a C-rate of C/25. For LFP cathodes, hysteresis effects present the biggest challenge, necessitating accurate reconstruction of OCV in both charge and discharge directions. The publication of the three-electrode aging dataset provides a methodology to replicate the study across different cell chemistries and address the challenges mentioned. The dataset already opens promising avenues for developing advanced state estimation algorithms and understanding anode impedance rise, enabling accurate characterization of lithium plating risk during degradation.

While there remains significant work to be done, this thesis provides essential building blocks for the future of mobility, both electric and digital. Through the development of advanced

OCV models, innovative neural network architectures and the provision of novel databases for battery state estimation, this research extends the current state of the art and contributes to the transition of the mobility sector towards climate-friendly alternatives.

References

[1] IEA. *Global Electric Vehicle Outlook 2025*. Ed. by International Energy Agency. 2025. URL: https://www.iea.org/reports/global-ev-outlook-2025.

[2] ZSW. *Datenservice Erneuerbare Energien: Bestand an Elektro-Pkw weltweit*. Ed. by Zentrum für Sonnenenergie- und Wasserstoff-Forschung Baden-Württemberg. 2025. URL: https://www.zsw-bw.de/mediathek/datenservice.html.

[3] R. Peng, Tang, J. H. C. G., X. Yang, M. Meng, J. Zhang, and C. Zhuge. "Investigating the factors influencing the electric vehicle market share: A comparative study of the European Union and United States". In: *Applied Energy* 355 (2024), p. 122327. DOI: 10.1016/j.apenergy.2023.122327.

[4] X. Zhang, J. Xie, R. Rao, and Y. Liang. "Policy Incentives for the Adoption of Electric Vehicles across Countries". In: *Sustainability* 6.11 (2014), pp. 8056–8078. DOI: 10.3390/su6118056.

[5] Z. Ling, C. R. Cherry, and Y. Wen. "Determining the Factors That Influence Electric Vehicle Adoption: A Stated Preference Survey Study in Beijing, China". In: *Sustainability* 13.21 (2021). DOI: 10.3390/su132111719.

[6] G. Dai and S. Yang. "A comparative study of motivations driving EV purchases in different-tier Chinese cities". In: *Transportation Research Part D: Transport and Environment* 126 (2024), p. 103993. DOI: 10.1016/j.trd.2023.103993.

[7] United Nations Economic Commission for Europe. *United Nations Global Technical Regulation on In-vehicle Battery Durability for Electrified Vehicles: Addendum 22*. 2022. URL: https://unece.org/sites/default/files/2023-01/ECE_TRANS_180a22e.pdf.

[8] J. Dornoff and F. Rodriguez. "Euro 7: The new emission standard for light-and heavy-duty vehicles in the European Union". In: *International Council on Clean Transportation* (2024). URL: https://theicct.org/wp-content/uploads/2024/03/ID-116-%E2%80%93-Euro-7-standard_final.pdf.

[9] J. C. Hamar. "Data-driven battery state estimation". PhD Thesis. Technische Universität München, 2024. URL: https://mediatum.ub.tum.de/1742640.

[10] S. K. Sharma, G. Sharma, A. Gaur, A. Arya, F. S. Mirsafi, R. Abolhassani, H.-G. Rubahn, J.-S. Yu, and Y. K. Mishra. "Progress in electrode and electrolyte materials: path to all-solid-state Li-ion batteries". In: *Energy Advances* 1.8 (2022), pp. 457–510. DOI: 10.1039/D2YA00043A.

[11] M. H. Hossain, M. A. Chowdhury, N. Hossain, M. A. Islam, and M. H. Mobarak. "Advances of lithium-ion batteries anode materials–A review". In: *Chemical Engineering Journal Advances* 16 (2023), p. 100569. DOI: 10.1016/j.ceja.2023.100569.

[12] N. Nitta, F. Wu, J. T. Lee, and G. Yushin. "Li-ion battery materials: present and future". In: *Materials Today* 18.5 (2015), pp. 252–264. DOI: 10.1016/j.mattod.2014.10.040.

[13] T. B. Reddy, ed. *Linden's Handbook of Batteries, Fourth Edition*. Fourth Edition. New York: McGraw-Hill Education, 2011. URL: https://www.accessengineeringlibrary.com/content/book/9780071624213.

[14] R. Korthauer, ed. *Handbuch Lithium-Ionen-Batterien*. Berlin, Heidelberg: Springer Berlin Heidelberg, 2013. URL: https://link.springer.com/book/10.1007/978-3-642-30653-2.

[15] D. Guyomard and J.-M. Tarascon. "Rocking-chair or lithium-ion rechargeable lithium batteries". In: *Advanced Materials* 6.5 (1994), pp. 408–412. DOI: 10.1002/adma.19940060516.

[16] J. Newman and N. P. Balsara. *Electrochemical Systems*. Fourth Edition. ECS, the Electrochemical Society series. John Wiley & Sons, 2021. URL: https://www.wiley.com/en-us/Electrochemical+Systems%2C+4th+Edition-p-9781119514602.

[17] D. U. Sauer, G. Bopp, A. Jossen, J. Garche, M. Rothert, and M. Wollny. "State of Charge-What do we really speak about". In: *The 21st international telecommunications energy conference*. 1999, pp. 6–9. URL: https://publications.rwth-aachen.de/record/760844.

[18] I.-Y. Jang. *SPECIFICATION OF PRODUCT: Lithium-ion rechargeable cell for power tools. Model name: INR18650-25R*. 2014. URL: https://www.dnkpower.com/wp-content/uploads/2018/04/Samsung-INR18650-25R-Datasheet.pdf.

[19] K. S. Oh. *PRODUCT SPECIFICATION: Rechargeable Lithium Ion Battery. Model: INR18650 MJ1 3500mAh*. 2014. URL: https://enerpower.de/wp/wp-content/uploads/2016/03/Specification_INR18650MJ1.pdf.

[20] H. Xiao, J. Zhao, Q. Gao, W. Zhang, X. Cheng, C. Song, and G. Li. "Recent advances in fast-charging lithium-ion batteries: Mechanism, materials, and future opportunities". In: *Chemical Engineering Journal* 506 (2025), p. 159927. DOI: 10.1016/j.cej.2025.159927.

[21] A. Farmann and D. U. Sauer. "A study on the dependency of the open-circuit voltage on temperature and actual aging state of lithium-ion batteries". In: *Journal of Power Sources* 347 (2017), pp. 1–13. DOI: 10.1016/j.jpowsour.2017.01.098.

[22] P. Keil. "Aging of Lithium-Ion Batteries in Electric Vehicles". PhD Thesis. Munich: Technical University Munich, 2017. URL: https://mediatum.ub.tum.de/1355829.

[23] C. R. Birkl, E. McTurk, M. R. Roberts, P. G. Bruce, and D. A. Howey. "A Parametric Open Circuit Voltage Model for Lithium Ion Batteries". In: *Journal of The Electrochemical Society* 162.12 (2015), A2271. DOI: 10.1149/2.0331512jes.

[24] F. Zheng, Y. Xing, J. Jiang, B. Sun, J. Kim, and M. Pecht. "Influence of different open circuit voltage tests on state of charge online estimation for lithium-ion batteries". In: *Applied Energy* 183 (2016), pp. 513–525. DOI: 10.1016/j.apenergy.2016.09.010.

[25] J. P. Schmidt, H. Y. Tran, J. Richter, E. Ivers-Tiffée, and M. Wohlfahrt-Mehrens. "Analysis and prediction of the open circuit potential of lithium-ion cells". In: *Journal of Power Sources* 239 (2013), pp. 696–704. DOI: 10.1016/j.jpowsour.2012.11.101.

[26] C. Kirst, A. Karger, J. P. Singer, and A. Jossen. "Non-destructive electrode potential and open-circuit voltage aging estimation for lithium-ion batteries". In: *Journal of Power Sources* 602 (2024), p. 234341. DOI: 10.1016/j.jpowsour.2024.234341.

[27] J. Schmitt, M. Rehm, A. Karger, and A. Jossen. "Capacity and degradation mode estimation for lithium-ion batteries based on partial charging curves at different current rates". In: *Journal of Energy Storage* 59 (2023), p. 106517. DOI: 10.1016/j.est.2022.106517.

[28] J. Schmitt, M. Schindler, and A. Jossen. "Change in the half-cell open-circuit potential curves of silicon-graphite and nickel-rich lithium nickel manganese cobalt oxide during cycle aging". In: *Journal of Power Sources* 506 (2021), p. 230240. DOI: 10.1016/j.jpowsour.2021.230240.

[29] D. P. Abraham, S. D. Poppen, A. N. Jansen, J. Liu, and D. W. Dees. "Application of a lithium-tin reference electrode to determine electrode contributions to impedance rise in high-power lithium-ion cells". In: *Electrochimica Acta* 49.26 (2004), pp. 4763–4775. DOI: 10.1016/j.electacta.2004.05.040.

[30] M. Klett, J. A. Gilbert, S. E. Trask, B. J. Polzin, A. N. Jansen, D. W. Dees, and D. P. Abraham. "Electrode Behavior RE-Visited: Monitoring Potential Windows, Capacity Loss, and Impedance Changes in Li1.03(Ni0.5Co0.2Mn0.3)0.97O2/Silicon-Graphite Full Cells". In: *Journal of The Electrochemical Society* 163.6 (2016), A875. DOI: 10.1149/2.0271606jes.

[31] B. Epding, A. Broda, B. Rumberg, H. Jahnke, and A. Kwade. "Development of Durable 3-Electrode Lithium-Ion Pouch Cells with LTO Reference Mesh: Aging and Performance Studies". In: *Journal of The Electrochemical Society* 166.8 (2019), A1550. DOI: 10.1149/2.0851908jes.

[32] M. Dubarry, C. Truchot, and B. Y. Liaw. "Synthesize battery degradation modes via a diagnostic and prognostic model". In: *Journal of Power Sources* 219 (2012), pp. 204–216. DOI: 10.1016/j.jpowsour.2012.07.016.

[33] J. Tao, S. Wang, W. Cao, P. Takyi-Aninakwa, C. Fernandez, and J. M. Guerrero. "A comprehensive review of state-of-charge and state-of-health estimation for lithium-ion battery energy storage systems". In: *Ionics* 30.10 (2024), pp. 5903–5927. DOI: 10.1007/s11581-024-05686-z.

[34] K. L. Quade, D. Jöst, D. U. Sauer, and W. Li. "Understanding the Energy Potential of Lithium-Ion Batteries: Definition and Estimation of the State of Energy". In: *Batteries & Supercaps* 6.8 (2023), e202300152. DOI: 10.1002/batt.202300152.

[35] D. Aurbach, M. D. Levi, E. Levi, H. Teller, B. Markovsky, G. Salitra, U. Heider, and L. Heider. "Common Electroanalytical Behavior of Li Intercalation Processes into Graphite and Transition Metal Oxides". In: *Journal of The Electrochemical Society* 145.9 (1998), p. 3024. DOI: 10.1149/1.1838758.

[36] A. Nyman, T. G. Zavalis, R. Elger, M. Behm, and G. Lindbergh. "Analysis of the Polarization in a Li-Ion Battery Cell by Numerical Simulations". In: *Journal of The Electrochemical Society* 157.11 (2010), A1236. DOI: 10.1149/1.3486161.

[37] T. R. Jow, M. B. Marx, and J. L. Allen. "Distinguishing Li+ Charge Transfer Kinetics at NCA/Electrolyte and Graphite/Electrolyte Interfaces, and NCA/Electrolyte and LFP/Electrolyte Interfaces in Li-Ion Cells". In: *Journal of The Electrochemical Society* 159.5 (2012), A604. DOI: 10.1149/2.079205jes.

[38] J. Kasnatscheew, U. Rodehorst, B. Streipert, S. Wiemers-Meyer, R. Jakelski, R. Wagner, I. C. Laskovic, and M. Winter. "Learning from Overpotentials in Lithium Ion Batteries: A Case Study on the LiNi1/3Co1/3Mn1/3O2 (NCM) Cathode". In: *Journal of The Electrochemical Society* 163.14 (2016), A2943. DOI: 10.1149/2.0461614jes.

[39] J. Schmalstieg. "Physikalisch-elektrochemische Simulation von Lithium-Ionen-Batterien: Implementierung, Parametrierung und Anwendung". Dissertation. Aachen: RWTH Aachen University, 2017. DOI: 10.18154/RWTH-2017-04693.

[40] W. Waag, S. Käbitz, and D. U. Sauer. "Experimental investigation of the lithium-ion battery impedance characteristic at various conditions and aging states and its influence on the application". In: *Applied Energy* 102 (2013), pp. 885–897. DOI: 10.1016/j.apenergy.2012.09.030.

[41] A. Barai, K. Uddin, W. D. Widanage, A. McGordon, and P. Jennings. "A study of the influence of measurement timescale on internal resistance characterisation methodologies for lithium-ion cells". In: *Scientific Reports* 8.1 (2018), p. 21. DOI: 10.1038/s41598-017-18424-5.

[42] C. H. Hamann and W. Vielstich. *Elektrochemie 4: vollständig überarbeitete und aktualisierte Auflage*. Weinheim: Wiley-VCH, 2005. URL: https://www.wiley-vch.de/de?option=com_eshop&view=product&isbn=9783527310685.

[43] C. R. Birkl, M. R. Roberts, E. McTurk, P. G. Bruce, and D. A. Howey. "Degradation diagnostics for lithium ion cells". In: *Journal of Power Sources* 341 (2017), pp. 373–386. DOI: 10.1016/j.jpowsour.2016.12.011.

[44] J. Vetter et al. "Ageing mechanisms in lithium-ion batteries". In: *Journal of Power Sources* 147.1 (2005), pp. 269–281. DOI: 10.1016/j.jpowsour.2005.01.006.

[45] W. Sarwar. "Hybridised energy storage systems for automotive powertrain applications". PhD Thesis. London: Imperial College London, 2017. DOI: 10.25560/44975.

[46] S. Schindler, G. Baure, M. A. Danzer, and M. Dubarry. "Kinetics accommodation in Li-ion mechanistic modeling". In: *Journal of Power Sources* 440 (2019), p. 227117. DOI: 10.1016/j.jpowsour.2019.227117.

[47] S. Lee, L. Su, A. Mesnier, Z. Cui, and A. Manthiram. "Cracking vs. surface reactivity in high-nickel cathodes for lithium-ion batteries". In: *Joule* 7.11 (2023), pp. 2430–2444. DOI: 10.1016/j.joule.2023.09.006.

[48] L. Su, K. Jarvis, H. Charalambous, A. Dolocan, and A. Manthiram. "Stabilizing High-Nickel Cathodes with High-Voltage Electrolytes". In: *Advanced Functional Materials* 33.12 (2023), p. 2213675. DOI: 10.1002/adfm.202213675.

[49] Q. Gan, N. Qin, H. Yuan, L. Lu, Z. Xu, and Z. Lu. "Critical review on the degradation mechanisms and recent progress of Ni-rich layered oxide cathodes for lithium-ion batteries". In: *EnergyChem* 5.5 (2023), p. 100103. DOI: 10.1016/j.enchem.2023.100103.

[50] R. Jung, M. Metzger, F. Maglia, C. Stinner, and H. A. Gasteiger. "Oxygen Release and Its Effect on the Cycling Stability of LiNixMnyCozO2 (NMC) Cathode Materials for Li-Ion Batteries". In: *Journal of The Electrochemical Society* 164.7 (2017), A1361. DOI: 10.1149/2.0021707jes.

[51] T. Hofmann, J. Hamar, B. Mager, S. Erhard, and J. P. Schmidt. "Physics-constrained transfer learning: Open-circuit voltage curve reconstruction and degradation mode estimation of lithium-ion batteries". In: *Energy and AI* 20 (2025), p. 100493. DOI: 10.1016/j.egyai.2025.100493.

[52] C. Mao, S. J. An, H. M. Meyer, J. Li, M. Wood, R. E. Ruther, and D. L. Wood. "Balancing formation time and electrochemical performance of high energy lithium-ion batteries". In: *Journal of Power Sources* 402 (2018), pp. 107–115. DOI: 10.1016/j.jpowsour.2018.09.019.

[53] X. Jia, C. Zhang, Y. Le Wang, L. Zhang, and W. Zhang. "The Degradation Characteristics and Mechanism of Li[Ni0.5Co0.2Mn0.3]O2 Batteries at Different Temperatures and Discharge Current Rates". In: *Journal of The Electrochemical Society* 167.2 (2020), p. 020503. DOI: 10.1149/1945-7111/ab61e9.

[54] D. Lu, S. M. Trimboli, G. Fan, R. Zhang, and G. L. Plett. "Implementation of a Physics-Based Model for Half-Cell Open-Circuit Potential and Full-Cell Open-Circuit Voltage Estimates: Part I. Processing Half-Cell Data". In: *Journal of The Electrochemical Society* 168.7 (2021), p. 070532. DOI: 10.1149/1945-7111/ac11a4.

[55] S. Yang, C. Zhang, J. Jiang, W. Zhang, Y. Gao, and L. Zhang. "A voltage reconstruction model based on partial charging curve for state-of-health estimation of lithium-ion batteries". In: *Journal of Energy Storage* 35 (2021), p. 102271. DOI: 10.1016/j.est.2021.102271.

[56] J. Guo, Y. Li, J. Meng, K. Pedersen, L. Gurevich, and D.-I. Stroe. "Understanding the mechanism of capacity increase during early cycling of commercial NMC/graphite lithium-ion batteries". In: *Journal of Energy Chemistry* 74 (2022), pp. 34–44. DOI: 10.1016/j.jechem.2022.07.005.

[57] S. Friedrich, J. Mährlein, A. Durdel, and A. Jossen. "Experimental Investigation of Fast Charging Protocols Over Aging Using Multilayer Pouch Cells with Silicon-Dominant Anodes". In: *Journal of The Electrochemical Society* 172.7 (2025), p. 070518. DOI: 10.1149/1945-7111/ade1ff.

[58] J. Schmitt. "State of health estimation for lithium-ion batteries". PhD Thesis. Technische Universität München, 2023. URL: https://mediatum.ub.tum.de/1694234.

[59] A. Karger. "Modeling the degradation of lithium-ion batteries during calendar and cycle aging". PhD Thesis. Technische Universität München, 2025. URL: https://mediatum.ub.tum.de/1750777.

[60] J. Schmalstieg, S. Käbitz, M. Ecker, and D. U. Sauer. "A holistic aging model for Li(NiMnCo)O2 based 18650 lithium-ion batteries". In: *Journal of Power Sources* 257 (2014), pp. 325–334. DOI: 10.1016/j.jpowsour.2014.02.012.

[61] J. Tian, R. Xiong, W. Shen, J. Lu, and X.-G. Yang. "Deep neural network battery charging curve prediction using 30 points collected in 10 min". In: *Joule* 5.6 (2021), pp. 1521–1534. DOI: 10.1016/j.joule.2021.05.012.

[62] N. Costa, L. Sánchez, D. Anseán, and M. Dubarry. "Li-ion battery degradation modes diagnosis via Convolutional Neural Networks". In: *Journal of Energy Storage* 55 (2022), p. 105558. DOI: 10.1016/j.est.2022.105558.

[63] J. Stadler, J. Fath, M. Ecker, and A. Latz. "Combining a Data Driven and Mechanistic Model to Predict Capacity and Potential Curve-Degradation". In: *Batteries & Supercaps* 7.10 (2024), e202400211. DOI: 10.1002/batt.202400211.

[64] H. Ruan, J. Chen, W. Ai, and B. Wu. "Generalised diagnostic framework for rapid battery degradation quantification with deep learning". In: *Energy and AI* 9 (2022), p. 100158. DOI: 10.1016/j.egyai.2022.100158.

[65] J. Tian, R. Xiong, W. Shen, and F. Sun. "Electrode ageing estimation and open circuit voltage reconstruction for lithium ion batteries". In: *Energy Storage Materials* 37 (2021), pp. 283–295. DOI: 10.1016/j.ensm.2021.02.018.

[66] R. Guo, Y. Xu, C. Hu, and W. Shen. "A Curve Relocation Approach for Robust Battery Open Circuit Voltage Reconstruction and Capacity Estimation Based on Partial Charging Data". In: *IEEE Transactions on Power Electronics* 39.3 (2024), pp. 3760–3773. DOI: 10.1109/TPEL.2023.3347236.

[67] K. Uddin, S. Perera, W. D. Widanage, L. Somerville, and J. Marco. "Characterising Lithium-Ion Battery Degradation through the Identification and Tracking of Electrochemical Battery Model Parameters". In: *Batteries* 2.2 (2016). DOI: 10.3390/batteries2020013.

[68] E. Miguel, G. L. Plett, M. S. Trimboli, L. Oca, U. Iraola, and E. Bekaert. "Review of computational parameter estimation methods for electrochemical models". In: *Journal of Energy Storage* 44 (2021), p. 103388. DOI: 10.1016/j.est.2021.103388.

[69] V. Laue, F. Röder, and U. Krewer. "Practical identifiability of electrochemical P2D models for lithium-ion batteries". In: *Journal of Applied Electrochemistry* 51.9 (2021), pp. 1253–1265. DOI: 10.1007/s10800-021-01579-5.

[70] J. Wang, P. Liu, J. Hicks-Garner, E. Sherman, S. Soukiazian, M. Verbrugge, H. Tataria, J. Musser, and P. Finamore. "Cycle-life model for graphite-LiFePO4 cells". In: *Journal of Power Sources* 196.8 (2011), pp. 3942–3948. DOI: 10.1016/j.jpowsour.2010.11.134.

[71] M. Ecker, J. B. Gerschler, J. Vogel, S. Käbitz, F. Hust, P. Dechent, and D. U. Sauer. "Development of a lifetime prediction model for lithium-ion batteries based on extended accelerated aging test data". In: *Journal of Power Sources* 215 (2012), pp. 248–257. DOI: 10.1016/j.jpowsour.2012.05.012.

[72] M. Petit, E. Prada, and V. Sauvant-Moynot. "Development of an empirical aging model for Li-ion batteries and application to assess the impact of Vehicle-to-Grid strategies on battery lifetime". In: *Applied Energy* 172 (2016), pp. 398–407. DOI: 10.1016/j.apenergy.2016.03.119.

[73] J. de Hoog, J.-M. Timmermans, D. Ioan-Stroe, M. Swierczynski, J. Jaguemont, S. Goutam, N. Omar, J. van Mierlo, and P. van den Bossche. "Combined cycling and calendar capacity fade modeling of a Nickel-Manganese-Cobalt Oxide Cell with real-life profile validation". In: *Applied Energy* 200 (2017), pp. 47–61. DOI: 10.1016/j.apenergy.2017.05.018.

[74] M. Naumann, M. Schimpe, P. Keil, H. C. Hesse, and A. Jossen. "Analysis and modeling of calendar aging of a commercial LiFePO4/graphite cell". In: *Journal of Energy Storage* 17 (2018), pp. 153–169. DOI: 10.1016/j.est.2018.01.019.

[75] M. Naumann, F. B. Spingler, and A. Jossen. "Analysis and modeling of cycle aging of a commercial LiFePO4/graphite cell". In: *Journal of Power Sources* 451 (2020), p. 227666. DOI: 10.1016/j.jpowsour.2019.227666.

[76] A. Karger, L. Wildfeuer, D. Aygül, A. Maheshwari, J. P. Singer, and A. Jossen. "Modeling capacity fade of lithium-ion batteries during dynamic cycling considering path dependence". In: *Journal of Energy Storage* 52 (2022), p. 104718. DOI: 10.1016/j.est.2022.104718.

[77] L. Wildfeuer, A. Karger, D. Aygül, N. Wassiliadis, A. Jossen, and M. Lienkamp. "Experimental degradation study of a commercial lithium-ion battery". In: *Journal of Power Sources* 560 (2023), p. 232498. DOI: 10.1016/j.jpowsour.2022.232498.

[78] F. Röder and S. Ramasubramanian. "A Review and Perspective on Path Dependency in Batteries". In: *Energy Technology* 10.11 (2022), p. 2200627. DOI: 10.1002/ente.202200627.

[79] A. Jokar, B. Rajabloo, M. Désilets, and M. Lacroix. "Review of simplified Pseudo-two-Dimensional models of lithium-ion batteries". In: *Journal of Power Sources* 327 (2016), pp. 44–55. DOI: 10.1016/j.jpowsour.2016.07.036.

[80] S. Dey, B. Ayalew, and P. Pisu. "Combined estimation of State-of-Charge and State-of-Health of Li-ion battery cells using SMO on electrochemical model". In: *2014 13th International Workshop on Variable Structure Systems (VSS)*. 2014, pp. 1–6. DOI: 10.1109/VSS.2014.6881140.

[81] M. Guo, G. Sikha, and R. E. White. "Single-Particle Model for a Lithium-Ion Cell: Thermal Behavior". In: *Journal of The Electrochemical Society* 158.2 (2011), A122. DOI: 10.1149/1.3521314.

[82] J. Li, K. Adewuyi, N. Lotfi, R. G. Landers, and J. Park. "A single particle model with chemical/mechanical degradation physics for lithium ion battery State of Health (SOH) estimation". In: *Applied Energy* 212 (2018), pp. 1178–1190. DOI: 10.1016/j.apenergy.2018.01.011.

[83] J. Li, R. G. Landers, and J. Park. "A comprehensive single-particle-degradation model for battery state-of-health prediction". In: *Journal of Power Sources* 456 (2020), p. 227950. DOI: 10.1016/j.jpowsour.2020.227950.

[84] M. Petit, E. Calas, and J. Bernard. "A simplified electrochemical model for modelling Li-ion batteries comprising blend and bidispersed electrodes for high power applications". In: *Journal of Power Sources* 479 (2020), p. 228766. DOI: 10.1016/j.jpowsour.2020.228766.

[85] M. Dubarry, A. Devie, and B. Y. Liaw. "The value of battery diagnostics and prognostics". In: *J. Energy Power Sources* 1.5 (2014), pp. 242–249. URL: https://api.semanticscholar.org/CorpusID:207914689.

[86] M. Dubarry, M. Berecibar, A. Devie, D. Anseán, N. Omar, and I. Villarreal. "State of health battery estimator enabling degradation diagnosis: Model and algorithm description". In: *Journal of Power Sources* 360 (2017), pp. 59–69. DOI: 10.1016/j.jpowsour.2017.05.121.

[87] J. P. Fath, D. Dragicevic, L. Bittel, A. Nuhic, J. Sieg, S. Hahn, L. Alsheimer, B. Spier, and T. Wetzel. "Quantification of aging mechanisms and inhomogeneity in cycled lithium-ion cells by differential voltage analysis". In: *Journal of Energy Storage* 25 (2019), p. 100813. DOI: 10.1016/j.est.2019.100813.

[88] D. Anseán, G. Baure, M. González, I. Cameán, A. B. García, and M. Dubarry. "Mechanistic investigation of silicon-graphite/LiNi0.8Mn0.1Co0.1O2 commercial cells for non-intrusive diagnosis and prognosis". In: *Journal of Power Sources* 459 (2020), p. 227882. DOI: 10.1016/j.jpowsour.2020.227882.

[89] M. Dubarry and D. Beck. "Perspective on Mechanistic Modeling of Li-Ion Batteries". In: *Accounts of Materials Research* 3.8 (2022), pp. 843–853. DOI: 10.1021/accountsmr.2c00082.

[90] M. Dubarry, V. Agrawal, M. Hüske, and M. Kuipers. "Accurate LLI and LAMPE Estimation Using the Mechanistic Modeling Approach with Layered Oxides". In: *Journal of The Electrochemical Society* 170.7 (2023), p. 070503. DOI: 10.1149/1945-7111/ace21c.

[91] J. Chen, M. N. Marlow, Q. Jiang, and B. Wu. "Peak-tracking method to quantify degradation modes in lithium-ion batteries via differential voltage and incremental capacity". In: *Journal of Energy Storage* 45 (2022), p. 103669. DOI: 10.1016/j.est.2021.103669.

[92] Z. Cui, N. Cui, C. Li, J. Lu, and C. Zhang. "Online Identification and Reconstruction of Open-Circuit Voltage for Capacity and Electrode Aging Estimation of Lithium-Ion Batteries". In: *IEEE Transactions on Industrial Electronics* 70.5 (2023), pp. 4716–4726. DOI: 10.1109/TIE.2022.3187596.

[93] I. Bin-Mat-Arishad, B. Wimarshana, and A. Fly. "Influence of voltage profile and fitting technique on the accuracy of lithium-ion battery degradation identification through the Voltage Profile Model". In: *Journal of Energy Storage* 70 (2023), p. 107884. DOI: 10.1016/j.est.2023.107884.

[94] S. Lee, J. B. Siegel, A. G. Stefanopoulou, J.-W. Lee, and T.-K. Lee. "Electrode State of Health Estimation for Lithium Ion Batteries Considering Half-cell Potential Change Due to Aging". In: *Journal of The Electrochemical Society* 167.9 (2020), p. 090531. DOI: 10.1149/1945-7111/ab8c83.

[95] Z. Ma, Z. Wang, R. Xiong, and J. Jiang. "A mechanism identification model based state-of-health diagnosis of lithium-ion batteries for energy storage applications". In: *Journal of Cleaner Production* 193 (2018), pp. 379–390. DOI: 10.1016/j.jclepro.2018.05.074.

[96] K. Mergo Mbeya, N. Damay, G. Friedrich, C. Forgez, and M. Juston. "Off-line method to determine the electrode balancing of Li-ion batteries". In: *Mathematics and Computers in Simulation* 183 (2021), pp. 34–47. DOI: 10.1016/j.matcom.2020.02.013.

[97] B. Pan, D. Dong, J. Wang, J. Nie, S. Liu, Y. Cao, and Y. Jiang. "Aging mechanism diagnosis of lithium ion battery by open circuit voltage analysis". In: *Electrochimica Acta* 362 (2020), p. 137101. DOI: 10.1016/j.electacta.2020.137101.

[98] C. Pastor-Fernández, T. F. Yu, W. D. Widanage, and J. Marco. "Critical review of non-invasive diagnosis techniques for quantification of degradation modes in lithium-ion batteries". In: *Renewable and Sustainable Energy Reviews* 109 (2019), pp. 138–159. DOI: 10.1016/j.rser.2019.03.060.

[99] S. Fernandez, I. Lopetegi, L. Oca, J. Yeregui, E. Garayalde, and U. Iraola. "Intuitive Degradation Mode Estimation Tool: ModEst". In: *2024 Energy Conversion Congress & Expo Europe (ECCE Europe)*. 2024, pp. 1–7. DOI: 10.1109/ECCEEurope62508.2024.10751868.

[100] T. Hofmann, J. Li, J. Hamar, S. Erhard, and J. P. Schmidt. "The ΔQ-method: State of health and degradation mode estimation for lithium-ion batteries using a mechanistic model with relaxed voltage points". In: *Journal of Power Sources* 596 (2024), p. 234107. DOI: 10.1016/j.jpowsour.2024.234107.

[101] A. Jaboob, O. Durrah, and A. Chakir. "Artificial Intelligence: An Overview". In: *Engineering Applications of Artificial Intelligence*. Ed. by A. Chakir, J. F. Andry, A. Ullah, R. Bansal, and M. Ghazouani. Cham: Springer Nature Switzerland, 2024, pp. 3–22. DOI: 10.1007/978-3-031-50300-9_1.

[102] J. C. Hamar, S. V. Erhard, A. Canesso, J. Kohlschmidt, N. Olivain, and A. Jossen. "State-of-health estimation using a neural network trained on vehicle data". In: *Journal of Power Sources* 512 (2021), p. 230493. DOI: 10.1016/j.jpowsour.2021.230493.

[103] H. Mawassi, G. Hermann, D. O. Abdeslam, and L. Idoumghar. "Enhanced co-estimation of state of health and state of charge in lithium-ion batteries using discharge voltage and an optimized feed-forward neural network". In: *Journal of Energy Storage* 109 (2025), p. 115034. DOI: 10.1016/j.est.2024.115034.

[104] M. Sedlařík, P. Vyroubal, D. Capková, E. Omerdic, M. Rae, M. Mačák, M. Šedina, and T. Kazda. "Advanced machine learning techniques for State-of-Health estimation in lithium-ion batteries: A comparative study". In: *Electrochimica Acta* 524 (2025), p. 145988. DOI: 10.1016/j.electacta.2025.145988.

[105] C. Qian, B. Xu, L. Chang, B. Sun, Q. Feng, D. Yang, Y. Ren, and Z. Wang. "Convolutional neural network based capacity estimation using random segments of the charging curves for lithium-ion batteries". In: *Energy* 227 (2021), p. 120333. DOI: 10.1016/j.energy.2021.120333.

[106] E. Chemali, P. J. Kollmeyer, M. Preindl, Y. Fahmy, and A. Emadi. "A Convolutional Neural Network Approach for Estimation of Li-Ion Battery State of Health from Charge Profiles". In: *Energies* 15.3 (2022). DOI: 10.3390/en15031185.

[107] J. Chen, M. Manivanan, J. Duque, P. Kollmeyer, S. Panchal, O. Gross, and A. Emadi. "A Convolutional Neural Network for Estimation of Lithium-Ion Battery State-of-Health during Constant Current Operation". In: *2023 IEEE Transportation Electrification Conference & Expo (ITEC)*. 2023, pp. 1–6. DOI: 10.1109/ITEC55900.2023.10186914.

[108] Z. Lu, Z. Fei, B. Wang, and F. Yang. "A feature fusion-based convolutional neural network for battery state-of-health estimation with mining of partial voltage curve". In: *Energy* 288 (2024), p. 129690. DOI: 10.1016/j.energy.2023.129690.

[109] M. Raman, V. Champa, and V. Prema. "State of Health Estimation of Lithium Ion Batteries using Recurrent Neural Network and its Variants". In: *2021 IEEE International Conference on Electronics, Computing and Communication Technologies (CONECCT)*. 2021, pp. 1–6. DOI: 10.1109/CONECCT52877.2021.9622557.

[110] R. S. D. Teixeira, R. F. Calili, M. F. Almeida, and D. R. Louzada. "Recurrent Neural Networks for Estimating the State of Health of Lithium-Ion Batteries". In: *Batteries* 10.3 (2024). DOI: 10.3390/batteries10030111.

[111] Y. Wu, Q. Xue, J. Shen, Z. Lei, Z. Chen, and Y. Liu. "State of Health Estimation for Lithium-Ion Batteries Based on Healthy Features and Long Short-Term Memory". In: *IEEE Access* 8 (2020), pp. 28533–28547. DOI: 10.1109/ACCESS.2020.2972344.

[112] W. Li, N. Sengupta, P. Dechent, D. Howey, A. Annaswamy, and D. U. Sauer. "Online capacity estimation of lithium-ion batteries with deep long short-term memory networks". In: *Journal of Power Sources* 482 (2021), p. 228863. DOI: 10.1016/j.jpowsour.2020.228863.

[113] Y. Gong, X. Zhang, D. Gao, H. Li, L. Yan, J. Peng, and Z. Huang. "State-of-health estimation of lithium-ion batteries based on improved long short-term memory algorithm". In: *Journal of Energy Storage* 53 (2022), p. 105046. DOI: 10.1016/j.est.2022.105046.

[114] S. Peng, Y. Sun, D. Liu, Q. Yu, J. Kan, and M. Pecht. "State of health estimation of lithium-ion batteries based on multi-health features extraction and improved long short-term memory neural network". In: *Energy* 282 (2023), p. 128956. DOI: 10.1016/j.energy.2023.128956.

[115] Z. Zhang, H. Min, H. Guo, Y. Yu, W. Sun, J. Jiang, and H. Zhao. "State of health estimation method for lithium-ion batteries using incremental capacity and long short-term memory network". In: *Journal of Energy Storage* 64 (2023), p. 107063. DOI: 10.1016/j.est.2023.107063.

[116] C. Lea, M. D. Flynn, R. Vidal, A. Reiter, and G. D. Hager. "Temporal Convolutional Networks for Action Segmentation and Detection". In: *IEEE Conference on Computer Vision and Pattern Recognition (CVPR)* (2017), pp. 1003–1012. DOI: 10.1109/CVPR.2017.113.

[117] D. Zhou, Z. Li, J. Zhu, H. Zhang, and L. Hou. "State of Health Monitoring and Remaining Useful Life Prediction of Lithium-Ion Batteries Based on Temporal Convolutional Network". In: *IEEE Access* 8 (2020), pp. 53307–53320. DOI: 10.1109/ACCESS.2020.2981261.

[118] D. Zhou and B. Wang. "Battery health prognosis using improved temporal convolutional network modeling". In: *Journal of Energy Storage* 51 (2022), p. 104480. DOI: 10.1016/j.est.2022.104480.

[119] C. Li, X. Han, Q. Zhang, M. Li, Z. Rao, W. Liao, X. Liu, X. Liu, and G. Li. "State-of-health and remaining-useful-life estimations of lithium-ion battery based on temporal convolutional network-long short-term memory". In: *Journal of Energy Storage* 74 (2023), p. 109498. DOI: 10.1016/j.est.2023.109498.

[120] S. Bockrath, V. Lorentz, and M. Pruckner. "State of health estimation of lithium-ion batteries with a temporal convolutional neural network using partial load profiles". In: *Applied Energy* 329 (2023), p. 120307. DOI: 10.1016/j.apenergy.2022.120307.

[121] S. Liu, Z. Chen, L. Yuan, Z. Xu, L. Jin, and C. Zhang. "State of health estimation of lithium-ion batteries based on multi-feature extraction and temporal convolutional network". In: *Journal of Energy Storage* 75 (2024), p. 109658. DOI: 10.1016/j.est.2023.109658.

[122] I. Goodfellow, Y. Bengio, and A. Courville. *Deep Learning*. MIT Press, 2016. URL: https://www.deeplearningbook.org/.

[123] J. Chen, X. Han, T. Sun, and Y. Zheng. "Analysis and prediction of battery aging modes based on transfer learning". In: *Applied Energy* 356 (2024), p. 122330. DOI: 10.1016/j.apenergy.2023.122330.

[124] X. Chen, T. Sun, X. Lai, Y. Zheng, and X. Han. "Transfer learning strategies for lithium-ion battery capacity estimation under domain shift differences". In: *Journal of Energy Storage* 90 (2024), p. 111860. DOI: 10.1016/j.est.2024.111860.

[125] S. Fu et al. "Data-driven capacity estimation for lithium-ion batteries with feature matching based transfer learning method". In: *Applied Energy* 353 (2024), p. 121991. DOI: 10.1016/j.apenergy.2023.121991.

[126] T. Hofmann, J. Hamar, B. Mager, S. Erhard, and J. P. Schmidt. "Transfer learning from synthetic data for open-circuit voltage curve reconstruction and state of health estimation of lithium-ion batteries from partial charging segments". In: *Energy and AI* 17 (2024), p. 100382. DOI: 10.1016/j.egyai.2024.100382.

[127] K. Huang, K. Yao, Y. Guo, and Z. Lv. "State of health estimation of lithium-ion batteries based on fine-tuning or rebuilding transfer learning strategies combined with new features mining". In: *Energy* 282 (2023), p. 128739. DOI: 10.1016/j.energy.2023.128739.

[128] S. Sahoo, K. S. Hariharan, S. Agarwal, S. B. Swernath, R. Bharti, S. Han, and S. Lee. "Transfer learning based generalized framework for state of health estimation of Li-ion cells". In: *Scientific Reports* 12.1 (2022), p. 13173. DOI: 10.1038/s41598-022-16692-4.

[129] S. Shen, M. Sadoughi, M. Li, Z. Wang, and C. Hu. "Deep convolutional neural networks with ensemble learning and transfer learning for capacity estimation of lithium-ion batteries". In: *Applied Energy* 260 (2020), p. 114296. DOI: 10.1016/j.apenergy.2019.114296.

[130] Y. Sun, H. Tian, F. Hu, and J. Du. "Method for Evaluating Degradation of Battery Capacity Based on Partial Charging Segments for Multi-Type Batteries". In: *Batteries* 10.6 (2024). DOI: 10.3390/batteries10060187.

[131] J. Tian, L. Ma, T. Zhang, T. Han, W. Mai, and C. Y. Chung. "Exploiting domain knowledge to reduce data requirements for battery health monitoring". In: *Energy Storage Materials* 67 (2024), p. 103270. DOI: 10.1016/j.ensm.2024.103270.

[132] J. Yao and T. Han. "Data-driven lithium-ion batteries capacity estimation based on deep transfer learning using partial segment of charging/discharging data". In: *Energy* 271 (2023), p. 127033. DOI: 10.1016/j.energy.2023.127033.

[133] Z. Zhou, Y. Liu, C. Zhang, W. Shen, and R. Xiong. "Deep neural network-enabled battery open-circuit voltage estimation based on partial charging data". In: *Journal of Energy Chemistry* 90 (2024), pp. 120–132. DOI: 10.1016/j.jechem.2023.11.009.

[134] G. Zou, Z. Yan, C. Zhang, and L. Song. "Transfer learning with CNN-LSTM model for capacity prediction of lithium-ion batteries under small sample". In: *Journal of Physics: Conference Series* 2258.1 (2022), p. 012042. DOI: 10.1088/1742-6596/2258/1/012042.

[135] A. Tian, L. He, T. Ding, K. Dong, Y. Wang, and J. Jiang. "A generic physics-informed neural network framework for lithium-ion batteries state of health estimation". In: *Energy* 332 (2025), p. 137215. DOI: 10.1016/j.energy.2025.137215.

[136] J. Kim, D. Han, P.-Y. Lee, and J. Kim. "Transfer learning applying electrochemical degradation indicator combined with long short-term memory network for flexible battery state-of-health estimation". In: *eTransportation* 18 (2023), p. 100293. DOI: 10.1016/j.etran.2023.100293.

[137] X. Lu, J. Qiu, G. Lei, and J. Zhu. "Degradation Mode Knowledge Transfer Method for LFP Batteries". In: *IEEE Transactions on Transportation Electrification* 9.1 (2023), pp. 1142–1152. DOI: 10.1109/TTE.2022.3196087.

[138] M. Lin, Y. You, J. Meng, W. Wang, J. Wu, and D.-I. Stroe. "Lithium-ion battery degradation trajectory early prediction with synthetic dataset and deep learning". In: *Journal of Energy Chemistry* 85 (2023), pp. 534–546. DOI: 10.1016/j.jechem.2023.06.036.

[139] Y. Wang, J. Zhu, L. Cao, B. Gopaluni, and Y. Cao. "Long Short-Term Memory Network with Transfer Learning for Lithium-ion Battery Capacity Fade and Cycle Life Prediction". In: *Applied Energy* 350 (2023), p. 121660. DOI: 10.1016/j.apenergy.2023.121660.

[140] Z. Deng, X. Lin, J. Cai, and X. Hu. "Battery health estimation with degradation pattern recognition and transfer learning". In: *Journal of Power Sources* 525 (2022), p. 231027. DOI: 10.1016/j.jpowsour.2022.231027.

[141] K. Liu, Q. Peng, Y. Che, Y. Zheng, K. Li, R. Teodorescu, D. Widanage, and A. Barai. "Transfer learning for battery smarter state estimation and ageing prognostics: Recent progress, challenges, and prospects". In: *Advances in Applied Energy* 9 (2023), p. 100117. DOI: 10.1016/j.adapen.2022.100117.

[142] H. Liu, Z. Deng, Y. Che, Le Xu, B. Wang, Z. Wang, Y. Xie, and X. Hu. "Big field data-driven battery pack health estimation for electric vehicles: A deep-fusion transfer learning approach". In: *Mechanical Systems and Signal Processing* 218 (2024), p. 111585. DOI: 10.1016/j.ymssp.2024.111585.

[143] G. Qi, G. Du, and K. Wang. "Progress in estimating the state of health using transfer learning-based electrochemical impedance spectroscopy of lithium-ion batteries". In: *Ionics* 31.3 (2025), pp. 2337–2349. DOI: 10.1007/s11581-025-06065-y.

[144] Q. Xing, M. Zhang, Y. Fu, and K. Wang. "Transfer learning to estimate lithium-ion battery state of health with electrochemical impedance spectroscopy". In: *Journal of Energy Storage* 110 (2025), p. 115345. DOI: 10.1016/j.est.2025.115345.

[145] Y. Yang, Y. Xu, Y. Nie, J. Li, S. Liu, L. Zhao, Q. Yu, and C. Zhang. "Deep transfer learning enables battery state of charge and state of health estimation". In: *Energy* 294 (2024), p. 130779. DOI: 10.1016/j.energy.2024.130779.

[146] J. Zhao and Z. Wang. "Specialized convolutional transformer networks for estimating battery health via transfer learning". In: *Energy Storage Materials* 71 (2024), p. 103668. DOI: 10.1016/j.ensm.2024.103668.

[147] M. Aykol et al. "Perspective–Combining Physics and Machine Learning to Predict Battery Lifetime". In: *Journal of The Electrochemical Society* 168.3 (2021), p. 030525. DOI: 10.1149/1945-7111/abec55.

[148] S. Kohtz, Y. Xu, Z. Zheng, and P. Wang. "Physics-informed machine learning model for battery state of health prognostics using partial charging segments". In: *Mechanical Systems and Signal Processing* 172 (2022), p. 109002. DOI: 10.1016/j.ymssp.2022.109002.

[149] T. Hofmann, J. Hamar, M. Rogge, C. Zoerr, S. Erhard, and J. P. Schmidt. "Physics-Informed Neural Networks for State of Health Estimation in Lithium-Ion Batteries". In: *Journal of The Electrochemical Society* 170.9 (2023), p. 090524. DOI: 10.1149/1945-7111/acf0ef.

[150] J. Ye, Q. Xie, M. Lin, and J. Wu. "A method for estimating the state of health of lithium-ion batteries based on physics-informed neural network". In: *Energy* 294 (2024), p. 130828. DOI: 10.1016/j.energy.2024.130828.

[151] L. Yang, M. He, Y. Ren, B. Gao, and H. Qi. "Physics-informed neural network for co-estimation of state of health, remaining useful life, and short-term degradation path in Lithium-ion batteries". In: *Applied Energy* 398 (2025), p. 126427. DOI: 10.1016/j.apenergy.2025.126427.

[152] L. Chen, C. Chang, X. Liu, J. Jiang, Y. Jiang, and A. Tian. "Physics-informed neural networks for small sample state of health estimation of lithium-ion batteries". In: *Journal of Energy Storage* 122 (2025), p. 116559. DOI: 10.1016/j.est.2025.116559.

[153] Y. Deng, C. Du, and Z. Ren. "A Novel Method for Estimating the State of Health of Lithium-Ion Batteries Based on Physics-Informed Neural Network". In: *Batteries* 11.2 (2025). DOI: 10.3390/batteries11020049.

[154] L. E, J. Wang, Y. Sun, W. Shen, and R. Xiong. "Physics-Informed Hybrid Neural Architecture for Coupled Degradation Modeling and Remaining Useful Life Prediction of LiFePO4 Batteries". In: *Journal of The Electrochemical Society* 172.6 (2025), p. 060505. DOI: 10.1149/1945-7111/addd4e.

[155] Y. Luo, S. Ju, P. Li, and H. Zhang. "A method for estimating lithium-ion battery state of health based on physics-informed hybrid neural network". In: *Electrochimica Acta* 525 (2025), p. 146110. DOI: 10.1016/j.electacta.2025.146110.

[156] F. J. Méndez-Corbacho, B. Larrarte-Lizarralde, R. Parra, J. Larrain, D. Del Olmo, H.-J. Grande, and E. Ayerbe. "Physics-Informed Neural Networks for Modeling Li-ion Batteries: Solving the Single Particle Model Without Labeled Data". In: *Journal of The Electrochemical Society* 171.11 (2024), p. 110534. DOI: 10.1149/1945-7111/ad940a.

[157] S. Singh, Y. E. Ebongue, S. Rezaei, and K. P. Birke. "Hybrid Modeling of Lithium-Ion Battery: Physics-Informed Neural Network for Battery State Estimation". In: *Batteries* 9.6 (2023). DOI: 10.3390/batteries9060301.

[158] G. Sun, Y. Liu, and X. Liu. "A method for estimating lithium-ion battery state of health based on physics-informed machine learning". In: *Journal of Power Sources* 627 (2025), p. 235767. DOI: 10.1016/j.jpowsour.2024.235767.

[159] F. Wang, Z. Zhai, Z. Zhao, Y. Di, and X. Chen. "Physics-informed neural network for lithium-ion battery degradation stable modeling and prognosis". In: *Nature Communications* 15.1 (2024), p. 4332. DOI: 10.1038/s41467-024-48779-z.

[160] L. Wang, T. Yang, and B. Hu. "A Battery State-of-Health Estimation Method for Real-World Electric Vehicles Based on Physics-Informed Neural Networks". In: *IEEE Sensors Journal* 25.9 (2025), pp. 15577–15587. DOI: 10.1109/JSEN.2025.3549486.

[161] R. Xiong, Y. He, Y. Sun, Y. Jia, and W. Shen. "Enhanced electrode-level diagnostics for lithium-ion battery degradation using physics-informed neural networks". In: *Journal of Energy Chemistry* 104 (2025), pp. 618–627. DOI: 10.1016/j.jechem.2025.01.019.

[162] A. Thelen, Y. H. Lui, S. Shen, S. Laflamme, S. Hu, H. Ye, and C. Hu. "Integrating physics-based modeling and machine learning for degradation diagnostics of lithium-ion batteries". In: *Energy Storage Materials* 50 (2022), pp. 668–695. DOI: 10.1016/j.ensm.2022.05.047.

[163] S. Navidi, A. Thelen, T. Li, and C. Hu. "Physics-informed machine learning for battery degradation diagnostics: A comparison of state-of-the-art methods". In: *Energy Storage Materials* 68 (2024), p. 103343. DOI: 10.1016/j.ensm.2024.103343.

[164] P. J. Weddle et al. "Battery state-of-health diagnostics during fast cycling using physics-informed deep-learning". In: *Journal of Power Sources* 585 (2023), p. 233582. DOI: 10.1016/j.jpowsour.2023.233582.

[165] C. Lin, X. Tuo, L. Wu, G. Zhang, Z. Lyu, and X. Zeng. "Physics-informed machine learning for accurate SOH estimation of lithium-ion batteries considering various temperatures and operating conditions". In: *Energy* 318 (2025), p. 134937. DOI: 10.1016/j.energy.2025.134937.

[166] S. Friedrich, F. Dengler, M. Bock, M. Stuckenberger, and A. Jossen. "Degradation Mode Analysis for Lithium-Ion Cells with Silicon-Dominant Anodes Using Reference Electrodes". In: *Journal of The Electrochemical Society* (2025). DOI: 10.1149/1945-7111/add4a0.

[167] J. Schmitt, M. Schindler, A. Oberbauer, and A. Jossen. "Determination of degradation modes of lithium-ion batteries considering aging-induced changes in the half-cell open-circuit potential curve of silicon-graphite". In: *Journal of Power Sources* 532 (2022), p. 231296. DOI: 10.1016/j.jpowsour.2022.231296.

[168] T. Insinna, E. N. Bassey, K. Märker, A. Collauto, A.-L. Barra, and C. P. Grey. "Graphite Anodes for Li-Ion Batteries: An Electron Paramagnetic Resonance Investigation". In: *Chemistry of Materials* 35.14 (2023), pp. 5497–5511. DOI: 10.1021/acs.chemmater.3c00860.

[169] P. Keil, S. F. Schuster, J. Wilhelm, J. Travi, A. Hauser, R. C. Karl, and A. Jossen. "Calendar Aging of Lithium-Ion Batteries". In: *Journal of The Electrochemical Society* 163.9 (2016), A1872. DOI: 10.1149/2.0411609jes.

[170] P. Keil and A. Jossen. "Calendar Aging of NCA Lithium-Ion Batteries Investigated by Differential Voltage Analysis and Coulomb Tracking". In: *Journal of The Electrochemical Society* 164.1 (2017), A6066. DOI: 10.1149/2.0091701jes.

[171] J. Zhu et al. "Investigation of lithium-ion battery degradation mechanisms by combining differential voltage analysis and alternating current impedance". In: *Journal of Power Sources* 448 (2020), p. 227575. DOI: 10.1016/j.jpowsour.2019.227575.

[172] M. Berecibar, M. Garmendia, I. Gandiaga, J. Crego, and I. Villarreal. "State of health estimation algorithm of LiFePO4 battery packs based on differential voltage curves for battery management system application". In: *Energy* 103 (2016), pp. 784–796. DOI: 10.1016/j.energy.2016.02.163.

[173] J. C. Hamar, M. Stuckenberger, J. Sturm, J. Schmitt, M. Rogge, S. V. Erhard, and A. Jossen. "Investigating the Path Dependent Aging Behavior of Nickel Cobalt Aluminum Oxide Cathode Batteries During High C-rate Cycling Conditions". In: *Journal of The Electrochemical Society* 171.2 (2024), p. 020555. DOI: 10.1149/1945-7111/ad2952.

[174] P. Bilfinger, P. Rosner, M. Schreiber, T. Kröger, K. A. Gamra, M. Ank, N. Wassiliadis, B. Dietermann, and M. Lienkamp. "Battery pack diagnostics for electric vehicles: Transfer of differential voltage and incremental capacity analysis from cell to vehicle level". In: *eTransportation* 22 (2024), p. 100356. DOI: 10.1016/j.etran.2024.100356.

[175] J. R. Dahn. "Phase diagram of LixC6". In: *Physical Review B* 44.17 (1991), pp. 9170–9177. DOI: 10.1103/PhysRevB.44.9170.

[176] D. Allart, M. Montaru, and H. Gualous. "Model of Lithium Intercalation into Graphite by Potentiometric Analysis with Equilibrium and Entropy Change Curves of Graphite Electrode". In: *Journal of The Electrochemical Society* 165.2 (2018), A380. DOI: 10.1149/2.1251802jes.

[177] D. M. Bernardi and J.-Y. Go. "Analysis of pulse and relaxation behavior in lithium-ion batteries". In: *Journal of Power Sources* 196.1 (2011), pp. 412–427. DOI: 10.1016/j.jpowsour.2010.06.107.

[178] I. Bloom, A. N. Jansen, D. P. Abraham, J. Knuth, S. A. Jones, V. S. Battaglia, and G. L. Henriksen. "Differential voltage analyses of high-power, lithium-ion cells: 1. Technique and application". In: *Journal of Power Sources* 139.1 (2005), pp. 295–303. DOI: 10.1016/j.jpowsour.2004.07.021.

[179] C. Xu, P. J. Reeves, Q. Jacquet, and C. P. Grey. "Phase Behavior during Electrochemical Cycling of Ni-Rich Cathode Materials for Li-Ion Batteries". In: *Advanced Energy Materials* 11.7 (2021), p. 2003404. DOI: 10.1002/aenm.202003404.

[180] X. Chen et al. "State of health (SoH) estimation and degradation modes analysis of pouch NMC532/graphite Li-ion battery". In: *Journal of Power Sources* 498 (2021), p. 229884. DOI: 10.1016/j.jpowsour.2021.229884.

[181] C. Weng, X. Feng, J. Sun, and H. Peng. "State-of-health monitoring of lithium-ion battery modules and packs via incremental capacity peak tracking". In: *Applied Energy* 180 (2016), pp. 360–368. DOI: 10.1016/j.apenergy.2016.07.126.

[182] D. Anseán, V. M. García, M. González, C. Blanco-Viejo, J. C. Viera, Y. F. Pulido, and L. Sánchez. "Lithium-Ion Battery Degradation Indicators Via Incremental Capacity Analysis". In: *IEEE Transactions on Industry Applications* 55.3 (2019), pp. 2992–3002. DOI: 10.1109/TIA.2019.2891213.

[183] D. P. Bertsekas. *Nonlinear Programming*. Athena scientific optimization and computation series. Athena Scientific, 1999. URL: https://books.google.de/books?id=TgMpAQAAMAAJ.

[184] J. Nocedal and S. J. Wright, eds. *Numerical Optimization*. New York, NY: Springer New York, 2006. URL: https://link.springer.com/book/10.1007/978-0-387-40065-5.

[185] X. Xu, Z. Xu, T. Wang, J. Xu, and L. Pei. "Open-circuit voltage curve reconstruction for degrading lithium-ion batteries utilizing discrete curve fragments from an online dataset". In: *Journal of Energy Storage* 56 (2022), p. 106003. DOI: 10.1016/j.est.2022.106003.

[186] A. Kunz, C. Kirst, A. Durdel, J. P. Singer, and A. Jossen. "Assessing degradation modes in cylindrical lithium-ion batteries: A non-invasive method using the entropic heat flow or surface temperature". In: *Journal of Power Sources* 627 (2025), p. 235732. DOI: 10.1016/j.jpowsour.2024.235732.

[187] A. Géron. *Hands-on machine learning with Scikit-Learn, Keras, and TensorFlow*. O'Reilly Media, Inc, 2019. URL: https://www.oreilly.com/library/view/hands-on-machine-learning/9781492032632/.

[188] C. C. Aggarwal, ed. *Neural Networks and Deep Learning: A Textbook*. Cham: Springer International Publishing, 2023. DOI: 10.1007/978-3-031-29642-0.

[189] A. Burkov. *The hundred-page machine learning book*. Quebec, Canada: Andriy Burkov, 2019. URL: https://themlbook.com/.

[190] M. Abadi et al. *TensorFlow: Large-Scale Machine Learning on Heterogeneous Systems*. 2015. URL: https://www.tensorflow.org/.

[191] F. Pedregosa et al. "Scikit-learn: Machine Learning in Python". In: *Journal of Machine Learning Research* 12 (2011), pp. 2825–2830. URL: https://jmlr.org/papers/volume12/pedregosa11a/pedregosa11a.pdf.

[192] A. Paszke et al. "PyTorch: An Imperative Style, High-Performance Deep Learning Library". In: *Advances in Neural Information Processing Systems 32*. Curran Associates, Inc, 2019, pp. 8024–8035. URL: http://papers.neurips.cc/paper/9015-pytorch-an-imperative-style-high-performance-deep-learning-library.pdf.

[193] S. Bai, J. Z. Kolter, and V. Koltun. "An Empirical Evaluation of Generic Convolutional and Recurrent Networks for Sequence Modeling". In: *CoRR* abs/1803.01271 (2018). DOI: 10.48550/arXiv.1803.01271.

[194] S. Hochreiter and J. Schmidhuber. "Long Short-Term Memory". In: *Neural Computation* 9.8 (1997), pp. 1735–1780. DOI: 10.1162/neco.1997.9.8.1735.

[195] B. Bole, C. S. Kulkarni, and M. Daigle. *Randomized Battery Usage Dataset*. Ed. by NASA. URL: https://data.nasa.gov/dataset?q=randomized+battery+usage&sort=score+desc%2C+metadata_modified+desc.

[196] C. Birkl. *Oxford Battery Degradation Dataset 1*. Ed. by University of Oxford. 2017. URL: https://ora.ox.ac.uk/objects/uuid:03ba4b01-cfed-46d3-9b1a-7d4a7bdf6fac.

[197] A. H. Victoria and G. Maragatham. "Automatic tuning of hyperparameters using Bayesian optimization". In: *Evolving Systems* 12.1 (2021), pp. 217–223. DOI: 10.1007/s12530-020-09345-2.

[198] P. Eleftheriadis, S. Giazitzis, J. Kowal, S. Leva, and E. Ogliari. "Joint State of Charge and State of Health Estimation Using Bidirectional LSTM and Bayesian Hyperparameter Optimization". In: *IEEE Access* 12 (2024), pp. 80244–80254. DOI: 10.1109/ACCESS.2024.3410675.

[199] D. Kong, S. Wang, and P. Ping. "State-of-health estimation and remaining useful life for lithium-ion battery based on deep learning with Bayesian hyperparameter optimization". In: *International Journal of Energy Research* 46.5 (2022), pp. 6081–6098. DOI: 10.1002/er.7548.

[200] P. Li, Z. Zhang, R. Grosu, Z. Deng, J. Hou, Y. Rong, and R. Wu. "An end-to-end neural network framework for state-of-health estimation and remaining useful life prediction of electric vehicle lithium batteries". In: *Renewable and Sustainable Energy Reviews* 156 (2022), p. 111843. DOI: 10.1016/j.rser.2021.111843.

[201] Y. Mazzi, H. Ben Sassi, and F. Errahimi. "Lithium-ion battery state of health estimation using a hybrid model based on a convolutional neural network and bidirectional gated recurrent unit". In: *Engineering Applications of Artificial Intelligence* 127 (2024), p. 107199. DOI: 10.1016/j.engappai.2023.107199.

[202] R. Simard and P. L'Ecuyer. "Computing the Two-Sided Kolmogorov-Smirnov Distribution". In: *Journal of Statistical Software* 39.11 (2011), pp. 1–18. DOI: 10.18637/jss.v039.i11.

[203] D. P. Kingma and J. Ba. "Adam: A Method for Stochastic Optimization". In: *arXiv* 1412.6980 (2017). DOI: 10.48550/arXiv.1412.6980.

[204] C. Tan, F. Sun, T. Kong, W. Zhang, C. Yang, and C. Liu. "A Survey on Deep Transfer Learning". In: *Artificial Neural Networks and Machine Learning - ICANN 2018*. Ed. by V. Kůrková, Y. Manolopoulos, B. Hammer, L. Iliadis, and I. Maglogiannis. Cham: Springer International Publishing, 2018, pp. 270–279. DOI: 10.48550/arXiv.1808.01974.

[205] M. Weber, M. Auch, C. Doblander, P. Mandl, and H.-A. Jacobsen. "Transfer Learning With Time Series Data: A Systematic Mapping Study". In: *IEEE Access* 9 (2021), pp. 165409–165432. DOI: 10.1109/ACCESS.2021.3134628.

[206] Y. Liu, J. Li, G. Zhang, B. Hua, and N. Xiong. "State of Charge Estimation of Lithium-Ion Batteries Based on Temporal Convolutional Network and Transfer Learning". In: *IEEE Access* 9 (2021), pp. 34177–34187. DOI: 10.1109/ACCESS.2021.3057371.

[207] M. Raissi, P. Perdikaris, and G. E. Karniadakis. "Physics Informed Deep Learning (Part I): Data-driven Solutions of Nonlinear Partial Differential Equations". In: *CoRR* abs/1711.10561 (2017). DOI: 10.48550/arXiv.1711.10561.

[208] M. Raissi and G. E. Karniadakis. "Hidden physics models: Machine learning of nonlinear partial differential equations". In: *Journal of Computational Physics* 357 (2018), pp. 125–141. DOI: 10.1016/j.jcp.2017.11.039.

[209] S. Barik and B. Saravanan. "Recent developments and challenges in state-of-charge estimation techniques for electric vehicle batteries: A review". In: *Journal of Energy Storage* 100 (2024), p. 113623. DOI: 10.1016/j.est.2024.113623.

[210] Y. Liang, S. Wang, Y. Fan, X. Hao, D. Liu, and C. Fernandez. "State of Health Prediction of Lithium-Ion Batteries Using Combined Machine Learning Model Based on Nonlinear Constraint Optimization". In: *Journal of The Electrochemical Society* 171.1 (2024), p. 010508. DOI: 10.1149/1945-7111/ad18e1.

[211] W. Xu et al. "Investigation of lithium-ion battery degradation by corrected differential voltage analysis based on reference electrode". In: *Applied Energy* 389 (2025), p. 125735. DOI: 10.1016/j.apenergy.2025.125735.

[212] J. R. Belt, D. M. Bernardi, and V. Utgikar. "Development and Use of a Lithium-Metal Reference Electrode in Aging Studies of Lithium-Ion Batteries". In: *Journal of The Electrochemical Society* 161.6 (2014), A1116. DOI: 10.1149/2.062406jes.

[213] S. Friedrich, M. Bock, and A. Jossen. "Cycling Aging in Different State of Charge Windows in Lithium-Ion Batteries with Silicon-Dominant Anodes". In: *Journal of The Electrochemical Society* 171.10 (2024), p. 100503. DOI: 10.1149/1945-7111/ad71f8.

[214] A. Bessman, R. Soares, O. Wallmark, P. Svens, and G. Lindbergh. "Aging effects of AC harmonics on lithium-ion cells". In: *Journal of Energy Storage* 21 (2019), pp. 741–749. DOI: 10.1016/j.est.2018.12.016.

[215] E. Catenaro and S. Onori. "Experimental data of lithium-ion batteries under galvanostatic discharge tests at different rates and temperatures of operation". In: *Data in Brief* 35 (2021), p. 106894. DOI: 10.1016/j.dib.2021.106894.

[216] X. Cui et al. "Data-driven analysis of battery formation reveals the role of electrode utilization in extending cycle life". In: *Joule* 8.11 (2024), pp. 3072–3087. DOI: 10.1016/j.joule.2024.07.024.

[217] G. Pozzato, A. Allam, and S. Onori. "Lithium-ion battery aging dataset based on electric vehicle real-driving profiles". In: *Data in Brief* 41 (2022), p. 107995. DOI: 10.1016/j.dib.2022.107995.

[218] A. Geslin, Le Xu, D. Ganapathi, K. Moy, W. C. Chueh, and S. Onori. "Dynamic cycling enhances battery lifetime". In: *Nature Energy* 10.2 (2025), pp. 172–180. DOI: 10.1038/s41560-024-01675-8.

[219] E. Goldammer, M. Gentejohann, M. Schlüter, D. Weber, W. Wondrak, S. Dieckerhoff, C. Gühmann, and J. Kowal. "The Impact of an Overlaid Ripple Current on Battery Aging: The Development of the SiCWell Dataset". In: *Batteries* 8.2 (2022). DOI: 10.3390/batteries8020011.

[220] V. N. Lam, X. Cui, F. Stroebl, M. Uppaluri, S. Onori, and W. C. Chueh. "A decade of insights: Delving into calendar aging trends and implications". In: *Joule* 9.1 (2025). DOI: 10.1016/j.joule.2024.11.013.

[221] R. Li, N. D. Kirkaldy, F. F. Oehler, M. Marinescu, G. J. Offer, and S. E. J. O'Kane. "The importance of degradation mode analysis in parameterising lifetime prediction models of lithium-ion battery degradation". In: *Nature Communications* 16.1 (2025), p. 2776. DOI: 10.1038/s41467-025-57968-3.

[222] W. Li, N. Sengupta, P. Dechent, D. Howey, A. Annaswamy, and D. U. Sauer. "One-shot battery degradation trajectory prediction with deep learning". In: *Journal of Power Sources* 506 (2021), p. 230024. DOI: 10.1016/j.jpowsour.2021.230024.

[223] W. Li, H. Zhang, B. van Vlijmen, P. Dechent, and D. U. Sauer. "Forecasting battery capacity and power degradation with multi-task learning". In: *Energy Storage Materials* 53 (2022), pp. 453–466. DOI: 10.1016/j.ensm.2022.09.013.

[224] M. Luh and T. Blank. "Comprehensive battery aging dataset: capacity and impedance fade measurements of a lithium-ion NMC/C-SiO cell". In: *Scientific Data* 11.1 (2024), p. 1004. DOI: 10.1038/s41597-024-03831-x.

[225] P. Mohtat, S. Lee, J. B. Siegel, and A. G. Stefanopoulou. "Reversible and Irreversible Expansion of Lithium-Ion Batteries Under a Wide Range of Stress Factors". In: *Journal of The Electrochemical Society* 168.10 (2021), p. 100520. DOI: 10.1149/1945-7111/ac2d3e.

[226] T. Raj, A. A. Wang, C. W. Monroe, and D. A. Howey. "Investigation of Path-Dependent Degradation in Lithium-Ion Batteries". In: *Batteries & Supercaps* 3.12 (2020), pp. 1377–1385. DOI: 10.1002/batt.202000160.

[227] F. Stroebl, R. Petersohn, B. Schricker, F. Schaeufl, O. Bohlen, and H. Palm. "A multi-stage lithium-ion battery aging dataset using various experimental design methodologies". In: *Scientific Data* 11.1 (2024), p. 1020. DOI: 10.1038/s41597-024-03859-z.

[228] B. van Vlijmen et al. "Interpretable data-driven modeling reveals complexity of battery aging". In: *ChemRxiv* (2023). DOI: 10.26434/chemrxiv-2023-zdl2n-v2.

[229] B. Bole, C. S. Kulkarni, and M. Daigle. "Adaptation of an Electrochemistry-based Li-Ion Battery Model to Account for Deterioration Observed Under Randomized Use". In: *Annual Conference of the PHM Society* 6 (2014), p. 1. DOI: 10.36001/phmconf.2014.v6i1.2490.

[230] C. Birkl. "Diagnosis and prognosis of degradation in lithium-ion batteries". PhD Thesis. University of Oxford, 2017. URL: https://ora.ox.ac.uk/objects/uuid:7d8ccb9c-1469-4209-9995-5871fc908b54.

[231] D. U. Sauer. *Time-series cyclic aging data on 48 commercial NMC/graphite Sanyo/Panasonic UR18650E cylindrical cells*. 2021. DOI: 10.18154/RWTH-2021-04545.

List of Figures

1.1 Current overview over the global EV market situation, with (a) the absolute BEV market share in 2024, (b) the BEV sales share in the same year, and (c) the development of the EV stock (including PHEVs and REEVs) for selected countries. Data for the maps in Subfigure (a) and (b) is taken from IEA [1]. A list of the included countries in the world map can be found online [1]. Data for the EV stock development (c) is taken from ZSW [2]. 1

1.2 Schematic illustration of the components and basic operating principle of a LiB. 4

1.3 Schematic illustration of the OCV and its underlying OCPs, including the de-/lithiation direction (adopted from [22]). 7

1.4 Pulse analysis for a NCA-graphite battery during a 1C pulse for 10 seconds at 50 % SOC including the schematic division of the overpotentials. An additional inlet shows the deviation of the measured voltage signal and the OCV 1 h after the applied pulse. 10

1.5 Relationship between the causes, degradation mechanisms, DMs, and effects of battery degradation, based on [43–45]. The color solely aims to guide the reader. 13

1.6 Schematic illustration of the degradation mechanisms occurring within a LiB, based on Birkl et al. [43]. 14

1.7 Relation of OCV changes, alignment parameter change, and underlying DMs for a NCA-graphite battery. (a) Initial cell balancing and resulting OCV including the alignment parameter set α_{NE}, α_{PE}, β_{NE}, and β_{PE}; (b) Resulting OCV after $\mathrm{LAM}_{\mathrm{NE}}$; (c) Resulting OCV after $\mathrm{LAM}_{\mathrm{PE}}$; and (d) Resulting OCV after LLI (Figure inspired by Birkl et al. [43]). 16

1.8 Overview of common SOH estimation models and their relation to cause, mechanisms, modes, and effects of battery degradation. (Figure inspired by Schmitt [58] and Karger [59]). 20

1.9 Schematic overview of a LiB and its modeling in the P2D model with its respective dimensions through the cell layers x and the pseudo dimension r within the particle radius. Figure adapted from Jokar et al. [79]. 23

1.10 Schematic visualization of the location of battery SOH estimation within the AI landscape in orange. The dashed, blue circles offer a more detailed perspective, where the methods solve regression problems with supervised learning approaches [9; 101]. 26
1.11 Different approaches for the cost function of the OCV model including the shifted and scaled OCPs, the reconstructed OCV, and the measured signal for an initial alignment parameter set of $[1.05, 1.1, -0.07, -0.18]$ for α_{NE}, α_{PE}, β_{NE}, β_{PE}, respectively. Subfigure (a) shows the voltage, (b) the differential voltage, and (c) the incremental capacity. 30
1.12 Illustration of the relation between the (a) OCV, (b) the ICA, and (c) the DVA for a NCA-graphite battery. The location of the phase transitions in the DVA (c) is related to the phase equilibria in the ICA (b). The length between these peaks/valleys can be used for peak-tracking, i.e., DM estimation. Figure is adapted from Karger et al. [59]. Subfigure (d) additionally illustrates the phase transitions of graphite during lithiation and the respective potential vs. $\mathrm{Li/Li^+}$ (Figure adapted from Insinna et al. [168]). 32
1.13 Illustration of potential input data for the OCV model derived from the mechanistic modeling approach. With higher C-rates of the voltage charging curve (a), the features in the ICA (b), and DVA (c) vanish. The complexity of the optimization process increases with higher C-rate values and narrower available charging windows. The displayed charging curves correspond to a pristine NCA-graphite battery. 36
1.14 (a) Representation of a neural network with two layers and one output, including the individual weights w and biases b. Figure adapted from Burkov [189] and Hamar et al. [9]. (b) Overview of the three most common activation functions. 39
1.15 Illustration of a neural network with two different layer architectures: (a) LSTM memory cell, adapted from Goodfellow et al. [122]. (b) Dilated causal convolution for a kernel size of 2 and dilation factors d within (c) a TCN residual block, which is interconnected with dropout and ReLU layers. Figure adapted from Bai et al. [193] and Bockrath et al. [120] 42

1.16 The problem of data scarcity and two possible solution approaches. (a) The model-based transfer learning approach solves the problem by pretraining a blank model on extensive data from other datasets $\mathcal{D}_{\text{Source}}$ prior and transferring the knowledge to another domain $\mathcal{D}_{\text{Target}}$. (b) The sequential PINN approach [147] accumulates more training data $\mathcal{D}_{\text{Source}}$ by running physics-based simulations with unlabeled data $\mathcal{D}_{\text{Source,PB}}$ prior. 47
1.17 The outline of this thesis indicating the used methods within the publication by the color shade. 54

2.1 The trimmed outline of the thesis structure with focus on this chapter. 55
2.2 The trimmed outline of the thesis structure with focus on this chapter. 73
2.3 The trimmed outline of the thesis structure with focus on this chapter. 100
2.4 The trimmed outline of the thesis structure with focus on this chapter. 121
2.5 The trimmed outline of the thesis structure with focus on this chapter. 143

3.1 The ΔQ-method applied on relaxed voltage points, gathered from the HPPC of the dataset introduced in Section 2.3. The true labels are generated from the measured electrode potentials, which are fitted based on the algorithm described in Section 2.3, and are compared to the estimated LAM_{NE} (a), LAM_{PE} (b) and LLI (c). 170
3.2 Relaxed voltage points and ΔQ-pairs, gathered from the HPPC of the dataset introduced in Section 2.3, in comparison to the measured OCV, OCPs (a), and DVA (b) from a pristine LiB. 171
3.3 Comparison of the proposed publications and their investigated system level and included features. 178

List of Tables

1.1 Comparison of the key properties of common cathode materials for LiBs [10; 12–14]. 5

3.1 Comparison of literature findings on the application of the mechanistic modeling approach to (partial) charging voltage curves with the novel ΔQ-method. 172